ON THE FLUTTER RESPONSE OF TWO-DEGREE-OF-FREEDOM FLAT PLATES FOR ENERGY HARVESTING APPLICATIONS

Dissertation

submitted to and approved by the

Department of Architecture, Civil Engineering and Environmental Sciences
University of Braunschweig – Institute of Technology

and the

Department of Civil and Environmental Engineering
University of Florence

in candidacy for the degree of a
Doktor-Ingenieur (Dr.-Ing.) /
Dottore di Ricerca in Civil and Environmental Engineering[*)]

by
Luca Pigolotti
born 09/09/1987
in Città di Castello, Italy

Submitted on	29/08/2016
Oral examination on	10/11/2016
Professorial advisors	Prof. Gianni Bartoli
	Prof. Klaus Thiele

2017

*) Either the German or the Italian form of the title may be used.

The dissertation is published in an electronic form by the Braunschweig University library at the address:

https://publikationsserver.tu-braunschweig.de/content/index.xml

Abstract

Among fluid-structure interaction phenomena, classical flutter is a dynamic instability that can occur in two-degree-of-freedom slender bodies with streamlined cross section, usually oscillating in the cross-flow (heaving) and rotational (pitching) components. The excitation mechanism relies on the strong energy exchange between modes and respective fluid-dynamic reactions that destabilises one of the modes at a certain critical flow speed, which then drives the system response toward large motion amplitudes. For energy harvesting applications, those flow-induced vibrations can be exploited to generate usable power by coupling the oscillating mechanical system with a specific conversion apparatus. In the case of flutter-based generators, a portion of the kinetic power related to the heaving motion component can be converted into *e.g.* electricity through electromagnetic transducers.

The capability of performing large-amplitude, self-sustained motion is a fundamental requirement for any flutter-based generators. However, the post-critical regime of classical flutter is not-well understood yet and its scientific study can significantly improve the design of such solutions. The main challenge is to understand how to design more unstable configurations, anticipating the instability threshold and enlarging the motion amplitudes.

A systematic literature review about energy harvesting systems is first carried out, organising the widespread achievements. Then, this thesis work is devoted to improve the understanding of the critical and post-critical behaviour of fluttering systems that consider sets of governing parameters describing energy-harvesting configurations, with the purpose of developing as reliable as possible scientific investigations. Linear analyses are conducted to systematically explore the parametric space influencing the instability threshold. Therefore, extensive experimental campaigns are conducted in both the Stahlbau Institute and CRIACIV wind tunnels to focus on the post-critical response of flat-plate models with, respectively, 15:1 (width-to-depth) and 25:1 cross sections. The experiments required the development of specific aeroelastic setups to observe also the large-amplitude motion and of damping devices, being necessary to simulate the energy extraction from the mechanical system. Thus, the study of a specific conversion apparatus is outside the scope of this work.

The results show that stable limit-cycle oscillations can occur in the post-critical regime due to the nonlinearity of the fluid-dynamic loads mainly, showing amplitudes that usually increase with the flow speed. Furthermore, the system is also able to oscillate in a limited range of sub-critical flow speeds, if triggered by certain initial conditions or if the stable solutions is reached from larger limit-cycle amplitudes at higher flow speeds. The influences of still-air uncoupled frequency ratio, inertial parameters and eccentricity of both elastic axis and mass centre are investigated in terms of both critical and post-critical response, outlining design guidelines for flutter-based generators. In particular, lighters configurations are more unstable and small mass unbalance downstream of the elastic axis is able to foster the instability even in the presence of high damping levels. Moreover, the study of optimal configurations for energy-harvesting applications explains that a generator has to be designed with a stiffness centre placed in the upstream half-chord of the section, depending on the level of power production.

This thesis work has both scientific and technological expected impacts, since it supplies a systematic and large database of results on classical flutter and various information for the development of the flutter-based energy harvesting technology.

Keywords: Flutter Instability, Post-Critical Regime, Energy Harvesting, Wind Tunnel

Zusammenfassung

Unter die Fluid-Körper Interaktionen, zählt das klassische Flattern als eine dynamische Instabilität, die zwei Freiheitsgradsystemen mit linienförmigen Profil als Summe von Traslation und Drehung gefährdet kann. Der lineare Mechanismus entsteht durch den Energieaustausch zwischen Schwingungsmoden, der zum Fluid-Körper Reaktionen führen. Bei der kritischen Windgeschwindigkeit, kann ein Schwingungsmode zur Instabilität mit großen Schwingungsamplituden erregt werden. Diese induzierten Bewegungen kann als Energiequelle angewendet werden. Die kinetische Energie der translatorischen Bewegung des Körpers quer zu Windrichtung kann es mit Hilfe von elektromagnetischen Geräten in elektrische Energie umgewandelt werden.

Die Erzeugung von konstanten, stabilen, großen Amplituden ist eine entscheidende Voraussetzung für eine Flattern-basierte Energiequelle. Allerdings, dieser kritische Zustand ist bisher noch nicht in Tiefe untersucht worden. Die größte Herausforderung liegt an das Verständnis des kritischen Bereichs, der Schwingungsamplitude und der Vorhersagen der Instabilitätsanfang.

Eine intensive Literaturrecherche zur Energieerzeugung wurde durchgeführt. Ziel dieser Arbeit ist das Verständnis des kritischen und überkritischen Bereichs des Flatterns zu erweitern. Dadurch wurden Parametern untersucht, die Einfluss auf die Energieerzeugung führen, um eine zuverlässige Forschung anzubieten. Lineare Analysen wurden durchgeführt, um das parametrische Raum des Instabilitätsbereichs zu untersuchen. An der TU Braunschweig und CRIACIV in Florenz wurden Windkanalversuche an Platenmodellen (Verhältnisse Breite zu Tiefe von 15:1 und 25:1) durchgeführt. Dabei wurden die aeroelastischen Eigenschaften mit unterschiedlichen Aufbaukombinationen variiert. Dämpfungsgrade wurden auch als Parameter zur Simulierung der Energieerzeugung betrachtet. Dementsprechend ist das Design einer mechanischen Vorrichtung in dieser Arbeit nicht betrachtet worden.

Die Ergebnisse zeigen, dass im transkritischen Bereich stabile Schwingungen zu beobachten sind. Grund dafür ist hauptsächlich die Nichtlinearität der Kräfte, die zu zunehmender Amplituden mit zunehmender Windgeschwindigkeit führen kann. Darüber hinaus kann das System auch im unterkritischen Bereich schwingen mit Hilfe einer Anfangsstörung oder nach der Erregung im kritischen Bereich. Der Einfluss der z.B. Trägheitsparameter und der Exzentrizität der elastischen Achse und Schwerkraftpunkt auf den kritischen und transkritischen Bereich wurde auch untersucht. Dadurch wurde bestätigt, wie für Kombinationen der genannten Parametern, die Schwingungen gefördert werden können trotz eines hohen Dämpfungsgrades. Die Studie der optimalen Energieerzeugung hat gezeigt, dass ein Generator mit dem Steifigkeitspunkt stromaufwärts der Sehne des Querschnitts als ideale Lösung gilt.

Diese Arbeit kombiniert wissenschaftliche und technologische Aspekte, die zu einem Zusammenspiel des klassischen Flattern Phänomens mit der aktuellen Problematik der Energie Erzeugung führt.

Schlüsselwörter: klassisches Flattern, transkritischer Bereich, Energie, Windkanal

Table of contents

List of Figures

List of Tables

Chapter 1

Introduction

1.1 General topic overview

This research deals with flow-induced vibrations of structures that can be exploited to produce usable power through the installation of specific energy conversion apparatus. Hence, the topic essentially combines the scientific research on fluid-structure interaction (FSI) and the recent research on energy-harvesting systems (EHS).

FSI (see § 2.2) is a discipline that studies the modelling of the interaction mechanism between a structure and a fluid. In this thesis context, the fluid is flowing with a certain velocity and surrounds an elastic structure that can vibrate in it, thus FSI relates flow-induced effects on deformable structures. On the other hand, EHS (see § 2.3) is a research field that try to answer to the general question: *is it possible to extract usable energy from any kind of available energy source, whatever it is and in efficient ways?*. In this thesis context, EHS relates to the exploitation of the kinetic energy of the vibrating structures (see § 2.3.4).

Several fluid-elastic phenomena can arise when slender structures are prone to self-induced fluid-dynamic loads, which can also include important nonlinear effects (see § 2.2.2). In some cases, the ensuing limit cycles of oscillation (LCOs) exhibit limited amplitudes in a range of flow velocities, as in the case of vortex-induced vibrations, or increasing LCO amplitude with the flow velocity after a critical threshold, as in the case of galloping and flutter. Among the latter, the classical flutter excitation mechanism represents the topic of this thesis. From the scientific point of view (see § 3), it involves a complex interaction between two (at least) structural modes and the respective fluid-dynamic reactions that leads to a violent dynamic instability at the critical flow velocity.

For energy-harvesting applications, the development of flutter-based generators requires an ad-hoc design. Two-degree-of-freedom (2-DoF) systems oscillating in the rotational (or pitching) and cross-flow translational (or heaving) DoFs are considered in this work (see § 3). Definitely, the capability of performing self-sustained motion with large amplitudes in the post-critical field is a fundamental characteristics of generator based on flow-induced vibrations and the knowledge of the system response in the post-critical regime is of crucial importance. Nevertheless, few scientific research works are available on the post-critical regime of flutter, being still a not well-known topic.

The main aim of the thesis is to understand the influence of some of the governing parameters of the flutter problem on its critical and post-critical regime, in order to exploit the results to outline some design guidelines that can lead to efficient power generators. However, this research mainly focuses on a portion of the whole energy generation process, which is explained in Fig. 1.1: the capability of a particular structural system to capture the energy of the fluid flow and to transform it into mechanical energy. In particular, the issue of the following conversion of the mechanical energy into other forms, for example electricity, is postponed, since the energy conversion apparatus can be preliminary simulated through equivalent mechanical damping added to the system (see next § 1.2.2 and 2.3.4). Thus, a simplified approach is followed in this work to preliminarily estimate the energy-harvesting performances. Indeed, any use of energy by the user means energy extraction from the device

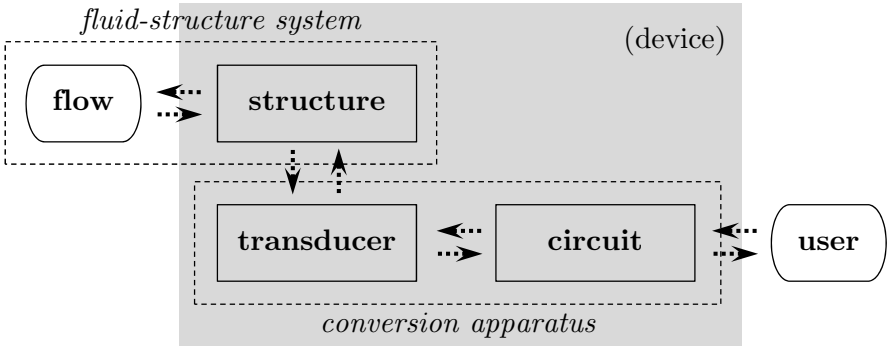

Figure 1.1. Logical process of energy generation from the fluid flow to the user through the fluid-structure-conversion apparatus interaction.

through the term proportional to the resistance of the electric circuit. Moreover, being the electric circuit coupled with the transducer, which in turn is coupled to the structure, it follows an additional damping in the mechanical system due to the negative work applied by the user. It is worth highlighting that this procedure is not well representing only the case of piezoelectric transducers, in which the feedback effect includes also a significant frequency modification. Hence, this thesis work considers a global performance factor (hereinafter identified by Γ) that describes the amount of energy potentially flowing in a next conversion apparatus.

The role of the damping in the fluid-structure interaction mechanism becomes important and it is crucial to understand how the system behaves, in terms of both critical and post-critical responses, when subjected to high damping levels. So far, this issue has not been studied sufficiently in the literature, since the damping influence can be neglected in common civil/aeronautical problems about flutter. Moreover, the achievement of performance enhancements requires the understanding of how to lower the critical flow speed, so that more unstable systems have to be conceived. Thus, the challenge is to study fluttering systems described by sets of governing parameters that have been never investigated so far, but which are proper of energy-harvesting configurations.

In this research, the experimental approach has been extensively implemented. While the critical condition can also be investigated through the more common analytical linear models (see § 3), which gives reliable results as supported by the extensive literature for civil/aeronautical engineering, the post-critical regime needs specific tools. Due to the large amplitude of oscillations in both degrees of freedom, important nonlinearities arise in the aerodynamic loads. Therefore, only semi-empirical numerical models are available, since the analytical formulation of the nonlinear self-excited loads is not available in closed-form. Thus, the problem can be faced by means of numerical or experimental approaches. Computational-fluid-dynamic (CFD) simulations require high performance computing and specific methods to take into account for the large amplitudes of the motion in both DoFs. On the other hand, wind-tunnel testing requires the development of aeroelastic setups to observe also the large-amplitude response, although requiring specific and complex design. Hence, wind-tunnel tests have been conducted in the facilities of Stahlbau Institut, in Braunschweig, Germany, and at CRIACIV laboratory, in Prato, Italy, (see § 5).

The experimental results carried out describe the system response for several configurations and outline some recurring dominant features of the post-critical paths (see § 7). This helps to understand how to get more unstable configurations playing on key parameters. Furthermore, according to the experimental results, the linear analytical model has been used as a parametric tool to investigate the instability threshold, looking for optimal configurations (see § 8). The results show that optimal configurations exist, and important performance enhancements can be achieved through a well-studied design of the system.

1.2 Energy transfer in generators based on flow-induced vibrations

1.2.1 Performance indicators

Observing Fig. 1.1, the energy transfer is the following:

1. the flow has its own energy;
2. the fluid-structure interaction mechanism governs the energy transfer between flow and mechanical system, that is the amount of energy captured by the device;
3. being the structure coupled with the transducer, there is an energy transfer from the mechanical system to the electrical circuit;
4. the design of the electric circuit governs the usable energy that can be stored or used and, in turns, produces the backward effect on the mechanical system;
5. the user network exploits the output energy from the device and definitely uses up the energy.

Hence, the energy transfer of a device based on flow-induced vibrations involves (i) the structural system, (ii) the transducer technology and (iii) the electric circuit at which the transducer is linked. Fig. 1.2 explains in more detail what showed in Fig. 1.1. During LCOs, the system response can be assumed harmonic and, considering the energies involved in a period of oscillation to obtain mean powers, several performance indicators can be identified:

- *Extraction factor*, ratio of the forcing power to the flow power

$$\Gamma' = \frac{P_F}{P_W} \ . \tag{1.1}$$

  It expresses the capability of the mechanical system to capture energy from the flow and it depends on the physical principle of the flow-induced mechanism, ruling the initial entry of energy in the device.

- *Conversion factor*, ratio of the electric power to the forcing power;

$$\Gamma'' = \frac{P_E}{P_F} = \frac{P_Q}{P_F} \cdot \frac{P_E}{P_Q} = \Gamma''_t \cdot \Gamma''_c \ . \tag{1.2}$$

  It expresses the capability of the conversion apparatus to convert the kinetic energy of the mechanical system into electricity and it depends on the characteristics of:

  - transducer, which converts movement/deformation into electric charge power P_Q (Γ''_t);
  - electric circuit, which transforms P_Q into electric power P_E (Γ''_c).

- *Operation factor*, ratio of the usable power to the electric power

$$\Gamma''' = \frac{P_U}{P_E} \ . \tag{1.3}$$

  It takes into account for the capability of the user network, at which the device is linked, to exploit the electric power provided.

Obviously, the global performance of the device is the product of all the previous factors:

$$\Gamma = \Gamma' \cdot \Gamma'' \cdot \Gamma''' \ . \tag{1.4}$$

Some comments have to be made about the extraction factor Γ'. The definition of Γ' (Eq. (1.1)) is not related to a thermodynamic efficiency but it is a simple and dimensionless indicator of performance. Moreover, when the flow power P_W considers the flow crossing the area A_{sw}, swept by the oscillating body (Fig. 1.3 shows an example with a 2-DoF system),

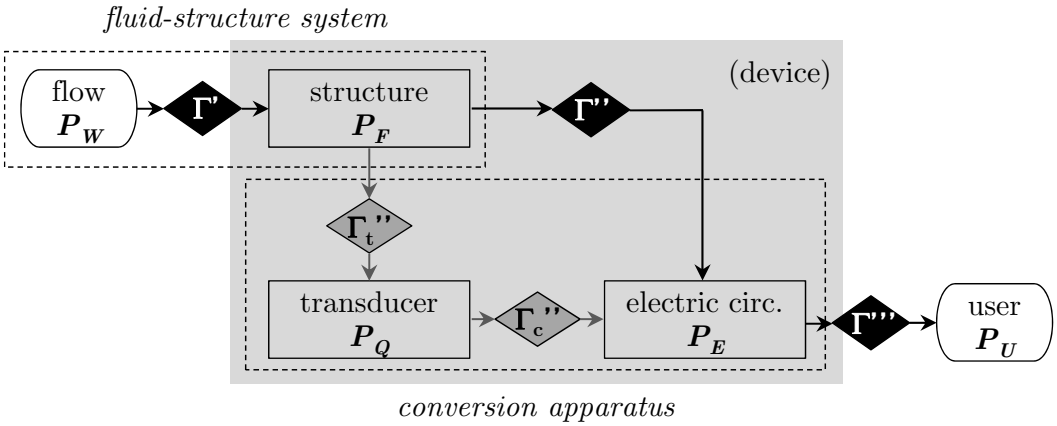

Figure 1.2. Energy-transfer diagram of a generator based on flow-induced vibrations.

Γ' can be related to the power coefficient of rotary wind turbines C_{PR} (this last explained in § 2.3.3.3). In particular, although the classical Betz analysis involves steady flows, a streamtube similar to the case of wind turbines can be identified also for oscillating systems in highly unsteady flows (due to the flow-structure interaction mechanism and the related wake vortices), if a time-averaged flow field over one cycle of oscillation is considered in the streamtube [219]. The streamlines locally tangent to extremal positions of the system during cross-flow oscillations, which identify the swept area, are the lateral boundaries of the streamtube. Thus, applying the equations of mass, momentum and mechanical energy conservation in that control volume, the Betz analysis of oscillating systems defines the theoretical maximum extraction factor. In some theoretical cases, *i.e.* two devices in a tandem configuration (see references cited in [219]), the limit value may overcome the classical Betz limit of 16/27, due to the effects of diffusion of unsteady momentum and kinetic energy across the time-averaged streamtube boundary (see § 2.3.5.4 and [219]).

The global factor Γ allows the calculation of the output power [W], or the output power per unit length [W m^{-1}], of such devices by multiplying it with the flow power referred to the, respectively, swept area or swept distance (A_{sw} or D_{sw} in Fig. 1.3). Nevertheless, other power indicators can be used to widen the typology of comparisons [30]:

- power with respect to the device volume [W m^{-3}];
- power with respect to the displaced volume [W m^{-3}], referring to the volume swept during the oscillations;
- power with respect to the footprint volume [W m^{-3}], considering the volume necessary for the flow-induced mechanism to develop that includes a virtual-wake length representing a hypothetical distance beyond which any obstacle placed in the wake does not disturb the body motiont;
- power with respect to the device weight [W kg^{-1}];
- power with respect to the device density [W kg^{-1} m^3], in which the density can be assumed equals to density of the device material or calculated using displaced volume or footprint volume;
- power with respect to the installation cost [W €$^{-1}$], which can include the cost of device, footprint volume, construction, *etc.*;

All of these power indicators can be considered to make comparisons among different technologies, and may become important at higher technology readiness levels, when relating real on-site installations (*e.g.* arranged in arrays or modules). In this case, constraints due to technology and context of the installation (*e.g.* available footprint volume) can drive the optimal system design, thus the evaluation of different power indicators can help the better

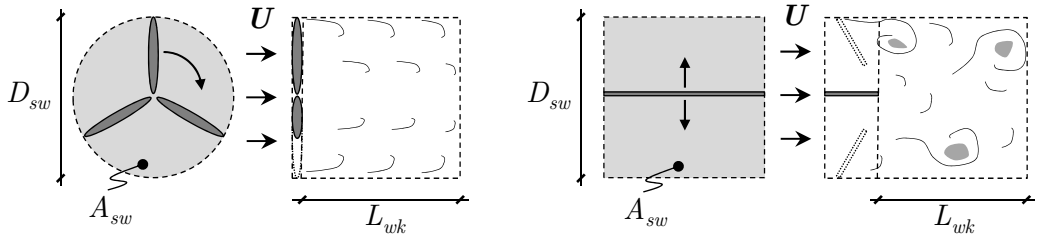

Figure 1.3. Similarity between wind turbine (left) and flutter-based generator (right) in terms of swept area A_{sw}, cross-flow swept distance D_{sw} and 'virtual'-wake length L_{wk}. This last, represents an hypothetical distance beyond which any obstacle placed in the wake does not disturb the body motion.

choice. Of course, the power output of real generators can be expressed also in terms of Watt provided continuously for one hour per year [kW h y^{-1}], which is a very common unit in the energy market. In this way, the probability distribution of velocity and direction of a real wind/water flow can be taken into account, and the system optimization could refer to this performance parameter instead.

1.2.2 Working principles

Let explain more in detail the energy-harvesting process, thus the energy flow from the fluid flow to the user network, by considering a 1-DoF oscillating system coupled with a conversion apparatus that comprises a RLC electric circuit (consisting of a resistor 'R', an inductor 'L' and a capacitor 'C'). The study of this simple problem is useful to explain some energetic issues that will support also the later discussion about 2-DoF generators (see § 4).

The general fluid-solid-electromagnetic system that describes the device can be modelled through the system of Eqs. (1.5) about the:

- mechanical system (a), identified by the displacement variable $x(t)$ and mechanical properties I (inertia), C (damping), K (stiffness), while $f(\ddot{x}, \dot{x}, x, t)$ represents the general self-excited force of the flow and $g_1(Q, t)$ describes the backward effect from the transducer;
- transducer (b), identified by the electric charge variable $Q(t)$, while $g_2(x, t)$ describes the forward effect from the structure and $h(V, t)$ is linked to the technology design of the transducer;
- electric circuit (c), identified by the electric potential $V(t)$ and circuit properties R_{ec}, L_{ec}, C_{ec} (the subscript ec is included to refer to the electric circuit, avoiding confusion with other variables used in this thesis).

$$
\begin{aligned}
& \overbrace{\qquad\qquad\qquad\qquad}^{fluid\text{–}structure\ interaction} \quad \overbrace{\qquad}^{transducer\ operation} \\
a)\quad & I\ddot{x}(t) + C\dot{x}(t) + Kx(t) = f(\ddot{x}, \dot{x}, x, t) \quad - \quad g_1(Q, t) \quad \rightarrow \text{ structure} \\
b)\quad & Q(x, t) = g_2(x, t) + h(V, t) \quad \rightarrow \text{ transducer} \\
c)\quad & L_{ec}\ddot{V}(t) + R_{ec}\dot{V}(t) + V(t)/C_{ec} = 0 \quad \rightarrow \text{ electric circuit}
\end{aligned}
\tag{1.5}
$$

While it is possible to study the fluid-structure interaction alone, without any transducer effect (simply not installing the conversion apparatus), the study of the conversion apparatus should always consider the transducer together with the respective circuit at which is linked (equation b+c in Eq. (1.5)). A simple way to overcome the modelling of a specific electric circuit without loss of physical meaning is to model a purely resistive circuit, in which all the energy flowing in it is dissipated by the resistance ($L_{ec} = 0$ and $C_{ec} = 0$ in Eq. (1.5)-c).

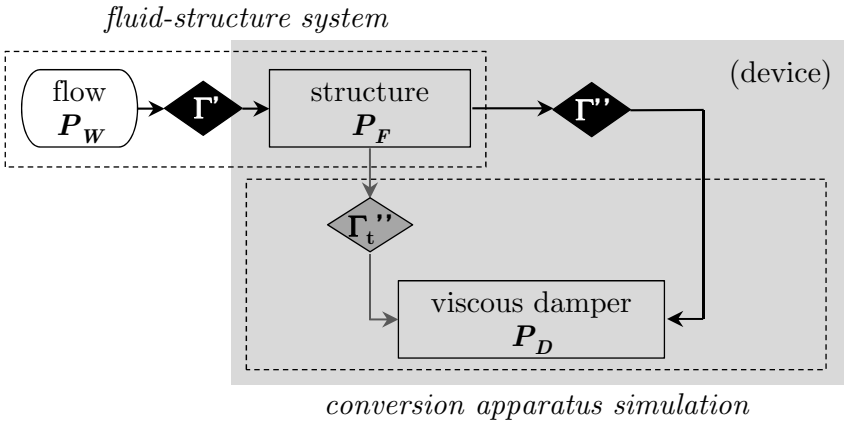

Figure 1.4. Energy-transfer diagram of the simplified approach through equivalent additional damping.

1.2.2.1 Assumptions on the conversion-apparatus modelling

A simplified approach is followed in this thesis to preliminarily estimate the extraction factor Γ' and, subsequently, the global performance Γ. This approach is not valid only in the case of piezoelectric transducers (see § 2.3.4).

Let consider a mechanical system that performs periodic motion. The equilibrium between inertial and potential energies holds over any oscillation cycle and the power pumped in by the flow-induced load P_F is balanced by the dissipated power P_D. In a classical fluid-structure interaction problem, the mechanical damping is the only responsible of the dissipated energy. By contrast, in the illustrative case of a generator that involves a purely resistive electric circuit (all the input energy of the circuit is dissipated by the resistance), any external use of energy consists in an energy extraction from the coupled mechanical-electrical system through the term proportional to the resistance. In turn, it follows an additional damping in the mechanical system due to the negative work done by the user. Within these assumptions, the device operation can be preliminarily simplified in a fluid-structure interaction problem if and only if additional damping is considered in the mechanical system: the dissipated power is the sum of the contribution of the damper P_{De} and that one of the structural damping P_{Ds}. Thus, the conversion apparatus is simulated by a viscous damper whose damping coefficient is proportional to the energy extracted (Fig. 1.4). In this way, it is possible to estimate P_F from the observation of the system response, avoiding the direct measurement/knowledge of the forcing term. This approach is particularly useful when an analytic expression of the forcing term in the post-critical regime is unknown, as in the case of classical flutter (see § 3.5). Then, the conversion factor is determined by the damper operation only, so that $\Gamma'' = \Gamma_t'' = P_{De}/P_F$, assuming that the electric circuit (not considered here) does not affect the performance ($\Gamma_c'' = 1$).

1.2.2.2 Power generators with 1-DoF

Let consider equation (a) in Eq. (1.5), in which now the damping coefficient $C = C_s + C_e$ is the sum of the structural and external contributions, the latter simulating the energy extraction through the conversion apparatus:

$$I\ddot{x}(t) + (C_s + C_e)\dot{x}(t) + Kx(t) = f(\ddot{x}, \dot{x}, x, t) \ . \tag{1.6}$$

When the steady-state regime can be described through a sinusoid of the form $x(t) = \hat{x}\sin(2\pi nt)$, being $\hat{x}$ the motion amplitude, n the motion frequency and t the time variable, the kinetic energy balances the potential energy in a cycle of oscillation of period T, since $K = (2\pi n_0)^2 I$ (n_0 is the natural frequency of the system in still air). Thus, the mean power

pumped in by the flow P_F equals the mean power dissipated by the damping:

$$P_F = \frac{1}{T}\int_0^T f(\ddot{x},\dot{x},x,t)\dot{x}dt = \frac{1}{T}\int_0^T C\dot{x}^2 dt = I\xi\hat{x}^2(2\pi n)^3\frac{n_0}{n} = P_D \ , \tag{1.7}$$

where $\xi = C/4\pi nI$ is the critical damping ratio.

The mean power P_F can be normalised by the flow power per unit length [W/m] (if two-dimensional problems are considered[1]), expressed as:

$$P_W = \frac{1}{2}\rho U^3 D_{sw} = \frac{1}{2}\rho U^3\left(\frac{B}{r} + 2\hat{x}\right) \ ; \tag{1.8}$$

where ρ is the flow density, U is the free-stream velocity, D_{sw} is the swept distance in the cross-flow direction during the oscillations, B is the reference dimension of the body used for normalisation and r is the ratio of B to the cross-flow dimension of the body. Therefore, the extraction factor can be expressed as[2]:

$$\Gamma' = \frac{P_F}{P_W} = 8\pi^3\frac{2I}{\rho B^2}\ \xi\ \left(\frac{\hat{x}}{B}\right)^2\ \frac{n_0}{n}\ \left(\frac{nB}{U}\right)^3 \Big/ \left[\frac{1}{r} + 2\frac{\hat{x}}{B}\right], \tag{1.9a}$$

The previous result can be considered to be representative of the case of translational motion, while for rotational motion (again identified with the variable x) the extraction factor becomes

$$\Gamma' = \frac{P_F}{P_W} = 8\pi^3\frac{2I}{\rho B^4}\ \xi\ \hat{x}^2\ \frac{n_0}{n}\ \left(\frac{nB}{U}\right)^3 \Big/ \left[\frac{\cos\hat{x}}{r} + (1 + 2|x_e|)\sin\hat{x}\right] \ , \tag{1.9b}$$

where the eccentricity of the rotation axis with respect to the midchord, $e = x_e B$, modifies the swept distance ($\hat{x}$ has to be kept equal to 90° for oscillations amplitudes larger than ±90°) and I is now the polar inertia of the system.

Observing Eq. (1.9), the following considerations can be made:

- The performance is proportional to the product of oscillating mass and damping, which is related to the Scruton number ($Sc = 4\pi I\xi/\rho B^2$ or $Sc = 4\pi I\xi/\rho B^4$); however, it is important to remind that this parameter strongly affects implicitly the motion amplitude as well. Therefore, the flow-induced vibration mechanism should be able to guarantee large amplitude of oscillation also in the presence of high values of the mass-damping parameter.
- If the reference dimension B is the width of the cross-section, r is the width-to-depth ratio and, in the case of elongated rectangular shapes, the quantity $1/r$ can be neglected; the performance is then proportional to the amplitude in the case of translational motion.
- The key parameter is the reduced velocity $U_R = U/nB$ since $\Gamma' \propto (1/U_R)^3$. Consequently, sustained vibrations with large amplitudes should appear for as low as possible values of U_R even in the presence of high damping levels, in order to enhance the performance.

The quantity $P_{De} = P_D - P_{Ds}$ is the one that can be effectively converted into electricity. Thus, the conversion factor takes the form:

$$\Gamma'' = \frac{P_{De}}{P_F} = \frac{\xi_e}{\xi_s + \xi_e} \ . \tag{1.10}$$

The ratio of structural to external damping rules the portion of the energy of the forcing term that is directed to the transducer and obviously should be as low as possible.

The expression of the global performance Γ is equivalent to eqns.(1.9a) or (1.9b) in which the parameter ξ_e is considered instead of ξ.

[1] In the case of three-dimensional problems, the flow power is referred to the swept area A_{sw} and the powers are expressed in Watt.

[2] The extraction factor is here calculated assuming that Eq. (1.7) holds and this is the only possible way when an analytical expression of the forcing term in the post-critical regime is not available.

1.3 Motivations and objectives

The motivations come from:

I *Scientific issues* (principal): current research trend and scientific interest; known *vs* unknown research area; establishment of design guidelines; challenging feature.

The knowledge of the system response in the critical and post-critical regime with respect to the governing parameters is a fundamental issues that has to be clarified and, itself, represents the main scientific and interesting open issue. In the conventional design of civil/aeronautical structures the common interest is to limit the flow-induced vibrations and, especially in case of flutter, to avoid the crossing of the instability threshold. Therefore, the literature mainly focused on the system response up to the critical condition, and analytical linear models have been developed to predict the instability threshold. Consequently, the problem of the way to stabilize a structure, outlining design expedients devoted to separate the service and critical conditions, is deeply debated in literature. On the contrary, a flutter-based generator needs to oscillate in the post-critical regime and, especially, with large amplitudes of the motion in presence of high damping levels. The topic has to be faced completely in the contrary way to the usual approach and the following questions need to be answered: *how to design configurations more unstable, anticipating the critical condition?*; *how to develop efficient solutions that are able to experience large amplitudes of oscillations in presence of very high damping levels?*. To get answers, the problem requires scientific understanding and the influence of the governing parameters has to be investigated with respect to the complete system response, including critical and post-critical regimes. The goal of the work also requires the study of configurations with sets of parameters that have never been investigated so far. Thus, there is a research gap on the evaluation of the fluid-elastic system response for energy production purposes.

II *Technological aspects* (secondary, but foregoing the former): energy-harvesting requirements; performance improvements and optimizations; technology simplifications.

Within the energy-harvesting framework, some authors have preliminary explored aero-/hydro-elastic generators based on several kinds of fluid-elastic phenomena (see § 2.3). The state of the art shows that the most promising results are obtained for two-Degree-of-Freedom (2-DoF) systems undergoing flapping motion. Anyway, these systems have two drawbacks: (*i*) the motion is artificially activated, where usually the pitching DoF is externally driven to adjust the phase with the heaving component and to control the lifting loads; (*ii*) specific airfoil-shaped cross sections are considered. Both (*i*) and (*ii*) can lead to expensive and technologically complex devices. In the present thesis, the problem is overcome through the exploitation of the spontaneous flutter instead of the flapping[3] mechanism, *i.e.* without any external manipulation of the flutter phenomenon, thus obtaining the natural system response according to the set of governing parameters. Moreover, oscillating bodies with simple, elongated rectangular cross sections, similar to flat plates, are considered.

III *Societal trends* (following the former): HORIZON 2020 guidelines and projects; sustainable development contributions; energy demand *vs* energy supply; future technology roadmaps.

The current international policy is strongly supporting sustainable development and clean energy production from alternative sources, looking for intelligent, conscious solutions that can be employed in many contexts. In particular, renewable energy sources (*i.e.* geophysical flows, solar, thermal gradients) are among the main purposes of the European Union project *Horizon 2020* for the many interesting features, such as

[3] In the technological literature, the flapping solutions relate two-degree-of-freedom systems with externally driven motion and, consequently, are not based on the classical flutter mechanism, as defined in the scientific literature. Indeed, in the same cases, the system oscillate even without any elastic suspension. Hence, flapping solutions have not to be confused with flutter-based solutions. See § 2.3.5 for more details.

the large natural availability and reduced environmental impact. Moreover, according to the current global world development and future trends, the energy demand is increasing due to custom requirements supply. High technology evolution and life standards are leading to an important growth of the electricity market in particular, in which the electrical energy scale is evolving too. The micro and small scale market is rapidly increasing, due to the development of low-energy networks. Also regarding the developing countries, where there is not a suitable organized network, local powering station could be very useful for the energy supply, for example at familiar scale. Finally, even the large-scale energy production waits for improvements, especially in terms of performance and realiability of the energy output. Multi-purpose energy platforms, wherein various powering systems (also with complementary features) work together, can become reliable power generation cores.

The general question is **'how should a flutter-based generator be designed to achieve the as high as possible performance, according to a given context?'** and it is considered the leading objective. As a preparatory answer, which also explains some recurring features, any power generator based on vibrations due to fluid-elastic phenomena needs to:

- get unstable at an as low as possible flow velocity;
- perform as large as possible amplitudes of oscillations, from the very beginning of the post-critical field;
- oscillate even in the presence of very high levels of external damping, which means the operation conditions of energy generation.

Hence, several sub-objectives coming from the discussion upon the state of the art can be identified:

A *Understanding of the influence of the governing parameters on the critical and post-critical regime.*

The critical condition of the classical flutter problem involves seven dimensionless governing parameters (see § 3) but few information are available on their influence on post-critical regime. Once the instability is started overcoming the critical condition, an initial relevant jump arises and the post-critical regime shows very large amplitudes, which almost linearly increase as the flow speed increases. Moreover, the instability usually shows to be of sub-critical type, with a stable branch with non-null amplitude below the critical onset that can be achieved under specific initial conditions. The objective is to evaluate this evolution of the system response with respect to different sets of parameters in order to outline some recurring dominant features in the post-critical response paths too.

B *Performing reliable experiments on the post-critical flutter of sectional models.*

The main issue is to design setups with linear or, at least, well-known mechanical properties in the whole range of measurement. This allows quantifying the nonlinearity due to fluid-dynamic forces only and performing reliable experiments even with large motion. Moreover, the energy production context requires experiments in which the production has to be, at least, simulated through equivalent mechanical damping. Thus, the development of specific dampers to introduce very high damping into the system is an important issue to be handled.

C *Identifying design guidelines to increase as much as possible the capability of a mechanical system to capture energy from the fluid flow.*

The several performance indicators (Γ', Γ'', Γ''') have to be as high as possible in order to enhance the global performance Γ. Observing Eq.(1.9), some key parameters can be identified to be mainly responsible of the system performance. Thus, the study of the parameters influence has to be addressed to understand how conceiving more unstable configurations, improving the design of flutter-based generators.

Putting together **A**, **B**, **C**, the final aim would be to develop optimal configurations that show the maximum performance with respect to a given context. The multiparametric space has to be explored looking for optimal configurations, understanding how a given set of governing parameters has to be established to provide a specific fluid-elastic response and thus performance, in order to capitalise on the available energy source.

1.4 Innovative contributions

- *Improvement of the knowledge about critical and post-critical flutter of flat plates.*

  The specific focus on the post-critical regime definitely contributes to the scientific understanding of the flutter problem, due to the very few research works conducted so far in this direction. Moreover, the investigation of fluttering systems with particular sets of governing parameters, according to the energy production goal, as well as the requirements of large amplitude of oscillations and very high levels of damping, are strongly different from the common design approach for civil/aeronautical applications. Thus, the design of flutter-based generators represents, itself, an innovative topic.

- *Systematic, large database about the flutter response of flat plates.*

  Combining the experimental campaigns and the analytical investigations, a large amount of configurations have been investigated and compared. The ensemble of results can constitute a new database about flutter of 2-DoF models with elongated rectangular cross sections. This database can also represent the basis for further analyses and studies, in particular it can be useful to support the development of analytical nonlinear models of the self-excited forces for the post-critical system response.

- *Experiments about energy harvesting with simulation of energy production.*

  So far, the majority of the literature studies (see § 2.3.5) are about theoretical predictions of the system performance, close to the critical condition. Experiments have been conducted too, but often without implementing the whole conversion apparatus. In this thesis there is a step forward in the study of the topic because, although the conversion apparatus is not directly implemented in the experiments, the energy production is simulated through real modifications of the damping in the degree of freedom in which the conversion apparatus acts. This approach allows also flexibility on the technical design of the conversion apparatus.

- *Preliminary design guidelines about flutter-based power generators.*

  The thesis is partially devoted to outline a methodology of designing a flutter-based generator, since the parametric space is wide. Configurations developed for low or high flow velocities, for small or large sizes, for open-sea or urban flows, *etc.* can be preliminary outlined combining the exploratory linear analyses and the experimental database, simplifying the development for the next higher levels of technology readiness.

1.5 Structure of the thesis

Overview of the problem

- *Chapter 1*: introduction to the energy-harvesting framework; performances of 1-DoF generators; motivations and objectives of this work; innovative contributions; how the research work is structured.

Scientific and technological background

- *Chapter 2*: review on aeroelastic phenomena; brief reviews of the wind turbine technology and the mechanical-to-electric conversion techniques; systematic review of energy-harvesting technologies; comparison of the main achievements; discussion of open issues.
- *Chapter 3*: review of 2-DoF classical flutter; analytical modelling; comments on the post-critical regime of flutter.
- *Chapter 4*: definition of performance for 2-DoF flutter-based generators.

Design of the experimental campaigns

- *Chapter 5*: description of facility, flow characteristics, equipment, setups, mechanical features of the setups at the Stahlbau Institute wind tunnel (Braunschweig, Germany) and at the CRIACIV wind tunnel (Florence, Italy).
- *Chapter 6*: description of the methodology of investigation; preliminary and results of explorative linear analyses to design the Stahlbau campaign.

Analyses of the experimental results

- *Chapter 7*: discussion of results of the Stahlbau experiments; preliminary discussion of the influence of some key parameters on the post-critical regime; discussion of the results of the CRIACIV experiments; improvement of the parameter-effect understanding; collection of complementary information; comments on the dominant features of the critical and post-critical responses and on the stability of the observed branches; evaluation of the performance of selected configurations from both campaigns.

Study of optimal configurations

- *Chapter 8*: systematic linear analysis of the parametric domain following the collected experimental results to look for optimal sets of parameters; experimental investigation of selected optimal configurations; evaluation of performances and influence of the governing parameters.

Discussion of specific issues

- *Chapter 9*: influence of the main governing parameters with a key role in the flutter problem; destabilizing effect of damping and very high damping levels; summarising comparison between selected configurations in terms of performance; comments on the validity of the linear predictions about the critical condition.

Concluding remarks

- *Chapter 10*: What has been done and what could be done next.

Chapter 2

State of the art

2.1 Introduction

The topic involves the research fields of fluid-elastic phenomena and energy-harvesting methods. Combining them, the resulting subject is multidisciplinary, requiring the knowledge of several disciplines (Fig. 2.1). Nevertheless, this research basically focuses on the two-degree-of-freedom flutter mechanism and on the investigation of the critical and post-critical regime, simulating the energy production through equivalent additional damping (see § 1.2). Thus, the multidisciplinary restricts to issues related to fluid-dynamics of bodies with streamlined cross sections and nonlinear dynamics due to the flow-induced vibrations, postponing the aspects related to the conversion apparatus.

The review about energy conversion solutions that exploit fluid-elastic phenomena as energy sources, in literature referred as energy-harvesting systems (this term is further discussed in § 2.3.1), has been systematically conducted. Indeed, a comprehensive review is not available yet, due to the developing and widespread character of the topic and only specific reviews on selected technologies are available [215, 217]. Moreover, brief overviews of the common wind turbine technology (§ 2.3.3) and basic methods to convert kinetic energy into electricity (§ 2.3.4) are included in this chapter.

Several types of flow-induced mechanisms have been considered so far as energy sources and this is why a discussion of them is required too. However, due to the extensive knowledge of the common fluid-elastic phenomena, which especially comes from the field of civil/aeronautical engineering, their review is synthetic. By contrast, a detailed description is given in § 3 for the classical flutter mechanism, and includes also an overview of the research field about the post-critical regime.

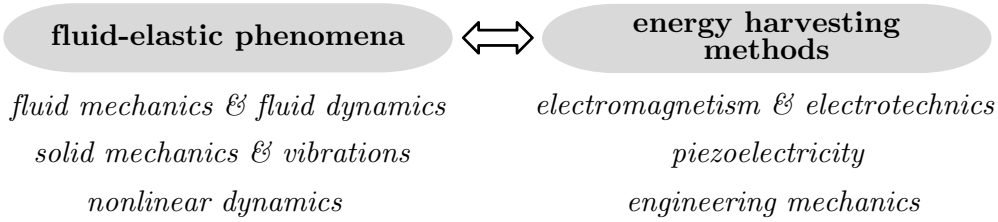

Figure 2.1. Multidisciplinary features of flow-induced-based energy-harvesting systems.

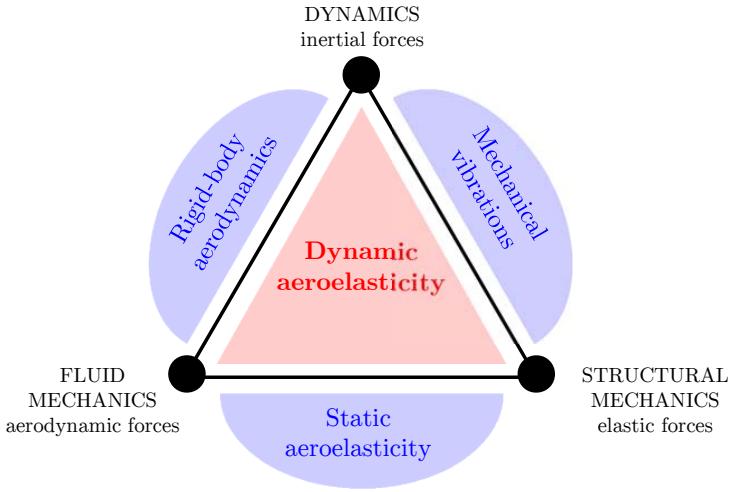

Figure 2.2. Collar's triangle describing the conceptual framework of aeroelasticity (or fluid-elasticity in general).

2.2 Discussion on fluid-elastic phenomena

2.2.1 Overview of fluid-structure interaction

In general terms, fluid-structure interaction (FSI) problems involve energy exchanges between a fluid system and a solid system. The solid system is usually identified as *structure*, because of the main practical applications in which a fluid flow interacts with civil or aeronautical structures. Along this line, the fluid is principally represented by air or water flows. More complex FSI problems can occur in other fields, such as aerospace engineering, where also thermal gradients, radiations, motion control and impacts participate in the interaction [33]. Anyway, these last are out of the topic of this thesis. Hence, the energy transfer takes place through the exchange of forces/displacements along the separating boundary between fluid and structure systems. Depending on their mechanical properties and constraints, several type of FSI can arise as explained in Fig. 2.2, because the structural system can manifest as a rigid or deformable body, as well as movable or restrained.

Disregarding the field of only structural vibrations, as represented in Fig. 2.2, and considering that the fluid can flow in a steady (laminar conditions, with uniform mean speed) or unsteady (turbulent conditions, with uniform or non-uniform both mean speed and fluctuations) way, the following FSI phenomena can be outlined:

- Fluid-rigid interaction
  - Static response
  - Dynamic response
- Fluid-elastic interaction:
  - 'Quasi-static' response
    - Stable systems
    - Unstable systems (divergence)
  - Dynamic response
    - Stable systems
    - Unstable systems (resonance and/or negative damping)
      - Limited-amplitude oscillations in a range of flow speed
      - Unlimited-amplitude oscillations with increasing flow speed

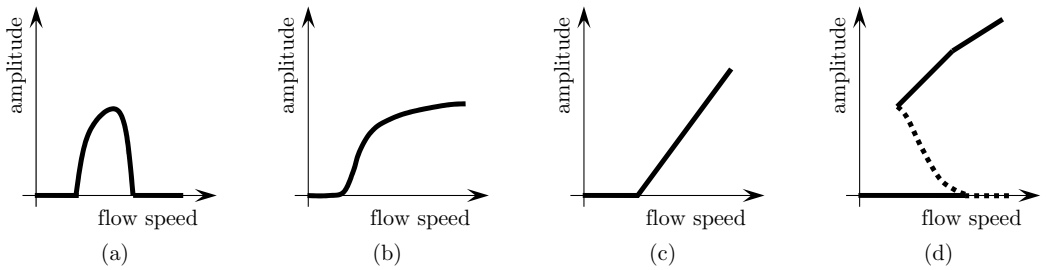

Figure 2.3. Sketch of the amplitude-velocity diagrams for several flow-induced excitation mechanisms: (a) lock-in resonance; (b) wake galloping; (c) transverse galloping; (d) flutter.

2.2.2 Main fluid-elastic mechanisms of oscillation

Focusing on elastic structural systems, the fluid-structure interaction is affected by the mechanical behaviour of the structure that can vibrate. The set of properties of stiffness, damping and mass become of fundamental importance and can be modified by the flow-induced effects, resulting in a coupled fluid-elastic system with different dynamic parameters. Hence, several typologies of oscillations (see Fig. 2.3), usually arising in the cross-flow direction, can be identified accordingly to the mechanisms that governs the interaction. The classification reported hereinafter recall Naudascher and Rockwell [162] and can combine with the previous, more general, classification of § 2.2.1.

2.2.2.1 Vortex-induced vibrations

- von Kármán excitations
- Lock-in resonance

The motion is due to coherent vorticity structures (Kármán vortices) that intrinsically arise around bodies with bluff shapes (also in the case of rigid bodies) and shed downstream alternately, producing important flow separations with pressure fluctuations on the body and pseudo-harmonic dynamic loads.

In the case of lock-in phenomenon, the body is left free to vibrate with a frequency close to the frequency of the vortex shedding, thus the following displacement field directly participates to the flow excitations, producing self-excited loads. The nonlinear response of the system in lock-in vibrations essentially involves resonance effects that amplify the motion, although characterised by limited amplitudes in a finite range of flow speeds (Fig. 2.3-a).

2.2.2.2 Motion-induced vibrations

- Nonlinear fluid-dynamic reactions
  - Bluff bodies
    - 1-DoF galloping (transverse or rotational)
    - 2-DoF galloping (cross-flow and along-flow motion)
  - Streamlined bodies & separated flow
    - Stall flutter
- Elastically & fluid-dynamically coupled modes
  - Streamlined bodies & attached flow
    - Classical flutter (bi-modal or multi-modal coupling)
  - Flexible plates in axial flows

The motion is due to nonlinear fluid-dynamic reactions and/or of fluid-elastically coupled modes of vibration that develop LCOs with large amplitude, usually increasing with the flow speed.

In particular, large flow separations can be produced by the movement of a bluff body with sharp edges or a streamlined body at high angles of attack, introducing important nonlinearities in the fluid-dynamic forces that lead to dynamic instabilities (*e.g.* galloping (Fig. 2.3-c) and stall flutter).

A different mechanism governs the classical flutter excitation. In this case, the energy exchange between two (at least) structural modes and the corresponding nonlinear fluid-dynamic reactions induces a dynamic coupling that modifies the inertia, stiffness and damping properties of the coupled fluid-structure system. Thus, even in the case of attached flow, the flow-induced actions produces the loss of damping in one of the involved structural modes, which becomes dynamically unstable, and drives the motion to large amplitudes (Fig. 2.3-d). A similar dynamic instability can involve flexible, continuous body when immersed in axial flow (*e.g.* panel flutter of flexible plates).

2.2.2.3 Turbulence-induced vibrations

- Buffeting
  - Flexible-body in unsteady flows or wake flows
- Wake-galloping

The motion is essentially due to fluctuations in the incoming flow velocity. These are proper of the unsteadiness of the stream fluid flow (buffeting) or produced by the wake of another upstream bluff body (wake effects) and are usually independent of any flow instability originating from the structure considered.

In the case of buffeting, the fluctuations can be also independent of the structural displacements if this do not exhibit fluid-elastic interaction. Otherwise, in the case of slender structures (line-like, plate-like, membranes, *etc.*), added-mass and fluid-damping effects participate in the interaction mechanism, leading to resonances and/or damping reductions. However, these vibrations are usually less powerful than the mechanisms previously considered and the following limit-cycle oscillations show smaller amplitudes although increasing with the flow speed.

Fluctuating coherent structures contained in incoming wake flows can also non-linearly excite bluff bodies let free to vibrate and placed downstream of the upline body, which produces the wake flow. This phenomenon may occur only under conditions where the frequencies of response of the downstream body are low compared to its vortex-shedding frequencies and to those of the upstream body (the latter may be also fixed), being also of crucial importance the relative position between the two bodies. Usually, the following limit-cycle oscillations show significant but limited amplitudes in a semi-infinite range with increasing the flow speed (Fig. 2.3-b).

2.3 Energy harvesting from fluid flows

2.3.1 Introduction

The concept of energy harvesting can find origins in 1826 when Thomas Johann Seebeck discovered the thermoelectric effect: the connection of dissimilar metals produced an electric current when exposed to a temperature gradient. Hence, *energy harvesting* started to be interpreted as the process by which energy is collected from whatever available sources (*e.g.*: solar and electromagnetic radiations; thermal, salinity and pressure gradients; wind and water flows; human movement and mechanical vibrations; *etc.*) and converted to usable power (see [90] or [71] for a general review of energy-harvesting history and methods).

Hence, energy harvesting is a wide concept and can comprehend many different solutions, even wind turbines and solar panels, for example. However, the literature usually restricts

the meaning of the term 'energy harvesting' to those solutions that (i) rely on innovative methods of energy recovery and (ii) produce energy exploiting energy sources that are scattered, free and largely available as ambient background (otherwise wasted). These solutions can be considered alternative to the more common and mature technologies and, so far, showed poor technology readiness level due to the emerging character of the topic. At the beginning, energy-harvesting systems based on flow-induced vibrations featured some limitations on the power output level, due to the small quantity of energy that was involved in most of the considered applications, mainly related to micro-/small-scale of energy supply (*e.g.*: self-powered micro-systems as wireless sensors, monitoring devices, structure-embedded instrumentation [71, 185]; remote stations; low-energy networks; *etc.*). Nevertheless, recent research progresses and achieved improvements suggest that these solutions may be competitive to the more mature wind turbine technology, which have achieved significantly higher levels of technology readiness and definitely takes place in the large-scale energy supply.

A systematic review of the main achievements of energy harvesting from fluid-elastic phenomena is here reported. Some preliminary aspects are also discussed, such as typology of available energy sources and the main methods for converting the kinetic energy (all relevant for this thesis work). In the framework of energy conversion from fluid flows, wind turbines represent the most advanced technology and therefore a brief overview on it is included too.

2.3.2 General framework of energy production

The conceptual framework of energy production considers an unidirectional transformation process, with priority rules, that involves the choice of the raw source, the form of available energy, the typology of technology that converts the energy and the form of the final usable output (Fig. 2.4). As a consequence, some classifications can be identified according to:

- type of source (Fig. 2.5);
- type of energy (Fig. 2.6);
- type of technology (Fig. 2.7);
- type of usable output (Fig. 2.8).

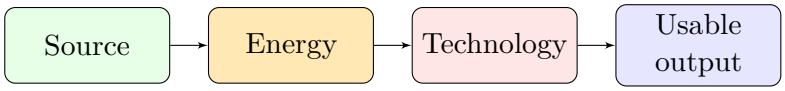

Figure 2.4. General path of the energy production framework.

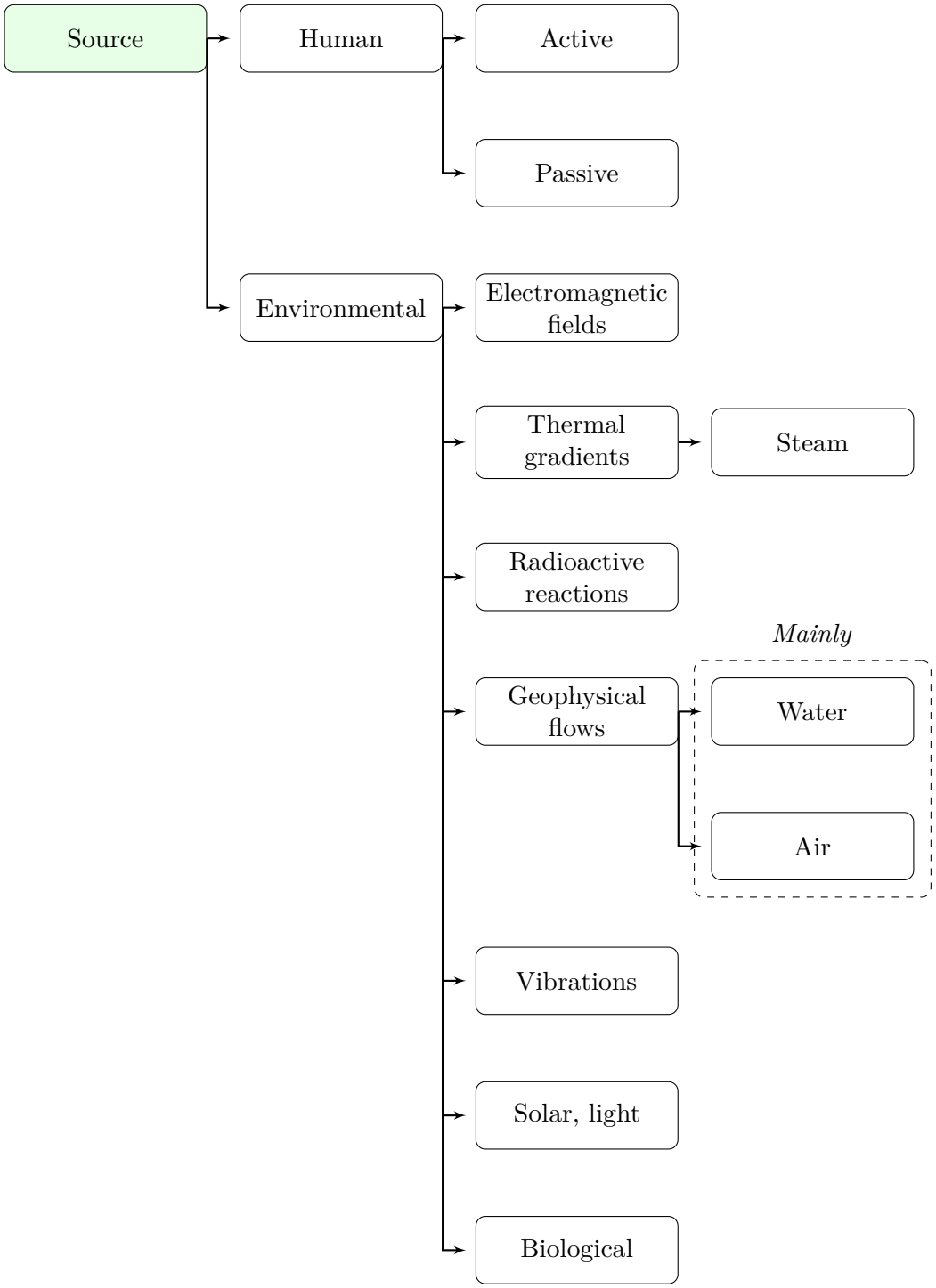

Figure 2.5. Energy production framework: classification by types of available source.

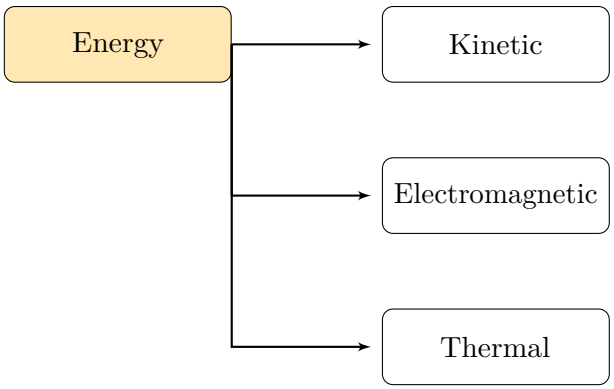

Figure 2.6. Energy production framework: classification by types of raw energy.

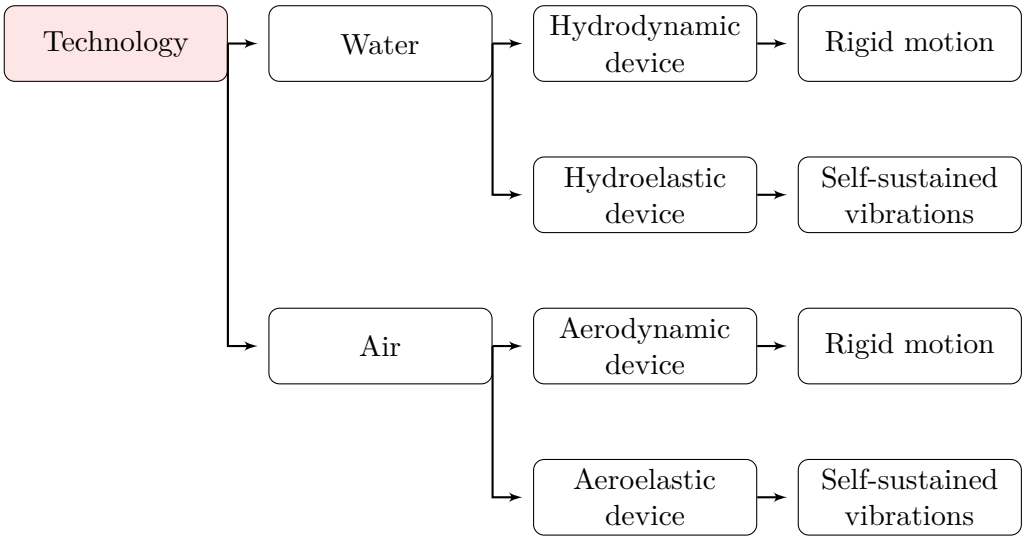

Figure 2.7. Energy production framework: classification by types of technology, relating the geophysical flows of air and water

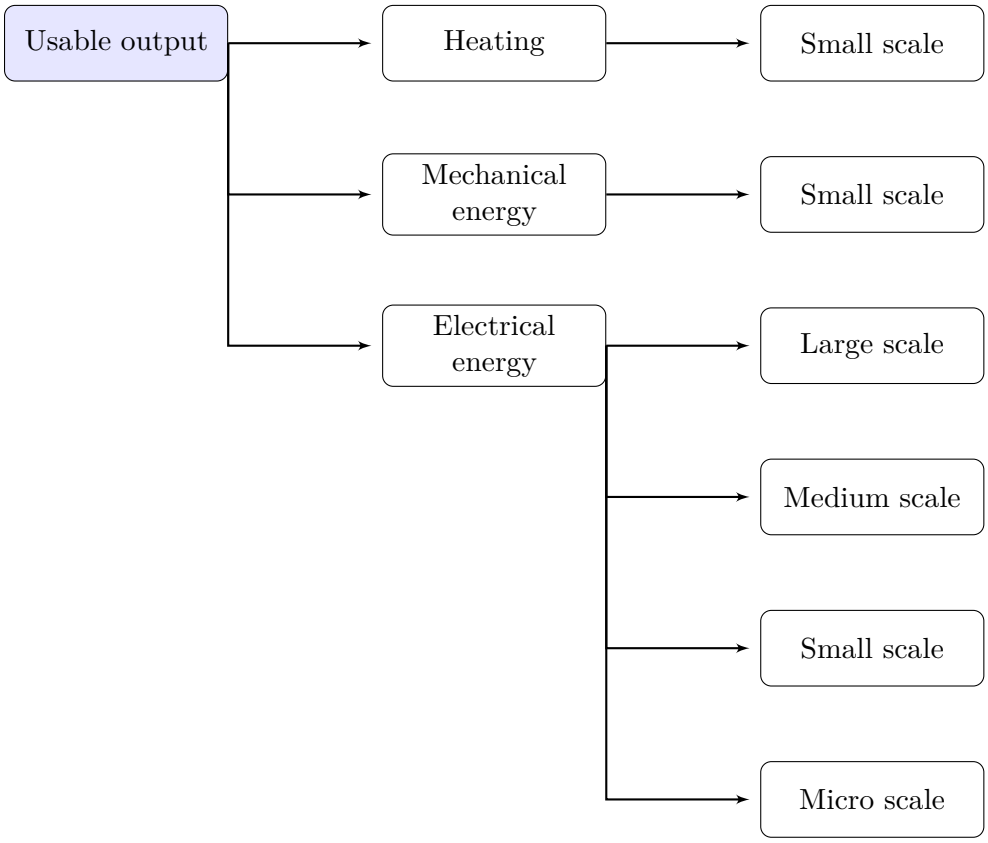

Figure 2.8. Energy production framework: classification by types of output energy.

2.3.3 The wind-turbine technology

2.3.3.1 Historical aspects

This historical review is based on the work of Ackermann *et al.*, dated 2000 [10].

At the beginning, wind-power systems were used to provide mechanical power [44]: the earliest recorded windmills are vertical-axis mills, as simple drag devices, used to grind grain since the 7^{th} century B.C. The first horizontal-axis mills appeared in the Mediterranean area during 11^{th} century A.D. and this technology was largely improved in Europe between the 12^{th} and 19^{th} centuries, until its introduction in North America by settlers for agricultural purposes. Nevertheless, after the 2^{nd} industrial revolution of 1870, the boost of fossil fuels strongly encouraged the development of other technologies for general energy production and wind-power systems moved to the background.

The first wind-turbine generating electricity was built in 1891 by Dane Poul la Cour although, until the early 20^{th} century, they were employed to provide mainly mechanical power. In 1942, a Danish Company designed a wind-turbine generator with rational knowledge of aerodynamics and further developments were achieved during the second World War. Anyway, the interest in the wind-power generation was secondary until the advent of the 3^{rd} industrial revolution during the 1970s, which fostered developments in the field of electronics and revolutionised the wind-power conversion. At the same time, the oil price shocked and the interest in the wind-power re-emerged, especially in Germany, USA and Sweden, to fit the increasing worldwide electricity demand and reduce the environmental impact. Hence, wind-power systems had the first boom in the history. The Danish prototypes were improved, particularly in USA due to special policy in the electric energy market, spreading the technology in other countries too (*e.g.* India).

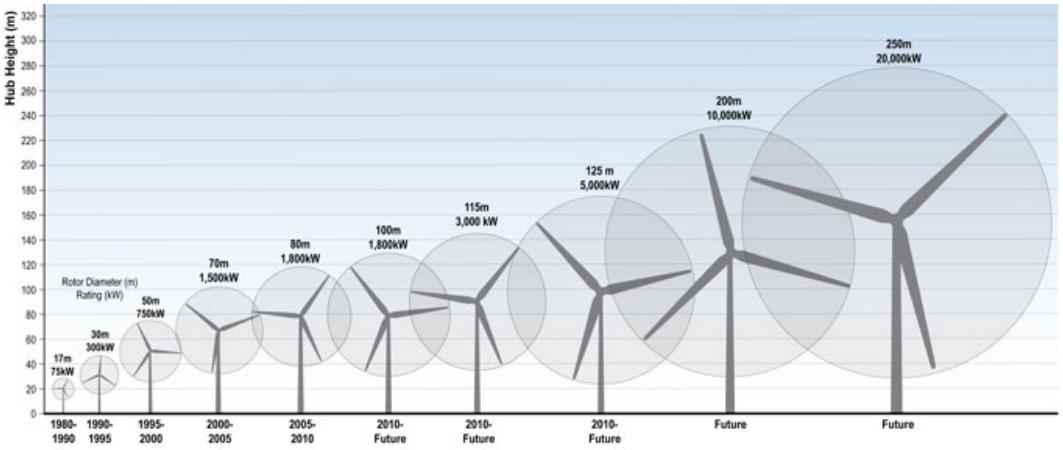

Figure 2.9. Evolution of the wind turbine technology, considering the rotor diameter, hub height and power with respect to the year. Source of the picture: National Renewable Energy Laboratory.

2.3.3.2 Wind-energy potential and current status

The wind-turbine technology has been improved step-by-step since the beginning of the 20^{th} century, passing from 300 kW on-shore wind-turbine with a 30 m rotor diameter (1989) to 6 MW on-shore/off-shore wind-turbine with a 154 m rotor diameter (2012), see Fig. 2.9, and becoming one of the most important sustainable energy solution. Ackermann *et al.* [10] stated that, at the beginning of 2000s, about 80% of the worldwide wind capacity was installed in only five countries[1]: Germany, USA, Denmark, India, Spain.

Concerning the features of the current installations, there are two types of wind-power generators: *grid-connected* and *stand-alone*. About the former, European policy is fostering the development toward off-shore installations, being the on-shore farms limited between 20 and 50 MW due to problems with population density and available space. About the latter, the common capacity is between few watts and 50 kW, usually used to power remote houses and remote technical applications. For village or rural electrification systems, the energy scale can increase up to 300 kW, otherwise providing mechanical power for pumping drinking and irrigation water. The demand of stand-alone installations is growing significantly, driven by the set-up of rural electrification programs in many parts of the world, supported by international aid programs.

According to the reports of the Global Wind Energy Council[2] (GWEC) about the wind energy market, there is a continued, although slightly evolving, growth for the rest of the decade. First, China and Brazil and, secondly, Mexico and South Africa (non-OEDEC[3] members) increased more than traditional markets in Europe and North America, wich are relatively stable markets. Looking ahead, GWEC expects that the growth will continue to be led by China and, secondly, by India. Latin America is becoming a strong regional market, led by Brazil, but with Mexico catching up quickly. Led by South Africa, Egypt and Morocco, GWEC looks for a number of new markets to emerge in the coming years which will make Africa the fastest growing regional market.

[1] The same authors [10] suggested the following organisations to consult regularly published statistics about wind energy: German Wind Energy Institute (http://www.dewi.de/); International Economic Platform for Renewable Energies (http://www.iwr.de/); Windpower Monthly (http://www.windpowermonthly.com/); Wind Force Reports of the European Wind Energy Associatio (http://www.inforse.org/, http://www.ewea.org/)

[2] http://www.gwec.net/.

[3] It is an international economic organisation of 34 countries founded in 1961 to stimulate economic progress and world trade, providing a platform to compare policy experiences, seek answers to common problems, identify good practices and coordinate domestic and international policies of its members (http://www.oecd.org/).

2.3.3.3 Betz's limit vs. wind-turbine performances

The Betz's limit[4] is derived from the principles of conservation of mass and momentum of any non-compressible, newtonian, axial fluid stream flowing through an idealized 'actuator disk', *i.e.* without hub and with an infinite number of blades (with no drag), that extracts the maximum possible amount of energy from the fluid stream (*e.g.* [41], [74]). With the additional assumptions of no heat transfer and uniform thrust over the disc, the analysis applies to the control volume indicated in Fig. 2.10, in which all the symbols appearing in the following formulas are also explained.

The power of the turbine is

$$W_t = (P_1 - P_2)A_t U_t \ , \tag{2.1}$$

the mass conservation is

$$A_u U_u = A_t U_t = A_d U_d \ , \tag{2.2}$$

and the momentum conservation, which expresses the force exerted on the disc due to the momentum change from upstream to downstream the disc, is

$$(P_1 - P_2)A_t = \rho A_u U_u (U_u - U_d) \ . \tag{2.3}$$

Then, considering the centreline of the stream tube (straight-dashed line in Fig. 2.10) the Bernoulli's theorem applies as

$$P_\infty + \frac{1}{2}\rho U_u^2 = P_1 + \frac{1}{2}\rho U_t^2 \tag{2.4a}$$

and

$$P_\infty + \frac{1}{2}\rho U_d^2 = P_2 + \frac{1}{2}\rho U_t^2 \ . \tag{2.4b}$$

The combination of equations (2.2), (2.3), (2.4a), (2.4b) gives

$$(P_1 - P_2) = \frac{1}{2}\rho\left(U_u^2 - U_d^2\right) = \rho\frac{A_u}{A_t}U_u(U_u - U_d) = \rho U_t(U_u - U_d) \ , \tag{2.5}$$

and

$$U_t = \frac{1}{2}(U_u + U_d) \ . \tag{2.6}$$

Hence, the power coefficient of the rotor C_{PR} can be defined as the ratio of the power of the turbine W_t to a virtual power of the oncoming flow in the stream tube at the disc position W_u. Combining Eqs. (2.5), (2.3) and (2.1), the power coefficient is

$$C_{PR} = \frac{W_t}{W_u} = \frac{(P_1 - P_2)A_t U_t}{\frac{1}{2}\rho A_t U_u^3} = \frac{1}{2}\left(1 - \frac{U_d}{U_u}\right)\left(1 + \frac{U_d}{U_u}\right)^2 \ . \tag{2.7}$$

Differentiating Eq. (2.7), the maximum power coefficient occurs when $U_d/U_u = 1/3$ (corresponding to $A_d/A_u = 3$) and it takes the limit $C_{PR} = 16/27 \simeq 59\%$.

Fig. 2.11 shows the rotor power coefficients of several wind turbines with respect to the tip-speed ratio (TSR, λ). The TSR is a fundamental parameter in the design of wind turbines and it represents the ratio of the velocity of the tip blade of a rotor with radius R_t, to a given free stream flow velocity [180]

$$\lambda = \frac{\omega R_t}{U} \ , \tag{2.8}$$

in which ω is the angular velocity of the rotor. The flow crossing the rotor area that has interacted with a blade is disturbed until a downstream distance s, reached at a time t_s, where it re-establishes itself according to the free stream condition:

$$t_s = \frac{s}{U} \ . \tag{2.9}$$

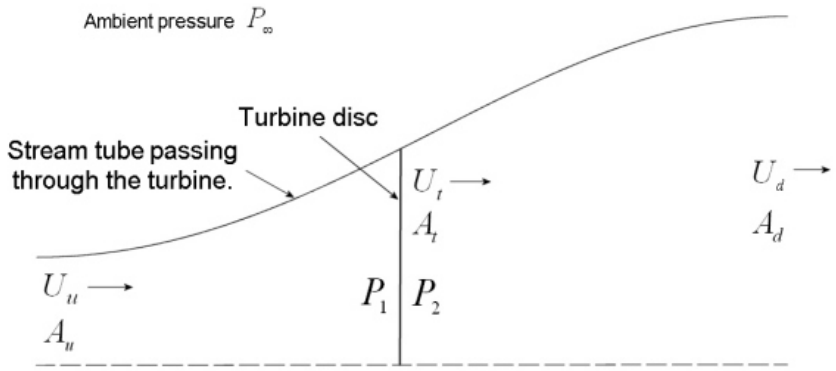

Figure 2.10. Sketch of the actuator disc theory for horizontal axis wind turbines, where $(U_u; A_u)$, $(U_t; A_t)$, $(U_d; A_d)$ state the flow velocity and area of the stream tube at the upstream, disc and downstream positions. P_1 and P_2 represent the pressures about the disc, inside the stream tube, while P_∞ states the ambient pressure. Picture from http://www.wind-power-program.com/betz.htm.

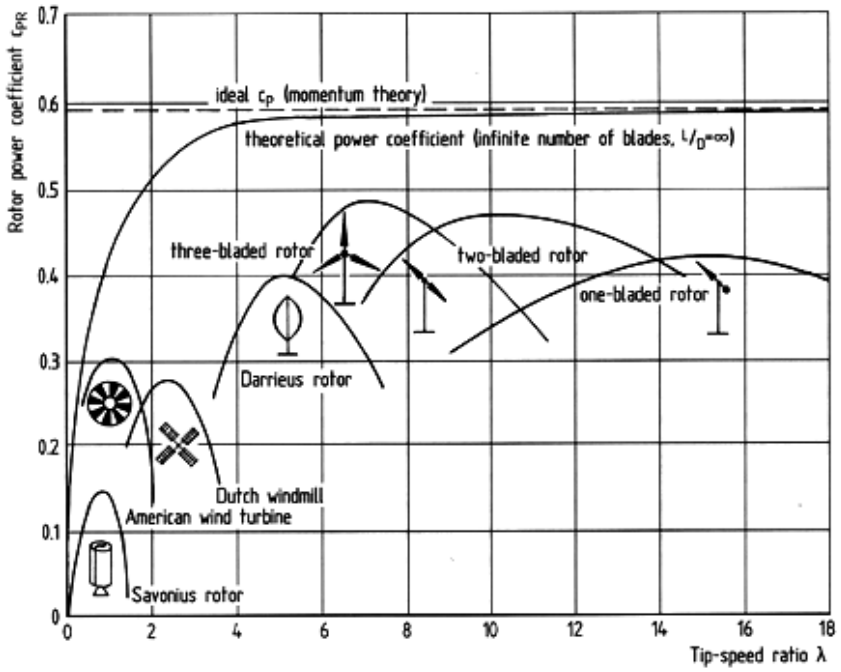

Figure 2.11. Comparison of wind-turbine performances, in terms of rotor power coefficient, with respect to the tip-speed ratio. Picture from [93].

Furthermore, the time needed by the next blade to pass in the same position is t_b:

$$t_b = \frac{2\pi}{\omega N_b} \ , \tag{2.10}$$

where N_b is the number of the blades in the rotor. If $t_s > t_b$, a certain amount of flow is unaffected by the rotor, while, if $t_s < t_b$, a certain amount of flow is not allowed to flow through the rotor area. Thus, the maximum power coefficient occurs when the two times are approximately the same:

$$\frac{s}{U} \simeq \frac{2\pi}{\omega N_b} \Rightarrow \omega_{opt} \simeq \frac{2\pi U}{s N_b} \ . \tag{2.11}$$

It follows that the optimal TSR is defined as

$$\lambda_{opt} \simeq \frac{\omega_{opt} R_t}{U} \simeq \frac{2\pi}{N_b} \left(\frac{R_t}{s} \right) \ , \tag{2.12}$$

which depends on the number of rotor blades: the smaller N_b, the faster the rotor must rotate to extract at the maximum C_{PR}. Moreover, from empirical observations [180], it is found that s is approximately equals to 50% or the rotor radius, thus $s/R_t \simeq 0.5$ and Eq. 2.12 becomes

$$\lambda_{opt} \approx \frac{4\pi}{N_b} \ . \tag{2.13}$$

However, the parameter s, usually called slip or slide number, depends on the fluid-dynamic efficiency of the blades and extensive research on it is ongoing, focusing on the way to reduce it. Thus, highly-efficient rotor blades, with airfoil shapes, increase the rotational speed of the rotor and the turbine can generate more power.

2.3.4 Mechanical-to-electric conversion techniques

In the field of energy-harvesting systems, inertial-transducer technology is the most used. It transforms some available kinetic energy into electricity (*e.g.* [179], [54] or the work by Angrist cited in [144]).

In general, the power output depends (i) the amount of convertible energy, (ii) the efficiency of the transducers and (iii) the characteristics of the electric circuit [144]. Moreover, two service situations can be distinguished:

- power consumption smaller than average harvested power (the device operates continuously);
- power consumption larger than average harvested power (the device operates discontinuously and an energy storage apparatus is fundamental for the device operation).

Dealing with flow-induced vibrations, the second service situation is more common, also due to the transient characteristics of natural flows. Moreover, kinetic energy transducers are needed and rely on spring-mass system (inertial transducers), being able to convert both displacement of a moving part and mechanical deformation of some structure inside the energy-harvesting device, or they depend strictly on the rate of deformation of a piezoelectric material (non-inertial transducers) [144, 156].

Hence, three different methods of mechanical-to-electric energy conversion can be identified [144, 179, 182], based on:

- *Electrostatic induction* (*e.g.* [154, 184] or the works by Miyazaki *et al.* and Sterken *et al.* cited in [182]).

  The principle relies on the relative motion between a fixed part of the transducer (fixed electrode) and a movable part (movable electrode). Constraining the electric charge

[4] Actually, this value was formulated independently by three authors: the German scientist Betz on 1920; the British scientist Lanchester on 1915; the Russian aerodynamic school leader Joukowsky on 1920. In order to honour all, this ideal efficiency should be named the 'Lanchester-Betz-Joukowsky limit' in scientific writing [209]

(or voltage) between the electrodes, the motion of the movable electrode changes the capacitance between the electrodes and thereby makes the applied voltage (or electric charge) change in proportion to the amplitude of the electrode's motion.

- *Electromagnetic induction* (*e.g.* the works by Amirtharajah and Chandrakasan, El-Hami *et al.*, Ching *et al.* cited in [182]).

  The principles relies on the Farady's law: variations of magnetic flux through an electric circuit produce electric current. This flux variation can be realized with a moving magnet whose flux is linked with a fixed coil or viceversa (the first solution is usually preferred [144]).

- *Piezoelectric effect* (*e.g.* [20, 47, 183] or the works by Ottman *et al.* and Glynne-Jones *et al.* cited in [182]).

  The piezoelectric effect (discovered by Jacques and Pierre Curie in 1880) arises if a certain material, when subjected to mechanical strain, exhibits en electrical polarization that is proportional to the applied strain. Mechanical strain depends on both the applied mechanical stress and the applied electric field, due to coupling terms in the constitutive equation of piezoelectric materials, and the electrical displacement depends on the same. A piezoelectric material mechanically stressed at a low frequency can be modelled electrically by a time-dependent charge source, that is accumulated in a capacitor [144].

When any transducer is activated, it produces both an equivalent damping into the mechanical system and a change of its oscillation frequency (*feedback effect* or *backward coupling* [108, 198]) . This is particular important in the case of piezoelectric transducers, for which the analysis has to consider the whole electro-mechanical interaction [91, 108, 132]. Anyway, the frequency modification can be neglected as compared to that of damping in the case of electrostatic or electromagnetic transducers, which essentially act as viscous generators [72, 91, 108]. Thus, the corresponding energy conversion process can be preliminary modelled through additional mechanical damping, as assumed in this work (see § 1.2.2.1).

2.3.5 Energy-harvesting systems from flow-induced vibrations

The extraction factor Γ' of Eq. (1.1) is used for the performance comparisons, allowing to include also works that did not consider the conversion apparatus, and it was evaluated from the data of the literature works if not directly reported. Furthermore, the flow power referred to the swept distance D_{sw} according to Fig. 1.3 is always used for the power normalisation.

2.3.5.1 Vortex-induced vibrations

In 2008, an important milestone of the energy-harvesting field was placed. The VIVACE project [30] demonstrated for the first time the capability of harvesting energy from vortex-induced vibrations (VIV), arising on cylinders elastically suspended and performing the energy extraction through electromagnetic transducers. VIVACE considers essentially water environments and a maximum extraction factor of 10% was verified, also through water channel tests that demonstrated the concept [28, 129]. In the experiments, the influence of the total critical damping ratio was evaluated up to a value about 27% and the effects of Reynolds number up to 10^5 was also discussed. Further theoretical investigations were recently conducted to systematically explore the parametric space and to improve the understanding of VIV-based solutions, explaining that the flow density plays a key role in the VIV-based generators [23]: the systems working with air flows are very sensitive to variations of the mass-damping parameter, being less efficient. Moreover, in the case of piezo-electric transducers in a air-based harvester, the electric load resistance strongly influenced the lock-in region [3], obtaining a widening of the width of the lock-in region with increasing it.

Continuous systems were approached too, facing the case study of tensioned cables [87]. The authors evaluated the lock-in response through a wake oscillator model [76] with respect to different distributions of the dampers along the beam (simulating the energy extraction),

confirming similar performances to the 1-DoF solution and a maximum extraction factor around 9-10%.

The same global resonant effect, as observed for piezoelectric flexible plates in axial flows [59], was investigated in 2013 for the vortex-induced vibrations of a circular cylinder when coupled with piezoelectric transducers [152]. The authors observed again that the lock-in region widens when electric load resistance increases and there is an optimal resistance for resonant condition, showing the maximum extraction factor that does not correspond to the case of largest amplitudes of oscillations.

2.3.5.2 Torsional and transverse galloping

In 1978, systematic studies on the energy production issue exploiting flow-induced excitations were started for the first time: Ahmadi explored the problem of torsional oscillations of H-shaped cross sections [11, 13, 14], talking about an aeroelastic wind energy converter. The author approached the problem from both the analytical and experimental points of view, facing for the first time the issue of how to quantify the performance of such generator. The setup considered a system without any spring but with a restoring force produced by a pendulum mechanism. The author immediately understood and highlighted the main features of energy-harvesting systems, which today have become their strongest points: [...] *although the efficiency of the model was very low, the system has the advantage of being capable of conversion of energy at very low wind speed. Furthermore, this wind energy converter is relatively simple and economical.* [...]. Indeed, low cut-in velocity, simplicity and cost-effectiveness are within the main aims of the current research. Power production through torsional vibrations was successively re-examined in 2010 [42], through a numerical approach on a wing section allowed to oscillate about its leading edge. In this case, a nonlinear elastic restoring force was considered, but the extraction factor was weakly improved up to 6%.

The first achievement on transverse galloping only dates back to 2010 [22]. The influence of several cross sections (square, isosceles triangles and D-shape) and mass-damping parameter was theoretically investigated, although showing poor extraction factors (maximum around 7%, obtained with 30°-isosceles triangle placed with the symmetry axis aligned to the flow with the corner upstream). Anyway, this paper introduced for the first time the universal plot of the performance with respect to a dimensionless flow velocity, which explains that the maximum extraction factor depends exclusively on the cross-section geometry and is independent of the mass and mechanical properties of the system. Other authors recently focused on the transducers counterpart, performing theoretical analysis within the quasi-steady assumption for the self-excited loads and exploiting both piezo-electric [4] and electromagnetic [49] transducers, looking for optimal set of electromechanical parameters.

The coupling with the transducer counterpart has recently been investigated through theoretical analyses with the quasi-steady assumption for the self-excited loads, considering both piezoelectric [4] and electromagnetic [49] transducers and looking for optimal sets of electromechanical parameters. Preliminary investigations of the fully-coupled electromechanical system for square and 2:3 (width-to-depth) rectangular sections were conducted in wind tunnel [95]. The several steps of performance indicators (as introduced in § 1.2.1) were discussed and, although the performances were very low, it was found that the optimal value of the electric load resistance is different if evaluated in terms of extraction or global factors.

In the framework of low-power generators, a viable alternative to a pure transverse galloping (although not studied yet) is the exploitation of the instability promoted by the interference of VIV and galloping. Recent discussions about this combined excitation mechanism can be found in [140, 141, 142]. Sustained vibrations can onset at low flow speed and the amplitude-velocity curves are expected to be rather independent of damping for an intermediate range of the mass-damping parameter, usually referred to as Scruton number.

2.3.5.3 Flexible plates behind bluff bodies and wake galloping

In 2001, a peculiar solution appeared, initially developed for applications in ocean currents. The concept of exploiting coherent structures contained in wake flows produced by bluff

bodies was investigated for the first time by Allen and Smith [18]. The goal was achieved through a piezoelectric membrane placed in the wake of the upstream bluff body, obtaining an extraction factor around 15% [204]. Dealing with the same concept, the influence of the shape of the upstream bluff body was also explored, considering different cross sections (*e.g.* circular, squared, exagonal, triangular, D-shaped), through numerical CFD simulations and experiments [175, 176, 177]. The particular case study of circular cross section was deeply investigated [15, 16], performing numerical simulations of the three-way coupled interaction that takes into account the aerodynamics (by Navier-Stokes equations), structural vibration (by Rayleigh-Ritz approximation), and electrical response (within the linear piezoelectricity assumption), as well as wind-tunnel experiments (including smoke-flow visualisations).

In 2009, wind-tunnel tests were conducted on two circular cylinders arranged in a tandem configuration [107]: the upstream cylinder was fixed, while the downstream one was placed at a certain distance in the wake of the former and elastically suspended to vibrate in the cross-flow direction, interacting with solenoid-based electromagnetic transducers. Thus, the energy source mechanism is the wake galloping, in which the distance between the two bodies plays a key role: in that case study it was found to be optimal 4-5 times the cross-flow dimension of the cross section [106]. Anyway, an extraction factor around 7% was experimentally obtained.

Recently, numerical CFD investigations with two turbulence models were conducted in a similar tandem configuration [56], with aim at defining the influence of the downstream cylinder arrangement on the energy-harvesting efficiency. A downstream longitudinal offset of $4D$ (D is the cylinder diameter) was found to be optimal, producing a maximum extraction factor of 10%. Moreover, if an offset of $1.5D$ is introduced also in the cross-flow direction, the capability to extract energy from the flow is improved up to 18.6%. Nevertheless, the cross-flow offset should be considered in the evaluation of the flow interacting with the tandem configuration, following the Betz analysis explained in [219]. This enlarges the area used for the flow power evaluation (P_W in Eq. (1.1)) and the actual extraction factor goes down to 14.7%. Water channel experiments were also conducted installing the downstream movable cylinder in a forced-motion rig, actively controlled to reproduce the response predicted by a VIV analytical model [26], measuring the flow-induced loads [55]. The observed performance depends on both the Reynolds number, which was varied from $2 \cdot 10^3$ to $15 \cdot 10^3$, and the phase between fluid force and oscillating cylinder. A maximum extraction factor of about 10.8% was attained (8.5% if the entire tandem configuration is considered) for configurations with downstream offset of 3.5-4.5D, cross-flow offset of 1-2D and small phase lag of 5-8°.

2.3.5.4 Flapping of 2-DoFs systems

In 1981, the effectiveness of energy production through flow-induced vibrations was definitely claimed: McKinney and DeLaurier [151] and Ly and Chasteau [138] theoretically and experimentally studied the first generator based on the flapping mechanism in an air-flow, coining the 'wingmill' concept. A wing model oscillated in vertical motion driven by a prescribed pitching angle, without any elastic support. Their solution showed an extraction factor around 17% at low wind-speed, competitive to the dam-turbines of that time. After 20 years, Jones and Platzer [105, 103] systematically explored the parametric space through numerical investigations based on the panel method that were compared with water channel tests, attesting the high extraction factor of this typology of systems around 26%. They also tried to define preliminary guidelines for the design of flapping systems and highlighted the importance of controlling, among the governing parameters, the maximum effective angle of attack achieved during the motion. Other investigations on 2-DoF NACA-0015 hydrofoils were extensively conducted through unsteady two-dimensional laminar-flow simulations using a finite volume CFD code and implementing a rigid-body mesh rotation in combination with a non-conformal sliding interface [110]. After discussing the inadequacy of the quasi-steady approach to study this unsteady problem, the work focused on the mapping of the energy-harvesting capability with respect to the reduced frequency of oscillation and pitching amplitudes (up to 90°). The investigations were restricted to a Reynolds number around 10^3, imposing the heaving amplitude equal to the section chord and the elastic axis fixed

upstream at one third of the chord. Extraction factors above 20% were observed for pitching amplitudes larger than 55°, which rose up to 34% for a maximum pitching amplitude of 76.3° and a frequency of $0.14U/B$ (B is the chord section and U the free-stream flow speed). Geometry and viscous parameters only weakly affected the results.

In 2008, hydrodynamic experiments [193] demonstrated an extraction factor of about 35% obtained with NACA-0012 hydrofoils with an aspect ratio of 7.9, performing harmonic motion in the two DoFs, at a Reynolds number of about $1.4 \cdot 10^4$, reduced velocity of about 14 and maximum pitching amplitude of about 34°. The motion parameters were continuously controlled to impose a motion phase of 90° and a heaving amplitude of 1.23 times the section chord. Decreasing the aspect ratio the performance was found to decrease. The efficiency was estimated without subtracting from the output energy the work done to drive the motion, which was relatively small at the highest efficiency point but which can become orders of magnitude higher depending on the motion parameters. Further parametric experimental investigations were recently conducted for a NACA-0012 hydrofoil vertically mounted in a specific device comprising an arms/gears mechanism that reproduced the heaving motion by means of rotations about a shaft [100]. In this system, the pitching motion was externally driven and the phase was directly adjusted by the device mechanism. A rotational viscous damper (dashpot) was used to simulate the energy converter. A maximum extraction factor of about 22% was found for a Reynolds number around $4.5 \cdot 10^4$.

An alternative solution for 2-DoF flapping systems was conceived in 2003 by Isogai *et al.* [102], who introduced for the first time an elastic suspension in the translational DoF, developing semi-active (or semi-passive) systems. The rotational DoF continued to be externally driven, in particular prescribing frequency and maximum amplitude, while the translational amplitude naturally adjusted according to the lifting load. After parametric numerical analyses and optimisations, conducted using a multi-objective evolutionary algorithm based on adaptive neighbouring search, a maximum extraction factor around 32% was predicted [191]. Further studies considered other variations on the flapping mechanism. In the work of Zhu *et al.* [222], the models included a pitching actuator and a damper support (without stiffness) in the heaving DoF. Both 2D and 3D numerical investigations using a Navier-Stokes solver were conducted investigating different aspect ratios (2 and 10) and cross sections (NACA-0005 and -0025), providing a maximum extraction factor of 25%. Subsequently, combining a two-dimensional asymptotic model based on the thin-plate approximation [205] and a three-dimensional boundary-element approach, a spring-dashpot model of the generator was used to map its performance with respect to mechanical and kinematic operational parameters [223]. The energy extraction process was idealized as a viscous damper. This model was improved solving the Navier-Stokes equations for Reynolds numbers around 10^3, in order to consider also the effects of the leading edge separation and the eddy detachment [223]. The results show that, when periodic pitching and heaving motions are performed, energy extraction at low values of the reduced flow velocity is possible, depending on the imposed pitching amplitude. Moreover, an optimal value of the damping coefficient was found, achieving a maximum extraction factor around 20% when the elastic axis is close to the hydrodynamic centre of pressure. Recently, Young *et al.* [216] conducted numerical CFD studies on a NACA-0012 model, simulating the motion according to different experimental setups. In particular, pitching-amplitude (four-bar linkage [114] and passive reversal-stroke [173] devices) or angle-of-attack (active pitching-control device [99, 193]) motion control techniques were considered, being representative of the typical supporting mechanisms for flapping systems. In the studied systems, a four-bar linkage mechanism for the pitching-heaving motion was considered with a purely passive flywheel (with null stiffness in both DoFs), in which the motion frequency was strongly dependent on the flow structures around the oscillating body [79]. Modifying the analytical model to include also the others control techniques, the higher energy extraction capability was obtained for angle-of-attack-controlled motion, supporting the results in [193]. Morevoer, with the aim at modelling more real flapping systems installations, the influence of the flow turbulence was preliminary investigated in [216] through Reynolds-averaged Navier-Stokes turbulence models, showing that the performance was slightly reduced in the case of low-turbulent flow at high Reynolds number ($Re = 1.1 \cdot 10^6$).

Over the years, more complex solutions were also proposed. A tandem configuration of flapping wings, placed at a certain distance in the streamwise direction and oscillating in quadrature thanks to a specific mechanical device composed by supporting arms and gears, was experimentally studied in water flows [104]. In that work, the problem was also numerically simulated through a modified panel code based on potential-flow theory, working in combination with a boundary layer code [105]. Further numerical and experimental investigations on a similar tandem configuration of hydrofoils confirmed efficiencies around 30% [111, 114]. On the basis of this experimental setup, a deeper numerical 2D-URANS study discussed the role of the distance between the upstream foil and that oscillating in its wake [112]. Favourable interactions between downstream foil and wake vortices seem to lead to theoretical extraction efficiencies up to 63%, if estimated for the ensemble of foils. Although the individual efficiencies of the foils were of about 30-35% (the downstream one is usually less efficient), the total performance may be considered as the sum, since the tandem configuration involves the same swept area for the upstream and downstream foil (see also [219] for a discussion about the Betz analysis of flapping systems). Numerical analyses were also conducted combining multiple foils in array arrangements [101] and evaluating the optimal phase shift between adjacent oscillating elements as well as their cross-flow distance, reaching extraction factors in the range 23-31% in the case of anti-phase mode of oscillation and adjacent wings at 2.5-3.0 chord-length distance.

Very recently, a NACA-0015 model with a flexible tail attached at its trailing edge was studied as a possible solution to enhance the performance [213]. Two-dimensional numerical simulations were conducted by setting an activated sinusoidal pitching DoF and an heaving motion component obtained by solving the flow-induced vibration problem. The pitching axis was located 1/3-chord downstream the leading edge and a damper was included in the heaving DoF to simulate the conversion apparatus. Effects of mass and flexibility of the tail, modelled as a continuous elastic plate, and of the pitching frequency were discussed for a laminar flow at $Re = 1100$. As compared to the case of rigid tail, a highly flexible tail can improve the performance, since the lifting load is increased due to the tail participation in the vortex-shedding mechanism. Another technological development of flapping systems considered the possibility to actively control the shape of the oscillating body [207]. In particular, the camber line of an airfoil cross-section was modified in time to be an arc of circle, with sinusoidal magnitude of the circle radius and parametric phase difference with respect to the pitching DoF [98]. The study was conducted though numerical CFD simulations, selecting a Reynolds number of 1100, and the power required to drive the camber deformation was taken into account in the evaluation of the extraction factor. In the case of constrained sinusoidal motion of a NACA-0015 model, imposing 76.33° of maximum pitching amplitude and 90° of heaving-to-pitching phase (following [110]), performance enhancements were obtained for camber deformation phases in a small range about 135°. At that value, a maximum relative efficiency increase of 7.5% was achieved. Furthermore, a semi-passive configuration was also investigated, considering the four-bar linkage mechanism with the circular flywheel to support both heaving and pitching DoFs, following a previous work [216] (more details on this setup can be found in [114]). The numerical results about a NACA-0012 section with pitching axis in the midchord position and $Re = 1100$ pointed out a small region of favourable effects, in which a maximum efficiency increase of 18.7% can be obtained in correspondence of a camber-line deformation phase of -157.5°.

Flapping bodies with cross section different from the airfoiled shape were investigated only by Matsumoto *et al.* in 2006 [147], who applied the concept of Isogai and co-workers to rectangular cross sections with 5 and 20 width-to-depth ratios. Theoretical and experimental investigations were focused on the assessment of the energy extraction opportunity either on the heaving or pitching DoF, working at Reynolds numbers of $4{\cdot}10^3$. The system was studied by means of a forced-motion setup, imposing a specific motion in one DoF at a time, and the extracted power was estimated through the measurement of forces and displacements. The results showed that the energy extraction in the heaving motion is more rentable. Indeed, the amount of the work done to drive the pitching motion is smaller and can be overcome at lower flow speed by the lift work. Finally, they investigated two levels of heaving damping (simulating the operation of the conversion apparatus) and suggested for the first time the

use of active flaps installed at the leading edge to control the flow around the section as possible solution to enhance the performance.

Finally, more information about the flapping-foil technology up to the end of 2013 can be found in two recent review papers focused on this specific topic [215, 217].

2.3.5.5 Classical flutter of 2-DoFs systems

In 1945, Duncan talked about a 'flutter engine' [65] during his fundamental study of flutter. However, this was the first machine constructed to scientifically discuss the flutter phenomenon and not for energy generation purposes.

Solutions essentially based on the classical flutter phenomenon were investigated only starting from the period 2009-2011. The starting point may be identified in the works of Bryant and Garcia in 2009 [36, 37], who preliminary explored the exploitation of aeroelastic vibrations of a NACA-0012 wing model attached to a cantilever beam with embedded piezo-patches. Consequently, they continued to study the problem through semi-empirical nonlinear models based on the finite state theory [170], performing also an experimental campaign, and predicted high extraction factors in the range of 32-42% [38, 39, 40].

Basing on the work of Bryant and Garcia, Ertuk *et al.* [75] experimentally investigated the theoretical critical condition for a 2-DoF sectional model of an airfoil with piezoelectric transducers embedded in the supporting elastic structures (cantilever beams), activating the energy extraction in the heaving DoF. The analytical modelling of the problem was also performed considering the fully coupled fluid-solid-electric system and the instability threshold was preliminarily investigated with respect to electric resistance variations. The same experimental setup was also investigated introducing nonlinearities in the mechanical support [196] and the results were compared with those of a theoretical state-space model for the unsteady loads, formulated according to [69]. It was found that a free-play gap (discontinuous stiffness, with a null value in a finite range about the rest position, producing a bilinear behaviour) in the pitching DoF can slightly anticipate the instability onset for some sets of parameters and allows limit-cycle oscillations also below the critical threshold. Moreover, combining this nonlinear effect with a cubic hardening rotational stiffness can limit the growth of the oscillation amplitude with the flow speed. The results about nonlinear stiffness were based on previous studies for civil/aeronautical design applications [61, 64], which were also carefully examined in [21] by means of numerical stability analyses based on root-locus and time-integration methods. An investigation of the electric resistance effect was also performed in [196].

De Marqui *et al.* [52, 53] continued studying piezo-aeroelastic solutions developing a specific electromechanically coupled finite element model combined with an unsteady aerodynamic model based on the vortex-/doublet-lattice method, thus achieving a complete piezo-aeroelastic model. They performed theoretical analyses through a state-space model with unsteady loads expressed according to the Jones's approximation of Wagner's function [84], calibrating the governing parameters based on the experimental campaign of Sousa *et al.* [196]. They discussed the capability of energy production through two different conversion methods, namely piezo-elements as in the previous cases and/or electromagnetic transducers in the heaving DoF. The analyses were conducted varying frequency ratio, electric load resistance, equivalent capacitance and electro-mechanical coupling factor [51]. Then, they also extended the investigations to the radius of polar inertia and position of the mass centre [57]. Finally, the possibility to introduce a control surface (flap) at the trailing edge was recently evaluated through analytical investigations[58], leading to the study of a 3-DoF (hybrid) piezo-inductive aeroelastic system. This solution increased considerably the complexity of the system, also increasing the number of optimisation variables. As compared with that of the 2-DoF solution [57], a weak improvement of the performance was achieved in a small region of the parametric space.

In parallel to these studies and between 2012 and 2014, the Abdelkefi's research team explored several similar problems about piezo-aeroelastic wing models, with piezo-electric elements installed in the translational DoF (*e.g.* [1, 2, 6, 7, 8]). They essentially investigated the nonlinear features of the system by means of theoretical analyses based on a quasi-

steady stall model [199] to describe the self-excited loads. In particular, they discussed the occurrence of sub-critical or super-critical limit-cycle oscillations (related to 'dangerous' or 'safe' Hopf bifurcation) in the design of such energy harvesters. In addition, they explored the possibility of anticipating the critical threshold through a suitable choice of the nonlinear pitching/heaving stiffness, considering a polynomial expansion of the force-displacement curve of at least second order. The width of a free-play gap (modelling and identification of these nonlinear effects were additionally discussed in [9]) and the distance of the centroid from the elastic axis were also investigated. A local minimum of the critical flutter speed was found for downstream mass eccentricity in the range between 7 and 10% of the chord, depending on the set of parameter and electric road resistance [7]. The same type of analysis was carried out in [1], focusing on the heaving stiffness, previously considered linear, and implementing a three-dimensional unsteady vortex lattice method to study the system response.

It is worth discussing a particular case of simplification of the semi-active (or semi-passive) flapping mechanism explained in § 2.3.5.4. Indeed, it was reduced to a fully passive flow-induced excitation mechanism, that is spontaneous flutter. Numerical investigations were conducted for a rigid hydro-foil model supported by a spring in the pitching DoF and just a damper in the heaving DoF [167]. Depending on the elastic axis location and pitching frequency, the system was found to oscillate about different equilibrium states, including irregular motions. In particular, periodic motion were observed for elastic axis positions between -0.2 and 0.5 times the chord (positive if aft the midchord) and the energy performance was almost constant for the elastic axis positions close to the midchord. An extraction factor of 20% was estimated in optimal conditions. Moreover, the capability of such system to extract energy was also numerically investigated in a linear shear flow [221].

Afterwards, the same authors investigated the relationship between flapping frequency and frequency of the wake vortices [220], stating that an extraction factor around 30% can be obtained when the system oscillates at a frequency of $0.15U/B$ and the two frequencies approach each others. In addition, the maximum pitching amplitude should reach 90°.

2.3.5.6 Classical flutter of continuous systems

In 2009, a fluttering 'belt' concept was patented by Frayne [81]. The system considers a flexible thin strip clamped at the ends, in which permanent magnets are embedded in the sections close to the ends and interact with a fixed coil. At the same time, this system was theoretically and experimentally explained [77, 78], although the electromagnetic transducers were placed in a different position with respect to that one considered in the patent.

2.3.5.7 Fluttering flexible plates in axial flows

During 2007-2009, another alternative and promising idea was developed by Tang *et al.* [201, 203]: the 'flutter windmill'. A cantilever flexible plate in axial flow was numerically and experimentally investigated, modelling the flow-induced forces through an unsteady lumped vortex model [202]. The energy production process considered electrostatic transducers placed along the plate and the predicted extraction factor was about 10%. This typology of systems can show a compact technological design, but high critical flow velocity was usually remarked, leading to applications in specific real cases in which the high speeds are verified. Few years later, a technological step was reached by Dunnmon *et al.* [68] and Doaré and Michelin [59] introducing piezoelectric patches, directly installed along the plate. The former investigated numerically, through a discretized vortex-lattice potential flow model, and experimentally the case with a single piezo-patch at a certain position along the plate, achieving a maximum extraction factor around 17%. On the other hand, Doaré and Michelin [59] assumed distributed piezo-patches in symmetric pairs along the upper and lower side. They performed accurate theoretical investigations to evaluate the fluid-solid-electromagnetic interaction on flexible plates in axial flow, adopting the extension of Lighthill's elongated body theory [134] to large-amplitude displacements in order to model the flow-induced forces. This work explained, for the first time, enhancements of the extraction factor at the global resonant condition, reached when the characteristic time of the electric circuit is close to that

one of the mechanical system. Consequently, further developments were reached [155, 194], optimizing the piezoelectric distribution along the plate and stating that discrete distributions are more powerful. A maximum extraction factor around 20% was achieved.

Further studies confirmed the possibility to produce energy from flexible plates in axial flows through piezo-patches. Deep numerical investigations, based on the immersed boundary approach coupled with a finite volume solver for incompressible, viscous flow, was performed in 2012 [17], also considering the effects of large beam deformation, membrane tension, and coupled electromechanical responses. Moreover, the authors discussed the differences between heavy plate in light flow and viceversa, stating that the former leads to configurations that become unstable at lower reduced velocities, involving the 2^{nd} mode of vibration and producing complex wake patterns and larger amplitudes. Finally, they pointed out the importance of evaluating the strain in the piezoelectrics during oscillations, which may exceed the limit as observed in their studies. A simplified approach that considered a bi-articulated, cantilever beam (representing the two-dimensional problem of a discrete flexible plate) was also presented [195]. The authors parametrically studied through a theoretical, nonlinear, reduced-order model the energy extraction capabilities, which was simulated by concentrated dampers in the joints.

2.3.5.8 Others

For the sake of completeness, it is worth mentioning that very particular solutions were recently explored, mainly based on piezo-electric transducers (*e.g.* [5, 94, 124, 125, 133, 197]) which received increasing interest during last years. Among them, a particular case study [97] studied flexible plates with embedded piezo-patches that were installed in the cross-flow direction, investigating the concept or 'piezoelectric grass', specifically developed for turbulent flow environments. Furthermore, a peculiar solution exploiting electromagnetic transducers is also remarkable [212]. All these recent studies try to explore innovative systems and confirm the constantly developing characteristics of the research topic about energy harvesting from flow-induced vibrations.

2.3.6 Summary of main achievements and comparisons

Considering literature studies can be classified combining the typology of mechanical system with the fluid-elastic phenomenon (as reviewed in § 2.2) and considering the conversion apparatus technology (see Table 2.1).

A more specific classification is reported in Table 2.2, which compares the main achievements also in terms of performance considering the extraction factor Γ'.

Table 2.1. Summary of the research studies subdivided according to the vibrating system, the relative excitation mechanism and the transducer technology (if specified).

System	Excitation mechanism	Transducer technology			
		Electrostatic	Electromagnetic	Piezoelectric	Undefined
1-DoF	Vortex-induced vibrations		[30]	[3, 152]	[23]
	Transverse galloping		[49, 95]	[4]	[22]
	Rotational galloping				[11, 13, 14, 42]
	Wake galloping		[106, 107]		[55, 56]
	Flapping (passive)		[111, 114]		[103, 138, 151, 216]
2-DoF	Classical flutter		[57, 58]	[36, 37, 38, 39, 40, 75] [21, 196] [51, 52, 53, 57, 58] [1, 2, 6, 7, 8]	[167, 221]
	Flapping (active)				[105, 110, 113, 193] [104] [98, 207, 220]
	Flapping (semi-active)				[101, 102, 191, 222, 223] [100] [98, 216] [213] [147]
	Axial-flow excitations				[195]
∞-DoF	Vortex-induced vibrations				[87]
	Classical flutter		[77, 78, 81]	[214]	
	Wake-flow excitations			[15, 16, 18, 175, 176, 177, 204]	
	Axial-flow excitations	[201, 203]		[17, 59, 68, 155, 194]	
Others			[212]	[5, 94, 97, 124, 125, 133, 197]	

Table 2.2. Main energy-harvesting system achievements, comparing the performances and the considered fluid ('a' stands for air, 'w' for water) and the type of investigation performed. Technologycal investigation means that the whole electromechanic system has been taken into account, modelling also the conversion apparatus. The marker '-' is inserted for not specified/inferable features.

Ref.	Year	Basic mechanism	Features		Investigation			
			Fluid	*Extraction factor*	*Analytical*	*Computational*	*Experimental*	*Technological*
[13], [12]*	1979	Torsional galloping of H-shaped section	a	2%	•		•	
[151]	1981	Flapping wing 2-DoF (active)	a	17%	•		•	
[103], [173]*	1999	Flapping wing 2-DoF (active)	w	26%		•	•	
[18, 204], [43]*	2001	Flexible plate behind a bluff body	w	15%	•	•	•	•
[102, 191]	2003/04	Flapping wing 2-DoF (semi-active)	a	32%	•	•		
[201, 155]	2007/13	Flexible plate in axial-flow	-	10-20%	•		•	•
[110, 193]	2008	Flapping wing 2-DoF (active)	w	34-35%	•	•	•	
[30], [29]*	2008/09	Lock-in resonance of cylinder	w	10%	•		•	•
[222]	2009	Flapping wing 2-DoF (semi-active)	w	25%	•	•		
[167]	2009	Fluttering wing 2-DoF	w	20%	•	•		
[22]	2010	Transverse galloping of triangular section	a	7%	•			
[42]	2010	Torsional galloping of wing section	a	6%	•	•		
[38, 40, 39]	2011/13	Fluttering wing on cantilever beam	a	32-42%	•	•	•	•
[106]	2011	Wake galloping of cylinders	a	7%	•		•	•
[101]	2012	Flapping multi-wings 2-DoF in array (active)	w	31%	•	•		
[111, 112]	2012	Flapping two-wings 2-DoF in tandem (active)	w	40-63%	•	•	•	
[78], [81]*	2012	Fluttering belt	a	-	•		•	•
[23, 87]	2012	Lock-in resonance of cylinder	w	9-10%	•			
[56, 55]	2014/15	Wake galloping of cylinders	w	8-14%	•	•	•	

(*) patent

2.3.7 Discussion about main features

The first observation concerns the density of the flowing fluid: for a given value of the extraction factor, the higher is the density, the higher is the power output. Thus, water-installations are supposed to be more powerful than air-installations, although they require more specific and complex technological solutions for the water environments. Moreover, it is worth noticing that a given device may not work simply in both air and water environments, because the important fluid difference, density (mainly) and viscosity, plays a key role in the development of the physical exciting mechanism itself and can alter both the operative range of reduced velocity and amplitudes of the motion.

In case of spontaneous phenomena due to fluid-elastic instability, some active or better passive solution should be provided to limit the maximum amplitudes and prevent structural failure, *i.e.* in case of galloping and (in particular) flutter. Among passive precautions, designing a stiffness term with hardening behaviour could be an interesting field to investigate. By contrast, excitation mechanisms due to turbulent wake from an upstream bluff body (*e.g.* wake galloping) or lock-in resonance mechanisms (*e.g.* VIV) usually show amplitudes of oscillation that are limited or vanish with increasing the flow velocity (see Fig. 2.3). This would avoid control system if the system is well-designed to be operative in a specific condition.

The state of the art revealed that the most performing solutions are those based on 2-DoF systems, so that flutter or flapping systems (see Table 2.2). Due to the presence of 1-DoF, at least, in the motion that is not affected by the operation of the conversion apparatus, the motion can be easier self-sustained. However, it is worth remarking that in the studies where the conversion apparatus was not directly modelled, the equivalent damping of a simulated energy extraction process has not always been considered and the actual amount of energy that can flow in the conversion apparatus is not quantifiable. Moreover, some works about flapping systems do not quantify the external work necessary to drive the pitching motion, although it is usually small compared to the extracted one when designing highly efficient configurations [193, 147].

Especially in the case of flutter, piezo-electric transducers have been recently preferred in order to develop low-powering solutions with compact design. Anyway, flapping systems received more attention along the years and they achieved the highest technology readiness level, as also demonstrated by the 'Dual Wing Generator' prototype of Festo[5]. Flapping systems usually involve electromagnetic transducers or directly produce mechanical energy (*e.g.* propulsion [146, 218]). Among the other solutions, flexible plates in axial flows showed remarkable performances, while the other excitation mechanisms based on 1-DoF motion seem to be not able to achieve high efficiency. Nevertheless, the exploitation of galloping, VIV or wake-induced excitations can lead to more cost-effective solutions, since 1-DoF technology is simpler than 2-DoF technology.

2.3.8 Open issues of interest

The following open issues can be identified and listed according to a priority criterion:

1. *Enhancement of the extraction factor.* Studying of the most efficient way to extract as much as possible energy from a given flow condition;
2. *Control of the cut-in velocity and of the operative range.* Understanding of the governing parameters influence and the most effective way to anticipate it, including the evaluation of fatigue-induced effects to safeguard the system serviceability;
3. *Turbulence effects of real flows.* Understanding of the influence of the turbulence-induced effects on the energy-harvesting mechanism and the way to safeguard the performance, considering the real flow properties acting on typical installations.
4. *Transient conditions of the mean flow velocity.* Evaluation and mitigation of the transient effects due to the non-stationary properties of real flows on the system response and development of specific energy storage apparatus.

[5] https://www.festo.com/group/en/cms/10222.htm

5. *Array configurations.* Possibility of arranging several systems in arrays (in parallel or series and vertical or horizontal dispositions), identifying the suitable configurations and the key parameters to enhance the global performance of a given module.

6. *Environmental impact assessment.* Assessment of the acoustic emissions of the system according to the comfort criteria of potential installation environments, as well as the electromagnetic emissions due to the energy transformation process.

2.3.9 Scientific aspects of post-critical flutter experiments

The studies about energy-harvesting systems exploiting classical flutter of § 2.3.5.5 are close to the topic of the present thesis and further considerations about the reliability of the experiments are necessary. In fact, since the generator need to oscillate in the post-critical regime, those studies can be also considered to supply scientific information about the post-critical flutter mechanism. However, from the scientific point of view, few reliable results are available in literature because few research works have been specifically conducted on this topic (*e.g.* [19]).

The setup of Bryant *et al.* (*e.g.* [38]) was not suitable for accurate LCO measurements, since it was only devised to the energy-harvesting purpose. The model had a span-to-chord ratio of 2.3 and endplates were not installed to ensure two-dimensional flow conditions. Moreover, the single-beam elastic support introduced an angle of attack due to the rotation of the tip of the cantilever beam during bending deflections.

From the scientific point of view about post-critical flutter, the setup developed by Sousa *et al.* [196] was not specifically devised to allow large oscillation amplitudes (no larger than 16% of the chord), but only to investigate the critical threshold and the effect of artificial nonlinearities in the pitching stiffness. Moreover, end-plates were not installed to enforce two-dimensional flow conditions and the model had a low aspect ratio of 2, jeopardizing the reliability of post-critical regime measurements.

Chapter 3

Two-degree-of-freedom classical flutter

3.1 Problem modelling

All the branches of classical physics, characterised by low-speed motion with respect to the light speed and large length scale with respect to the atomic scale, follows the same fundamental laws (continuity equation, cardinal equations, constitutive equations, energy balances). This thesis takes place in the branch of classical mechanics and, in particular, focuses on continuum mechanics of Newtonian fluids and linear elastic solid systems.

For dynamic continuum systems, the state-space equation is a second-order, differential equation respect to the time, as derived from the second principle of dynamics (Newton's Law and/or the following extensions of D'Alambert's and Hamilton's principles [86, 153]). The approach can be adapted to work correctly with both continuum and discrete systems. Moreover, a body that does not change shape (and volume), namely a *rigid body*, can be regarded as a discrete system with finite DoFs (generally six: three translations and three rotations) even if it is assumed to be continuous. In case of a continuous system that can change shape (and volume), namely *elastic body* with distributed elasticity, it has infinite DoFs. However, specific decomposition techniques (usually based on modal dynamic analysis if certain assumptions are verified) can reduce a continuous system with ∞^n DoFs (for n-dimensional body) into ∞^n sub-systems of one DoF.

In the present thesis, the dynamic modelling refers to the motion of the structural body, while the fluid system is indirectly considered through the actions exchanged along the interface due to fluid-elastic interaction (see Fig. 3.1). The structural body is considered rigid, with fixed shape, and the elasticity and damping parameters are concentrated in a specific point (centre of elasticity, EC) linked to the body. The fluid system is modelled according to common methods of fluid mechanics and it produces non-conservative actions on the structure, resulting from the pressures distribution along the boundary. The following flow-induced loads usually can be concentrated to act in a specific point of the structural body (centre of fluid-dynamic loads, FC).

3.1.1 General 2nd-order differential equation

Within the assumption of holonomic constraints, the system motion can be described, at any time t, by independent *generalised coordinates* $\mathbf{q}(t) = \{\mathrm{q}_k(t)\}$.

Extending the generalised principle of D'Alamber to a variational approach over the time interval $[t_1, t_2]$, the extended Hamilton's principle states that

$$\int_{t_1}^{t_2} (\delta\mathcal{T} + \delta\mathcal{W})\ dt\ = 0 \quad , \quad \forall\ \delta\mathrm{q}_k\Big|_{t_1}^{t_2} = 0\ , \tag{3.1}$$

where $\delta\mathcal{W} = \delta\mathcal{W}(\mathrm{q}_k)$ is the virtual work of all the forces acting in the system and $\delta\mathcal{T} = \delta\mathcal{T}(\mathrm{q}_k, \dot{\mathrm{q}}_k)$ is the virtual kinetic energy of the whole system, both corresponding to the virtual

increments δq_k. Moreover, the work can be decomposed in a conservative part $\mathcal{W}_C$, which admits an associated potential form $\Pi = -\mathcal{W}_C$ (or potential energy), and a non-conservative part $\mathcal{W}_{NC}$ that verifies $\delta\mathcal{W}_{NC} = \sum_k \mathcal{Q}_k \delta q_k$, in which $\mathcal{Q}_k$ is the generalised non-conservative term. Thus, Eq. (3.1) becomes

$$\int_{t_1}^{t_2} \sum_k \left(\frac{d}{dt}\frac{\partial \mathcal{T}}{\partial \dot{q}_k} - \frac{\partial \mathcal{T}}{\partial q_k} + \frac{\partial \Pi}{\partial q_k} - \mathcal{Q}_k \right) \delta q_k \; dt \; = 0 \tag{3.2}$$

and, since the arbitrariness of δq_k, Eq. (3.2) is verified if and only if

$$\frac{d}{dt}\left(\frac{\partial \mathcal{L}}{\partial \dot{q}_k}\right) - \frac{\partial \mathcal{L}}{\partial q_k} = \mathcal{Q}_k \quad , \quad \forall \; k \; , \tag{3.3}$$

being $\mathcal{L} = \mathcal{T} - \Pi$ the lagrangian function. Generalised friction forces $\mathcal{D}_k$, so far omitted due to the holonomic constraints assumption allowing reversible virtual displacements, can be added through a contribution to the non-conservative part in the form of the Rayleigh's dissipation function $\mathcal{F} = \mathcal{F}(\dot{q}_k)$ [86], within the following assumption

$$\mathcal{D}_k = -\frac{\partial \mathcal{F}}{\partial \dot{q}_k} \; , \quad \forall \; k \; . \tag{3.4}$$

This leads Eq. (3.3) to the general form

$$\frac{d}{dt}\left(\frac{\partial \mathcal{L}}{\partial \dot{q}_k}\right) - \frac{\partial \mathcal{L}}{\partial q_k} = \mathcal{Q}_k + \mathcal{D}_k \quad , \quad \forall \; k \; . \tag{3.5}$$

The solution of Euler–Lagrange's equations of the 2$^{\text{nd}}$-type, Eq. (3.5), describes the true path of the evolution of the system response, which generally has a nonlinear behaviour. However, within the interest of identifying an equilibrium position $\mathbf{q_e}$, and the assumption of small amplitudes perturbation ($\tilde{\mathbf{q}}$), the problem can be linearised according to:

$$q_k(t) = q_{e_k} + \tilde{q}_k(t) \; ; \tag{3.6a}$$

$$\dot{q}_k(t) = \dot{\tilde{q}}_k(t) \; . \tag{3.6b}$$

Then, the kinetic and potential energies can be expressed in Taylor expansions, truncated to $\mathcal{O}\left(\tilde{\mathbf{q}}^2, \dot{\tilde{\mathbf{q}}}^2\right)$:

$$\mathcal{T} \cong \frac{1}{2}\sum_k \sum_h \frac{\partial^2 \mathcal{T}}{\partial \dot{q}_k \partial \dot{q}_h}\Big|_{\mathbf{q}=\mathbf{q_e}} \dot{\tilde{q}}_k \dot{\tilde{q}}_h = \frac{1}{2}\dot{\tilde{\mathbf{q}}}^T \mathbf{M} \dot{\tilde{\mathbf{q}}} \; ; \tag{3.7}$$

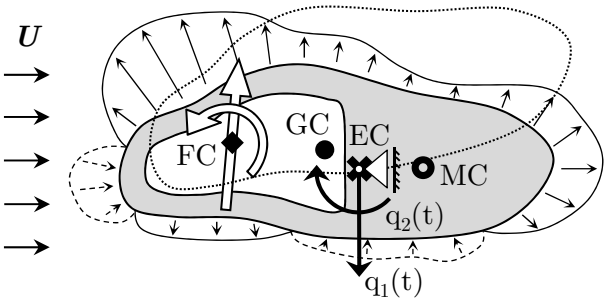

Figure 3.1. General two-dimensional fluid-structure interaction problem, with 2-DoFs (q_1, q_2). The pressure distribution along the body surface gives a resultant force at the fluid-dynamic centre (FC). The centre of geometry (GC) may not coincide with the centre of mass (MC), *e.g.* in case of cavity or non-homogeneous material. The body motion is about the elastic centre (EC), where the mechanical properties are concentrated.

$$\begin{aligned}\Pi &\cong \Pi(\mathbf{q_e}) + \sum_k \frac{\partial \Pi}{\partial q_k}\Big|_{\mathbf{q}=\mathbf{q_e}} \tilde{q}_k + \frac{1}{2}\sum_k\sum_h \frac{\partial^2 \Pi}{\partial q_k \partial q_h}\Big|_{\mathbf{q}=\mathbf{q_e}} \tilde{q}_k \tilde{q}_h = \\ &= \Pi(\mathbf{q_e}) + \sum_k \frac{\partial \Pi}{\partial q_k}\Big|_{\mathbf{q}=\mathbf{q_e}} \tilde{q}_k + \frac{1}{2}\tilde{\mathbf{q}}^T \mathbf{K} \tilde{\mathbf{q}} \ .\end{aligned} \tag{3.8}$$

In the case of linear viscous forces, the Rayleigh's dissipation function follows the quadratic form

$$\mathcal{F} \cong \frac{1}{2}\sum_k\sum_h \frac{\partial^2 \mathcal{F}}{\partial \dot{q}_k \partial \dot{q}_h}\Big|_{\mathbf{q}=\mathbf{q_e}} \dot{\tilde{q}}_k \dot{\tilde{q}}_h = \frac{1}{2}\dot{\tilde{\mathbf{q}}}^T \mathbf{C} \dot{\tilde{\mathbf{q}}} \ , \tag{3.9}$$

which implies symmetric coefficient in $\mathbf{C}$.

The combination of Eqs. (3.7)-(3.8)-(3.9) in (3.5) leads to the linearised version of the Lagran's equations:

$$\sum_h \left(m_{kh} \ddot{\tilde{q}}_h + c_{kh} \dot{\tilde{q}}_h + k_{kh} \tilde{q}_h \right) + \frac{\partial \Pi}{\partial q_k}\Big|_{\mathbf{q}=\mathbf{q_e}} = \mathcal{Q}_k \quad , \quad \forall k \ . \tag{3.10}$$

Eq. (3.10) is composed by a constant part (expected mean value) and a small perturbative part (fluctuating value). Separating them, the *equilibrium equations* are

$$\frac{\partial \Pi}{\partial q_k}\Big|_{\mathbf{q}=\mathbf{q_e}} = \mathcal{Q}_{k,m} \quad , \quad \forall k \ , \tag{3.11}$$

and the *linearised equations about the equilibrium positions* are

$$\sum_h m_{kh} \ddot{\tilde{q}}_h(t) + c_{kh} \dot{\tilde{q}}_h(t) + k_{kh} \tilde{q}_h(t) = \mathcal{Q}_k(t) - \mathcal{Q}_{k,m} \quad , \quad \forall k \ . \tag{3.12}$$

The characteristic 2$^{\text{nd}}$-order differential equations (3.12), within the assumption of small perturbations about the equilibrium position, can be expressed in the matrix form

$$\mathbf{M}\ddot{\mathbf{q}}(t) + \mathbf{C}\dot{\mathbf{q}}(t) + \mathbf{K}\mathbf{q}(t) = \mathbf{Q}(t) \ , \tag{3.13}$$

where the over-tildes are omitted and the non-conservative term is assumed to be zero-mean, for simplicity of notation.

In the classical mechanics field, the coefficients $\mathbf{M}$, $\mathbf{C}$ and $\mathbf{K}$ are, respectively, the mass, damping and stiffness[1] matrix and, in most applications, they are independent on time and on the system response (constant coefficients). $\mathbf{Q}(t)$ represents the generalised external forcing term. Since closed systems[2] are usually considered in classical mechanics, the external action is linked to the energy that the environment exchanges with the system. In the case of fluid-elastic interaction, it explains the flow-induced loads acting on the structural system and its more general form takes into account also the dependence on the system response,

$$\mathbf{Q} = \mathbf{Q}\left(\mathcal{J}\{\mathbf{q}(t)\}, t\right) \ , \tag{3.14}$$

through the linear operator $\mathcal{J} : \mathbf{q}(t) \mapsto \mathcal{J}\{\mathbf{q}(t)\} \in \mathbb{R}^3$ that usually involves time derivatives[3].

In addition, some of the mechanical coefficients can show out-diagonal terms (non-diagonal matrices). Hence, the final differential equations (as much as the number of

[1] The stiffness term $\mathbf{K}\mathbf{q}(t)$ can be generally represented by $\mathcal{G}\{\mathbf{q}(t)\}$, suitable for the continuous approach, where $\mathcal{G} : \mathbf{q}(t) \mapsto \mathcal{G}\{\mathbf{q}(t)\} \in \mathbb{R}^3$ is a linear operator which describes the kinematic deformation of the body and involves spatial derivatives of the potential elastic energy.

[2] Variations of energy between the system and the environment are allowed; variations of mass between the system and the environment are not allowed.

[3] The term $\mathbf{Q}\left(\mathcal{J}\{\mathbf{q}(t)\}, t\right)$ can be replaced by $\mathcal{A}\left\{\mathcal{J}\{\mathbf{q}(t)\}, t\right\}$, where $\mathcal{A} : \mathbf{q}(t), t \mapsto \mathcal{A}\{\mathbf{q}(t), t\} \in (\mathbb{R}^3 \times \mathbb{R}^+)$ is a linear operator (called *fluid-dynamic operator* [32]) that takes into account the local distribution of the flow-induced effects along the whole boundary of the structural body. Indeed, $\mathbf{Q}\left(\mathcal{J}\{\mathbf{q}(t)\}, t\right)$ contains the lagrangian components of the resultant action, without explaining its local distribution. The use of $\mathcal{A}\left\{\mathcal{J}\{\mathbf{q}(t)\}, t\right\}$ is fundamental in fluid-elastic problems that involve deformable structures, that is with distributed elasticity, where the local fluid-elastic interaction affects the whole system response and can be modelled through *influence functions* [84].

lagrangian coordinates) are generally coupled. Decoupling techniques assume that the system response $\mathbf{q}(t) = (\mathrm{q}_1(t), ..., \mathrm{q}_N(t))^T$ can be expressed as a linear combination of a new set of principal coordinates $\boldsymbol{a}(t) = (a_1(t), ..., a_N(t))^T$ and N principal coefficients (vectors) $\boldsymbol{\sigma_k} = (\sigma_{1k}(t), ..., \sigma_{Nk}(t))^T$, stocked in the $N \times N$ transformation matrix $\boldsymbol{\Sigma}$, according to the linear transformation

$$\mathbf{q}(t) = \sum_k \boldsymbol{\sigma_k} a_k(t) = \boldsymbol{\Sigma} \boldsymbol{a}(t) \ . \tag{3.15}$$

The transformation matrix is usually determined through the *modal analysis*, considering a free-vibration problem of the un-damped system or, at least, within the assumption of 'proportional damping' $\mathbf{C} = c_1\mathbf{M} + c_2\mathbf{K}$ (Rayleigh's damping [153]). In the case of symmetric mass and stiffness matrices, also the transformation matrix is symmetric and can be calculated by solving the eigenvalue problem

$$(\mathbf{K} - \lambda_k \mathbf{M})\boldsymbol{\sigma_k} = \mathbf{0} \ , \tag{3.16}$$

in which $\lambda_k = \omega_k^2$ is the k-th eigenvalue and participates to the diagonal eigenvalue matrix $\boldsymbol{\Omega} = \{\omega_1^2, ..., \omega_N^2\}$. In this way, the transformation process simultaneously diagonalises $\mathbf{M}$ and $\mathbf{K}$ (as well as $\mathbf{C} = c_1\mathbf{M} + c_2\mathbf{K}$) and the set of principal coefficients forms the modal basis $\{\boldsymbol{\sigma}_k\}$, while $\omega_1 \leq \omega_2 \leq ... \leq \omega_N$ represents the N natural or modal circulatory frequencies ($\omega_k = 2\pi n_k$, where n_k is the frequency in Hz) of the dynamic system.

Hence, $a_k(t) = \langle \boldsymbol{\sigma}_k, \boldsymbol{q}(t) \rangle$, where $\langle \cdot, \cdot \rangle$ is the scalar product according to the considered space domain, becomes the k-th modal coordinate and the system can be decoupled into N independent oscillators:

$$m_i \ddot{a}_i(t) + c_i \dot{a}_i(t) + k_i a_i(t) = f_i(\ddot{a}_i(t), \dot{a}_i(t), a_i(t), t) \quad , \quad \forall i \ , \tag{3.17a}$$

or

$$m_i \left[\ddot{a}_i(t) + 2\omega_i \xi_i \dot{a}_i(t) + \omega_i^2 a_i(t) \right] = f_i(\ddot{a}_i(t), \dot{a}_i(t), a_i(t), t) \quad . \quad \forall i \ , \tag{3.17b}$$

The coefficients and the forcing terms are:

$$m_i = \langle \boldsymbol{\phi}_i, \mathbf{M}\boldsymbol{\phi}_i \rangle \ ; \tag{3.18a}$$

$$c_i = \langle \boldsymbol{\sigma}_i, \mathbf{C}\boldsymbol{\sigma}_i \rangle = 2\omega_i \xi_i m_i \ ; \tag{3.18b}$$

$$k_i = \langle \boldsymbol{\sigma}_i, \mathbf{K}\boldsymbol{\sigma}_i \rangle = \omega_i^2 m_i \ ; \tag{3.18c}$$

$$f_i = \langle \boldsymbol{\sigma}_i, \mathbf{Q}\left(\mathcal{J}\{\mathbf{q}(t)\}, t\right) \rangle \ ; \tag{3.18d}$$

where ξ_i is the critical damping ratio of the i-th modal coordinate

$$\xi_i = \frac{c_i}{2\omega_i m_i} \ . \tag{3.19}$$

Indeed, considering the case without forcing term and a non-zero initial condition, the condition $\xi_i = 1 \rightarrow c_i = 2\omega_i m_i$ states the critical damping that separates over-damped systems (hard damping, $\xi_i > 1$), characterised by exponential decays only, and under-damped systems (soft damping, $\xi_i < 1$) that can perform oscillatory motion with decreasing amplitudes.

Being both Eqs. (3.17a) and (3.17b) differential equations, initial conditions are required to solve the problem. Thus, the general solution is composed by the transient contribution that evolves to match the steady-state contribution due to the forcing action. In the common vibrating problems of under-damped systems ($\xi_i < 1$) undergoing flow-induced excitations, the steady state dominates, whereas initial conditions (corresponding to the homogeneous equations) are fundamental for free-vibration problems (without forcing action). Only in the case of nonlinear systems, *e.g.* with forcing term depending on the system response as for fluid-elastic phenomena, the initial condition can play a key role even in the achieved steady-state regime.

The core of the problem-solving relates a convolution product between each i-th impulse-response function of the set $\{h_i(t)\} \in R$, with $t \subset \mathbb{R}^+$, and the i-th forcing action

$$a_i(t) = f_i \star h_i(t) = \int_{-\infty}^{+\infty} f_i\left(\ddot{a}_i(t-\tau), \dot{a}_i(t-\tau), a_i(t-\tau), t-\tau\right) \cdot h_i(\tau) \ d\tau \ , \tag{3.20}$$

with:

$$h_i(t) = \frac{1}{m_i \omega_{d,i}} e^{-\xi_i \omega_i t} \sin\left(\omega_{d,i} t\right) \; ; \tag{3.21a}$$

$$\omega_{d,i} = \omega_i \sqrt{1 - \xi_i^2} \; . \tag{3.21b}$$

Since any linear forcing term could be approximately expressed as superposition of harmonics[4] (Fourier's expansion), the special case of harmonic forcing term is explained to discuss some important features. Considering Eq. (3.17a) in the form

$$m_i \ddot{a}_i(t) + c_i \dot{a}_i(t) + k_i a_i(t) = f_0 e^{j\omega t} \quad , \quad \forall i \; , \tag{3.22}$$

the system response at the steady-state regime becomes

$$\mathbf{q}(t) = \sum_i \boldsymbol{\sigma_i} \left(a_{0,i} \; e^{j\omega t}\right) \mathcal{G}_i \; , \tag{3.23}$$

in which $a_{0,i}$ is a 'quasi-static' response of the i-th modal oscillator under the action f_0 and $\mathcal{G}_i$ is the *transfer function* that describes the dynamical properties of the i-th modal oscillator. The latter can both amplify (or reduce) and delay (or anticipate) the system response with respect to the quasi-static part driven by the same harmonic of the action. In particular, these terms assume the expressions

$$a_{0,i} = \frac{f_0}{k_i} \tag{3.24}$$

and

$$\mathcal{G}_i = \mathcal{G}_i\left(\frac{\omega}{\omega_i}, \xi_i\right) = 1 \Big/ \left[1 - (\omega/\omega_i)^2 + 2j\,(\omega/\omega_i)\,\xi_i\right] \; ; \tag{3.25a}$$

$$|\mathcal{G}_i| = 1 \Big/ \sqrt{\left[1 - (\omega/\omega_i)^2\right]^2 + \left[2\,(\omega/\omega_i)\,\xi_i\right]^2} \; ; \tag{3.25b}$$

$$\tan\varphi_i = \frac{\mathrm{Im}(\mathcal{G}_i)}{\mathrm{Re}(\mathcal{G}_i)} = \frac{2\,(\omega/\omega_i)\,\xi_i}{1 - (\omega/\omega_i)^2} \; . \tag{3.25c}$$

Since $m_i > 0 \; \forall i$, it is easy to verify from Eqs. (3.22), (3.23), (3.24) and (3.25) that:

- if $c_i > 0$ and $k_i > 0 \Rightarrow$ *stable motion* (subsidence or damped oscillation);
- if $c_i > 0$ and $k_i = 0 \Rightarrow$ *statically unstable motion* (divergence);
- if $c_i = 0$ and $k_i > 0 \Rightarrow$ *undamped resonance when* $\omega/\omega_i \simeq 1$ (divergent oscillations);
- if $c_i < 0 \Rightarrow$ *dynamically unstable motion* (growing oscillations).

For a real mechanical system, the changes of signs of the stiffness and damping terms are responsible of the unstable motions and these particular situations are usually called *critical conditions*. These become of crucial importance in fluid-elasticity because the self-excited loads can be proportional to displacement, velocity and acceleration of the system, thus contributing to alterate the global mechanical properties, as explained in the next section.

3.1.2 Two-degrees-of-freedom fluid-elastic systems

Let consider the results obtained in the previous § 3.1.1 applied to the case study of a two-dimensional problem with 2-DoFs that involves a rigid body (with fixed shape) with concentrated mechanical properties of mass, damping and stiffness. The body interacts with a surrounding fluid in a homogeneous, steady flow (Fig. 3.1).

[4] In case of non-periodic forcing terms, these can be windowed and extended in time, repeating infinitely times the windows thus becoming periodic.

The body occupies a certain closed area of the plane and the motion is described by the pairs of lagrangian coordinates (q_1, q_2). According to Eqs. (3.7), (3.8), (3.9) and (3.13), the governing equation of the motion is

$$\begin{bmatrix} M_{11} & M_{12} \\ M_{21} & M_{22} \end{bmatrix} \begin{bmatrix} \ddot{q}_1(t) \\ \ddot{q}_2(t) \end{bmatrix} + \begin{bmatrix} C_{11} & C_{12} \\ C_{21} & C_{22} \end{bmatrix} \begin{bmatrix} \dot{q}_1(t) \\ \dot{q}_2(t) \end{bmatrix} + \begin{bmatrix} K_{11} & K_{12} \\ K_{21} & K_{22} \end{bmatrix} \begin{bmatrix} q_1(t) \\ q_2(t) \end{bmatrix} = \\ = \begin{bmatrix} Q_1(t) \\ Q_2(t) \end{bmatrix} . \tag{3.26}$$

In case of fluid-elastic interaction, the forcing term follows the general expression of Eq. (3.14) where, due to the assumption of small perturbations about the equilibrium position, linearised self-excited forces (approximated to first order) are considered. In particular, these are proportional to the reference force $\frac{1}{2}\rho U^2 B^*$ ($\frac{1}{2}\rho U^2$ is the kinetic pressure and B^* is a reference length) and depend on the linear combination of the kinematic coordinates, $\ddot{\mathbf{q}}$, $\dot{\mathbf{q}}$, $\mathbf{q}$, through the respective *fluid-elastic coefficients*, $\{\Theta_{kh}\}$, $\{\Theta'_{kh}\}$, $\{\Theta''_{kh}\}$:

$$\begin{aligned} \mathbf{Q}(t) &= \mathbf{Q}\left(\rho, U, B^*, \mathbf{\Theta}'', \mathbf{\Theta}', \mathbf{\Theta}, \ddot{\mathbf{q}}, \dot{\mathbf{q}}, \mathbf{q}, t\right) = \\ &= \frac{1}{2}\rho U^2 B^* \left(\mathbf{\Theta}''\ddot{\mathbf{q}}(t) + \mathbf{\Theta}'\dot{\mathbf{q}}(t) + \mathbf{\Theta}\mathbf{q}(t)\right) = \frac{1}{2}\rho U^2 B^* \cdot \\ &\cdot \left(\begin{bmatrix} \Theta''_{11} & \Theta''_{12} \\ \Theta''_{21} & \Theta''_{22} \end{bmatrix} \begin{bmatrix} \ddot{q}_1(t) \\ \ddot{q}_2(t) \end{bmatrix} + \begin{bmatrix} \Theta'_{11} & \Theta'_{12} \\ \Theta'_{21} & \Theta'_{22} \end{bmatrix} \begin{bmatrix} \dot{q}_1(t) \\ \dot{q}_2(t) \end{bmatrix} + \begin{bmatrix} \Theta_{11} & \Theta_{12} \\ \Theta_{21} & \Theta_{22} \end{bmatrix} \begin{bmatrix} q_1(t) \\ q_2(t) \end{bmatrix} \right) . \end{aligned} \tag{3.27}$$

The fluid-elastic coefficients are $n \times n$ matrices (n is the number of DoFs) with, generally, complex values because they have to describe the relationships between motion and fluid-dynamic reactions, including the phase shift. Moreover, they depend intrinsecally on the characteristics of the problem configuration, that is body shape and position of the elastic axis (in the case of two-dimensional problems), while they are supposed to be independent on the motion amplitude (within the small-perturbation approach). Hence, *e.g.* Θ_{kh} relates the flow-induced effect on the k-th DoF (q_k) due to the component on the h-th DoF of the displacement field during the motion. Then, it follows similarly for the others coefficients Θ'_{kh} and Θ''_{kh} related to, respectively, the velocity and acceleration field.

When Eq. (3.27) is considered into Eq. (3.26), it produces an important coupling on the fluid-elastic system. At a given flow velocity U, the self-excited loads combine with $\mathbf{M}$, $\mathbf{C}$, $\mathbf{K}$ to achieve a form similar to[5]

$$\left(\mathbf{M} + \mathbf{M_{se}}\right)\ddot{\mathbf{q}}(t) + \left(\mathbf{C} + \mathbf{C_{se}}\right)\dot{\mathbf{q}}(t) + \left(\mathbf{K} + \mathbf{K_{se}}\right)\mathbf{q}(t) = \mathbf{0} , \tag{3.28a}$$

or

$$\tilde{\mathbf{M}}\ddot{\mathbf{q}}(t) + \tilde{\mathbf{C}}\dot{\mathbf{q}}(t) + \tilde{\mathbf{K}}\mathbf{q}(t) = \mathbf{0} , \tag{3.28b}$$

where $\mathbf{M_{se}}$, $\mathbf{C_{se}}$ and $\mathbf{K_{se}}$ contain the effects of the fluid-elastic loads, being non-symmetric and depending on $\frac{1}{2}\rho U^2 B^*$, $\mathbf{\Theta}$, $\mathbf{\Theta}'$ and $\mathbf{\Theta}''$. Eq. (3.28) can be solved:

- in the *time domain*, through several time-integration schemes directly applied to the governing equation or the state-space representation, otherwise transforming the differential form in an algebraic system of equations by the use of the Laplace transform;
- in the *frequency domain*, describing the system response through a superposition of harmonic motions.

Time-domain methods allow a more general study of the system response, even in the case of transient effects, although they may require larger computational efforts. Frequency-domain

[5] It is worth remarking that the right-hand side of Eq. (3.28) is the empty vector because, in case of homogeneous, steady flow (without fluctuations in the free-stream velocity), the only self-excited actions are present. However, the calculation of the state-space modal basis (see § 3.3.1) always applies to the associated homogeneous system of a general differential problem.

methods consider the assumption of harmonic motion and linear combination through the modal basis, and this may restricts the field of application, although they are computationally simpler and more intuitive.

Some observations can be made about the steady-state regime due to self-excited harmonic excitations (*e.g.* at the flutter condition). At a fixed flow velocity U, the system will oscillate in two fluid-elastic modes ($\tilde{\boldsymbol{\sigma}}_{\mathbf{1}}$ and $\tilde{\boldsymbol{\sigma}}_{\mathbf{2}}$) that generally have components in both the DoFs, and evolve as the flow velocity increases:

$$\tilde{\boldsymbol{\sigma}}_{\mathbf{1}}(U) = \begin{pmatrix} \mathrm{q}_{1,1} \\ \mathrm{q}_{1,2} \end{pmatrix} \quad ; \quad \tilde{\boldsymbol{\sigma}}_{\mathbf{2}}(U) = \begin{pmatrix} \mathrm{q}_{2,1} \\ \mathrm{q}_{2,1} \end{pmatrix} . \tag{3.29}$$

The modal basis $\{\tilde{\sigma}_i\}$ can be determined setting up Eq. (3.28) in the state-space form, as described after in § 3.3.1, and it takes into account of the self-excited loads that modify the resulting mechanical properties. In the case of 'free vibrations', that is in still-air conditions, the fluid-elastic coefficients continue to contribute, although their influence is negligible for small amplitudes of oscillation, when they essentially relate the fluid-dynamic damping and added-mass in still air. Thus, the free-vibration problem leads to the following approximation

$$\boldsymbol{\sigma}_{\mathbf{1}} \simeq \tilde{\boldsymbol{\sigma}}_{\mathbf{1}}(U = 0) \quad ; \quad \boldsymbol{\sigma}_{\mathbf{2}} \simeq \tilde{\boldsymbol{\sigma}}_{\mathbf{2}}(U = 0) , \tag{3.30}$$

in which the natural modes $\boldsymbol{\sigma}_{\mathbf{1}}$ and $\boldsymbol{\sigma}_{\mathbf{2}}$ (coming from the modal analysis of Eq. (3.16)) might not coincide with the lagrangian coordinates because of the possible mechanical coupling due to out-diagonal components in the mass, damping and stiffness matrices[6].

Summarising, the following considerations can be made:

a) The fluid-elastic coefficients generally couple the two DoFs, because of the influence in the k-th DoF of the motion component in the h-th DoF, due to the generic fluid-elastic mode that exhibits both components.

b) The self-excited loads introduce (positive/negative) additional mass, additional damping and additional stiffness, because they are proportional to the acceleration, velocity and displacement fields (within the linearised problem). Moreover, they are proportional to the kinetic pressure $1/2\rho U^2$ and this means that the vanishing of total damping or stiffness can be achieved at a certain flow velocity, producing unstable motion or divergence (see § 3.1.1).

c) Eq. (3.26), including Eq. (3.27), could be projected into the modal space produced by $\{\tilde{\boldsymbol{\sigma}}_{\boldsymbol{i}}\}$. However, the fluid-elastic modes evolve with the flow velocity and consequently the modal basis changes too, being different at each flow velocity and complicating the analysis. Furthermore, the approach based on the two DoFs $(\mathrm{q}_1, \mathrm{q}_2)$ is strictly related to the experimental field, in which the elastic suspension reproduces the motion in the pairs $(\mathrm{q}_1, \mathrm{q}_2)$ and these are the only DoFs that can be practically observed (same considerations about fluid-elastic forces because only the components in q_1 and q_2 can be measured).

d) The linear equations previously introduced, Eqs. (3.26) and (3.27), are specific for the stability evaluation about equilibrium positions, within the assumption of small perturbations. Thus, they represent linear analytical models to investigate the system stability in the whole range of flow velocities up to the critical condition. Neither the post-critical field nor possible sub-critical stable branches can be predicted, because of the small amplitude hypothesis.

e) The critical condition, as explained in § 3.1.1, is mainly affected by only one of the modes of the system, which drives the instability or divergence. Indeed, once the instability/divergence is embarked, the energetic content of the driving mode becomes markedly larger than the other, becoming possible to neglect the contribution of the latter. Moreover, the damping of the secondary mode strongly increases when approaching the instability onset [33].

[6] The modal basis coincides with the lagrangian basis, that is $(\mathrm{q}_1\ 0)^T$ and $(0\ \mathrm{q}_2)^T$, only in the case of diagonal matrices $\mathbf{M}$, $\mathbf{C}$, $\mathbf{K}$.

3.2 The case study of 2-DoF classical flutter

3.2.1 Governing equations

In the two-degree-of-freedom classical-flutter problem within the assumption of two-dimensional conditions (*e.g.* [84]), streamlined cross sections can vibrate in the translational DoF (or heaving η) and rotational DoF (or pitching α), as reported on Fig. 3.2. The structure is excited by the fluid-dynamic forces of lift L and moment M, which react to the body motion. Moreover, the structure is elastically suspended, including the damping, about the elastic axis (EC) in both the DoFs, and the typical problem is supposed to consider *null out-diagonal terms for damping and stiffness matrices.*

This two-dimensional model can describe real problems in which the structure has finite span, provided that the bi-dimensional flow conditions are ensured. In those cases, both mechanical properties and fluid-elastic loads can be referred to unit span.

Considering the positive motion of Fig. 3.2, a generic point of the cross section $\mathcal{A}$ with material density ρ_m, at positive distance x aft the elastic axis, has the following horizontal and vertical components (u and w) of displacement:

$$\begin{cases} u(s) = x\,[\cos(\alpha) - 1] \\ w(s) = -\eta - x\sin(\alpha) \end{cases} \quad \rightarrow \quad \begin{cases} u(s) \simeq 0 \\ w(s) \simeq -\eta - x\alpha \end{cases} \qquad if \quad \alpha \simeq 0\ . \tag{3.31}$$

Hence, the kinetic, potential and damping energies are:

$$\mathcal{T} \simeq \frac{1}{2}\rho_m \int_{\mathcal{A}} \dot{w}^2 dx = \frac{1}{2} I_\eta \dot{\eta}^2 + S\dot{\eta}\dot{\alpha} + \frac{1}{2} I_\alpha \dot{\alpha}^2\ ; \tag{3.32a}$$

$$\Pi \simeq \frac{1}{2} K_\eta \eta^2 + \frac{1}{2} K_\alpha \alpha^2\ ; \tag{3.32b}$$

$$\mathcal{D} \simeq \frac{1}{2} C_\eta \dot{\eta}^2 + \frac{1}{2} C_\alpha \dot{\alpha}^2\ . \tag{3.32c}$$

Considering Eq. (3.32) with respect to Eqs. (3.7), (3.13) and Eqs. (3.26), (3.27), the reference equation becomes

$$\begin{aligned} &\begin{bmatrix} I_\alpha & S \\ S & I_\eta \end{bmatrix} \begin{bmatrix} \ddot{\alpha}(t) \\ \ddot{\eta}(t) \end{bmatrix} + \begin{bmatrix} C_\alpha & 0 \\ 0 & C_\eta \end{bmatrix} \begin{bmatrix} \dot{\alpha}(t) \\ \dot{\eta}(t) \end{bmatrix} + \begin{bmatrix} K_\alpha & 0 \\ 0 & K_\eta \end{bmatrix} \begin{bmatrix} \alpha(t) \\ \eta(t) \end{bmatrix} = \\ &= \frac{1}{2}\rho U^2 l \begin{bmatrix} B^2 \cdot \overline{M}(\Theta''_{\alpha\alpha}\ddot{\alpha}, \Theta'_{\alpha\alpha}\dot{\alpha}, \Theta_{\alpha\alpha}\alpha, \Theta''_{\alpha\eta}\ddot{\eta}, \Theta'_{\alpha\eta}\dot{\eta}, \Theta_{\alpha\eta}\eta, U, t) \\ B \cdot \overline{L}(\Theta''_{\eta\alpha}\ddot{\alpha}, \Theta'_{\eta\alpha}\dot{\alpha}, \Theta_{\eta\alpha}\alpha, \Theta''_{\eta\eta}\ddot{\eta}, \Theta'_{\eta\eta}\dot{\eta}, \Theta_{\eta\eta}\eta, U, t) \end{bmatrix}\ , \end{aligned} \tag{3.33}$$

in which:

- t [s] is the time variable;
- α [rad] and η [m] are the pitching and heaving DoFS referred to the elastic centre (EC, see Fig. 3.2);
- I_α [kg m^2] and I_η [kg] are the inertia in, respectively, the pitching and heaving DoF, calculated with respect to the elastic centre (EC, see Fig. 3.2);
- C_α [N m s rad^{-1}] and C_η [N s m^{-1}] are the damping in, respectively, the pitching and heaving DoF;
- K_α [N m rad^{-1}] and K_η [N m^{-1}] are the stiffness in, respectively, the pitching and heaving DoF;
- S [kg m] is the static mass unbalance;
- $\frac{1}{2}\rho U^2$ [N m^{-2}] is the kinetic pressure of the flow, with density ρ [kg m^{-3}] and velocity U [m s^{-1}];
- l [m] is the model span, which can be placed to multiply the loads (as here considered) or to divide the mechanical properties.

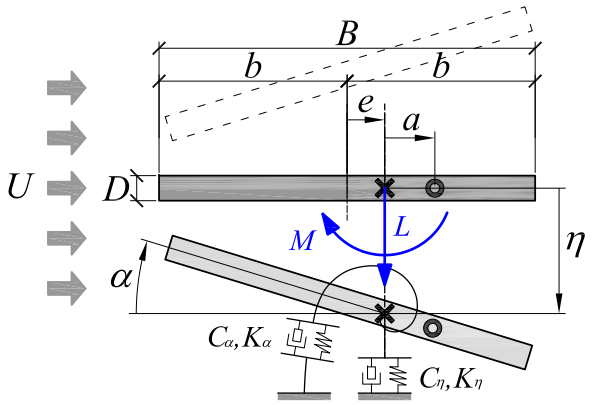

Figure 3.2. Sketch of the 2-DoF classical-flutter problem, being α the pitching and η the heaving DoF, in the case of elongated rectangular cross section of depth D and width B. The mass centre is located at a distance $a > 0$ aft the elastic axis, which is located $e > 0$ aft the midchord. The stiffness and damping (K_α, C_α, K_η, C_η) are supposed to be concentrated in the elastic axis and the self-excited loads of lift L and moment M and the polar inertia are referred to that point.

- B [m] is the specific length to normalise the moment and lift loads (previously called B^*), which in this case represents the chord of the cross section;
- $\overline{M}$ [-] and $\overline{L}$ [-] are the dimensionless self-excited moment and lift (positive if agree with positive α and η).

Important: $\overline{M}$ and $\overline{L}$ contain the (complex) fluid-elastic coefficients, which depend on the characteristic of the motion. Since the motion is referred to the position of the elastic axis e (see Fig. 3.2), they intrinsically include the influence of the elastic axis as well. With particular regard to the experimental field, in which the fluid-elastic coefficients are usually estimated through specific dynamic tests, it is always important to specify the position of the elastic axis assumed during the tests in order to properly apply them in the fluid-elastic model.

The following relations are also valid:

$$I_\alpha = r_I^2 I_\eta, \tag{3.34a}$$
$$S = a I_\eta, \tag{3.34b}$$
$$K_\alpha = \omega_{\alpha 0}^2 I_\alpha = (2\pi n_{\alpha 0})^2 I_\alpha \ , \tag{3.34c}$$
$$K_\eta = \omega_{\eta 0}^2 I_\eta = (2\pi n_{\eta 0})^2 I_\eta \ , \tag{3.34d}$$
$$C_\alpha = 2\xi_{\alpha 0}\omega_{\alpha 0} I_\alpha = 4\pi\xi_{\alpha 0} n_{\alpha 0} I_\alpha \ , \tag{3.34e}$$
$$C_\eta = 2\xi_{\eta 0}\omega_{\eta 0} I_\eta = 4\pi\xi_{\eta 0} n_{\eta 0} I_\eta \ , \tag{3.34f}$$

in which:

- a is the eccentricity of the mass centre (CM, see Fig. 3.2), positive downstream to the elastic centre (EC);
- r_I is the radius of polar inertia;
- $\omega_{\alpha 0}$ (or $n_{\alpha 0}$) and $\omega_{\eta 0}$ (or $n_{\eta 0}$) are the pulsation [rad] (or frequency [Hz]) of the, respectively, pitching and heaving DoF, in still air, for the uncoupled system (when $S_\alpha = 0$);
- $\xi_{\alpha 0}$ and $\xi_{\eta 0}$ are the ratio-to-critical damping coefficients of the, respectively, pitching and heaving DoF, in still air, for the uncoupled system (when $S = 0$).

Defining the dimensionless kinematic variables

$$\begin{aligned} \overline{\alpha}(t) &= \alpha(t) \ , \quad \dot{\overline{\alpha}}(t) = \frac{\dot{\alpha}(t)}{\omega} \ , \quad \ddot{\overline{\alpha}}(t) = \frac{\ddot{\alpha}(t)}{\omega^2} \ , \\ \overline{\eta}(t) &= \frac{\eta(t)}{B} \ , \quad \dot{\overline{\eta}}(t) = \frac{\dot{\eta}(t)}{\omega B} \ , \quad \ddot{\overline{\eta}}(t) = \frac{\ddot{\eta}(t)}{\omega^2 B} \ , \end{aligned} \tag{3.35}$$

the governing dimensionless equation is

$$\begin{aligned} \mu \left(\begin{bmatrix} r_\alpha^2 & x_m \\ x_m & 1 \end{bmatrix} \begin{bmatrix} \ddot{\overline{\alpha}} \\ \ddot{\overline{\eta}} \end{bmatrix} + \begin{bmatrix} 2\xi_{\alpha 0} r_\alpha^2 \sqrt{X} & 0 \\ 0 & 2\xi_{\eta 0}\sqrt{X}/\gamma_n \end{bmatrix} \begin{bmatrix} \dot{\overline{\alpha}} \\ \dot{\overline{\eta}} \end{bmatrix} + \right. \\ \left. + \begin{bmatrix} r_\alpha^2 X & 0 \\ 0 & X/\gamma_n^2 \end{bmatrix} \begin{bmatrix} \overline{\alpha} \\ \overline{\eta} \end{bmatrix} \right) = \\ = \frac{1}{K^2} \begin{bmatrix} \overline{M}(A_\alpha^{''}, A_\alpha^{'}, A_\alpha, A_\eta^{''}, A_\eta^{'}, A_\eta, \ddot{\overline{\alpha}}, \dot{\overline{\alpha}}, \overline{\alpha}, \ddot{\overline{\eta}}, \dot{\overline{\eta}}, \overline{\eta}, K, t) \\ \overline{L}(H_\alpha^{''}, H_\alpha^{'}, H_\alpha, H_\eta^{''}, H_\eta^{'}, H_\eta, \ddot{\overline{\alpha}}, \dot{\overline{\alpha}}, \overline{\alpha}, \ddot{\overline{\eta}}, \dot{\overline{\eta}}, \overline{\eta}, K, t) \end{bmatrix} \ , \end{aligned} \tag{3.36}$$

where, due to the use of Eq. (3.35), the dependence of the self-excited loads on the flow velocity U is traduced in the dependence on the reduced frequency K and the fluid-elastic coefficients follow the relationships:

$$\begin{array}{ccccccccc} \omega^2 \Theta_{\alpha\alpha}^{''} & , & \omega \Theta_{\alpha\alpha}^{'} & , & \Theta_{\alpha\alpha} & \leftrightarrow & K^2 A_\alpha^{''} & , & K^2 A_\alpha^{'} & , & K^2 A_\alpha & ; \\ \omega^2 B \Theta_{\alpha\eta}^{''} & , & \omega B \Theta_{\alpha\eta}^{'} & , & B\Theta_{\alpha\eta} & \leftrightarrow & K^2 A_\eta^{''} & , & K^2 A_\eta^{'} & , & K^2 A_\eta & ; \\ \omega^2 \Theta_{\eta\eta}^{''} & , & \omega \Theta_{\eta\eta}^{'} & , & \Theta_{\eta\eta} & \leftrightarrow & K^2 H_\eta^{''} & , & K^2 H_\eta^{'} & , & K^2 H_\eta & ; \\ \omega^2 B \Theta_{\eta\alpha}^{''} & , & \omega B \Theta_{\eta\alpha}^{'} & , & B\Theta_{\eta\alpha} & \leftrightarrow & K^2 H_\alpha^{''} & , & K^2 H_\alpha^{'} & , & K^2 H_\alpha & . \end{array} \tag{3.37}$$

Due to the assumption of small perturbations about equilibrium positions that requires linearised quantities, the dimensionless self-excited loads can take the form:

$$\begin{aligned} \overline{M} &= K^2 \left(A_\alpha^{''} \ddot{\overline{\alpha}} + A_\alpha^{'} \dot{\overline{\alpha}} + A_\alpha \overline{\alpha} + A_\eta^{''} \ddot{\overline{\eta}} + A_\eta^{'} \dot{\overline{\eta}} + A_\eta \overline{\eta} \right) \ ; \\ \overline{L} &= K^2 \left(H_\alpha^{''} \ddot{\overline{\alpha}} + H_\alpha^{'} \dot{\overline{\alpha}} + H_\alpha \overline{\alpha} + H_\eta^{''} \ddot{\overline{\eta}} + H_\eta^{'} \dot{\overline{\eta}} + H_\eta \overline{\eta} \right) \ ; \end{aligned} \tag{3.38}$$

where the dimensionless fluid-elastic coefficients $\{A_i^{''}\}$, $\{A_i^{'}\}$, $\{A_i\}$, $\{H_i^{''}\}$, $\{H_i^{'}\}$, $\{H_i\}$ (for $i = \eta, \alpha$) can be explained according to several linearised models (see § 3.4).

Observing Eq. (3.36) and the previous comments on elastic axis eccentricity e, the governing parameters of the problem can be identified:

- (*inertia parameters*: μ, mass ratio; r_α, dimensionless radius of inertia)

$$\mu = \frac{2I_\eta}{\rho B^2 l} \quad ; \tag{3.39a}$$

$$r_\alpha = \frac{r_I}{B} = \sqrt{I_\alpha / I_\eta B^2} \quad ; \tag{3.39b}$$

- (*damping parameters*: ξ_α, ratio-to-critical damping coefficient of pitching; ξ_η, ratio-to-critical damping coefficient of pitching)

$$\xi_{\alpha 0} = \frac{C_\alpha}{2\omega_{\alpha 0} I_\alpha} \quad ; \tag{3.40a}$$

$$\xi_{\eta 0} = \frac{C_\eta}{2\omega_{\eta 0} I_\eta} \quad ; \tag{3.40b}$$

- (*geometry parameters*: x_m, dimensionless eccentricity of the mass centre, positive if aft to the elastic centre; x_e, dimensionless eccentricity of elastic centre, positive if aft to the geometrical centre)

$$x_m = \frac{a}{B} \quad ; \tag{3.41a}$$

$$x_e = \frac{e}{B} \quad ; \tag{3.41b}$$

- (*frequency parameters*: γ_n, ratio of pitching to heaving frequency, in still air for the uncoupled system; $\sqrt{X}$, ratio of still-air pitching frequency to a reference frequency used for normalisations, which usually is the flutter frequency)

$$\gamma_n = \frac{n_{\alpha 0}}{n_{\eta 0}} = \frac{\omega_{\alpha 0}}{\omega_{\eta 0}} \quad ; \tag{3.42a}$$

$$\sqrt{X} = \frac{n_{\alpha 0}}{n} = \frac{\omega_{\alpha 0}}{\omega} \quad ; \tag{3.42b}$$

- (*flow parameters*: K, reduced frequency, referred to a certain frequency of oscillation ω, or dually, U_R, reduced velocity)

$$K = \frac{\omega B}{U} = 2\pi / U_R \quad \Rightarrow \quad U_R = \frac{U}{nB} \quad . \tag{3.43}$$

The governing dimensionless equation of the classical-flutter problem results:

$$\begin{aligned}
&\mu\left(\begin{bmatrix} r_\alpha^2 & x_m \\ x_m & 1 \end{bmatrix} \begin{bmatrix} \ddot{\overline{\alpha}}(t) \\ \ddot{\overline{\eta}}(t) \end{bmatrix} + \right. \\
&+ \begin{bmatrix} 2\xi_{\alpha 0} r_\alpha^2 \sqrt{X} & 0 \\ 0 & 2\xi_{\eta 0}\sqrt{X}/\gamma_n \end{bmatrix} \begin{bmatrix} \dot{\overline{\alpha}}(t) \\ \dot{\overline{\eta}}(t) \end{bmatrix} + \\
&+ \left. \begin{bmatrix} r_\alpha^2 X & 0 \\ 0 & X/\gamma_n^2 \end{bmatrix} \begin{bmatrix} \overline{\alpha}(t) \\ \overline{\eta}(t) \end{bmatrix} \right) = \\
&= \begin{bmatrix} A_\alpha'' & A_\eta'' \\ H_\alpha'' & H_\eta'' \end{bmatrix} \begin{bmatrix} \ddot{\overline{\alpha}}(t) \\ \ddot{\overline{\eta}}(t) \end{bmatrix} + \\
&\begin{bmatrix} A_\alpha' & A_\eta' \\ H_\alpha' & H_\eta' \end{bmatrix} \begin{bmatrix} \dot{\overline{\alpha}}(t) \\ \dot{\overline{\eta}}(t) \end{bmatrix} + \\
&\begin{bmatrix} A_\alpha & A_\eta \\ H_\alpha & H_\eta \end{bmatrix} \begin{bmatrix} \overline{\alpha}(t) \\ \overline{\eta}(t) \end{bmatrix} \quad ,
\end{aligned} \tag{3.44a}$$

or, in compact form,

$$\begin{aligned}
&\begin{bmatrix} \mu r_\alpha^2 - A_\alpha'' & \mu x_m - A_\eta'' \\ \mu x_m - H_\alpha'' & \mu - H_\eta'' \end{bmatrix} \begin{bmatrix} \ddot{\overline{\alpha}}(t) \\ \ddot{\overline{\eta}}(t) \end{bmatrix} + \\
&+ \begin{bmatrix} 2\mu\xi_{\alpha 0} r_\alpha^2 \sqrt{X} - A_\alpha' & -A_\eta' \\ -H_\alpha' & 2\mu\xi_{\eta 0}\sqrt{X}/\gamma_n - H_\eta' \end{bmatrix} \begin{bmatrix} \dot{\overline{\alpha}}(t) \\ \dot{\overline{\eta}}(t) \end{bmatrix} + \\
&+ \begin{bmatrix} \mu r_\alpha^2 X - A_\alpha & A_\eta \\ -H_\alpha & \mu X/\gamma_n^2 - H_\eta \end{bmatrix} \begin{bmatrix} \overline{\alpha}(t) \\ \overline{\eta}(t) \end{bmatrix} = 0 \quad .
\end{aligned} \tag{3.44b}$$

3.2.2 Comments on the solving methods

Eq. (3.44) is similar to Eq. (3.28) and can be solved through different methods as preliminary explained in § 3.1.2. The choice essentially depends on how the self-excited loads are expressed (see § 3.4) and the main difference is between time-domain and frequency-domain approaches:

- *Time-domain methods*

  The problem can be solved by a direct integration of the governing equation. Analytical methods apply rarely and only under suitable conditions, although leading to closed form solutions. On the other hands, numerical methods (finite difference, Runge-Kutta, *etc.*) are effective tools for time-integration of ODEs.

  Being in the time domain, the self-excited loads have to be expressed accordingly. Thus, the more general form of the fluid-elastic coefficients describes the impulsive

response of the system to an impulse step in the system motion (see § 3.4.2.1). They generally consider convolution integrals between impulsive-transfer functions (usually called 'indicial functions') and displacement, velocity, acceleration fields corresponding to the impulse step on the motion.

The use of fluid-elastic coefficients that come from the frequency domain, *i.e.* the flutter derivatives of § 3.4.3, is conceptually contradictory in time-domain methods. Nevertheless, they could be considered as well, with the payback of introducing approximations and deficiency of physical meaning, because time-domain methods do not consider the presence of fluid-elastic modes as a prerequisite for the problem modelling. Furthermore, it is not possible to correctly express the self-excited loads as the combination of fluid-elastic modes, as more clear from the next item.

- *Frequency-domain methods*

  The system response can be described by a superposition of the harmonic motion corresponding to the fluid-elastic modes. In this case, the fluid-elastic coefficients are affected by both frequencies ω_1 and ω_2 of the fluid-elastic modes (acting through the corresponding reduced frequencies K_1 and K_2) that apply according to the respective modal shapes $\tilde{\boldsymbol{\sigma}}_{\mathbf{1}}$ and $\tilde{\boldsymbol{\sigma}}_{\mathbf{2}}$. Thus, the generic fluid-elastic coefficient[7] becomes *e.g.* $\boldsymbol{\Theta}^i = \boldsymbol{\Theta}(\tilde{\boldsymbol{\sigma}}_{\boldsymbol{i}}, K_i)$ and this constitutes a problem in the case of flutter evaluation, because the frequencies of oscillations are unknown a priori, as well as the corresponding modal shapes. Thus, the modal decomposition on the basis $\{\tilde{\sigma}_i\}$ cannot apply and further simplifications are usually introduced to overcome this issue [32, 84], which are alternatively[8]:

  S1 the independence of the fluid-elastic coefficients on both reduced frequency and modal shape (see also footnote at pag. 228 in [84]);

  S2 the predominance of only one mode, being the dominant one, in the flutter motion (consider also observation (e) in § 3.1.2).

Time-domain methods return the exact response for a given set of flow speeds. The contributions of each fluid-elastic mode can be evaluated a posteriori, observing the evolution of the system eigenvalues within a state-space formulation, and the critical condition can be identified directly from the system response in time or from changes in the roots sign, as explained in § 3.3.1. On the other hands, frequency-domain methods are extremely efficient tools to evaluate the stability only. Through an approximated description of the system response, they look for the condition in the frequency domain that eventually verifies the assumptions introduced for the instability evaluation, as explained in § 3.3.2.

3.3 Critical-condition evaluation

3.3.1 State-space formulation

The self-excited loads have to be described through impulsive transfer functions (see § 3.4.2.1). Alternatively, one of simplifications S1 and S2 introduced in § 3.2.2 could be used to approximate the fluid-elastic coefficients as:

- *e.g.* $\boldsymbol{\Theta} = \boldsymbol{\Theta}(K)$, where K is due to the frequency ω of the dominant mode only, without dependence on the modal shape (being ω unknown a priori, an iterative approach is required);
- *e.g.* $\boldsymbol{\Theta}$ is constant, thus without dependence on both reduced frequency and modal shape.

[7] In case of harmonic motion, the total amount of fluid-elastic coefficients may be calculated as:

$$(\#\text{ of modes}) \times (\#\text{ of kinematic fields}) \times (\#\text{ of DoF})^2 \ .$$

[8] Assumptions (S1) and (S2) can be applied even simultaneously, leading to the quasi-steady approach of § 3.4.1.

Let refer to the general governing equation in the form of Eq. (3.28). The resultant damping matrix $\tilde{\mathbf{C}}$ usually cannot be considered 'proportional', so that $\tilde{\mathbf{C}} = \tilde{c_1}\tilde{\mathbf{M}} + \tilde{c_2}\tilde{\mathbf{K}}$ is not verified. Thus, the modal analysis performed through Eq. (3.16) certainly does not diagonalise $\tilde{\mathbf{C}}$ and no analytical solution of the equations of motion in that modal space is possible. Nevertheless, the problem can be re-formulated in the state-space form

$$\begin{cases} \dot{\mathbf{q}}(t) = \dot{\mathbf{q}}(t) \\ \ddot{\mathbf{q}}(t) = -\tilde{\mathbf{M}}^{-1}\tilde{\mathbf{C}}\dot{\mathbf{q}}(t) - \tilde{\mathbf{M}}^{-1}\tilde{\mathbf{K}}\mathbf{q}(t) \end{cases} , \tag{3.45a}$$

or

$$\begin{bmatrix} \dot{\mathbf{q}}(t) \\ \ddot{\mathbf{q}}(t) \end{bmatrix} = \begin{bmatrix} \mathbf{0} & \mathbf{I} \\ -\tilde{\mathbf{M}}^{-1}\tilde{\mathbf{K}} & -\tilde{\mathbf{M}}^{-1}\tilde{\mathbf{C}} \end{bmatrix} \begin{bmatrix} \mathbf{q}(t) \\ \dot{\mathbf{q}}(t) \end{bmatrix} , \tag{3.45b}$$

or

$$\dot{\mathbf{x}}(t) = \mathbf{A}\mathbf{x}(t) , \tag{3.45c}$$

where $\mathbf{x}(t) = (\mathbf{q}(t),\ \dot{\mathbf{q}}(t))^T$ is the 'state vector'. Eq. (3.45c) constitutes a set of ordinary differential equations and, since these have constant coefficients, solution in the form

$$\mathbf{x}(t) = e^{\lambda t}\mathbf{x} \tag{3.46}$$

can be assumed, leading to the *complex eigenvalue problem*

$$\mathbf{A}\mathbf{x} = \lambda\mathbf{x} , \tag{3.47}$$

which returns the necessary modal basis. This is complex and with no longer orthogonal eigenvectors because $\mathbf{A}$ in not symmetric. However, $\mathbf{A} \in \mathbb{R}$ and this allows λ_i and its complex conjugate λ_i^* $(\forall i = 1, 2, \dots 2n)$ to be both eigenvalues of $\mathbf{A}$, with $\mathbf{x}_i$ and $\mathbf{x}_i^*$ their complex eigenvectors. Since $\mathbf{A}^T \neq \mathbf{A}$ and $\det(\mathbf{A}^T) = \det(\mathbf{A})$ because $\mathbf{A} \in \mathbb{R}$, the adjoint complex eigenvalue problem is

$$\mathbf{A}^T\mathbf{y} = \lambda\mathbf{y} , \tag{3.48}$$

being $\mathbf{y}_j$ the adjoint eigenvectors. Collecting $\mathbf{x}_i$ (right eigenvectors) and $\mathbf{y}_j$ (left eigenvectors) in $\mathbf{X} = [\mathbf{x}_1, \mathbf{x}_2, \dots, \mathbf{x}_{2n}]$ and $\mathbf{Y} = [\mathbf{y}_1, \mathbf{y}_2, \dots, \mathbf{y}_{2n}]$, the combination of Eqs. (3.47) and (3.48) leads to the 'biorthogonality relations'

$$\mathbf{Y}^T\mathbf{X} = \mathbf{I} , \quad \mathbf{Y}^T\mathbf{A}\mathbf{X} = \mathbf{\Lambda} \tag{3.49}$$

in which $\mathbf{\Lambda}$ stocks the set of complex eigenvalues $\{\lambda_i\}$ along its diagonal. The 'dual expansion theorem' can be finally applied to a generic vector $\mathbf{v} \in \mathbb{C}$:

$$\mathbf{v} = \mathbf{X}\mathbf{a} , \quad \mathbf{a} = \mathbf{Y}^T\mathbf{v} , \tag{3.50a}$$

or

$$\mathbf{v} = \mathbf{Y}\mathbf{b} , \quad \mathbf{b} = \mathbf{X}^T\mathbf{v} . \tag{3.50b}$$

Recalling Eq. (3.46) and observing that $2n$ ways of solving Eq. (3.45c) exist (because λ_i and λ_i^* are both valid eigenvalues), the state vector can be expressed as linear combination in the state-space modal basis $\{\mathbf{x}_i\}$, so that

$$\mathbf{x}(t) = \sum_1^{2n} \mathbf{x}_i e^{\lambda_i t} a_i = \mathbf{X} e^{\mathbf{\Lambda} t}\mathbf{a} . \tag{3.51}$$

The coefficients a_i, $\forall i = 1, 2, \dots 2n$, depend on the initial conditions and can be calculated from Eq. (3.54) using Eqs. (3.49) and (3.50) to obtain

$$a_i = \mathbf{y}_i^T\mathbf{x}(0) \ , i = 1, 2, \dots 2n \tag{3.52}$$

which leads to the final solution in the form

$$\mathbf{x}(t) = \sum_1^{2n} \mathbf{x}_i e^{\lambda_i t}\mathbf{y}_i^T\mathbf{x}(0) = \mathbf{X} e^{\mathbf{\Lambda} t}\mathbf{Y}^T\mathbf{x}(0) . \tag{3.53}$$

The final system response depends on both left $\mathbf{Y}$ and right $\mathbf{X}$ eigenvectors. Nevertheless, the complex eigenvalue problem has to be solved only once, because $\mathbf{Y}^T = \mathbf{X}^{-1}$ thanks to Eq. (3.49). Moreover, the i-th coefficient a_k describes the effects of the initial conditions on the system response through the k-th state-space oscillator, and can be moved backward when discussing the state-space modal decomposition. Hence, each state-space modal oscillator is definitely described by $\lambda_k = -\xi_k\omega_k + j\omega_{d,k} \in \mathbb{C}$ (λ_k are *poles* of the system, defining its stability) and $\mathbf{x}_k \in \mathbb{C}$ according to

$$\mathbf{x}_k(t) \propto \mathbf{x}_k \cdot e^{-\xi_k\omega_k t} \cdot e^{j\omega_{d,k}t} \ , \quad k = 1, 2, \dots 2n \ , \tag{3.54}$$

in which:

- $e^{j\omega_{d,k}t}$ decribes an harmonic behaviour, where $\omega_{d,k}$ is the damped frequency of oscillation of Eq. (3.21b), thus involving the natural frequency $\omega_k = |\lambda_k|$ and ratio-to-critical damping $\xi_k = -\mathrm{Re}(\lambda_k)/|\lambda_k|$;
- $e^{-\xi_k\omega_k t}$ represents, since $\omega_k \geq 0 \ \forall k$, a growing motion (amplification) if $\xi_k < 0$, or a neutral condition if $\xi_k\omega_k = 0$ (static divergence if $\omega_k = 0$ or dynamic instability if $\xi_k = 0$), or a decaying motion if $\xi_k > 0$;
- $\mathbf{x}_k$, being complex, contains information about both amplitude and phase of the k-th state-space mode, the components of $\mathbf{x}_k$ refer to the lagrangian coordinates $(\mathrm{q}_1, \mathrm{q}_2)$, which in are complex values, according to:

$$\begin{gathered}
\mathbf{x}_k = \begin{bmatrix} \mathbf{q} \\ \dot{\mathbf{q}} \end{bmatrix}_k = \begin{bmatrix} \mathrm{q}_1 \\ \mathrm{q}_2 \\ \dot{\mathrm{q}}_1 \\ \dot{\mathrm{q}}_2 \end{bmatrix}_k \quad ; \quad \mathbf{x}_k^* = \begin{bmatrix} \mathbf{q}^* \\ \dot{\mathbf{q}}^* \end{bmatrix}_k = \begin{bmatrix} \mathrm{q}_1^* \\ \mathrm{q}_2^* \\ \dot{\mathrm{q}}_1^* \\ \dot{\mathrm{q}}_2^* \end{bmatrix}_k \quad ; \quad k = 1, 2 \\
\Rightarrow \mathbf{X} = \begin{bmatrix} \mathbf{x}_1 & \mathbf{x}_1^* & \mathbf{x}_2 & \mathbf{x}_2^* \end{bmatrix} = \left[\begin{bmatrix} \mathrm{q}_1 \\ \mathrm{q}_2 \\ \dot{\mathrm{q}}_1 \\ \dot{\mathrm{q}}_2 \end{bmatrix}_1 \begin{bmatrix} \mathrm{q}_1 \\ \mathrm{q}_2 \\ \dot{\mathrm{q}}_1 \\ \dot{\mathrm{q}}_2 \end{bmatrix}_1^* \begin{bmatrix} \mathrm{q}_1 \\ \mathrm{q}_2 \\ \dot{\mathrm{q}}_1 \\ \dot{\mathrm{q}}_2 \end{bmatrix}_2 \begin{bmatrix} \mathrm{q}_1 \\ \mathrm{q}_2 \\ \dot{\mathrm{q}}_1 \\ \dot{\mathrm{q}}_2 \end{bmatrix}_2^* \right] .
\end{gathered} \tag{3.55}$$

From this last point, it is possible to identify the information about the fluid-elastic modes corresponding to a given flow velocity U:

$$\tilde{\boldsymbol{\sigma}}_{\mathbf{1}}(U) = \begin{pmatrix} \mathrm{X}_{11} \\ \mathrm{X}_{21} \end{pmatrix} \ ; \quad \tilde{\boldsymbol{\sigma}}_{\mathbf{2}}(U) = \begin{pmatrix} \mathrm{X}_{13} \\ \mathrm{X}_{23} \end{pmatrix} \ , \quad \text{where} \quad \tilde{\boldsymbol{\sigma}}_{\boldsymbol{i}} \in \mathbb{C} \ . \tag{3.56}$$

In the approximated case of fluid-elastic coefficients that depend on the reduced frequency of the dominant mode only (simplification S2 in § 3.2.2), the following algorithm can be followed to solve the iterative process:

0. define a domain of flow velocities $[U_1, U_2, \dots, U_N]$ and set $i = 2$;
1. consider the flow velocity U_i;
2. assume the starting value of the unknown frequency ratio $\sqrt{X}^*$, which returns a guess ω^* of flutter and the corresponding reduced frequency K^*;
3. determine the fluid-elastic coefficients due to K^* and the ratio-independent damping coefficients due to ω^*;
4. solve the state-space problem of Eq. (3.45), with known coefficients, calculating the complex roots λ_1 and λ_2;
5. exit the frequencies ω_1 and ω_2, as well as the damping coefficient ξ_1 and ξ_2, and identify the destabilising mode:
   - if $\xi_k\big|_i < \xi_k\big|_{i-1}$, then use ω_k to determine the new $\sqrt{X}$;
6. if $|\sqrt{X} - \sqrt{X}^*|$ is smaller than a certain threshold go to step (7), else:

- update $\sqrt{X}^* = \sqrt{X}$;
- go to step (2) and continue till a limit number of iterations.

7. if $\xi_k \leq 0$, the critical flow velocity of flutter lies in the range $[U_{i-1}, U_i]$ and stop the process; else, set $i = i + 1$ and go to step (1) till $i \leq N$.

When the self-excited loads are formulated directly in the time domain, the previous algorithm simplifies avoiding steps 2-3-6.

3.3.2 Complex-determinant method

Within the frequency-domain methods, the simplification (S2) in § 3.2.2 is here recalled and combined with the observation (e) in § 3.1.2. In fact, it is supposed *negligible contribute of the secondary fluid-elastic mode during the evaluation of the critical condition*, in order to allow the representation of the motion through a single harmonic component at the flutter frequency:

$$\overline{\alpha}(t) = \overline{\hat{\alpha}} e^{j\omega t} \ , \quad \overline{\eta}(t) = \overline{\hat{\eta}} e^{j\omega t} \ , \quad \overline{\hat{\alpha}}, \overline{\hat{\eta}} \in \mathbb{C} \ . \tag{3.57}$$

Only the unstable mode (or dominant fluid-elastic mode) is considered and the approach is valid just for stability evaluation at the critical condition. The fluid-elastic coefficients are:

- *e.g.* $\boldsymbol{\Theta} = \boldsymbol{\Theta}(K)$, where K is due to the frequency ω of the dominant mode, without dependence on the modal shape (being ω unknown a priori, an iterative approach is required).

Eq. (3.57) simplifies Eq. (3.44) in

$$\begin{aligned} \mu \left(- \begin{bmatrix} r_\alpha^2 & x_m \\ x_m & 1 \end{bmatrix} \begin{bmatrix} \overline{\hat{\alpha}} \\ \overline{\hat{\eta}} \end{bmatrix} + j \begin{bmatrix} 2\xi_{\alpha 0} r_\alpha^2 \sqrt{X} & 0 \\ 0 & 2\xi_{\eta 0} \sqrt{X}/\gamma_{n0} \end{bmatrix} \begin{bmatrix} \overline{\hat{\alpha}} \\ \overline{\hat{\eta}} \end{bmatrix} + \right. \\ \left. + \begin{bmatrix} r_\alpha^2 X & 0 \\ 0 & X/\gamma_{n0}^2 \end{bmatrix} \begin{bmatrix} \overline{\hat{\alpha}} \\ \overline{\hat{\alpha}} \end{bmatrix} \right) = \\ = \frac{1}{K^2} \begin{bmatrix} \overline{M}(K, A_\alpha'', A_\alpha', A_\alpha, A_\eta'', A_\eta', A_\eta, \overline{\hat{\alpha}}, \overline{\hat{\eta}}) \\ \overline{L}(K, H_\alpha'', H_\alpha', H_\alpha, H_\eta'', H_\eta', H_\eta, \overline{\hat{\alpha}}, \overline{\hat{\eta}}) \end{bmatrix} . \end{aligned} \tag{3.58}$$

The presence on $\sqrt{X}$ can be simplified if the coefficients of rate-independent damping are introduced leading to the so called *U-g method* to solve the flutter equation [84]:

$$g_{\alpha 0} = 2\xi_{\alpha 0} \frac{\omega}{\omega_{\alpha 0}} \ , \quad g_{\eta 0} = 2\xi_{\eta 0} \frac{\omega}{\omega_{\eta 0}} \ . \tag{3.59}$$

This is an artefact to include the damping in the stiffness term[9]. The rate-independent damping simplify Eq. (3.58) into the more compact form

$$\begin{aligned} \begin{bmatrix} \mu r_\alpha^2 [(1 + j g_{\alpha 0}) X - 1] & -\mu r_\alpha^2 x_m \\ -\mu x_m & \mu [(1 + j g_{\eta 0}) X/\gamma_n^2 - 1] \end{bmatrix} \begin{bmatrix} \overline{\alpha}_0 \\ \overline{\eta}_0 \end{bmatrix} = \\ = \frac{1}{K^2} \begin{bmatrix} \overline{M}(K, A_\alpha'', A_\alpha', A_\alpha, A_\eta'', A_\eta', A_\eta, \overline{\hat{\alpha}}, \overline{\hat{\eta}}) \\ \overline{L}(K, H_\alpha'', H_\alpha', H_\alpha, H_\eta'', H_\eta', H_\eta, \overline{\hat{\alpha}}, \overline{\hat{\eta}}) \end{bmatrix} . \end{aligned} \tag{3.60}$$

[9]The introduction of the rate-independent damping coefficients $g_{\eta 0}$ or $g_{\alpha 0}$ comes from the assumption of 'proportional damping' (see § 3.1.1), where the damping depends only on the energy dissipated E_d through the hysteresis cycle, whatever shape it behaves. Thus, E_d is proportional to the squared amplitude of oscillation, in case of harmonic motion, and this introduces a time-shift of the elastic force. Hence, this assumption leads to damping forces proportional to the module of the elastic forces and in phase with the velocity of the motion [84]. Also in case of external additional damping introduced by the eddy-current dampers, as described in § 5, this holds because of purely viscous forces.

Once the dimensionless fluid-elastic loads $\overline{M}$ and $\overline{L}$ are formally expressed (see § 3.4), they follow Eq. (3.38) and the system becomes

$$\begin{bmatrix} \mu r_\alpha^2[(1+jg_{\alpha 0})X-1]+\overline{M}_\alpha & -\mu r_\alpha^2 x_m+\overline{M}_\eta \\ -\mu x_m+\overline{L}_\alpha & \mu[(1+jg_{\eta 0})X/\gamma_n^2-1]+\overline{L}_\eta \end{bmatrix} \begin{bmatrix} \overline{\hat{\alpha}} \\ \overline{\hat{\eta}} \end{bmatrix} = \begin{bmatrix} 0 \\ 0 \end{bmatrix} \tag{3.61a}$$

or

$$\begin{bmatrix} P_{11}(X) & P_{12} \\ P_{21} & P_{22}(X) \end{bmatrix} \begin{bmatrix} \overline{\hat{\alpha}} \\ \overline{\hat{\eta}} \end{bmatrix} = \begin{bmatrix} 0 \\ 0 \end{bmatrix} \quad , \tag{3.61b}$$

being $\overline{M}_\alpha$, $\overline{M}_\eta$, $\overline{L}_\alpha$, $\overline{L}_\eta$ the complex terms:

$$\overline{M}_\alpha = A_\alpha'' - A_\alpha - jA_\alpha' \quad ; \tag{3.62a}$$

$$\overline{M}_\eta = A_\eta'' - A_\eta - jA_\eta' \quad ; \tag{3.62b}$$

$$\overline{L}_\alpha = H_\alpha'' - H_\alpha - jH_\alpha' \quad ; \tag{3.62c}$$

$$\overline{L}_\eta = H_\eta'' - H_\eta - jH_\eta' \quad . \tag{3.62d}$$

Definitely, $\mathbf{P} \in \mathbb{C}$ depends on the unknown flutter frequency X, and Eq. (3.61) requires the solution of its complex determinant, usually by iterative methods [66, 84]. If the flutter condition exists in the flow velocity domain $[U_{min}, U_{max}]$, the determinant of $\mathbf{P}(X)$ vanishes:

$$\Delta_P(X) = \det \mathbf{P}(X) = P_{11}(X) \cdot P_{22}(X) - P_{12} \cdot P_{21} = 0 \quad . \tag{3.63}$$

A simple approach, usually referred as Theodorsen's approach [84], splits the determinant into its real and imaginary parts

$$\Delta_P(X) = \mathrm{Re}\{\Delta_P(X)\} + j\,\mathrm{Im}\{\Delta_P(X)\} \quad , \tag{3.64}$$

and considers the solutions of two algebraic 2^{nd}-order equations about its real and imaginary parts

$$\Delta_P(X) = 0 \;\Leftrightarrow\; \begin{cases} \mathrm{Re}\{\Delta_P(X)\} = 0 \\ \mathrm{Im}\{\Delta_P(X)\} = 0 \end{cases} . \tag{3.65}$$

Thus, plotting the solutions of the real and imaginary terms with respect to the reduced frequency, the critical condition will correspond to their intersection and the following iterative scheme can be followed:

0. define a domain of reduced frequency $[K_1, K_2, \ldots, K_N]$ and set $i = 2$;
1. consider the reduced frequeny K_i;
2. determine the fluid-elastic coefficients due to K_i;
3. solve Eq. (3.61) separately for $\mathrm{Re}\{\Delta_P(X)\} = 0$ and $\mathrm{Im}\{\Delta_P(X)\} = 0$:
   (a) assume a starting value of the unknown flutter frequency ω^* and calculate the ratio-independent damping coefficients;
   (b) solve the complex determinant of $\mathbf{P}$ for the unknown X and exit the new frequency ω;
   (c) if $|\omega - \omega^*|$ is smaller than a certain threshold go to step (4), else:
   - update $\omega^* = \omega$;
   - go to step (a) and continue until a limit number of iterations.
4. given K_i and K_{i-1}, if $(\omega|_{Re,i} - \omega|_{Im,i}) \cdot (\omega|_{Re,i-1} - \omega|_{Im,i-1}) \leq 0$, so that they intersect, the critical reduced frequency of flutter lies in the range $[K_{i-1}, K_i]$ and stop the process; else, set $i = i + 1$ and go to step (1) untill $i \leq N$.

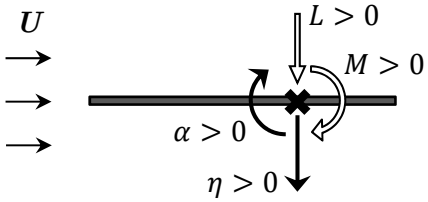

Figure 3.3. Positive convention of lift (L) and moment (M) loads with respect to the heaving (η) and pitching (α) DoFs, all referred to the position of the elastic axis (symbol ×).

3.4 Linearised fluid-elastic loads

The positive convention of the self-excited loads is represented in Fig. 3.3 and follows the positive convention of the motion components.

The self-excited loads of this section are considered **per unit span**.

3.4.1 Quasi-steady approach

The reduced frequency of oscillation (K) is proportional to the ratio

$$\frac{\text{time needed by the flow to stream the structure}}{\text{time needed by the structure to perform a cycle of oscillation}} = \frac{B/U}{2\pi/\omega} = K \ . \tag{3.66}$$

Dually, the particle disturbed by the body motion waves with the flow velocity U and frequency $n = \omega/2\pi$, exhibiting a certain wave length. Thus, the the reduced frequency is also proportional to

$$\frac{\text{body dimension}}{\text{flowing-wave length}} = \frac{B}{U/n} = K \ . \tag{3.67}$$

Hence, $K < 1$ means that a particle of flow streams quickly over the structure interacting with it only in a portion of its cycle of oscillation or, dually, that the disturbance arising at a certain point of the body is not felt by other points.

When $K \ll 1$, the flow interacts with structure without *memory effects*, and the quasi-steady assumption relies on this: the flow that interacts with the structure at time t considers the structure as it is stationary, with instantaneous values of both displacements and velocity calculated at the same time t, disregarding its motion history. The quasi-steady theory considers fluid-elastic loads that come from vorticity and circulation only (Fig. 3.4), but neglecting both memory effects and apparent masses, which always arise for unsteady motions [84]. This introduces important approximations and quasi-steady theory has to be carefully used in the case of flutter [139].

The quasi-steady theory explained in the following is formulated for streamlined bodies, and takes place within the following assumptions:

1. two-dimensional problem (or *'strip' assumption*[10]);
2. incompressible flow (subsonic regime, $\mathrm{M}^2 = (U_{flow}/U_{sound})^2 \ll 1$);
3. steady flow with constant mean value (fluctuations could be included as well [139]);
4. small perturbations about equilibrium conditions (infinitesimal displacements and first-order approximation of flow-induced loads);
5. surface on the body differing only infinitesimally from a flat plate.

[10]This assumption regards the finite-span effect of tridimensional structures: the fluid-elastic forces at any position along the span of the structure can be calculated considering the cross section at that position as situated in a two-dimensional flow (being like an infinite cylinder with fixed cross section).

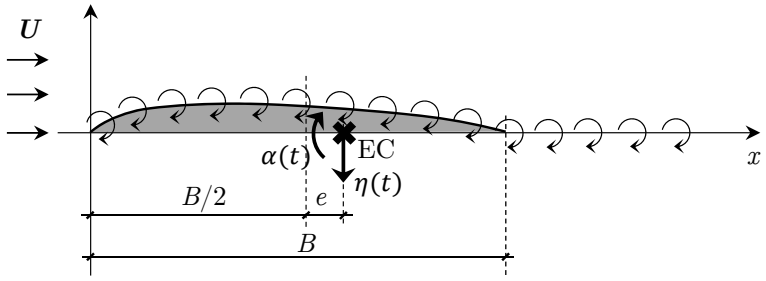

Figure 3.4. Distribution of the vorticity circulation due to unsteady motion of pitching α and heaving η about the elastic centre (EC), under the steady flow velocity U.

An infinitesimal disturbance on the angle of attack of the free-stream flow produces fluid-elastic loads due to a resultant flow velocity that has to be tangent to the section boundary, leaving the trailing edge in a smooth way (Kutta's condition). Thus, the body can be replaced by a continuous distribution of vortices (vortex street), which gives the resultant lift according to Joukowsky's theorem. The lift acts at the 1/4-chord aft of the leading edge. Therefore, the resultant dimensionless loads of lift and moment, referred to the leading edge ($x = 0$, see Fig. 3.4), are [84]:

$$\overline{L} = -\frac{d\overline{L}}{d\alpha}\left[\alpha + \frac{\dot{\eta}}{U} + \left(\frac{1}{4} - x_e\right)\frac{B\dot{\alpha}}{U}\right] \quad ; \tag{3.68a}$$

$$\overline{M}\big|_{l.e.} = -\frac{\pi}{8}\frac{B\dot{\alpha}}{U} + \frac{1}{4}\overline{L} \quad . \tag{3.68b}$$

In Eq. (3.68a), the term contained in $[\dots]$ represents the apparent angle of attack due to the velocity field of the motion. Inside it, the term contained in $(\dots)$ identifies the point that is representative, for the whole section, of the variable angle of attack along the section due to the angular velocity $\dot{\alpha}$, located $\frac{3}{4}B$ aft of the leading edge. In Eq. (3.68b), the lift is acting at the quarter-chord aft of the leading edge, and also contains a damping couple. Eq. (3.68) can be re-arranged so to evaluate the moment about the elastic axis. Thus, if the vortex street is assumed to be concentrated at the upstream $\frac{1}{4}$-chord point and if the downwash angle is evaluated about the $\frac{3}{4}$-chord point, it becomes:

$$\overline{L} = -\frac{d\overline{L}}{d\alpha}\left[\alpha + \frac{\dot{\eta}}{U} + \left(\frac{1}{4} - x_e\right)\frac{B\dot{\alpha}}{U}\right] \quad ; \tag{3.69a}$$

$$\overline{M} = \overline{M}\big|_{l.e.} - \left(\frac{1}{2} + x_e\right)\overline{L} = -\frac{\pi}{8}\frac{B\dot{\alpha}}{U} - \left(\frac{1}{4} + x_e\right)\overline{L} \quad . \tag{3.69b}$$

Developing Eq. (3.69b), the following expression is obtained

$$\overline{M} = \left(\frac{d\overline{L}/d\alpha - 2\pi}{16} - \frac{d\overline{L}}{d\alpha}x_e^2\right)\frac{B\dot{\alpha}}{U} + \frac{d\overline{L}}{d\alpha}\left(\frac{1}{4} + x_e\right)\left(\alpha + \frac{\dot{\eta}}{U}\right) \quad , \tag{3.70}$$

in which, under the assumption of flat plate ($d\overline{L}/d\alpha = 2\pi$), the damping couple depends only on the eccentricity of the elastic axis and vanishes for symmetric configurations. The corresponding dimensionless fluid-elastic coefficients are reported in Table 3.1.

Table 3.1. Dimensionless fluid-elastic coefficients from quasi-steady theory.

A_α''	0
A_α'	$\left[-\frac{\pi}{8}+\left(\frac{1}{16}-x_e^2\right)\frac{d\overline{L}}{d\alpha}\right]/K$
A_α	$\frac{d\overline{L}}{d\alpha}(\frac{1}{4}+x_e)/K^2$
A_η''	0
A_η'	$\frac{d\overline{L}}{d\alpha}(\frac{1}{4}+x_e)/K$
A_η	0
H_α''	0
H_α'	$-\frac{d\overline{L}}{d\alpha}(\frac{1}{4}-x_e)/K$
H_α	$-\frac{d\overline{L}}{d\alpha}/K^2$
H_η''	0
H_η'	$-\frac{d\overline{L}}{d\alpha}/K$
H_η	0
$\overline{M}_\alpha$	$-\frac{d\overline{L}}{d\alpha}(\frac{1}{4}+x_e)/K^2-j\left[(\frac{d\overline{L}}{d\alpha}-2\pi)/16-\frac{d\overline{L}}{d\alpha}x_e^2\right]/K$
$\overline{M}_\eta$	$-j\frac{d\overline{L}}{d\alpha}(\frac{1}{4}+x_e)/K$
$\overline{L}_\alpha$	$\frac{d\overline{L}}{d\alpha}/K^2+j\frac{d\overline{L}}{d\alpha}(\frac{1}{4}-x_e)/K$
$\overline{L}_\eta$	$j\frac{d\overline{L}}{d\alpha}/K$

3.4.2 Unsteady approaches

The hypothesis of quasi-steady theory can be removed, considering the memory effects of unsteady motion. Again for streamlined bodies, the assumptions behind this more general approach are:

1. two-dimensional problem (or *'strip' assumption*, see footnote 10);
2. steady flow with constant mean value;
3. non-stationary potential-flow theory (piezotropic, isentropic, irrotational and inviscid fluid);
4. no flow separation and shear-layer development (Kutta-Yukoswky's assumption at the trailing edge);
5. incompressible flow (subsonic regime, $\mathrm{M}^2 = \left(U_{flow}/U_{sound}\right)^2 \ll 1$);
6. small perturbations about equilibrium conditions (infinitesimal displacements and first-order approximation of flow-induced loads);
7. surface on the body differing only infinitesimally from a flat plate.

The self-excited loads have been obtained in closed-form solution for airfoil due to a step response (either to a pitch input [211] or to a gust [123, 189, 190, 210]), due to airfoil oscillations in the frequency domain [206] and due to generalized airfoil motions in the Laplace domain [69]. Moreover, the unsteady motion can be arranged in the state-space form, thus in terms of ordinary differential equations that approximate the airfoil and flow-field response [169, 170].

3.4.2.1 Wagner's model

In this paragraph, the reference length is the semi-chord $b = B/2$ and the dimensionless eccentricity of the elastic axis is referred to the semichord, so that $x_e^* = e/b = 2x_e$. Let consider the unsteady aerodynamic forces acting on a streamlined cross section undergoing unsteady motion in the η and α DoFs (Fig. 3.5), which are due to [211, 84]:

- *circulatory origin*:
  - vorticity circulation;
  - centrifugal effect;
- *non-circulatory origin*:
  - apparent mass on the heaving and pitching DoFs.

At a given flow velocity U, an impulsive step at time $t_0 = 0$ on the motion generates a growth of circulation that gives the following lift (with resultant acting at $\frac{1}{4}$-chord aft the leading edge):

$$L_1(\tau) = -\frac{1}{2}\rho U^2(2b) \cdot \frac{d\overline{L}}{d\alpha} \cdot \frac{w}{U} \cdot \psi(\tau) \quad ; \tag{3.71}$$

in which

- $d\overline{L}/d\alpha$, is the slope of the lift coefficient that corresponds to 2π in case of ideal flat plate;
- w/U , is the angle of attack produced by the vertical velocity component of the fluid (w, called 'downwash') within the assumption that the flow must be tangent to the body surface;

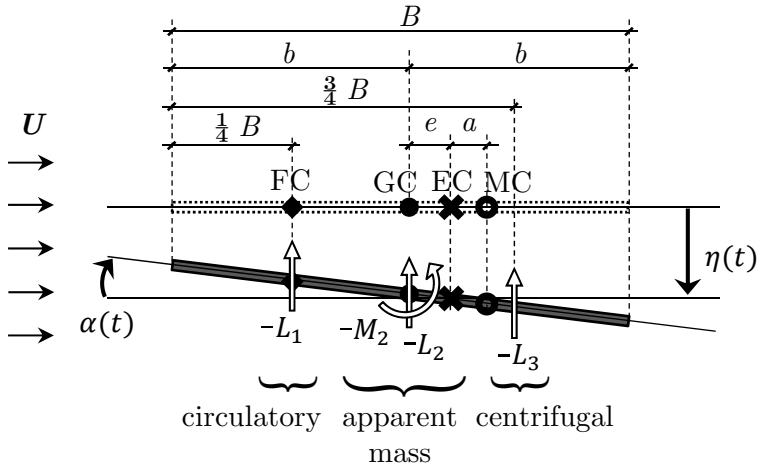

Figure 3.5. Schematic of the self-excited loads acting on a 2-DoF fluttering flat plate, due to: vorticity circulation (L_1), acting at the $\frac{1}{4}$-chord point; apparent masses in heaving (L_2), acting at the mid-chord point and in pitching (M_2); centrifugal effect (L_3), acting at the $\frac{3}{4}$-chord point.

- $\sigma(\tau)$, is the *Wagner's function* that represents the growth of circulation due to a sudden step in the downwash:

$$\psi(\tau) = 1 - \int_0^\infty \left[(Y_0 + Y_1)^2 + \pi^2 (J_0 + J_1)^2 \right]^{-1} e^{-x\tau} x^{-2} dx \quad , \tag{3.72}$$

  where J_0 and J_1, Y_0 and Y_1 are modified Bessel's function of, respectively, first and second kind, with argument x implied;

- τ , is a dimensionless quantity proportional to the time that describes the distance travelled at the fixed velocity U:

$$\tau = Ut/b \quad . \tag{3.73}$$

In case of 2-DoF motion, the downwash can be determined referring to the $\frac{3}{4}$-chord point aft of the leading edge according to

$$w(t) = U\alpha(t) + \dot{\eta}(t) + \left(\frac{1}{2} - x_e^*\right) b\, \dot{\alpha}(t) \quad , \tag{3.74a}$$

or

$$w(\tau) = U\alpha(\tau) + \frac{U}{b}\eta'(\tau) + \left(\frac{1}{2} - x_e^*\right) U\, \alpha'(\tau) \quad , \tag{3.74b}$$

introducing the differentiation with respect to the dimensionless time $\dot{(\,)} = (\,)'\, U/b$. An impulsive increment of downwash $dw(\kappa)$ at time κ produces the lift growth

$$dL_1(\tau) = -\frac{1}{2}\rho U^2 (2b) \cdot \frac{d\overline{L}}{d\alpha} \cdot \frac{dw(\kappa)}{U} \cdot \psi(\tau - \kappa) \tag{3.75}$$

and, assuming that $w = 0$ for $\tau \leq 0$ and $\psi(\tau - \kappa) = 0$ for $\tau < \kappa$, the resulting lift is obtained combining Eqs. (3.74b) and (3.75) through Duhamel's integral:

$$\begin{aligned} L_1(\tau) = &-\frac{1}{2}\rho U^2 (2b) \cdot \frac{d\overline{L}}{d\alpha} \cdot \\ &\cdot \int_0^\tau \psi(\tau - \kappa) \left[\alpha'(\tau) + \frac{\eta''(\tau)}{b} + \left(\frac{1}{2} - x_e^*\right) \alpha''(\tau) \right] d\kappa \quad . \end{aligned} \tag{3.76}$$

The apparent masses in the heaving and pitching DoFs are:

$$L_2 = -\rho\pi b^2 \left(\ddot{\eta} - x_e^* b\ \ddot{\alpha}\right) = -\frac{1}{2}\rho U^2 (2b) \cdot \pi \left(\frac{\eta''}{b} - x_e^*\ \alpha''\right) \quad ; \tag{3.77a}$$

$$M_2 = -\frac{\rho\pi b^4}{8}\ddot{\alpha} = -\frac{1}{2}\rho U^2 (2b)^2 \cdot \frac{\pi}{16}\ \alpha'' \quad ; \tag{3.77b}$$

which act about the mid-chord point. The centrigural force is

$$L_3 = -\rho\pi b^2 U\ \dot{\alpha} = -\frac{1}{2}\rho U^2 (2b) \cdot \pi\ \alpha' \quad , \tag{3.78}$$

with center at the $\frac{3}{4}$-chord point aft of the leading edge. Finally, the unsteady loads of lift and moment are

$$L(\tau) = L_1(\tau) + L_2(\tau) + L_3(\tau) \quad , \tag{3.79a}$$

$$M(\tau) = -L_1(\tau) \cdot b\left(\frac{1}{2} + x_e^*\right) - L_2(\tau) \cdot b x_e^* + L_3(\tau) \cdot b\left(\frac{1}{2} - x_e^*\right) + M_2 \quad , \tag{3.79b}$$

and assume the dimensionless forms:

$$\begin{aligned} \overline{L}(\tau) &= \frac{L(\tau)}{\frac{1}{2}\rho U^2 (2b)} = \\ &= -\pi\left(\frac{\eta''}{b} - x_e^*\ \alpha'' + \alpha'\right) - \\ &- \frac{d\overline{L}}{d\alpha} \cdot \int_0^\tau \psi(\tau - \kappa)\left[\alpha'(\tau) + \frac{\eta''(\tau)}{b} + \left(\frac{1}{2} - x_e^*\right)\alpha''(\tau)\right] d\kappa \ ; \end{aligned} \tag{3.80a}$$

$$\begin{aligned} \overline{M}(\tau) &= \frac{M(\tau)}{\frac{1}{2}\rho U^2 (2b)^2} = \\ &= \pi\left[\ \frac{\eta''}{b}\frac{x_e^*}{2} - \left(\frac{x_e^{*2}}{2} + \frac{1}{16}\right)\alpha'' - \left(\frac{1}{4} - \frac{x_e^*}{2}\right)\alpha'\ \right] + \\ &+ \left(\frac{1}{4} + \frac{x_e^*}{2}\right)\frac{d\overline{L}}{d\alpha} \cdot \int_0^\tau \psi(\tau - \kappa)\left[\alpha'(\tau) + \frac{\eta''(\tau)}{b} + \left(\frac{1}{2} - x_e^*\right)\alpha''(\tau)\right] d\kappa \ . \end{aligned} \tag{3.80b}$$

3.4.2.2 Theodorsen's model

Theodorsen's approach [206] considers the theoretical case of potential-flow theory applied to a flat plate undergoing harmonic motion, and has been developed to evaluate the critical condition of flutter in the frequency domain. The motion is supposed to be driven by the dominant fluid-elastic mode alone:

$$\alpha = \hat{\alpha} e^{j\omega t} = \hat{\alpha} e^{jk\tau} \quad , \quad \eta = \hat{\eta} e^{j\omega t} = \hat{\eta} e^{jk\tau} \quad , \quad \hat{\alpha}, \hat{\eta} \in \mathbb{C} \ , \tag{3.81}$$

where $k = \omega b/U = K/2$ is the reduced frequency referred to the semichord. In this case, the self-excited loads of Eq. (3.80) can be expressed as [84]:

$$\begin{aligned} \overline{L}(k) &= \frac{L(\tau) \cdot e^{-jk\tau}}{\frac{1}{2}\rho U^2 (2b)} = \\ &= -\pi\left[-k^2\left(\frac{\hat{\eta}}{b} - x_e^*\ \hat{\alpha}\right) + jk\hat{\alpha}\right] - \\ &- \frac{d\overline{L}}{d\alpha} C(k)\left[\hat{\alpha} + jk\frac{\hat{\eta}}{b} + jk\left(\frac{1}{2} - x_e^*\right)\hat{\alpha}\right] \quad ; \end{aligned} \tag{3.82a}$$

$$\begin{aligned} \overline{M}(k) &= \frac{M(\tau) \cdot e^{-jk\tau}}{\frac{1}{2}\rho U^2 (2b)^2} = \\ &= \pi\left\{\ -k^2\left[\frac{\hat{\eta}}{b}\frac{x_e^*}{2} - \left(\frac{x_e^{*2}}{2} + \frac{1}{16}\right)\hat{\alpha}\right] - jk\left(\frac{1}{4} - \frac{x_e^*}{2}\right)\hat{\alpha}\ \right\} + \\ &+ \left(\frac{1}{4} + \frac{x_e^*}{2}\right)\frac{d\overline{L}}{d\alpha} C(k)\left[\hat{\alpha} + jk\frac{\hat{\eta}}{b} + jk\left(\frac{1}{2} - x_e^*\right)\hat{\alpha}\right] \quad ; \end{aligned} \tag{3.82b}$$

in which

$$C(k) = F(k) + jG(k) = \frac{H_1^{(2)}(k)}{H_1^{(2)}(k) + jH_0^{(2)}(k)} \tag{3.83}$$

is the *Theodorsen's circulatory function*[11] and contains the Hänkel's functions

$$H_n^{(2)}(k) = J_n(k) - jY_n(k) \tag{3.84}$$

with the modified Bessel's functions $J_n(k)$ and $Y_n(k)$ of first and second kind.

Arranging Eq. (3.82) to consider the dimensionless variables of Eq. (3.35), the dimensionless loads are

$$\begin{aligned}
\frac{\overline{L}(t)}{K^2} &= \frac{L(K)\cdot e^{j\omega t}}{\frac{1}{2}\rho U^2 B\cdot K^2} = \\
&= -\frac{\pi}{2}\left[\ddot{\overline{\eta}}(t) + \frac{\dot{\overline{\alpha}}(t)}{K} - x_e\ddot{\overline{\alpha}}(t)\right] - \\
&- \frac{d\overline{L}}{d\alpha}C(k)\left[\frac{\dot{\overline{\eta}}(t)}{K} + \frac{\overline{\alpha}(t)}{K^2} + \left(\frac{1}{4} - x_e\right)\frac{\dot{\overline{\alpha}}(t)}{K}\right] ;
\end{aligned} \tag{3.85a}$$

$$\begin{aligned}
\frac{\overline{M}(t)}{K^2} &= \frac{M(K)\cdot e^{j\omega t}}{\frac{1}{2}\rho U^2 B^2\cdot K^2} = \\
&= \frac{\pi}{2}\left[x_e\ddot{\overline{\eta}}(t) - \left(\frac{1}{4} - x_e\right)\frac{\dot{\overline{\alpha}}(t)}{K} - \left(\frac{1}{32} + x_e^2\right)\ddot{\overline{\alpha}}(t)\right] + \\
&+ \left(\frac{1}{4} + x_e\right)\frac{d\overline{L}}{d\alpha}C(k)\left[\frac{\dot{\overline{\eta}}(t)}{K} + \frac{\overline{\alpha}(t)}{K^2} + \left(\frac{1}{4} - x_e\right)\frac{\dot{\overline{\alpha}}(t)}{K}\right] ;
\end{aligned} \tag{3.85b}$$

from which the fluid-elastic coefficients can be identified, as reported in Table 3.2.

[11] The circulatory function $C(k)$ is linked to the Wagner's function through the Fourier transform

$$\psi(\tau) = \frac{1}{2\pi}\int_{-\infty}^{+\infty}\frac{C(k)}{jk}e^{jk\tau}dk \ .$$

Table 3.2. Dimensionless fluid-elastic coefficients from unsteady approach in the frequency domain, using the Theodorsen's approach.

$A_{\alpha}^{''}$	$-\left(\frac{1}{32}+x_e^2\right)\frac{\pi}{2}$
$A_{\alpha}^{'}$	$-\left(\frac{1}{4}-x_e\right)\frac{\pi}{2}/K+\left(\frac{1}{16}-x_e^2\right)\frac{d\overline{L}}{d\alpha}C(k)/K$
A_{α}	$\left(\frac{1}{4}+x_e\right)\frac{d\overline{L}}{d\alpha}C(k)/K^2$
$A_{\eta}^{''}$	$x_e\frac{\pi}{2}$
$A_{\eta}^{'}$	$\left(\frac{1}{4}+x_e\right)\frac{d\overline{L}}{d\alpha}C(k)/K$
A_{η}	0
$H_{\alpha}^{''}$	$\frac{\pi}{2}x_e$
$H_{\alpha}^{'}$	$-\frac{\pi}{2}/K-\left(\frac{1}{4}-x_e\right)\frac{d\overline{L}}{d\alpha}C(k)/K$
H_{α}	$-\frac{d\overline{L}}{d\alpha}C(k)/K^2$
$H_{\eta}^{''}$	$-\frac{\pi}{2}$
$H_{\eta}^{'}$	$-\frac{d\overline{L}}{d\alpha}C(k)/K$
H_{η}	0
$\overline{M}_{\alpha}$	$\left(\frac{1}{32}+x_e^2\right)\frac{\pi}{2}+\left(\frac{1}{4}+x_e\right)\frac{d\overline{L}}{d\alpha}C(k)/K^2-$ $-j\left(\frac{1}{4}-x_e\right)\left[\frac{\pi}{2}+\left(\frac{1}{4}+x_e\right)\frac{d\overline{L}}{d\alpha}C(k)\right]/K$
$\overline{M}_{\eta}$	$-x_e\frac{\pi}{2}+j\left(\frac{1}{4}+x_e\right)\frac{d\overline{L}}{d\alpha}C(k)/K$
$\overline{L}_{\alpha}$	$-\frac{\pi}{2}x_e-\frac{d\overline{L}}{d\alpha}C(k)/K^2-j\left[\frac{\pi}{2}+\left(\frac{1}{4}-x_e\right)\frac{d\overline{L}}{d\alpha}C(k)\right]/K$
$\overline{L}_{\eta}$	$\frac{\pi}{2}-j\frac{d\overline{L}}{d\alpha}C(k)/K$

3.4.3 Flutter-derivative approach

Flutter-derivative approach has been developed for civil engineering purposes and, in particular, to evaluate the wind-induced effects on bridges ([187, 192]). Indeed, this approach can be seen as an extension of the Theodorsen's approach to problems different to the flat-plate case study. When specific or complex cross sections are involved, provided that the system is still prone to flutter, the study of the critical condition is performed by evaluating the fluid-elastic coefficients proper of that case study, in the frequency domain, which are called 'flutter derivatives'.

This approach comes from the experimental field, in which specific tests are performed to determine the flutter derivatives. These are intrinsically dependent on the geometry of the cross section and position of the elastic centre, while they can be expressed as functions of the reduced frequency of the motion [25], within the assumption of small perturbations about the equilibrium position. The tests can be performed in two ways:

1. through forced-harmonic motion (according to the DoFs, separately and combined) for several flow velocities, during which the fluid-dynamic forces are measured and used to calculate the flutter derivatives;
2. through free-decay oscillations (according to the DoFs, separately and combined) from a given small initial condition, for several flow velocities and measuring the displacements to extract the flutter derivatives.

Flutter-derivative approach considers empirical, real-valued fluid-elastic coefficients connected to the velocity and displacement fields[12]. It applies to the case of harmonic motion during the flutter instability, when only the principal fluid-elastic mode is considered as responsible of the motion, since the contribution of the secondary fluid-elastic is hardly quantifiable through experiments and has negligible influence.

The self excited loads are:

$$\overline{M} = KA_1^*(K)\frac{\dot{\eta}}{U} + KA_2^*(K)\frac{B\dot{\alpha}}{U} + K^2A_3^*(K)\alpha + K^2A_4^*(K)\frac{\eta}{B} \quad ; \tag{3.86a}$$

$$\overline{L} = KH_1^*(K)\frac{\dot{\eta}}{U} + KH_2^*(K)\frac{B\dot{\alpha}}{U} + K^2H_3^*(K)\alpha + K^2H_4^*(K)\frac{\eta}{B} \quad ; \tag{3.86b}$$

in which A_i^*, H_i^*, for $i = 1, 2, 3, 4$, are the dimensionless flutter derivatives, following the notation of [187]. The corresponding dimensionless fluid-elastic coefficients are reported in Table 3.3. Comparing the terms $\overline{M}_\alpha$, $\overline{M}_\eta$, $\overline{L}_\alpha$, $\overline{L}_\eta$ of Table 3.2 with those of Table 3.3, the flutter derivatives can be linked to the fluid-elastic coefficients from Theodorsen's theory as reported on Table 3.4.

Moreover, the determination of the flutter derivatives depends on the position of the elastic axis (§ 3.2.1). Assuming that circulatory/centrifugal forces and apparent masses follow the same structure of those for the unsteady theory, the flutter derivatives of any configuration with $x_e \neq 0$ can be calculated from those obtained for the symmetric configuration ($x_e = 0$),

[12] The contributions proportional to the acceleration field, so that the apparent masses, can be neglected for civil engineering applications [187].

here called $H^*_{i,0}$ and $A^*_{i,0}$ for $i = 1, 2, 3, 4$, according to:

$$
\begin{aligned}
A^*_1(K) &= A^*_{1,0}(K)\,(1 + 4x_e) \quad ; \\
A^*_2(K) &= \left[A^*_{2,0}(K) + \frac{\pi}{8K}\right](1 + 4x_e) - \frac{\pi}{8K} - x_e A^*_1(K) + \frac{\pi x_e}{2K} \quad ; \\
A^*_3(K) &= \left[A^*_{3,0}(K) - \frac{\pi}{64}\right](1 + 4x_e) + \frac{\pi}{64} - x_e A^*_4(K) \quad ; \\
A^*_4(K) &= A^*_{4,0}(K)\,(1 + 4x_e) - \frac{\pi x_e}{2} \quad ; \\
H^*_1(K) &= H^*_{1,0}(K) \quad ; \\
H^*_2(K) &= H^*_{2,0}(K) - x_e H^*_1(K) \quad ; \\
H^*_3(K) &= H^*_{3,0}(K) - x_e H^*_4(K) \quad ; \\
H^*_4(K) &= H^*_{4,0}(K) \quad .
\end{aligned}
\tag{3.87}
$$

This relationship has also been sought in [150], but the Authors do not explain the formal expressions, although they compare the calculated results with the experimental measurements finding quite good agreement.

Table 3.3. Dimensionless fluid-elastic coefficients from flutter derivatives approach.

A''_α	0
A'_α	$A^*_2(K)$
A_α	$A^*_3(K)$
A''_η	0
A'_η	$A^*_1(K)$
A_η	$A^*_4(K)$
H''_α	0
H'_α	$H^*_2(K)$
H_α	$H^*_3(K)$
H''_η	0
H'_η	$H^*_1(K)$
H_η	$H^*_4(K)$
$\overline{M}_\alpha$	$jA^*_2(K) + A^*_3(K)$
$\overline{M}_\eta$	$jA^*_1(K) + A^*_4(K)$
$\overline{L}_\alpha$	$jH^*_2(K) + H^*_3(K)$
$\overline{L}_\eta$	$jH^*_1(K) + H^*_4(K)$

Table 3.4. Relationships between flutter derivatives and fluid-elastic coefficients from Theodorsen's theory, in which *e.g.* $\mathrm{Re}[L_{1\dot\eta}]$ indicates the part proportional to the real part of the circulatory lift due to $\dot\eta$ of Eq. (3.85). It follows similarly for the others. The terms inside $[\cdots]$ represent the dimensionless distances of each lift contributions to evaluate the respective moments about the elastic centre.

$$A_1^*(K) = \pi\left\{ \underbrace{\frac{F(k)}{k}\frac{d\overline{L}/d\alpha}{2\pi}}_{\mathrm{Re}[L_{1\dot\eta}]} \cdot \left[\tfrac{1}{2}\left(\tfrac{1}{2}+x_e^*\right)\right] \right\}$$

$$A_2^*(K) = -\frac{\pi}{2k}\left\{ \underbrace{\tfrac{1}{2}}_{L_{3\dot\alpha}} \cdot \left[\tfrac{1}{2}\left(\tfrac{1}{2}-x_e^*\right)\right] - \underbrace{\left(\tfrac{1}{2}-x_e^*\right)F(k)\frac{d\overline{L}/d\alpha}{2\pi}}_{\mathrm{Re}[L_{1\dot\alpha}]} \cdot \left[\tfrac{1}{2}\left(\tfrac{1}{2}+x_e^*\right)\right] - \right.$$
$$\left. - \underbrace{\frac{G(k)}{k}\frac{d\overline{L}/d\alpha}{2\pi}}_{\mathrm{Im}[L_{1\alpha}]} \cdot \left[\tfrac{1}{2}\left(\tfrac{1}{2}+x_e^*\right)\right] \right\}$$

$$A_3^*(K) = -\frac{\pi}{2k^2}\left\{ \underbrace{\frac{x_e^* k^2}{2}}_{L_{2\ddot\alpha}} \cdot \left[\frac{x_e^*}{2}\right] + \underbrace{\frac{k^2}{32}}_{M_\alpha} + \underbrace{F(k)\frac{d\overline{L}/d\alpha}{2\pi}}_{\mathrm{Re}[L_{1\alpha}]} \cdot \left[\tfrac{1}{2}\left(\tfrac{1}{2}+x_e^*\right)\right] - \right.$$
$$\left. \underbrace{\left(\tfrac{1}{2}-x_e^*\right)kG(k)\frac{d\overline{L}/d\alpha}{2\pi}}_{\mathrm{Im}[L_{1\dot\alpha}]} \cdot \left[\tfrac{1}{2}\left(\tfrac{1}{2}+x_e^*\right)\right] \right\}$$

$$A_4^*(K) = -\pi\left\{ \underbrace{\tfrac{1}{2}}_{L_{2\ddot\eta}} \cdot \left[\frac{x_e^*}{2}\right] + \underbrace{\frac{G(k)}{k}\frac{d\overline{L}/d\alpha}{2\pi}}_{\mathrm{Im}[L_{1\dot\eta}]} \cdot \left[\tfrac{1}{2}\left(\tfrac{1}{2}+x_e^*\right)\right] \right\}$$

$$-H_1^*(K) = \pi\left\{ \underbrace{\frac{F(k)}{k}\frac{d\overline{L}/d\alpha}{2\pi}}_{\mathrm{Re}[L_{1\dot\eta}]} \right\}$$

$$-H_2^*(K) = \frac{\pi}{2k}\left\{ \underbrace{\tfrac{1}{2}}_{L_{3\dot\alpha}} + \underbrace{\left(\tfrac{1}{2}-x_e^*\right)F(k)\frac{d\overline{L}/d\alpha}{2\pi}}_{\mathrm{Re}[L_{1\dot\alpha}]} + \underbrace{\frac{G(k)}{k}\frac{d\overline{L}/d\alpha}{2\pi}}_{\mathrm{Im}[L_{1\alpha}]} \right\}$$

$$-H_3^*(K) = \frac{\pi}{2k^2}\left\{ \underbrace{\frac{x_e^* k^2}{2}}_{L_{2\ddot\alpha}} + \underbrace{F(k)\frac{d\overline{L}/d\alpha}{2\pi}}_{\mathrm{Re}[L_{1\alpha}]} - \underbrace{\left(\tfrac{1}{2}-x_e^*\right)kG(k)\frac{d\overline{L}/d\alpha}{2\pi}}_{\mathrm{Im}[L_{1\dot\alpha}]} \right\}$$

$$-H_4^*(K) = -\pi\left\{ \underbrace{\tfrac{1}{2}}_{L_{2\ddot\eta}} + \underbrace{\frac{G(k)}{k}\frac{d\overline{L}/d\alpha}{2\pi}}_{\mathrm{Im}[L_{1\dot\eta}]} \right\}$$

3.5 Overview of post-critical modelling

3.5.1 Nonlinearity sources

In case of classical-flutter mechanism, the energy transfer between flowstream and structure relies on elastic and/or fluid-dynamic coupling between the two fluid-elastic modes ($\tilde{\boldsymbol{\sigma}}_{\mathbf{1}}$ and $\tilde{\boldsymbol{\sigma}}_{\mathbf{2}}$, as indicated in § 3.1.2). The key effect is the modification of the phase lags involved in the mechanism:

A) phase lag between $\tilde{\boldsymbol{\sigma}}_{\mathbf{1}}$ and $\tilde{\boldsymbol{\sigma}}_{\mathbf{2}}$,

B) phase lags between each $\tilde{\boldsymbol{\sigma}}_{\boldsymbol{k}}$ and the respective fluid-dynamic reactions,

in order to pump energy from the flow into the mechanical system. The phase adjustment at the instability onset generates loss of damping in one of the fluid-elastic mode, which then drives the instability.

Considering some practical applications [48, 60, 61, 64, 83], nonlinearity sources can come from the:

- *mechanical system*:
  - free play or nonlinear stiffness arising from structural components (*e.g* control surface/flap [199], loose joints, hardening springs, see also [73])
  - strain displacement or geometric effects (*e.g.* nonlinear stiffness arising from large displacements gradients)
  - dry friction or nonlinear damping (*e.g.* structural components in sliding contacts).
- *fluid-dynamic reactions*:
  - shock motion in transonic flows (see also [188]);
  - separated flows, due to transonic flows or large angles of attack (see also [67]).

Thus, provided that the mechanical properties of the system are linear within the range of interest and the subsonic regime holds, the nonlinearity source is in the fluid-dynamic reactions only. The linearised theory predicts exponentially growing oscillations, describing a dynamically divergent phenomenon at the flutter boundary. Nevertheless, as time unfolds, the oscillation amplitudes increase and nonlinear excitation mechanisms can affect the motion, so to modify the total mass, damping and stiffness matrices of the coupled fluid-elastic system. In particular, in case of post-critical oscillations evolving from the classical-flutter instability, the nonlinearity is essentially due to important flow separation encountered crossing the stall angle that produces hysteresis in the load-displacement path. Limit-cycle oscillations appear, and the following amplitude-velocity path manifests very large amplitudes in both the DoFs that increase with the flow velocity, after a steep and large jump at the instability threshold. Furthermore, the system manifests a sub-critical bifurcation, thus exhibiting a significant stable branch for flow speeds lower than the critical one (*e.g.* see Fig. 3.6).

3.5.2 Nonlinear models and approaches

Although the classical-flutter phenomenon is well studied in terms of prediction of the instability threshold, a few research studies are available in its post-critical regime, and the majority are focused on practical applications related to aeronautical engineering problems (see also [128] for an extensive review on nonlinear-aeroelasticity investigations). In addition, these problems come from flight experience about high-speed aircrafts and helicopters, and the nonlinearity sources are often in the mechanical system [61, 63, 64]. Thus, the modelling of the nonlinear fluid-dynamic reactions is still an open issue.

The post-critical regime of flutter can be faced through analytical, computational and experimental approaches.

Analitical models are not available in closed form. The main problem is the modelling of the self-excited loads in the post-critical regime. The simplest way to explore the post-critical

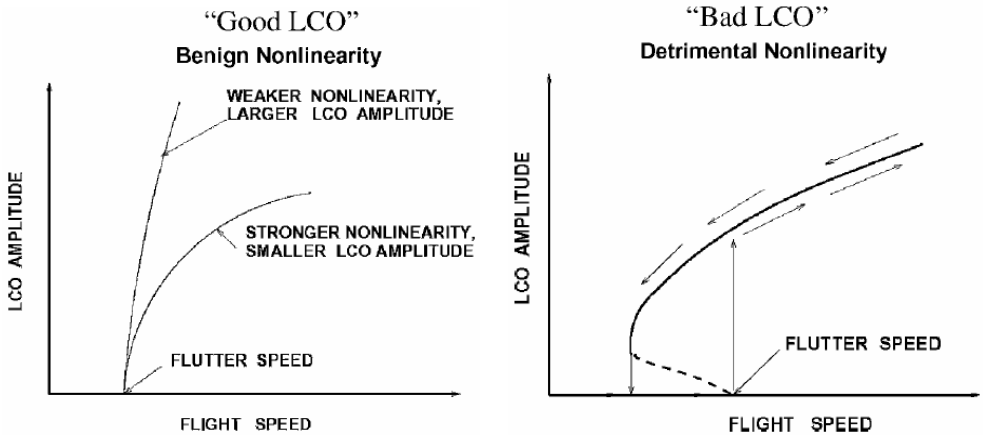

Figure 3.6. Influence of nonlinearities on the evolution of the LCO amplitude with respect to the flow velocity, and difference between super-critical and sub-critical bifurcation. Picture from [61].

regime, although introducing approximations, is by the use of the quasi-steady theory. Indeed, the linear model presented in § 3.4.1) can be extended to the large-amplitude motion by considering the actual not-linearised displacements (see also [139] for further details) and the aerodynamic (static) force coefficients if measured until large amplitudes. Alternatively, simplified stall models can be used to describe the aerodynamic nonlinearity due to the massive flow separation associated to the large-amplitude motion (*e.g.* [73], as introduced in the next paragraph). This approach has been followed in some studies about nonlinear control of aeroelastic flutter on aircraft wing through the feedback action of flaps (*e.g.* [199, 119, 117, 118]).

Semi-empirical models are available for dynamic-stall flutter, that is involving the pitching DoF only. Nevertheless, although classical-flutter instability has different origin with respect to stall flutter, it takes into account the same nonlinearity source of stall flutter (large flow separations) once the post-critical regime is embarked. Moreover, the main consequence of the 2-DoF motion of classical flutter is an effective angle of attack that is influenced by both DoFs. Thus, the heaving component can be considered to modify the effective angle of attack, and the dynamic stall model can be exploited to determine the self-excited loads also in the case of a 2-DoF motion. These models have been developed to describe the hysteretical behaviour about the stall angle featured during oscillations at large angles of attack (*e.g.* models of: ONERA [208, 171]; Beddoes-Leishman [131]; Larsen-Nielsen-Krenk [127]). A static relationship between lift coefficient and angle of attack is commonly used as backbone curve, and the nonstationary effects are included essentially through delays of the lift, depending on the flow separation mechanisms at leading and trailing edges. Otherwise, the dynamic evolution of lift force within the range of interest of the angles of attack is considered, although experimental tests are required to empirically calibrate the parameters of the model. See also [45, 80] for applications of the dynamic-stall model to the response prediction of nonlinear systems.

Other analytical investigations focused on the stability of nonlinear systems, from the theoretical point of view. These aimed at the identification of stability domains with respect to some governing parameters (*e.g.* [161]), also by the use of Lyapunov's function (*e.g.* [158, 157]). To infer something beyond the critical onset, a posteriori assumption was introduced on the expression of the self-excited loads, based on the experience coming from the experimental results and being inspired by similar 1-DoF nonlinear systems (*e.g.* [160, 159]). The nonlinearity of the self-excited loads contributes to modify mainly the stiffness and damping matrices of the system, thus producing Duffing-van der Pol type

oscillator[13] [160] of the form

$$\ddot{q} \underbrace{-\delta\left(1-\epsilon q^2\right)\dot{q}}_{van\ der\ Pol\ term} \underbrace{+\gamma\left(1+\nu q^2\right)q}_{Duffing\ term} = f(t) \quad , \tag{3.88}$$

where $q(t)$ is a generic state variable, $f(t)$ an additional external input and δ, ϵ, γ, ν are real constants. Indeed, the shapes of the experimental amplitude-velocity diagrams suggest that the response is dominated by a van der Pol nonlinear damping and the self-excited loads could be represented as the superposition of a linear term (from linear theory) and higher order terms [122] (similarly to the polynomial expansion of [166], in case of the galloping phenomenon). The polynomial coefficients would depend only on the flow velocity and have to be derived from experimental tests.

Computational modelling deals with a general fluid-structure interaction problem, and usually requires to model both the structural and the flow fields. However, in the specific case of 2-DoF flutter of rigid models, elastically suspended, the region occupied by the body can be considered as a boundary condition for the flow domain, and the problem modelling essentially considers the flow field only. Thus, the Navier-Stokes equations can be approached in several ways according to the detail of the analysis, boundary conditions and technical constraints (*e.g.* [62, 50]): (i) directly solving the Navier-Stokes equations, or (ii) applying the potential-flow theory, or introducing further simplifications [109], such as (iii) the vortex-lattice method.

The computational approach is out the scope of this thesis. Nevertheless, several numerical works can be found in the literature (see § 2), although the CFD simulation of a large-amplitude post-critical response, as in the case of flutter-induced motion, generally are time/cost expensive.

Due to the very large amplitudes of oscillations both in translation and rotation, the management of the flow domain mesh needs particular expedients to avoid computational problems. Movable meshes are required, in which the mesh grid is assumed to be deformable accordingly to some artificial elastic properties, following the body motion while remaining fixed at the outer boundary. However, large rotations beyond 90° cannot be considered in this way. On the other hand, multi-block meshes can be considered to overcome the large rotations. In this case, there are two undeformable meshes for the flow domain: one fixed about the body section that moves together with its motion (responsible of modelling the fluid-dynamic effects of the section, shear layers and vortex formation) and one that occupies the whole domain, being a backward layer fixed in time. During the motion, the information are exchanged between the two grids by interpolations among the grids nodes. This method usually produces larger numerical errors.

Experimental investigation requires specific setups to allow even large amplitudes of oscillations in both DoFs, with well-known and simple-to-control mechanical properties. The common setup used in wind-tunnel tests involves coil-spring suspension, where the pitching stiffness can be modified by varying the distance between the pairs of springs. Recently, setup with blade-spring suspensions for the heaving DoF have been developed (*e.g.* [19, 186, 188, 196]). Other more complex setups are also considered ([85, 121]), specifically designed for an easier control of the parameters.

The main difficulty is to design a setup that is suitable for both small and large oscillations at the same time, allowing to control the governing parameters of the flutter problem (see § 3.2.1). Setups for large oscillations require specific attentions to provide the desired stiffness in the range od amplitudes tested, and this usually induces detrimental effects on the mass and damping of the oscillating system. In fact, the structural design of the elastic supports

[13] The Duffing and van der Pol oscillators belong to the more general Liénard equations:

$$\ddot{d} + h(q)\dot{q} + g(q) = 0 \ ,$$

being $h(q)$ and $g(q)$ two continuously differentiable functions on $\mathbb{R}$, with g an odd function and h an even function. Under certain additional assumptions, Liénard's theorem guarantees the uniqueness and existence of a limit cycle for such a system.

introduces a significant amount of additional mass, participating to the oscillations, and this mass increases with the stiffness of the setup. Moreover, although the stiffness can be easly modified (*e.g.* torsional stiffness with freeplay [9] and polynomial restoring force [164]), the structural damping represents a key issue: it is easy to be increased, *e.g.* through electromagnetic dampers, but the lower limit, which depends on the setup characteristics, is difficult to be decreased (being impossible in reality to achieve null damping, with exception of the case of active control). On the other hand, setups for small oscillations allow easier the design of solution specific for low-damping levels, but importantly limit the maximum amplitude of oscillations.

The study of two-dimensional problems entails the simulation of two-dimensional flow conditions (using end-plates linked to the model ends or smooth walls to bound the flow about the test section), and also the motion should be composed by just 2-DoF. In the case of a sectional model, the rolling DoF (rotations about the symmetry axis of the model parallel to the stream flow) is usually free to manifest and could disturb the energy exchange [188]. Particular attentions have to be devoted to set up as symmetric as possible mass distributions in the cross-flow direction, avoiding large masses to be concentrated close to the model ends.

Chapter 4

Performance of classical-flutter-based generators

4.1 The energy transfer in 2-DoF systems

The discussion in § 1.2.2 can be referred to any powering systems that exploit a 1-DoF motion. In the case of flutter, Eq. (1.5) has to be modified so to introduce the contribution of the pitching DoF, leading to Eq. (4.2) within small-amplitude oscillations or to Eq. (4.12) for oscillations with large amplitudes. It is worth highlighting that the conversion apparatus is preferred to act in the heaving DoF [172], because the pitching DoF has a primary role in the excitation mechanism, and any disturbance on it can have significant detrimental effects on the system response [84, 147].

Observing Eqs. (4.2) or (4.12), the importance of the mass unbalance S is apparent, because it rules the energy exchange between the pitching and heaving DoFs in addition to the coupling due to the fluid-elastic forces, which usually is weaker. Thus, the energy associated to the mass unbalance is actually not dissipated by the global mechanical system, since remains in it. This is the main advantage with respect to 1-DoF systems that, being present only one DoF, are more sensitive to external disturbances, because the flow-induced mechanism relies only on that DoF.

Additional considerations have to be made, according to what shown in Fig. 4.1. Since the mechanical system involves two DoFs, two fluid-elastic modes $\tilde{\boldsymbol{\sigma}}_{\mathbf{1}}$ and $\tilde{\boldsymbol{\sigma}}_{\mathbf{2}}$ exist (§ 3.1.2). Both modes participate in the energy transfer at the instability threshold, resulting $P_F = P_{F1} + P_{F2}$, $P_D = P_{D1} + P_{D2}$ and $P_S = P_{S1} + P_{S2}$. However, the energetic contribution of the secondary fluid-elastic mode is markedly smaller than the one of the principal fluid-elastic mode, during flutter oscillations. Thus, the approximation of neglecting the presence of the secondary mode ($P_F \approx P_{F1}$, $P_D \approx P_{D1}$ and $P_S \approx P_{S1}$), as commonly assumed in the theoretical calculation of the critical condition, does not affect the evaluation of the performance and the governing-parameter influence. In addition, it has to be remarked that during post-critical LCOs the system is nonlinear, thus idea of modes of vibrations losses of physical meaning, being the motion characterised just by a certain shape and phase relationship between the DoFs.

In addition to the previous comment, it has to point out that the energy extraction is performed in the heaving DoF only, therefore the energy balance has to be referred to that DoF. Since $P_F = P_{F\alpha} + P_{F\eta}$ in general, only $P_{F\eta}$ is of interest and the actual extraction factor is

$$\Gamma'_\eta = \frac{P_{F\eta}}{P_W} = \frac{P_F}{P_W} \cdot \frac{1}{1 + P_{F\alpha}/P_{F\eta}} \,, \tag{4.1}$$

being $P_{F\eta}$ linked to the amount of energy that can be effectively converted, while $P_{F\alpha}$ circulates in the pitching DoF and sustains the flutter mechanism.

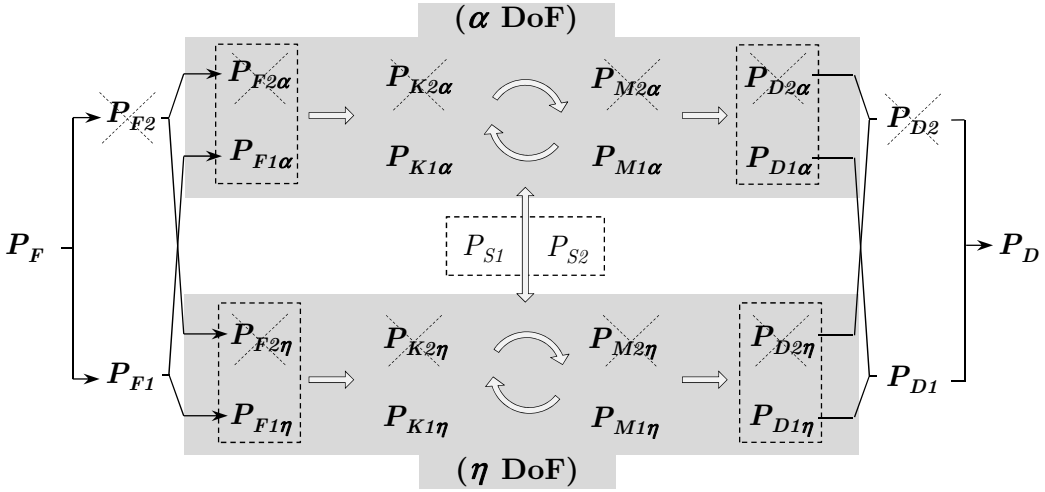

Figure 4.1. Energy transfer in a 2-DoF system approaching the instability threshold. The forcing mean power (P_F) is split into the contributions due to the two fluid-elastic modes, which in turn can have components on both DoFs. The inertial (P_{Mi}) and potential (P_{Ki}) mean powers are balanced, and those associated to the mass unbalance (P_{Si}) circulate between the DoFs. Then, in each DoF the dissipated energy is due to contributions of both fluid-elastic modes, which add to produce the total dissipated mean power (P_D).

4.1.1 Extraction factor for small oscillations

The energy-harvesting process can be described through the following equations:

$$\begin{aligned}
&a_1)\ I_\alpha\ddot{\alpha}(t) + C_\alpha\dot{\alpha}(t) + K_\alpha\alpha(t) + S\ddot{\eta}(t) = M(\ddot{\alpha},\dot{\alpha},\alpha,\ddot{\eta},\dot{\eta},\eta,U,t) && \rightarrow \text{ pitching DoF ;}\\
&a_2)\ I_\eta\ddot{\eta}(t) + C_\eta\dot{\eta}(t) + K_\eta\eta(t) + S\ddot{\alpha}(t) = L(\ddot{\alpha},\dot{\alpha},\alpha,\ddot{\eta},\dot{\eta},\eta,U,t) - && \rightarrow \text{ heaving DoF ;}\\
&\qquad\qquad - g_1(Q,t) \ ; &&\\
&b)\ \ Q(\eta,t) = g_2(\eta,t) + h(V,t) && \rightarrow \text{ transducer ;}\\
&c)\ \ L_{ec}\ddot{V}(t) + R_{ec}\dot{V}(t) + V(t)/C_{ec} = 0 && \rightarrow \text{ electric circuit ;}
\end{aligned} \tag{4.2}$$

in which the symbols description can be found in § 1.2 and § 3.2. According to what said about in the previous § 1.2.2 and Fig. 1.4, the estimation of the extraction factor Γ' can consider the part of equation (a_2) in Eq. (4.2) related to the fluid-structure interaction, that is

$$I_\eta\ddot{\eta}(t) + C_\eta\dot{\eta}(t) + K_\eta\eta(t) + S\ddot{\alpha}(t) = L(\ddot{\alpha},\dot{\alpha},\alpha,\ddot{\eta},\dot{\eta},\eta,t) \ , \tag{4.3}$$

where the the damping coefficient $C_\eta = C_{\eta s} + C_{\eta e}$ is now the sum of structural and external contributions, this last assumed as $g_1(Q,t) \propto C_{\eta e}\dot{\eta}(t)$.

During steady-state oscillations, the system response can be described through the harmonics

$$\begin{cases} \eta(t) = \hat{\eta}\sin(\omega t) \\ \alpha(t) = \hat{\alpha}\sin(\omega t + \hat{\phi}) \end{cases} . \tag{4.4}$$

Thus, the kinetic energy related to the inertial mass I_η balances the potential energy in a cycle of oscillation[1] of period $T = 2\pi/\omega$, and the mean power pumped in by the flow in the

[1] Let consider to amount of energy flowing in the heaving DoF only. The potential energy is $\Pi = \frac{1}{2}K_\eta\eta^2$ and the kinetic energy, excluding the contribution from the static mass unbalance, is $\mathcal{T} = \frac{1}{2}I_\eta\dot{\eta}^2$. Since $K_\eta = \omega_{\eta 0}^2 I_\eta$ and $\dot{\eta} = j\omega\eta$, it follows that $\Delta(t) = \Pi + \mathcal{T} = \frac{1}{2}I_\eta\omega^2\left[(\omega_{\eta 0}/\omega)^2 - 1\right]\eta^2 = \frac{1}{2}I_\eta\omega^2\left[X/\gamma_n^2 - 1\right]\eta^2$. During flutter motion, the frequency of oscillation ω is different from the

heaving DoF (where the conversion apparatus is supposed to act) is:

$$\begin{aligned} P_F &= \frac{1}{T}\int_0^T L(\ddot{\alpha},\dot{\alpha},\alpha,\ddot{\eta},\dot{\eta},\eta,t)\dot{\eta}\ dt = \\ &= \frac{1}{T}\int_0^T C_\eta \dot{\eta}^2\ dt + \frac{1}{T}\int_0^T S\ddot{\alpha}\dot{\eta}\ dt = P_{D\eta} + P_S = \\ &= I_\eta \cdot \hat{\eta}^2 \cdot (2\pi n)^3 \cdot \xi_{\eta 0}\frac{\sqrt{X}}{\gamma_n} - I_\eta \cdot \hat{\eta}^2 \cdot (2\pi n)^3 \cdot \frac{a\hat{\alpha}}{\hat{\eta}}\frac{\sin\hat{\phi}}{2} = \\ &= I_\eta \cdot \hat{\eta}^2 \cdot (2\pi n)^3 \cdot \frac{\sqrt{X}}{\gamma_n} \cdot \left[\xi_{\eta 0} - \frac{a\hat{\alpha}}{\hat{\eta}}\frac{\sin\hat{\phi}}{2}\frac{\gamma_n}{\sqrt{X}}\right]\ ; \end{aligned} \tag{4.5}$$

where a is the distance of the mass centre with respect the elastic axis, as defined in § 3.2. It is worth remarking that in 2-DoF systems, the energy circulating between the DoFs P_S (proportional to the mass unbalance) participates as a 'virtual' sink or source of energy with for the heaving DoF.

The power P_F can be normalised by the flow power per unit length P_W, expressed as

$$P_W = \frac{1}{2}\rho U^3 D_{sw} = \frac{1}{2}\rho U^3 B\hat{\psi}_{sw}\ , \tag{4.6}$$

taking into account the spanned distance $D_{sw} = \hat{\psi}_{sw}B$ due to both heaving and pitching components. If compared to the case of 1-DoF systems, the evaluation of $\hat{\psi}_{sw}$ is more complicated for 2-DoF systems. In particular, assuming $1/r \sim 0$ (valid for large width-to-depth ratios), the bounds of the area swept by the model during LCOs can be related to the extremal positions of the leading ($\hat{\psi}_{sw,l}$) or trailing ($\hat{\psi}_{sw,t}$) edge:

$$\begin{aligned} \hat{\psi}_{sw,l} &= \max\left\{\left|\sin\alpha(t)\,(1+2x_e) - 2\eta(t)/B\right|\right\}\ ; \\ \hat{\psi}_{sw,t} &= \max\left\{\left|-\sin\alpha(t)\,(1-2x_e) - 2\eta(t)/B\right|\right\}\ ; \\ \hat{\psi}_{sw} &= \max\left\{\hat{\psi}_{sw,l};\hat{\psi}_{sw,t}\right\}\ . \end{aligned} \tag{4.7}$$

Fig. 4.2 illustrates how to identify the streamtube for a 2-DoF motion, which is fundamental to determine the swept distance D_{sw} and to set a Betz analysis (as pointed out in § 1.2.1 referring to the work in [219]).

Finally, the extraction factor takes the following form:

$$\Gamma'_\eta = \frac{P_{F\eta}}{P_W} = 8\pi^3 \cdot \mu \cdot [\xi_{\eta 0} + \beta^*] \cdot \frac{1}{U_R^3} \cdot \left(\frac{\hat{\eta}}{B}\right)^2 \cdot \frac{\sqrt{X}}{\gamma_n} \cdot \frac{1}{\hat{\psi}_{sw}}\ , \tag{4.8}$$

which can also be expressed in terms of $U_{R\alpha} = U/n_{\alpha 0}B = U_R/\sqrt{X}$. The parameter β^* is defined as

$$\beta^* = -x_m \cdot \frac{B\hat{\alpha}}{\hat{\eta}} \cdot \frac{\gamma_n}{\sqrt{X}} \cdot \frac{\sin\hat{\phi}}{2}\ , \tag{4.9}$$

and is due to the presence of the mass unbalance $x_m \neq 0$, acting like an apparent (positive or negative) damping coefficient. Observing Eqs. (4.8) and (4.9), it results that when the heaving motion leads the pitching motion, that is with phase $-180° < \hat{\phi} < 0$, the sign of β^* depends on the mass unbalance only and, when downstream mass eccentricity is considered, it enhances Γ'_η.

It is to note the influence of the pitching amplitude and of the pitching-to-heaving phase difference on the calculation of $\hat{\psi}_{sw}$ in Eq. (4.7). Indeed, for a motion with a given heaving amplitude (that is generated power), the swept distance can significantly depend on both $\hat{\alpha}$ and $\hat{\phi}$ (Fig. 4.3), and the efficiency of the generator is affected in turn. The position of the elastic axis also plays a key role in the determination of the swept distance, since it rules, together with the phase $\hat{\phi}$, the maximum displacement to occur at the leading or trailing edge. For a given heaving amplitude, the configuration with the minimum swept distance is the one characterised by a motion with quadrature of phase.

natural one $\omega_{\eta 0}$ and, in usual applications, the ratio X/γ_n^2 is in the range from 0.9 to 1.2. Anyway,

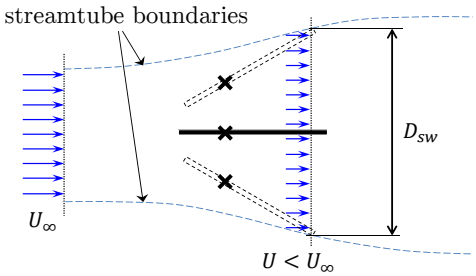

Figure 4.2. Streamtube for a flutter-based generator during a two-degree-of-freedom motion. U_∞ is the freestream flow speed, and the symbol $\times$ indicates the elastic axis.

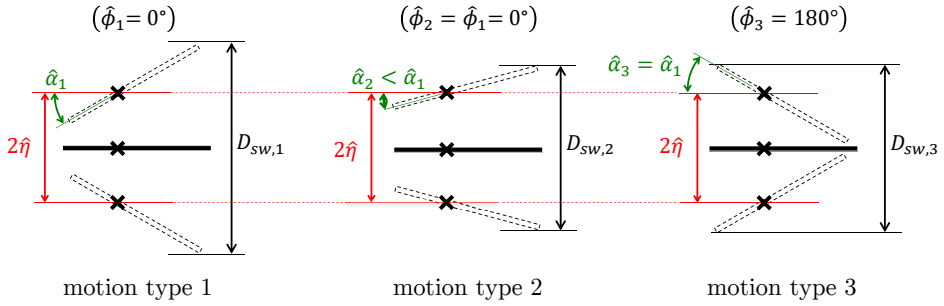

Figure 4.3. Swept distances for different types of motion with a constant heaving amplitude, for configurations with the elastic axis located in the upstream half-chord.

4.1.2 Extraction factor for large oscillations

In the previous section, the assumption of small perturbations about equilibrium is applied, as explained in § 3.2.1. Thus, since the post-critical response involves large pitching angles, the assumption $\alpha \approx 0$ has to be removed. By contrast, the assumption that the mechanical system show linear stiffness and damping on the whole oscillation range continues to hold.

Recalling Fig. 3.2, the large-displacement motion of a generic point of the cross section at a distance x from the elastic axis is

$$\begin{cases} u(s) = x\,[\cos\alpha - 1] \\ w(s) = -\eta - x\sin\alpha \end{cases} \tag{4.10}$$

and the respective kinetic energy takes the form:

$$\mathcal{T} = \frac{1}{2}\rho_m \int_{\mathcal{A}} \dot{w}^2 dx = \frac{1}{2} I_\eta \dot{\eta}^2 + S\dot{\eta}\dot{\alpha}\cos\alpha + \frac{1}{2} I_\alpha \dot{\alpha}^2 \ . \tag{4.11}$$

The energies associated to the stiffness and damping terms follow the same expressions reported in Eq. (3.32) of § 3.2.1. Then, applying the lagrangian Eq. (3.5) of § 3.1.1, the governing equations for the mechanical system during large motion amplitudes are:

$$\begin{cases} I_\alpha \ddot{\alpha} + C_\alpha \dot{\alpha} + K_\alpha \alpha + S\ddot{\eta}\cos\alpha = M\left(\ddot{\alpha}, \dot{\alpha}, \alpha, \ddot{\eta}, \dot{\eta}, \eta, U, t\right) \\ I_\eta \ddot{\eta} + C_\eta \dot{\eta} + K_\eta \eta + S\left(\ddot{\alpha}\cos\alpha - \dot{\alpha}^2\sin\alpha\right) = L\left(\ddot{\alpha}, \dot{\alpha}, \alpha, \ddot{\eta}, \dot{\eta}, \eta, U, t\right) \end{cases} . \tag{4.12}$$

An analytical expression of the self-excited loads M and L is not available in this case.

---

the average over a cycle $[0, T]$ of the instantaneous energy $\Delta(t)$ vanishes because $\eta^2(T) = \eta^2(0)$ and independence on the displacement path for the conservative contributions.

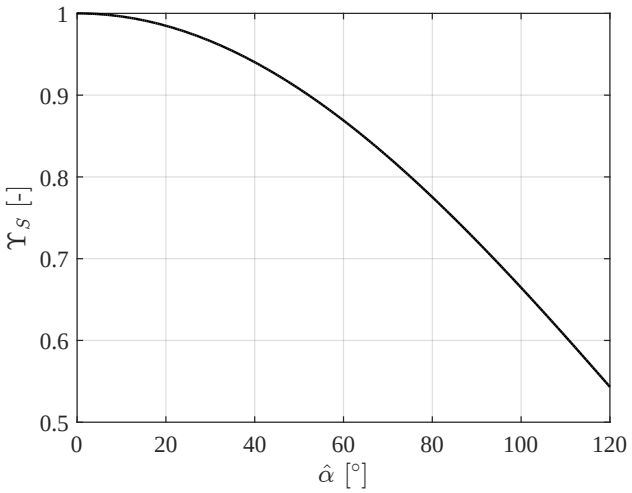

Figure 4.4. Dependence of the coefficient Υ_S on the pitching amplitude.

Comparing Eq. (4.12) with Eqs. (4.2)-a1 and (4.2)-a2, and considering that the energy extraction still acts in the heaving DoF only, the estimation of the extraction factor modifies just the term related to the static mass unbalance:

$$\begin{aligned} P_F &= \frac{1}{T}\int_0^T L(\ddot{\alpha},\dot{\alpha},\alpha,\ddot{\eta},\dot{\eta},\eta,t)\dot{\eta}\ dt = \\ &= \frac{1}{T}\int_0^T C_\eta \dot{\eta}^2\ dt + \frac{1}{T}\int_0^T S\left(\ddot{\alpha}\cos\alpha - \dot{\alpha}^2\sin\alpha\right)\dot{\eta}\ dt = P_{D\eta} + P_S = \\ &= I_\eta \cdot \hat{\eta}^2 \cdot (2\pi n)^3 \cdot \frac{n_{\alpha 0}/\hat{n}}{\gamma_n} \cdot [\xi_{\eta 0} + \beta]\ . \end{aligned} \tag{4.13}$$

In Eq. 4.13, the damping related to the mass unbalance is now expressed as

$$\beta = \frac{\frac{1}{T}\int_0^T S\left(\ddot{\alpha}\cos\alpha - \dot{\alpha}^2\sin\alpha\right)\dot{\eta}\ dt}{I_\eta \cdot \hat{\eta}^2 \cdot (2\pi n)^3 \cdot \frac{n_{\alpha 0}/\hat{n}}{\gamma_n}} = \beta^* \cdot \Upsilon_S\ , \tag{4.14}$$

in which β^* refers to the values obtained for small oscillation (Eq. (4.9)), while the coefficient Υ_S is:

$$\Upsilon_S = \frac{2}{\sin\hat{\phi}} \cdot \frac{1}{T}\int_0^T \left[\sin\left(\omega t + \hat{\phi}\right)\cos\alpha + \hat{\alpha}\cos^2\left(\omega t + \hat{\phi}\right)\sin\alpha\right]\cos(\omega t)dt\ . \tag{4.15}$$

Fig. 4.4 shows the influence of the pitching amplitude on Υ_S, indicating that the coefficient β is about 75% of β^* for a system oscillating at $\hat{\alpha} = 90°$.

Finally, the extraction factor takes the following form:

$$\Gamma'_\eta = \frac{P_{F\eta}}{P_W} = 8\pi^3 \cdot \mu \cdot [\xi_{\eta 0} + \beta] \cdot \frac{1}{U_R^3} \cdot \left(\frac{\hat{\eta}}{B}\right)^2 \cdot \frac{n_{\alpha 0}/\hat{n}}{\gamma_n} \cdot \frac{1}{\hat{\psi}_{sw}}\ , \tag{4.16}$$

4.1.3 Conversion factor and global-performance

According to the simplified approach explained in § 1.2.2, the conversion factor relates to the amount of power dissipated by the external dampers $P_{D\eta e}$. Then, excluding the contributions of structural damping $P_{D\eta s}$ and mass unbalance P_S, it takes the form:

$$\Gamma''_\eta = \frac{P_{D\eta e}}{P_{D\eta e} + P_{D\eta s} + P_S} = \frac{\xi_{\eta 0 e}}{\xi_{\eta 0 s} + \xi_{\eta 0 e} + \beta}\ . \tag{4.17}$$

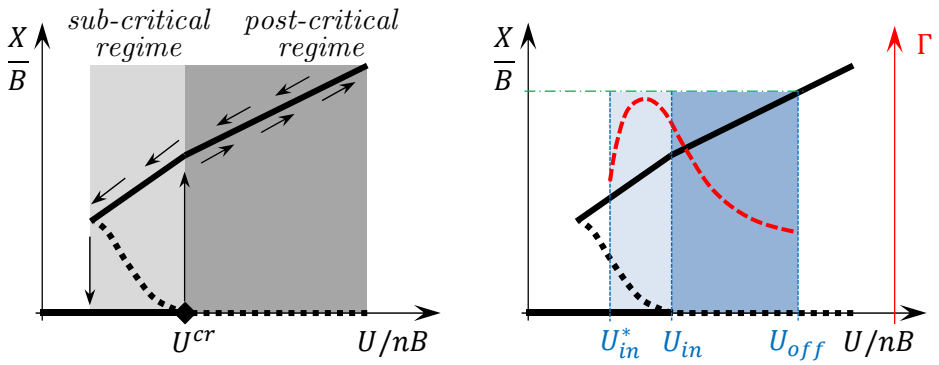

Figure 4.5. (left) Typical amplitude-velocity path of flutter, where solid lines represent stable branches, while dashed lines represent unstable branches. (right) Operative range for flutter-based generators, with indication of the cut-off velocity U_{off} and the cut-in velocity U_{in} (or U^*_{in}).

Then, the global performance of the device, Γ_η, is given by:

$$\Gamma_\eta = \Gamma'_\eta \cdot \Gamma''_\eta = 8\pi^3 \cdot \mu \cdot \xi_{\eta 0 e} \cdot \frac{1}{U_R^3} \cdot \left(\frac{\hat{\eta}}{B}\right)^2 \cdot \frac{n_{\alpha 0}/\hat{n}}{\gamma_n} \cdot \frac{1}{\hat{\psi}_{sw}} \ . \tag{4.18}$$

From Eqs. (4.8) and (4.18), and additionally to what said about in § 1.2.2, the following considerations can be made:

- the pitching motion can increase the swept distance for motion far from the quadrature of phase, producing a detrimental effect on both Γ'_η and Γ_η, in particular when the pitching-to-heaving amplitude ratio is large;
- the performance is affected by the difference between natural and flutter frequency of oscillation $n_{\alpha 0}/\hat{n}/\gamma_n = n_{\eta 0}/\hat{n}$, although the ratio $n_{\eta 0}/\hat{n}$ is usually close to unity;
- the influence of the mass unbalance through the parameter β does not directly affect the global performance, but is implicitly included in the amplitude-velocity path of the system response.

In the context of flutter-based generators, Eq. (4.18) highlights the key parameters. In particular, the reduced velocity U_R clearly and strongly influences the performance, while some other parameters ($\hat{\eta}$, $\hat{\alpha}$, $\hat{n}$ and $\hat{\alpha}$) complicate the problem, since they implicitly depend on U_R (see § 7). The operative range of the generator (Fig. 4.5) is identified by a cut-off velocity U_{off}, limiting the maximum amplitude of motion to preserve the structural integrity of the device, and a cut-in velocity U_{in}, which usually corresponds to the critical velocity U^c at which flutter starts spontaneously. It is worth highlighting that, in case of exploitation of the sub-critical branch, a lower cut-in velocity U^*_{in} can be activated through initial conditions that are large enough to cross the unstable branch. In view of these considerations, the linear analysis is a useful parametric tool to investigate the most effective way to anticipate the instability threshold.

Chapter 5

Experimental setups

5.1 Introduction and motivations

The PhD programme is joined between University of Florence and University of Braunschweig. Therefore, the investigations were conducted in the CRIACIV Boundary Layer Wind Tunnel in Prato (IT) and in the Stahlbau Wind Tunnel in Braunschweig (DE).

The main objective of the experimental campaign was to observe the post-critical regime of flutter, shedding light on it and collecting information on the system response with respect to different sets of governing parameters that have been never investigated so far. Being in the energy-harvesting context, the implementation of viscous dampers received large importance, since the control of the heaving damping preliminary simulated the operation of a conversion apparatus (see § 1.2.2, § 2.3.4 and § 4.1). Thus, large attention was devoted to the evaluation of the system response to various heaving damping levels, returning information on the capability of flutter-based generators.

The possibility to systematically modify the governing parameters drove the design of the experimental setup. Large attention was devoted to obtain as linear (or well-known, at least) as possible mechanical properties of the setup in the whole range of attained displacement field, up to very large amplitude of oscillations. The main difficulty was to conciliate technical/structural requirements for small amplitudes with those for large amplitudes, being often in contrast, and to respect the capabilities of the measuring equipment.

Performing reliable investigations that aim to study both efficient energy-harvesting configurations and scientific aspects of post-critical regime of flutter, at the same time, cannot be easily carried out. In particular, optimal powering configurations would require low critical reduced velocity and low values of the oscillating inertias (see § 8 and § 9). This requires sectional models with large span and high slenderness, thus the internal flexibility of the model can affect the reliability of the measurements of a pure 2-DoF motion. Moreover, the amplitudes of oscillation of low-inertia systems can be so high to exceed the range of measurement of the available instrumentation (*e.g.* range of the analog displacement sensors). By contrast, if reliable measurements of the post-critical regime are pursued, the setup should involve as rigid as possible sectional models, thus shorter and heavier systems, and more complex solutions of the supporting system to limit any disturbance. The objective becomes providing high-quality 2-DoF motion, and the respective setup design usually increases the oscillating inertia in both DoFs (also considering the importance of installing end-plates to enforce two-dimensional flow conditions) and limits the maximum oscillation amplitude. In this case, the achievable critical flow speed will not be as low as desired for energy-harvesting purposes.

In the present thesis, performing reliable observations of the post-critical regime of flutter has been preferred. The investigation of a portion of the parametric space was not compromised, being possible to understand the influence of the governing parameters and to identify some design guidelines for flutter-based generators at the same time, although with the drawback of achieving limited values of the maximum performances.

5.2 Stahlbau wind tunnel

The first part of the experimental campaign was conducted in the facility[1] of the 'Institut für Stahlbau' of the 'Technische Universität' of Braunschweig, in Germany. The Eiffel-type (open-return), boundary layer wind tunnel (Fig. 5.1) has the following features:

- supporting structure made of wood, with some parts of the walls made of glass and plexiglass.
- cross-section width of 1.40 m and height of 1.20-1.35 m (with adjustable ceiling);
- test-section length of 8.75 m;
- 55 kW fan, placed at the outlet;
- velocity range of 2-25 m/s^{-1}, controlled through of the inverter RPM;
- turntable floor (circle of 1.2 m diameter) at the downstream part of the test section, controlled by a computer;
- lowest turbulence intensity $\approx 1\%$;
- turbulators (vortex generators) and roughness patches.

Since flows with boundary layer are not of interest for this thesis, the aeroelastic setup was placed close to the starting part of the test section, that is close to the inlet (Fig. 5.1b). In that position, smooth-flow condition can be better provided.

5.2.1 Equipment

The following instruments were adopted.

- *A Prandtl tube* (Fig. 5.2a). It measures the mean dynamic pressure of the oncoming flow, that is the mean flow velocity. It was fixed to the lateral wall of the test section, in a position downline of the model, as apparent in Fig. 5.4-up. It was used to measure the flow speed during the investigations and to infer the flow speed at the model centerline by means of flow maps and velocity conversions (see § 5.2.2).
- *A Cobra probe* (Fig. 5.2b). It is a three components Cobra-246 probe and allows to measure unsteady flows. It was used in combination with the Prandtl tube to map the flow mean speed and turbulence intensity in the area swept by the oscillating model. It was installed in a specific support (Fig. 5.6). The operative sampling frequency was 2000 Hz.
- *A digital micromanometer* (Fig. 5.2d). It is a universal differential pressure micromanometer 'ManoAir500' that indicates beside Pa, mbar and mmH_2O directly the flow velocity of gaseous media by means of an anemometer placed inside the wind tunnel (as visible on Fig. 5.4). Thereby (after compensation) media temperature, effective ambient pressure and humidity were measured.
- *Four displacement lasers* (Fig. 5.2e). Analog laser displament transducers ('WayCon', LAS-T5-250-10V) were used to measure the motion of the model (installed as indicated in Fig. 5.13, Fig. 5.15). The analog output is in the range 0-10 V and corresponds to the measuring range 50-300 mm, with the specifications as indicated in Table 5.1 and Fig. 5.3. These were connected to the data acquisition (DAQ) system through 5-m-long cables (K5P5M-S-M12, 5 pole, shielded, with mating M12 connector). The operative sampling frequency was set to 1000 Hz.

[1] http://www.is.tu-braunschweig.de/index.php/menu-labor-de/menu-laboreinrichtung/menu-windkanal

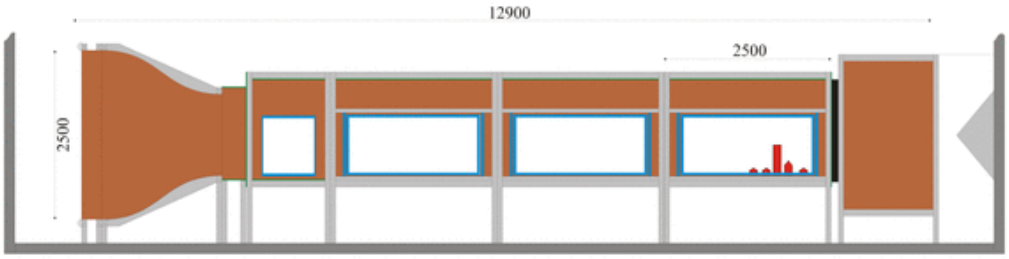

(a) Sketch of the wind-tunnel geometry.

(b) Frontal view, from the inlet.

(c) Frontal view, from the outlet.

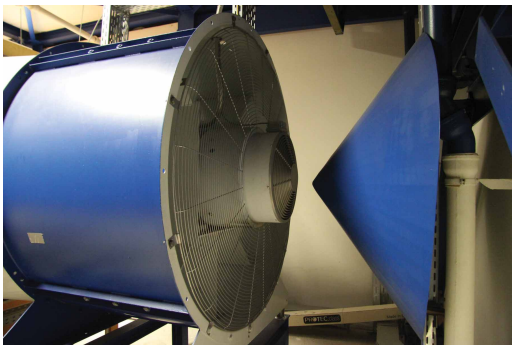

(d) Close-up of the motor fan.

Figure 5.1. Geometry and photos of the Stahlbau wind tunnel.

Table 5.1. Summary of technical features of the analog displacement lasers [Stahlbau Institute].

Sensor type		Laser-sensor
Model		LAS-T5
Type		250
Operative voltage	[V]	0 ... 10
Measuring range	[mm]	50 ... 300
Stand-off midrange	[mm]	175
Resolution	μm	0.01 ... 0.33
Sampling frequency	[kHz]	> 1000
Light source		laser diode (pulsed)
Wavelength	[nm]	650 (red)

- *Two electromagnets* (Fig. 5.2f). The damping of the heaving motion was controlled by an electromagnetic system (Fig. 5.15, Fig. **??**), composed by a pair of circular 80 mm × 38 mm cylindrical electromagnets (GTo80-0.5000, with a nominal power of 15 W corresponding to a force of about 2800 N on a 9 mm iron plate in contact), combined with a power supply and voltmeter (Fig. 5.2g).
- *Data acquisition (DAQ) system* (Fig. 5.2h). Analog-to-digital converter by National Instruments, which sent the measured signals to the computer.

5.2.2 Flow characteristics

The choice of the grid of points for the flow mapping depended on the displacement field achieved in the tests. The investigations of the flow characteristics were conducted about 1 m downstream the contraction zone of the wind tunnel, where the smooth flow conditions are better satisfied. The aeroelastic tests involved 2-DoFs oscillations and the maximum allowed heaving amplitude was less than 100 mm, being this last value imposed by the plexiglass vertical walls that have a circular hole of 200 mm diameter (Fig. 5.5-left). These holes allowed the installation of the model inside the wind tunnel and its connection with the aeroelastic setup. Since the model was equipped with cylinders of 20 mm diameter at the lateral edges, which link with the springs setup, the maximum heaving amplitude was ±90 mm. An example of admissible flutter motion, with quadrature-phase between heaving and pitching DoFs, is showed in (Fig. 5.5-up-right).

The main flow that interacts with the model is contained in the swept area spanned during the oscillations. Thus, the grid was chosen according to the maximum amplitude of oscillation in the vertical direction (Fig. 5.5-right), and 15 points were evaluated, being distributed to cover almost 70% of the swept area. The lateral portions between the boundary points of the grids and the vertical walls were not investigated, due to excessive vibrations of the structure used to support the Cobra probe (Fig. 5.6).

The Cobra probe measured the three components of the flow velocity and their respective turbulence intensities:

- U [m s^{-1}] and I_u [%] along the longitudinal direction;
- V [m s^{-1}] and I_v [%] along the vertical direction;
- W [m s^{-1}] and I_w [%] along the transversal direction.

The supporting structure is a vertical, thin, steel cylinder welded to a horizontal steel plate that was fixed with screws to the floor of the test section. Due to problems of excessive vibrations, a stiffening element was installed in the top of the cylinder to reduce transversal oscillations, and an inclined steel cylinder was welded between the vertical cylinder and the plate to avoid alongwind oscillations. Moreover, an insulating material was placed in

(a) Prandtl tube.

(b) Cobra probe.

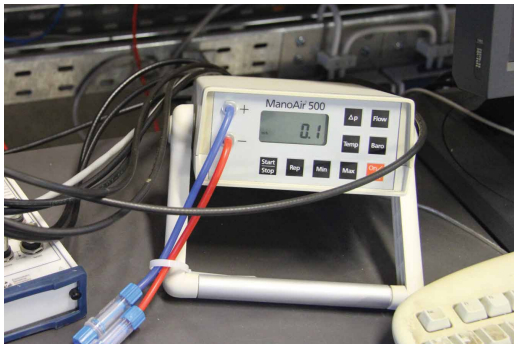

(c) Micromanometer.

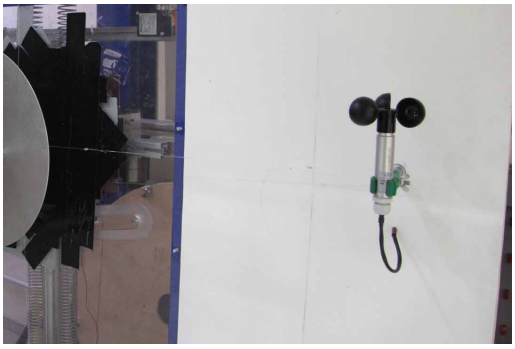

(d) Anemometer.

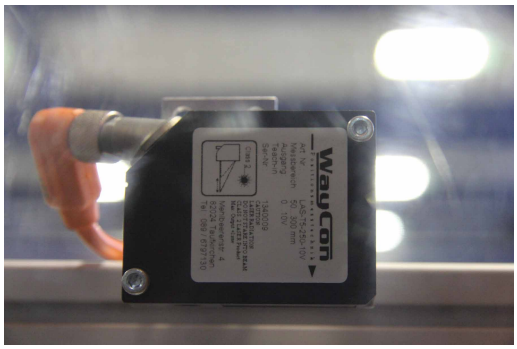

(e) Displacement laser.

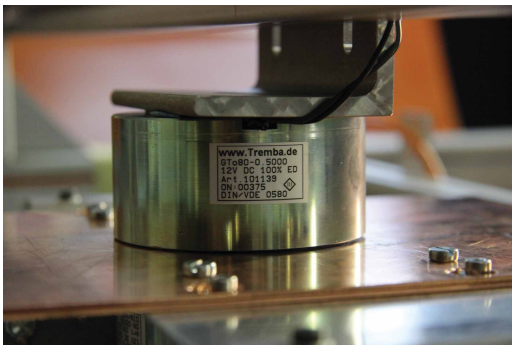

(f) Electromagnet.

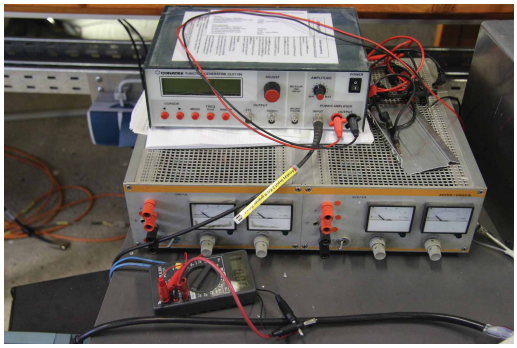

(g) Power supply and voltmeter.

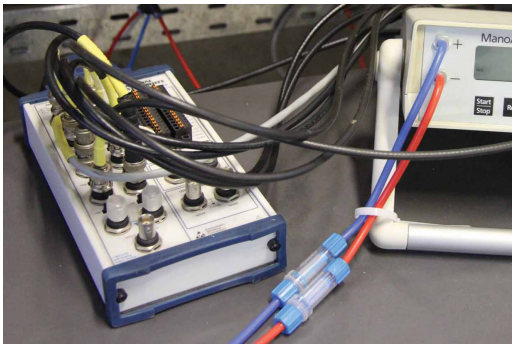

(h) Data acquisition system.

Figure 5.2. Instrumentations of the Stahlbau facility.

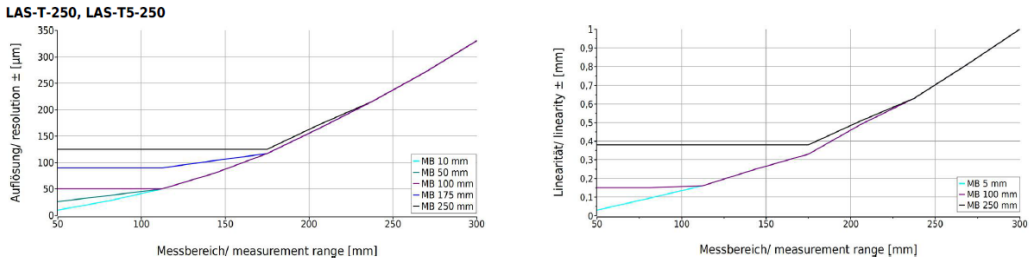

Figure 5.3. Linearity and resolution of the displacement transducers [Stahlbau Institute].

(a)

Test No.	Inverter [rpm]	Prandtl speed [m s^{-1}]
1	340	8.1
2	415	10.1
3	490	12.1
4	565	14.1
5	640	16.1
6	720	18.1-18.2

(b)

Test No.	Inverter [rpm]	Prandtl speed [m s^{-1}]
1'	300	7.0
2'	380	9.1
3'	455	11.1
4'	530	13.1
5'	605	15.0
6'	680	17.1

Table 5.2. Main reference flow speeds that are investigated, for all the points of the grid (a) and additional flow speeds for the central point of the grid (b), that is point #8.

between the plate and the floor, in order to reduce the transmission of vibrations due to the fundamental eigenfrequency of the wind tunnel (about 135 Hz). The probe was linked to the supporting structure through movable hinges and a steel cylinder (Fig. 5.6), which kept the correct position of the probe respect to the supporting structure. The displacement of the probe, both in vertical and horizontal directions, were allowed by the hinges that were fixed when the suitable configuration was reached.

The flow characterization was conducted in smooth flow conditions. For each point of the grid, first the calibration of the probe was performed, calibrating also the Prandtl tube for the reference mean speed. Then, the flow velocities were investigated as reported on Table 5.2-left. Furthermore, for the central point of the grid, namely point 8 of Fig. 5.5, additional flow speeds were investigated, in order to evaluate a more refined spacing of flow velocities, as reported in Table 5.2-right. The sampling frequency was set to 2000 Hz and the duration of the acquisitions was 60 s, excepted for all the measurements of the central point (point 8) that was 120 s. The flow velocity conversion between the Prandtl tube installed in the later wall of the test section and the Cobra probe arranged in the point 8 of the grid is reported in Table 5.3 and Fig. 5.7. The piecewise interpolation returns a mean conversion factor of 0.969, meaning that the flow in correspondence of the model position was slightly slower than in the Prandtl tube position.

The time histories of the three components of the flow velocity (U, V, W) and the respective autospectra (S_{uu}, S_{vv}, S_{ww}) were calculated in order to evaluate the frequency content and to identify the noise to remove. An example of the filtering procedure to reduce the disturbances is reported in Appendix A, conducted with a low-pass filter at 90 Hz. In the Appendix A are reported also the maps of mean flow velocity, for the longitudinal component of the velocity vector (U) and the maps of the respective turbulence intensity (I_u), as obtained without and with the filter. Each map refers to a test case according to Table 5.2 and to the reference flow speed as measured by the Prandtl probe.

Large attention was devoted to find the correct position of the Cobra probe, in order to be aligned with the longitudinal flow direction. The very low mean values of the transversal and vertical components of the flow velocity confirmed the correct installation of the probe.

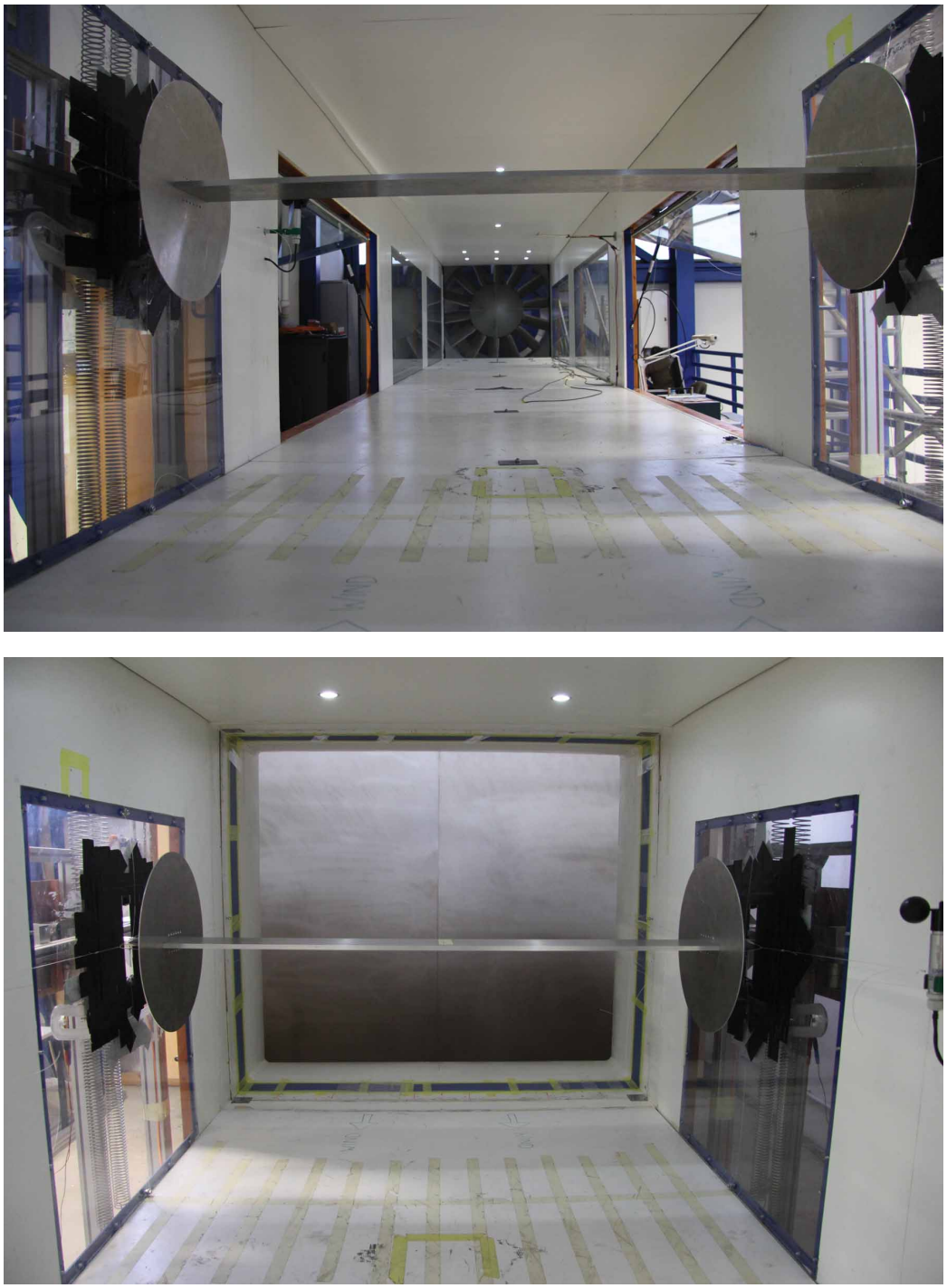

Figure 5.4. (up) Upstream view of the model, with the Prandtl tube and anemometer installed as visible in the background; (down) downstream view of the model, with the anemometer on the right [Stahlbau Institute].

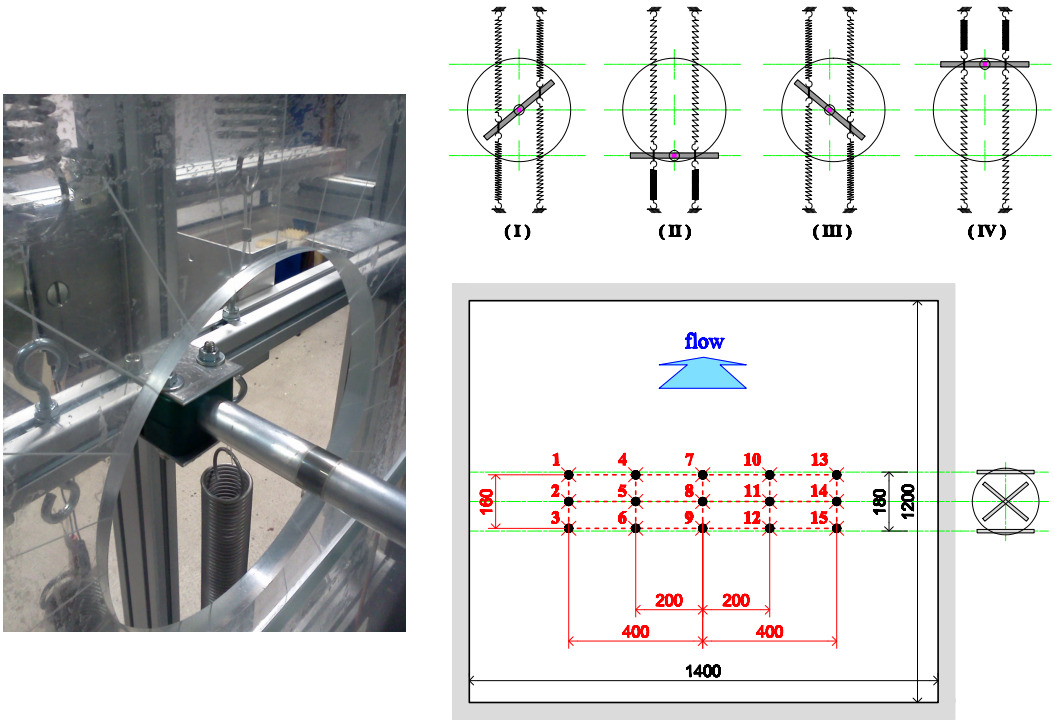

Figure 5.5. Distribution of the points of the grid for the flow mapping (right-down) and a typical motion in quadrature of phase (right-up). In the latter, the circle represents the round window in the plexiglass walls of the wind tunnel, visible in the left figure, where is also visible the connection between the model axis and the rod of the elastic suspension. Distances are in millimetres.

Figure 5.6. Views of the Cobra probe installed in the supporting structure.

Table 5.3. Piecewise velocity conversion.

U_i - U_{i+1} [m/s]	K_{Ui} [m/s]
7.0 - 8.1	0.936
8.1 - 9.1	1.070
9.1 - 10.1	0.790
10.1 - 11.1	1.040
11.1 - 12.1	0.940
12.1 - 13.1	1.040
13.1 - 14.1	0.930
14.1 - 15.0	1.044
15.0 - 16.1	0.927
16.1 - 17.1	1.050
17.1 - 18.1	0.820

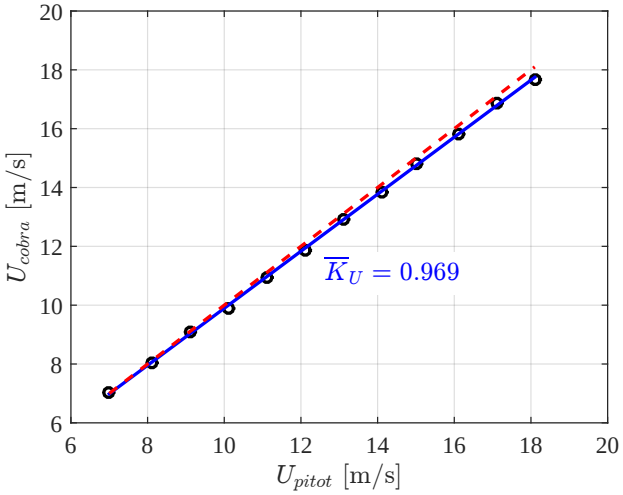

Figure 5.7. Mean velocity conversion.

The results are good, although some problems of the flow were identified:

1. Four main peaks in the spectra can be identified: (i) 135 Hz; (ii) 170 Hz; (iii) 455 Hz; (iv) 730 Hz (see Appendix A). The two first peaks are close and may be due to the fundamental eigenfrequencies of the wind tunnel and of the supporting structure. In a preliminary configuration in which the supporting structure was not fixed to the floor but just placed upon it, including an insulating element in between, these peaks were not found. These peaks involve mainly the longitudinal component of the flow velocity and partially the vertical ones; no presence of them was detected in the transversal component. The others peaks at higher frequency may be due to electrical noise.

2. The signals of some grid points, as indicated in Fig. 5.8-left, show isolated fluctuations of velocities of about ±1 m/s, which seems to be not appropriate for this low level of turbulence intensity, thus they may be linked to electrical disturbances.

3. The maps of the mean speed (Appendix A) reveal a weak low-speed zone about the central point of the grid, as indicated in Fig. 5.8-right. The relative difference between minimum and maximum values in the mean speed field is around 3.5%, calculated at all flow speeds.

4. The maps of turbulence intensity (Appendix A) reveal a high-turbulence zone in the up-left part the grid, as indicated in Fig. 5.8-right. The highest values of I_U reached about 1.3% at low mean speed and 1% at high mean speed, while in the remaining grid points was always lower than 1% (lowest values around 0.35%). It is worth highlighting that the turbulence intensity calculated without filtering the signals was 25% to 70% higher.

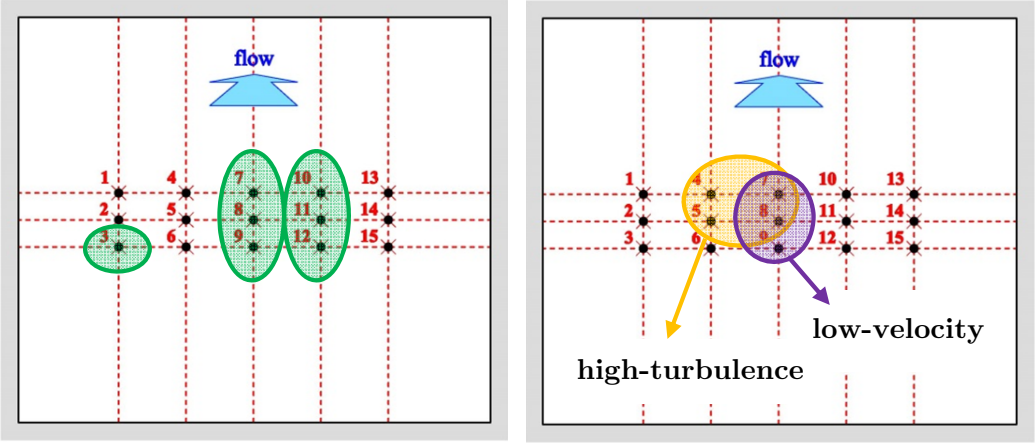

Figure 5.8. Summary of the flow maps results at the Stahlbau wind tunnel.

5.2.3 Aeroelastic setup

The aeroelastic setup, arranged immediately downstream of the inlet (Fig. 5.1b), was composed by several items:

- *External structure.*

  This independent aluminium structures externally enveloped the test section and supported the coil springs (Fig. 5.1b , Fig. 5.14-left), providing a fixed constraint. It was composed by Bosch Rexroth profiles arranged in a frame, placed on the floor of the laboratory. No fixing elements were installed, although the frame was charged by additional weights. Being disconnected to the test section, the aeroelastic setup was better isolated from the wind tunnel and its vibrations.

- *Supporting structure.*

  Four coil springs[2] (with an individual nominal stiffness of 220 N m^{-1}, as reported on Table 5.4) were installed at both ends of the model as sketched in Fig. 5.12, being in a total of 8 springs, to provide the pitching and heaving supports. In this classical design of the elastic suspension, the coils springs were installed vertically at a certain horizontal distance, and were responsible of both heaving and pitching stiffnesses. The latter can be controlled by varying the horizontal distance d, as indicated on Fig. 5.13.

  During 2-DoFs oscillations, the pitching component produced a stretching/shortening of the springs, in addition to the one due to the heaving component. Thus, one of the four springs installed at each ends of the model experienced the maximum elongation or reduction. In addition, the springs in the upper side were also charged by the dead load of the oscillating system. Considering all contributions, the largest expected elongation drove the selection of the springs, which was chosen with a maximum elongation of 833 mm. It is worth highlighting that the springs experiencing the maximum reduction of length had not to show contact between adjacent wires, avoiding alteration of stiffness and damping. Thus, all springs had to be elongated even when the model was in the rest position. The selection of this configuration was an important issue, in order to ensure the reliability of the mechanical characteristics of the setup during the whole oscillation range, providing the springs to operate in the linear field.

  The coil springs were connected to an aluminium rod (Bosch Rexroth, 40×40 mm profile), which in turns was linked to the model axis represented by the cylinder of the hooking element. The connecting element between springs and rod was a steel hook (Fig. 5.16c) at first, but during the experiments it was substituted by smooth bearings with spherical junction (Fig. 5.16d). In between the springs and the hooks, a short

[2] http://www.federnshop.com/Zugfedern/ZugfedernSuchergebnis.aspx

Table 5.4. Techical details of the coils springs (code RZ-162U-07I, material EN 10270-3-1.4310), according to Fig. 5.9.

Oest	180	degree	loop position
d	3	mm	wire diameter
De	40	mm	outer coil diameter
F0	9.2	N	initial tension
Fn	176.9	N	maximum spring force
Lk	211.5	mm	length of unstressed spring body
L0	266	mm	length of unstressed spring
sn	833.28	mm	maximum spring deflection
Lh	27.25	mm	distance of inner edge of loop from the spring body
R	0.201	N/mm	spring rate
Gew	462.9002	g	weight of one spring

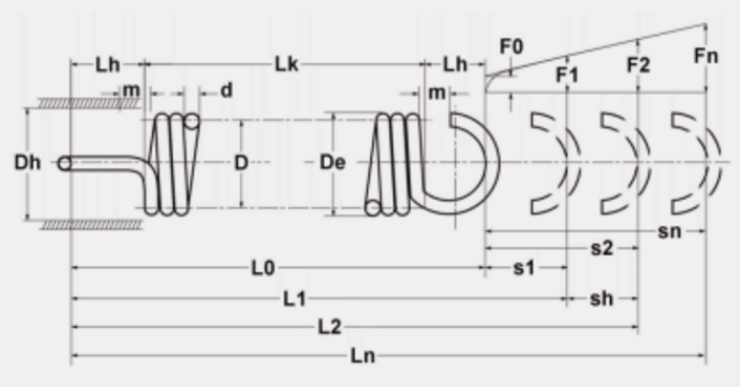

Figure 5.9. Geometry characteristics of the coil spring.

plastic noose was installed to avoid steel-to-steel dry friction during the motion. The rod allowed also to install additional known-masses (as clear on Fig. 5.15-down) to shift the mass-centre position. Due to the operative mechanism of the elastic suspension, these additional masses modified both the total oscillating mass and polar inertia. Playing with added mass and distance to the elastic centre, or modifying the distance between pairs of coil, it was possible to control some of the governing parameters one at a time.

- *Sectional model.*

  The aluminium model, shown in Fig. 5.4 and 5.11, had a rectangular cross section with sharp edges. It was 150 mm wide (B), 10 mm deep (D) and 1200 mm long (l); the smaller dimension D is the one facing the wind. Circular aluminium end-plates, 400 mm large and 2 mm thick, were provided to ensure time-averaged bi-dimensional flow conditions. The end-plates were placed between the model lateral side and an aluminium element (Fig. 5.11), the latter being responsible to allow the connection with the spring suspension. In particular, it was designed to provide a cylindrical attachment in order to allow rotations of the model, adjusting the angle of attack. Moreover, this ad-hoc designed system allowed also to vary the position of the elastic centre, by simply changing the position of the bolts that fixed to the model ends.

  The bending deflection of the model during the oscillations had to be limited in order to not affect flow-induced effects and measurements. The calculations of the expected deflection f_m is conducted according to the static scheme of Fig. 5.10 that considers the real assembled system, thus comprising aluminium model and aluminium axis tubes (the joints between model and tubes are modelled through rotational springs).

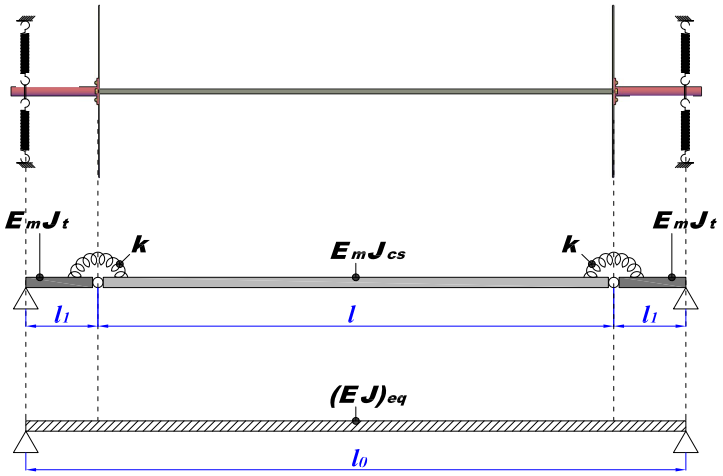

Figure 5.10. Static schemes used to estimate the bending deformation and the fundamental frequency of the model. The model is described by the elastic modulus E_m and flexural inertia J_{cs}, while the axis tube by E_m and J_t. In the scheme, $l = 1.2$ m and $l_1 = 0.15$ m, while $l_0 = l + 2l_1$.

Then, the axis tubes are assumed to be hinged at the external ends. The wind load normal to the cross section and the inertial load, both acting during oscillations, are defined as:

$$F_N = \frac{1}{2} \cdot \rho_f \cdot U^2 \cdot B/2 \cdot C_N \cdot C_d \ ; \tag{5.1a}$$

$$F_A = g\omega^2 \hat{\eta} I_\eta / l_0 \ ; \tag{5.1b}$$

in which:

- $g \cong 9.81$ is the gravitational acceleration [m s^{-2}];
- ω is the circular frequency of the oscillating body during flutter [rad];
- $\hat{\eta}$ is the heaving amplitude during flutter oscillation [m];
- I_η is the total heaving inertia [kg];
- l_0 is the total span [m];
- ρ_f is the density of the fluid [kg m^{-3}], assumed equal to 1.25;
- U is the flow speed [m s^{-1}];
- C_N is aerodynamic coefficient corresponding to the normal load [-];
- C_d is an amplification coefficient to take into account possible dynamical effects of the model [-], assumed equal to 1.5.

The expected deformation was calculated by solving the structure through the iterative method of Cross (from the theory of Science of Constructions), giving the values reported in Table 5.5.

The model was designed to be rigid enough to avoid dynamic interference during flutter oscillations: the natural frequency of oscillation of the model was designed to be larger than 5-6 times the flutter frequency. The same static scheme used for the calculation of the deflection was used to calculate an equivalent stiffness $(EJ)_{eq}$, which can be applied to a homogeneous beam spanning l_0, as depicted by the static scheme in the lower side of Fig. 5.10. Then, the expected frequency n_m of the model can be calculated as:

$$n_{m,eq} = \frac{\pi}{2} \cdot \frac{1}{l_0^2} \cdot \sqrt{\frac{(EJ)_{eq}}{I_\eta / l_0}} \ ; \tag{5.2}$$

in which (in addition the variable defined for Eq. (5.1)):

Table 5.5. Bending deflection and fundamental frequency of the models at the Stahlbau wind tunnel. The total free span, used in the calculation schemes, is l_0 = 1.5 m.

			15:1	23:1	25:1
Bending deflection	f_m	[mm]	5.6	9.3	10.0
Equivalent beam stiffness	$(EJ)_{eq}$	[N m^2]	2350.61	2906.59	3013.51
Fundamental frequency	$n_{m,eq}$	[Hz]	16.14	15.17	14.92

  - E_m is the Young's modulus of the model material [N m^{-2}];
  - $J_{cs} = \frac{1}{12}BD^3$ is the cross-section flexural inertia moment [m^4], being D the cross-section depth.

  The results are reported in Table 5.5.

  Three sectional models were constructed, with different cross sections. In particular, the 15:1, 23:1, 25:1 width-to-depth ratios were selected because:

  - the 15:1 is between the limit of torsional flutter and two-degrees-of-freedom flutter [145, 149];
  - the 23:1 is close to the experimental test of Amandolese [19], so that can be used for comparisons;
  - the 25:1 can be considered very similar to a flat plate, so that can be compared with several available results about flat plates;
  - for all these ratios, the linear theory can be used with good results, allowing a simple calculation of the critical condition;
  - several literature studies can supply useful information about these 'standard' geometries [145].

  However, due to limitation of time, only the 15:1 cross section has been tested so far.

- *Damping system.*

  The system (Fig. 5.15) was developed by Jonas Pons [178], during his Master Thesis at the Stahlbau Institut TU Braunschweig in 2014. Setting the current intensity in a pair of electromagnets placed at a small face-to-face distance (about 7-8 mm) and arranged so to attract each other, as visible on Fig. 5.14-right, the magnetic field produced eddy currents in a 2 mm aluminium or 3 mm copper[3] plate connected to the oscillating system. This latter moved in the gap, and thus a damping force was produced on the system. Summarising, the damping force depends on:

  - relative velocity between magnetic source and conductor;
  - orientation between magnetic field and conductor surface;
  - conductivity of the conductor;
  - geometry of the conductor;
  - geometry of the magnetic source;
  - distance between magnetic sources;
  - value of the magnetic flux.

- *Along-wind motion constraint.*

  The along-wind motion was suppressed connecting plastic cables to the cylinders of the model axis, close to the internal walls of the test section (Fig. 5.16a). The cables

[3]The 3 mm copper plate was obtained by placing side-by-side a pair of 1.5 mm plates and keeping them fixed through bolts.

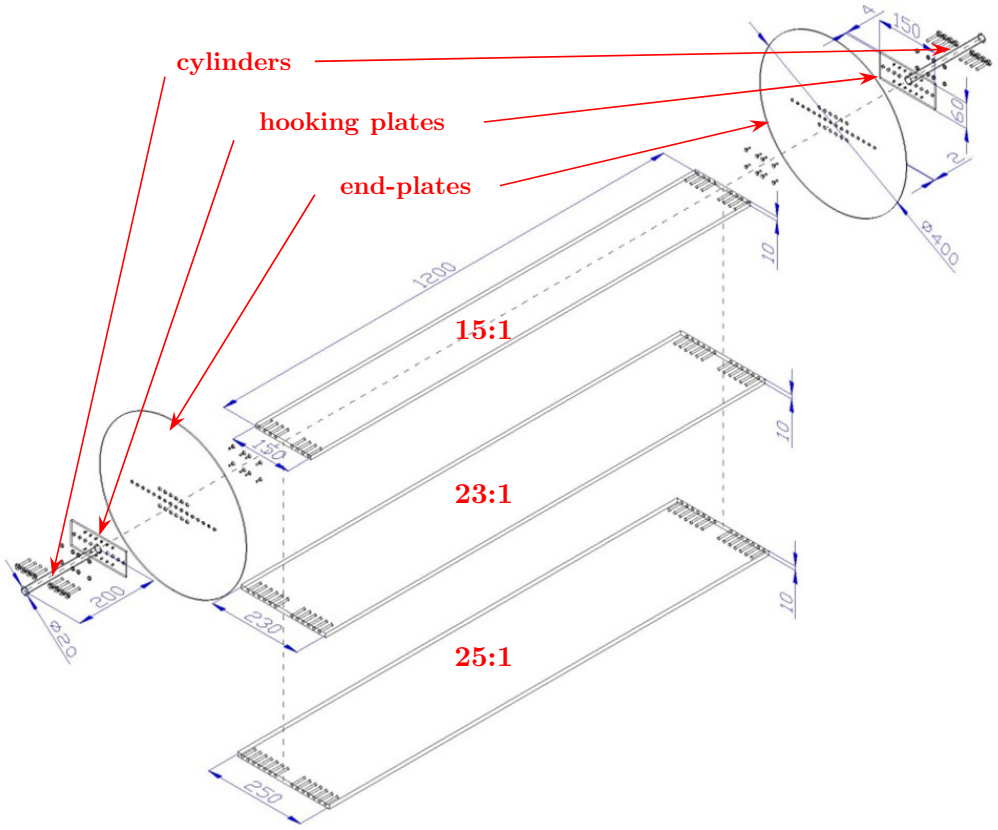

Figure 5.11. Exploded view of the model, with end-plates and connecting elements.

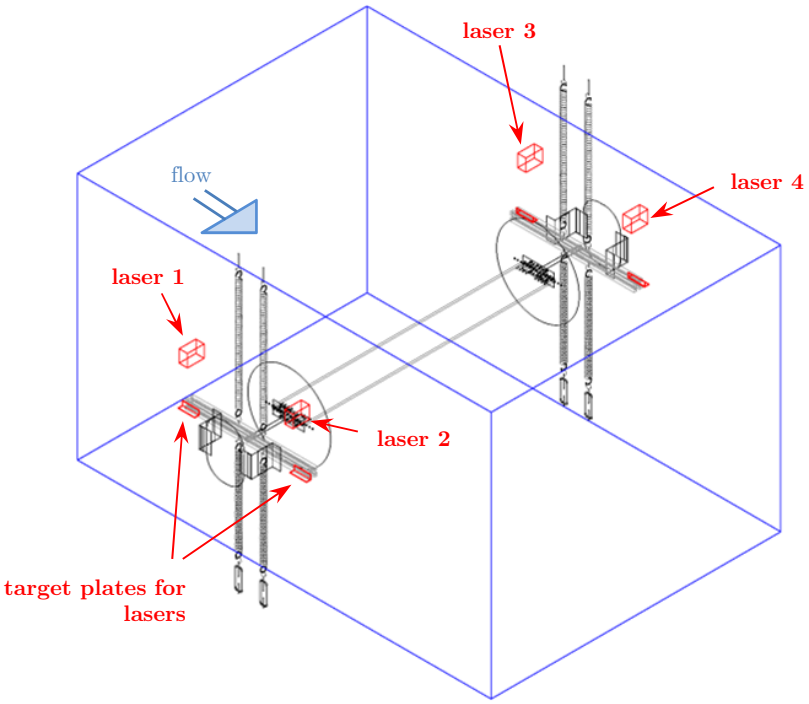

Figure 5.12. Sketch of the elastic suspension of the aeroelastic setup at Stahlbau Institut.

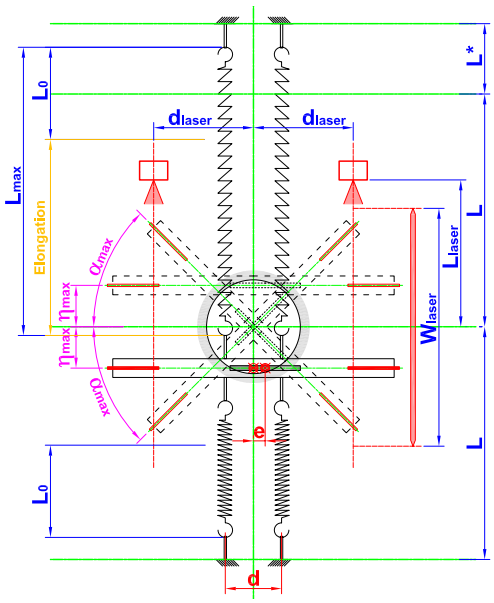

Figure 5.13. Sketch of the working principle of the measuring system of the aeroelasic setup at the Stahlbau Institute. L_0 is the nominal length of the coil springs and elongation; W_{laser} is the operative range of the displacement lasers. The elongation due to the dead load (L*) has to be compensated by distancing the fixing points of the upper springs.

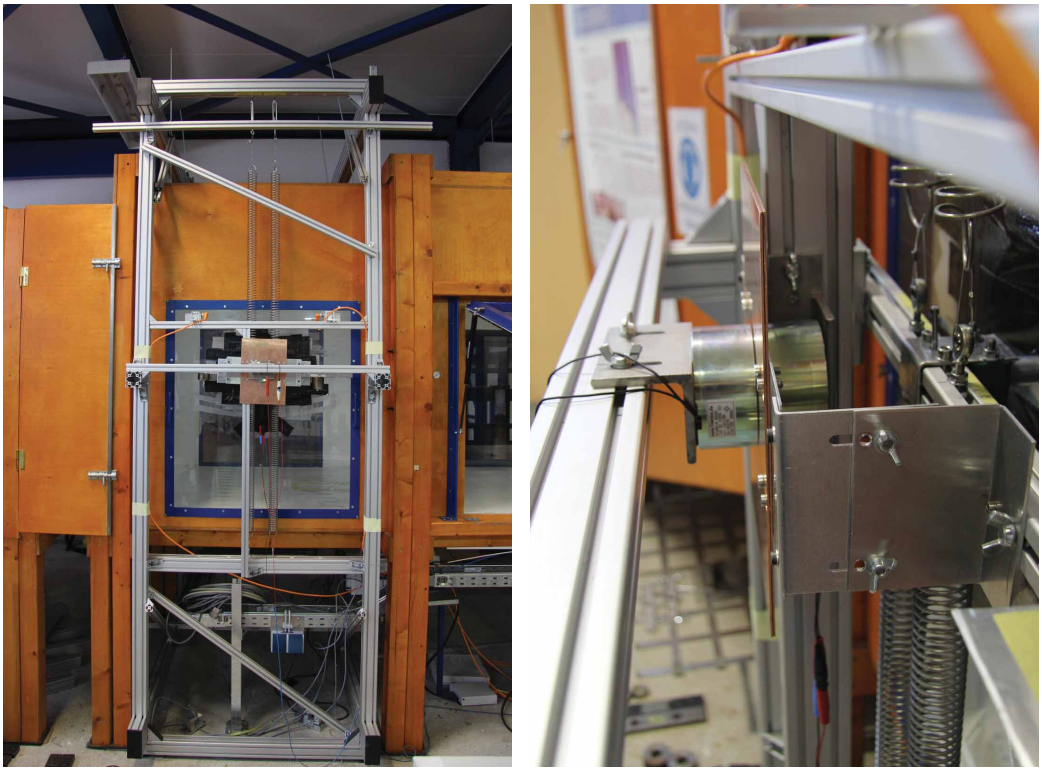

Figure 5.14. Frontal view of the aeroelastic setup (left) and detail of the damper (right), with the pair of electromagnets and copper plate in the gap, this last linked to the rod and to the model motion in turn.

Figure 5.15. Views of the measuring system and dampers of the Stahlbau's setup. The displacement lasers and the respective target plates are clearly visible on the upper photo, while the additional masses installed in the rod are visible in the lower photo.

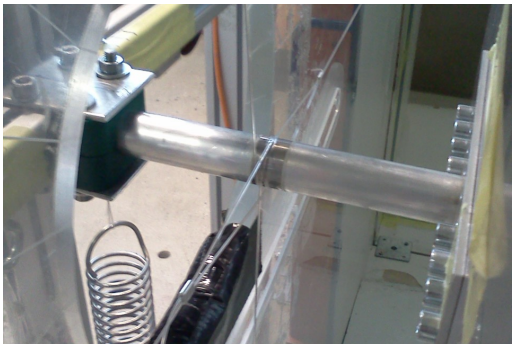

(a) Anti-drag plastic cables with noose.

(b) Anti-drag cables with bearing.

(c) Steel hooks.

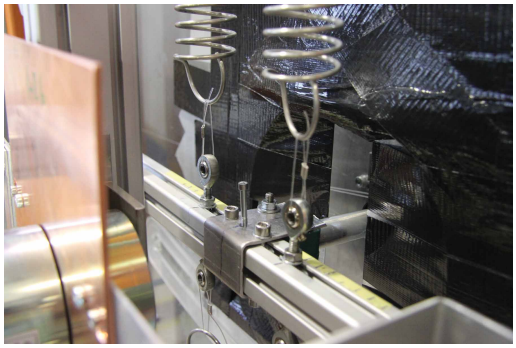

(d) Spherical bearing hooks.

Figure 5.16. Addditional details of the aeroelastic setup of the Stahlbau Institute.

were in turn fixed to the internal walls of the wind tunnel, at a distance of about 1.7 m from the model axis. The variations of the vertical and torsional stiffness during motion were verified to be negligible, although a small increments of heaving nominal stiffness was observed with respect that one of the coils springs only.

A very thin sheet, made of polished stainless steel, was inserted from the beginning of the campaign between the noose and the cylinder, in order to lower the friction. However, as time unfolds the cyclic motion altered the contact surface and dry friction seemed to appear at large oscillations amplitudes (see § 5.2.4). Unfortunately, this problem was noticed only at the end of the experimental campaign, when the noose was released and the surface appeared damaged. Fig. 5.16b shows a possible solution to this problem, obtained inserting a radial ball bearing to produce rolling friction. Due to limitations of time, configurations with this solution were not investigated, performing just free-decay tests.

- *Measuring system.*

  The analog laser displacement transducers were installed as indicated in Fig. 5.12, 5.13 and 5.15-up and measured the displacement of the aluminum plates fixed in the rod of the elastic suspension (target flat elements). A sheet of paper tape was arranged in the target surface to avoid reflection of the laser light. Then, the motion of the model was calculated from these displacements, extracting the contribution of heaving (η), pitching (α) and rolling (δ) according to:

$$\begin{aligned} \eta &= (L_1 + L_2 + L_3 + L_4)/4; \\ \alpha &= \left[\arctan\left(\frac{L_2 - L_1}{b_1 + b_2}\right) + \arctan\left(\frac{L_4 - L_3}{b_3 + b_4}\right)\right]/2\ ; \\ \delta &= \left(\frac{L_1 + L_2}{2} - \frac{L_3 + L_4}{2}\right)/2\ ; \end{aligned} \tag{5.3}$$

where L_i is the displacement measure by the i-th laser and b_i the respective distance from the elastic center, being the lasers placed as in Fig. 5.13. Attention was paid to identify the largest pitching angle at which the laser light loses the target surface ($\alpha_{max} \approx 14°$). For this reason, the target element was elongated in order to enlarge the observable surface during rotations. It is worth highlighting that positive displacements are: downside-vertical heaving, clockwise pitching and counter-clockwise rolling (assuming to observe the model from the upstream side).

5.2.4 Mechanical features

The stiffness linearity of the aeroelastic setup, in both the pitching and heaving degrees of freedom, were verified through static tests (Fig. 5.17), measuring static displacements for different known loads. This characterisation was repeated for each different arrangement of the setup adopted for the investigations of the configurations listed in Table 6.2. The participating inertia in pitching and heaving motions, I_α and I_η, were calculated from the previously estimated stiffness and the corresponding frequency of oscillation in still air. Dynamic tests, in which the frequencies were measured for different additional inertias, confirmed the results.

For each configuration, several free-decay tests[4] were performed in still air for different initial conditions and post-processed through the Modified Unified Least-Square (MULS) method ([88], [181] and [24]). First, the natural frequencies of oscillation ($n_{\alpha 0}$, $n_{\eta 0}$) and the structural ratio-to-critical damping coefficients ($\xi_{\alpha 0}$, $\xi_{\eta 0}$) were evaluated for the un-coupled mechanical system. The only-pitching motion was obtained by constraining the heaving DoF through a plastic cable that linked with a noose to the cylinder of the model axis (similarly to the anti-drag solution). The only-heaving motion was difficult to be performed with coil-spring setups. In this campaign, it was provided only for the configurations with symmetric mass distribution ($S = 0$), where a small heaving displacement was imposed in the model centerline and then released. The quality of the oscillations was then verified a posteriori, post-processing the signals and repeating the procedure if necessary.

The measured damping coefficients were $\xi_{\alpha 0} \approx 0.17\%$ and $\xi_{\eta 0} \approx 0.07\%$, as obtained processing the last part of the decaying signal, where the amplitude started to be lower than 0.2-0.3° of pithing rotations and 2-3 mm of heaving displacements. The length of the processed signal was 70-90 s. In Fig. 5.18 are reported examples of the free-decay tests analysis. The indentification procedure gives good results, stating that the system behaved linearly both in frequency and damping for small oscillations. The aerodynamic damping in still-air oscillations, which is a non-visous contribution, had low effect in these free-decay tests, as demonstrated by the identified signals that well agree with the measured signal even in those large-size windows. Also the cases with external damping introduced by the dampers give very good results, comfirming that the eddy-current damping device introduced purely viscous damping. The identified parameters were considered to be reliable for the estimation of the critical condition of flutter.

By constrast, Fig. 5.19 show examples of free-decay oscillations that started from larger amplitudes. The tests refers to a symmetric configuration undergoing uncoupled oscillations, obtained as explaied in the previous paragraph. Observing the heaving DoF, the MULS identification was performed in the first part of signal, returning a damping coefficient higher than in the case of small-amplitude oscillations. However, those free-decay tests were performed with the model at null angle of attack, thus the chord section facing the still-air flow produced non-negligible aerodynamic damping. This aeroelastic effect due to just the heaving velocity was supposed to be responsible of the higher damping value obtained at larger amplitudes. Observing the pitching DoF in Fig. 5.19-right, the free-decay oscillations seem to depend importantly on damping and the MULS identification does not give good results. In fact, Fig. 5.20a shows that the pitching damping strongly varies from 4° to 2° pitching amplitudes. This behaviour is supposed to be related mainly to the anti-drag system

[4] At least three free-decay tests were performed to allow a minimal statistical characterisation of the parameters.

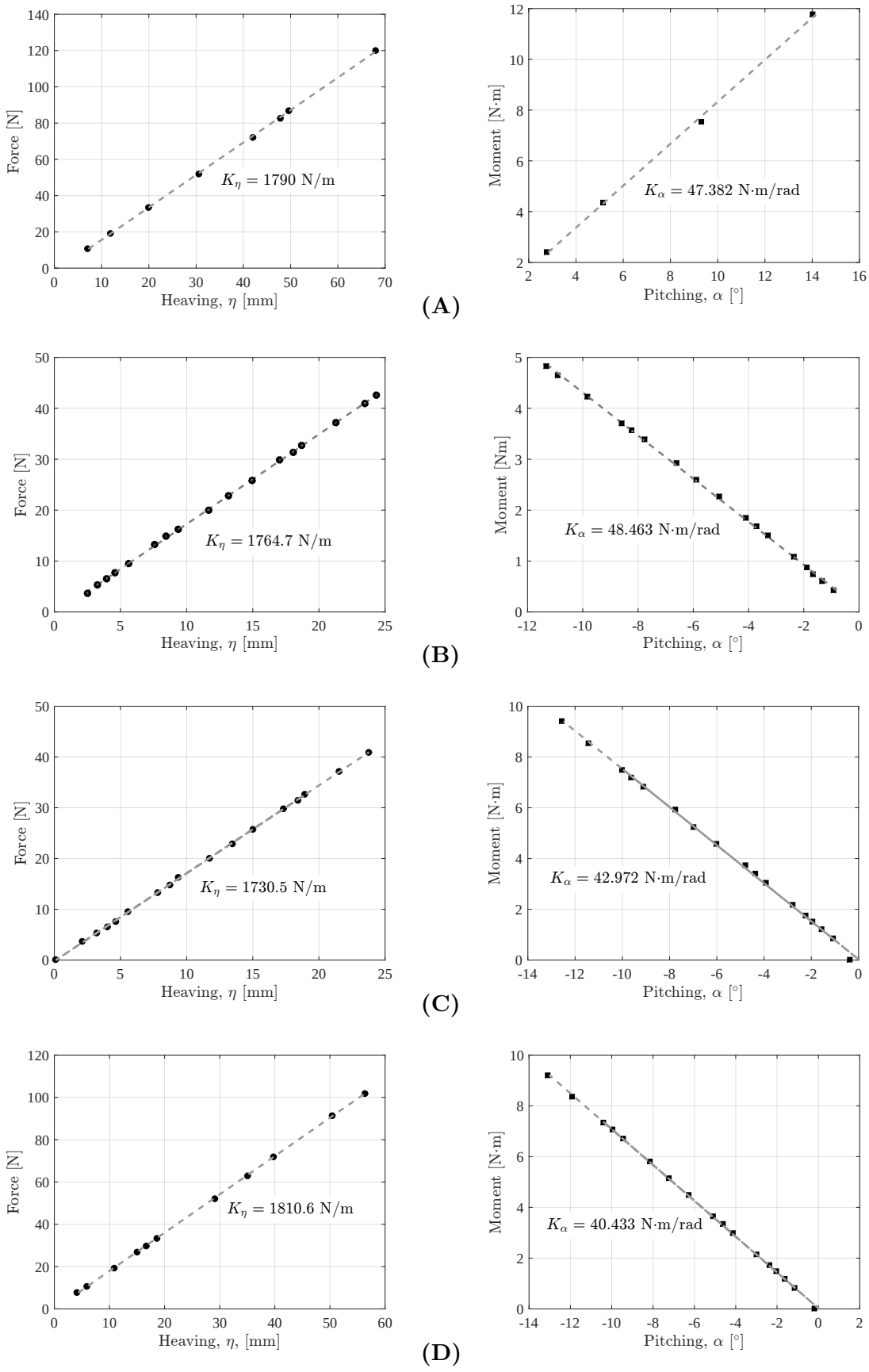

Figure 5.17. Results of the static tests to verify the heaving and pitching stiffnesses, for the used typologies of setups A, B, C and D, as indicated in Table 6.1.

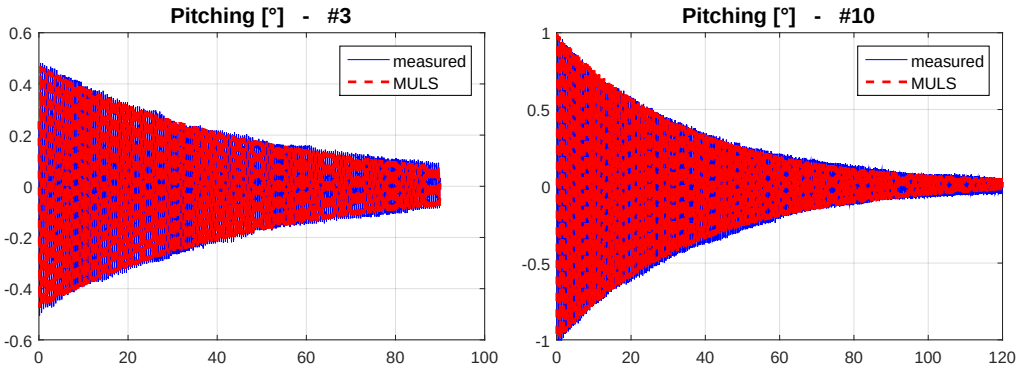

(a) Pitching oscillations with constrained heaving, for different configurations and initial amplitudes.

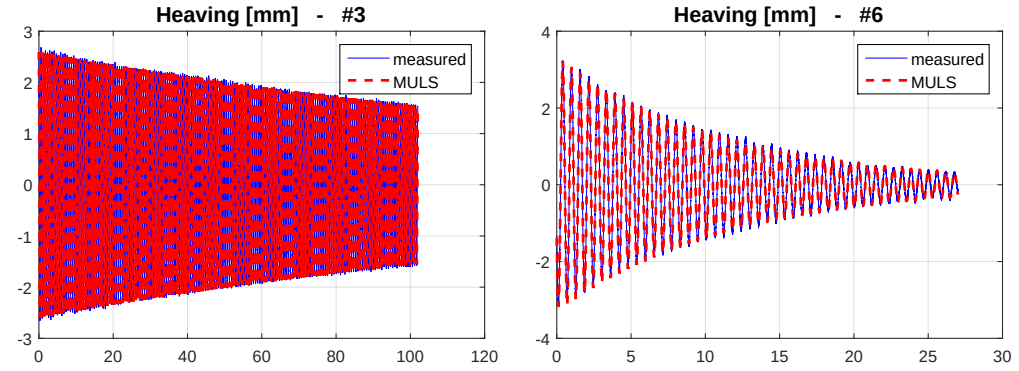

(b) Symmetric configurations with different heaving damping levels ($\xi_{\eta 0} = 0.05\%$ and $\xi_{\eta 0} = 2.57\%$).

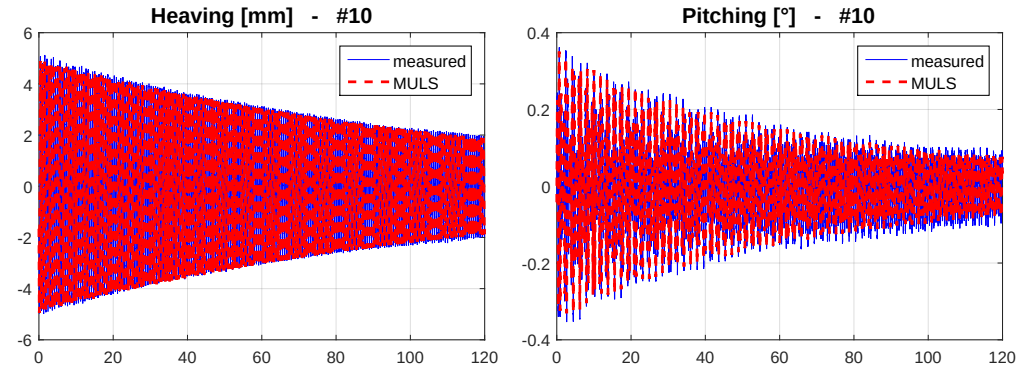

(c) Identification of coupled η-α motion, with low heaving damping level ($\xi_{\eta 0} = 0.07\%$).

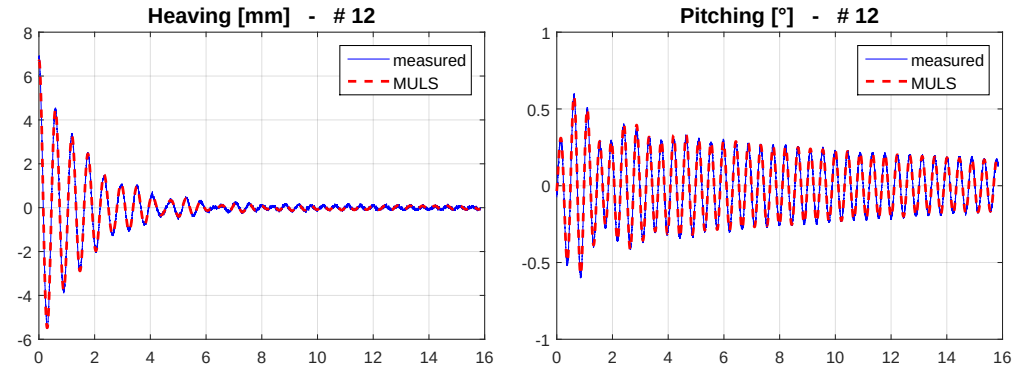

(d) Identification of coupled η-α motion, with high heaving damping level ($\xi_{\eta 0} = 5.67\%$).

Figure 5.18. Some examples of results of free-decays tests. In the figures, the abscissa is the time [s].

used in the experiments, although a small contribution can also be due to the aerodynamic damping arising from the pitching velocity in the still-air flow. For large pitching amplitudes, higher values of damping were expected to be enhanced by the friction between the anti-drag cable and the model-axis tube. In the right-side of Fig. 5.20a, the MULS identification was applied to 2 s windowed signals, moving the window centre along the the time axis by steps of 1 s. The results indicate that the system can be considered linear for small oscillations amplitudes, as the damping (and frequency) values are almost constant. The ball-bearing solution adopted at the end of experimental campaign only (see § 5.2.3), confirmed the expected considerations about the pitching-damping increments. Observing Fig. 5.20b, the MULS algorithm identified a viscous damping almost constant in all 50 s signal. In this case, only the aerodynamic pitching damping was responsible to the damping modifications. In the right-side of Fig. 5.20b, the MULS identification was applied to signal windows with increasing length, starting from the same inital time value. Damping (and frequency) variations are apparent but are small if compared to the obtained values. The same figure also reports the system identification when performed in the last 10 s of the signal, so that small amplitudes are considered. It is remarkable to state that the system identification through the MULS algorithm depends on the length of the windowed signal, although the differences reduce as the system is closer to be perfectly linear.

Higher levels of $\xi_{\eta 0}$ were reached through the electromagnetic system, up to a value of 5.67%, by varying the current intensity in the electromagnets. The corresponding free-decay oscillations showed a few cycles to end the decay and the identification procedure was difficult. In some cases, an additional mass, ΔI_η, was installed in the suspension system to temporary reduce the critical damping ratio to a smaller value $\xi^*_{\eta 0}$ allowing more cycles of oscillation in order to better identify the signal. Since the damping coefficient C_η has to be the same (depending only on the characteristics of the dampers), the obtained critical damping ratio can be corrected to remove the effect of the additional mass according to:

$$C_\eta = 2\sqrt{K_\eta (I_\eta + \Delta I_\eta)}\xi^*_{\eta 0} \quad \rightarrow \quad \xi_{\eta 0} = \xi^*_{\eta 0}\sqrt{1 + \frac{\Delta I_\eta}{I_\eta}} \ . \tag{5.4}$$

The static mass unbalance S was experimentally estimated by measuring the frequencies of oscillations of the system during coupled pitching-heaving motion, namely $n_{\alpha 1}$ and $n_{\eta 1}$, using the following formula [19, 32]:

$$S = \left[I_\eta I_\alpha \left(1 - \frac{\omega^2_{\eta 0} + \omega^2_{\alpha 0}}{\omega^2_{\eta 1} + \omega^2_{\alpha 1}} \right) \right]^{0.5} \tag{5.5}$$

This equation is derived from the transfer function of a general linear dynamic system with 2-DoFs when subjected to harmonic motion.

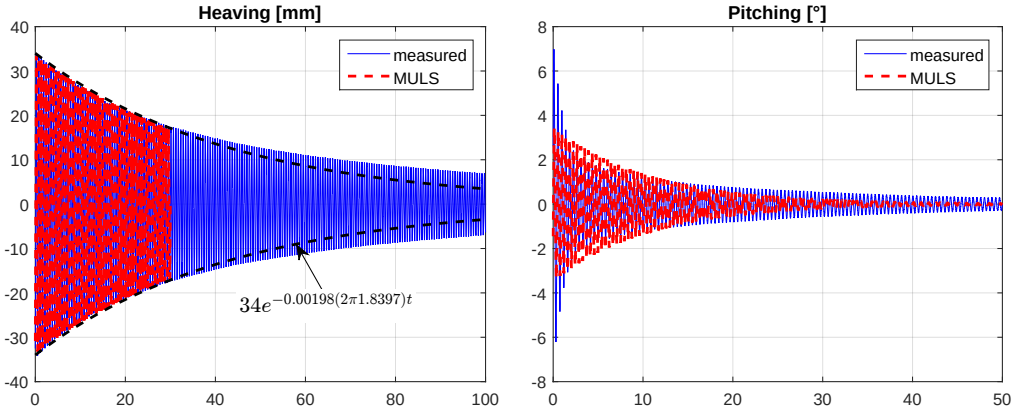

Figure 5.19. Examples of free-decay tests starting at large amplitudes; the anti-drag system was without ball-bearings. In the figures, the abscissa is the time [s].

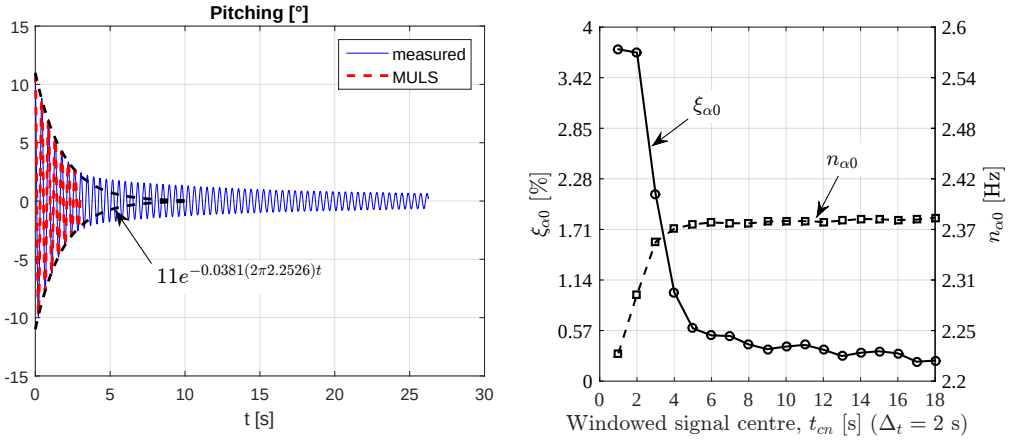

(a) Pitching component (without ball-bearings in the anti-drag system).

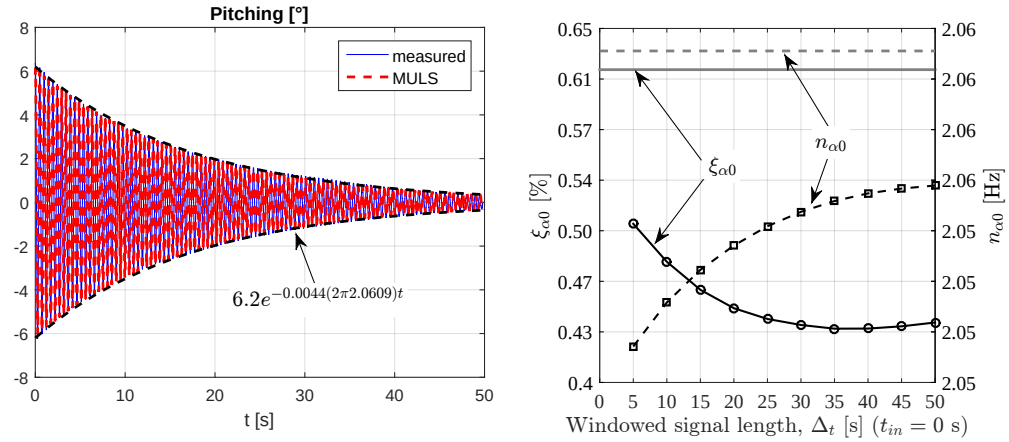

(b) Pitching component (with ball-bearings in the anti-drag system).

Figure 5.20. Examples of results of free-decays tests starting at large amplitudes to study the influence of the ball-bearings in the anti-drag systems by applying the MULS algorithm to different signal windows.

5.3 CRIACIV wind tunnel

The second part of the experimental campaign was conducted in the facility of the 'Centro di Ricerca Interuniversitario di Aerodinamica delle Costruzioni e Ingegneria del Vento (CRIACIV)[5]' in Prato, of the 'Università degli Studi di Firenze' of Florence, Italy. The open-circuit, boundary layer wind tunnel (Fig. 5.21) is about 22 m long and has the following features:

- supporting structure made of steel, floor covered with wood and walls covered with wood or made of glass and plexiglass.
- cross-section width of 2.20 m and height of 1.60 m (inlet), width of 2.40 m and height of 1.60 m (test section);
- length of the test section of 11 m;
- 156 kW fan, placed at the outlet;
- velocity range of 0.1-27.6 m s^{-1}, by regulation of the ange of the rotor blades (0-15.4°) and the inverter RPM;
- turntable floor (circle of 2.2 m diameter) at the test section;
- lowest turbulence intensity ≈ 0.7%;
- turbulators (vortex generators), grids for homogeneous turbulence and roughness patches;

5.3.1 Equipment

The following instruments were adopted.

- *A Prandtl tube* (Fig. 5.22a). It was connected to a pressure transducer (model 239 by Setra System) to convert the flow pressure to electric signal, which was sent to the acquisition system by an interconnecting coaxial BCN cable. The probe was placed in a position upstream to the test section, fixed to the floor, at a distance of about 4 m in order to limit possible turbulent wake flows disturbing the model. It was used to measure the flow speed during the investigations and to infer the flow speed at the model centerline by means of flow maps and velocity conversions (see § 5.3.2).
- *An ambient measuring sensor.* The instrument (model HD2001.1 by Delta OHM, with RS232C serial port) is composed by a probe, an interconnecting cable, a digital display and and output cable. It is able to measure ambient pressure (the accuracy is ±0.5 mbar at 25°C), temperature (the accuracy is ±0.3 °C) and humidity and it allows analog measurements with voltage or ampere output signal. The probe was placed close to the Prandtl tube.
- *An hot-wire anemometer.* It is a straight single-sensor miniature wire probe, made of platinum-plated tungsten with a diameter of 5 μm and length of 1.25 mm (model 55P11 by Dantec), which is installed in a 1.9 mm diameter ceramic tube, 30 mm long, equipped with gold-plated connector pins that connect to the probe support by means of a plug-and-socket arrangement. The body of the probe is arranged in a specific tube that holds the probe aligned to the flow and allows the installation on other supports to perform flow measurements. The sensor works together with a Wheatstone bridge (model CTA 56C17) that is installed in the relative box (model CTA 56C01 for 4 modules); this last contains also a signal conditioner module (model CTA 56N20) for each Wheatstone bridge to amplify/filter the signals before the analog-to-digital conversion. The instrument measures mean and fluctuating components of one-dimensional flows with an accuracy of ≤ ±0.2 m s^{-1} and sampling frequency up to 250 kHz.

[5] Interuniversity Research Centre on Building Aerodynamics and Wind Engineering

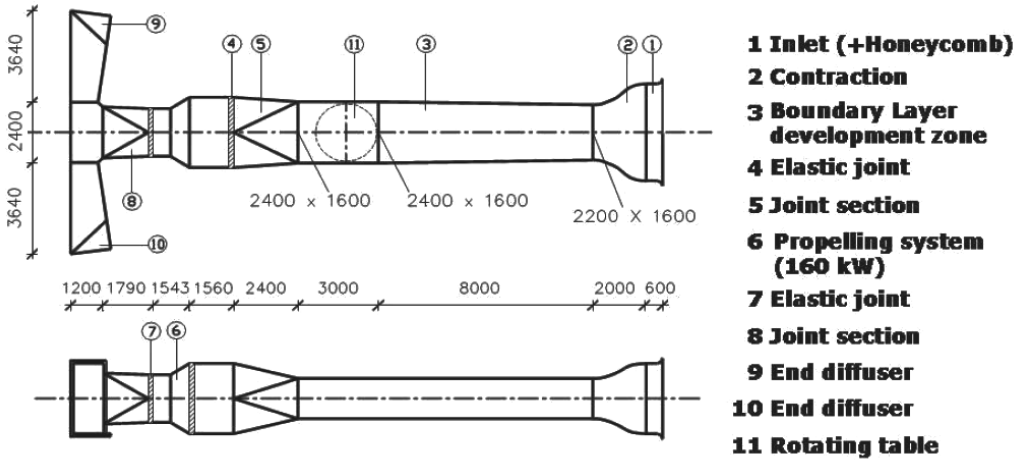

(a) Sketch of the geometry.

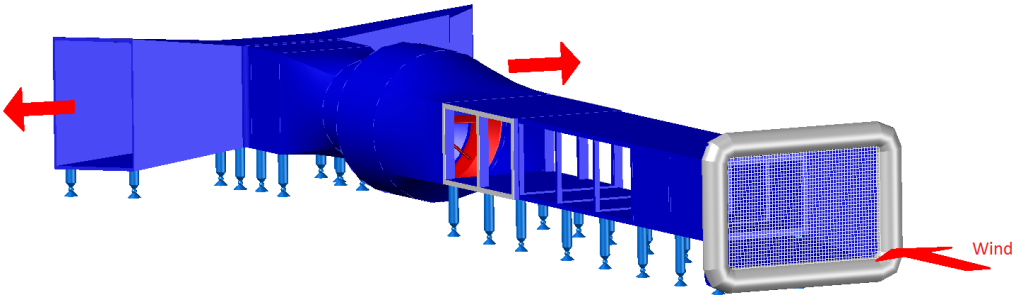

(b) 3D model of the facility.

(c) Later view, from the inlet (number 1 in (a)).

Figure 5.21. Geometry and views of the CRIACIV wind tunnel.

- *Three displacement lasers.* Analog laser displacement transducers of the type:

  a) n° 2 of OptoNCDT 1605-200 by Micro-epsilon (Fig. 5.22h). The analog output is in the range ±10 V and corresponds to the measuring range 240-440 mm, with the specifications indicated in Table 5.6. These were connected to the power supply (model PS 1605 working at 220 V-AC in input and 24 V-DC in output, with a 25-pol. D-Pin-Connector) by a 3 m long interconnecting cable (model PC 1605-3 with 7-pin) and then to the digital acquisition system.

  b) n° 1 of OptoNCDT ILD 1700-200 by Micro-epsilon. The analog output is in the range 0-10 V and corresponds to the measuring range 70-270 mm, with the specifications indicated in Table 5.6. This was connected to the digital acquisition system through a supply/output cable (model PC 1700-3, with 14 coaxial pins), which also allowed the direct connection to the amplifier.

  Both typologies of lasers were linked to the amplifier (Fig. 5.22i) that supplied 24 V.

- *Two miniaturised accelerometers* (Fig. 5.22e). Piezoelectric ceramic shear sensors of the type ICP (model 352C42 by PCB piezotronics), with technical features reported on Table 5.8. During different sessions of the experimental campaign, these were connected to:

  a) 9 m long, low-noise coaxial cables (model 003A30 with 10-32 coaxial plug at both ends by PCB piezotronics, with one end that has been modified to BNC plug), Fig. 5.22f;

  b) 6 m long, twisted red/white cables (model 031A20 with 10-32 AW solder adaptor at both ends), which required a scope input adaptor (model 070A02, 10-32 jack to BNC plug), Fig. 5.22g.

  Cables a) are quite ridig in bending and their installation was complicated by the large rotations, and the cables were damaged after some tests due to the large bending curvatures achieved in particular points of the cables. By contrast, cables b) are more flexible due to the twisted arrangement, and substituted the former during the last experimental session (SESSION III in § 6.3.2). In both cases, the cables were linked to a power supply box (model 442B104 by PCB piezotronics), placed in an intermediate position between accelerometers and acquisition system, which amplified (×10) and conditioned the returning signals before the DAQ system.

- *Two groups of four permanent magnets* (type 60 × 5 of Fig. 5.22c and 35 × 20 of Fig. 5.22d). A pair of circular, neodymium, permanent magnets of the type a) or b) (technical features listed on Table 5.7), were installed in a supporting structure, specifically designed for these tests in order to allow linear viscous damping even during large motion amplitudes. Thus, a damper requires two magnets, at least. Since a damper was installed in each side of the model, introducing symmetric damping forces, the global damping system involved two dampers, that is four permanent magnets at least.

- *Data acquisition (DAQ) system* (Fig. 5.22i). Analog-to-digital converter (A/D USB NI-cDAQ-9172 by National Instruments), equipped with modules NI-9239 working at 24 bit and with anti-aliasing filter, which sends the measured signals to the computer for the next post-processing. It was linked to an amplifier (Fig. 5.22i), which supplied 24 V. Every instrument sent the signal to the DAQ system through coaxial BNC cables, but short specific cables were inserted to modify the BNC plugs in order to link to the DAQ module. The operative sampling frequency was set to 2000 Hz.

5.3.2 Flow characteristics

The mapping of the flow at the test section is necessary to know the flow characteristic in the position where the model oscillates. It was conducted for smooth flow conditions and

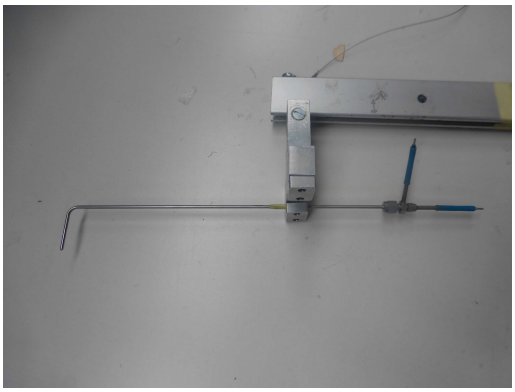

(a) Prandtl tube.

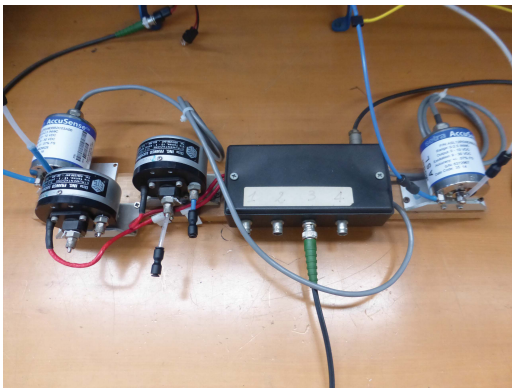

(b) Setra equipment.

(c) Permanent magnet 60×5.

(d) Permanent magnet 35×20.

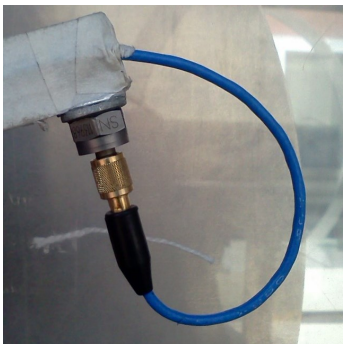

(e) Miniaturized accelerometer.

(f) Low-noise coaxial cable 003A30.

(g) Twisted-red/white cable 031A20.

(h) Displacement laser.

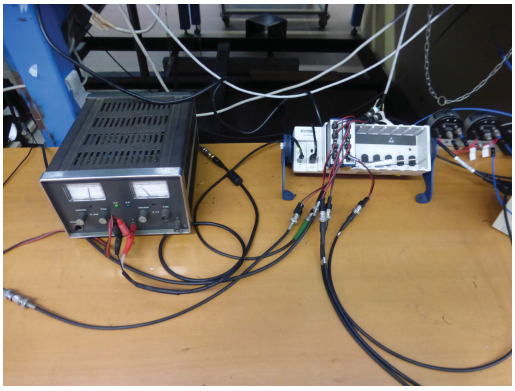

(i) Power supply (left) and DAQ system (right).

Figure 5.22. Instrumentations of the CRIACIV facility.

Table 5.6. Summary of technical features of the analog displacement lasers.

		a)	b)
Sensor type		Laser-sensor	Laser-sensor
Model		LD 1605	ILD 1700
Type		200	200
Operative voltage	[V]	±10	0-10
Measuring range	[mm]	±100	±100
Stand-off midrange	[mm]	340	170
Resolution	μm	60	12
Sampling frequency	[kHz]	40	2.5 (adjustable)
Light source		laser 1mW	semiconductor laser ≤1mW
Wavelength	[nm]	675 (red)	670 (red)

Table 5.7. Summary of technical features of the permanent magnets.

		(a)	(b)
ID article		S-35-20-N	S-60-05-N
Material		NdFeB	NdFeB
Shape		disk	disk
Magnetization		N45	N45
Covering		nikel-plated (Ni-Cu-Ni)	nikel-plated (Ni-Cu-Ni)
Diameter	[mm]	30	60
Thickness	[mm]	20	5
Actraction force*	[kg]	≈ 38	≈ 22
Weight	[g]	150	110

* on a plate of 10 mm thick, made of pure steel, placed in contact with the magnet face.

Table 5.8. Summary of technical features of accelerometers.

Sensitivity (±10%)	[mV/g]	100
Measurement range	[g pk]	±50
Frequency range (±5%)	[Hz]	1.0 to 9000
Frequency range (±10%)	[Hz]	0.5 to 10000
Frequency range (±3 dB)	[Hz]	0.3 to 15000
Resonant frequency	[kHz]	≥ 30
Broadband resolution (1 to 10000 Hz)	[g rms]	0.0005
Overload limit	[g pk]	±5000
Excitation voltage	[VDC]	22 to 30
Constant current excitation	[mA]	2 to 20
Size - height	[mm]	9.7
Weight	[gm]	2.8
Housing material		titanium
Electrical connector		10-32 coaxial jack
Electrical connection position		top

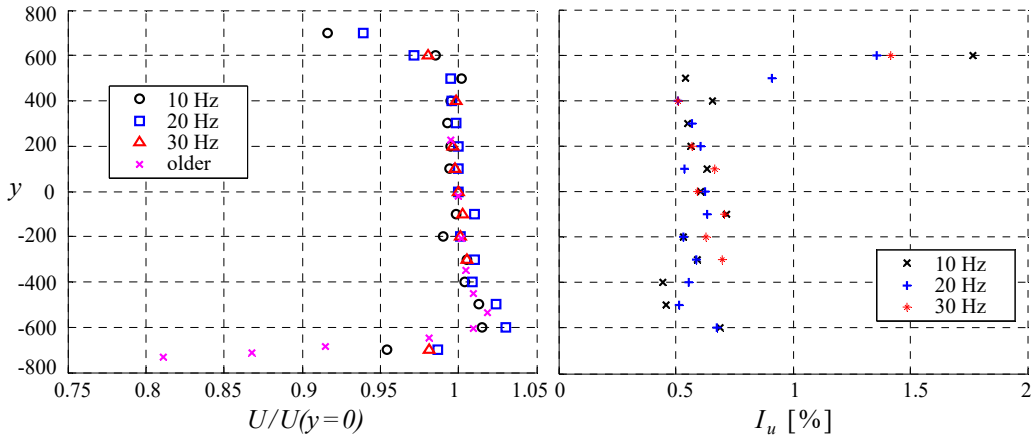

Figure 5.23. Characteristics of the flow in the free-test section, where y [mm] indicates the vertical position along the vertical centerline of the test section.

for the configuration of the experimental setup adopted during the first two parts of the experimental campaign (SESSION I and SESSION II, see § 6.3.2). The displacement lasers, which pointed the frames of the heaving suspension and the dampers, were both installed during the flow characterisation in order to take into account for their possible disturbances.

The flow features in the case of free-test section, that is without elements installed inside the wind tunnel with the exception of the devices required to measure the flow (Prandtl tube and hot-wire anemometer), are reported in Fig. 5.23, and show good mean velocity and turbulence intensity distributions. However, the experimental setup considered the installation of screens to shelter the elastic suspension from the interaction with the oncoming flow (see § 5.3.3). Since the screens were developed for the first time for these tests, the characterisation of the flow flowing between them was required.

A grid of measured points was identified with respect to the allowed displacement field, as indicted in Fig. 5.24. The maximum vertical displacement of the oscillating model was ±100 mm and corresponds to the range of measurement of the displacement lasers. The vertical holes on the plexiglass walls of the carters allowed this displacement. Although the model can show a rotation different from zero at the maximum heaving amplitude position, which can enlarge the swept area during oscillations and thus the area of the oncoming flow that directly impacts the model, the upper and lower line of the investigated points were chosen to correspond to the ±100 mm alignments. This grid was considered to be representative of the flow interacting with the model during oscillations.

The flow mapping was performed installing the hot-wire anemometer in the respective supporting probe, which was linked in turn to a specific support (Fig. 5.25). At the same time and in the same support, both a Prandtl tube and a temperature probe were installed allowing the calculation of the mean velocity to be compared to the that one calculated through the anemometer. The Prandtl tube and the anemometer were arranged to be at as close as possible distance (28 mm, calculated at the measuring points of the two instruments). The points belonging to the vertical alignment CN of Fig. 5.24 were investigated arranging the Prandtl tube and the anemometer in vertical position, while the other lateral points were measured rotating the instruments of ±90°. The support of the instruments was linked through bolts to a vertical aluminium Bosch profile with 10×40 mm^2 cross section, which was fixed to floor and ceiling of the wind tunnel. The support was also stiffened through two steel cables connected to the floor and arranged to form a triangle. The vertical movement of the measuring apparatus to points at different height was simply obtained releasing the bolts, moving the support along the vertical Bosch profile and fixing again the bolts. By contrast, the horizontal movement required the modification of the position of the whole Bosch profile and stiffening elements.

Another Prandtl tube was placed in a position upstream of the test section, which was

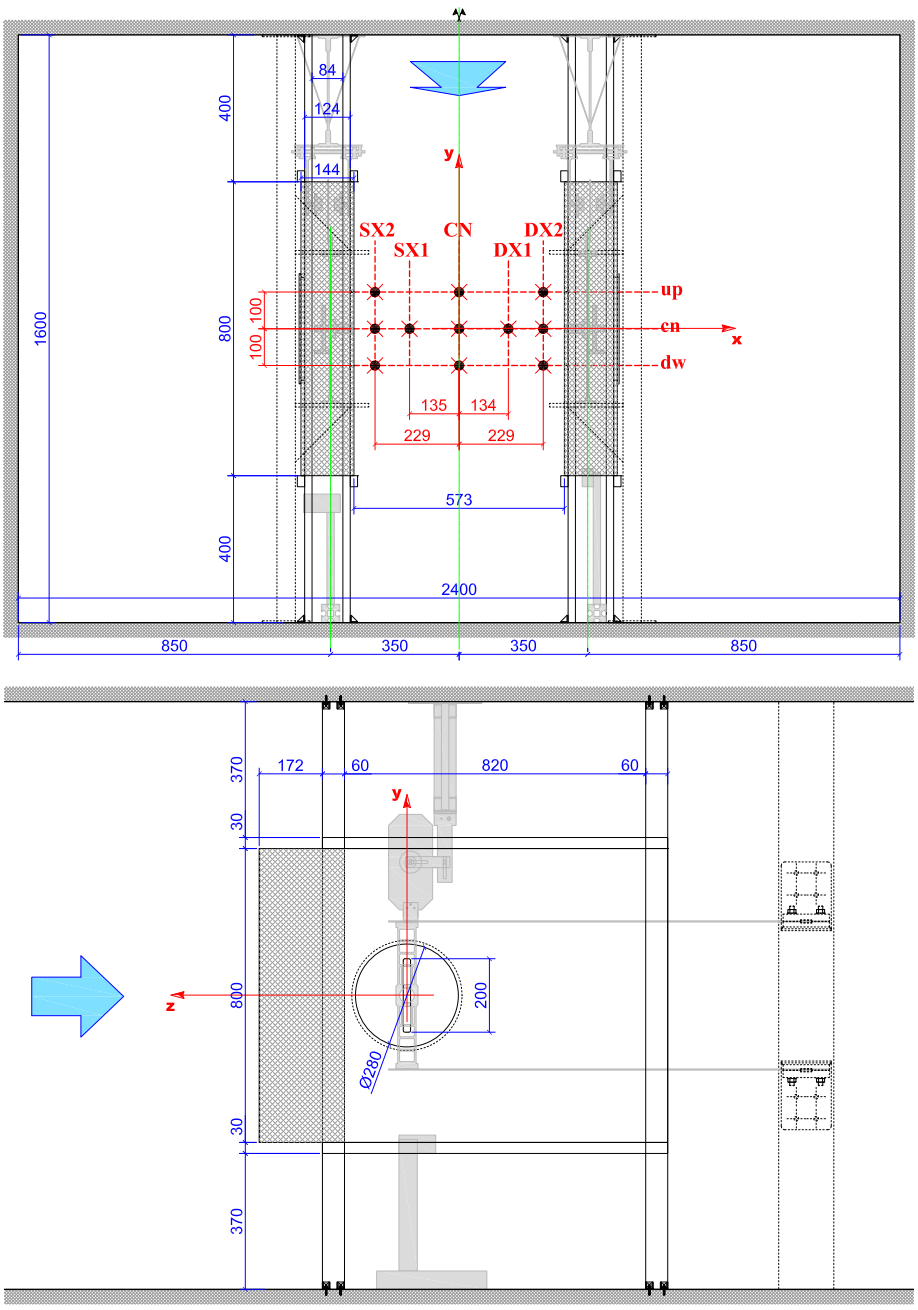

Figure 5.24. Distribution of the grid points in the test section between the carters.

Figure 5.25. View from upstream (left) and downstream (right) of the installed equipment for the flow measurements; the shorter tube is the support of the hot-wire anemometer.

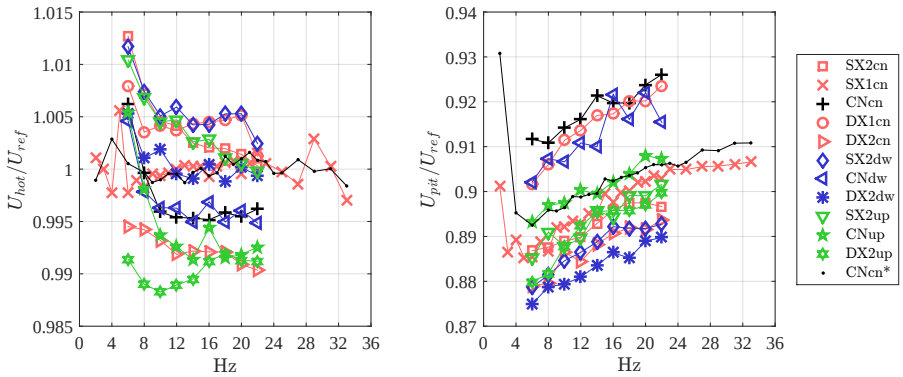

Figure 5.26. Mean velocity in the points of the grid measured through the hot-wire anemometer U_{hot} (left) and the up-stream Prandtl tube U_{pit} (right), normalised by the mean velocity obtained with the Prandtl tube at the test section U_{ref}, and displayed with respect to the frequency of the inverter.

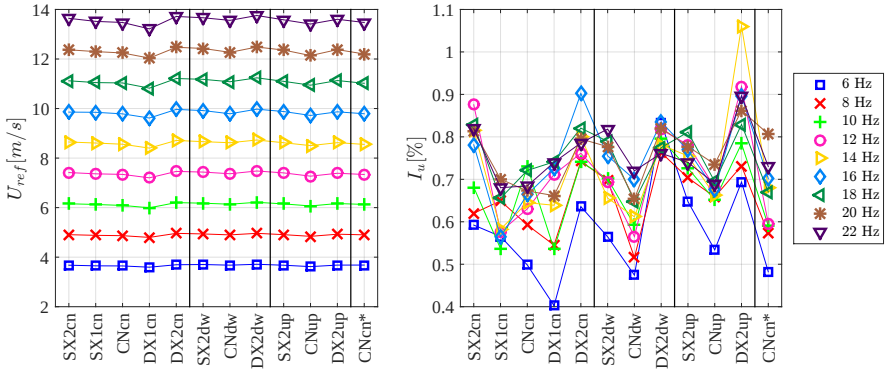

Figure 5.27. Distributions of the mean velocity (left) and turbulence intensity (right) with respect to the points of the grid, as measured for several values of the inverter frequency.

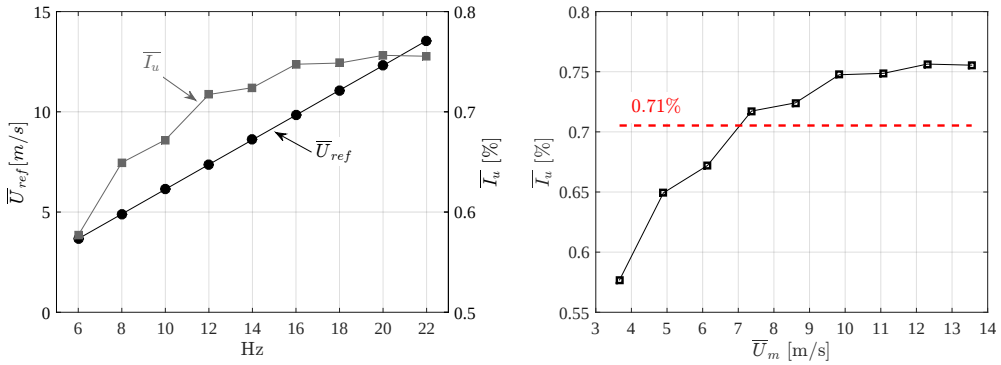

Figure 5.28. Mean values of mean velocity and turbulence intensity over all the points of the grid with respect to the inverter frequency (left), and their relative evolution (right).

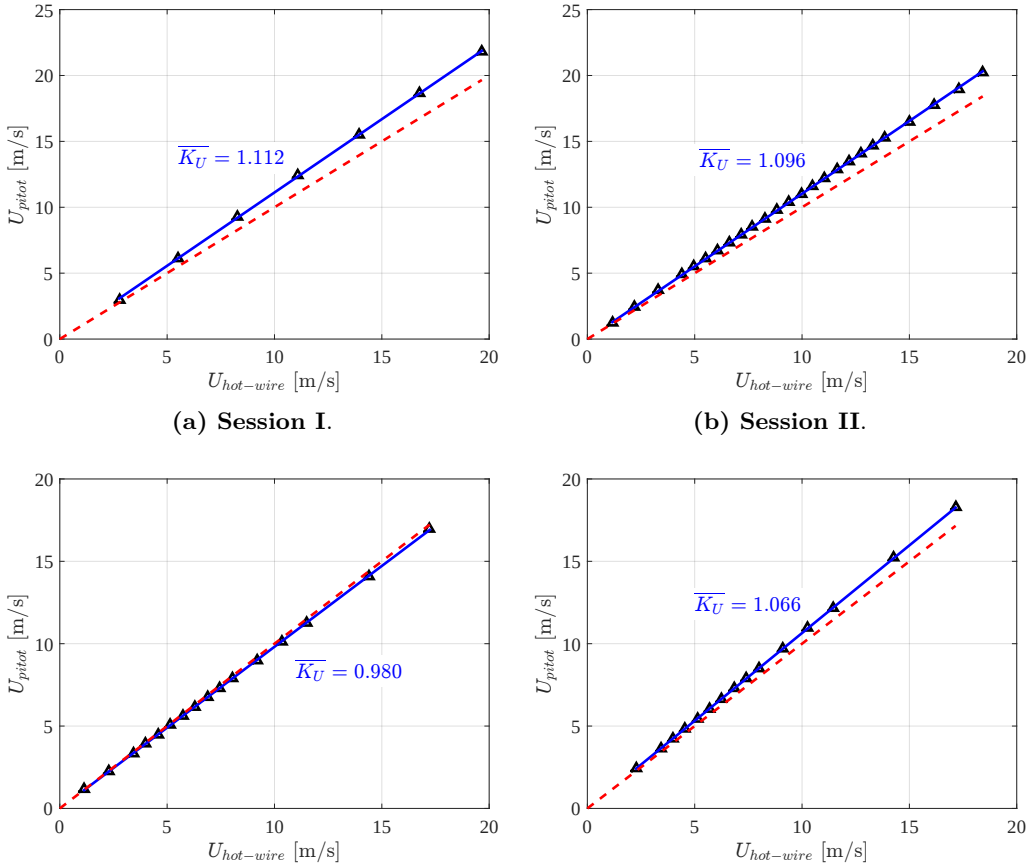

(a) Session I. **(b) Session II.**

(c) Session III - without carters. **(d) Session III** - with carters.

Figure 5.29. Mean-flow velocity conversions for the CRIACIV tests. In the ordinates, U_{pitot} refers to the flow speed measured by the upstream Prandtl tube.

maintained also during the aeroelastic tests, in order to obtain the velocity conversion that infers the flow velocity at the model position. The Prandtl tube was installed in a short piece of a similar aluminium Bosch profile, which in turn was stiffened to the floor with two steel cables. It is worth highlighting that the position of the upstream Prandtl tube with respect to the model is usually of low importance. However, the arrangement in Fig. 5.25 (identified as P1) produced a wake flow able to increase the turbulence intensity measured in some points of the grid, especially in the points CNcn and CNdw of Fig. 5.24. For this reason, the upstream Prandtl tube was moved in a position closer to the later wall of the wind tunnel and installed in a shorter Bosch profile. This second configuration (identified as P2) was adopted in the last part of the experimental campaign (SESSION III, in § 6.3.2).

The flow mapping was performed for several flow velocities and the results, in terms of flow maps, are reported in the Appendix B. Hereinafter, only the main results are reported, and refer to the position P2 of the upstream Prandtl tube. Fig. 5.26-left shows that the mean flow velocity calculated by the hot-wire anemometer well agrees with that one obtained from the Prandtl tube, placed at close distance. Furthermore, Fig. 5.26-right shows the velocity-conversion factors as calculated for several inverter frequencies. It is also possible to note the difference between velocity-conversion factors calculated for the same point of the grid but with different position of the upstream Prandtl tube (CNcn derives from the position P2 while CNcn* from P1).

Fig. 5.27 summarises the mean flow speeds, as measured by the Prandtl tube close to the anemometer (U_{ref}), and the turbulence intensity of the alongwind velocity component, measured with the anemometer (I_u); both are reported for all the grid points. It is apparent that the smooth flow condition features a homogeneous flow, in terms of both mean speed and turbulence intensity. Considering the mean value of the mean speeds ($\overline{U}_m$) and of the turbulence intensities ($\overline{I_u}$), calculated from all the points of the grid (Fig. 5.28), $\overline{U}_m$ linearly increases with the inverter frequency and $\overline{I_u}$ is contained in the range $[0.57\%, 0.76\%]$, slightly increasing with the mean flow speed. In smooth flow conditions, the mean turbulence intensity experienced during the tests is 0.71%. Fig. 5.29 reports all the mean flow velocity conversions required during the CRIACIV campaign and, comparing Figs. 5.29c and 5.29d, the presence of the carters slightly altered the flow speed at the model centreline.

All these results were obtained with the opened vertical slots on the plexiglass walls, without covering them. The measurements at the grid point DX2cn were repeated covering the closer slot with duct tape but the results were not influenced. Moreover, the flow characterisation was completed with additional checks, observing the behaviour of small wool strings attached along the surface and performing simple smoke visualisations.

As said at the beginning of this section, this flow characterisation is valid for SESSION I and SESSION II of the experimental campaign. During SESSION III, a longer model was used, thus the carters were placed at a larger distance. For these reasons, the previous results can not directly apply to the characterisation of the flow experienced during SESSION III. However, the flow characterisation was not repeated because of the previous validation of the carters effectiveness. Due to the quality of the flow flowing between them when placed at the closer distance required for SESSION I and SESSION II, it was assumed that they continued to provide good quality of the flow also when placed at a larger distance. Finally, the first tests of SESSION III were conducted without carters at all. Moreover, in this case the flow mapping can refer to the results obtained for the free test section, with good approximation. The elastic frame for the heaving motion can be considered to not affect significantly the oncoming flow when the model is at rest, although it can affect the system response during the flow-induced motion because of its aeroleastic effects. In Appendix C is explained the influence of the carters in the post-critical response of the system.

5.3.3 Aeroelastic setup

The aeroelastic setup was specifically designed for these tests to allow large amplitudes of oscillations. The setup was composed by (i) an oscillating part, which comprised the elastic supports and the model, and (ii) a fixed counterpart (Figs. 5.30, 5.36, 5.37 and 5.38). This last comprised the constraint, which was composed by two hollow-rectangular steel

(a) External view.

(b) Upper support.

(c) Lower support.

Figure 5.30. Arrangement of the linear springs, according to Fig. 5.31 and Fig. 5.32.

pillars that constrained the elastic suspension to the wind tunnel, the carters and the other equipment (displacement lasers and dampers), as described in the following items. In this way, the model was hold in the horizontal position at the mid-height line of the test section. The pillars were placed about 10 m downstream the inlet, in correspondence of stiffening steel frames, which externally enveloped the wind-tunnel section.

Hence, the setup is composed by the following items belonging to the oscillating part (i):

- *Flexible supporting structure*

  The adopted solution of the elastic suspension is depicted in Figs. 5.31 and 5.32. The stiffness of the heaving DoF was controlled through the free length (selected between 900 and 1008 mm) of two pairs of aluminium beams (or blade-springs, 50 mm wide and 3 mm thick). Each pair was arranged to provide a frame with shear-type deformation thanks to a Vierendeel girder connecting the free ends of the beams through bolted joints, while the other ends were clamped to the fixed support, as visible on Fig. 5.32.

  Due to the large free length of the beams of the shear-type frames and being the model arranged in the horizontal position, the gravity force importantly deformed the frames. Thus, the static deflection needed to be compensated in order to obtain a rest position of the model in which the blades of the frames were almost undeformed. The adopted solution consisted on the installation of two pairs of linear springs (with stiffnesses of 95 or 195 N m^{-1}, see Table 5.9 and Fig. 5.34a) linked to the upper (Fig. 5.30b) and lower (Fig. 5.30c) sides of the free ends of each frame. These additional springs were placed outside to the test section through steel cables linking the springs to the free ends of each frame, in order to be not disturbed by the oncoming flow. The upper springs were installed in a way to communicate each other, that is closing the force transmission, in order to balance asymmetric loads. This was obtained linking together the upper springs by a steel cable that past through two wheel bearings, each one installed in steel scaffolds (Figs. 5.31 and 5.30b) that was fixed to the outer side of the wind tunnel ceiling and held the springs vertically aligned. By contrast, the lower

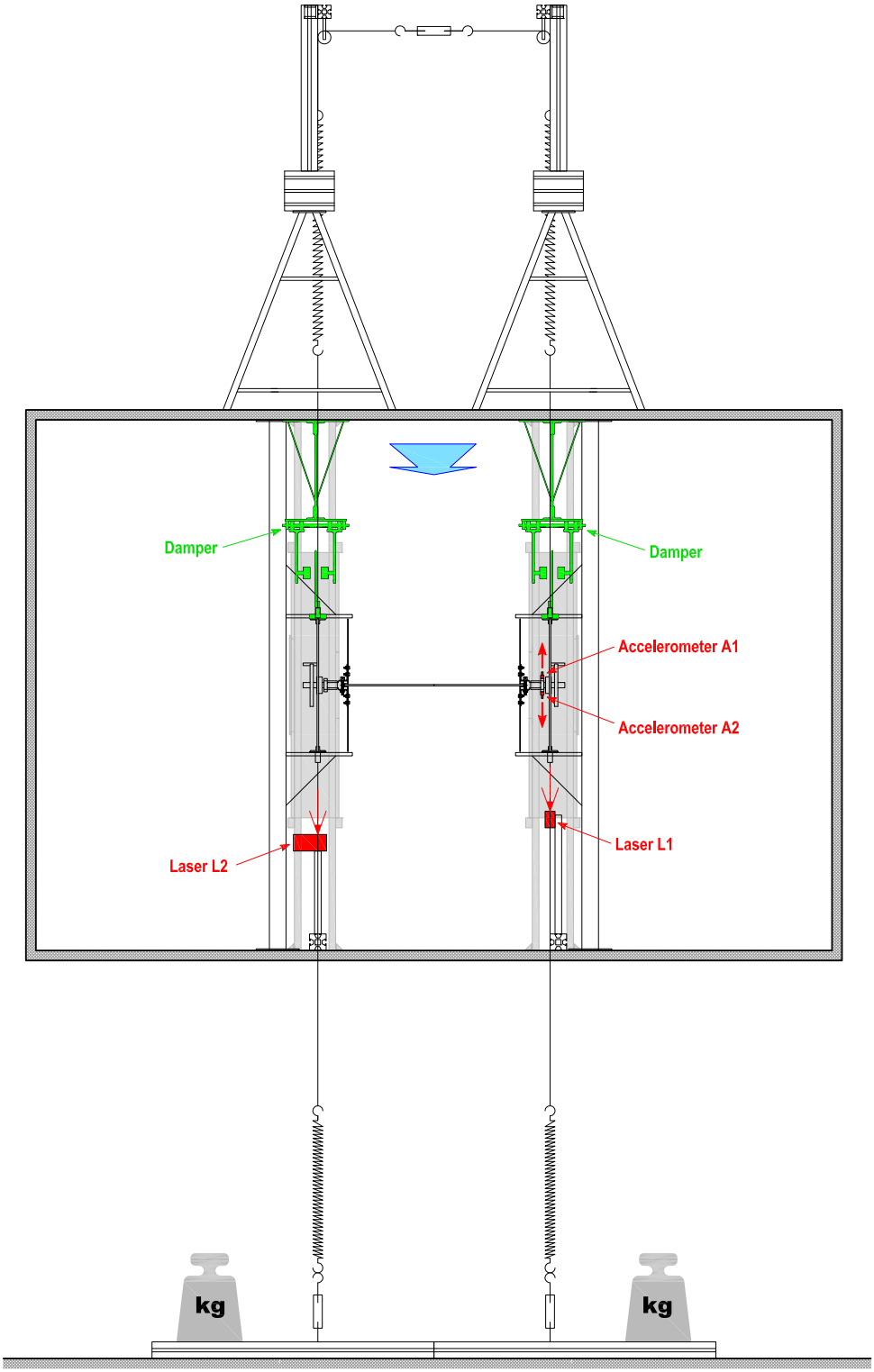

Figure 5.31. Schematic of the aeroelastic setup at CRIACIV wind tunnel (frontal view).

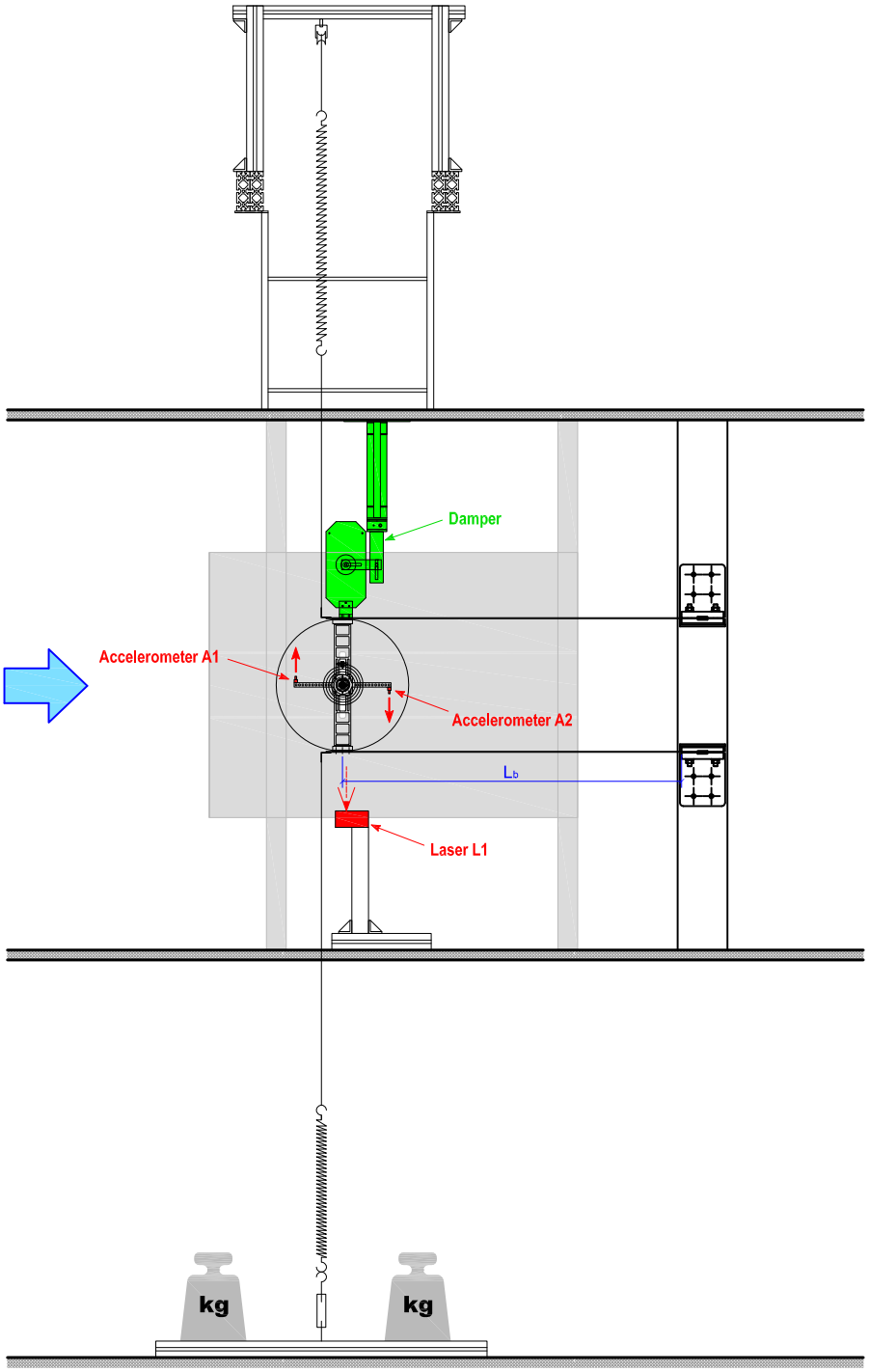

Figure 5.32. Schematic of the aeroelastic setup at CRIACIV wind tunnel (lateral view).

springs were fixed to a ballast, lying on the floor under the wind tunnel (Fig. 5.30c). Obviously, the linear springs contributed also to the heaving stiffness and this was taken into account.

Each frame was equipped with a clock spring as depicted in Figs. 5.39 and 5.43 (with a rotational stiffnesses of 0.923, 1.381 or 2.057 N m rad^{-1}, see Table 5.10 and Fig. 5.34b), which was fixed in a coaxial position with respect to the model axis. The inner end of the clock spring was fixed to the model axis, while the outer end was clamped to a specific element, fixed in turn to the Vierendeel girder (Figs. 5.39 and 5.41). Moreover, the model axis was connected to the elastic supporting frames by means of radial ball bearings (model 7303 BEP by SKF, 109 g heavy, see Fig. 5.34c) installed directly in the Vierendeed girder (as also visible on Fig. 5.43 and Fig. 5.32-right), inserted through a hole with a slightly larger diameter in the Vierendeel girder and fixed to this last with a special glue. The bearing system decoupled the two degrees of freedom. This arrangement (identified as BL) was used during almost all the experimental campaign. A different arrangement (as visible on Fig. 5.32-left and identified as BS2) was designed with the aim to reduce the free play of the joint due to the out-of-plane rotations allowed, which are typical of bearing with a single row of balls. In this solution, a pair of smaller single-row ball bearings (model 61803 by SKF, 8.2 g heavy, see Fig. 5.34c) were installed inside a special interconnecting case (65.8 g heavy, see Fig. 5.34d), linked to the Vierendeed girder, in order to better limit the out-of-plane rotations of this joint. However, this solution was hyperstatic and suffered the not perfect arrangement of the setup, which strongly stressed the bearings producing a distorted motion. Thus, only the inner bearing was installed (configuration identified as BS1) and this arrangement was adopted in the earliest part of SESSION III until the damage of the bearings, happened because the bearings were too much small to endure against the stress arising from the motion at large amplitudes. In Appendix C is discussed the influence of the ball-bearing systems BS1 and BL.

- *Sectional model*

  Two sectional model were investigated (identified as M25S and M25L and comparable observing Figs. 5.36 and 5.37), both made of steel and with a rectangular cross section with sharp edges that was 100 mm wide (B) and 4 mm deep (D), the smaller dimension being the one facing the wind. The free span of the model M25S, calculated as the distance between end-plates[6], was 517 mm and it was installed during SESSION I and SESSION II. During SESSION III, the model M25L was installed and it was 1008 mm long. Circular aluminium end-plates, 400 mm large and 1.5 mm thick, were also provided to the model ends during SESSION I and SESSION II in order to ensure time-averaged two-dimensional flow conditions. During SESSION III the end-plates were not installed.

  Each sectional model was provided with a special interconnecting element that represented the 'model axis', and connected the model to the elastic support (see Figs. 5.34e, 5.39 and 5.41). It comprised a clamp to hold the model, a joint to adjust the angle of attack of the model and a piece of an aluminium tube that past through the ball bearing and linked to the clock spring. This ensemble of parts allowed also to control the position of the elastic axis by simply clamping the model in different positions. Two rocker arms were devised to the same element to vary the mass centre position by adding calibrated masses. During SESSION I and SESSION II, the rocker arm RAa was installed, as indicated in the upper side of Fig. 5.40 (see also Figs. 5.42 and 5.43) and, while during SESSION III the typology RAb was used (lower side in Fig. 5.40, and also Figs. 5.42 and 5.43). The RAa typology introduced a weak eccentricity of the mass centre in the direction perpendicular to the width of the cross section, being the rocker arm not aligned with the elastic centre. Moreover, since it was permanently fixed the upper part of the interconnecting element, it was not possible to obtain its

[6]The model was actually long 541 mm, but few centimetres were occupied by the clamps and end-plates were not in correspondence of the exact model ends.

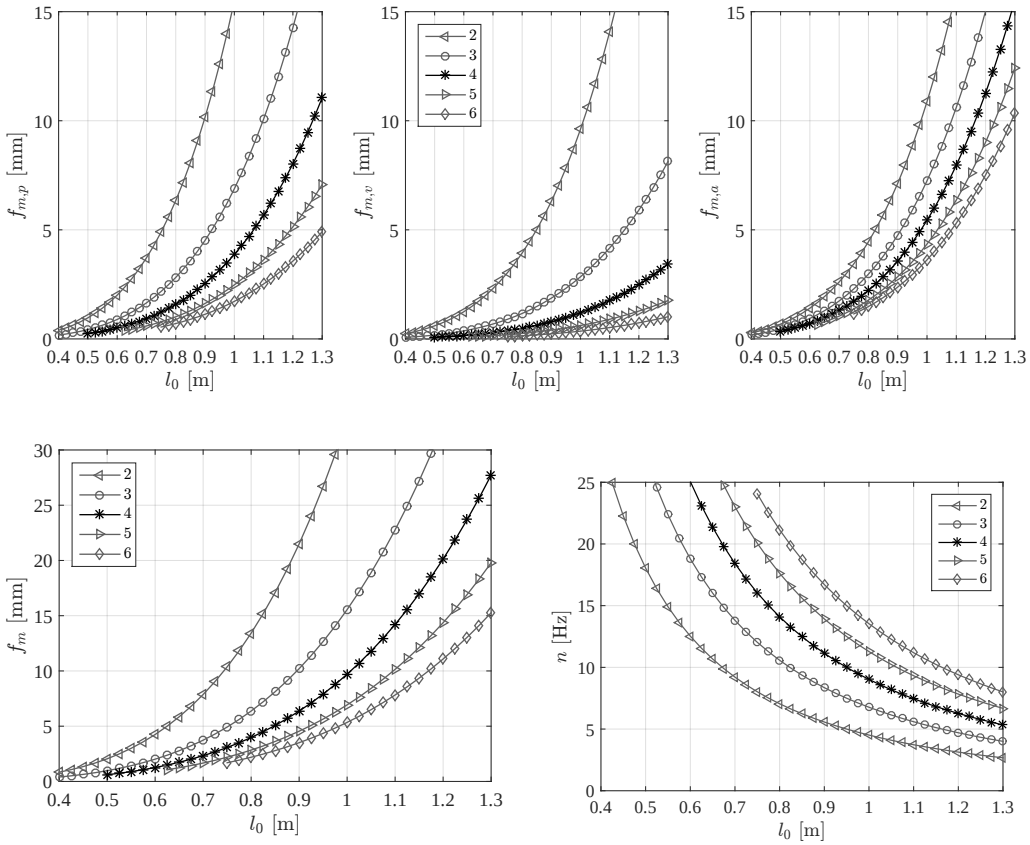

Figure 5.33. Bending deflections due to the dead load ($f_{m,p}$), wind load ($f_{m,v}$) and inertial load ($f_{m,a}$) and the combination of them during the motion in most onerous condition. The fundamental frequency of the model (n) is also reported, as calculated assuming the model simply supported.

horizontal alignment during the rest position of the model for configurations with mass unbalance. The RAb model was designed to solve this problem.

The sectional models were designed following the same principles reported in § 5.2.3. In this case, according to Eqs. (5.6) and (5.7), the system is assumed to behave like a simply-hinged homogeneous beam undergoing bending deformations for the estimation of the expected deflection f_m and frequency n_m.

$$
\begin{aligned}
q_a &= \rho_m \gamma_A r D^2 \omega^2 \hat{\eta} r D = \rho_a \cdot g \gamma_A r D^2 \ ; \\
q_v &= \frac{\rho_f}{2} U^2 \frac{rD}{2} C_N C_d = \rho_v \cdot g \gamma_A r D^2 \ ; \\
f_{m,p} &= g \cdot \frac{5}{32} \cdot \frac{l_0}{(D/l_0)^3} \cdot \frac{D}{(E_m/\rho_m)} \cdot \frac{\gamma_A}{\gamma_J} \ ; \\
f_{m,v} &= f_{m,p} \cdot \frac{\rho_v}{\rho_m} \ ; \\
f_{m,a} &= f_{m,p} \cdot \frac{\rho_a}{\rho_m} \ ; \\
f_m &= f_{m,v} + \left(f_{m,p} + f_{m,a} \cos \hat{\phi} \right) \cos \hat{\alpha} \ .
\end{aligned}
\tag{5.6}
$$

$$
n_m = \frac{\pi}{4\sqrt{3}} \cdot \frac{1}{\sqrt{l_0}} \cdot \left(\frac{D}{l_0} \right)^{\frac{3}{2}} \cdot \sqrt{\frac{E_m D}{\rho_m}} \cdot \sqrt{\frac{\gamma_J}{\gamma_A}} \ . \tag{5.7}
$$

In eqns.(5.6) and (5.7), the variables are:

- D is the cross-section depth [m];
- r is the width-to-depth ratio of the cross-section [-];
- l_0 is the total span [m];
- ρ_m is the density of the model material [kg m^{-3}];
- E_m is the Young's modulus of the model material [N m^{-2}];
- $\gamma_A = A_{cs}/rD^2$ is the ratio of the cross-section area A_{cs} to a reference area [-];
- $\gamma_J = J_{cs}/(rD^4/12)$ is the ratio of the cross-section flexural inertia moment J_{cs} to a reference moment of inertia [-];
- ω is the circular frequency of the oscillating body during flutter [rad];
- $\hat{\eta}$ is the heaving amplitude during flutter oscillation [m];
- $\hat{\alpha}$ is the pitching amplitude during flutter oscillation [rad];
- $\hat{\phi}$ is the pitching-to-heaving phase during flutter oscillation [rad];
- ρ_f is the density of the fluid [kg m^{-3}], assumed equal to 1.25;
- U is the flow speed [m s^{-1}];
- C_N is aerodynamic coefficient corresponding to the normal load [-];
- C_d is an amplification coefficient to take into account possible dynamical effects of the model [-], assumed equal to 1.5;
- $g \cong 9.81$ is the gravitational acceleration [m s^{-2}] .

As inferable from Fig. 5.33, the shorter model M25S would experience a maximum bending deflection lower than half time its cross-section depth ($f_m \leq 0.5D$), vibrating at a fundamental frequency higher than 25 Hz. Thus, the M25S model can be effectively considered as a rigid model and its deformations weakly affected the flow-induced vibrations. By contrast, the M25L model would experience bending deflections up to about two times and half its cross-section depth ($f_m \approx 2.5D$) and its fundamental frequency is around 7 Hz. This means that, although the frequency is larger than 3 times the typical frequencies achieved during flow-induced motion (see § 7), the model flexibility could affect the flow-induced loads. However, it is worth highlighting that this calculation is conservative. In fact, the deformations achieved during the experiments were smaller, since it was assumed a flow speed of 13 m s^{-1} in the theoretical calculation, which was rarely achieved during the tests.

Also for this experimental campaign, three width-to-depth ratios were selected. In particular, the 15:1 and 25:1 were considered in order to have the possibility to compare the results with those of the German experimental campaign, while the 20:1 was selected to add an intermediate value in addition to the 23:1, which was considered for the campaign at the Stahlbau Institut. **Anyway, due to limitation of time, only the 25:1 cross section has been tested so far.**

The items belonging to the fixed counterpart (ii) are:

- *Sheltering screens (or carters)*

  The suspension system was sheltered from the flow by means of two screens, composed by an aluminium nose (1 mm thick) shaped on a wood centering skeleton with the geometry of a NACA0020 profile, installed in a wooden frame fixed to the test section. Plexiglass panels were installed in the frame to cover the lateral walls between the frame beams (see Figs. 5.36, 5.37 and 5.38), limiting both the disturbances produced by the setup to the incident flow and the unwanted aeroelastic effects of the oscillating supporting elements (mainly the blade-springs). It is worth highlighting that the sheltering part of the carters covered only a portion of the test section height, that is a volume sufficiently larger than the swept volume of the suspension system.

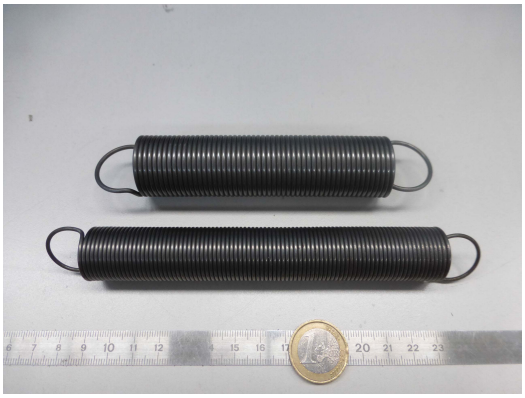

(a) Coil springs.

(b) Clock springs.

(c) Radial ball-bearings.

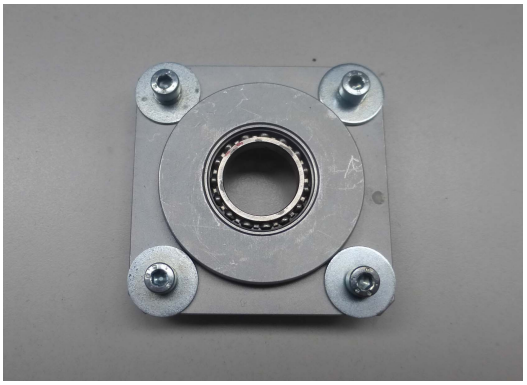

(d) Small-bearing supporting case.

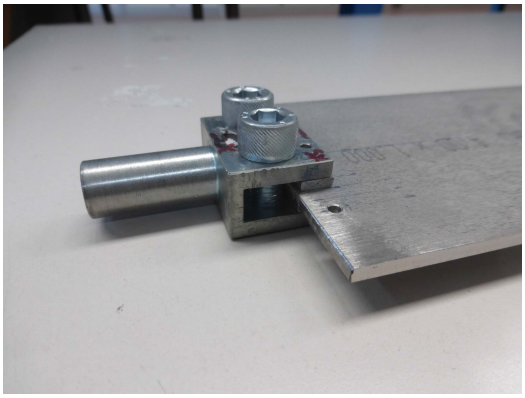

(e) Clamp for the model axis.

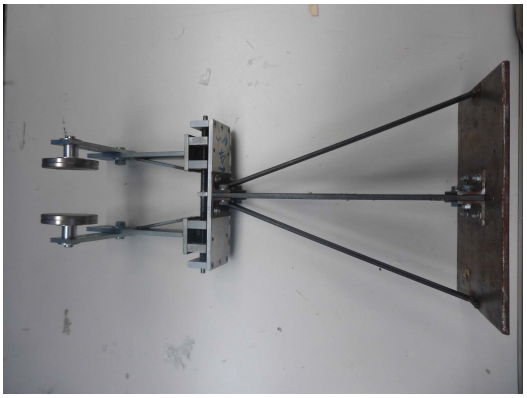

(f) Damper.

Figure 5.34. Photos of some elements installed in the aeroelastic setup.

- *Damping system*

  The damping device is shown in Figs. 5.31, 5.32 and 5.44. It is based on the eddy-current dissipation generated on an aluminium plate (5 mm thick, 120 mm wide and 260 mm long) that moved between a pair of circular permanent magnets. The magnets were placed at a close face-to-face distance (Fig. 5.44a), and were installed in supports to hold them in the correct position, as in Fig. 5.34f (the magnets have to be arranged to attract each others). The plates were long enough to ensure the magnetic flux, always crossing the plate during the maximum oscillation amplitudes. In this way linear viscous damping was introduced in the heaving DoF. By varying the face-to-face distance between the magnets (usual values were in the range 9 mm to 50 mm), the heaving damping coefficient was controlled. The configurations without additional damping were simply obtained moving away the damper (see Figs. 5.44b and 5.44c).

  The damper operates better when the face-to-face distance is small with respect to the magnet diameter, because the magnetic flux becomes more confined and homogeneous. Thus, if low values of damping were desired, it is preferable to install magnets with a bigger diameter when larger distances are required or to change the thickness of the plate maintaining the smaller distance. By contrast, if high values of the damping have to be achieved, it is preferable to change the material of the plate (*e.g.* copper has a larger electric conductivity than aluminium) or to install thicker magnets, instead of reaching too much small face-to-face distances enabling the risk to touch the plate during oscillations.

- *Measuring system*

  The heaving motion was recorded through two analogic laser displacement transducers, pointing the ends of the shear-type frames (Figs. 5.31, 5.32, 5.36, 5.37 and 5.38). They were installed in aluminium Bosch profiles, fixed to the floor of the test section, in order to be held at the mid-range of measure when the model was in the rest position. Being one laser in each of the model ends, they enabled also the monitoring of the possible rolling motion. During SESSION I, a third laser transducer was installed in correspondence to approximately the midspan of the model, as visible in Fig. 5.36, pointing directly the model to check for a possible mean pitching rotation with increasing flow speed.

  Due to the large pitching amplitudes, the displacement lasers were not able to correctly record the pitching motion (the maximum angle allowed, when the rotation axis is parallel to the triangulation plane, is about 35°). Thus, two miniaturized accelerometers were installed through a thin layer of 'loctite super attack' glue at the ends of one of the rocker arms to record the pitching motion. The accelerometers were installed in a way to experience positive accelerations during positive pitching rotations (clock-wise), as visible in Fig. 5.32. After same problems encountered at the end of SESSION I due to small, but cyclic, bending radius and stretching of the cables in some critic points, large attention was paid to arrange the cables in order to not be stressed during large rotation amplitudes and, at the same time, to disturb as low as possible the pitching dynamics. The cable arrangements can be compared in Fig. 5.42.

  The arrangement of the measuring instruments is outlined in Figs. 5.31 and 5.32. The motion components were calculated according to Eq. (5.8). The pitching displacement is obtained by integrating the pitching acceleration after the application of an high-pass filter (cutting frequency at 0.9 Hz), eliminating also a section of the signal ends (about a 1 s window for each end) at each integration step to remove numerical noise due to the integration. An additional low-pass filter, with cutting frequency at 150 Hz, was applied to clean the signals from undesired high-frequency vibrations, which were observed through the accelerometers only. The sampling frequency during the tests was 2000 Hz.

$$\begin{aligned} \eta &= -\left(L_1 + L_2\right)/2 \ , \\ \ddot{\alpha} &= \left(A_1 + A_2\right)/\left(b_1 + b_2\right) \quad \longrightarrow \quad \alpha \ , \\ \delta &= \left(L_1 - L_2\right)/2 \ . \end{aligned} \tag{5.8}$$

Table 5.9. Techical details of the coils springs LS095 (code Z-118DI, material EN 10270-1) and LS195 (code Z-133AI, material EN 10270-1), according to Fig. 5.9.

	LS095	LS195		
Oest	180	180	degree	loop position
d	1.6	2	mm	wire diameter
De	21.6	27	mm	outer coil diameter
F0	3.991	6.881	N	initial tension
Fn	67.4	101.2	N	maximum spring force
Lk	141.6	109	mm	length of unstressed spring body
L0	172	146	mm	length of unstressed spring
sn	664.83	483.84	mm	maximum spring deflection
Lh	15.2	18.5	mm	inner edge loop distance from the spring body
R	0.095	0.195	N mm^{-1}	spring rate
Gew	89.15	107.793	g	weight of one spring

Table 5.10. Technical details of the clock springs CS161 (cat. no. 0924), CS241 (cat. no. 0925) and CS359 (cat. no. 0928), according to Fig. 5.35. The material is stainless steel EN 10270-3-1.4310.

	CS161	CS241	CS359		
t	1.5	1.5	2	mm	material thickness
b	10	15	12	mm	material width
A	20	20	24	mm	shaft (recommended)
r	33	33	43	mm	spring centre to locating centre distance
n	5	5	5	#	number of coils
B	7	7	8	mm	length of inner end
C	6.3	6.3	8.4	mm	distance of the outer end
D	9	9	12	mm	length of the outer end
R	16.1	24.1	35.9	N mm $(°)^{-1}$	spring rate
	923	1381	2057	N mm rad^{-1}	
gwe	70.0	105.0	142.25	g	weight

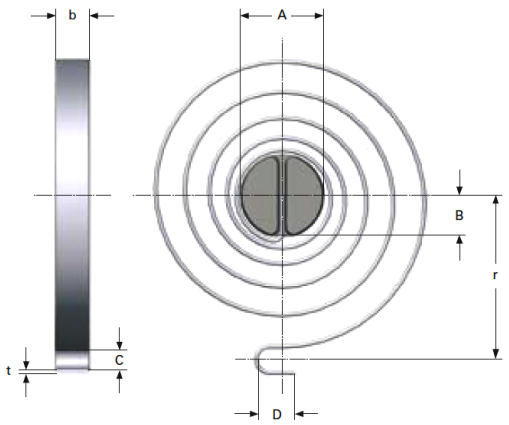

Figure 5.35. Geometry of the clock springs and design parameters.

(a) Frontal view.

(b) Rear view.

Figure 5.36. Views of the setup used in the experimental campaign during SESSION I and SESSION II. From the rear views are visible also the up-stream Prandtl tube and the temperature probe.

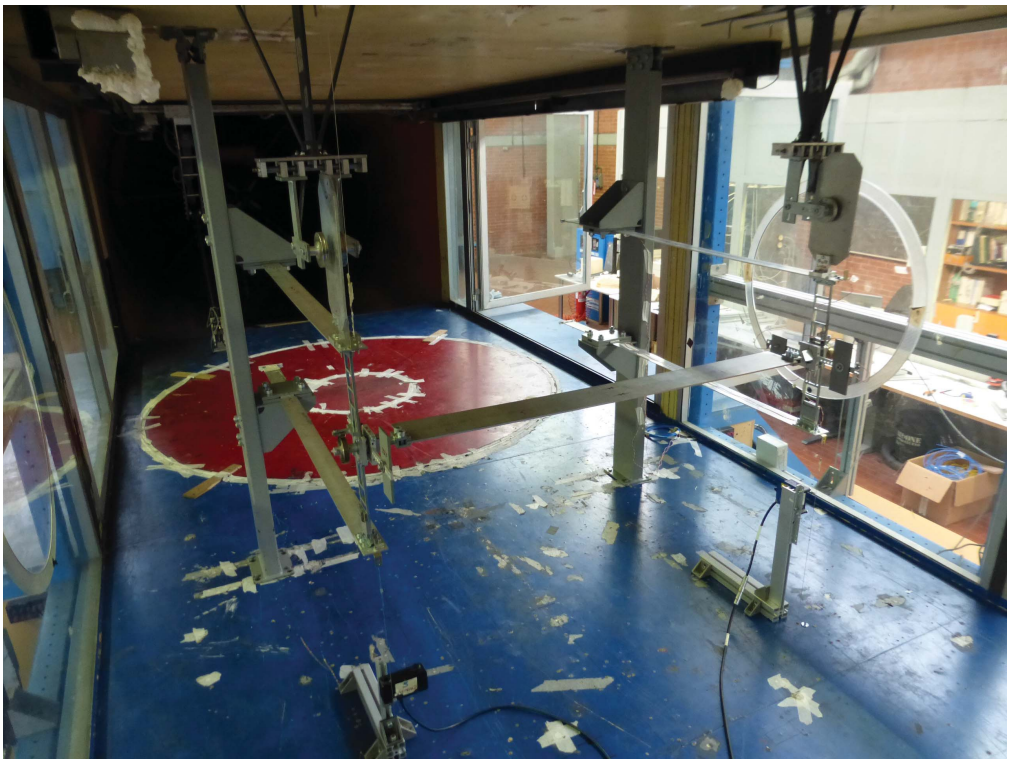

(a) Frontal view.

(b) Rear view.

Figure 5.37. Views of the setup used in the experimental campaign during SESSION III-A.

(a) Frontal view.

(b) Rear view.

Figure 5.38. Views of the setup used in the experimental campaign during Session III-b and Session III-c.

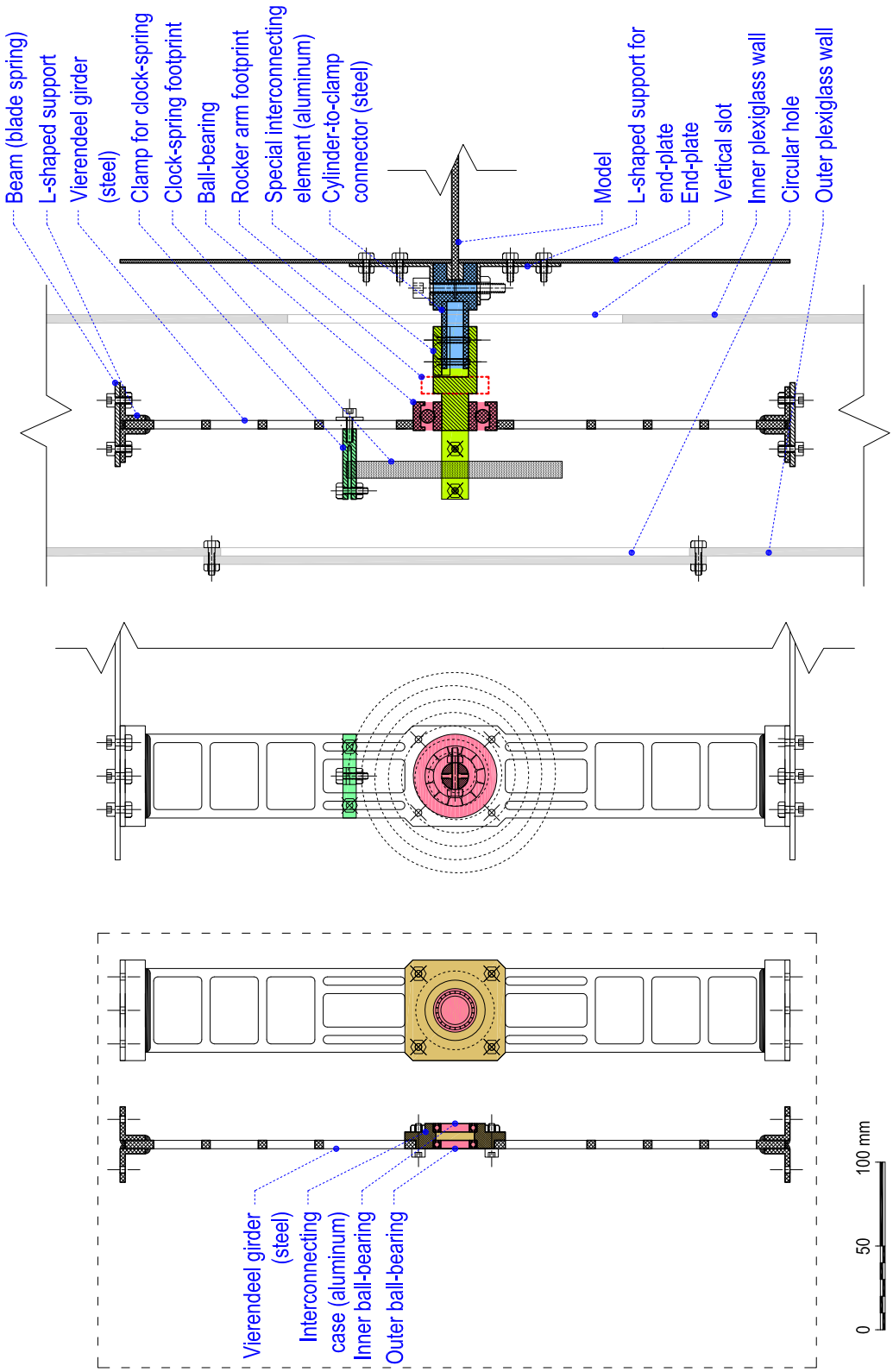

Figure 5.39. Schematic of the junction system between heaving and pitching DoFs, installing the ball bearing directly in the Vierendeel girder. Within the dashed-box, an alternative solution is indicated, which considers the aluminium case containing the smaller ball bearings, bolted to the Vierendeel girder.

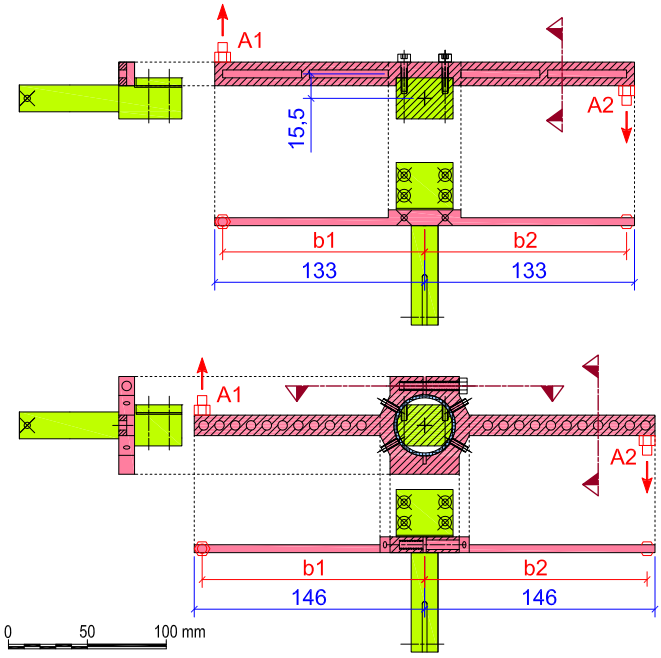

Figure 5.40. Schematic of the rocker arms: model RAa (upper side), producing a small eccentricity of about 15 mm between the elastic centre and the mass centre of the additional weights, and model RAb (lower side).

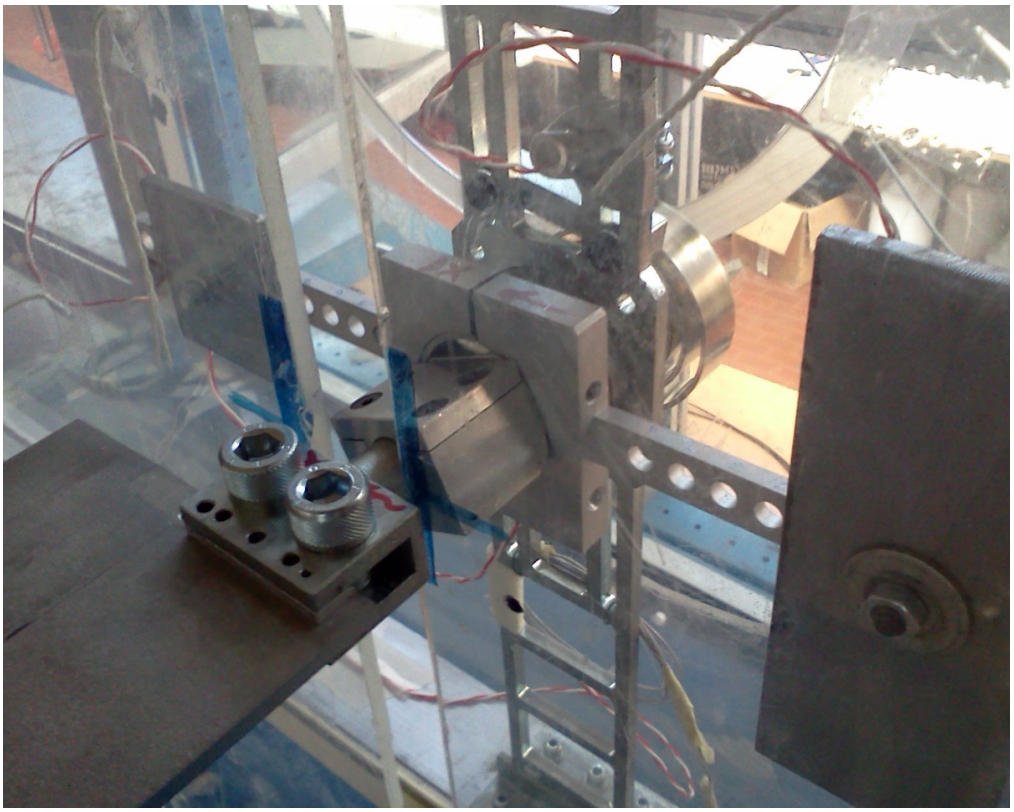

Figure 5.41. View of the connection between model axis and elastic suspension (the rocker arm RAb is installed, SESSION III), being also visible the vertical slot on the plexiglass wall and the device clamping the model.

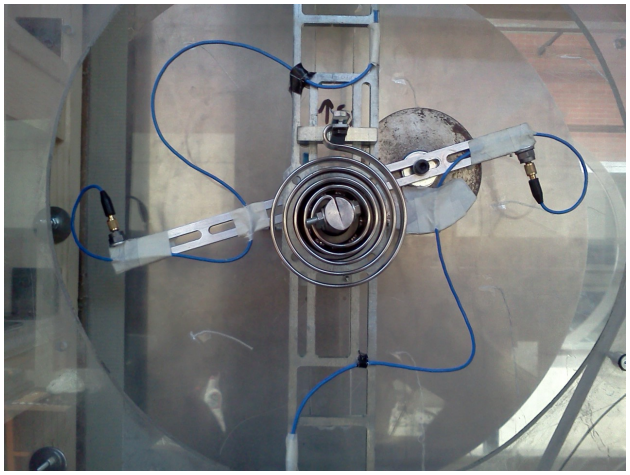

(a) Session I.

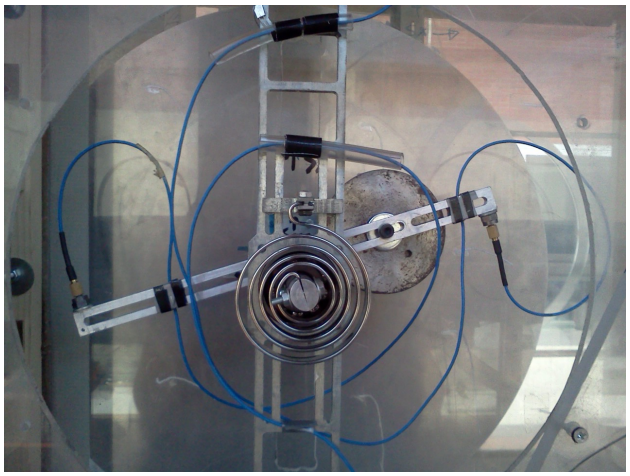

(b) Session II.

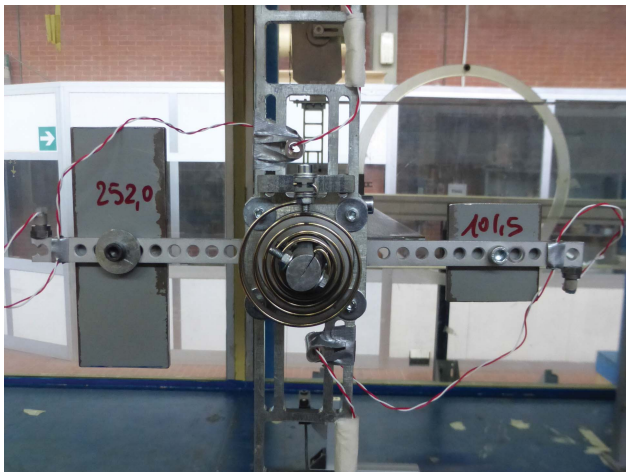

(c) Session III.

Figure 5.42. Views of the different arrangement of the cables of the accelerometers as evolved during the experimental campaign. In all cases, the cables were then arranged in order to follow the frame geometry, placed along the upper and lower beams and the vertical pillar, down to the floor of the test section.

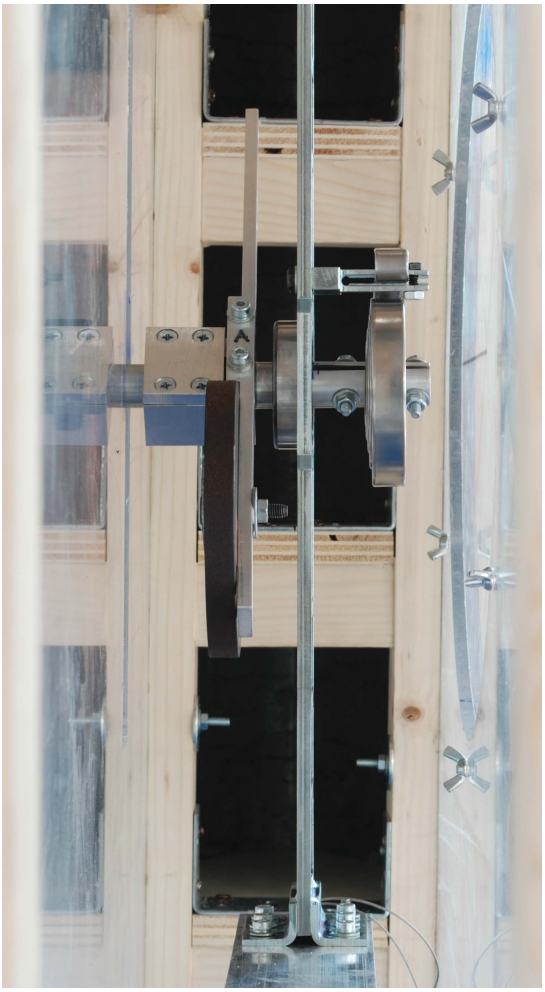

(a) Internal view.

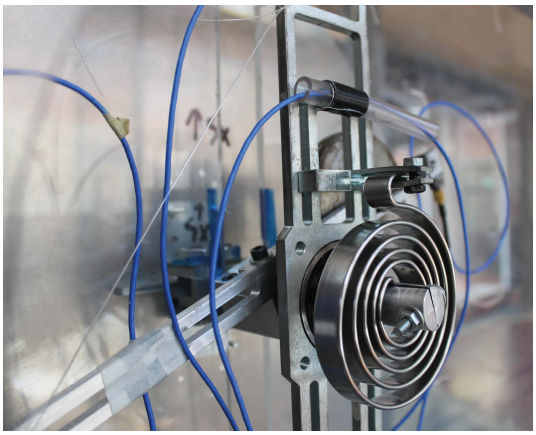

(b) Session I and Session II.

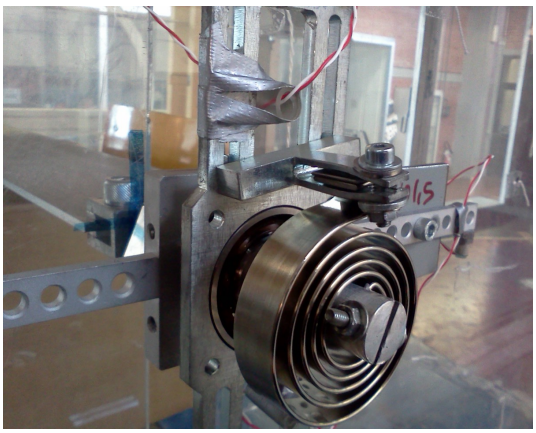

(c) Session III - external view.

Figure 5.43. Views of the internal junction between heaving and pithing motion (a). In picture (a) and (b) the rocker arm RAa is installed. In the latter, it is possible to see also a nylon cable used to block the pitching DoF during un-coupled free oscillations. In picture (c) the rocker arm RAb is installed.

(a) Frontal view.

(b) Damper on.

(c) Damper off.

Figure 5.44. Views of dampers: (a) frontal view, being apparent the face-to-face distance between magnets; (b) configuration of damper activated; (c) configuration of damper de-activated. This last configuration is preferred instead of taking out entirely the dampers in order to preserve the same flow disturbances. This picture also shows several installations of magnets: (a) double-pair of M60 magnets; (b) single-pair of M60 magnets; (c) single-pair of M35 magnets.

5.3.4 Mechanical features

The stiffness linearity of the aeroelastic setup, both in the pitching and heaving degrees of freedom, was verified through static tests (Fig. 5.45 and Fig. 5.46), measuring static displacements for different known masses. This characterisation was conducted for the setup used during SESSION I and SESSION II, in which the free length of the blade springs (L_b) and the clock springs were not modified, and only the coil springs were changed to set up different configurations during those sessions. The experimental stiffness of the heaving DoF well agreed with the theoretical estimation. The latter is evaluated according to the linear spring details in Table 5.9, and calculating the contributions of the shear-type frame to the heaving stiffness as:

$$K_{\eta,f} = 4 \cdot \left(\frac{12 E J_b}{L_b^3} \right) \tag{5.9a}$$

where

$$J_b = \frac{1}{12} B_b H_b^3 \ , \tag{5.9b}$$

is the inertial modulus of the cross section of the beam, $E = 73.1$ GPa is the elastic modulus of 2024-T3 aluminum allow, $B_b = 50$ mm is the beam width and $H_b = 3$ mm is the beam thickness. Thus, considering $L_b = 1040$ mm as used during SESSION I and SESSION II, it results $K_{\eta,f} = 350.92$ N/m. Adding the contributions of the linear springs, the total heaving stiffness (see Table 5.11) result in very good agreement with the experimental ones of Fig. 5.45.

For the pitching DoF, the total stiffness of two clock springs CS359, from the datasheet (Table 5.10), is 4.114 N m rad^{-1} and it slightly differs from the experimental values of Fig. 5.46a. However, it is worth highlighting that, since the displacement laser were not able to measure large rotation amplitudes (see Fig. 5.46c), the measurement of the static pitching angles was manually performed using a dual-axis digital inclinometer (model DXL360S Level Box 0.01°). The accuracy of this instrument is $\Delta\alpha = \pm 0.05°$ and, taking into account also the accuracy of the scale, which is $\Delta M = \pm 0.5$ g, the stiffness calculated considering two adjacent points of the polar-inertia vs. rotation diagram, that is $(\alpha_i, I_{\alpha,i})$ and $(\alpha_j, I_{\alpha,j})$, is:

$$\begin{aligned} K^*_{\alpha,ij} &= g \cdot \frac{(I_{\alpha,j} \pm \Delta I_\alpha) - (I_{\alpha,i} \pm \Delta I_\alpha)}{(\alpha_j \pm \Delta\alpha) - (\alpha_i \pm \Delta\alpha)} \approx \\ &\approx K_{\alpha,ij} \cdot \left(1 \pm \frac{2\Delta I_\alpha}{I_{\alpha,j} - I_{\alpha,i}} \right) \Big/ \left(1 \pm \frac{2\Delta\alpha}{\alpha_j - \alpha_i} \right) \ , \end{aligned} \tag{5.10}$$

where g is the gravity acceleration, $\Delta I_\alpha = \Delta M \cdot d = 0.01$ g m^2 is the accuracy in terms of polar inertia (with $d \approx 137$ mm is the distance of the masses from the elastic centre) and $K_{\alpha,ij}$ is the stiffness without effects of instruments accuracies. Observing Eq. (5.10), points of measure that differ of small quantities, both in terms of pitching angle and polar inertia, can be more affected by the instrument errors. Moreover, assuming as typical intervals of the polar inertia $I_{\alpha,j} - I_{\alpha,i} \approx 0.05$ kg m^{-2}, and $\alpha_j - \alpha_i \approx 5°$ for the pitching angle (as understandable from Fig. 5.46), it follows that the modified stiffness is:

$$K^*_{\alpha,ij} \approx K_{\alpha,ij} \cdot \left(1 \pm \frac{0.00002}{0.05} \right) \Big/ \left(1 \pm \frac{0.1}{5} \right) \approx K_{\alpha,ij} / \left(1 \pm 0.02 \right) \ . \tag{5.11}$$

Table 5.11. Theoretical estimation of heaving stiffness.

	Upper springs [N/m]	Lower springs [N/m]	Shear-type frames [N/m]	Suspension [N/m]
SESSION I	390 (n.2 LS195)	390 (n.2 LS195)	350.92	1130.92
SESSION II	390 (n.2 LS195)	190 (n.2 LS095)	350.92	930.92

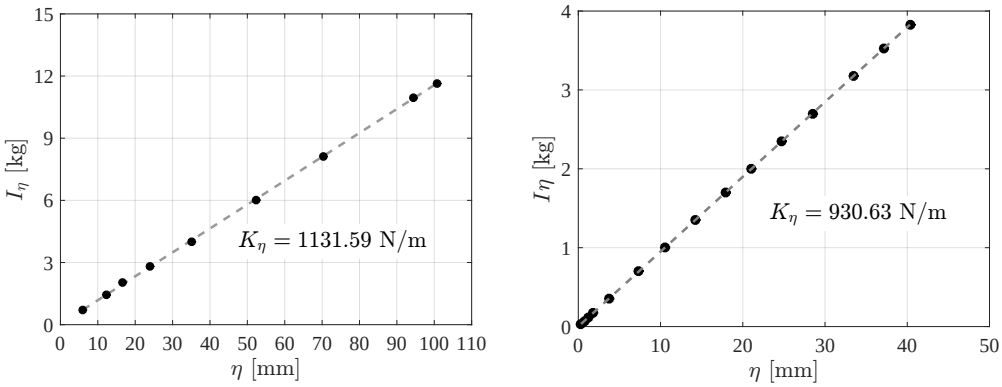

Figure 5.45. Results of the static tests to verify the heaving stiffness, for the setups of SESSION I (left) and SESSION II (right).

Thus, the stiffness from the datasheet could be altered by the instrument accuracy and detected in the range 4.033 to 4.198 N m rad^{-1}.

Attempting to clarify this problem, the test was repeated for smaller rotational angles (Fig. 5.46b), and also trying to use the displacement lasers (Fig. 5.46c). In Fig. 5.46d, the global stiffness as obtained interpolating both small and large pitching amplitudes (without the points from the lasers of Fig. 5.46c), is superimposed to the others, showing that all the stiffnesses slightly differ. The previous tests were performed during SESSION I, while Fig. 5.46e includes in the comparison the stiffness characterisation conducted during SESSION II. Finally, it has been assumed to be representative the stiffness obtained from the datasheet, because of the uncertainty due to the instrument accuracy. Moreover, it is closer to that one measured for large angles, which is more related to the steady state regime.

The inertia of the oscillating system in the heaving and pitching motions, I_η and I_α, were calculated from the previously estimated stiffnesses and the corresponding frequencies of oscillation in still air. Moreover, for each configuration, several free decay tests (some examples are shown in Fig. 5.47) were performed in still air for different initial conditions, in order to evaluate the natural frequencies of oscillation ($n_{\eta 0}$, $n_{\alpha 0}$) and the critical damping ratios ($\xi_{\eta 0}$, $\xi_{\alpha 0}$). The MULS algorithm [24] was applied for the system identification. The only-heaving motion was obtained by constraining the pitching DoF, simply linking the rocker arm to the Vierendeel girder through a cable (Fig. 5.43b). The only-pitching was obtained constraining the shear-type frame by means of cables fixed to the floor/ceiling of the test section or installing a wood diagonal beam inside the frame, similarly to a cross-bracing. By contrast, the free oscillations during coupled motion give the frequencies of the modes of the coupled system ($n_{\eta 1}$, $n_{\alpha 1}$), with components in both DoFs. The static unbalance, S, was then estimated according to Eq. 5.5.

The structural damping coefficients were $\xi_{\eta 0,s} \approx 0.46\%$, $\xi_{\alpha 0} \approx 1.26\%$, as obtained processing the last part of the decaying signals where the amplitude started to be lower than 4-5 mm for the heaving component and 3-4° for the pitching component (Fig. 5.48a). Nevertheless, it is worth highlighting that the pitching DoF showed a damping that seemed to be not of viscous type in the case of small oscillation amplitudes. In particular, in the very last part of the decaying signal, that is when lower than 2-3°, the amplitude decreased almost linearly, suggesting a Coulomb-type damping or dry-friction [46] (Fig. 5.48b). The reason may lie on the operation principle of the ball bearings, which introduce also a static friction in addition to the rolling friction that can become relevant for small amplitudes of oscillation. For larger pitching amplitudes (Fig. 5.48b-right), the damping was better described by the viscous type. By contrast, the heaving damping was almost perfectly linear viscous for both large amplitudes and higher levels of $\xi_{\eta 0}$ (*e.g.* Figs. 5.47 and 5.49), up to a value of about 18% in same cases. In the case of very high ξ_η, additional know masses were installed to participate in the heaving oscillation only, in order to increase the number of oscillation cycles and to

better identify the signal though the MULS algorithm (see Eq. (5.4)).

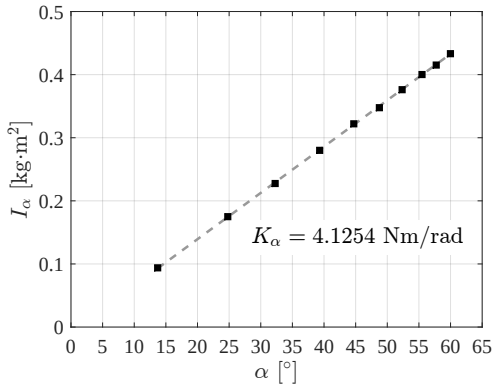

(a) Large angles, with digital inclinometer.

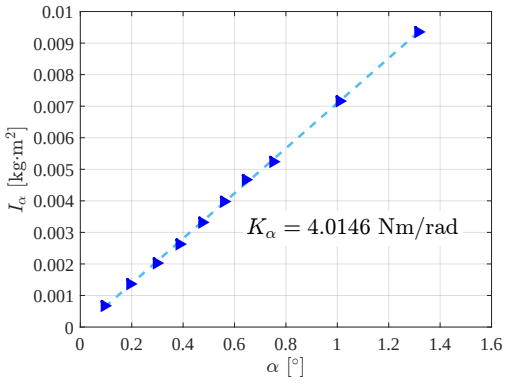

(b) Small angles, with digital inclinometer.

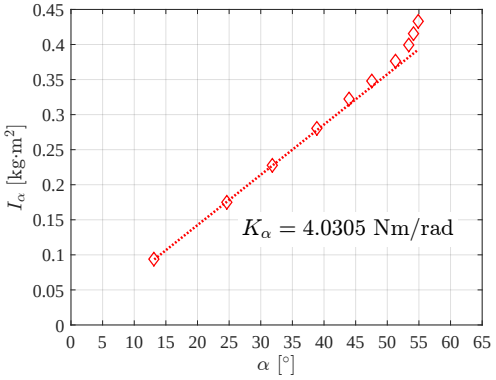

(c) Large angles, with displacement lasers.

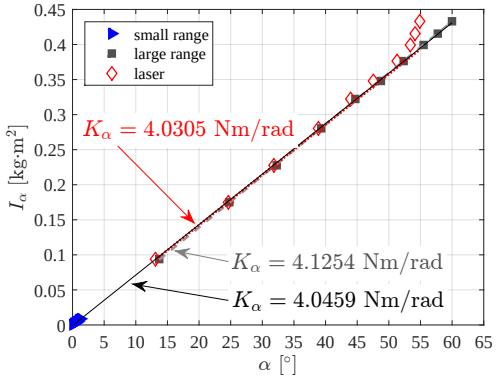

(d) Superimposed diagrams.

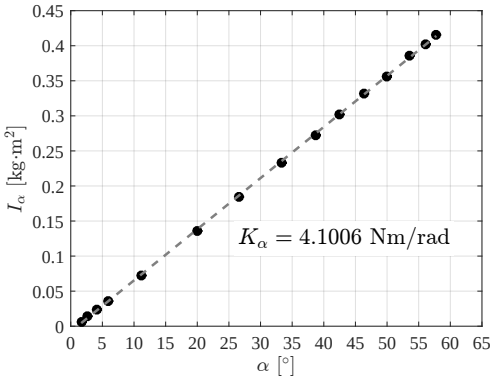

(e) Session II.

Figure 5.46. Results of the static tests for the pitching stiffness. The small and large ranges were manually recorder through the digital inclinometer. In the figure (c), the interpolation of the stiffness was implemented considering the first three points. In the figure (d), the solid-black line represent the interpolation of the total diagram obtained considering the points of both figure (a) and (b).

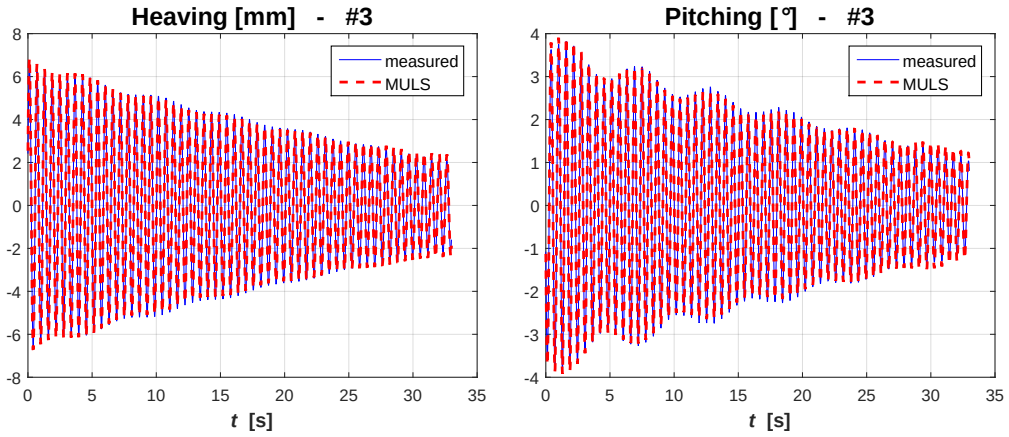

(a) $\xi_\eta = 0.04\%$

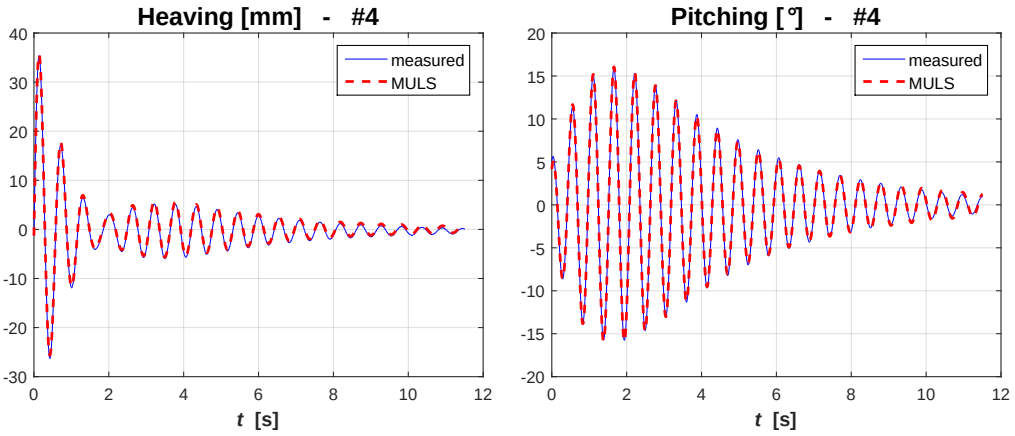

(b) $\xi_\eta = 9.52\%$

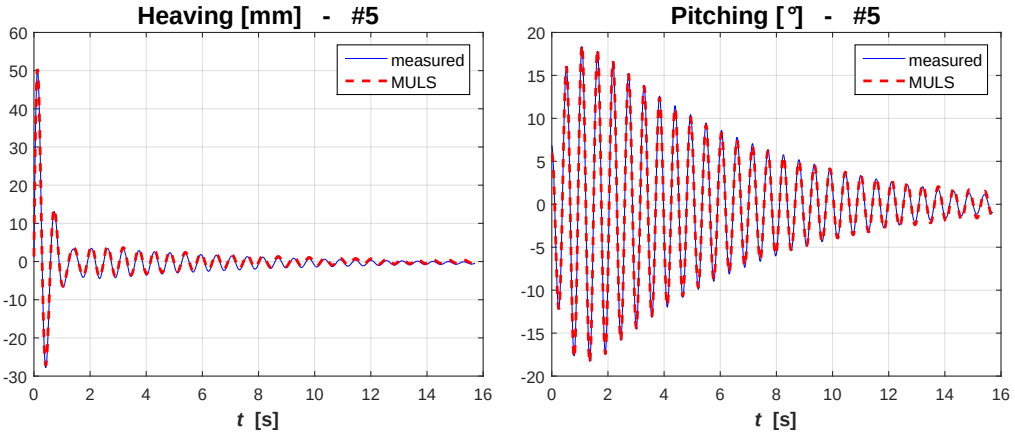

(c) $\xi_\eta = 18.13\%$

Figure 5.47. System identification through MULS algorithm of free-decay oscillations for several heaving damping values [CRIACIV campaign].

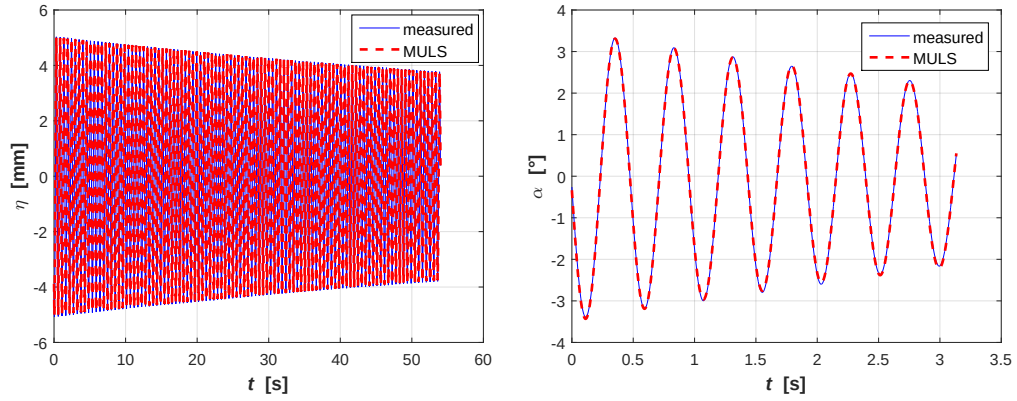

(a) Small-amplitude oscillations.

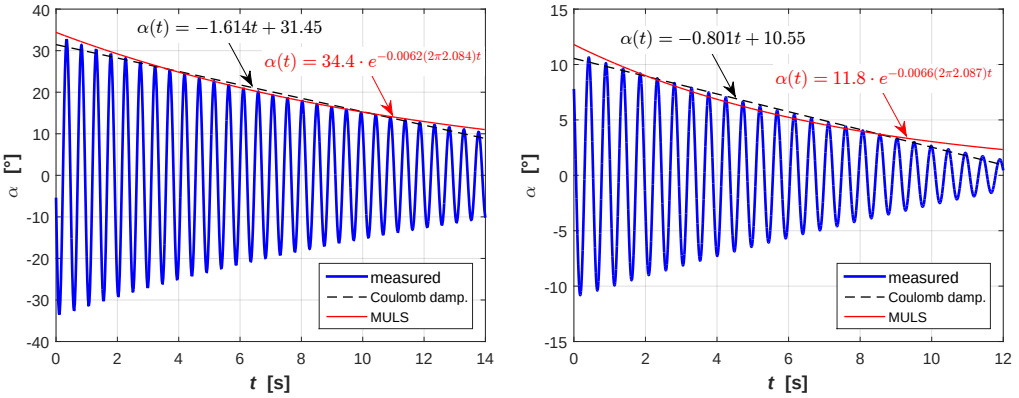

(b) Large-amplitude oscillations for the pitching DoF.

Figure 5.48. Influence of the oscillations amplitude in the pitching-damping value estimation [CRIACIV campaign].

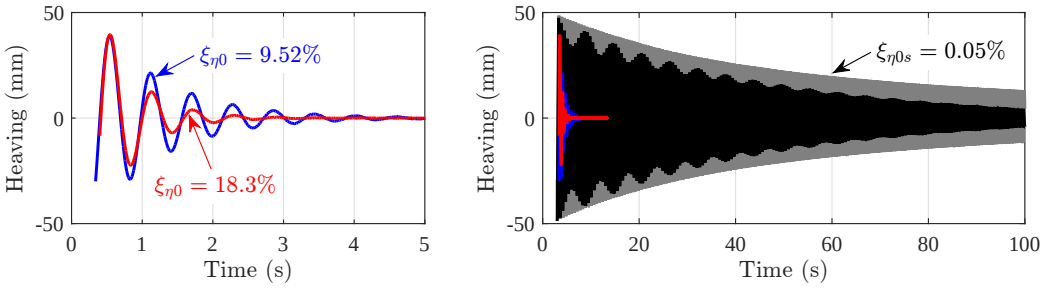

Figure 5.49. Example of free decay oscillations for the symmetric configuration, with large values of the heaving damping (left) and due to the structural damping only (right). In the right-hand figure, the black signal represents the free decay oscillations of a configuration with positive mass unbalance.

Chapter 6

Tested configurations overview

Linear analyses anticipated and supported the experimental campaigns, with the aim to design the configurations to be tested and to improve the understanding of the influence of the governing parameters on the instability threshold. Then, wind-tunnel tests firstly aimed to experimentally verify the influence of the governing parameters, mainly the position of the stiffness centre x_e, the position of the mass centre x_m, the still-air frequency ratio γ_n and the ratio-to-critical damping coefficient in the heaving DoF ξ_η, on the instability threshold. Subsequently, the core of the investigations was devoted to characterise the evolution of the LCO in terms of motion amplitude, frequency and phase, with both increasing and decreasing the flow speed. The evaluation of the stability features of the observed LCO branches was also conducted, observing the system response after the release of several manually-induced disturbances of different magnitudes. The instability threshold was verified through similar tests.

6.1 Framework of investigation

The framework followed in the investigation is outlined hereinafter:

(1) Exploratory linear analyses to set up the first experimental campaign at the Stahlbau wind tunnel; discussed in § 6.2.

(2) Preliminary experiments at the Stahlbau wind tunnel to verify the linear predictions and to explore the post-critical regime features; introduced in § 6.3.1 and discussed in § 7.1.

(3) Experimental campaign at the CRIACIV wind tunnel (SESSION I and SESSION II), following the results of steps (1) and (2), with a completely different setup in order to widen the range of tested parameters and cross-check the results; introduced in § 6.3.2 and discussed in § 7.2.

(4) Detailed examination of all collected results from steps (1), (2) and (3) to set up an extensive and systematic parametric linear analysis, with the aim at looking for optimal configurations; discussed in § 8.1.

(5) Experimental investigations at CRIACIV wind tunnel (SESSION III) to observe the post-critical regime of the designed optimal configurations; introduced in § 6.3.2 and discussed in § 8.2.

6.2 Exploratory analytical investigations

Exploratory investigations about the critical condition were conducted to set up the first experimental campaign at the Stahlbau laboratory.

The candidate ranges of the governing parameters (Table 6.1) were identified with the aim at designing feasible and reliable wind-tunnel tests (as explained in the next § 6.2.1). Thus, these values of the parameters are in agreement with the expected mechanical parameters

involved in the following experimental campaign (Table 6.2). Theoretical analyses based on Theodorsen's linear theory were thus conducted with a twofold objective: (i) performing an exploratory parametric analysis to understand the effect of the governing parameters in the instability threshold and to calibrate the design of the experimentally tested configurations; (ii) identifying the critical condition to be compared with the experimental results (discussed in § 7.3).

6.2.1 Comments on the analysis arrangement

The features of the Stahlbau wind tunnel (see § 5.2) constrained the model design and some values of the flutter governing parameters, in particular the mass ratio μ.

Since the aeroelastic setup was placed externally to the test section (see § 5.2.3), the model had to span the whole test section width. Thus, the depth of the model was selected to avoid large deflections during oscillations. Consequently, given the 15:1 width-to-depth ratio, the depth imposed the cross-section chord and the model size in turn.

Considering the passive oscillating inertias due to the suspension system, which was imposed by the technology of the coil-spring setup, the mass ratio μ could not be reduced as desired. The selection of another material for the model (*e.g.* carbon fibre) could be the only possibility to decrease the inertia. Moreover, since the experiments were conducted to vary one parameter at a time, extra masses were installed from the beginning of a given configuration in order to have always the same μ while modifying, for example, the centre of mass or centre of stiffness. Similar considerations can be made for the polar radius of inertia, which was markedly influenced by the end-plates. Being these designed large enough to enforce two-dimensional flow conditions during the motion (about 2.6 times the section chord), the parameter r_α was hard to be decreased.

Concerning the still-air frequency ratio γ_n, the coil-spring setup typology can not allow values too close to the unity. In fact, the distance between pairs of springs control the rotational stiffness, and springs too much close each others can touch during large oscillations.

It is worth remarking that the width-to-depth ratio of the cross section investigated in the Stahlbau campaign was 15:1, so that the flat plate assumption is not fully suitable. Thus, Theodorsen's results (always considered as reference) were supported with the results obtained from the exploitation of aeroelastic coefficients, as explained in § 3.4.3. Therefore, flutter derivatives available from the experiments of Matsumoto *et al.* [145] were used. In that work, the measurements were conducted up to reduced velocities lower than those of interest here, so that a 3$^{\text{rd}}$-order polynomial was used to extrapolate the coefficients. Moreover, the correction presented in Eq. (3.87) was applied, since the flutter derivatives were provided for a symmetrical elastic suspension. Nevertheless, in this way non-negligible approximations were introduced in the flutter derivative model following this approach.

Table 6.1. Domains of the parameters investigated through numerical analyses (B = 0.15 m and $n_{\alpha 0}$ = 2.28 Hz). Δ indicates the discretization step of the generic interval [· , ·], while { · ; · ; · ; ··· } denotes a set of values.

Configuration	$\xi_{\eta 0}$ [%]	$\xi_{\alpha 0}$ [%]	x_e [-]	μ [-]	x_m [-]	r_α [-]	γ_n [-]
reference	0.09	0.17	0.00	948.8	0.00	0.84	1.28
x-0-0-0-0-0-0	[0.09,40] Δ = 2	"	"	"	"	"	"
0-**x**-0-0-0-0-0	"	[0.17,4] Δ = 0.2	"	"	"	"	"
0-0-**x**-0-0-0-0	"	"	[-0.5,0.5] Δ = 0.05	"	"	"	"
0-0-0-**x**-0-0-0	"	"	"	[628.3 , 1256.6] Δ = 31.4	"	"	"
0-0-0-0-**x**-0-0	"	"	"	"	[-0.5 , 0.5] Δ = 0.05	"	"
0-0-0-0-0-**x**-0	"	"	"	"	"	[-0.5, 0.5] Δ = 0.05	"
0-0-0-0-0-0-**x**	"	"	"	"	"	"	[1 , 3] Δ = 0.1
x-0-**x**-0-0-0-0	[0.09,40] Δ = 2	"	{-0.1; 0.1; 0.2; 0.3; 0.4}	"	"	"	"
x-0-0-**x**-0-0-0	[0.09,40] Δ = 2	"	"	"	{0.05; 0.15; 0.25; 0.35; 0.45}	"	"

6.2.2 Parametric linear analyses

In the following, the critical reduced velocity is always expressed as $U^c_{R\alpha} = U^c/n_{\alpha 0}B$, in order to be more easily compared with the experimental results. Therefore, Eqs. (4.8) and (4.18) have to be considered by setting $U_R = U_{R\alpha}\sqrt{X}$. Referring to the mechanical parameters involved in the experimental campaign (Table 6.2), the numerical analysis aimed at studying the dependence of the critical reduced velocity $U^c_{R\alpha}$ and, thought less important, also of $\sqrt{X^c}$ on the variation of one parameter at a time. In addition, the linear model would allow estimating the ratio of the motion amplitudes, that is $(B\alpha/\eta)^c$, and the phase difference ϕ^c. Nevertheless, the parameters describing the critical condition, except for $U^c_{R\alpha}$, can provide only indicative information because they are restricted to the unstable mode appearing during the starting part of the instability build up. The system is nonlinear when oscillates at the large-amplitude limit cycle, thus the results of the linear analysis has to be mainly considered in terms of critical reduced velocity.

It is worth remembering that the flutter derivatives reported in [145], used to model the linear self-excited loads for the 15:1 cross section as explained in § 3.4.3, were affected by the approximation due to the extrapolation procedure (see § 6.2.1). Therefore, the results from the flutter derivatives's approach provide only qualitative information in addition to those from Theodorsen's approach, this last considered as reference.

The complete set of tested configurations is summarised in Table 6.1.

Fig. 6.1 shows that both the critical reduced velocity and $\sqrt{X^c}$ decrease with decreasing the frequency ratio γ_n. A lower bound of $U^c_{R\alpha}$ is reached for values of γ_n tending to unity. This condition enables fast coupling and energy exchange between the modes, fostering the flutter instability. In this case, also $\sqrt{X^c}$ is close to 1, thus playing a minor role in the energy performance.

It is also clear in Fig. 6.1 that the critical reduced velocity decreases if the inertial parameter μ or r_α decreases, meaning that lighter systems get unstable earlier. While $\sqrt{X^c}$ is almost constant with μ, it rises with decreasing r_α, but the global effect is usually favourable for the performance. The parameter r_α, unlike μ, does not directly appear in the performance equations. However, r_α and μ can strongly affect the pitching-to-heaving amplitude ratio during post-critical motion: a lower value of r_α usually enhances the pitching component, thus the maximum rotation should be limited in order to avoid detrimental effects on both structural system and performance.

Key parameters to modify the critical reduced velocity are the positions of elastic and mass centres. In the case of low heaving damping, the design of systems with large stiffness eccentricity downstream of the midchord of the cross section entails significant reduction of $U^c_{R\alpha}$. In Fig. 6.1, decrements above 25% were simply achieved moving the elastic centre to the downstream of the quarter-chord position. A decrease of the critical reduced velocity was also obtained moving the mass centre downstream the elastic centre. In particular, observing Theodosen's model predictions, which can be considered representative of width-to-depth ratios above 20:1 [145], a local minimum of $U^c_{R\alpha}$ occurs around $x_m = 0.2$ for the reference set of the other governing parameters. By contrast, $\sqrt{X^c}$ increases with both x_e and x_m and can slightly affect the energy performance, especially due to the remarkable dependence on x_m.

Generally, a damping increase postpones the critical condition and/or reduces the oscillation amplitudes. This is the case for the pitching damping, which significantly influences the instability threshold, since the flutter mechanism mainly needs the pitching DoF to develop. In fact, a fluid-elastic mode becomes unstable when the corresponding negative aerodynamic damping overcomes the mechanical damping and, considering that a mode can have components in both DoFs, a lower pitching damping usually corresponds to a lower force required to reach the instability, thus a lower $U^c_{R\alpha}$.

The understanding of the system response to significant increments of the heaving damping is crucial, as the latter simulates the energy generation process. An effect similar to those due to $\xi_{\alpha 0}$ is shown in Fig. 6.1, which reports the evolution of $U^c_{R\alpha}$ and $\sqrt{X^c}$ with the critical heaving damping ratio $\xi_{\eta 0}$. However, this type of response is specific of the symmetric configuration, for which both x_e and x_m are null. Considering configurations without mass unbalance and positive eccentricity of the elastic centre (right-hand side of Fig. 6.2), which

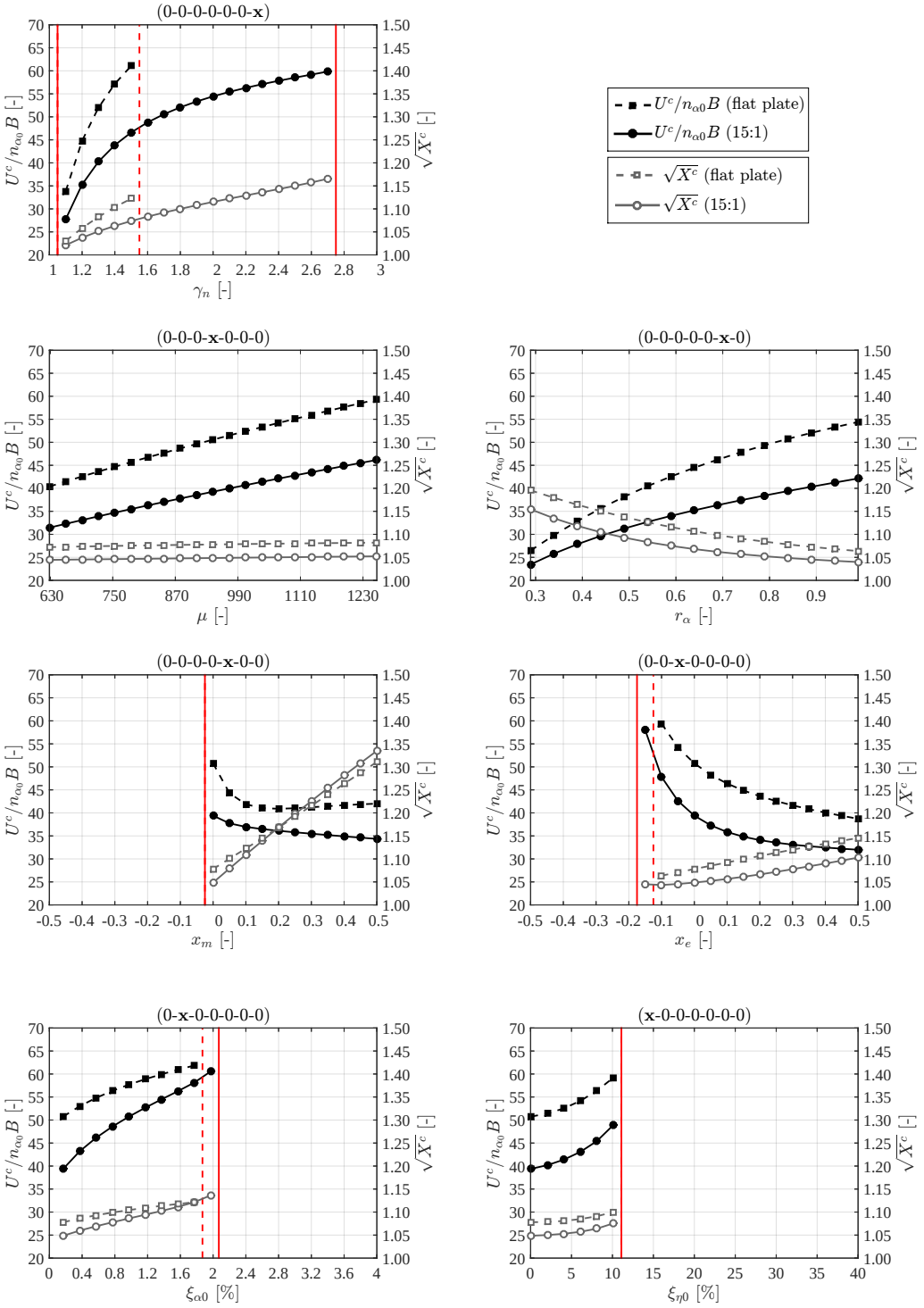

Figure 6.1. Results of the preliminary linear analyses to design the Stahlbau experimental campaign. The parameters are varied one by one according to Table 6.1 and the results are reported in terms of critical reduced velocity ($U^c/n_{\alpha 0}B$) and ratio of pitching still-air frequency to flutter frequency ($\sqrt{X^c}$). The vertical lines delimit no-flutter regions within the range of parameters and velocities investigated (solid-line for flutter derivative's model and dashed-line for Theodorsen's model).

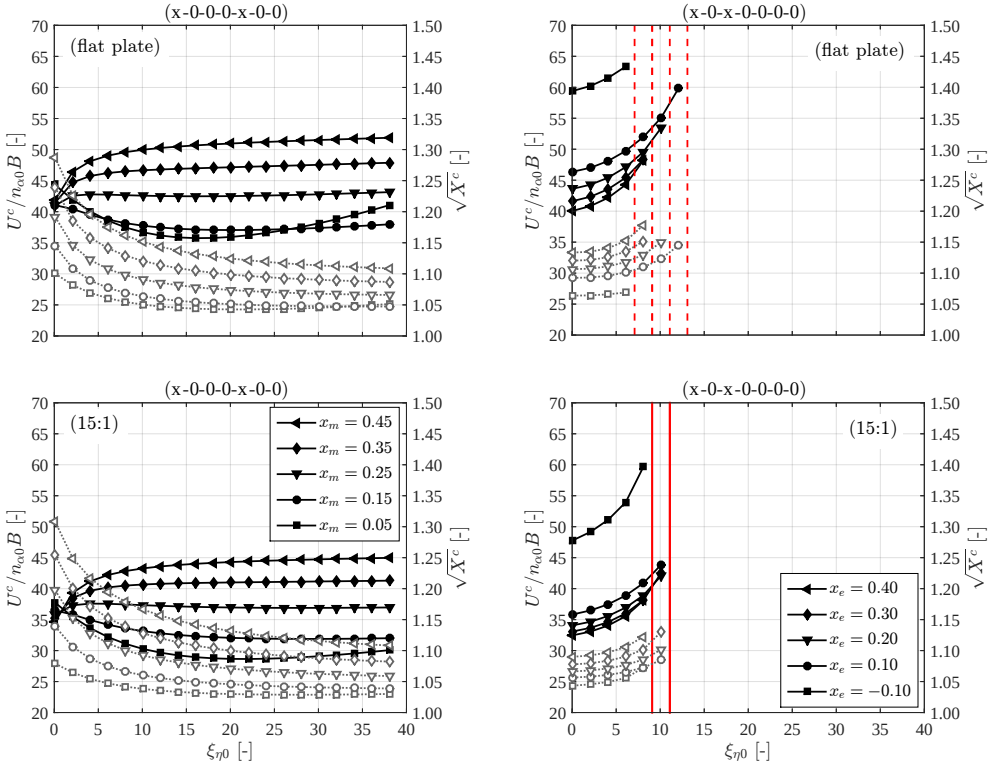

Figure 6.2. Results of linear analyses obtained varying the heaving-damping level and the position of the mass centre (left) or of the elastic centre (right), according to Table 6.1. Filled markers refer to $U^c/n_{\alpha 0}B$ while empty markers refer to $\sqrt{X^c}$.

is an effective solution to reduce the critical velocity when $\xi_{\eta 0}$ is low, high increments of $\xi_{\eta 0}$ tend to stabilize the system, with negative consequences for energy harvesting purposes.

By contrast, for configurations with positive eccentricity of the mass centre (left-hand side of Fig. 6.2), a significant increase of heaving damping produces only small increments of $U^c_{R\alpha}$ but considerable reductions of $\sqrt{X^c}$. In particular, for large positive mass eccentricity, the reduced critical flow speed saturates for values of $\xi_{\eta 0}$ beyond 20-25%, meaning that higher levels of power production are supposed not to affect the stability threshold considerably. Then, in the case of small eccentricity of the mass centre ($x_m \simeq 0.05$), both Theodorsen's model and flutter derivative approach even predict a reduction of the critical reduced velocity due to an increase of the heaving damping, up to a minimum for values of $\xi_{\eta 0}$ around 15-20%.

Finally, it is worth mentioning that the damping-induced anticipation of the instability has also been observed for other configurations during the CRIACIV campaign (see § 9.1.2), which involved different sets of the governing parameters. In particular, increments of ξ_η can destabilize systems for which the elastic axis is located at the upstream quarter chord, provided that a small positive mass unbalance is present. Thus, the influence of the elastic axis on the critical condition importantly depends on the level of heaving damping.

6.3 Experimental investigations

6.3.1 Stahlbau campaign

For each configuration, the rest position of the model was firstly checked through the bubble device in order to impose a zero angle of attack. Then, the system response was observed when subjected to flow-induced excitations, in particular:

I - The flow speed was increased starting from values markedly below the theoretical critical condition.

II - Incrementing the flow speed by small steps, the experimental critical condition was identified, and corresponded to the speed value at which the flutter motion started spontaneously, while the system was stable in the rest position for the flow speed before the last increment.

III - The amplitude-velocity response was observed with increasing the flow speed, up to a maximum flow speed value compatible with both wind-tunnel and aeroelastic-setup capabilities.

IV - Points with decreasing flow speeds were then observed till the system stopped the motion spontaneously, usually at a flow speed markedly lower than the critical one.

V - The stability of some points of the sub-critical and post-critical branches, and others close to the instability onset, were verified through the observation of the system response to externally imposed disturbances.

During the tests, the operative Reynolds number was in the range 70,000-180,000 ($Re = UB/\nu$, with $\nu = 15$ mm^2 s^{-1}). The mean flow speed was measured through a Prandtl tube installed downstream of the model and flow conversion maps were used to infer the velocity at the model centreline (see § 5.2.2). The maximum blockage ratio was about 2.4%, reached when the model oscillated at $\alpha \approx 14°$.

Table 6.2 summarizes the governing parameters of the experimental configurations. The investigation focused mainly on the understanding of the influence of the positions of the mass and stiffness centres, that is x_m and x_e. These parameters were selected according to the preliminary exploratory analyses performed through the linear theory (see § 6.2.2). In particular, the tested model was provided with additional masses to obtain positions of the mass centre near to 0.06 chords, downstream of the stiffness centre (see § 5.2.3), since the linear analyses showed the presence of a minimum of the critical reduced velocity about that x_m value (see Figs. 6.1 and 6.2). The position of the elastic axis was varied clamping the model in different positions and eccentricities downstream and upstream of the midchord ($x_e = \pm 0.1$) were considered, also to verify the theoretical results.

Table 6.2. Parameters of the configurations tested during the experimental campaign in Braunschweig (the cross-section width is $B = 150$ mm and the model span is $l = 1200$ mm).

Setup	Code	Info	ρ [kg m^{-3}]	I_η [kg]	I_α [kg m^2]	S [kg m]	$n_{\eta 0}$ [Hz]	$n_{\alpha 0}$ [Hz]	$\xi_{\eta 0}$ [%]	$\xi_{\alpha 0}$ [%]	x_e [–]	μ [–]	x_m [–]	r_α [–]	γ_n [–]
A	#1	0-0-0	1.19	13.404	0.2107	0.047	1.839	2.387	0.09	0.20	0.00	831.9	0.023	0.836	1.298
A	#2	0-0-1	"	"	"	"	"	"	0.93	"	"	832.5	"	"	"
B	#3	0-0-0	"	15.364	0.2521	0.079	1.706	2.207	0.05	0.13	"	953.8	0.034	0.854	1.294
B	#4	0-0-1	1.20	"	"	"	"	"	0.86	"	"	947.5	"	"	"
B	#5	0-0-1*	"	"	"	"	"	"	"	"	"	951.3	"	"	"
B	#6	0-0-2	1.19	"	"	"	"	"	2.57	"	"	953.2	"	"	"
B	#7	0-1-0	1.20	"	0.2439	0.306	"	2.244	0.11	0.17	"	947.5	0.133	0.840	1.315
B	#8	0-1-2a	"	"	"	"	"	"	2.01	"	"	"	"	"	"
B	#9	0-1-2b	"	"	"	"	"	"	3.08	"	"	"	"	"	"
B	#10	0-2-0	1.19	"	0.2438	0.130	"	"	0.07	"	"	953.8	0.056	"	1.316
B	#11	0-2-2	1.20	"	"	"	"	"	3.11	"	"	945.0	"	"	"
B	#12	0-2-3	1.19	"	"	"	"	"	5.67	"	"	956.9	"	"	"
C	#13	0-2-0	"	"	"	0.185	"	2.357	0.08	0.21	"	"	0.080	"	1.382
C	#14	0-2-3	"	"	"	"	"	"	5.40	"	"	"	"	"	"
D	#15	0-0-0	1.17	14.822	0.2308	0.073	1.720	2.172	0.05	0.17	"	935.6	0.033	0.832	1.263
D	#16	0-0-0*	1.19	"	"	"	"	"	"	"	"	925.5	"	"	"
D	#17	0-0-3	1.17	"	"	"	"	"	5.66	"	"	941.8	"	"	"
D	#18	0-0-3*	1.19	"	"	"	"	"	"	"	"	926.1	"	"	"
D	#19	1-0-0	"	14.850	0.2386	0.092	1.718	2.136	0.07	0.14	−0.10	926.8	0.041	0.845	1.243
D	#20	1-0-0*	"	"	"	"	"	"	"	"	"	"	"	"	"
D	#21	2-0-0	"	"	0.2352	0.029	"	2.151	"	0.15	0.10		0.013	0.839	1.252
D	#22	2-0-3	"	"	"	"	"	"	4.95	"	"	924.3	"	"	"

6.3.2 CRIACIV campaign

The model was arranged with a nose-up angle of about 0.43° to compensate the vertical incidence of the flow in the test section.

The investigation procedure was similar to that one adopted in the experimental campaign at Stahlbau Institut (see § 6.3.1).

Large attention was paid to arrange the whole setup as symmetric as possible with respect to the along-wind centreline of the model in order to limit the unwanted rolling motion. The blockage ratio, calculated in a vertical plane crossing the model in the rest position, was about 0.25%. This value increased up to 6.25% when the model experienced pitching amplitudes around 90°. The tests were conducted in smooth flow conditions with a free-stream turbulence intensity of about 0.7% (see § 5.3.2). The mean flow speed was measured by means of a Prandtl tube installed upstream the model and corrected through known flow maps to infer the velocity at the model centreline. The Reynolds numbers (defined as $Re = UB/\nu$, with $\nu = 15$ mm^2 s^{-1}) during the tests were in the range 33,000 to 107,000.

Table 6.3 summarises the characteristics of the principal configurations. Moreover, Table 6.4 reports the governing parameters of additional configurations tested to verify the influence of some technological alternatives for the setup (*e.g.* different ball bearings or presence of the shelters), and also to explore the influence of homogeneous high turbulence and cross-section modifications (*e.g.* installation of small porous barriers on the short sides of the plate).

The investigations conducted in SESSION I and SESSION II limited to the case of no eccentricity of the elastic centre, whereas the influence of the still-air frequency ratio was explored when combined with the static mass unbalance. The effects of high damping levels were instigated as well. In these first sessions, large attention was paid to perform as reliable as possible post-critical regime measurements. Thus the sectional model with shorter span (M25S) was installed, having higher bending rigidity, to improve the quality of the results.

The investigations conducted in SESSION III evaluated the post-critical regime of configurations with elastic axis at the upstream quarter-chord, being the optimal value for energy harvesting applications as suggested by the linear analysis (see § 9). With the aim at lowering the mass-ratio parameter μ, the sectional model with longer span (M25L) was installed in order to reduce the effect of the passive mass of the setup that oscillated during the motion. Nevertheless, the model had now higher bending flexibility and the quality of the post-critical results may be affected by dynamic deflections of the model during very large amplitude oscillations.

Some more information about the characteristics of the aerolastic-setup arrangement are reported in Table 6.5.

Table 6.3. Parameters of the configurations tested during the experimental campaign at CRIACIV (the cross-section width is $B = 250$ mm, and the model span is $l = 517$ mm for setup-type S0 and $l = 1008$ mm for setup-type S1-S2-S3).

Session	Setup	Code	Info	ρ [kg m^{-3}]	I_η [kg]	I_α [kg m^2]	S [kg m]	$n_{\eta 0}$ [Hz]	$n_{\alpha 0}$ [Hz]	$\xi_{\eta 0}$ [%]	$\xi_{\alpha 0}$ [%]	x_e [–]	μ [–]	x_m [–]	r_α [–]	γ_n [–]
I	S0a	♯1	0-2-0	1.151	8.058	0.0315	0.073	1.886	1.820	0.05	1.67	0.00	2708.9	0.091	0.625	0.965
I	S0a	♯2	0-0-0	1.143	"	0.0240	0.006	"	2.085	0.04	1.17	"	2726.8	0.008	0.545	1.105
I	S0a	♯3*bis*	0-1-0**	1.144	7.872	0.0306	0.034	1.731	1.844	0.05	0.82	"	2661.8	0.043	0.624	1.066
II	S0b	♯3	0-1-0*	1.235	7.867	0.0317	0.045	"	1.814	0.04	1.24	"	2604.7	0.057	0.634	1.048
II	S0b	♯4	0-1-1*	1.168	"	"	"	"	"	9.52	"	"	2605.3	"	"	"
II	S0b	♯5	0-1-2*	1.164	"	"	"	"	"	18.13	"	"	2615.4	"	"	"
II	S0b	♯6	0-0-0*	1.164	7.872	0.0290	0.000	"	1.895	0.05	1.23	"	2617.1	0.000	0.607	1.095
II	S0b	♯7	0-0-2*	1.145	"	"	"	"	"	9.52	"	"	2660.6	"	"	"
II	S0b	♯3*ter*	0-1-0***	1.159	"	0.0317	0.045	"	1.814	0.05	1.24	"	2627.6	0.057	0.634	1.048
III-c	S1	♯13	1-1-0	1.204	8.491	0.0136	0.045	1.829	2.273	0.05	1.04	−0.25	1398.9	0.053	0.401	1.243
III-c	S1	♯14	1-1-1	1.223	"	"	"	"	"	9.38	"	"	1377.4	"	"	"
III-c	S1	♯15	1-1-2	1.214	"	"	"	"	"	14.57	"	"	1387.5	"	"	"
III-c	S2	♯16	1-2-0	1.230	8.525	0.0176	0.0482	1.982	1.995	0.05	0.88	"	1374.9	0.057	0.454	1.007
III-c	S2	♯17	1-2-1	1.219	"	"	"	"	"	8.99	"	"	1387.4	"	"	"
III-c	S2	♯18	1-2-2	1.215	"	"	"	"	"	14.98	"	"	1392.0	"	"	"
III-c	S3	♯19	1-3-0	"	"	0.0212	0.0477	1.982	1.817	0.05	0.75	"	1392.0	0.056	0.499	0.917
III-c	S3	♯20	1-3-1	1.187	"	"	"	"	"	1.04	"	"	1424.4	"	"	"
III-c	S3	♯21	1-3-2	1.191	"	"	"	"	"	2.60	"	"	1420.5	"	"	"
III-c	S3	♯22	1-3-3	1.190	"	"	"	"	"	4.82	"	"	1421.9	"	"	"
III-c	S3	♯23	1-3-4	1.213	"	"	"	"	"	6.81	"	"	1394.9	"	"	"
III-c	S3	♯24	1-3-5	1.205	"	"	"	"	"	8.96	"	"	1403.2	"	"	"
III-c	S3	♯25	1-3-6	1.206	"	"	"	"	"	11.85	"	"	1402.9	"	"	"
III-c	S3	♯26	1-3-7	1.201	"	"	"	"	"	14.98	"	"	1408.8	"	"	"
III-c	S1	♯27	0-1-0	1.197	8.589	0.0135	0.048	1.819	2.280	0.06	1.25	0.00	1423.5	0.056	0.396	1.254

Table 6.4. Parameters of the extra configurations tested during the experimental campaign at CRIACIV (the cross-section width is B = 250 mm, and the model span is l = 517 mm for setup-type S0 and l = 1008 mm for setup-type Sc*-ScC).

Session	Setup	Code	Info	ρ [kg m^{-3}]	I_η [kg]	I_α [kg m^2]	S [kg m]	$n_{\eta 0}$ [Hz]	$n_{\alpha 0}$ [Hz]	$\xi_{\eta 0}$ [%]	$\xi_{\alpha 0}$ [%]	x_e [–]	μ [–]	x_m [–]	r_α [–]	γ_n [–]
I	S0a	♯b1	0-0-0-H00	1.141	8.058	0.0240	0.006	1.886	2.085	0.04	1.17	0.00	2733.1	0.008	0.545	1.105
I	S0a	♯b2	0-0-0-H25	1.131	"	"	"	"	"	"	"	"	2756.9	"	"	"
I	S0a	♯b3	0-0-0-H50	1.143	"	"	"	"	"	"	"	"	2728.3	"	"	"
I	S0a	♯b4	0-0-0-U00	1.140	"	"	"	"	"	"	"	"	2735.5	"	"	"
I	S0a	♯b5	0-0-0-U50	1.158	"	"	"	"	"	"	"	"	2691.9	"	"	"
II	S0b	♯s1	0-1-0****	1.170	7.875	0.0317	0.031	1.730	1.814	0.04	1.24	0.00	2604.3	0.039	0.634	1.049
II	S0	b ♯s2	0-1-1****	1.176	"	"	"	"	"	1.47	"	"	2590.1	"	"	"
II	S0b	♯s3	0-1-2****	1.179	"	"	"	"	"	2.41	"	"	2582.9	"	"	"
II	S0b	♯s4	0-1-3****	1.166	"	"	"	"	"	4.62	"	"	2613.5	"	"	"
II	S0b	♯s4T1	0-1-3****-t	1.162	"	"	"	"	"	4.62	"	"	2620.6	"	"	"
II	S0b	♯s4T2	0-1-3****-T	"	"	"	"	"	"	4.62	"	"	2621.5	"	"	"
III-A	Sc*	♯p1	1-1-0	1.235	8.415	0.0131	0.037	1.837	1.893	0.06	3.54	−0.25	1352.4	0.044	0.393	1.030
III-A	Sc*	♯p2	1-1-1	1.236	"	"	"	"	"	9.38	"	"	1350.9	"	"	"
III-A	Sc*	♯p3	1-1-2	1.230	"	"	"	"	"	15.19	"	"	1357.0	"	"	"
III-A	Sc	♯g2	1-1-2	1.233	8.448	0.0125	0.048	1.833	1.932	9.48	2.21	"	1359.3	0.057	0.385	1.053
III-B	ScC	♯ 8	1-1-0	1.218	8.454	0.0123	"	"	1.951	0.05	2.25	"	1377.7	"	0.381	1.064
III-B	ScC	♯ 9	1-1-1	1.217	"	"	"	"	"	6.66	"	"	1378.4	"	"	"
III-B	ScC	♯ 10	1-1-2	"	"	"	"	"	"	9.31	"	"	1377.9	"	"	"
III-B	ScC	♯ 11	1-1-3	1.219	"	"	"	"	"	12.23	"	"	1375.9	"	"	"
III-B	ScC	♯ 12	1-1-4	1.227	"	"	"	"	"	15.06	"	"	1367.3	"	"	"

Table 6.5. Arrangement of the aeroelastic setups in the CRIACIV campaign. The codes of the element types are described in § 5.3.3.

Setup	Sectional-model type	Leaf-spring cantilever (Fig. 5.32)	Upper-coil-spring type (Table 5.9)	Lower-coil-spring type (Table 5.9)	Clock-spring type (Table 5.10)	Rocker-arm type (Fig. 5.40)	Ball-bearing type (Fig. 5.34c)	Flow-sheltering carters	End-plates
S0a	M25S	1040 mm	LS195	LS195	CS359	RAa	BL	yes	yes
S0b	"	"	"	LS095	"	"	"	"	"
Sc*	M25L	900 mm	"	"	CS161	RAb	BS1	no	no
Sc	"	"	"	"	"	"	BL	"	"
ScC	"	"	"	"	"	"	"	yes	"
S1	"	"	"	"	CS241	"	"	"	"
S2	"	"	"	LS195	"	"	"	"	"
S3	"	"	"	"	"	"	"	"	"

6.4 Theoretical flutter predictions

The theoretical predictions of the critical conditions, as evaluated by the linear analytical model proposed in § 3.3.2, are discussed in this section. The analysis was set up using the governing parameters according to Table 6.2 for the campaign at the Stahlbau Institute and to Tables 6.3 and 6.4 for the campaign at CRIACIV.

Figs. 6.3, 6.4 and 6.5 show the critical condition evaluations, in terms of critical reduced velocity U_R^c or $U_{R\alpha}^c = U_R^c/\sqrt{X^c}$, flutter frequency at the instability threshold $\sqrt{X^c}$, phase difference ϕ^c and pitching-to-heaving amplitude ratio $(B\hat{\alpha}/\hat{\eta})^c$.

It is worth highlighting that the reduced velocity $U_R = U/nB$, in which n is the dominant frequency during the oscillations, agrees with the one derived from the theoretical flutter evaluation (§ 3.3.2). However, the dimensionless form $U_{R\alpha} = U/n_{\alpha 0}B$ is preferred to show the experimental results of this research work, since it can be related easily to the physical flow speed in the wind tunnel (being not affected by the variations of n with the flow speed). Moreover, the system oscillates randomly due to buffeting for flow velocities below the critical condition. Since no flutter oscillations are present yet, two different dominant frequencies can be detected, which correspond to the modes of oscillations. Therefore, they would complicate the displaying of the results if in terms of U_R. For these reasons, the following results about the critical condition are described in terms of both U_R and $U_{R\alpha}$.

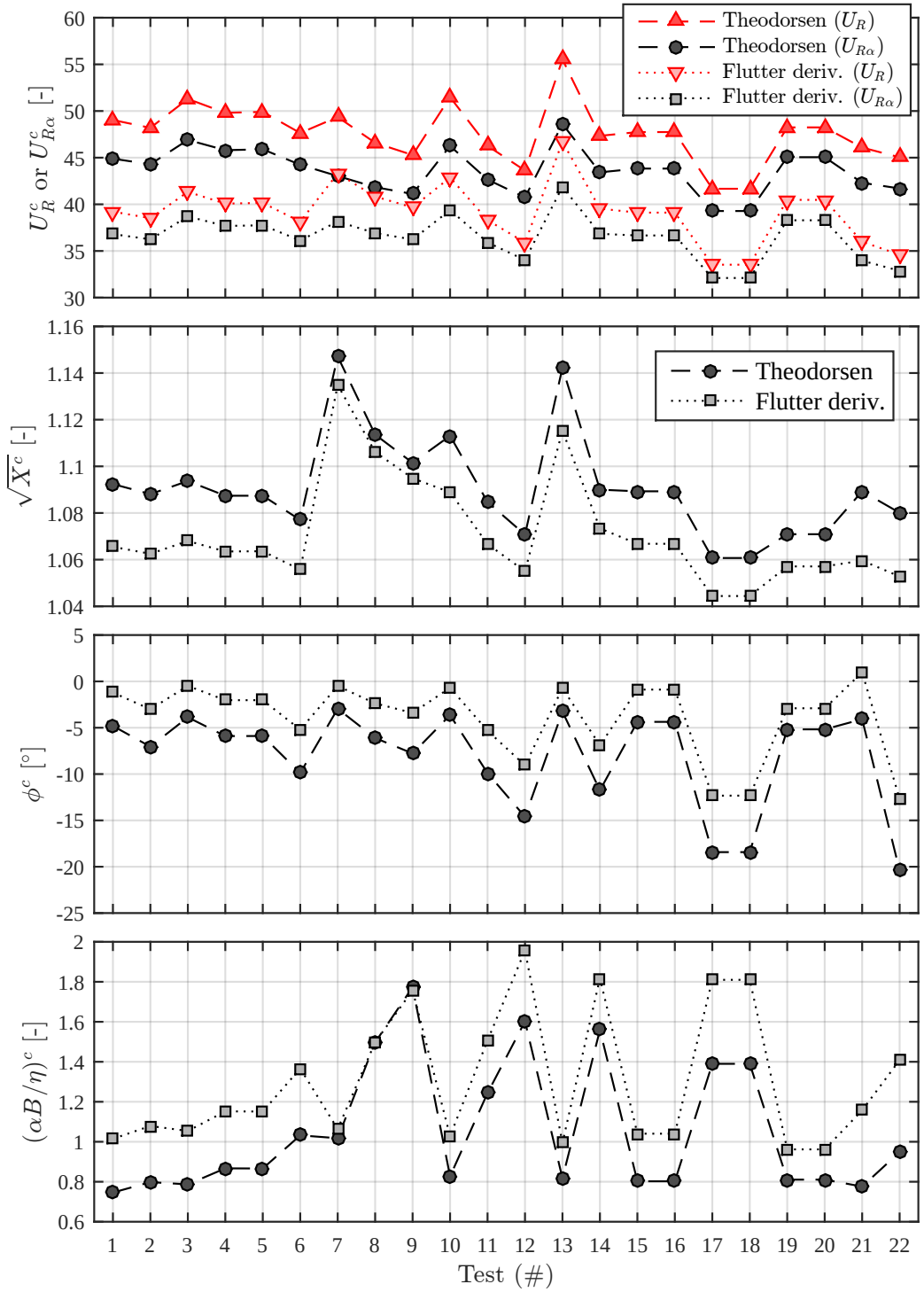

Figure 6.3. Theoretical flutter predictions for the configurations tested during the Stahlbau campaign.

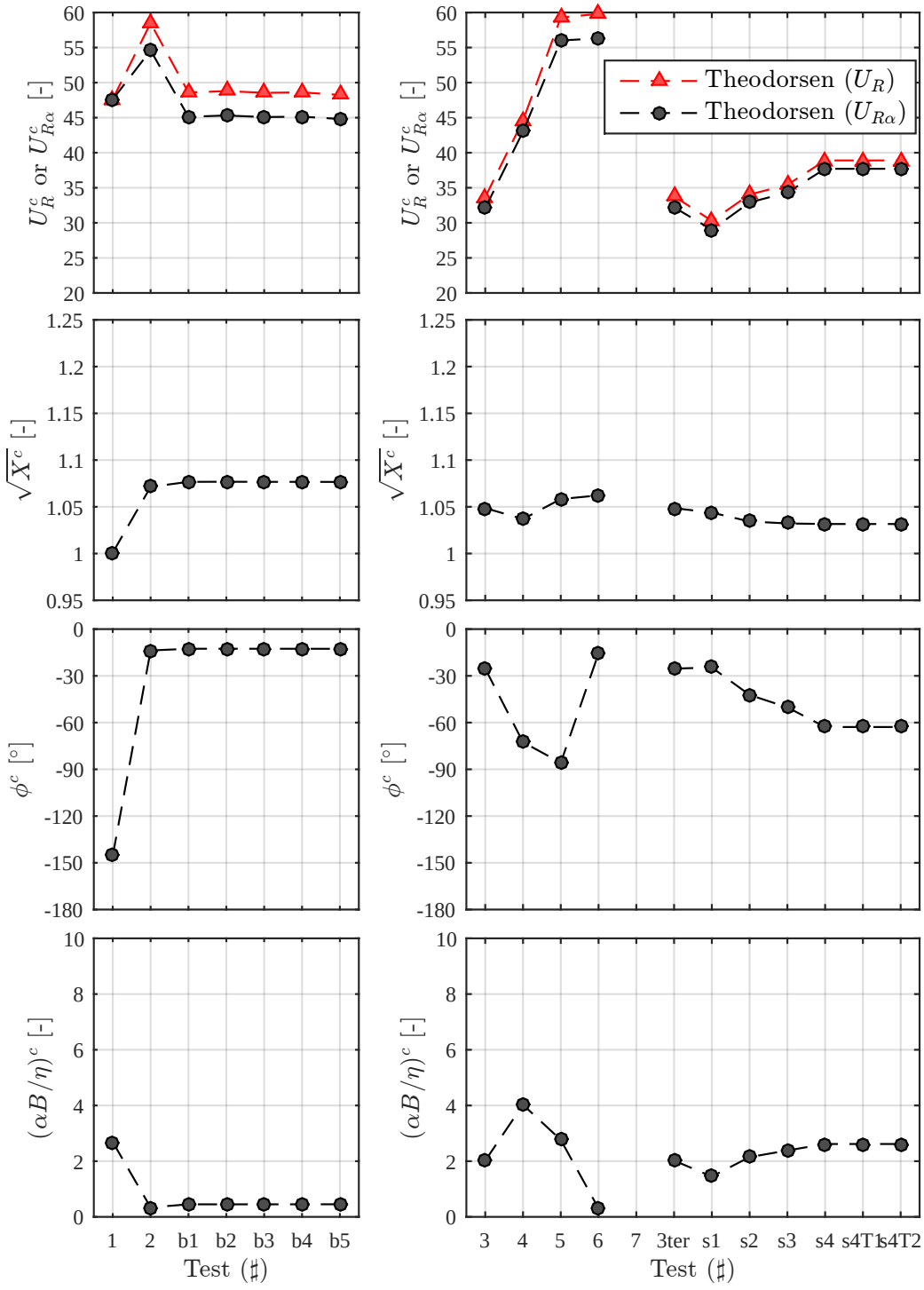

Figure 6.4. Theoretical flutter predictions for the configurations tested during SESSION I (left) and SESSION II (right) in the CRIACIV campaign. Any values is associated with ♯7, because the linear theory did not predict flutter instability in the tested flow velocity domain $U_R \in (0, 100)$.

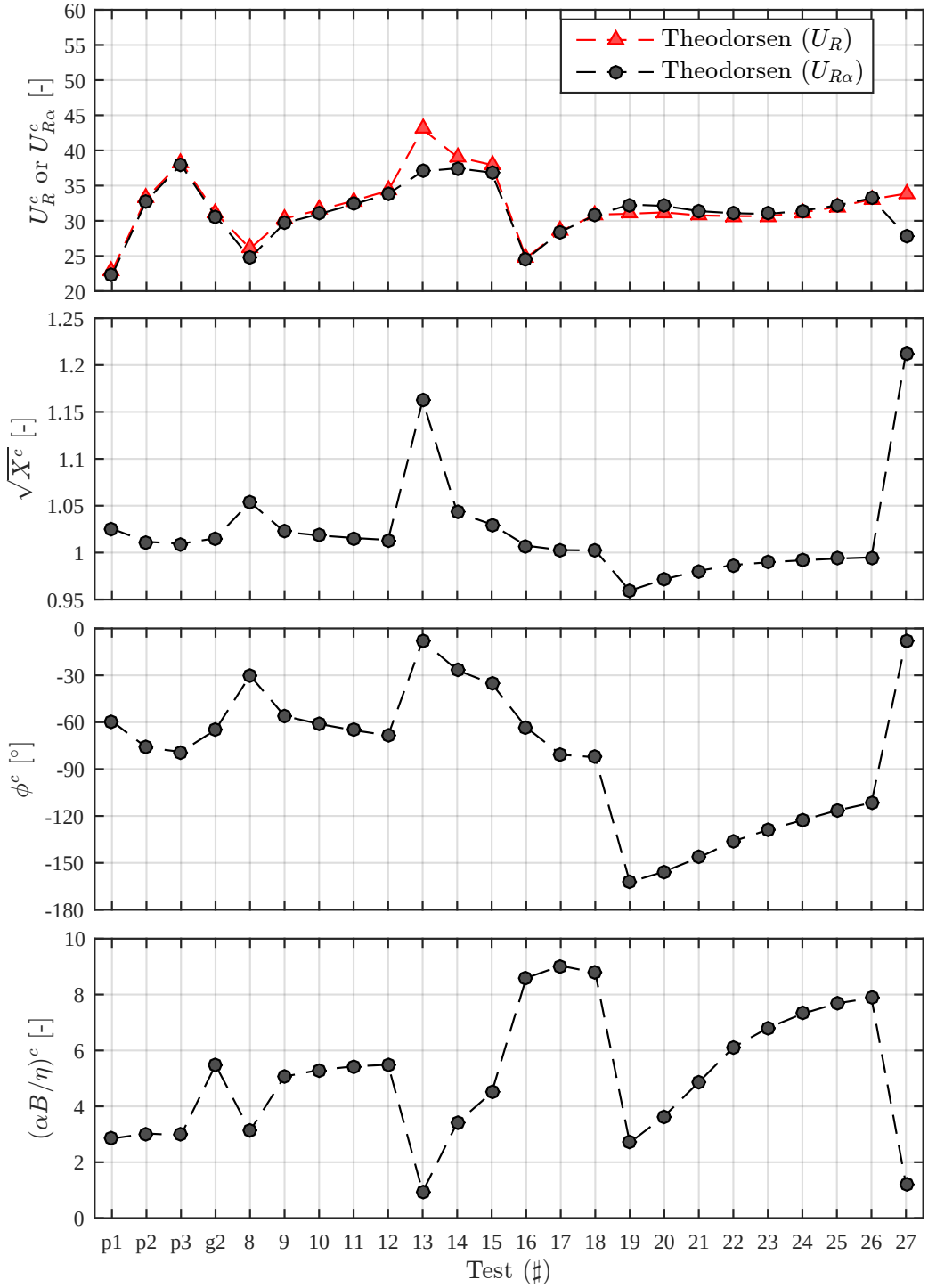

Figure 6.5. Theoretical flutter predictions for the configurations tested during SESSION III (CRIACIV campaign).

Chapter 7

Post-critical-regime analysis

Large attention was paid to characterise the amplitude-velocity diagrams with increasing and decreasing flow speed. Moreover, the stability features of the observed LCO branches was also investigated through the observation of the system response to several manually-induced disturbances of different magnitudes.

It has to be remembered that some problems related to the pitching damping during the tests in both laboratories (see § 5.2.4 and § 5.3.4). In the Stahlbau campaign, undesired increments of the pitching mechanical damping were encountered for large amplitudes of oscillation, due to the friction between the tensioned cables used to restrain the sway motion and the model axis tubes. Since the instability observed in the tests seems to be of pitching-branch type [148], this effect could have non-negligibly influenced the evolution of the LCOs. Consequently, the slope of the amplitude-velocity curves may have been slightly higher in the ideal case of constant viscous damping. By contrast, during the CRIACIV campaign, the ball-bearing system used to decouple the heaving and pitching DoFs influenced the pitching damping for very small amplitudes of oscillation. Due to the introduction of static friction, which produced a Coulomb-type damping, the system was not able to starts the motion spontaneously (exception for configuration ♯13). Thus, manually induced perturbations of very small amplitude were introduced to trigger the motion when the flow speed reached a value close to the theoretical onset.

The post-critical regime was described in terms of heaving and pitching amplitudes, $\hat{\eta}$ and $\hat{\alpha}$, performed during the LCOS. They were calculated as the mean value of the envelope of the displacement time histories, obtained through the Hilbert Transform. In addition, the phase shift between the two DoFs $\hat{\phi}$, the oscillation frequency $\hat{n}$ and the amplitudes ratio $B\hat{\alpha}/\hat{\eta}$ were evaluated to complete the characterisation of the motion during the LCOs. $\hat{n}$ was evaluated by detecting the peaks in the displacement spectra, while $\hat{\phi}$ was determined from the cross-spectra between $\eta(t)$ and $\alpha(t)$, calculating the phase corresponding to the peak at the oscillation frequency.

The figures reported in § 7, § 8 and § 9 always show those motion parameters. Moreover:

- solid markers refer to tests with increasing flow speed;
- empty markers refer to tests with decreasing flow speed;
- vertical dashed lines refer to the experimental critical threshold, corresponding to the flow speed at which the system started to oscillate spontaneously or after a manually-induced initial condition of very small amplitude;
- vertical dotted lines refer to the end of the sub-critical branch, corresponding to the constant flow speed during which the system stopped to oscillate spontaneously.

7.1 Model 15:1

A selected subset of the tested configurations of Table 6.2 is here discussed.

The analysed configurations show mainly the effects of mass unbalance x_m, eccentricity of the elastic axis x_e and heaving damping $\xi_{\eta 0}$. The other parameters were keeps as constant as possible: mass ratio $\mu \in (924.3, 953.8)$; polar-inertia radius $r_\alpha \in (0.832, 0.854)$; still-air frequency ratio $\gamma_n \in (1.243, 1.382)$; pitching damping $\xi_{\alpha 0} \in (0.13\%, 0.21\%)$.

7.1.1 Effects of mass unbalance and stiffness eccentricity

This investigation was conducted for configurations with no-added damping in the heaving DoF, that is only the structural damping $\xi_{\eta 0} \equiv \xi_{\eta 0 s} \simeq 0.1\%$ was present.

Observing Fig. 7.1, the experiments confirmed that a significant reduction of the instability threshold is obtained when a positive eccentricity of the centre of mass is introduced. In particular, there is an optimal value in the range $x_m \in (0.05, 0.1)$, as also suggested by linear analyses (see 6.2), which is in agreement with the discussion reported in [32, pg. 250]. Configuration #3 has an experimentally estimated mass unbalance of $x_m = 0.034$, and it is assumed to be symmetric [1]. If compared with configuration #10, which has an experimentally estimated mass unbalance of $x_m = 0.056$, the instability threshold is markedly anticipated. Now, if introducing configuration #13 in the comparison, which has a larger mass unbalance ($x_m = 0.08$), the critical reduced velocity is slightly increased with respect to that of #10, confirming the presence of an optimal value of x_m. Indeed, configuration #13 shows an intermediate behaviour between #3 and #10 also in terms of amplitudes of the heaving and pitching DoFs. Observing the other parameters of the motion, the evolution of the phase of #13 is again in between those of #3 and #10, confirming the intermediate behaviour also in terms of shape of the motion.

Again observing Fig. 7.1, the critical threshold can be anticipated also if positive stiffness eccentricity ($x_e = 0.1$) is introduced, as demonstrated by the configuration #21. In particular, the slope of the heaving-amplitude vs. reduced-velocity curve is higher than for the other test cases, while relative moderate pitching amplitudes are observed. In the case of configuration #20, that is when the opposite eccentricity of the elastic axis ($x_e = -0.1$) is considered, the system gets more stable, postponing the critical condition and reducing the amplitude of the motion in both DoFs. As also confirmed by linear analyses (see § 6.2), the elastic axis position plays a key role in the system stability, since it directly participates in the self-excited forces formulation modifying the flow-induced loads effect (see Eq. 3.4).

The effect of the elastic axis position and mass unbalance can be better understood if the distance between steady-state-flow aerodynamic centre (FC) and mass centre (MC) is considered (see Figs. 3.2 and 3.5 to clarify the mentioned positions), that is $d^* = \frac{1}{2} + x_e + x_m$. Since the circulatory forces act at the aerodynamic centre (FC), while the inertia is concentrated at the mass centre[2] (MC), there is a 'lever' between FC and MC with 'fulcrum' on the elastic centre (EC). Thus, a small mass unbalance x_m is extremely useful to facilitate the effect of the flow forces on the system motion because. Since $x_m \neq 0$ basically enhances the mechanical/fluid-dynamic coupling between DoFs, any energy exchange between flow and structure (even weak) produces marked effects on the excitation mechanism. By contrast, when the MC is moved too much aft from the EC, the lever becomes hard and larger work is required to move the mass centre, thus increasing the system stability. The influence of the EC position in the system response is more complicated. Since it directly participates in the self-excited-loads definition. However, in the case of very small heaving damping, it is shown that the flow-induced excitations are facilitated as the EC is moved downstream of the FC. This behaviour may be explained by the increment of the arm of the forces on the lever mechanism (when $x_m \neq 0$), or simply because the rotation of the section is facilitated thanks to a larger distance between FC and EC. According to this, in the case of small damping

[1] This configuration was conceived to be symmetric, that is with $x_m \approx 0$. However, the arrangement of the masses of the setup may have introduced experimental errors, as well as the estimation of the coupled and decoupled oscillation frequencies from free-decay tests can have affected the mass-unbalance evaluation. Despite these uncertainties, configuration #3 is assumed as a symmetric configuration.

[2] It is important to remark that, in continuum mechanics, the mass centre is a key reference point in the evaluation of the motion of a certain rigid body.

levels the stabilizing effect of the elastic axis, when upstream of the midchord, is also justified by the fact that it approaches the fluid-dynamic centre (see also [32, Figs. 6 and 20]).

Some additional considerations can be made on the shape of the motion of the tested configurations. Configuration #10 shows the largest pitching amplitudes, which affect the amplitude ratio $B\hat{\alpha}/\hat{\eta}$ in turns. Moreover, it is worth noting the modification of the phase due to the mass unbalance and elastic-axis eccentricity, which both move away from the in-phase motion typical of the symmetric configuration, in the range of flow speed beyond the instability threshold. Then, the phases evolution are almost linear with increasing the reduced flow speed. It is also interesting to note a similarity between the symmetric configuration (#3) and the configuration with negative elastic-axis eccentricity (#20), which mainly differ in terms of x_e. Although the size of the motion amplitudes are markedly different, the other parameters of the motion ($\hat{\phi}$ and $\hat{n}$) are similar, and the two amplitude ratios almost coincide. This behaviour seems to suggest that the effects of the elastic-axis position on the characteristics of the excitation mechanism reduce when the EC gets closer to the force centre. In fact, the characteristics of the excitation mechanism seem to be not distorted, while the energy of the fluid forces is reduced, producing smaller motion amplitudes. It follows that, when the elastic axis approaches the upstream quarter-chord and coincides with the circulatory-force centre, the energy of the fluid forces will vanish if the system is assumed perfectly symmetric ($x_m = 0$), and no flutter instability will occur. These considerations seem to agree with the results of the linear analysis in Fig. 6.1 and with the results reported in [32, Figs. 6-20], where in both cases a vertical asymptote appears when approaching $x_e = -0.25$.

Finally, is it worth highlighting again that all this discussion refers to the case with very small mechanical damping. In the cases with higher levels of the heaving damping (see § 7.1.2), as for energy-harvesting applications, the phase between the DoFs is modified affecting the motion, and also the phases with the flow-induced loads may be altered. Thus, the new shape of the motion can lead to other considerations with respect to optimal positions of the elastic axis (the mass centre plays always the same role of enhancing the coupling between DoFs). See next sections and § 8 for further considerations on this topic.

7.1.2 Effects of heaving damping

For symmetric configurations, the increase of the heaving damping is expected to produce system stabilizations, as predicted by the linear theory (see § 6.2 and [32]). However, configurations based on #3 are not perfectly symmetric, since the experimentally estimated mass unbalance is $x_m = 0.034$, and the linear theory predicted a weak destabilizing effect of damping (see Fig. 6.3). The tested configurations involved heaving-damping increments up to a value of $\xi_{\eta 0} = 2.57\%$, which seem to reduce the LCO amplitude in the range of reduced flow velocity immediately beyond the instability onset (Fig. 7.2). Unfortunately, the excessively coarse increase of the flow speed during the wind-tunnel tests does not enable further considerations about the critical flow speed anticipation with increasing $\xi_{\eta 0}$. No significant modifications of the amplitude ratio $B\hat{\alpha}/\hat{\eta}$ and motion frequency are noted, while the phase seems to be linearly translated away from the in-phase motion, as showed in Fig. 7.6a. The phase shift values of Fig. 7.6a have been calculated by a linear fitting of the last part of the phase curves.

In the case of $x_e > 0$, moderate damping levels (up to 4.95%) do not considerably affect the critical velocity, in agreement with the results of Fig. 6.2 (right-hand side). By contrast, the damping weakly decreases the slope of both heaving and pitching LCOs and strongly reduces the amplitudes in the subcritical branch (Fig. 7.3). Also in this case, no significant modifications of the pitching-to-heaving amplitude ratio and motion frequency are noted, while the phase seems to be linearly translated away from the in-phase motion of about 10°.

The experimental results of Fig. 7.4 confirm that the instability threshold is anticipated by heaving damping increments for small positive eccentricity of the mass centre ($x_m \simeq 0.05$), in agreement with the results discussed in § 6.2 and left-hand side of Fig. 6.2. In addition, the damping variation almost do not affect the LCO amplitude of the heaving DoF. The system seems to be able to compensate the increment of heaving viscous forces increasing the phase shift between the motion components and producing larger pitching amplitudes. In

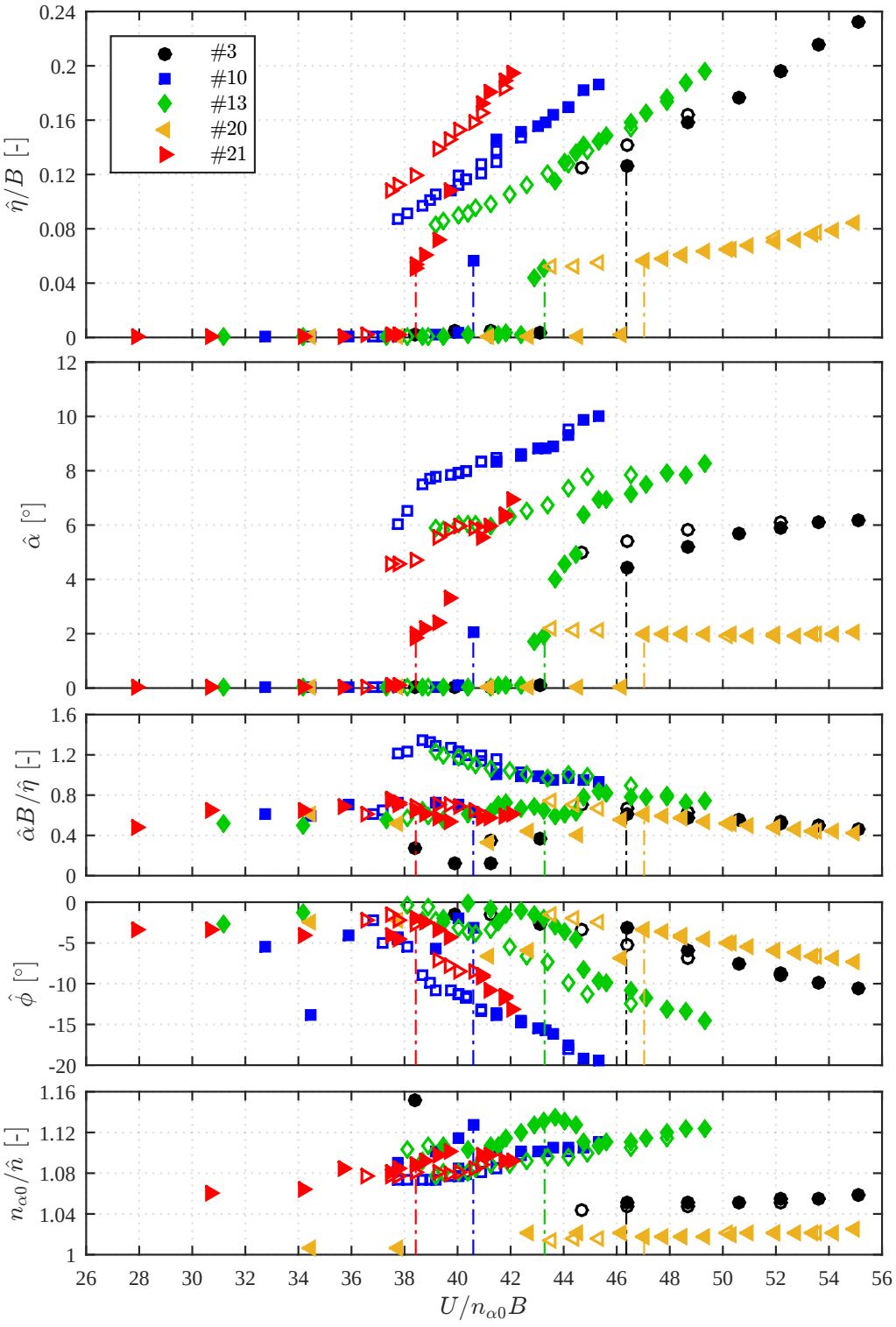

Figure 7.1. Amplitude-velocity diagrams for some cases without added damping: symmetrical configuration (#3), configurations with positive eccentricity of the mass centre (#10 and #13), configurations with eccentricity of the elastic axis upstream (#20) and downstream (#21) of the midchord.

this case, no significant modification of the motion frequency $\hat{n}$ is noted, while the amplitude ratio $B\hat{\alpha}/\hat{\eta}$ is slightly affected due to the pitching-amplitude increment. The evolution of the phase shift with respect to heaving-damping increments is reported in Fig. 7.6b. Similar considerations can be made if observing results of Fig. 7.5, which refers to a configuration with slightly larger mass unbalance and still-air frequency ratio ($x_m \approx 0.08$, $\gamma_n \approx 1.38$). It is worth observing that configuration #13 was arranged in a later step with respect to configuration #10, after modification of some elements of the setup. The observation of this destabilizing effect on a differently arranged configuration can exclude the influence of problems related to the setup operation.

The presence of a steady-state solution with small amplitude, arising in a small flow-speed range suddenly beyond the instability threshold, is apparent in Fig. 7.4 for configuration #10 and in Fig. 7.5 for configuration #13; both configurations describes low-damped systems. These small-amplitude branches of LCOs are expected to occur during attached-flow conditions, and may be due to some nonlinearities on the self-excited loads or to a peculiar condition of the energy exchange between the mechanical system and the flow-induced loads.

The coherence of the results was confirmed by modifying the damping level during real-time measurements, that is skipping from higher values of the heaving damping to the pure mechanical one and vice versa, by turning on/off the electromagnets, as it is clear in the left-hand side of Fig. 7.7. In addition, the right-hand side of the same figure support this result also in terms of build-up, obtained from an imposed rest position for a post-critical flow velocity. This destabilizing effect of heaving damping is in a similar way to the results obtained for others 2-DoF dynamical systems subjected to non-conservative loads (*e.g.* Ziegler's column with dry-friction [31]), although no experimental evidence had been provided so far for 2-DoF fluid-elastic systems.

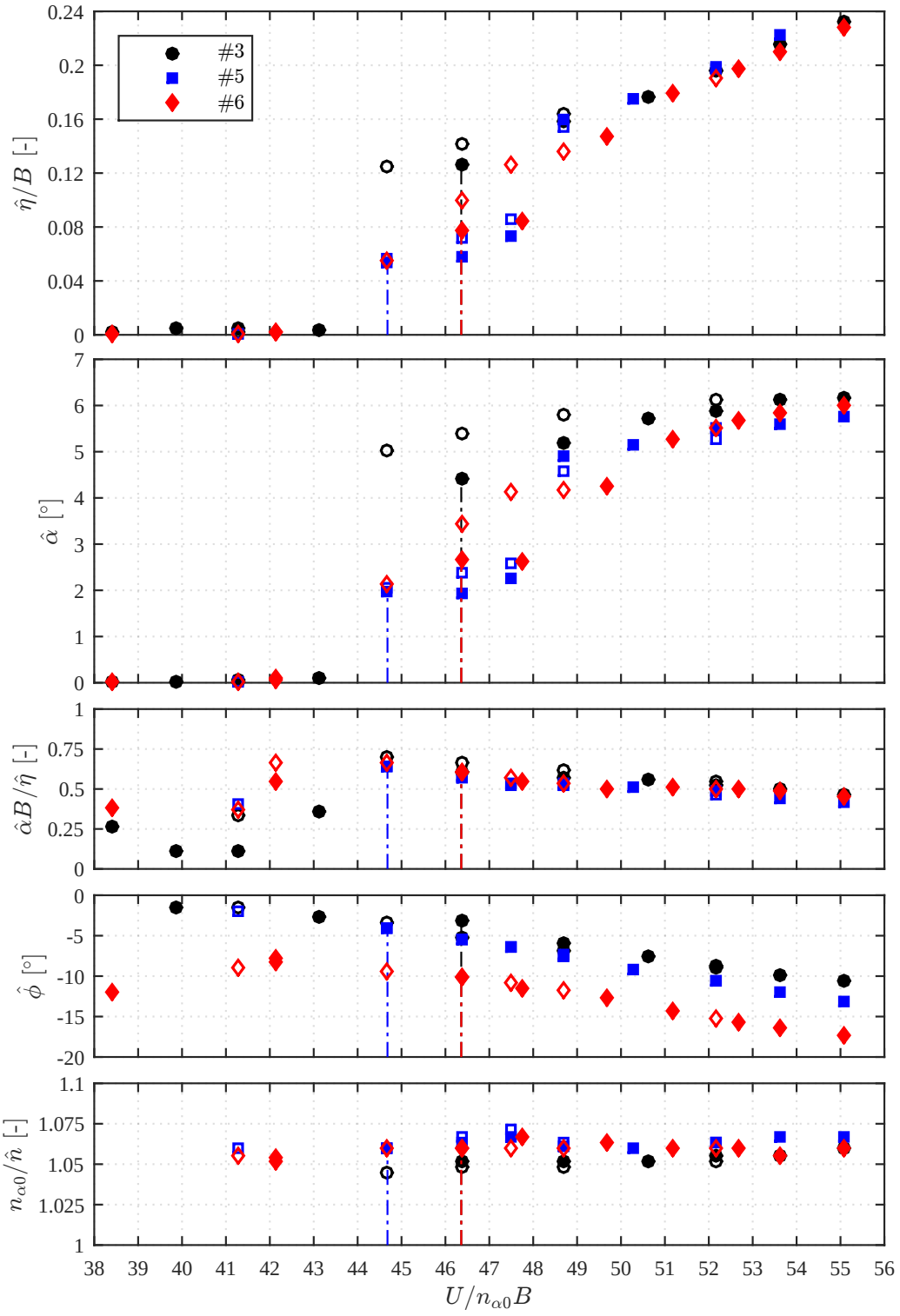

Figure 7.2. Effect of heaving-damping increments for nearly-symmetric configurations ($x_e = 0$, $x_m = 0.034$). The value of $\xi_{\eta 0}$ is 0.05% for #3, 0.86% for #5 and 2.57% for #6.

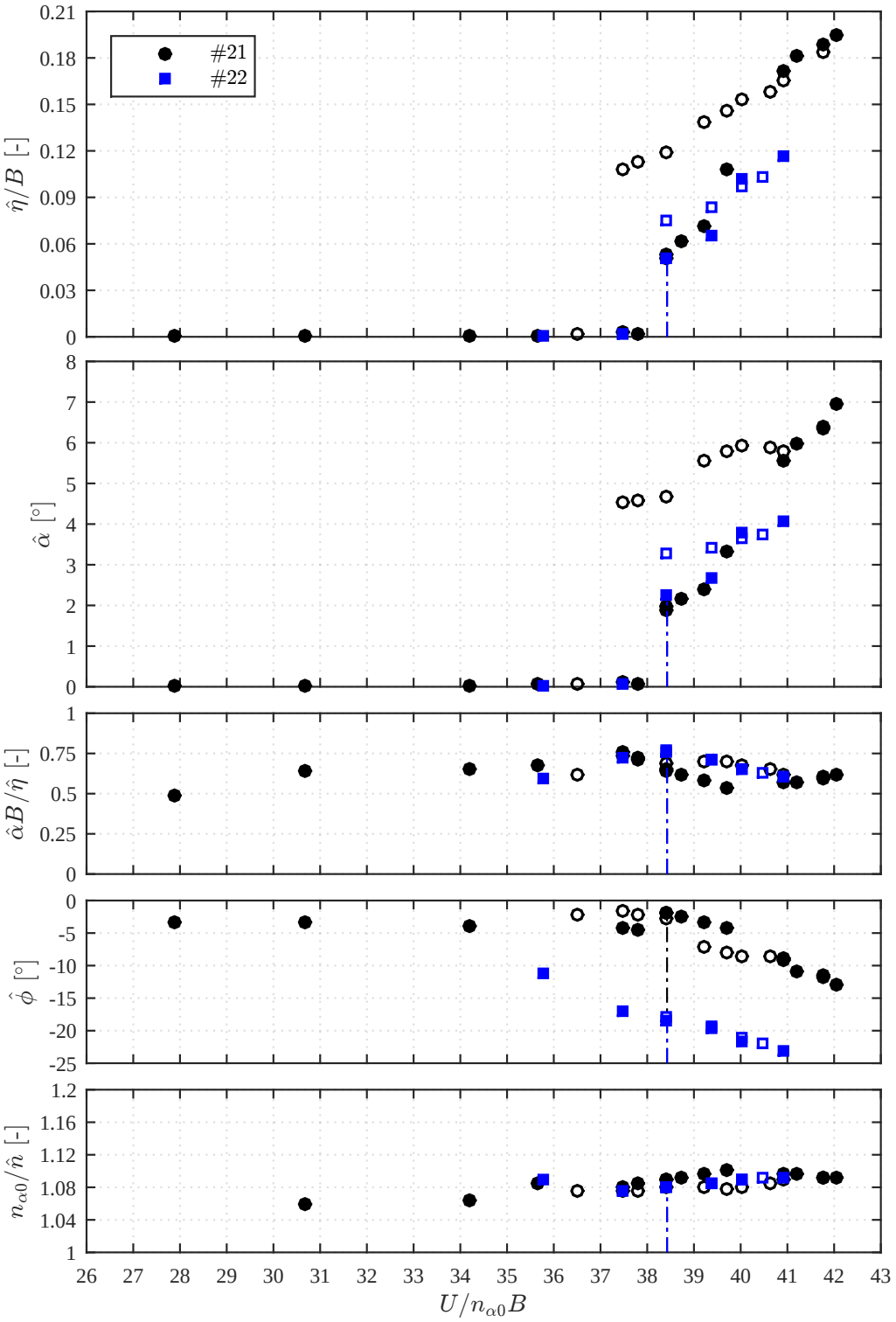

Figure 7.3. Effect of heaving-damping increments for test cases with positive eccentricity of the elastic centre ($x_e = -0.1$). The value of $\xi_{\eta 0}$ is 0.07% for #21 and 4.95% for #22.

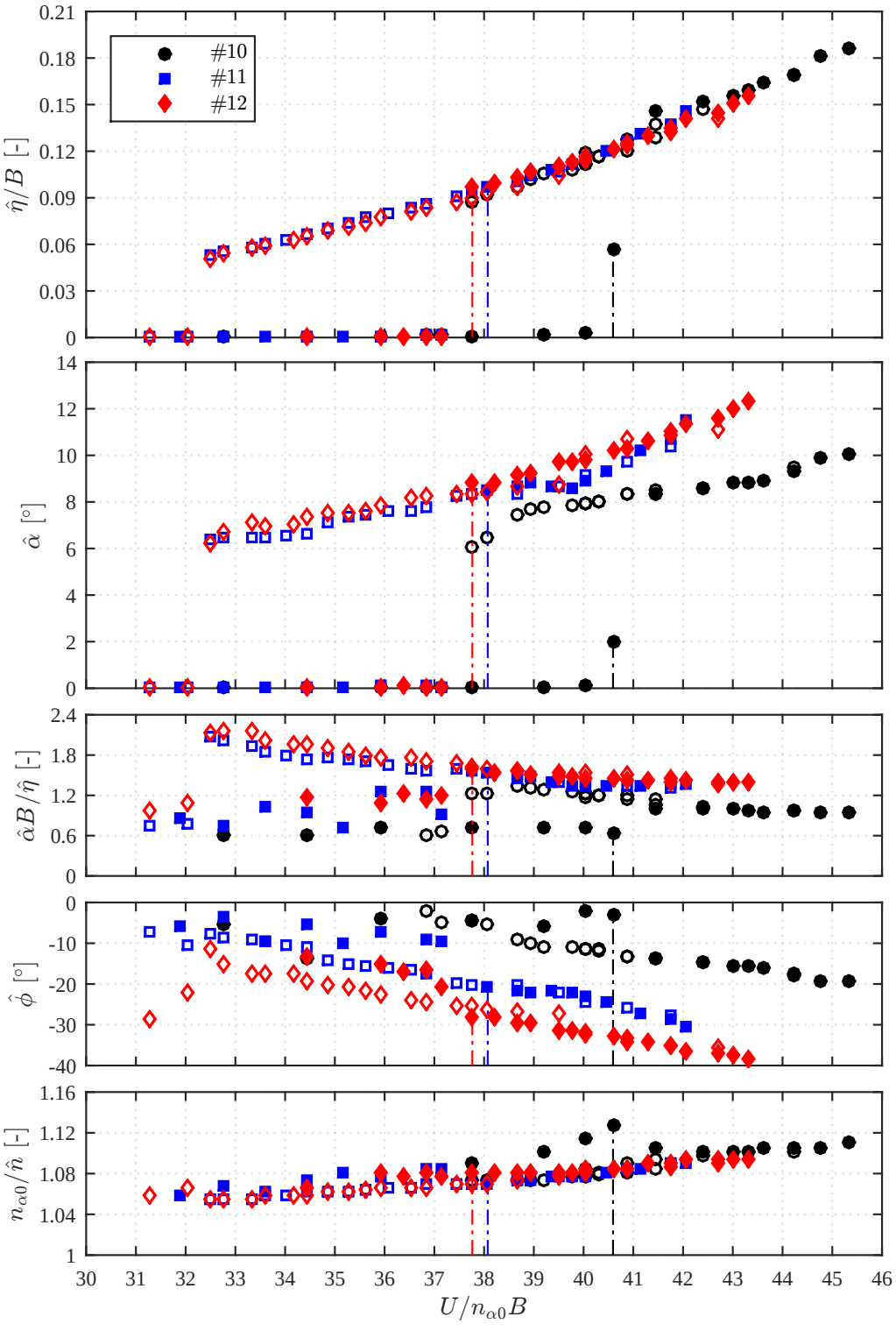

Figure 7.4. Effect of heaving-damping increments for cases with positive eccentricity of the mass centre (x_m = 0.056) and γ_n = 1.316. The value of $\xi_{\eta 0}$ is 0.07% for #10, 3.11% for #11 and 5.67% for #12.

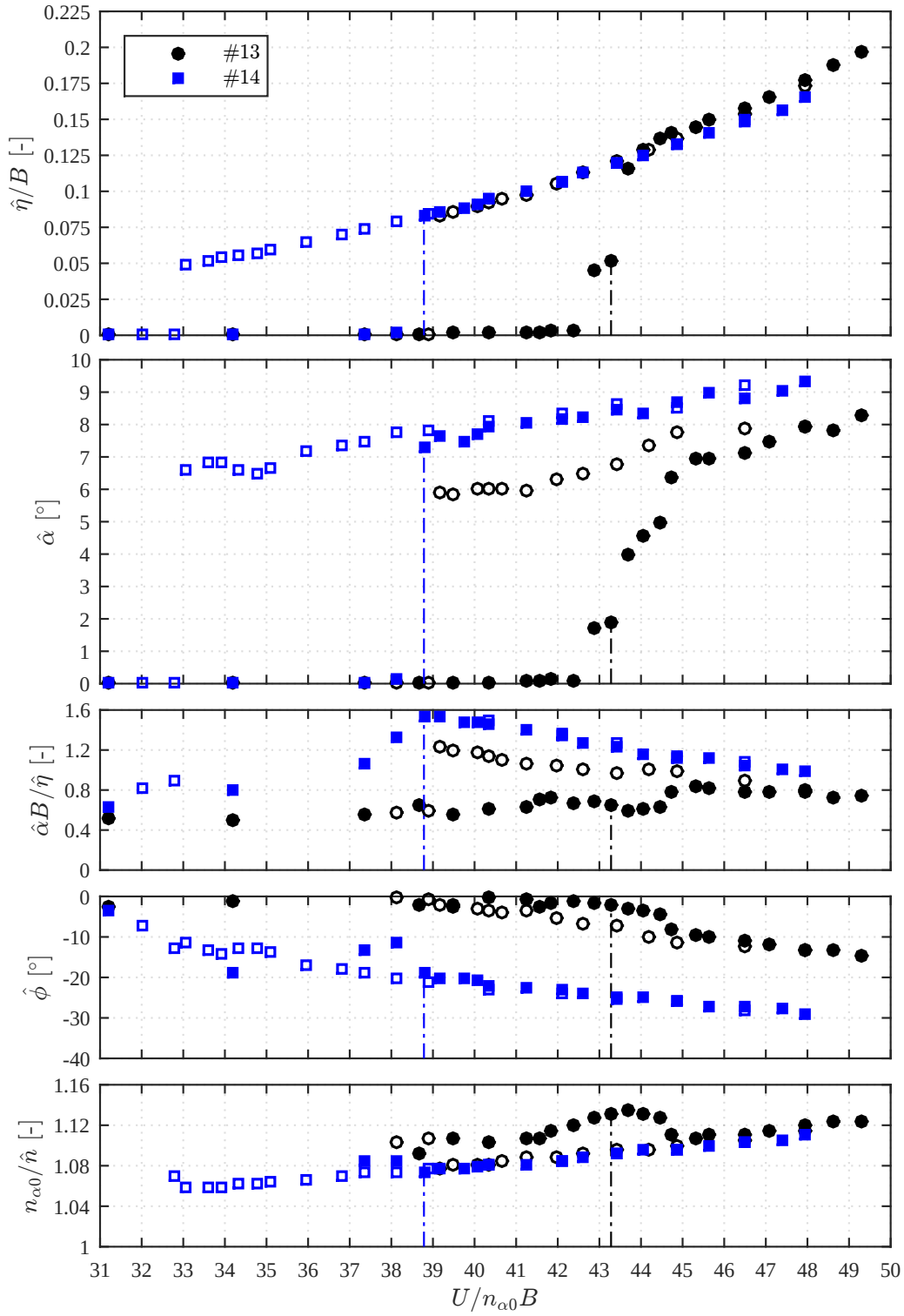

Figure 7.5. Effect of heaving-damping increments for cases with positive eccentricity of the mass centre (x_m = 0.080) and γ_n = 1.382. The value of $\xi_{\eta 0}$ is 0.08% for #13 and 5.40% for #14.

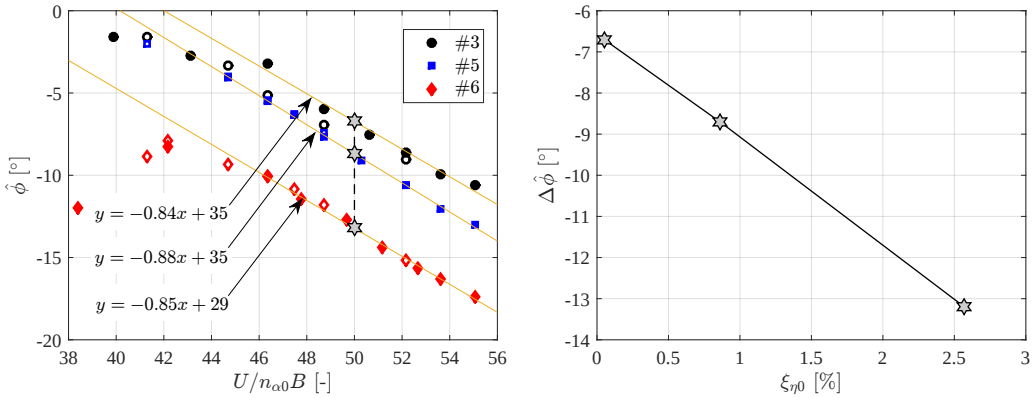

(a) Nearly-symmetric configurations. $\xi_{\eta 0}$ is 0.05% for #3, 0.86% for #5 and 2.57% for #6.

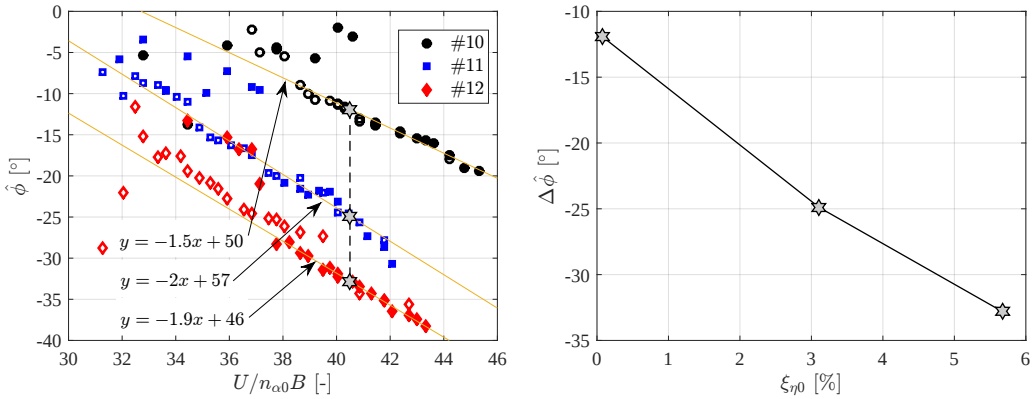

(b) Configurations with small mass unbalance (x_m = 0.056). $\xi_{\eta 0}$ is 0.07% for #10, 3.11% for #11 and 5.67% for #12.

Figure 7.6. Evaluation of the phase shift $\Delta\hat{\phi}$ due to increments of heaving damping $\xi_{\eta 0}$.

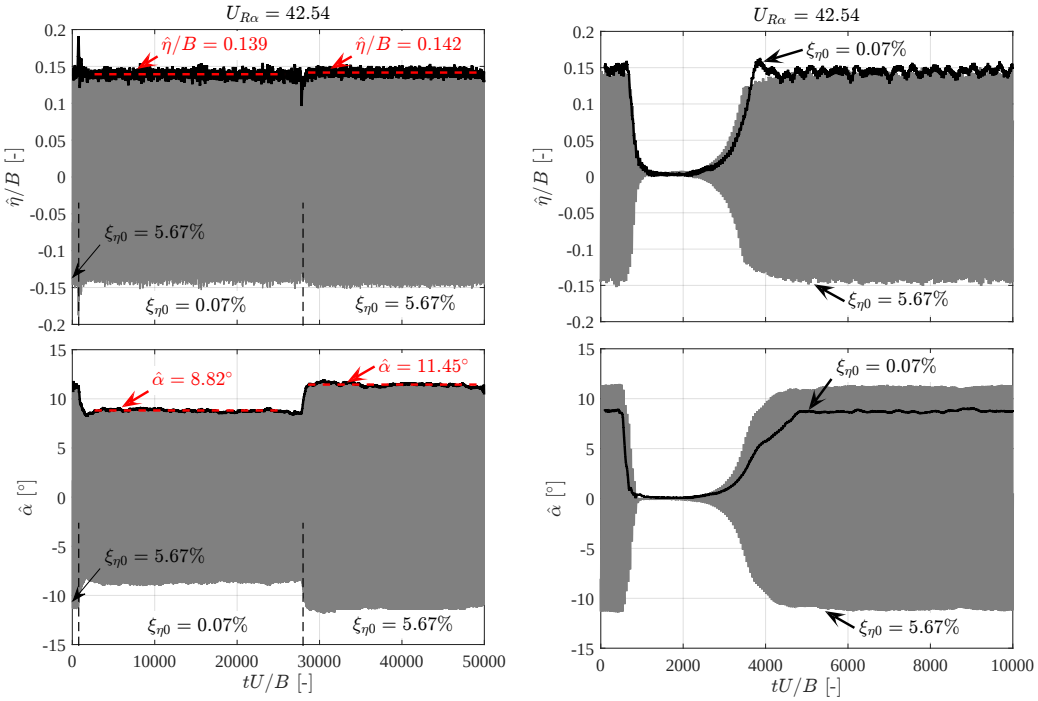

Figure 7.7. (left) Example of a measurement with variations of heaving damping from an higher to a lower value and vice versa, that is between configurations #10 and #12, during oscillations at constant flow speed; (right) comparison of the post-critical build-ups for the two configurations #10 and #12. Black lines describe the envelope of the motion signal.

7.2 Model 25:1 (sessions I and II)

A selected subset of the tested configurations of Table 6.3 is here discussed.

The analysed configurations show mainly the effects of mass unbalance x_m, still-air frequency ratio γ_n and heaving damping $\xi_{\eta 0}$. The other parameters were keeps as constant as possible: mass ratio $\mu \in (2582.9, 2756.9)$; polar-inertia radius $r_\alpha \in (0.545, 0.634)$; stiffness eccentricity $x_e = 0$; pitching damping $\xi_{\alpha 0} \in (0.82\%, 1.67\%)$.

7.2.1 Effects of mass and still-air frequency ratio

The instability threshold can be significantly anticipated if small positive mass eccentricity is introduced, as clear if comparing configurations ♯6 and ♯3 in Fig. 7.8. Furthermore, it is interesting to note the important modification of the motion shape due to a small positive x_m. The still-air frequency ratios of ♯6 and ♯3 are comparable, that is respectively $\gamma_n \approx 1.1$ and $\gamma_n \approx 1.05$, and close to the resonant condition. Due to this, small variations of the inertial parameter move the region in which the centre of the motion rotation lies from upstream to downstream of the midchord, as clarified from the phase that changes from about $-10°$ to about $-155°$. Also the motion frequency ($\sqrt{\hat{X}}$) confirms a different behaviour, since the system shows $\hat{n} > 1$ for the symmetric configuration and $\sqrt{\hat{X}} < 1$ for the mass unbalanced configuration.

Since these configurations have markedly different still-air frequency ratio and mass ratio if compared to those of the German campaign, these tests confirm the destabilizing effect of small mass unbalance for different sets of governing parameters and also for the case of 25:1 width-to-depth ratio (closer to the flat-plate assumption). Thus, small $x_m \neq 0$ is able to enhance the energy exchange, fostering the flutter instability.

Comparing configurations ♯6 and ♯1 in Fig. 7.8, the ratio $B\hat{\alpha}/\hat{\eta}$ seems to be importantly affected by γ_n. In fact, in the case of $\gamma_n<1$, the centre of rotation lies in a small region downstream the midchord, as suggested by the decrease of the phase angle to about -164°, and the heaving component is enhanced. Due to the presence of small mass unbalance ($x_m \approx 0.09$), the instability threshold is again anticipated with respect to the symmetric configuration ♯6. It is worth highlighting that the combination of mass centre position and still-air frequency ratio can lead to optimal configurations, which show low critical reduced velocity and heaving-dominated motion. In fact, while the amplitude ratio $B\hat{\alpha}/\hat{\eta}$ of ♯3 is markedly larger, configurations with small mass unbalance can be calibrated by weak modifications of γ_n to compensate the heaving amplitude reduction without affecting too much the instability threshold.

7.2.2 Effects of heaving damping

For the specific case of configuration ♯2 reported in Fig. 7.9, it is clear that the pitching and especially the heaving amplitudes first significantly reduce for an increment of the heaving damping from 0.05% to 9.5%. By contrast, a further increase of the damping, up to 18.3%, does not produce any dramatic reduction of the oscillation amplitude. In addition, the critical condition is postponed, but the amplitude-velocity paths preserve the main qualitative features, such as the sudden jump at the instability threshold and the drop-down at the lower bound of the sub-critical branch, or the nearly linear evolution with the flow speed of the sub-critical and post-critical branches. Similar considerations can be made about configuration ♯$s1$ in Fig. 7.10. Between configurations ♯2 and ♯$s1$, the only difference was in the mass centre position, which are respectively 0.057 and 0.039, confirming the heaving-damping effect. It is worth highlighting that this small difference of x_m seems to weakly modify the transition toward the sub-critical branch in the heaving and pitching amplitudes. In particular, a small discontinuity is more marked for configuration ♯$s1$, for both DoFs. This discontinuity in the amplitude-velocity paths arises also for the configurations with increasing heaving damping, although gradually vanishing as increasing $\xi_{\eta 0}$.

According to the linear theory, the increase of external damping in the case of the symmetric configuration ♯6 fully stabilizes the system. Therefore, although configuration

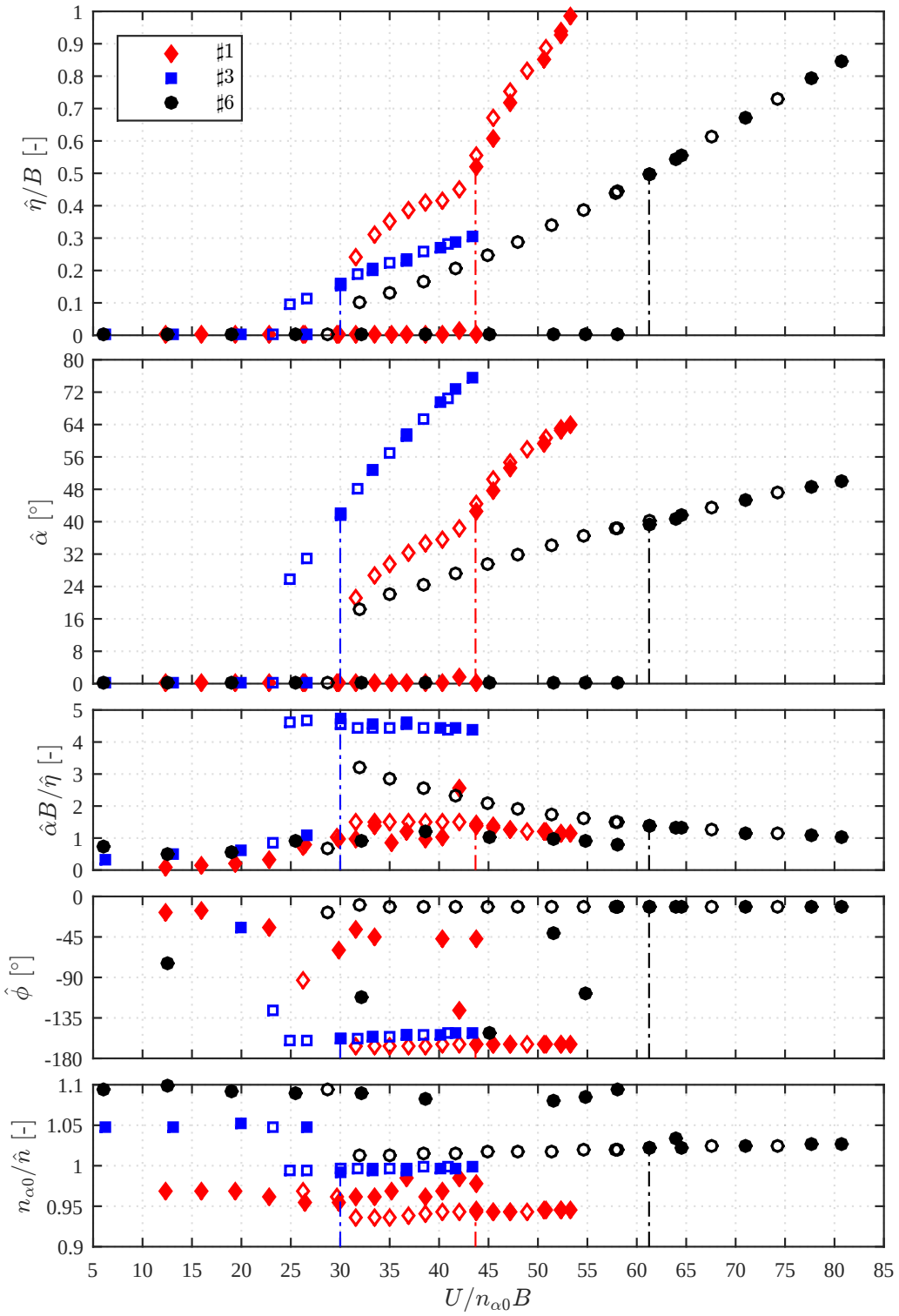

Figure 7.8. Comparison between symmetric (x_m = 0 and γ_n = 1.095 for ♯6) and mass-unbalanced configurations with different still-air uncoupled frequency ratio (x_m = 0.091 and γ_n = 0.956 for ♯1, x_m = 0.057 and γ_n = 1.048 for ♯3).

♯7 is theoretically not prone to flutter instability, steady-state oscillations were achieved, as shown in Fig. 7.11, provided that the system was artificially disturbed through large initial conditions, so that an amplitude-velocity diagram was obtained anyway. This result highlights the differences between the self-excited loads that dominate the steady-state regime and those responsible for the incipient classical-flutter instability. In particular, while the latter relies on the aeroelastic coupling between structural modes and respective fluid-dynamic reactions that leads to phase adjustment and loss of damping, the motion is governed by hysteresis loops in the nonlinear fluid-dynamic loads when massive flow separation occurs at high angles of attack due to dynamic stall.

In the case of small mass unbalance (*e.g.* Fig. 7.9), the phase $\hat{\phi}$ increases from about $-152°$ for low heaving damping ($\xi_{\eta 0} = 0.05\%$) to about $-133°$ for ($\xi_{\eta 0} = 9.52\%$) and to about $-121°$ for ($\xi_{\eta 0} = 18.13\%$). By contrast, for the symmetric configuration (Fig. 7.11) the phase angle starts from about $-12°$ and decreases down to about $-61°$ if the heaving damping is equal to 9.52%. In general, $\hat{\phi}$ seems to tend to $-90°$ for very high heaving damping, suggesting that the system adjusts the motion to an optimal condition while exhibiting self-sustained oscillations in the case of very high mechanical dissipation. See § 9.1.2 for more details on this issue.

Definitely, the increase of heaving damping nonlinearly modifies the characteristics of the motion, as better clarified in Fig. 7.12 and Fig. 7.13. The linear fitting has been applied to the post-critical stable branch of the heaving and pitching amplitudes and phase curves with the reduced flow speed. In this case, the system response seems to saturate as the heaving damping increases.

7.2.3 Tests repeatability and sensitivity to mass-ratio parameter

Some configurations were repeated, after disassembling and reassembling the setup, to verify that undesired intrinsic problems due to the setup are not present and/or the repeatability of the post-critical measurements. In particular, it is possible to compare in Fig. 7.14 the results of configurations ♯3 and ♯3*ter* (configuration ♯3*ter* was reassembled after testing configurations from ♯3 to ♯7) that have the same parameters exception of the mass ratio μ, which slightly differs due to variations of the temperature (thus of the airflow density). Good overlapping is found, with weak differences on the amplitude ratio $B\hat{\alpha}/\hat{\eta}$ due to slightly smaller heaving amplitudes. Moreover, if introducing configuration ♯*s*1 in the comparison, which was tested in a different step during the campaign, the results continue to be in agreement.

It is worth highlighting that ♯*s*1 has an experimentally estimated $x_m = 0.039$ that slightly differs from $x_m = 0.057$ of configurations ♯3 and ♯3*ter*. Since the set up of these configurations considered the same inertias and geometry, and following the good overlapping of the results, it can be concluded that they can be considered to be similar. The difference on the mass centre position may be due to errors during the identification of x_m from the frequencies of the uncoupled and coupled free-decay tests. The parameter x_m, estimated by Eq. (5.5), is very sensitive to the frequencies of the coupled and uncoupled motion, and the third decimal digit becomes usually significant. Thus, uncertainties on this parameter estimation cannot be avoided, getting close to the spectra resolution.

Continuing to observe Fig. 7.14, the comparison between configurations ♯2 and ♯6 shows the sensitivity of the system response to small variations of the mass-ratio parameter, being respectively $\mu = 2762.8$ and $\mu = 2617.1$ (this difference is due to a variation of about 200 g of heaving mass). It is interesting to note that the amplitude of the motion is simply reduced if slightly increasing μ, without affecting the other parameters of the motion. This linear 'scaling' effect of the mass-ratio parameter seems to agree with the linear trend of the critical reduced velocity with μ, as depicted in Fig. 6.1, concluding that a lighter system experiences larger motion amplitudes.

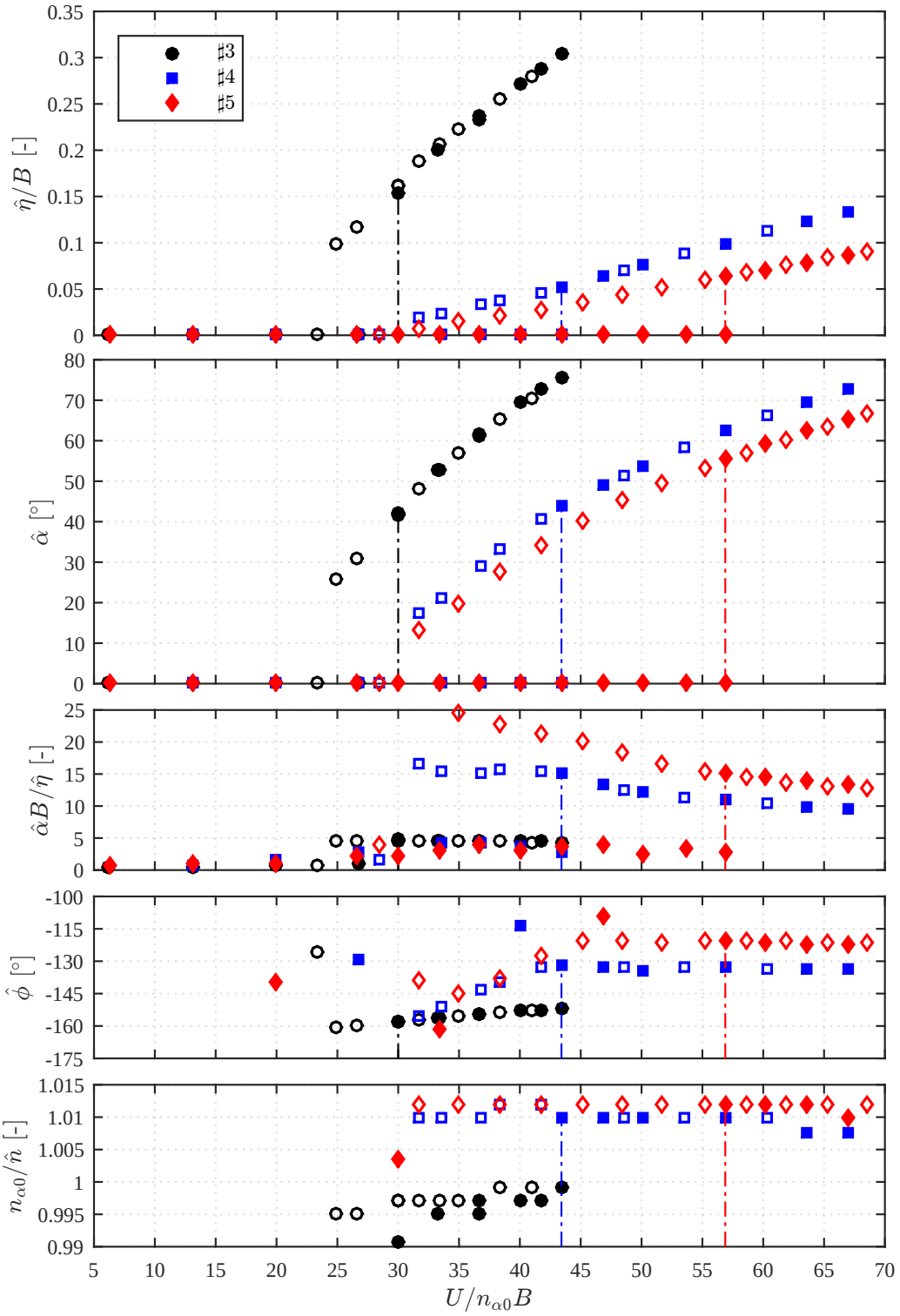

Figure 7.9. Effect of heaving-damping increments for the cases with a positive mass unbalance of x_m = 0.057. $\xi_{\eta 0}$ is 0.04% for ♯3, 9.52% for ♯4 and 18.13% for ♯5.

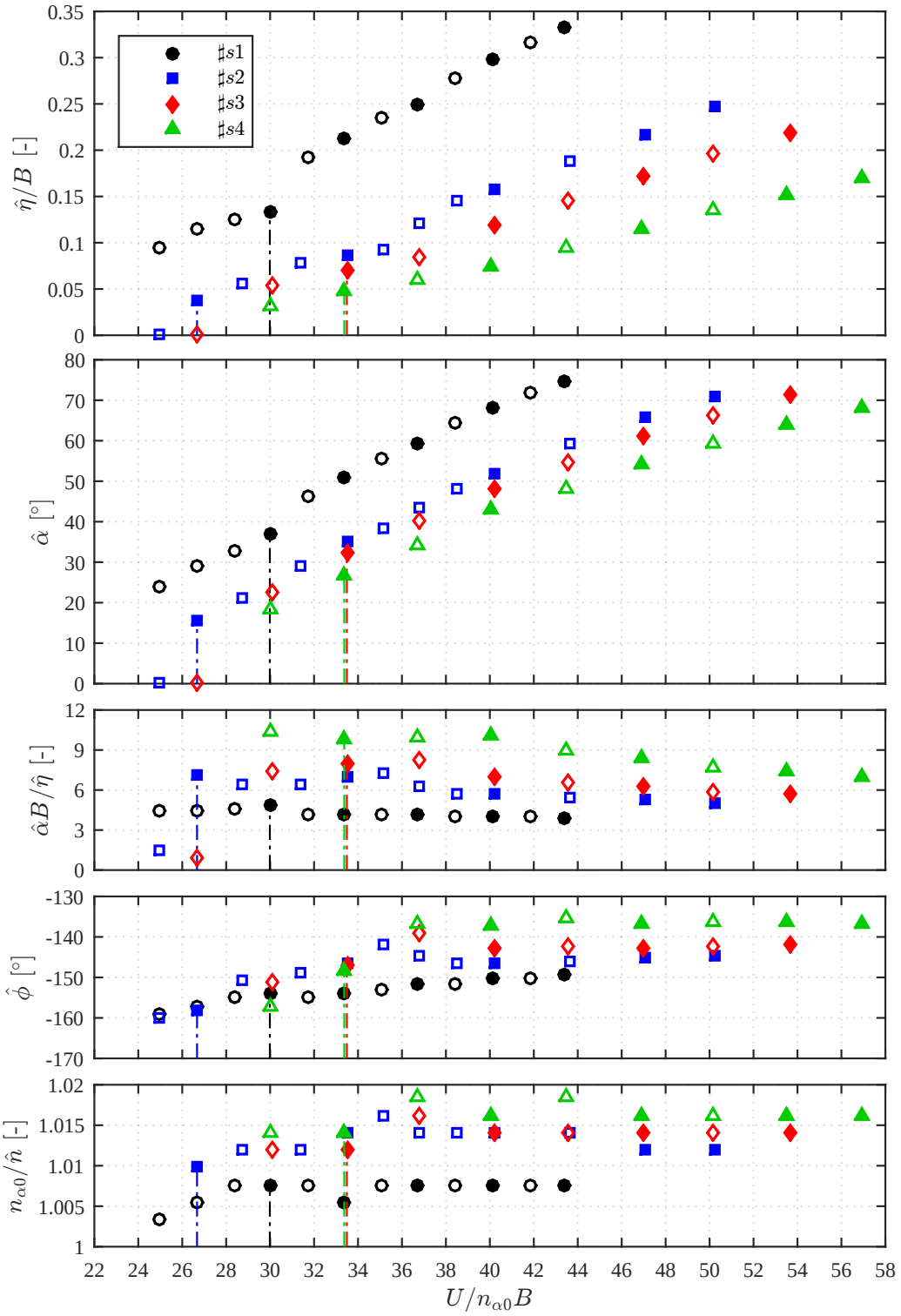

Figure 7.10. Effect of heaving-damping increments for the cases with a positive mass unbalance of $x_m = 0.039$. $\xi_{\eta 0}$ is 0.04% for ♯$s1$, 1.47% for ♯$s2$, 2.41% for ♯$s3$ and 4.62% for ♯$s4$.

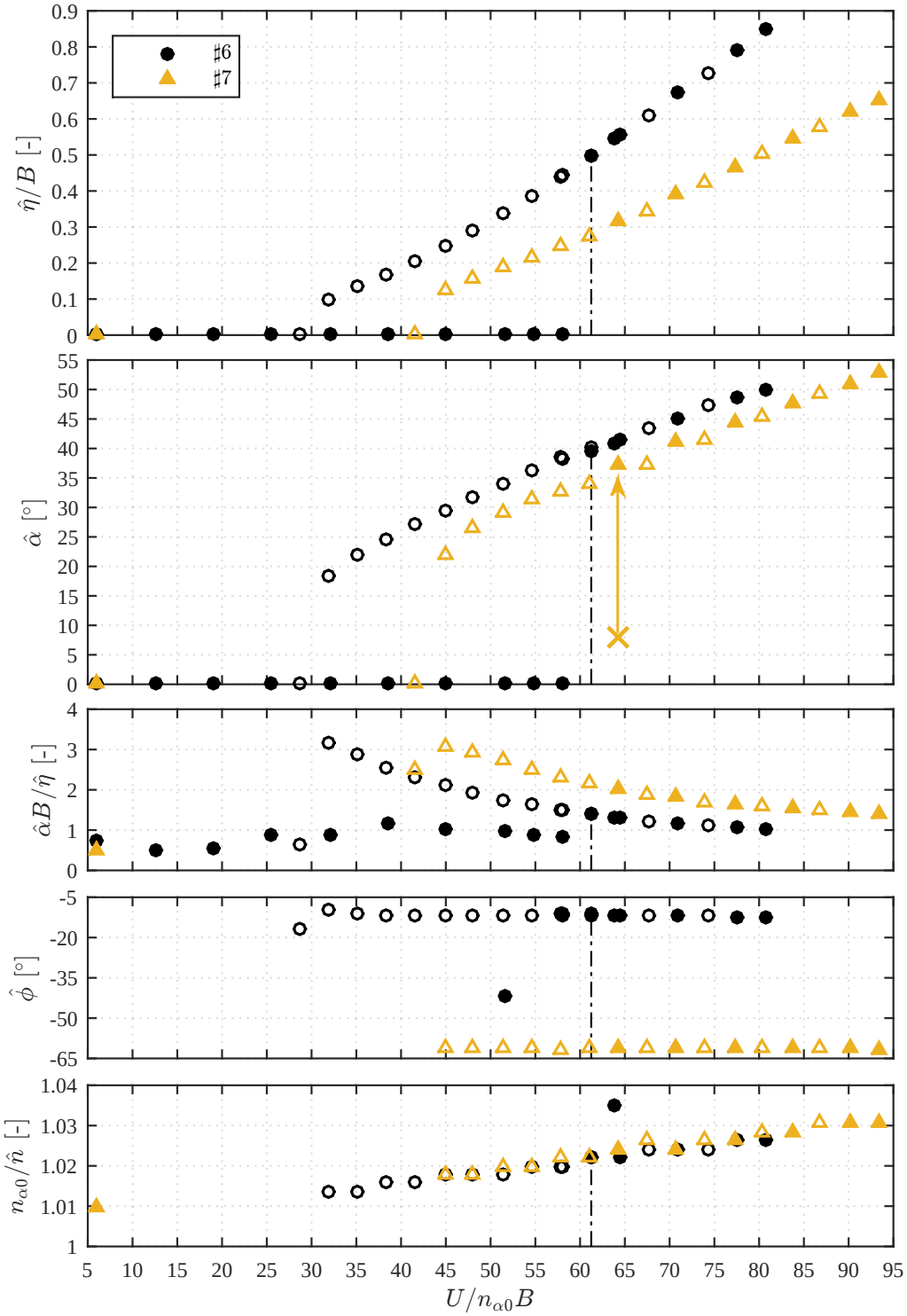

Figure 7.11. Effect of heaving-damping increments for the symmetric configuration. In the pitching-velocity curve, the symbol '×' indicates the initial condition imposed to trigger the motion. $\xi_{\eta 0}$ is 0.05% for ♯6 and 9.52% for ♯7.

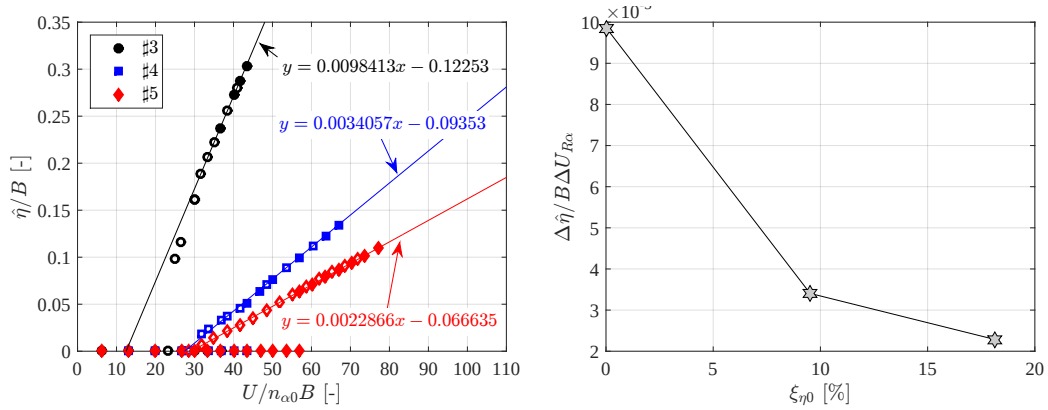

(a) Heaving DoF.

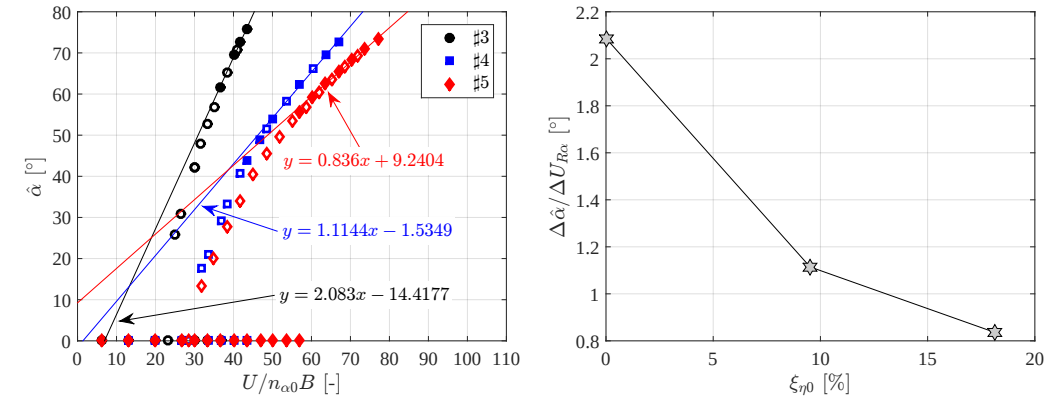

(b) Pitching DoF.

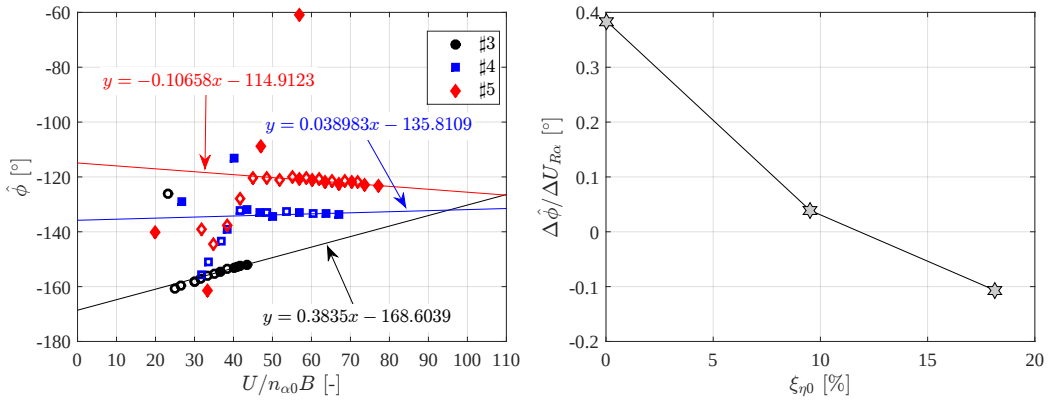

(c) Phase difference.

Figure 7.12. Evaluation of heaving ($\Delta\hat{\eta}/B$), pitching ($\Delta\hat{\alpha}$) and phase ($\Delta\hat{\phi}$) variations with respect to reduced-flow-velocity variations ($\Delta U/Bn_{\alpha 0}$) due to increments of heaving damping $\xi_{\eta 0}$, for configurations derived from ♯3.

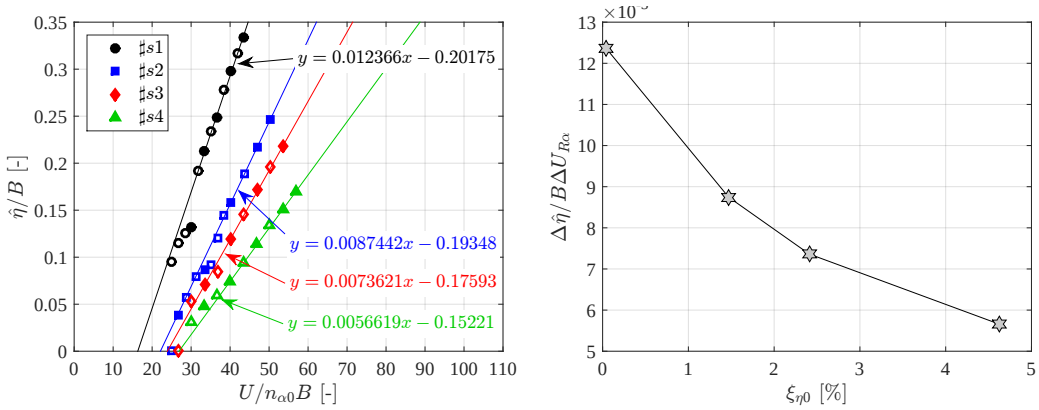

(a) Heaving DoF.

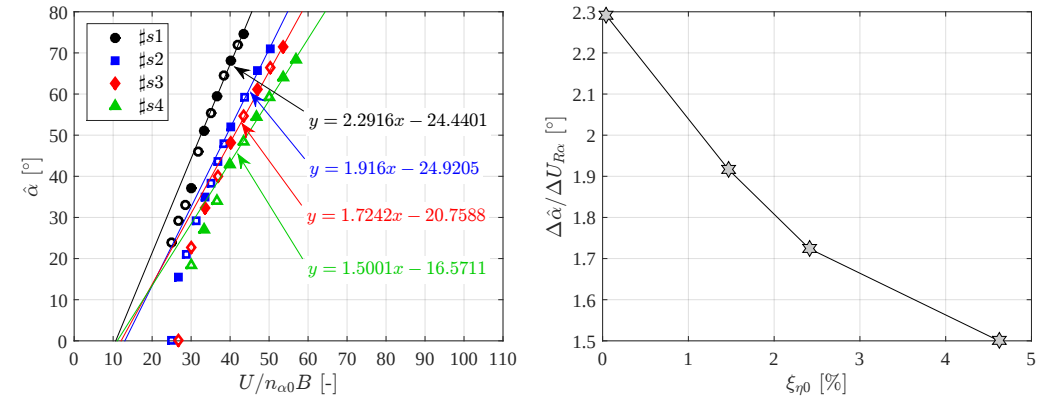

(b) Pitching DoF.

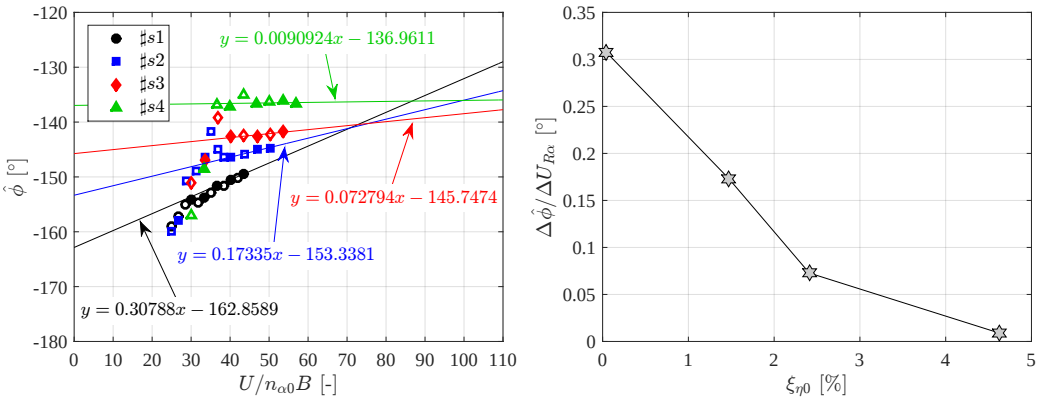

(c) Phase difference.

Figure 7.13. Evaluation of heaving ($\Delta\hat{\eta}/B$), pitching ($\Delta\hat{\alpha}$) and phase ($\Delta\hat{\phi}$) variations with respect to reduced-flow-velocity variations ($\Delta U/Bn_{\alpha 0}$) due to increments of heaving damping $\xi_{\eta 0}$, for configurations derived from $\sharp\, s1$.

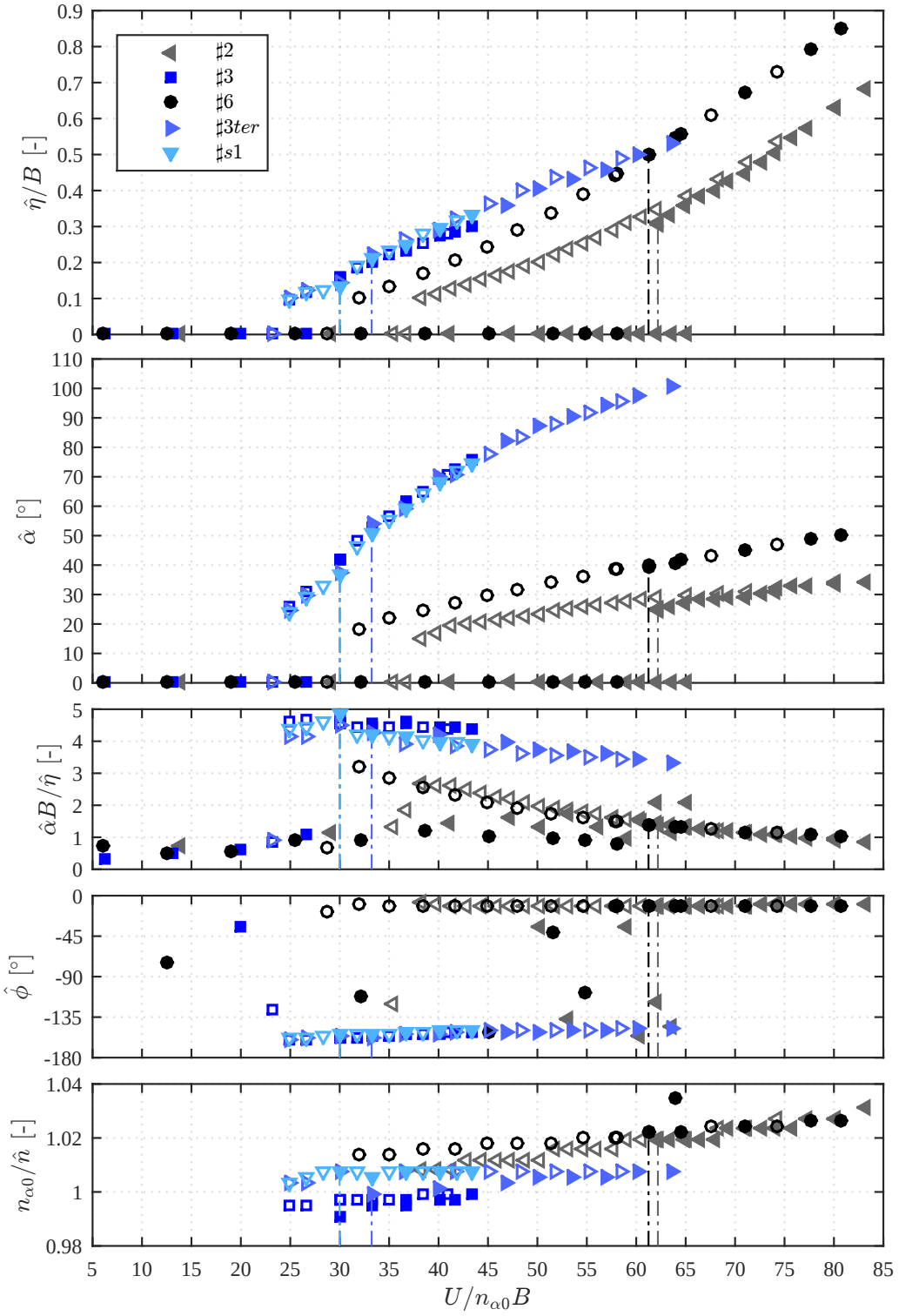

Figure 7.14. Comparisons between several similar configurations to discuss the test repeatability and sensitivity to the mass-ratio parameter. For cases ♯2 and ♯6: $\xi_{\eta 0} \approx 0.04$, $\xi_{\alpha 0} \approx 1.2$, $x_e = 0$, $\mu \approx 2700$, $x_m \approx 0$, $r_\alpha \approx 0.57$, $\gamma_n \approx 1.1$. For cases ♯3, ♯3*ter* and ♯*s*1: $\xi_{\eta 0} \approx 0.04$, $\xi_{\alpha 0} = 1.24$, $x_e = 0$, $\mu \approx 2610$, $x_m \approx 0.05$, $r_\alpha = 0.634$, $\gamma_n = 1.048$.

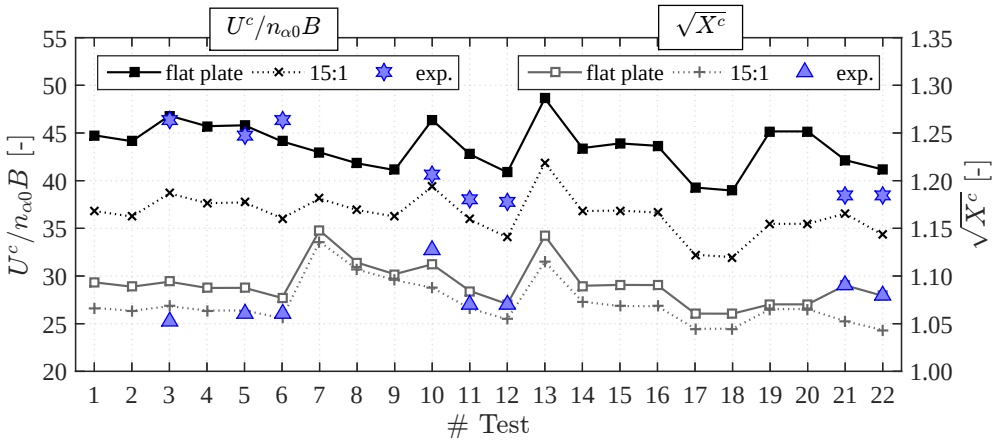

Figure 7.15. Comparison between linear flutter predictions and experimental critical conditions for some configurations tested during the Stahlbau campaign (see Table 6.2).

7.3 Comments on the critical condition and post-critical regime

7.3.1 Experimental critical conditions

The aeroelastic setup used at the Stahlbau campaign allowed spontaneous flutter oscillations, thanks to its linear mechanical properties for very small oscillation amplitudes. Thus, the experimental critical threshold simply correspond to the constant flow speed at which the system becomes unstable, while it was stable one step value of the constant flow speed before. Fig. 7.15 shows the flutter critical condition predicted by Theodorsen's linear model (see § 3.4.2.2) for the test cases reported in Table 6.2 compared to some of those experimentally obtained; some differences can be remarked. In this regard, the flutter problem is very sensitive to the mass unbalance and still-air frequency ratio, as it is clear from Fig. 6.1 when observing the predictions for $x_m \in [0; 0.1]$ and $\gamma_n \in [1.2; 1.4]$. Thus, small errors in their estimation can importantly affect the prediction of the instability threshold. Furthermore, the influence of the aerodynamic properties of the rectangular 15:1 cross section, as compared to the flat-plate assumption, is important. Nevertheless, despite the non-negligible approximations introduced in the flutter-derivative model (see § 6.2.1), the results show that this approach allows a better agreement with the experiments in the case of mass-unbalanced configurations (#10 to #12).

In all the configurations tested during SESSION I and SESSION II at the CRIACIV wind tunnel (results related to SESSION III are discussed in § 8.2), the theoretical (calculated with the flat-plate assumption of Theodorsen's model) and experimental critical conditions are in good agreement (Fig. 7.16). In this case, the experimental critical condition was identified through a systematic procedure, which introduced initial conditions of different amplitudes and at different flow speeds before the theoretical critical velocity. Thus, the instability onset corresponded to the value of flow speed at which the motion builds up after the release of the smallest initial condition. It is worth highlighting that, in the case of configurations characterised by $\gamma_n \lesssim 1$, the instability threshold seems to lies close to the change of slope between the sub-critical and the post-critical branch (*e.g.* ♯1 in Fig. 7.8 and ♯s1 in Fig. 7.10). This behaviour probably suggests a slightly different excitation mechanism in the two regimes.

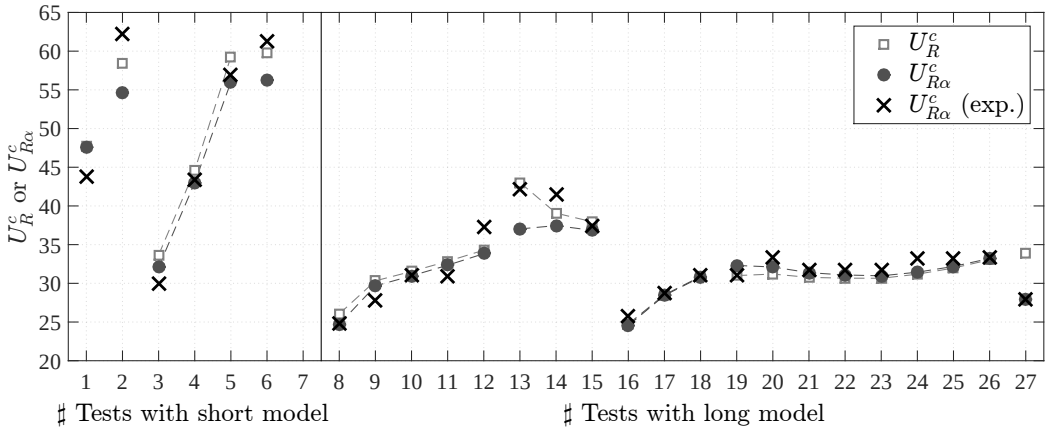

Figure 7.16. Comparison between linear flutter predictions and experimental critical conditions for some configurations tested during the SESSION II in the CRIACIV campaign (see Tables 6.3 and 6.4).

7.3.2 Sub-critical actractor basin

Fig. 7.17 and Fig. 7.18 show some time histories of the system response to different initial conditions, for the configurations #10 and #12 with positive mass unbalance and respectively $\xi_{\eta 0} = 0.07\%$ and $\xi_{\eta 0} = 5.67\%$.

The sub-critical nature of the bifurcation is apparent in the figures, showing a stable branch below the critical threshold for decreasing wind speed, in agreement with previous results [19]. This sub-critical branch is particularly remarkable for these configurations with a positive mass unbalance, where the system is able to oscillate down to about $0.85U^c$, featuring a modulated steady-state response (lighter background signals (b) in Fig. 7.17 and signals (c)-(d)-(e) in 7.18). The path of the unstable solution branch, which separates rest positions and sub-critical branch, can be outlined observing the system response following initial condition of different amplitude. Comparing the amplitudes of the initial conditions, configuration #12 ($\xi_\eta = 5.67\%$) seems to have the separating branch closer to the zero-amplitude solution.

It is also worth highlighting that, in the case of low damping (#10), the transition from the zero-amplitude branch to the non-null-amplitude branch is more complicated, showing an intermediate steady state (isolated point in correspondence of the instability threshold in the amplitude-velocity diagrams) with a smaller amplitude of oscillation. The existence of other equilibrium states in the vicinity of the critical condition is also supported by the time history following the perturbation described by the dark-foreground signal (c) in Fig. 7.18: as compared to the larger-initial condition case, the system oscillates with nearly the same heaving amplitude but with a significantly lower pitching amplitude.

7.3.3 Recurring features of the post-critical regime

Generally in the tests, long build-ups were required to reach stable LCO regimes, especially for symmetric configurations where neither a stiffness nor a mass eccentricity promote the instability. This behaviour is clarified in Fig. 7.19, which considers the system response of two different configurations, namely one symmetric (♯6) and the other with mass unbalance (♯3). It is possible to identify three regions of oscillation regimes:

A) Exponentially growing oscillations, which can be approximated through the linear theory.

B) Transitory regime in which the nonlinear self-excited loads adjust the motion and, in particular, the phase and amplitude ratio (modulation), driving the system to the next item C).

C) Steady-state oscillation at the limit cycle.

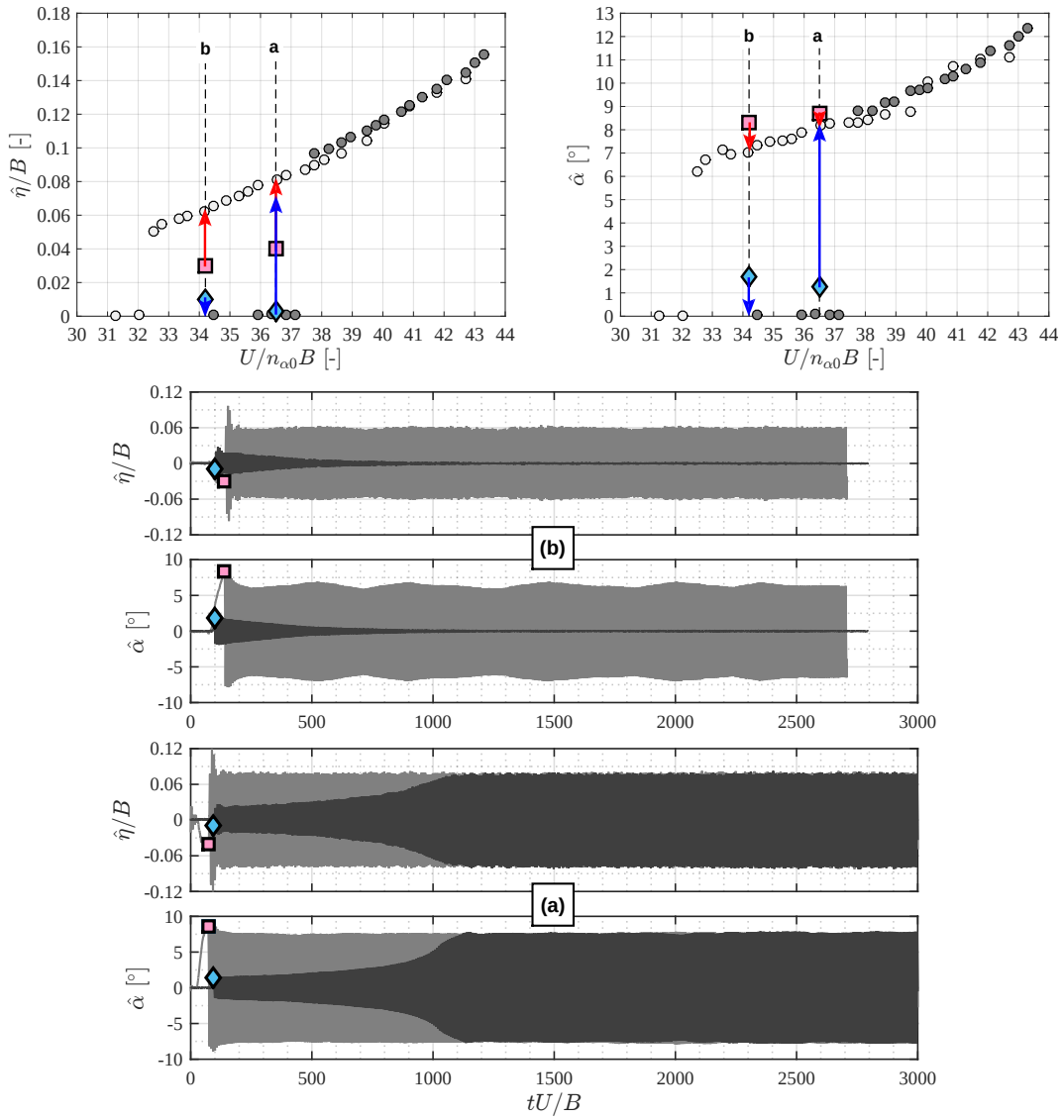

Figure 7.17. Time histories of the oscillations following the release of different initial conditions, imposed mainly in the pitching DoF, for the configuration with positive mass unbalance and increased damping (#12). Lighter background signals correspond to larger initial conditions (identified with the squared markers), while darker foreground signals correspond to smaller initial conditions (identified with the diamond markers).

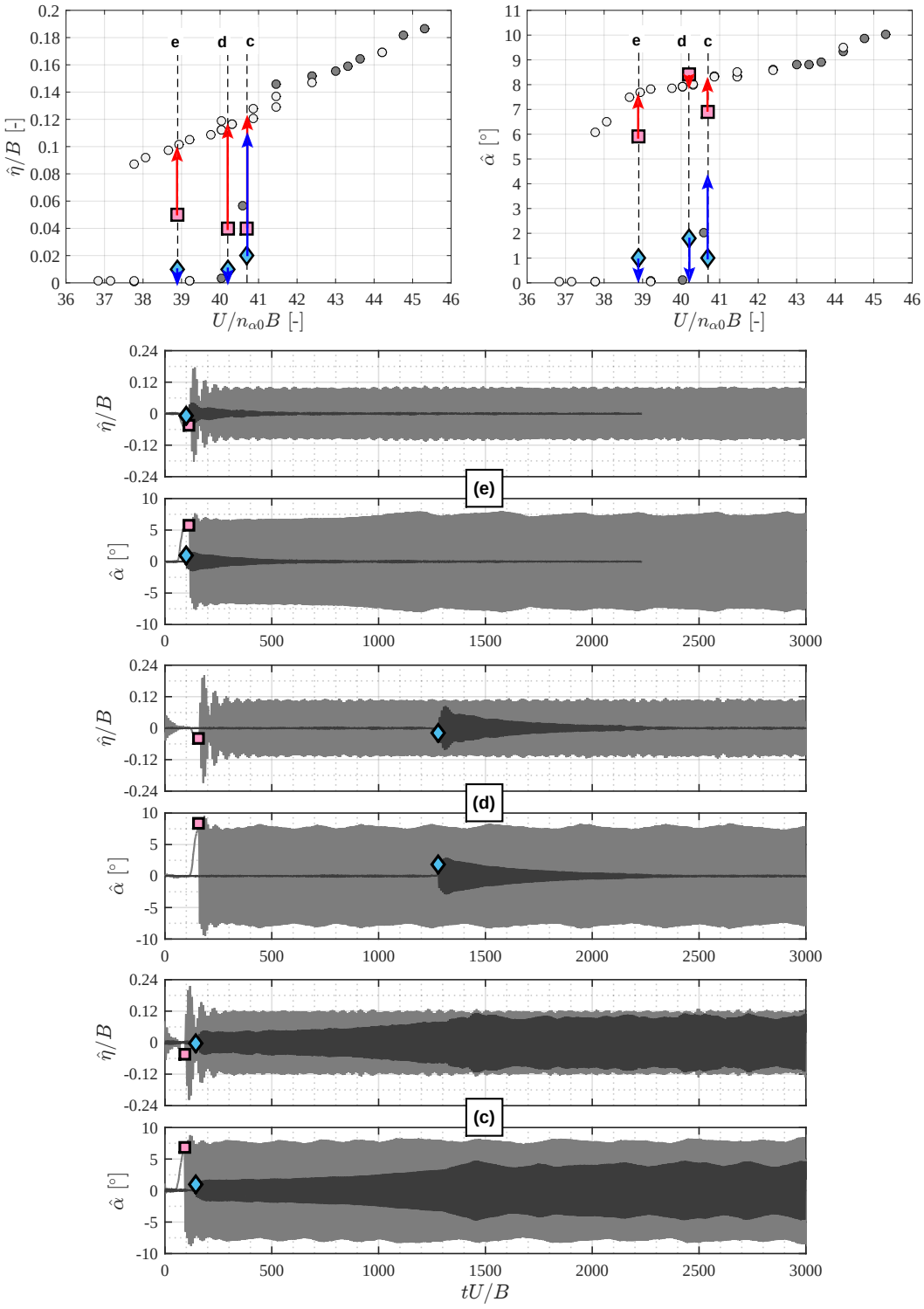

Figure 7.18. Time histories of the oscillations following the release of different initial conditions, imposed mainly in the pitching DoF, for the configuration with positive mass unbalance (#10). Lighter background signals correspond to larger initial conditions (identified with the squared markers), while darker foreground signals correspond to smaller initial conditions (identified with the diamond markers).

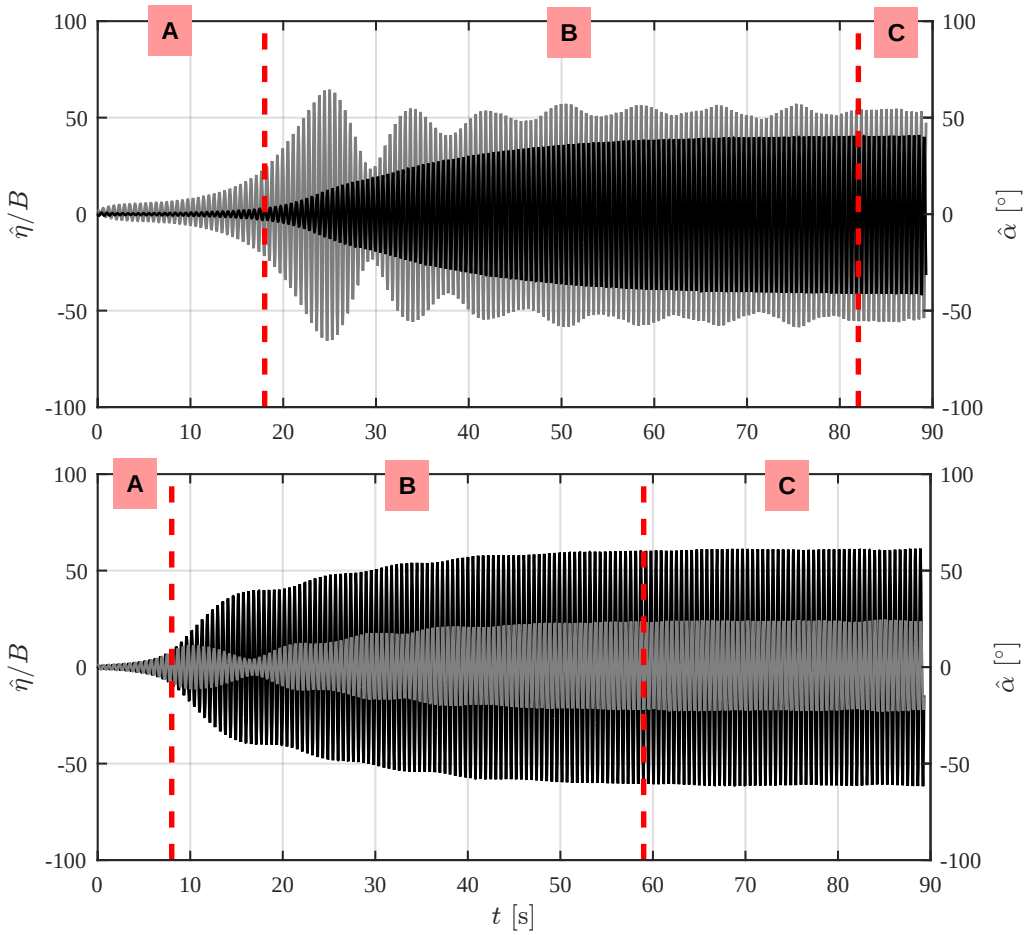

Figure 7.19. Build ups of a symmetric configuration (♯6, in the top side) and a mass unbalanced configuration (♯3, in the bottom side), with identification of the exponential growth (A), transitory regime (B) and steady-state oscillations (C).

Fig. 7.19 shows also that $x_m \neq 0$ produces a shorter transitory regime and a faster motion adjustment, confirming the more unstable behaviour of the mass-unbalanced configurations.

Observing all figures about amplitude-velocity diagrams collected so far in §7, it is apparent that the post-critical regime of flutter shows some dominant recurring features, as outlined in Fig. 7.20:

a - Marked jump at the instability threshold in both heaving and pitching DoFs.

b - Almost constant slope of the post-critical branch of the motion parameters.

c - Weak modification of slope and trend in the sub-critical branch.

d - Sub-critical branch that is stable down to flow speeds in the range from 0.7 to 0.85 times the critical flow speed U^c.

e - High gradients in the variations of the motion characteristics with increasing the heaving damping.

f - The 'shape' of the curves of the motion parameters with the flow speed is not distorted by varying the dynamic parameters, that is considerations from (a) to (e) continue to be valid for different sets of parameters.

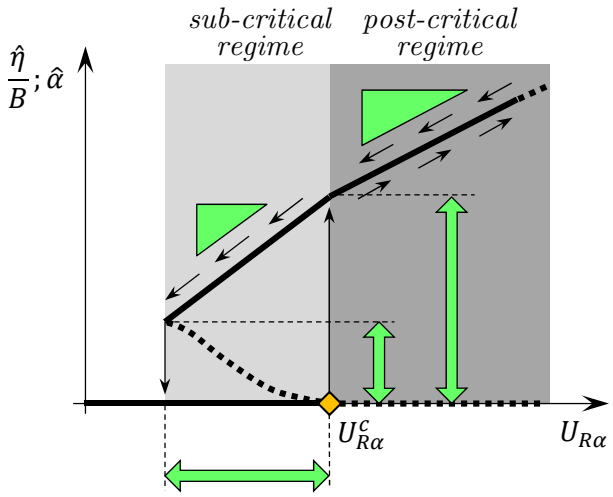

Figure 7.20. Recurring dominant features of the post-critical regime of flutter for both heaving and pitching DoFs.

7.4 Energy-harvesting performances

Before discussing the results in terms of energy-harvesting performance, it is worth pointing out that these preliminary experiments were mainly designed according to the characteristics of wind-tunnel facility and setup, with the aim at performing as reliable as possible post-critical measurements. Thus, although the linear analyses suggested optimal configurations, it had not been possible to calibrate the system for power generation purposes as will. In particular, too much high values of the reduced critical wind speed were present due to the high values of the mass-ratio parameter (μ), and considerably reduced the performance.

7.4.1 Selected configurations with 15:1 model

Considering the main configurations for energy-harvesting applications, that is #12 with positive mass unbalance and #22 with positive stiffness eccentricity, the system performances are shown in Fig. 7.21 in term of extraction factor Γ'_η and global performance factor Γ_η. They are calculated by setting $U_R = U_{R\alpha}\ n_{\alpha 0}/\hat{n}$ in Eqs.(4.8) and (4.18) respectively. Assuming a linear trend of the LCO motion properties ($\hat{\eta}$, $\hat{\alpha}$, $\hat{\phi}$, $\hat{n}$), as suggested by the experimental results, the system performance is extended to higher reduced velocities. The path of the extraction factor curve confirms the typical presence of an optimal value.

The complementary features of configurations #12 and #22 have to be highlighted. In fact, for the investigated set of parameters, the mass unbalanced configuration (#12) is more efficient in the lower range of reduced flow velocities, while the configuration with stiffness eccentricity (#22) seems to operate better at higher flow speeds. In the perspective of power-generator design, it would be possible to conceive modules or arrays, comprising different oscillating elements with complementary characteristics in order to harness as much as possible energy from the flow. This should also allow to operate in various scenarios, installation typologies and environments.

Specific comments are worth for the left-hand side of Fig. 7.21, which shows the evolution with the reduced flow speed of the parameter β of Eq. (4.9). As it is clear from Eqs. (4.8) and (4.17) respectively for the extraction (Γ'_η) and the conversion (Γ''_η) factors, these directly depend on β. Large values of β means lower available energy that can flow in the conversion apparatus. In fact, in the configurations with mass unbalance, a large amount of energy remains in the mechanical system, circulating between the DoFs, and cannot be transformed into usable power (already outlined in § 4.1). This means that the position of the mass centre has to be carefully chosen and its eccentricity has to be limited to small values, in order not to compromise the amount of convertible energy. The comparison between Γ'_η

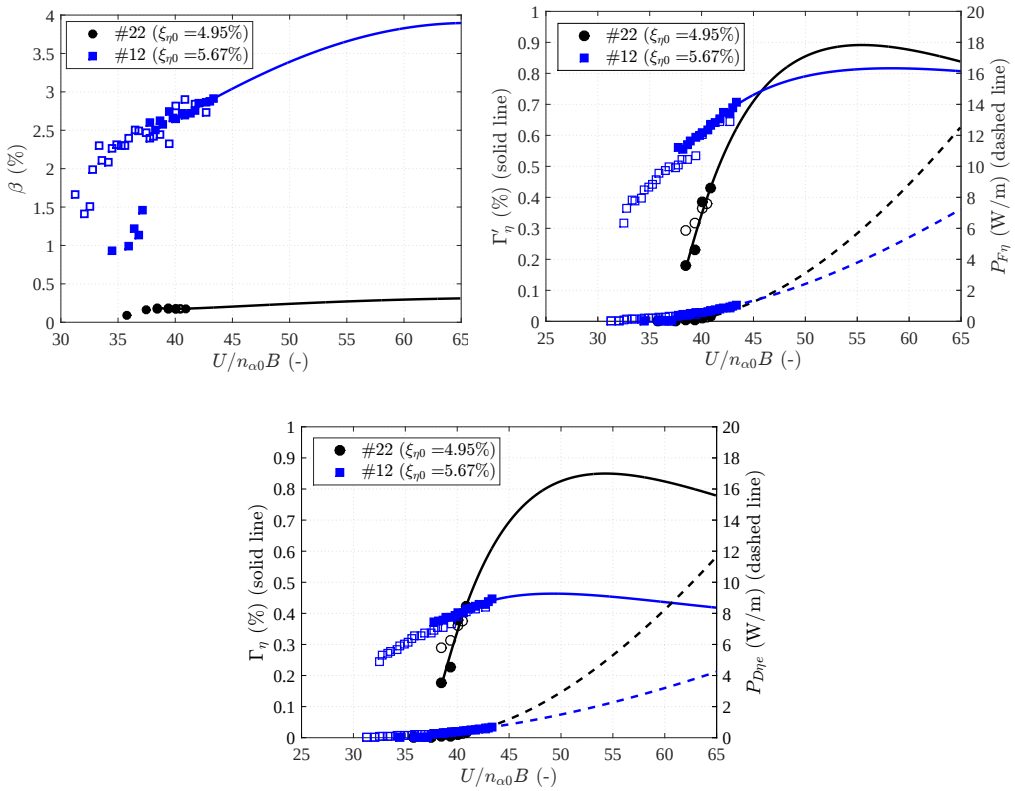

Figure 7.21. Evolution of parameter β (up-left), extraction factor Γ'_η with the respective forcing power $P_{F\eta}$ (up-right), and global factor Γ_η with the respective output power $P_{D\eta e}$ (down), for the configurations with positive eccentricity of mass and elastic centres. [Stahlbau Institut campaign]

and Γ_η in Fig 7.21 clarifies this point, as shown by the larger reduction of the Γ_η values for configuration #12, which is characterised by a small mass unbalance.

7.4.2 Selected configurations with 25:1 model

Considering the configurations analysed in § 7.2, that is ♯3 and ♯s1 with positive mass unbalance and the symmetric configuration ♯6, their energy-harvesting performances are evaluated. The performances are shown in Fig. 7.22, Fig. 7.23 and Fig. 7.24 and are reported in terms of the performance parameters explained in § 1.2.1 and § 4, that is: extraction factor Γ'_η; forcing power of the self-excited lift P_η; conversion factor Γ''_η; equivalent damping of the static mass unbalance β; global performance factor $\Gamma_\eta = \Gamma'_\eta \cdot \Gamma''_\eta$; output power to be introduced in a next electric circuit $P_{D_{E\eta}}$.

The CRIACIV setup allowed to test a wider range of flow speeds beyond the instability threshold. As apparent in both Fig. 7.22 and Fig. 7.23, the experimental amplitude-velocity diagrams contain enough flow speed measurements to experimentally verify the presence of the maxima in the Γ'_η and Γ_η curves. The shape of these curves well agrees with those reported in literature.

Observing the shape of the Γ'_η curves, in both Fig. 7.22 and Fig. 7.23, it is interesting to note a variation of the optimal operative flow speed at which the maximum of Γ'_η occurs (here defined as $U_{R\alpha}^{opt}$) with increasing the heaving damping. In particular, it moves toward higher velocities, and it seems to follow a nonlinear trend with increasing $\xi_{\eta 0}$. Moreover, the reduction of Γ'_η with increasing $\xi_{\eta 0}$ indicates a reduction of the ability of the mechanical system to capture energy from the flow, since in this case it oscillates with smaller amplitudes.

Similar considerations can be made observing the evolution of the global performance factor Γ_η in both Fig. 7.22 and Fig. 7.23. By contrast, while $U_{R\alpha}^{opt}$ continues to increase with increasing $\xi_{\eta 0}$, the magnitudes of Γ_η increase too, since the energy flowing in the dampers (or equivalently in a virtual transducer of the conversion apparatus) is larger.

It is worth observing that the values of $U_{R\alpha}^{opt}$ evaluated in the Γ'_η curves differ to those identified for the Γ_η curves, being the latter higher. This result suggests that the optimization should be conducted directly in terms of Γ_η instead of Γ'_η, in order to be sure to correctly identify the optimal configuration. Moreover, the conversion factor Γ''_η seems to linearly increase with $U_{R\alpha}$ after the critical condition, meaning that the system is improving its operation as power generator for larger oscillation amplitudes. This fact is essentially due to the evolution of the β parameter. Since it reduces with increasing $U_{R\alpha}$, the energy exchanged between heaving and pitching DoFs is lower at large oscillation amplitudes. From a different point of view, a larger exchange of energy between the two DoFs is required at low flow speeds, closer to the instability threshold, to self-sustain the steady-state motion; the heaving and pitching DoFs help each others.

The performance of configuration ♯7, that is the symmetric configuration ♯6 in which the heaving damping was set to $\xi_{\eta 0} = 9.52\%$, is markedly higher than the those of the other configurations. This is due to absence of the static mass unbalance that did not subtract energy in the heaving DoF, producing $\beta = 0$ and $\Gamma''_\eta \approx 1\%$ (see Eq. (4.17)). Moreover, this configuration showed lower values of the amplitude ratio ($B\hat{\alpha}/\hat{\eta}$ are about 1/3 of those of ♯s4 and about 1/5 of those of ♯4), producing a better attitude for energy-harvesting applications. However, this configuration was not able to start spontaneously the motion, since no flutter instability can occur for that given set of governing parameters and high heaving damping. Thus, external perturbations are necessary to trigger the motion, and this can complicate the design of the following device technology.

7.4.3 Additional comments

- In the common practice of civil/aeronautical design of structures, a sub-critical instability is a dangerous mechanism that has to be carefully avoided. Some authors maintained this way of thinking for energy-harvesting system too (*e.g.* [8, 6]), stating that supercritical bifurcation has to be preferred to limit the damage of the generator. Nevertheless, energy-harvesting systems based on flow-induced excitations are intentionally designed to exhibit large-amplitude LCOs, so that the sub-critical branch can be considered as an additional range of operative flow velocity, which can widen the harnessing capability of such systems. The only drawback of the sub-critical range is that the system can be operative only if the flow speed is reduced from post-critical values, or if the motion is artificially triggered through initial conditions (see Fig. 7.18 or Fig. 7.17).
- The possibility to activate the motion through the buffeting of incoming turbulence of real flows or wake flows could be a valuable alternative, which should be investigated in the future.
- The destabilizing effect of damping suggests the possibility to extract higher levels of energy from heaving vibrations by simply increasing the heaving damping. An optimal value of $\xi_{\eta 0}$ is expected, given the upper bound represented by the over-damped configurations, in which oscillations cannot occur.
- The positions of stiffness and mass centres play as tuning parameters in the design of more unstable, thus more efficient, configurations (*i.e.* with a lower reduced critical flow speed).
- As a general remark for the design of generators based on fluid-elastic phenomena, the structural damping $\xi_{\eta 0s}$ should be kept as low as possible.
- Since the performance evaluation is arranged using dimensionless parameters, the flutter-based generator can be designed accordingly. It has to be provided that the resulting design variables (*e.g.* model size, mechanical frequencies, inertias distributions,

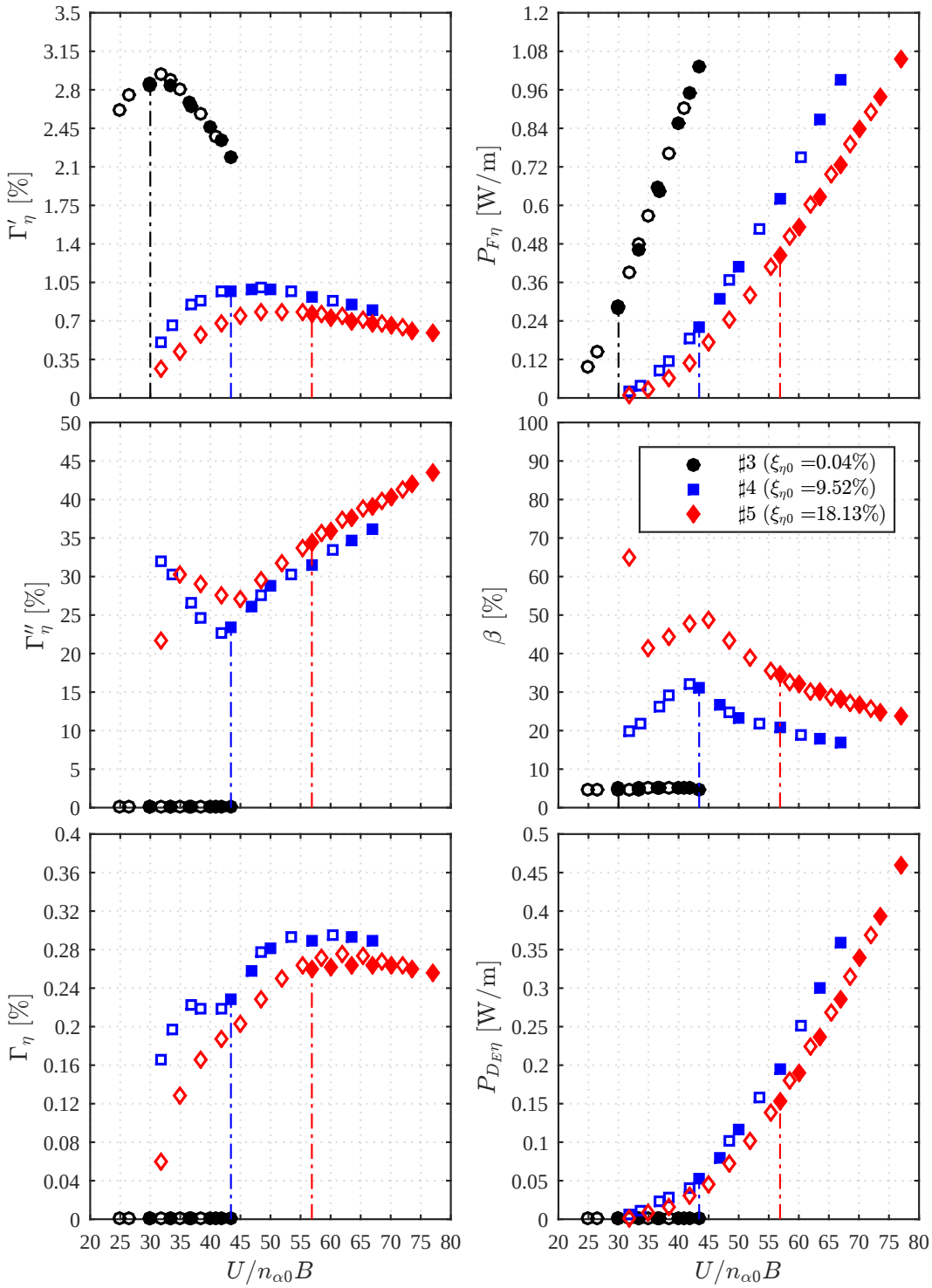

Figure 7.22. Performance evaluation for configurations with a downstream mass unbalance of $x_m = 0.057$ and different heaving damping levels [CRIACIV campaign].

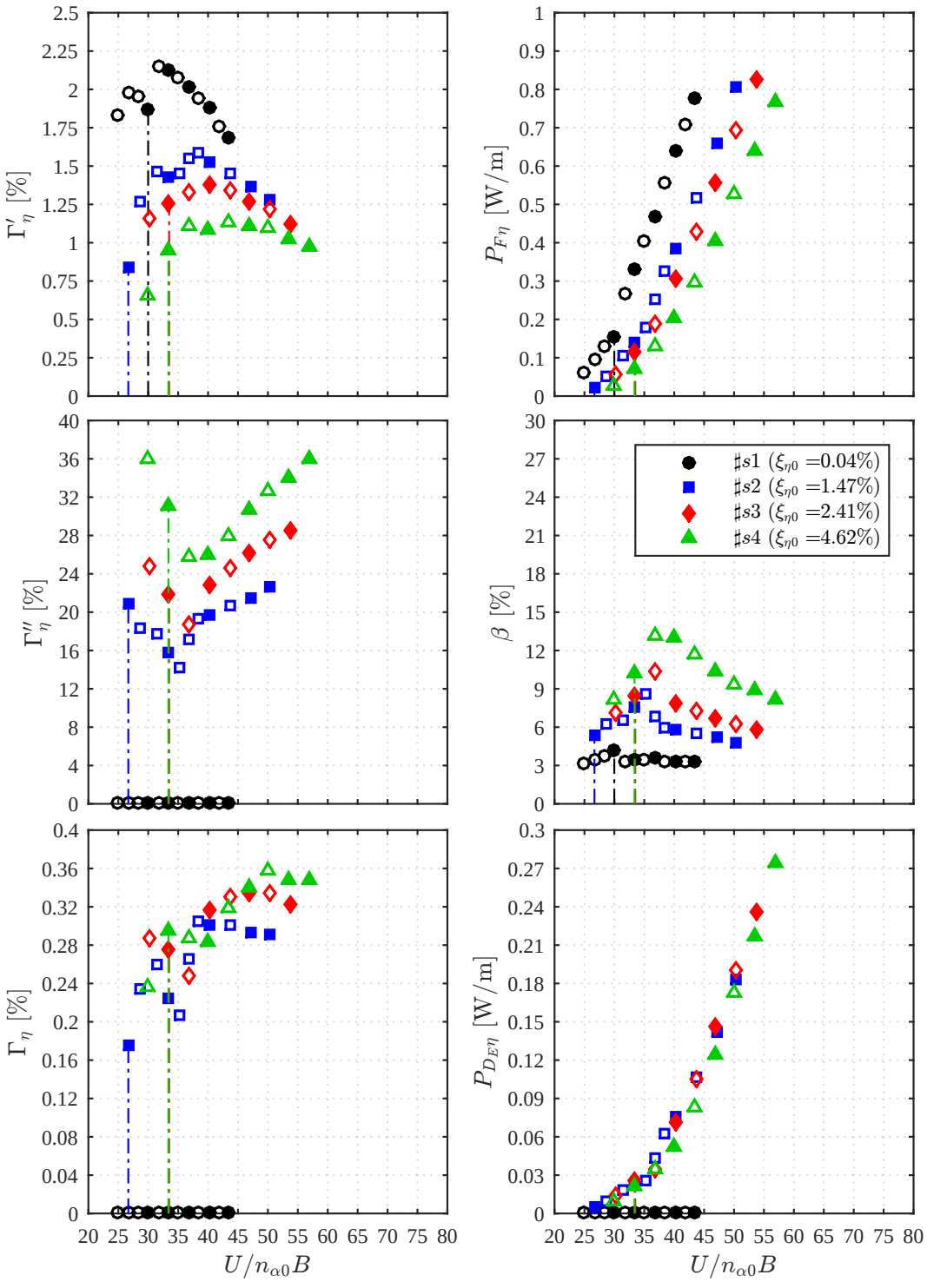

Figure 7.23. Performance evaluation for configurations with a downstream mass unbalance of x_m = 0.039 and different heaving damping levels. [CRIACIV campaign]

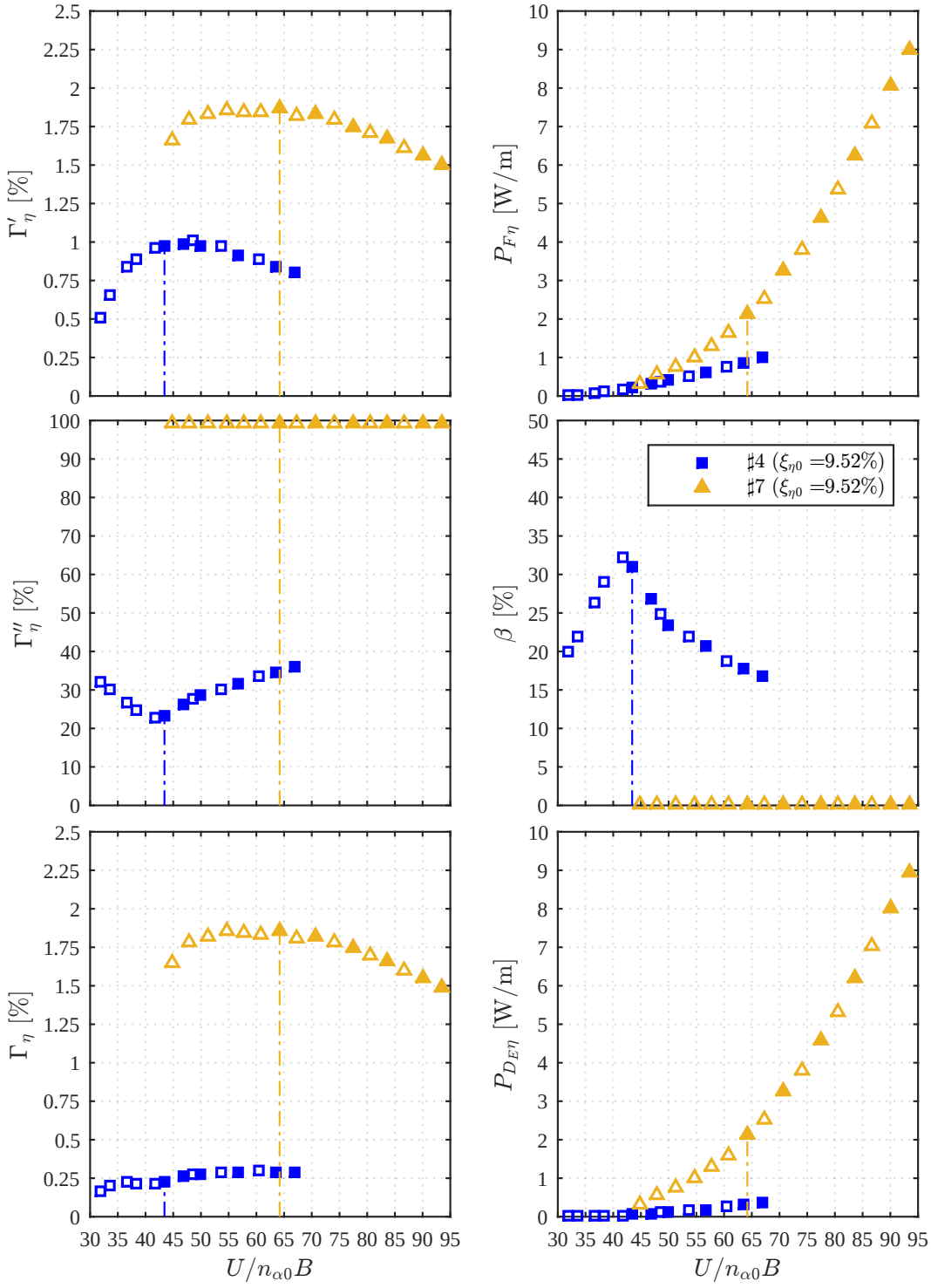

Figure 7.24. Performance comparisons between a symmetric (#7) and a mass-unbalanced (#4, with x_m = 0.057) configuration, both with similar heaving damping ($\xi_{\eta 0}$ = 9.52%). [CRIACIV campaign]

etc.) have physical meaning and are technically feasible. Considering for example configuration ♯7, which showed the highest performance, 5 W/m can be converted into electricity when the system oscillates at $U/n_{\alpha 0}B \approx 77$. Thus, it can be conceived a large-size system, oscillating at low frequency, or a small-size system, oscillating at high frequency, which both provide the same output energy. Moreover, considering for example a wind flow[3] with a service speed of about 2 m/s (typical of urban environments), the dimensional product $n_{\alpha 0}B$ should be about 0.026 m/s. Thus, assuming a frequency of oscillation or 1 Hz, the section chord of the device should be about 26 mm and would provide about 5 W/m at 2 m/s wind speed.

[3]The wind flow is considered instead of water currents, because of the tested values of mass-ratio parameter μ that are more typical for air-flow installations. Feasible water-flow installations usually show much lower values of μ

Chapter 8

Study of optimal configurations

8.1 Systematic analysis through linear theory

The frequency-domain linear model presented in § 3.4.2.2 is here applied to look for optimal configurations, and to explore the influence of the governing parameters of the flutter problem (see § 3.2) on the critical-condition characteristics. The parameters describing the instability threshold are critical reduced velocity U_R^c (this formulation is here used instead of $U_{R\alpha}^c = U_R^c \cdot n^c/n_{\alpha 0}$), dimensionless flutter frequency $\sqrt{X^c} = n_{\alpha 0}/n^c$, phase difference ϕ^c and amplitude ratio $(B\alpha/\eta)^c$. Among them, the critical reduced velocity is the most important parameter for the performance factors (see § 4.1.2).

The 'optimal' means a configuration with the lowest value of the critical reduced velocity. However, it is to note that this optimal condition relates the system about the instability threshold, and may differ to the optimal condition for a system that performs large-amplitude LCOs. Nevertheless, the performance is mainly affected by the flow speed at which the system operate (see Eq. (4.18)), thus the parameter U_R^c is expected to importantly influence the optimal condition in the post-critical regime as well.

The setting up of this systematic parametric linear analysis takes into account the results of the first experimental campaigns (Stahlbau campaign and SESSION I and SESSION II at CRIACIV), as discussed in § 7. The investigated sets of governing parameters were imposed to be in specific ranges, which were selected according to the values of the experimental tests, as reported in Table 8.1. In this way, optimal and realistically feasible configurations can be designed.

The results are shown through two-dimensional contour maps, plotted with respect to the mass-unbalance parameter (x_m) in the abscissa and the elastic eccentricity parameter (x_e) in the ordinate. Among all, they showed a key role as 'tuning' parameters for the optimal configuration, revealing minimum points of U_R^c that are identified with the superscript $*$ (*e.g.* U_R^*). Considering the pairs $(x_m; x_e)$ at which corresponds U_R^*, the other parameters of the optimal critical condition are identified in the respective maps as $\sqrt{X^*}$, ϕ^* and $(B\alpha/\eta)^*$. Then, the evolution of those optimal parameters with respect to increments of heaving damping $\xi_{\eta 0}$ is also showed, understanding the influence of the (simulated) energy-extraction process.

It is worth highlighting that the spacing of the parametric domain was set as small as possible according to the performance of the processor used in the numerical analyses. Nevertheless, due to the coarse spacing of the domain some 'jumps' appears in displaying the results.

8.1.1 Refined study on previously tested configurations

A more specific investigation was conducted by considering sets of parameters typical of the experimental configurations. According to Table 8.1, the configurations investigated during the campaign at Stahlbau Institut can be identified in $C2337$, while $C1221$-$C1223$-$C1224$

Table 8.1. Values of the governing parameters used in the linear analysis. A code-value combination identifies an investigated configuration, *i.e.* $C1223$ stands for the configuration with $\xi_{\alpha 0} = 1.2\%$, $\mu = 2650$, $r_\alpha = 0.60$ and $\gamma_n = 1.05$.

Parameter \ Code value	1	2	3	4	5	6	7
$\xi_{\alpha 0}$ [%]	1.2	0.15	0.6	-	-	-	-
μ [-]	1600	2650	950	-	-	-	-
r_α [-]	0.34	0.60	0.85	-	-	-	-
γ_n [-]	0.95	1.00	1.05	1.10	1.15	1.20	1.25

can well represent the configurations investigated during SESSION I and SESSION II at the CRIACIV wind tunnel.

The aim is to compare the position, in the parametric space, of the tested configurations with respect to those of the optimal configurations, in terms of critical reduced velocity U_R^c. Then, the observation of the instability features described by $n_{\alpha 0}/n^c$, ϕ^c and $(B\alpha/\eta)^c$ can also improve the identification of preliminary design guidelines, since they give information on the incipient-motion characteristics.

The results shown in Fig. 8.1 are related to the Stahlbau campaign. Fig. 8.1a, obtained for $\xi_{\eta 0} = 0$, explains that optimal configurations would require elastic-axis positions close to the trailing edge, as previously discussed in § 6.2.2, and this requirement dominates for all values of x_m. However, low values of $\xi_{\eta 0}$ do not allow energy extraction, thus high-damping levels have to be considered instead. As the heaving damping increases, the mass unbalance x_m becomes extremely important, and a narrow band of low U_R^c values (dark valley) appears around $x_m \approx 0.09$. Fixing the attention to the point in both Fig. 8.1a and Fig. 8.1b identified by $x_e = 0$ and $x_m \simeq 0.05$, the destabilizing effect of damping introduced in § 7.1.2 and discussed in § 7.1.2 (see also Fig. 6.2 and Fig. 7.4) can be better understood. In particular, the position of the global minimum of U_R^* in the $(x_m; x_e)$ space is varying with increasing $\xi_{\eta 0}$ and different gradient modifications appear in different regions, as showed by the shapes of the isolines. Thus, although the value of the global minimum of U_R^c (called U_R^*) is not markedly varying, the local value of U_R^c in a certain point $(x_m; x_e)$ can be importantly reduced.

The results shown in Fig. 8.2, Fig. 8.3 and Fig. 8.4 relate to the CRIACIV campaign. The observations of all these figures preliminary explains the effect of the still-air frequency parameter γ_n. This parameter markedly influences the characteristics of the motion, as discussed in § 7.2.1, and this has important consequences on the position of the global minimum U_R^*. In fact, for low values of $\xi_{\eta 0}$, U_R^* is in the windward half-chord of the section for $\gamma_n < 1$ and in the leeward half-chord for $\gamma_n > 1$. Moreover, it is interesting to preliminary note the trend of the U_R^* positions in the $(x_m; x_e)$ space with increasing the heaving damping, since it moves upstream when $\gamma_n > 1$. Also in this case, U_R^* shows small mass-unbalance values, that is $x_m \simeq 0.05$. This global minimum lies again in a narrow region stretched along the x_e direction, thus confirming the high sensitivity of the system response to the x_m parameter. Taking as example the experimental configurations derived from ♯3 (see Table 6.3), the optimal configuration (having U_R^*) was close to ♯4 only, that is for $\xi_{\eta 0} \simeq 10\%$; more discussions are in § 8.1.2.

For all sets of governing parameters of Stahlbau Institut and CRIACIV campaigns, the shapes of the isolines of $n_{\alpha 0}/n^c$, ϕ^c and $(B\alpha/\eta)^c$ seem to weakly modify with increasing the heaving damping. Moreover, a good regularity of the isolines shapes is always apparent.

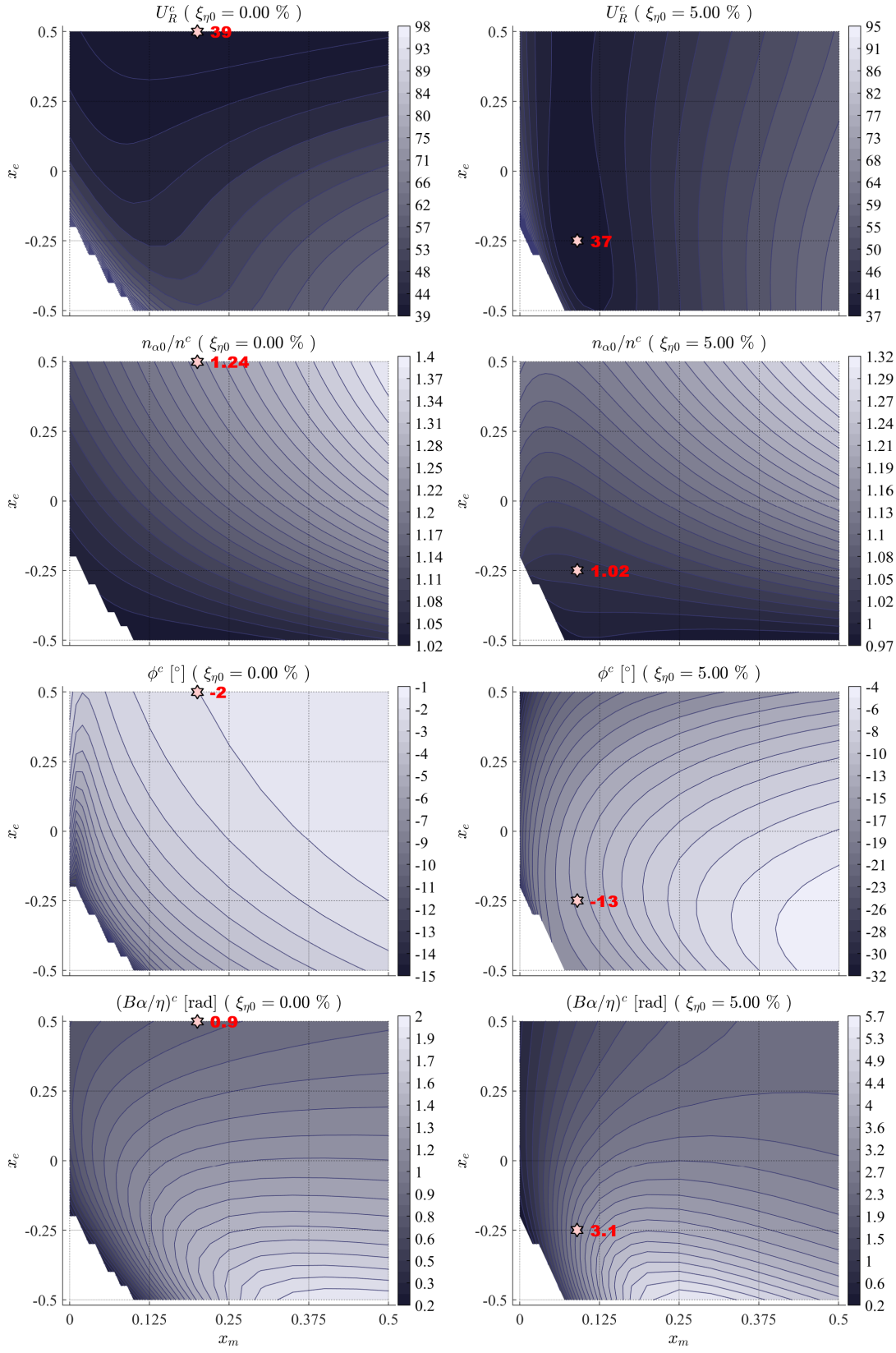

(a) $C2337$ ($\xi_{\eta 0}$ = 0%). **(b)** $C2337$ ($\xi_{\eta 0}$ = 5%).

Figure 8.1. Stahlbau Institut campaign. The other parameters are $\xi_{\alpha 0}$ = 0.15%, μ = 950, r_α = 0.85 and γ_n = 1.25.

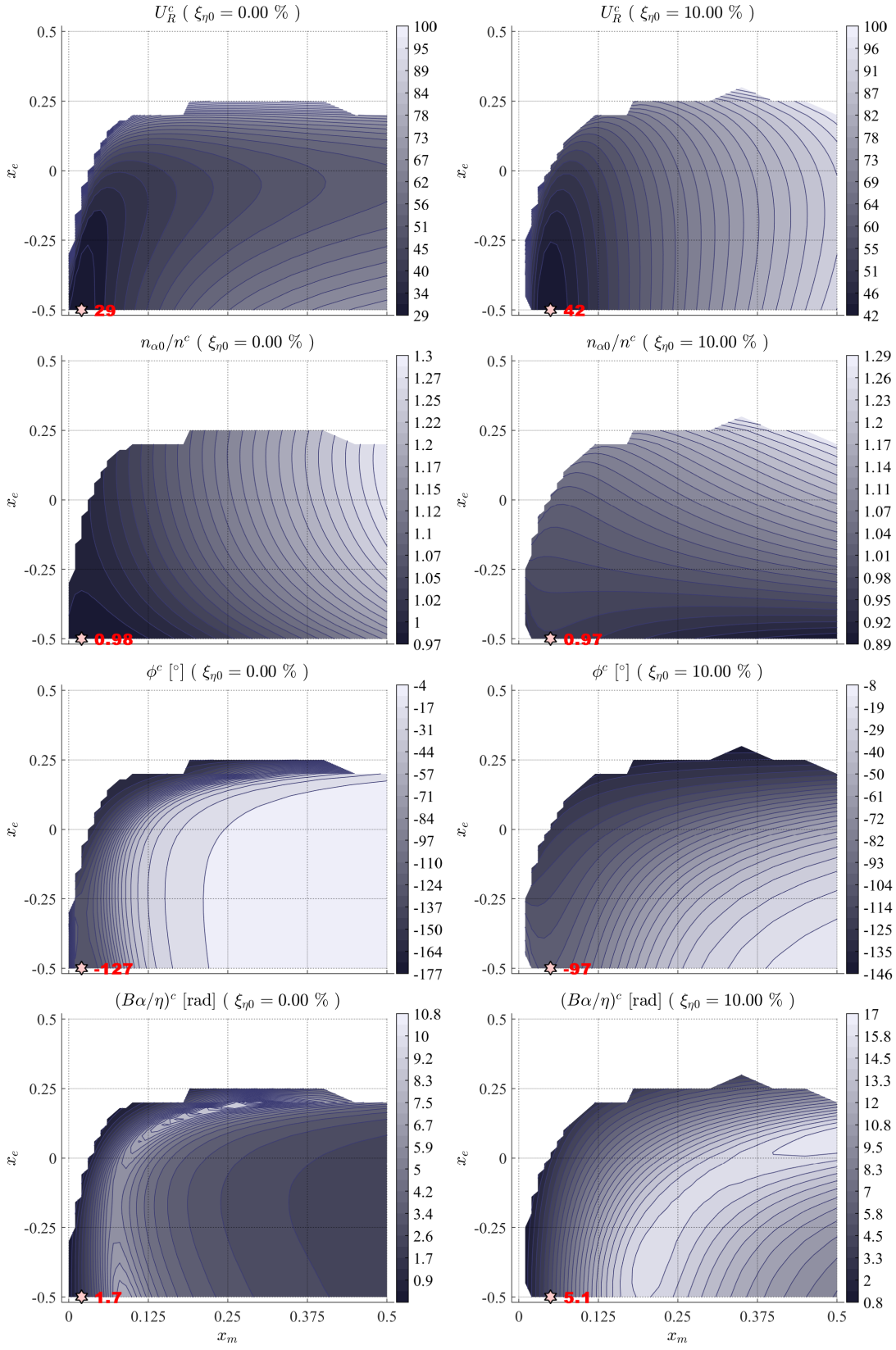

(a) $C1221$ ($\xi_{\eta 0}$ = 0%). **(b)** $C1221$ ($\xi_{\eta 0}$ = 10%).

Figure 8.2. CRIACIV campaign. The other parameters are $\xi_{\alpha 0}$ = 1.2%, μ = 2650, r_α = 0.60 and γ_n = 0.95.

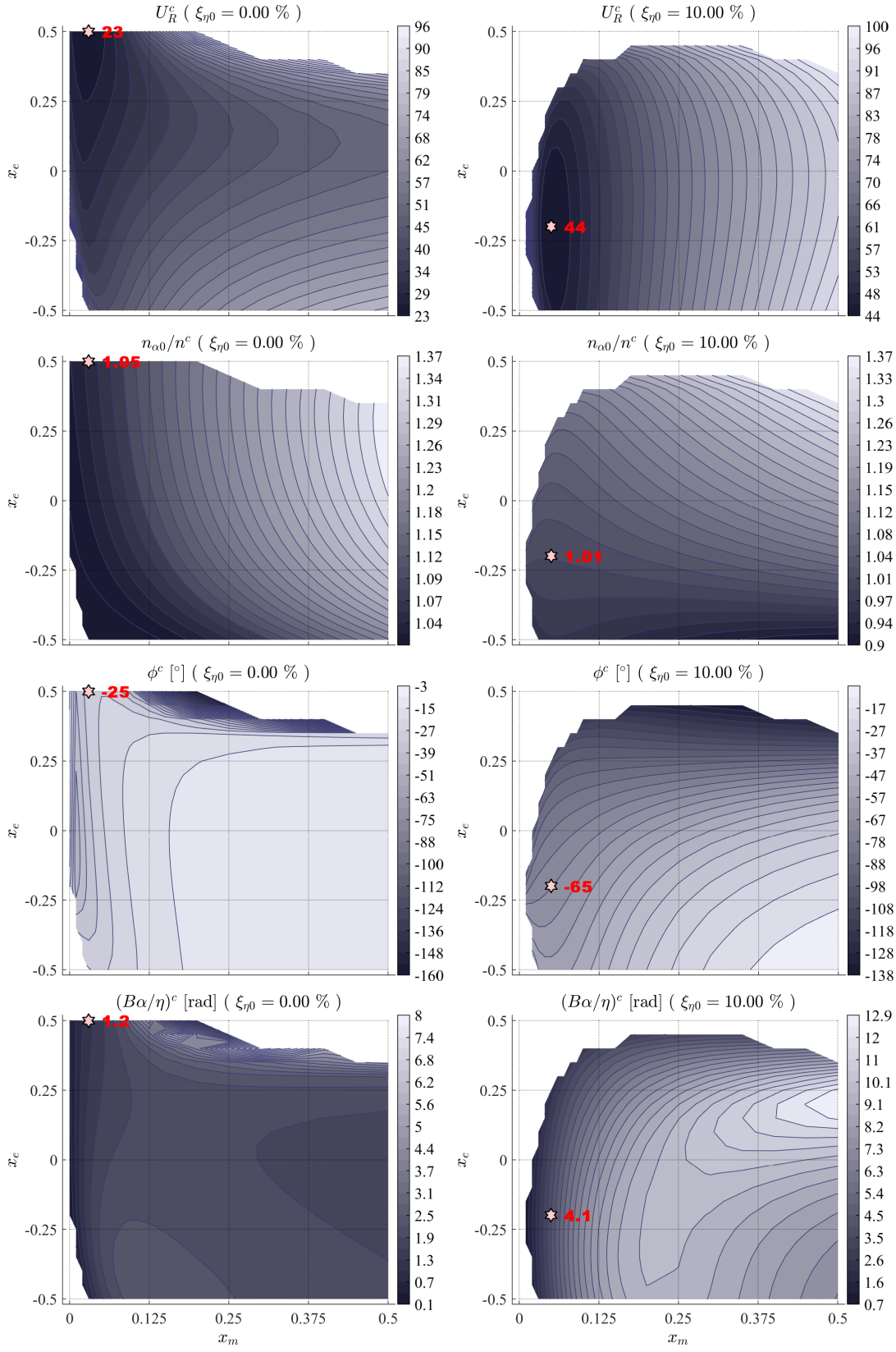

(a) $C1223$ ($\xi_{\eta 0}$ = 0%). **(b)** $C1223$ ($\xi_{\eta 0}$ = 10%).

Figure 8.3. CRIACIV campaign. The other parameters are $\xi_{\alpha 0}$ = 1.2%, μ = 2650, r_α = 0.60 and γ_n = 1.05.

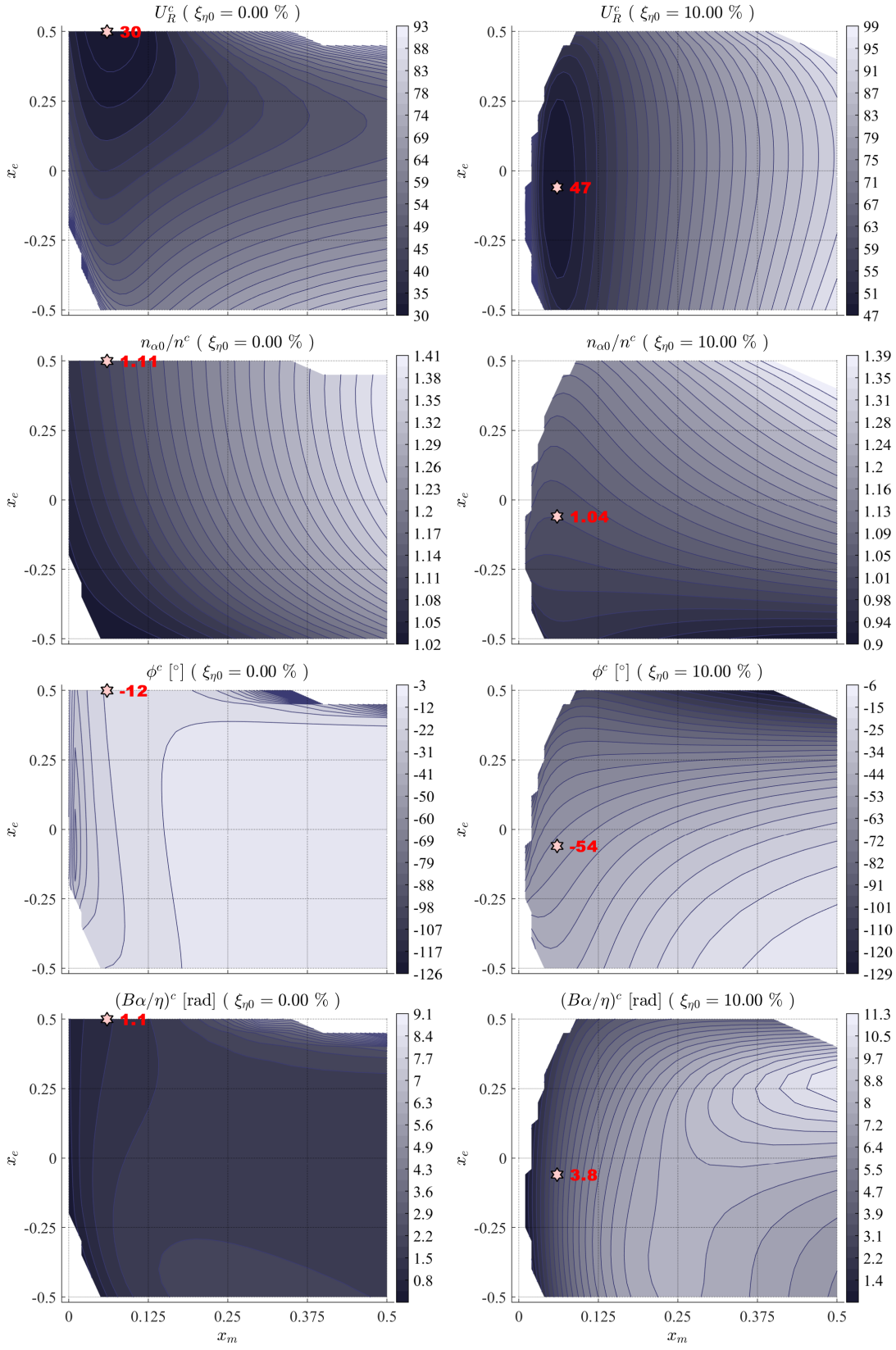

(a) $C1224$ ($\xi_{\eta 0}$ = 0%). **(b)** $C1224$ ($\xi_{\eta 0}$ = 10%).

Figure 8.4. CRIACIV campaign. The other parameters are $\xi_{\alpha 0}$ = 1.2%, μ = 2650, r_α = 0.60 and γ_n = 1.10.

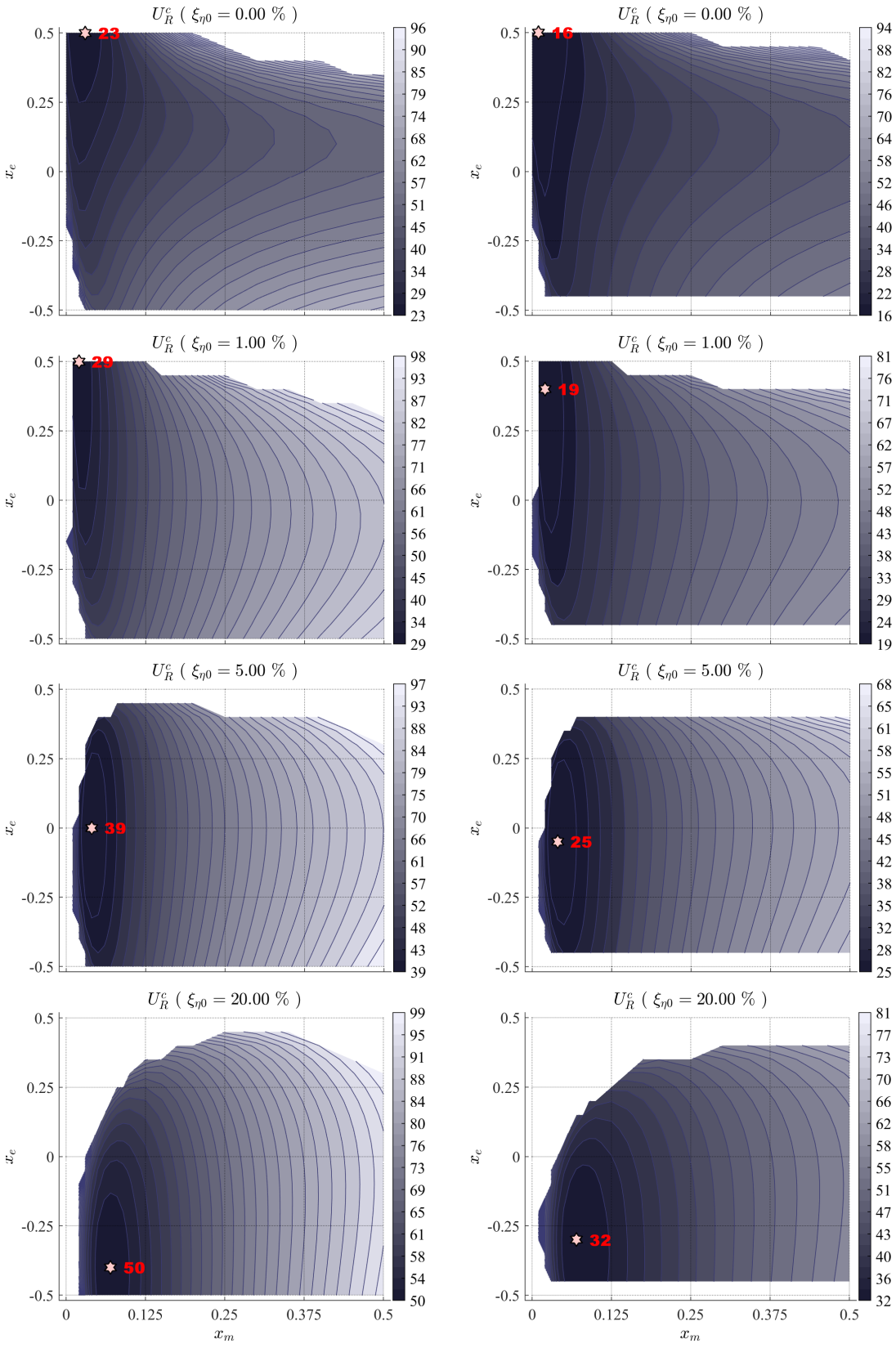

Figure 8.5. $C1223$ (μ = 2650, $\xi_{\alpha 0}$ = 1.2%, r_α = 0.6, γ_n = 1.05).

Figure 8.6. $C1323$ (μ = 950, $\xi_{\alpha 0}$ = 1.2%, r_α = 0.6, γ_n = 1.05).

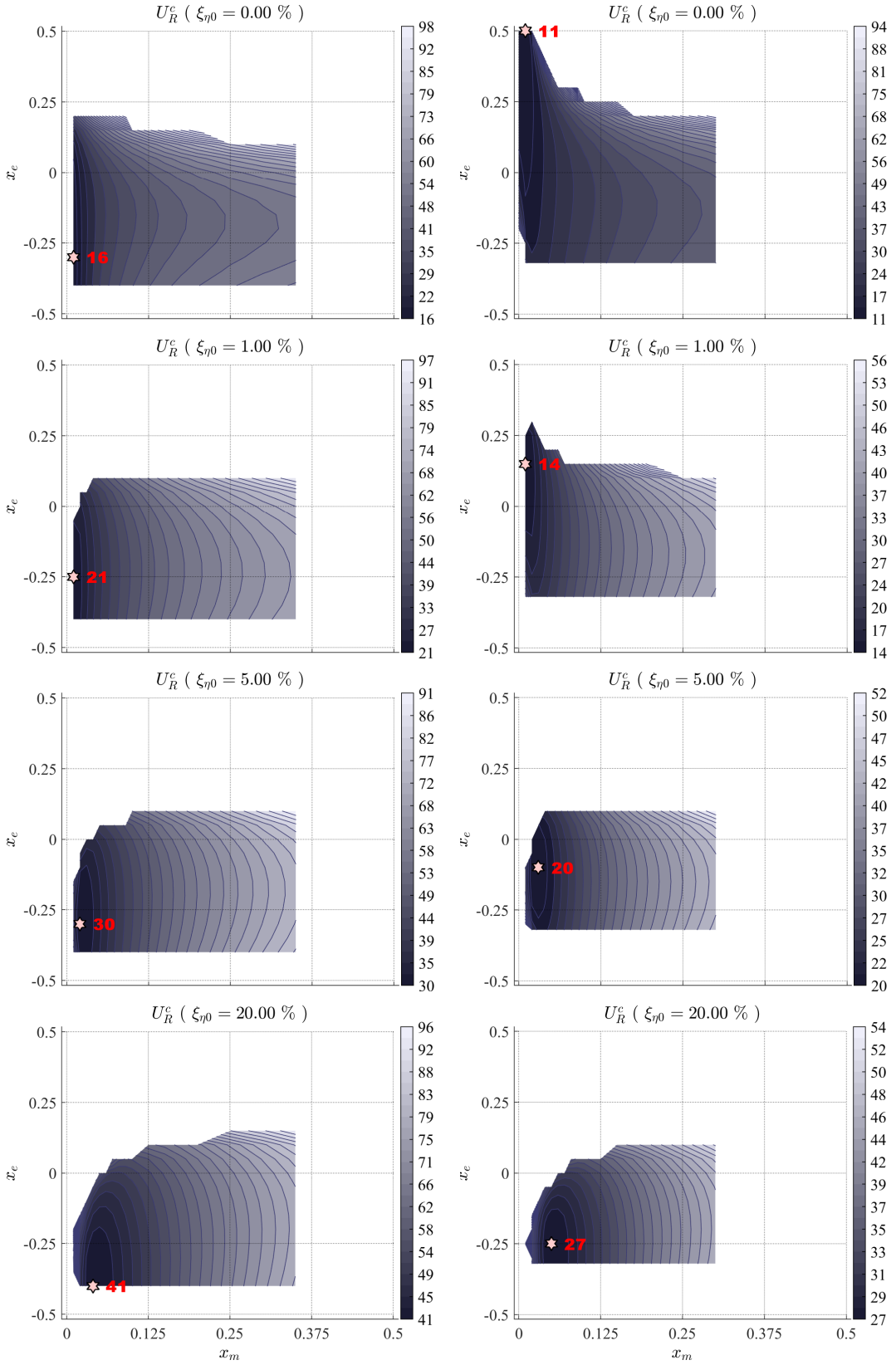

Figure 8.7. $C1213$ ($\xi_{\alpha 0} = 1.2\%$, $\mu = 2650$, $r_\alpha = 0.34$, $\gamma_n = 1.05$).

Figure 8.8. $C1313$ ($\xi_{\alpha 0} = 1.2\%$, $\mu = 950$, $r_\alpha = 0.34$, $\gamma_n = 1.05$).

8.1.2 Sensitivity to governing parameters

In this section, the influence of the dynamic parameters governing the flutter problem is discussed more in detail, examining the main results obtained for the sets of parameters according to Table 8.1, which are useful to highlight some dominant features.

Comparing Fig. 8.5 and Fig. 8.6, that is switching from $\mu = 2650$ of $C1223$ to $\mu = 950$ of $C1323$ (the other parameters are fixed), the mass ratio seems to linearly scale U_R^c, while it slightly modifies the shape of the isolines. This is in agreement with Fig. 6.1 of § 6.2.2, in which the quasi-linear evolution of U_R^c with μ was clear. Moreover, the global minimum value U_R^* can be markedly reduced by decreasing μ, only slightly distorting the $(x_m; x_e)$ position and this consideration holds for all values of $\xi_{\eta 0}$. Comparing Fig. 8.7 and Fig. 8.8, it is also possible to widen the discussion about the mass-ratio parameter influence, since μ varies from 2650 to 950 but for configurations with $r_\alpha = 0.34$. The parameter μ seems to markedly influence the system response, weakly modifying also the position of U_R^* along the x_e axis. In particular, lower μ would require optimal x_e values closer to the trailing edge. However, it is worth highlighting that this effect seems to gradually decrease as the heaving damping increases. The pairs Fig. 8.9-Fig. 8.10 and Fig. 8.11-Fig. 8.12 (about configurations $C1221$-$C1321$ and $C2221$-$C2321$), obtained by varying μ for configurations with $r_\alpha = 0.60$, $\gamma_n = 0.95$ and, respectively, $\xi_{\alpha 0} = 1.2\%$ and $\xi_{\alpha 0} = 0.15\%$, corroborate the comments about the μ influence, which are valid also for other sets of governing parameters.

Fig. 8.7 refers to $C1213$, while Fig. 8.8 refers to $C1313$, which are respectively obtained from $C1223$ and $C1323$ by reducing r_α from 0.6 to 0.34. In both cases, it is apparent that smaller values of r_α reduce the region of the $x_m - x_e$ space in which the system can get unstable. The right-hand-side limit in the x_m axis is equal to r_α, because it is not physically possible to design mass distributions in which the mass center position is larger than the polar inertia radius[1]. By contrast, the lower limit in the x_e axis may be due to too much extreme combinations of the parameters, which compromises the physical mechanism behind the classical flutter. This effect of r_α is also well apparent observing Fig. 8.13 ($C2323$) and Fig. 8.14 ($C2313$), which differ from the previous pair only by $\xi_{\eta 0}$, which is now reduced to $\xi_{\alpha 0} = 0.15\%$.

Comparing the pairs Fig. 8.9-Fig. 8.11, Fig. 8.10-Fig. 8.12, Fig. 8.8-Fig. 8.14 and Fig. 8.15-Fig. 8.16 (that is the pairs of configurations $C1221$-$C2221$, $C1321$-$C2321$, $C1313$-$C2313$ and $C1325$-$C2325$), it is possible to note the influence of the ratio-to-critical pitching damping $\xi_{\alpha 0}$ when switching between 1.2% and 0.15%, for different sets of the other governing parameters. The typical effect due to lower values of $\xi_{\alpha 0}$ is to simply reduce U_R^c in all points of the $x_m - x_e$ space, slightly altering the shapes of the isolines.

It is worth highlighting the influence of the heaving damping and, in particular, the marked modification of the shapes of the isolines in both Fig. 8.5 and Fig. 8.6 when skipping from $\xi_{\eta 0} = 0$ to $\xi_{\eta 0} = 1\%$. It seems that very small damping levels are able to importantly alter the system response, and the gradient of the effect decreases as the damping increases. This consideration is in agreement with the experimental results discussed in § 7.2.2. Moreover, the damping level influences the optimal position of the elastic axis x_e, which seems to tend closer to the quarter-chord point upstream of the midchord of the section.

All this discussion is supported by Fig. 8.17 and Fig. 8.18, which show the evolution of the critical-condition parameters characterising the optimal configuration, that is point U_R^* as identified through the special mark ($\star$) in all the previously mentioned figures. In addition, Fig. 8.19, Fig. 8.20, Fig. 8.21 and Fig. 8.22 increase the information about the ensemble of parameters combinations that are admissible according to Table 8.1.

As previously discussed in § 8.1.1, the heaving-damping increment seems to move the optimal position of the elastic axis toward the leading edge and, in particular, in a region between the upstream quarter-chord ($x_e = -0.25$) and the leading edge ($x_e = -0.5$). Moreover, the optimal position of the mass-unbalance parameter seems to be weakly affected by large heaving damping, although almost linearly increasing in the range $x_m \in (0.01; 0.08)$, confirming what said in § 8.1.1 and in the experimental results (§ 7.1.1 and § 7.2.1). Figures

[1] In the theoretical case of concentrated mass in a point, the case $x_m \equiv r_\alpha$ is possible, otherwise is always $x_m < r_\alpha$.

from Fig. 8.17 to Fig. 8.22 show also information about the other critical-condition parameters, such as ϕ^*, $\sqrt{X^*}$ and $(B\alpha/\eta)^*$, about which the maps are not here reported for sake of brevity. It is interesting to note that there is a trend of ϕ^* that seems to converge toward $-90°$ for very high damping levels, and this can be stated for all investigated configurations. Moreover, the amplitude ratio $(B\alpha/\eta)^*$ usually increases as the heaving damping increases and this is in agreement with the experimental results discussed in § 7. A peculiarity characterises the evolution of the flutter frequency of the optimal configurations, $\sqrt{X^*}$, with increasing the heaving damping. It seems to follows a common slope after $\xi_{\eta 0} = 10\% - 15\%$, producing almost parallel curves, despite coming from different sets of governing parameters.

Generally, the critical reduced velocity of flutter of optimal configurations, U_R^*, increases with the heaving damping. However, it is worth noting the very particular response of configuration $C2325$ in which U_R^* shows a local minimum in the range $\xi_{\eta 0} \in (8\%; 17\%)$. A more refined investigation, showed in Fig. 8.23, explains that this destabilizing effect of damping on the global minimum U_R^* seems to manifest only for configurations with large still-air frequency ratio, large polar inertia radius and small pitching damping, independently on μ. With respect to the tested configurations, these considerations can be identified through $\gamma_n > 1.1$, $r_\alpha \geq 0.6$ and $\xi_{\alpha 0} < 1.2\%$.

Nevertheless, it is to point out that all these considerations are based on the results of linear analyses, thus they refer to the incipient flutter condition only. The dynamic parameters examined govern the flutter instability and are expected to influence the post-critical response as well. However, the identification of the optimal configuration may be different when considering the large-amplitude response, since the influence of the dynamic parameters may be different in this regime. Thus, the optimal configurations described in this section have to be considered as 'potentially' optimal configurations for energy harvesting.

In conclusion, the influence of the governing parameters on the features of the instability condition for the investigated configurations can be summarised:

- The optimal position of the elastic axis is expected to depend on the heaving-damping level, moving toward the leading edge as increasing $\xi_{\eta 0}$.
- The optimal position of the mass centre usually lies in the range $x_m^* \in (0.05; 0.08)$.
- For high levels of heaving damping, the sensitivity to x_e is smaller than to x_m, since the minimum region of U_R^c are stretched along the x_e axis and narrowed in the x_m direction.
- The parameters μ and $\xi_{\alpha 0}$ generally scale the whole U_R^c distribution and slightly alter the gradient.
- The parameter r_α importantly modifies the boundary region of the $x_m - x_e$ plane in which the system can get unstable, and also slightly scales the U_R^c distribution.
- A common configuration with $\phi \simeq -90°$ seems to manifest for very high heaving-damping levels, which is approached from different sets of governing parameters.
- Generally, the increments of heaving damping seem to make uniform the critical-condition parameters of optimal configurations, reducing the effects of the other governing parameters.

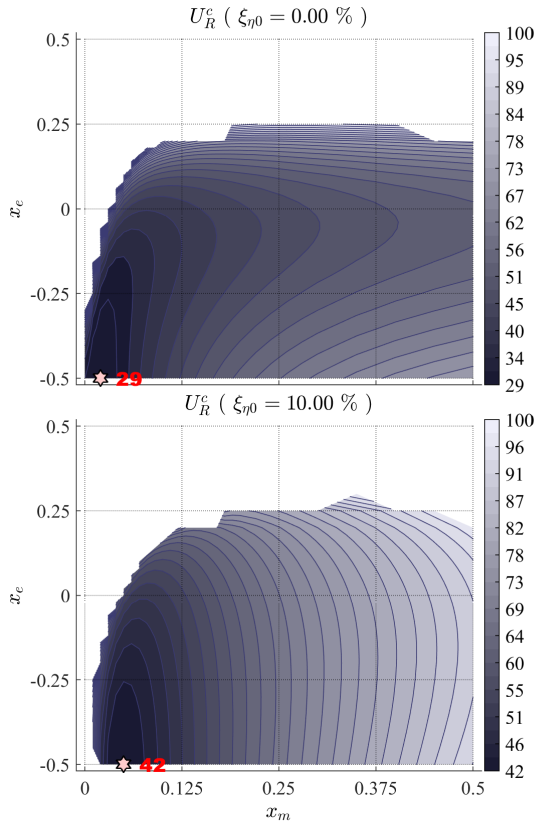

Figure 8.9. $C1221$ ($\xi_{\alpha 0}$ = 1.2%, μ = 2650, r_α = 0.60, γ_n = 0.95).

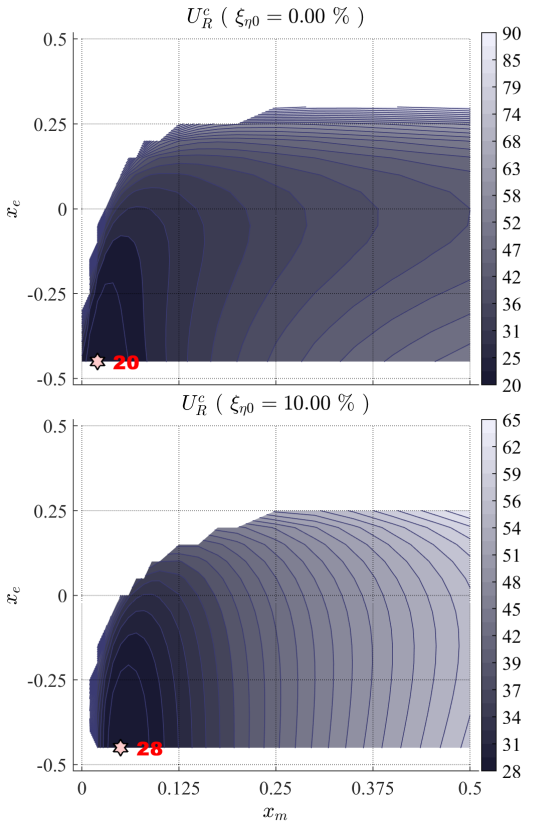

Figure 8.10. $C1321$ ($\xi_{\alpha 0}$ = 1.2%, μ = 950, r_α = 0.60, γ_n = 0.95).

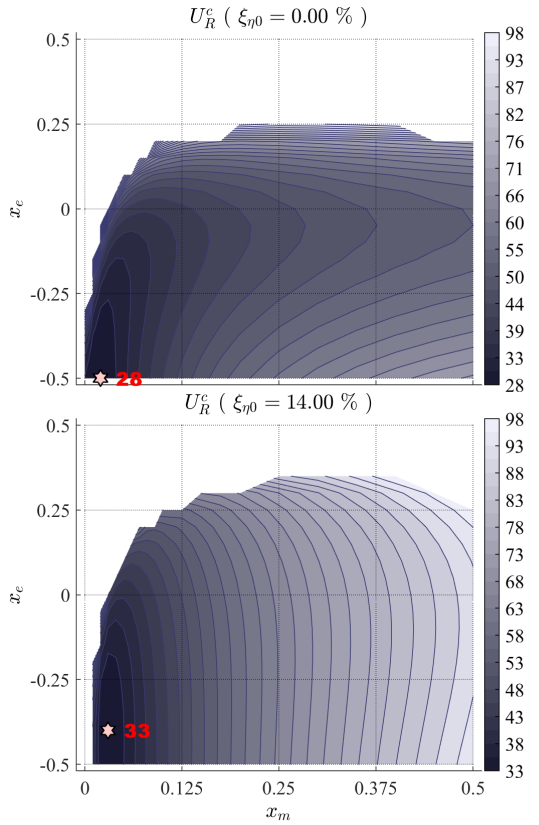

Figure 8.11. $C2221$ ($\xi_{\alpha 0}$ = 0.15%, μ = 2650, r_α = 0.60, γ_n = 0.95).

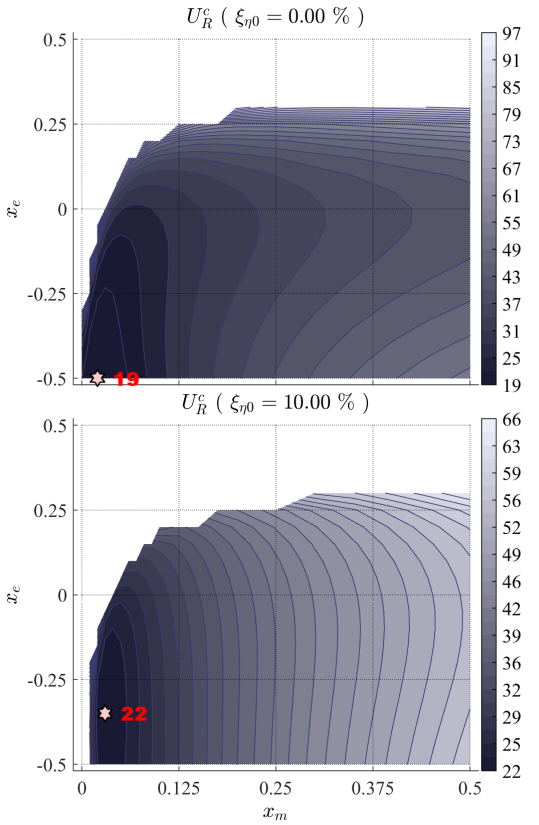

Figure 8.12. $C2321$ ($\xi_{\alpha 0}$ = 0.15%, μ = 950, r_α = 0.60, γ_n = 0.95).

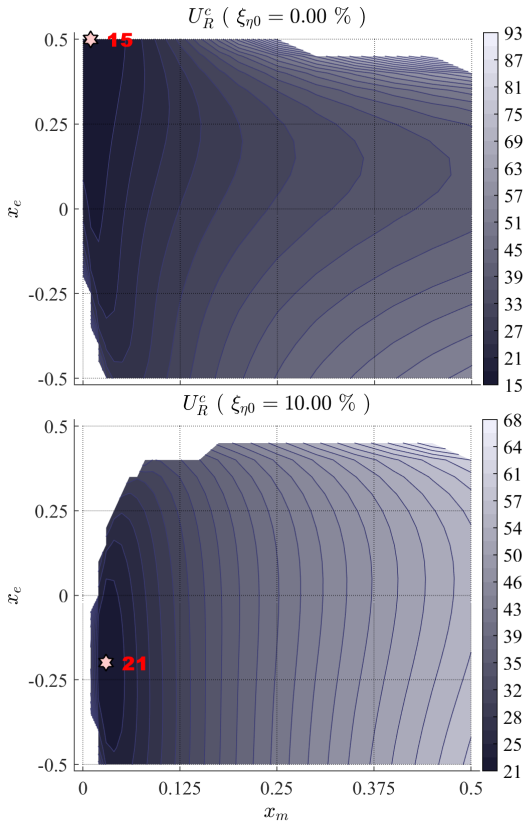

Figure 8.13. $C2323$ ($\xi_{\alpha 0}$ = 0.15%, μ = 950, r_α = 0.60, γ_n = 1.05).

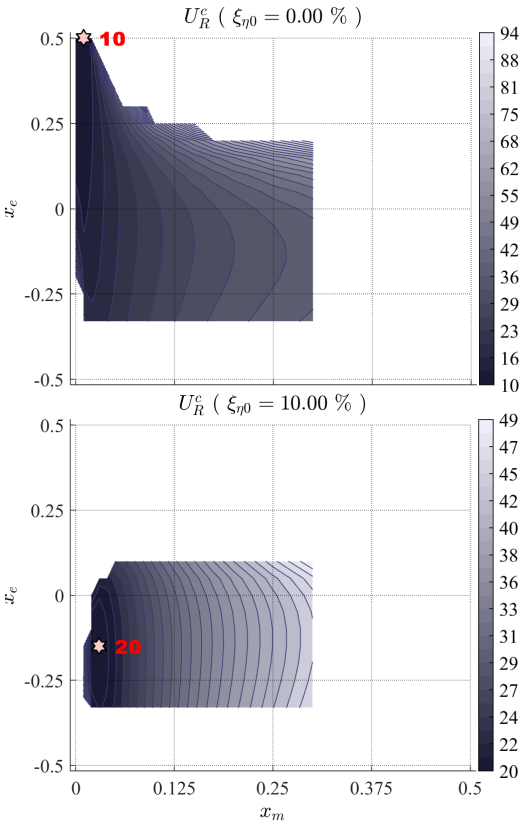

Figure 8.14. $C2313$ ($\xi_{\alpha 0}$ = 0.15%, μ = 950, r_α = 0.34, γ_n = 1.05).

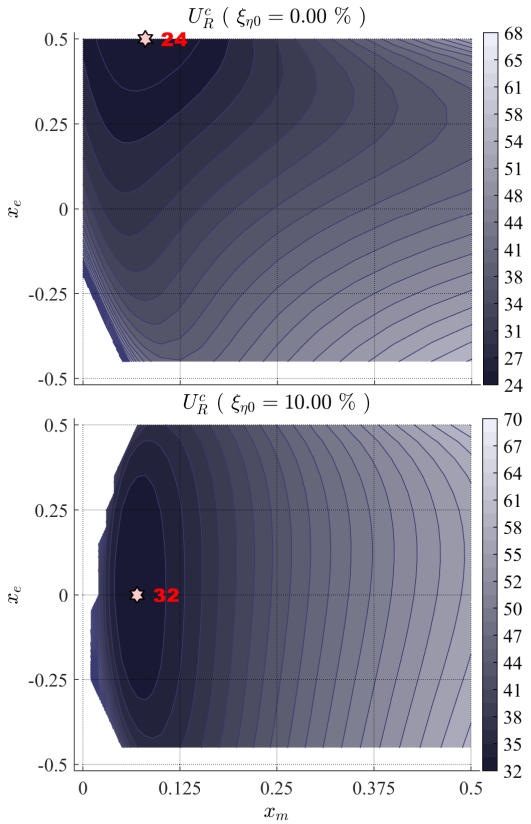

Figure 8.15. $C1325$ ($\xi_{\alpha 0}$ = 1.20%, μ = 950, r_α = 0.60, γ_n = 1.15).

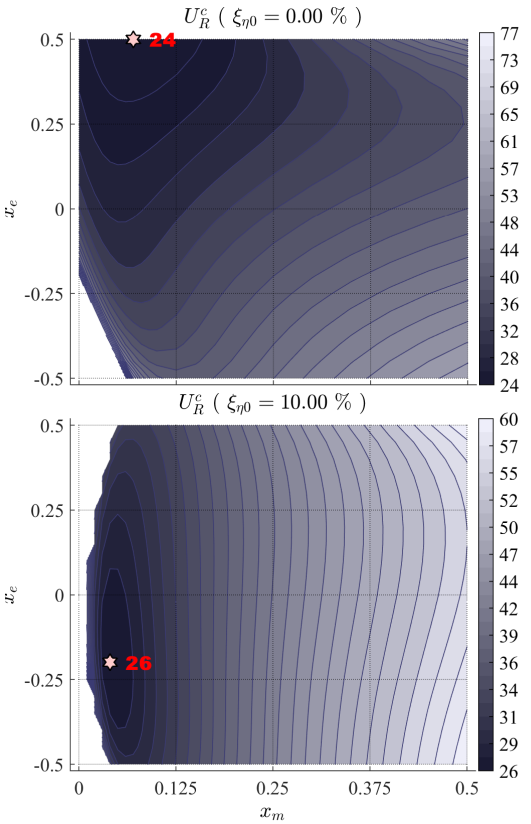

Figure 8.16. $C2325$ ($\xi_{\alpha 0}$ = 0.15%, μ = 950, r_α = 0.60, γ_n = 1.15).

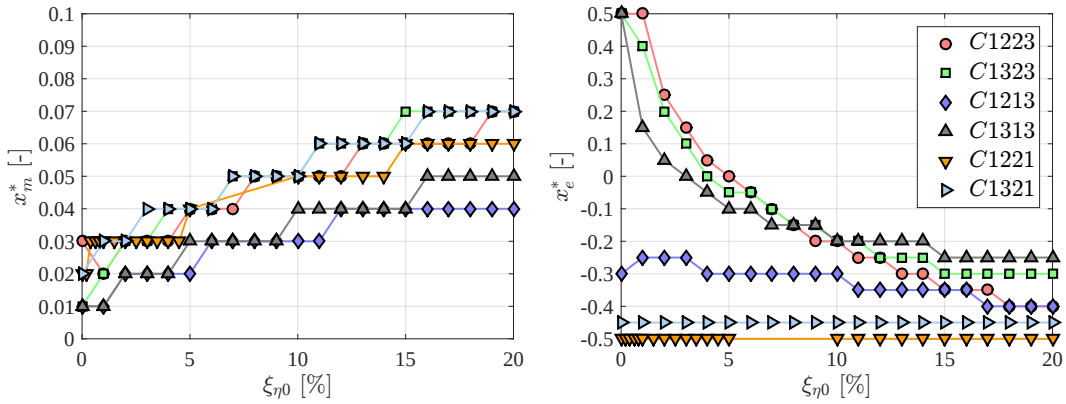

(a) Optimum values of the mass unbalance and elastic-axis eccentricity.

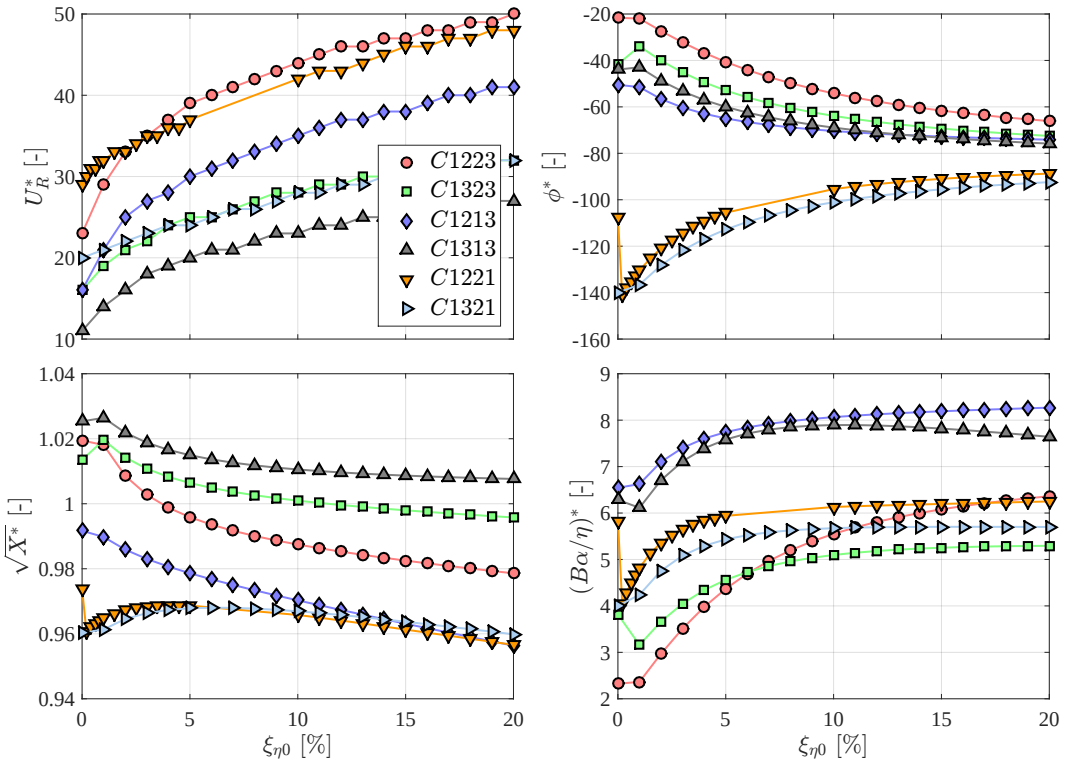

(b) Critical-condition parameters.

Figure 8.17. Critical-condition characteristics corresponding to the optimum points - PART I.

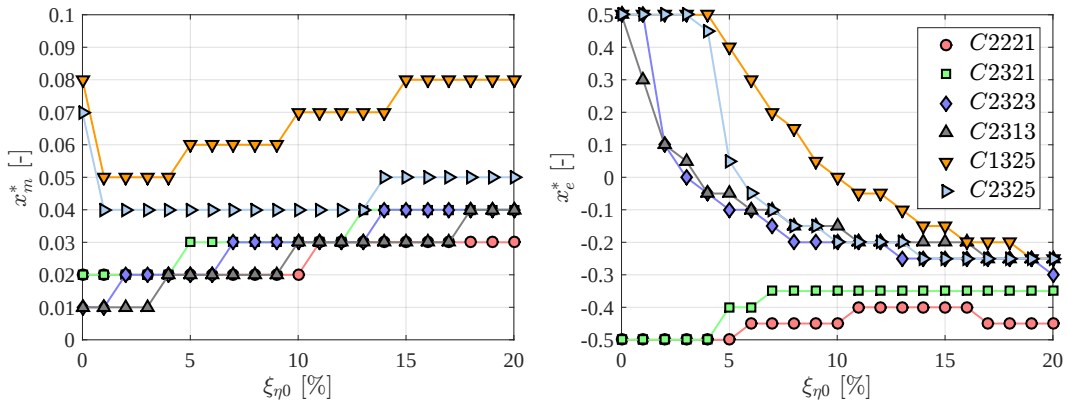

(a) Optimum values of the mass unbalance and elastic-axis eccentricity.

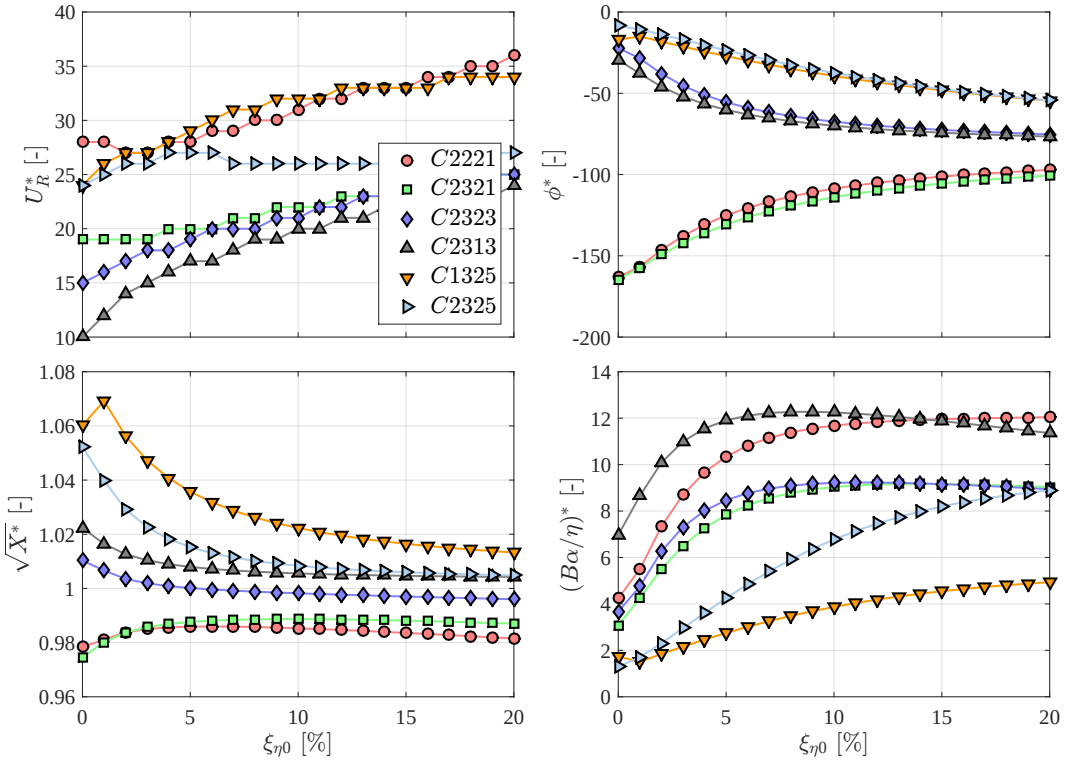

(b) Critical-condition parameters.

Figure 8.18. Critical-condition characteristics corresponding to the optimum points - PART II.

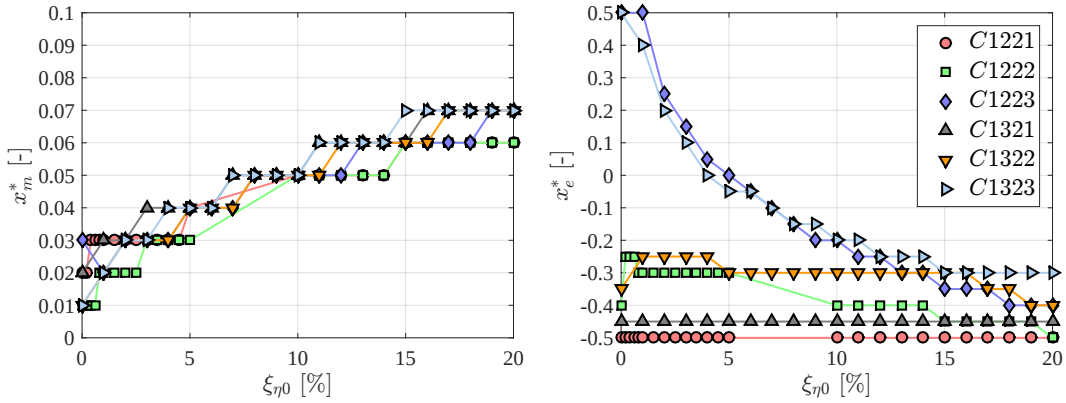

(a) Optimum values of the mass unbalance and elastic-axis eccentricity.

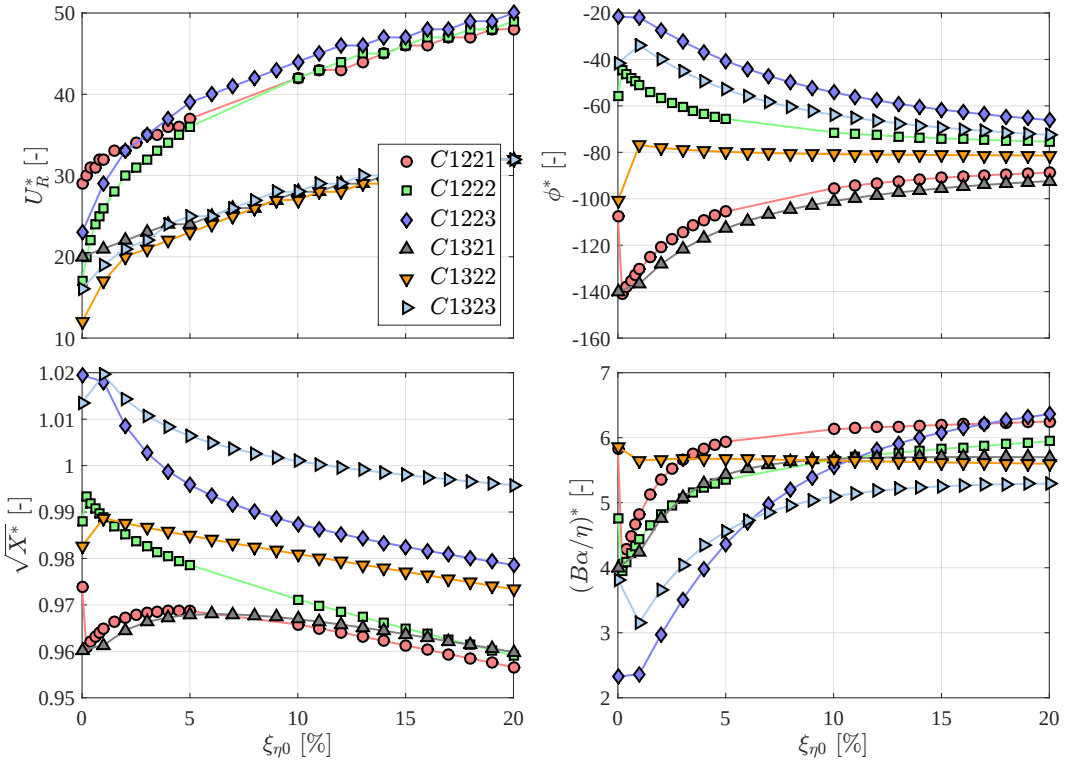

(b) Critical-condition characteristics of optimum points.

Figure 8.19. Critical-condition characteristics corresponding to the optimum points - PART III.

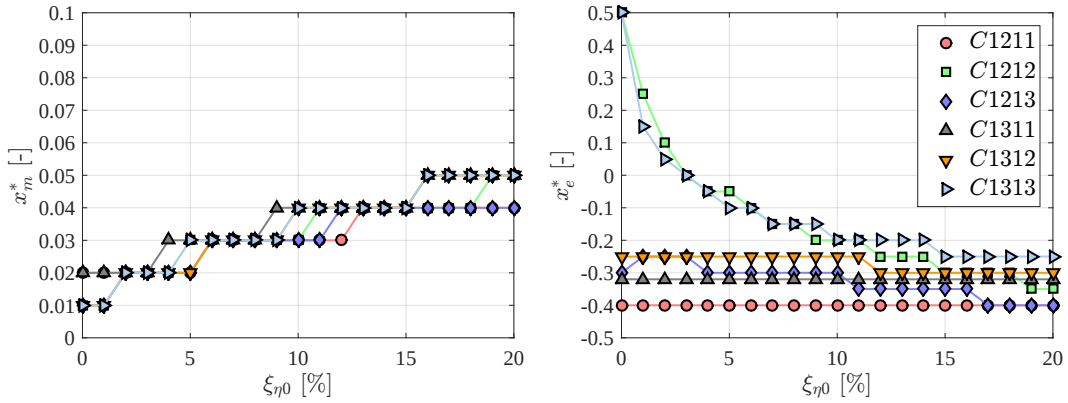

(a) Optimum values of the mass unbalance and elastic-axis eccentricity.

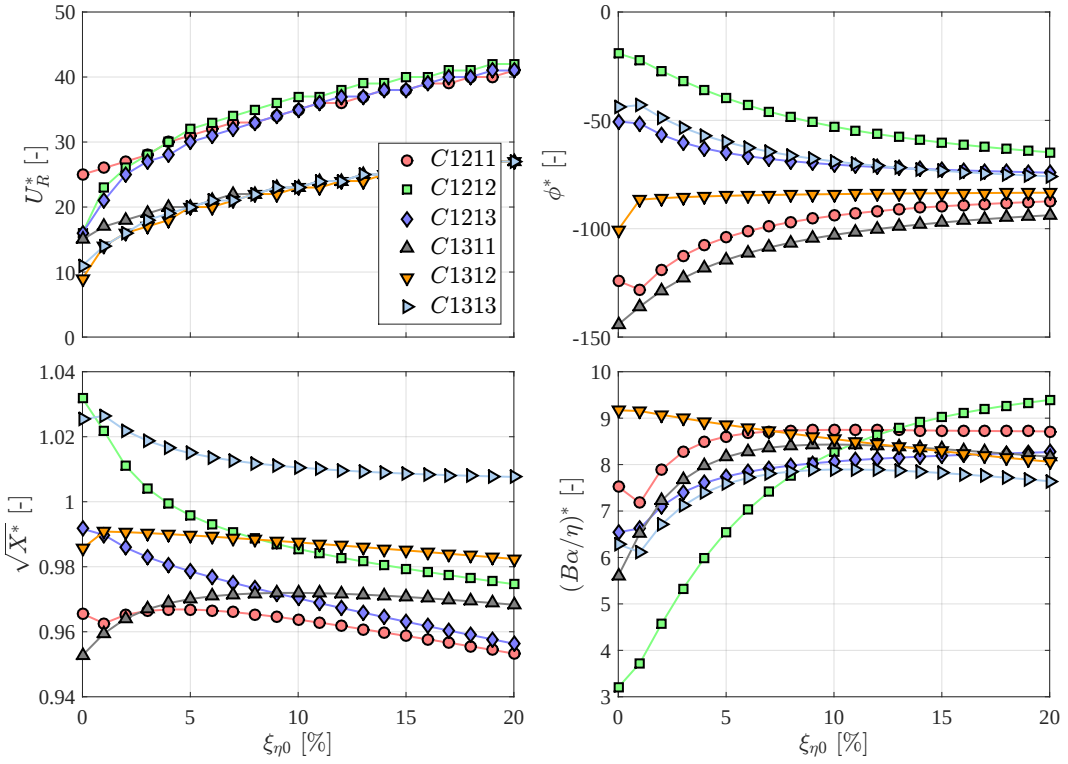

(b) Critical-condition parameters.

Figure 8.20. Critical-condition characteristics corresponding to the optimum points - PART IV.

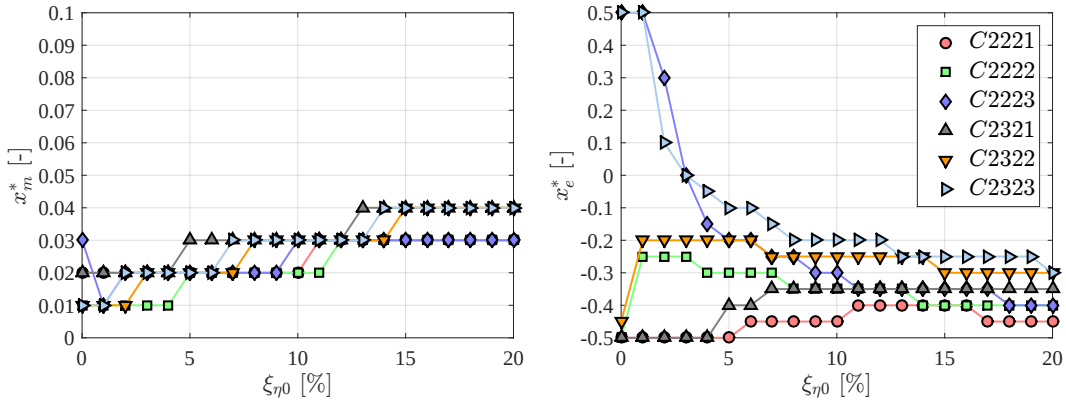

(a) Optimum values of the mass unbalance and elastic-axis eccentricity.

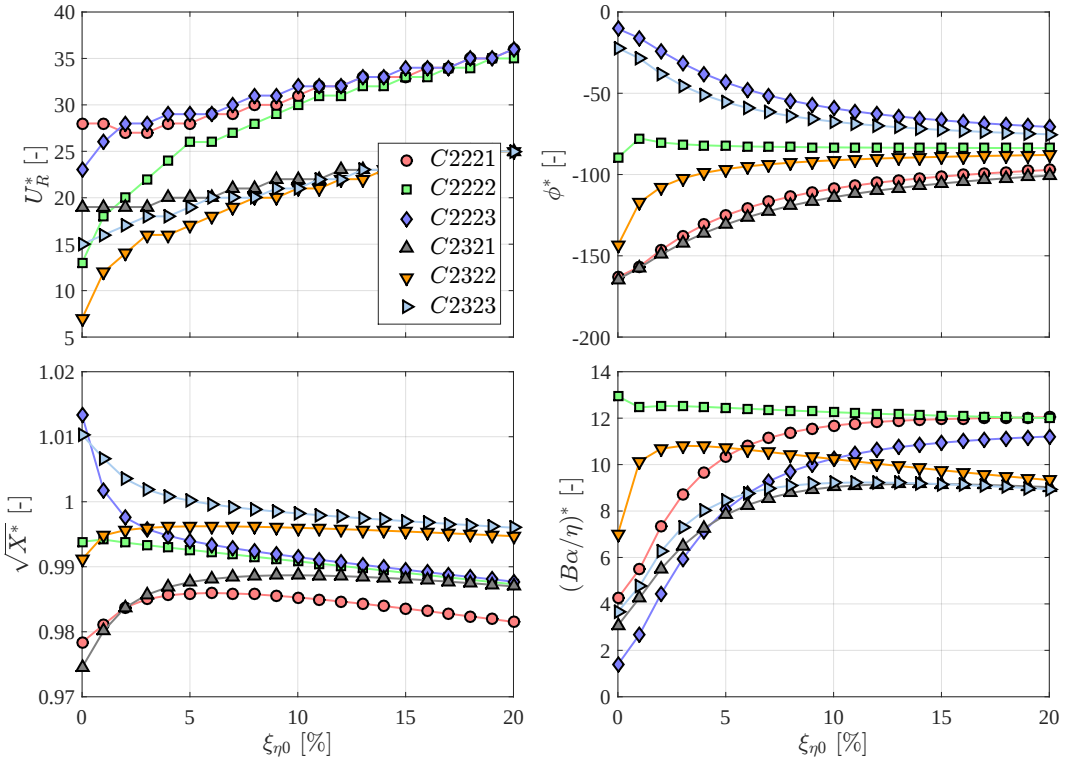

(b) Critical-condition parameters.

Figure 8.21. Critical-condition characteristics corresponding to the optimum points - PART V.

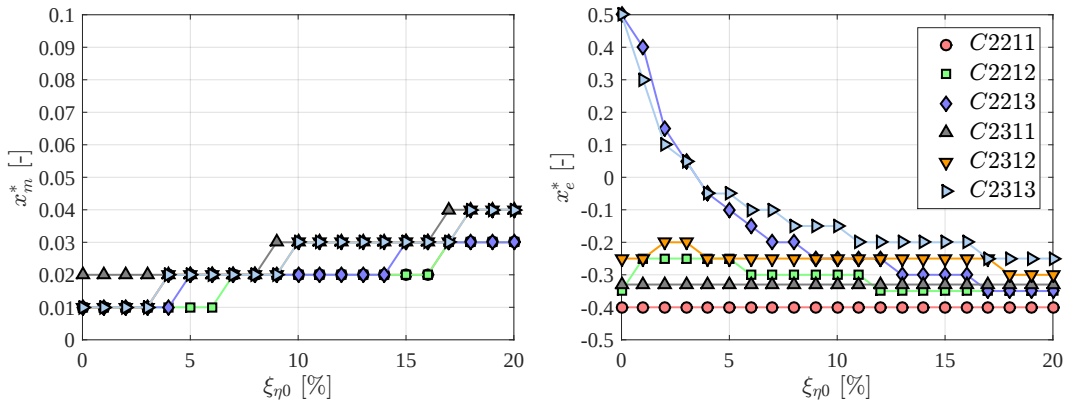

(a) Optimum values of the mass unbalance and elastic-axis eccentricity.

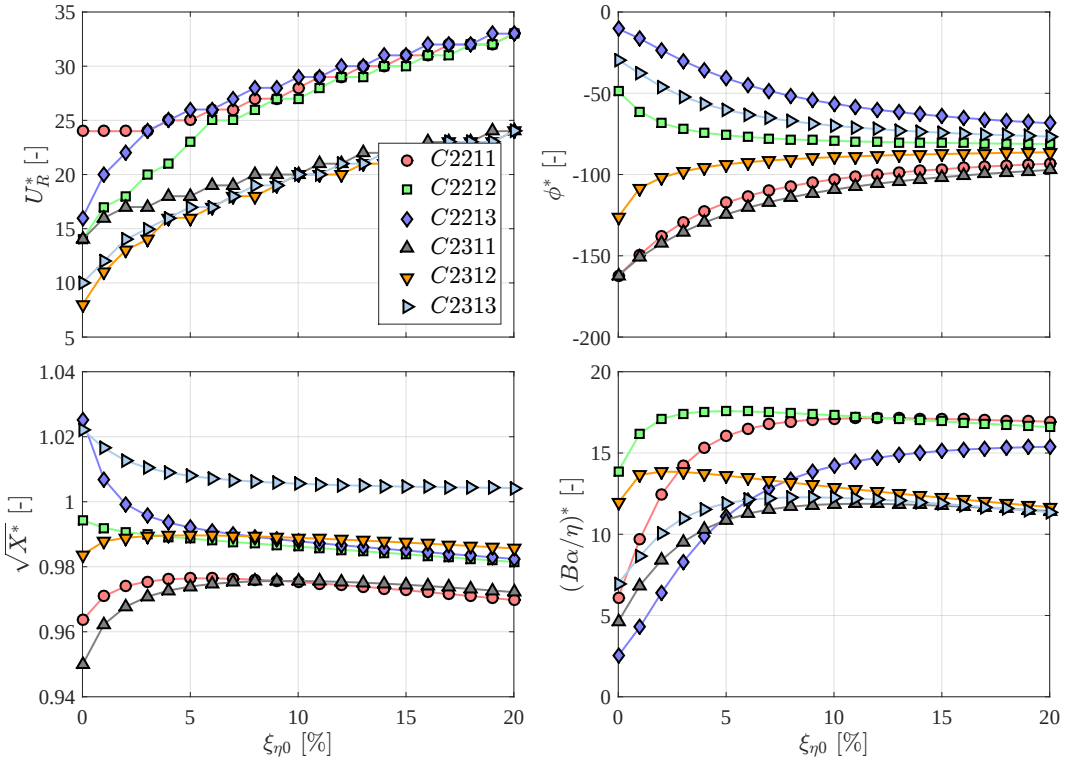

(b) Critical-condition parameters.

Figure 8.22. Critical-condition characteristics corresponding to the optimum points - PART VI.

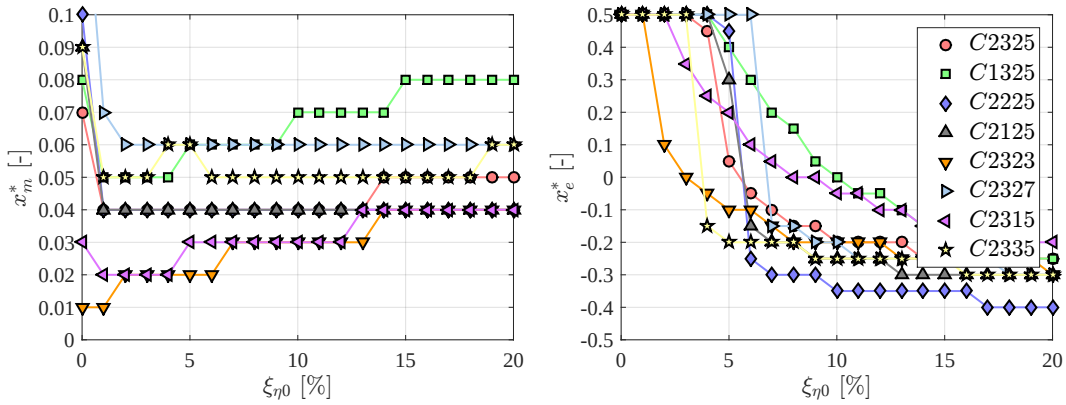

(a) Optimum values of the mass unbalance and elastic-axis eccentricity.

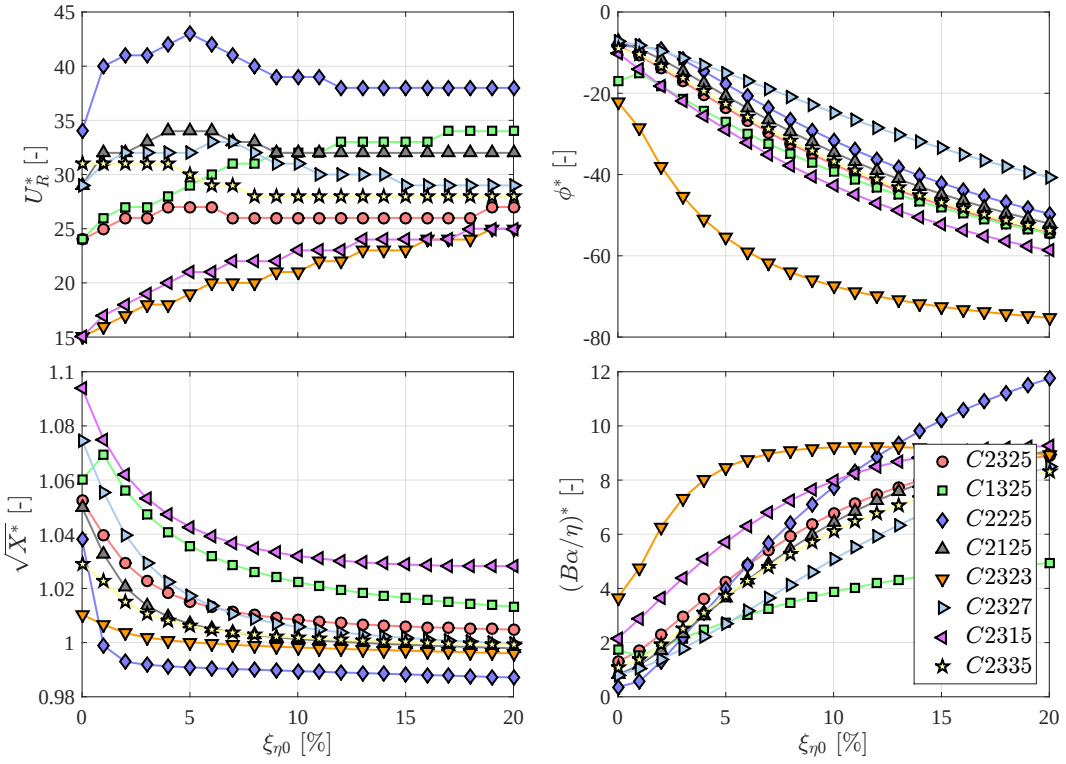

(b) Critical-condition parameters.

Figure 8.23. Critical-condition characteristics corresponding to the optimum points - PART VII.

8.1.3 Design of experimental optimal configurations

The analyses discussed in the previous section § 8.1.2 indicated that the configurations showing the lowest values of the global minimum of critical reduced velocity (U_R^*) requires as low as possible inertial parameters (μ and r_α) and small mass unbalance. Moreover, the pitching damping should be limited.

Considering the technical features of the aeroelastic setup at the CRIACIV laboratory, used for SESSION I and SESSION II, and its compatibility with the governing parameters of the theoretical optimal configurations, some expedients were applied to design realistically feasible configurations.

In particular, the critical damping ratio of pitching $\xi_{\alpha 0}$ could not be reduced as will, since it strictly depends on the ball-bearing system used to decouple the 2-DoF motion (see § 5.3.3 and § 5.3.4), which provides a nominal damping force. Thus, the only way to reduce it was to increase the polar inertia (I_α) or the pitching frequency ($n_\alpha 0$). Nevertheless, the increment of I_α is contrary to the optimal design because it increases r_α too. Furthermore, the increment of $n_\alpha 0$ complicates the post-critical regime measurements, since higher frequencies of oscillations would enhance the inertial and fatigue loads acting on the system Hence, $\xi_{\alpha 0}$ was kept around $1 - 1.2\%$.

By contrast, the mass-ratio parameter can be reduced to values about 1400 by simply increasing to 1 m the span of the model. Indeed, the passive oscillating masses of the elastic suspension were almost the same and a larger span, keeping the same material of the model, reduces μ. An alternative can also be to enlarge the section chord B. However, a larger B will produce larger dimensional amplitude of oscillations in heaving, which will go earlier out of the measuring range of the laser displacement sensors (see § 5.3.1 and Table 5.6).

The polar inertia radius was possible to be reduced to values about 0.40 by simply taking off the end-plates from the model ends.

Thus, only the model span and the presence of the end-plates were modified to set up SESSION III. It is worth highlighting that the longer span increased the bending flexibility of the model, as indicated in Fig. 5.33, and the post-critical measurement could be slightly altered. Moreover, the absence of end-plates had negligible effects because of the presence of the shelters, which contributed to enforce two-dimensional flow conditions in a similar way.

Once the parameters μ, r_α and $\xi_{\alpha 0}$ were fixed, the theoretical investigation indicated the optimal combinations of x_e and x_m, for different values of the still-air frequency ratio γ_n. Table 8.2 shows the governing parameters used for the linear analysis and the results are reported in Fig. 8.24 and Fig. 8.25. A smaller spacing for the domain of the mass-unbalance parameter x_m domain is used, narrowing the investigated range to $x_m \in (0; 0.1)$ (the previous analyses indicated that x_m^* always lies within this range); the identification of the optimal configuration is improved.

The evolution of the critical-condition parameters of the optimal configurations is showed in Fig. 8.26. It is clear the dependence on γ_n, confirming again the considerations made at the end of § 8.1.2, allowing to be also extended for these investigated sets of governing parameters. Moreover, observing the evolutions of U_R^* in Fig. 8.26b, the lowest value of U_R^* is produced by the configuration with $\gamma_n = 1.00$; its curve is always slightly below the others for all $\xi_{\eta 0}$ levels.

Table 8.2. Governing parameters for linear analysis of experimental optimal configurations.

$\xi_{\alpha 0}$ [%]	μ [-]	r_α [-]	γ_n [-]
1.20	1400	0.39	0.95 ; 1.00 ; 1.05 ; 1.10

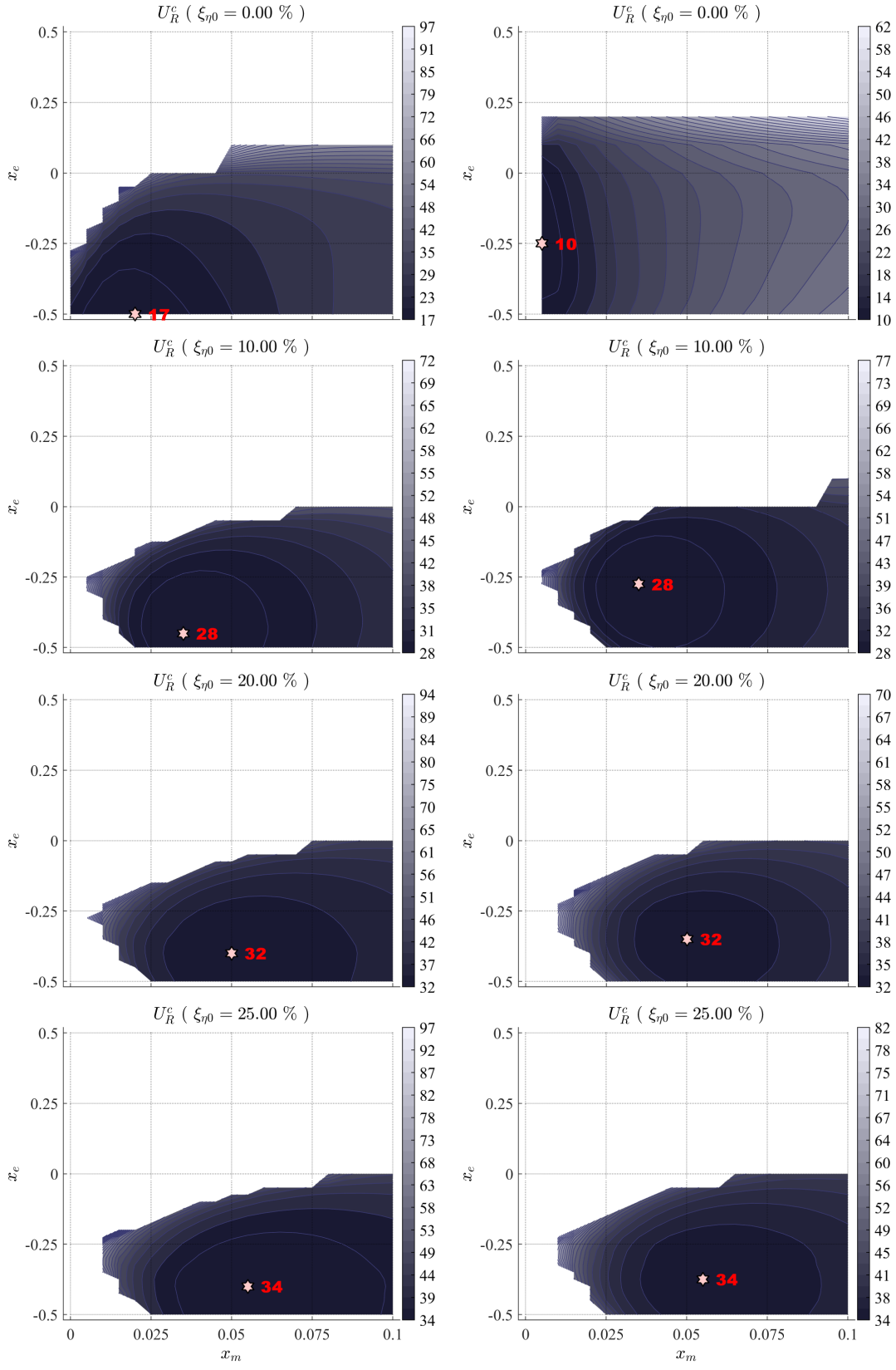

(a) $\gamma_n = 0.95$. **(b)** $\gamma_n = 1.00$.

Figure 8.24. Maps about experimental optimal configurations - PART I. The other parameters are $\xi_{\alpha 0} = 1.2\%$, $\mu = 1400$ and $r_\alpha = 0.39$.

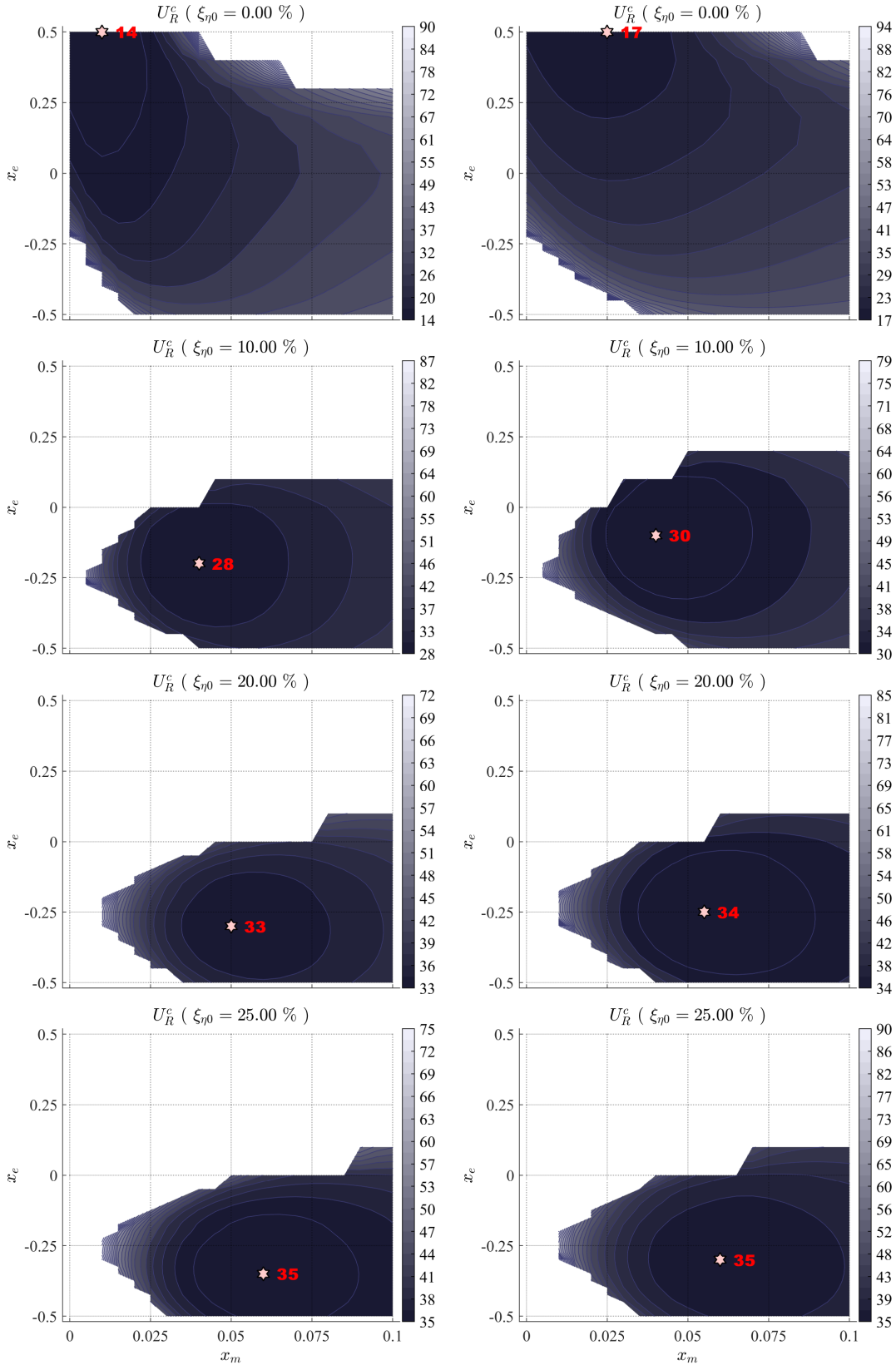

(a) $\gamma_n = 1.05$. **(b)** $\gamma_n = 1.10$.

Figure 8.25. Maps about experimental optimal configurations - PART II. The other parameters are $\xi_{\alpha 0} = 1.2\%$, $\mu = 1400$ and $r_\alpha = 0.39$.

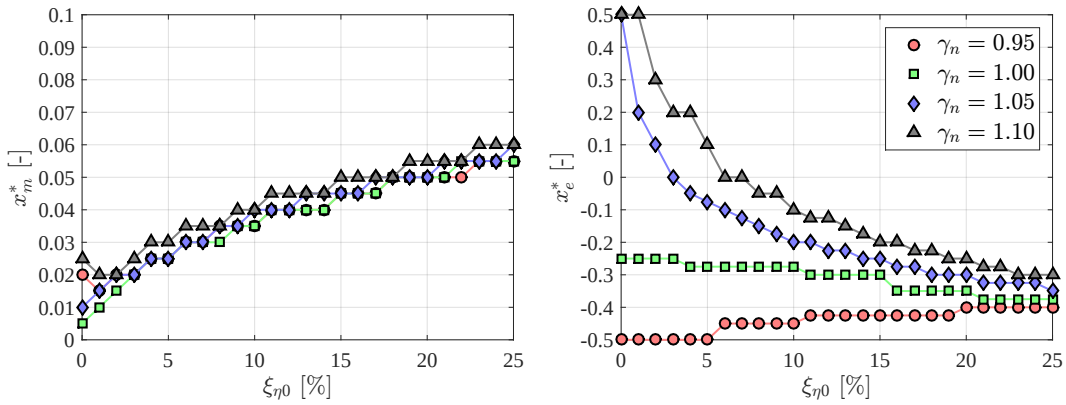

(a) Optimum values of the mass unbalance and elastic-axis eccentricity.

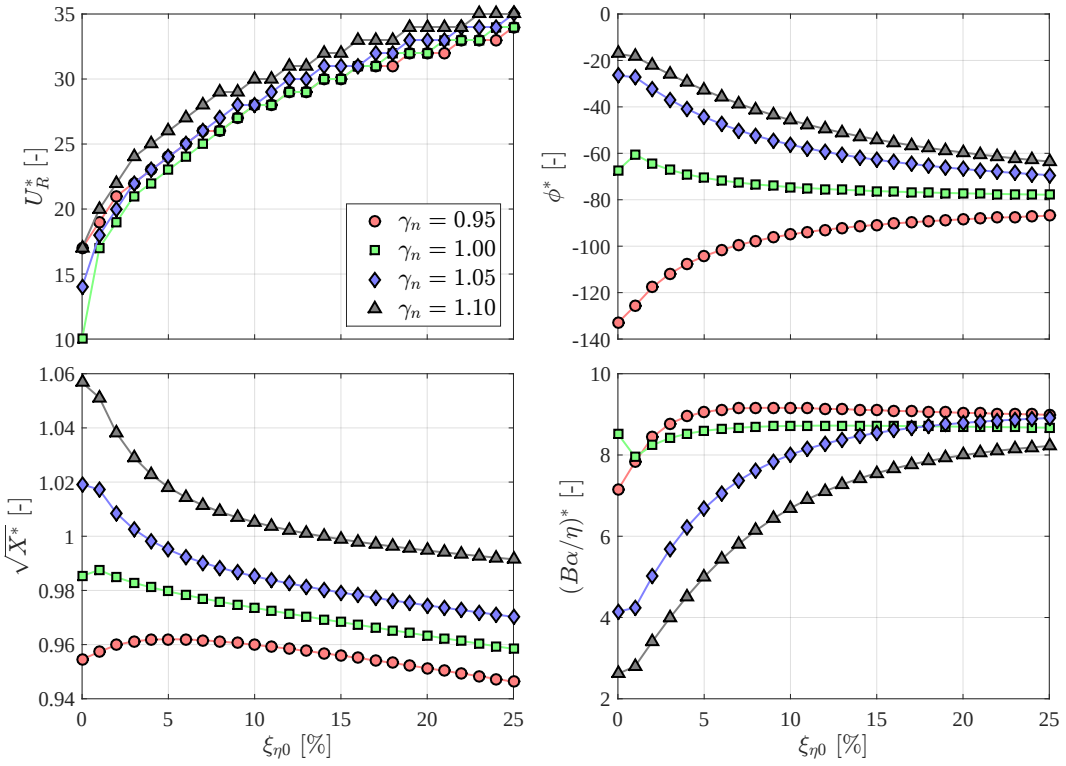

(b) Critical-condition characteristics of optimum points.

Figure 8.26. Critical-condition characteristics corresponding to the optimum points from Figs. 8.24 and 8.25.

8.2 Experimental investigations (25:1 model, session III)

The trend of the parameter x_e^* in Fig. 8.26a imposed the design value of the elastic-axis position. In particular, since it depends on the heaving-damping level, $x_e = -0.25$ was selected for the configurations tested in SESSION III (exception of ♯27 with $x_e = 0$, tested for cross-comparisons). With this value, the configuration with $\gamma_n = 1.00$ is almost always close to the optimal value for all levels of $\xi_{\eta 0}$, while it is a good compromise among configurations with $\gamma_n = 0.95$, $\gamma_n = 1.05$ and $\gamma_n = 1.10$ when $\xi_{\eta 0}$ is about 15% (typical value reached during the experiments).

The configurations were designed to have a mass-unbalance parameter x_m in the range $(0.05; 0.06)$. These values are suggested by Fig. 8.26a, which shows that x_m^* get closer to that range as the heaving damping is increased above 15%. However, it is worth highlighting that x_m is very difficult to be designed with high precision, and the optimal range is even very narrow. In particular, x_m is experimentally evaluated through Eq. (5.5) from the frequencies estimation of the coupled and un-coupled oscillating system, and indirect experimental errors could be introduced, also coming from the accuracy of the instruments.

The parameters of the investigated configurations are reported in Table 6.3 and Table 6.4. A selected subset of those configurations is here discussed.

8.2.1 Still-air frequency ratio influence on large motion amplitudes

Fig. 8.27 shows the comparison among three configurations that mainly differ[2] in terms of still-air frequency ratio γ_n, which varies between 1.064 to 0.917.

In all cases, these configurations are markedly more unstable if compared with those presented in § 7.2, which essentially differ in terms of mass-ratio parameter (it was $\mu \approx 2650$ in SESSION I and SESSION II, while now it is $\mu \approx 1400$). Indeed, the system is able to experience very large oscillation amplitudes in both DoFs from the very beginning of the post-critical regime, since the jump at the instability threshold is more pronounced. Moreover, the slopes of the post-critical amplitude-velocity branches are higher.

Continuing to observe Fig. 8.27, configuration ♯19, that is with $\gamma_n = 0.917$, shows the smallest amplitude ratio and the largest phase differences (close to $-170°$). Moreover, this configuration shows also the biggest heaving jump at the instability threshold, which reaches almost $0.8B$. Configuration ♯8, that is with $\gamma_n = 1.064$, gets unstable at the lowest reduced velocity. Nevertheless, configuration ♯16 with $\gamma_n = 1.007$ shows the largest sub-critical branch that ends at a reduced velocity of about 0.78 times the critical one. Also in this case, both configurations perform a motion with almost anti-phase DoFs.

It is interesting to note the evolution of the motion frequency $\hat{n}$, which slightly decreases for ♯19 ($\gamma_n < 1$) while increases for both ♯8 and ♯16 ($\gamma_n \geq 1$).

Finally, it is worth highlighting the very good agreement between linear analysis and experiments, in terms of critical reduced velocity, comparing the vertical dashed lines in Fig. 8.27 with results in Fig. 6.5.

8.2.2 Detailed study of heaving-damping influence

Despite the very high motion amplitudes of the low-damped configurations discussed in § 8.2.1, the increments of heaving damping importantly reduced the motion amplitudes of both DoFs.

Observing Fig. 8.28, the strong nonlinear influence of even small values of $\xi_{\eta 0}$ is clearly apparent. Moreover, the pitching amplitude-velocity path seems to follows a parabolic trend in the range of flow speeds beyond the critical one, and this is remarkable for all

[2]The other parameters sligtlty varied due to problems with the calibration of mechanical features of the aeroelastic setups. The required clock spring (designed according to the optimal configurations features) brake after very few experiments and the following configurations were arranged trying to exploit other available clock springs that had different stiffness. Thus, additional masses were installed to adjust the still-air frequency ratio and, consequently, the mass-centre position, producing small variations of polar inertia radius and (weaker) mass ratio.

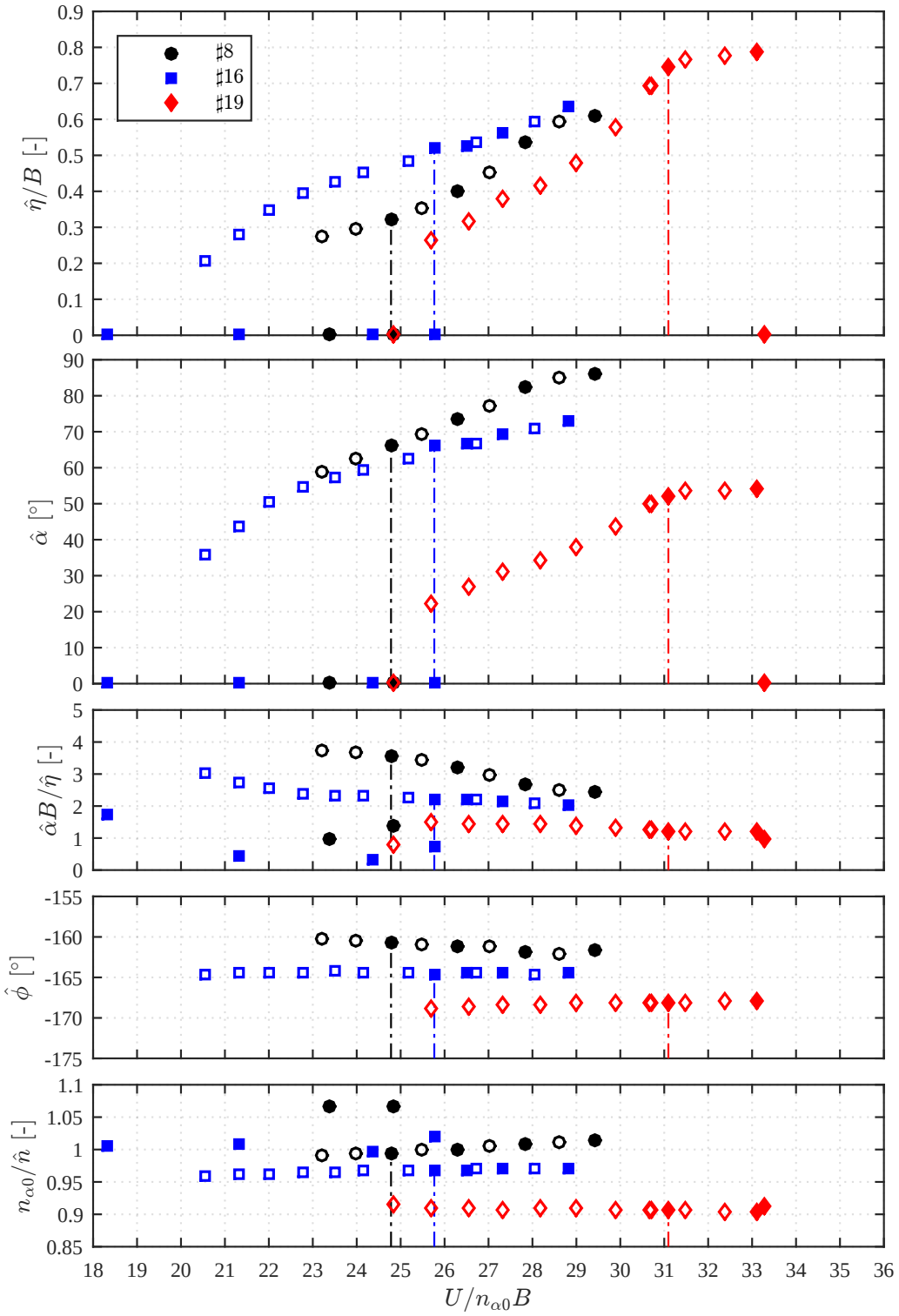

Figure 8.27. Comparison of LCO features among configurations with low heaving damping ($\xi_{\eta 0}$ = 0.05%) and with different still-air frequency ratio (γ_n = 1.064 for ♯8, γ_n = 1.007 for ♯16 and γ_n = 0.917 for ♯19).

heaving-damping levels. This marked effect of heaving damping can be noted also for the other configurations, as shown in Figs. 8.29 and 8.30. This last shows a refined study of heaving-damping influence, since that parameter was more gradually varied in the range from 0.05% to 14.98%.

The phases evolution confirms what concluded in § 8.1.2 and § 8.1.3, that is the trend toward −90° as the heaving damping increases. Moreover, it is interesting to note the evolution of the motion frequencies in all Figs. 8.28, 8.29 and 8.30. For configuration based on ♯8 and ♯16, that is when $\gamma_n \geq 1$, any increment of $\xi_{\eta 0}$ changes the slope from positive to negative and the motion frequency decreases with the flow speed. By contrast, configurations based on ♯19, that is with $\gamma_n < 1$, show motion frequencies that do not invert the slope with increasing the heaving damping.

Furthermore, it seems to be present a discontinuity in the amplitude-velocity diagrams in correspondence of the instability threshold, as previously introduced in § 7.3.1. In particular, a change of slope between the sub-critical and post-critical branches is usually observed. Nevertheless, the marked slope change in the amplitude-velocity curve of configuration ♯19 in Fig. 8.30 is also due to a weak sliding contact between the model-axis tube and the vertical hole in the plexiglass walls of the shelters. Indeed, during very-large heaving oscillations, a small displacement in the along-wind direction was produced by the second-order deformation of the leaf-spring suspension. Therefore, at large heaving amplitudes the along-wind displacement used up the available gap of the model-axis tube inside the vertical slot.

Finally, it is worth highlighting that, for all configurations with additional heaving damping, the amplitude-velocity diagrams seem to origin from a common point, which could be obtained by extrapolating the sub-critical branch toward lower flow speed (close to the point identified by the high-damped configuration). Moreover, the system was able to perform steady-state oscillations even at the very end of the sub-critical branch, where the motion amplitudes were extremely low if compared to those in the post-critical regime.

8.2.3 Performance evaluation

Considering the analyses discussed in § 8.2.2, that is about configurations with additional heaving damping derived from ♯8, ♯16 and ♯19 (all with $x_e = -0.25$ and $x_m \approx 0.06$), their energy-harvesting performances are hereinafter evaluated.

The performances are shown in Fig. 8.31 (configurations from ♯8 to ♯12), in Fig. 8.32 (configurations from ♯16 to ♯18) and in Fig. 8.33 (configurations from ♯19 to ♯26), and are reported in terms of the performance parameters explained in § 4.1.2, that is: extraction factor Γ'_η; mean power of the lifting load P_η; conversion factor Γ''_η; equivalent damping due to the static mass unbalance β; global performance factor $\Gamma_\eta = \Gamma'_\eta \cdot \Gamma''_\eta$; output mean power available for a next electric circuit $P_{D_{E\eta}}$.

Concerning the shape of the curves of Γ'_η and Γ_η, all cases show an almost linear evolution in the range of flow speeds corresponding to the sub-critical branch. Then, the slope seems to be gradually varied at a certain point after the instability threshold, so to follow a polynomial curve with concavity oriented to the bottom-side of the performance-factor axis. It is clear that this evolution always produces a maximum of efficiency and this is in agreement with discussions in § 7.4. By contrast, the evolution of Γ''_η seems to be linear in the post-critical range and following some polynomial shape in the connection toward the sub-critical range. It is worth highlighting the comparisons with the β curves of the investigated configurations during SESSION I and SESSION II, as discussed in § 7.4.2, for which the sub-critical branches were shorter, and β did not manifest the falling trend in its left-hand side at the lower flow speeds.

Observing the evolution of the Γ'_η curves of configurations based on ♯8 (Fig. 8.31) and ♯16 (Fig. 8.32), the increment of the heaving damping strongly reduces the capability to extract energy from the flow. Since the heaving motion component is markedly reduced, the energy flowing in the heaving DoF is limited, although the system continues to perform self-sustained motion. Nevertheless, the evolution of the Γ_η curves states that, in both cases, the usable energy for a next conversion apparatus is larger as increasing $\xi_{\eta 0}$. Moreover, the

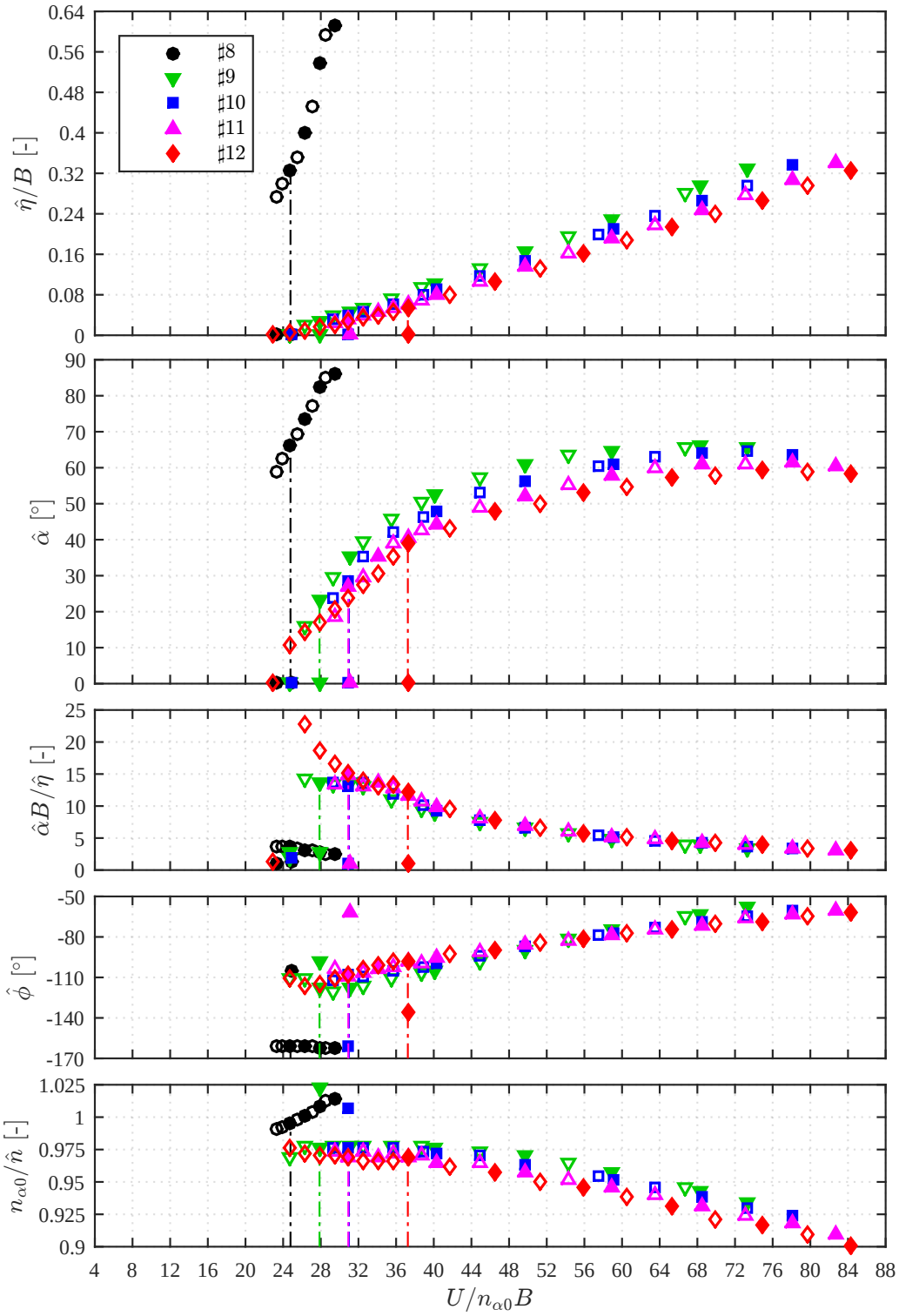

Figure 8.28. Detailed study of heaving-damping influence on the LCO amplitudes for the configurations with $\gamma_n = 1.064$. The value of $\xi_{\eta 0}$ is 0.05% for ♯8, 6.66% for ♯9, 9.31% for ♯10, 12.23% for ♯11 and 15.06% for ♯12.

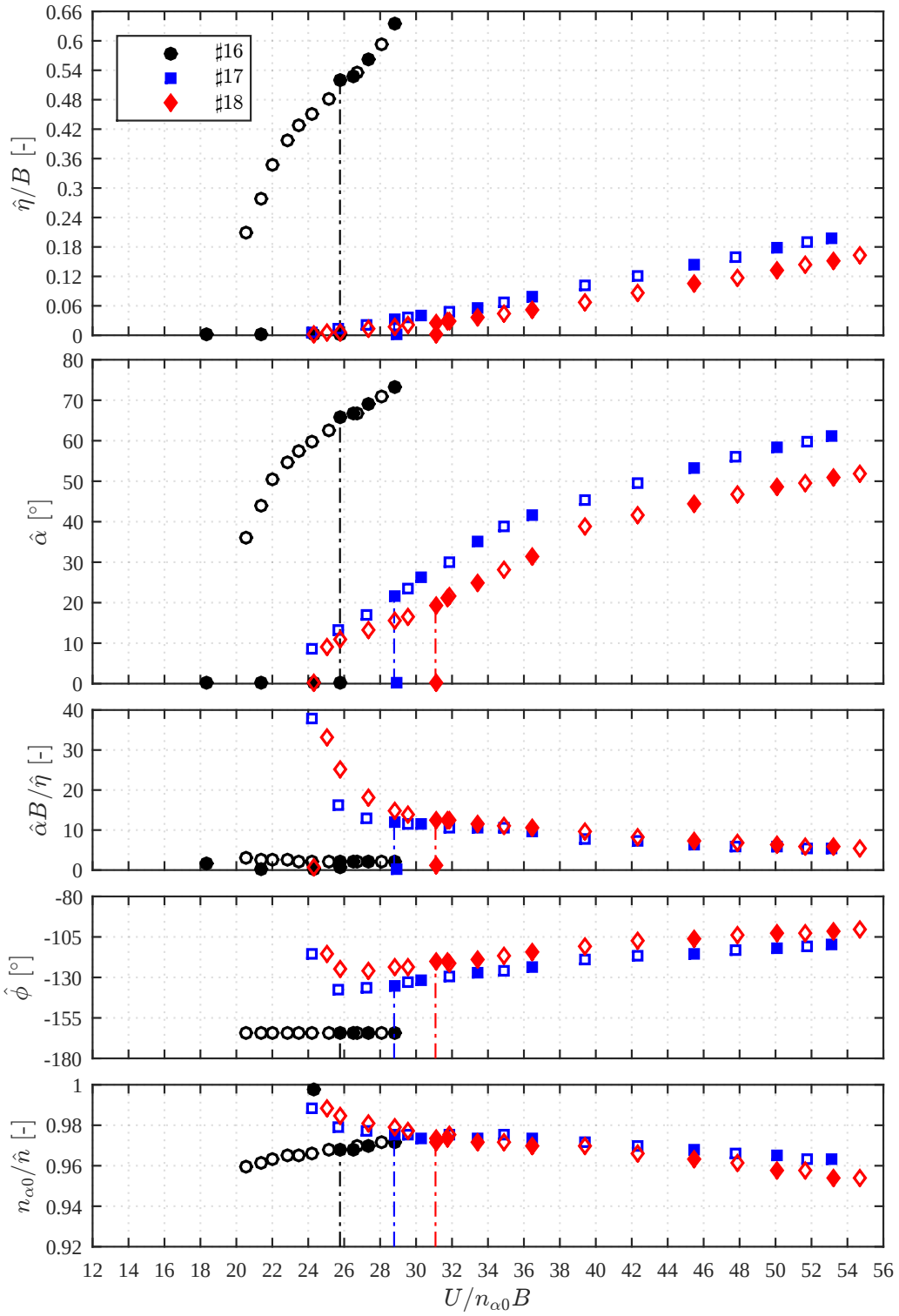

Figure 8.29. heaving-damping influence on the LCO amplitudes for the configurations with $\gamma_n = 1.007$. The value of $\xi_{\eta 0}$ is 0.05% for ♯16, 8.99% for ♯17 and 14.98% for ♯18.

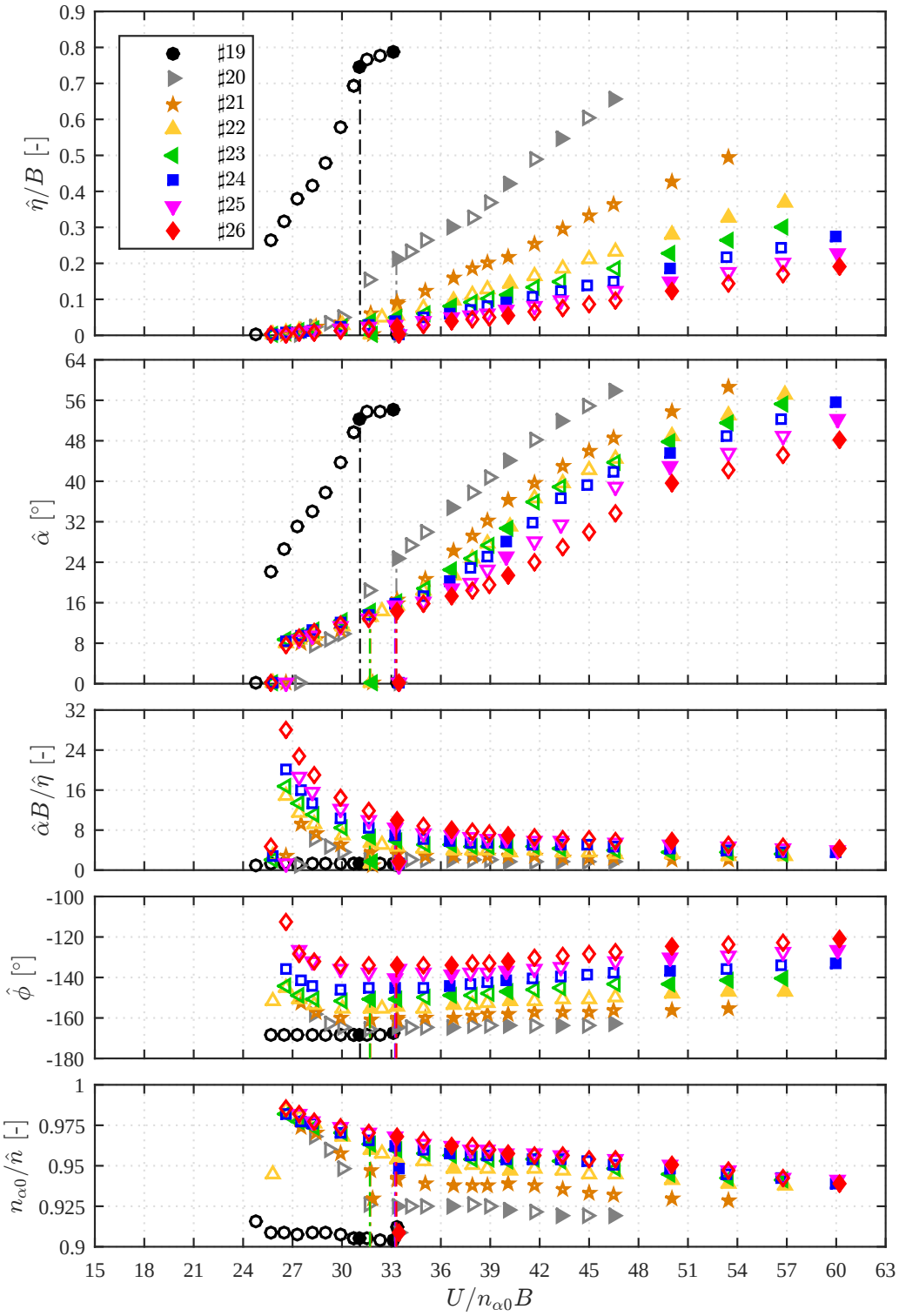

Figure 8.30. Detailed study of heaving-damping influence on the LCO amplitudes for the configurations with $\gamma_n = 0.917$. The value of $\xi_{\eta 0}$ is 0.05% for ♯19, 1.04% for ♯20, 2.60% for ♯21, 4.82% for ♯22, 6.81% for ♯23, 8.96% for ♯24, 11.85% for ♯25 and 14.98% for ♯26.

shape of Γ_η curves of configurations based on ♯8, differently to those based on ♯16, show a limited dependence on the reduced flow speed after a certain value around 60, being almost horizontal in the last part.

A peculiar behaviour is showed by the configurations derived from ♯19, as shown in Fig. 8.33. In this case, the study of the heaving-damping influence through a more refined spacing clearly indicates the presence of an optimal value of the heaving damping at which corresponds the maximum performance, both in terms of Γ'_η and Γ_η. Furthermore, configurations based on ♯19 reach the highest performance factors and, in particular, configuration ♯23 with $\xi_{\eta 0} = 6.81\%$ shows $\Gamma_\eta \approx 1.45\%$. The higher energy-harvesting capabilities of configurations derived from ♯19 can be also clarified observing Fig. 8.34, which compares different configurations with similar heaving damping.

Fig. 8.35, Fig. 8.36 and Fig. 8.37 explain the evolution of $U_{R\alpha}^{opt}$ and the corresponding values of extraction and global factor, that is Γ'_η and Γ_η, with respect to the heaving-damping variations as obtained for all configurations based on ♯8, ♯16 and ♯19. For the tested configurations based on ♯8 and ♯16, Γ_η increases with $\xi_{\eta 0}$. By contrast, $U_{R\alpha}^{opt}$ manifests a minimum when $\xi_{\eta 0}$ is about 10% for configurations based on ♯8. Concerning the case of $\gamma_n < 1$, Fig. 8.37 remarks the presence of an optimal value of $\xi_{\eta 0}$, while $U_{R\alpha}^{opt}$ is always increasing.

Finally, comparing the results of this section with those of § 7.4.2, it is worth highlighting the improvements of performance obtained through the design of optimal configurations, which manifest a more unstable behaviour and start to oscillate at lower reduced flow speed. Anyway, the maximum values of the performance factors, Γ'_η or Γ_η in Fig. 8.34, are still lower then those achieved in literature (see Table 2.2 in § 2.3.5). The optimisation procedure suggested optimal configurations, but these are affected by the technical features of the aeroelastic setup used to perform as reliable as possible measurements of the post-critical regime oscillations (these two issues are in contrast). More discussions on this topic are reported in § 9.

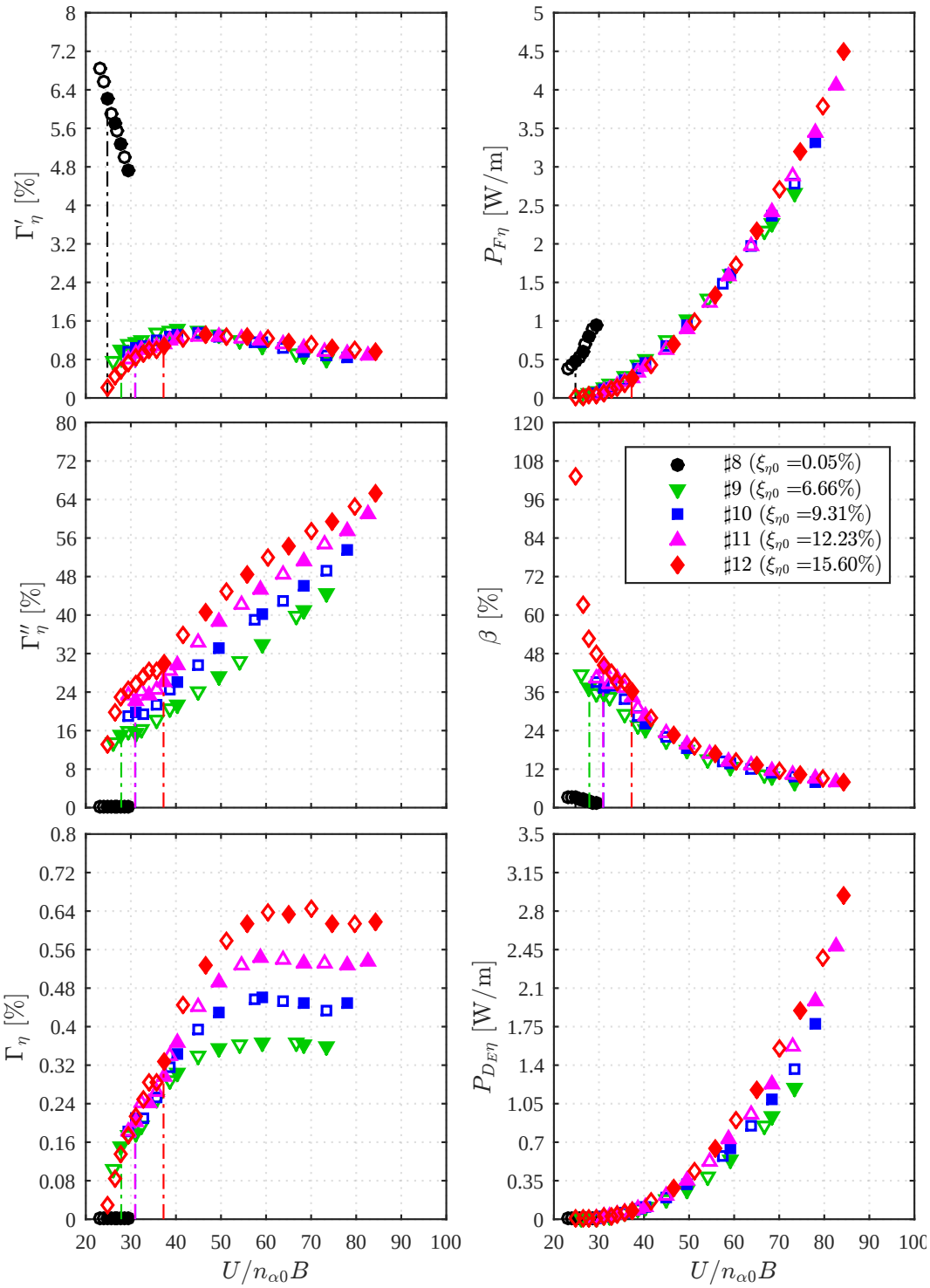

Figure 8.31. Performance evaluation for configurations with still-air frequency ratio γ_n = 1.064 and different heaving-damping levels.

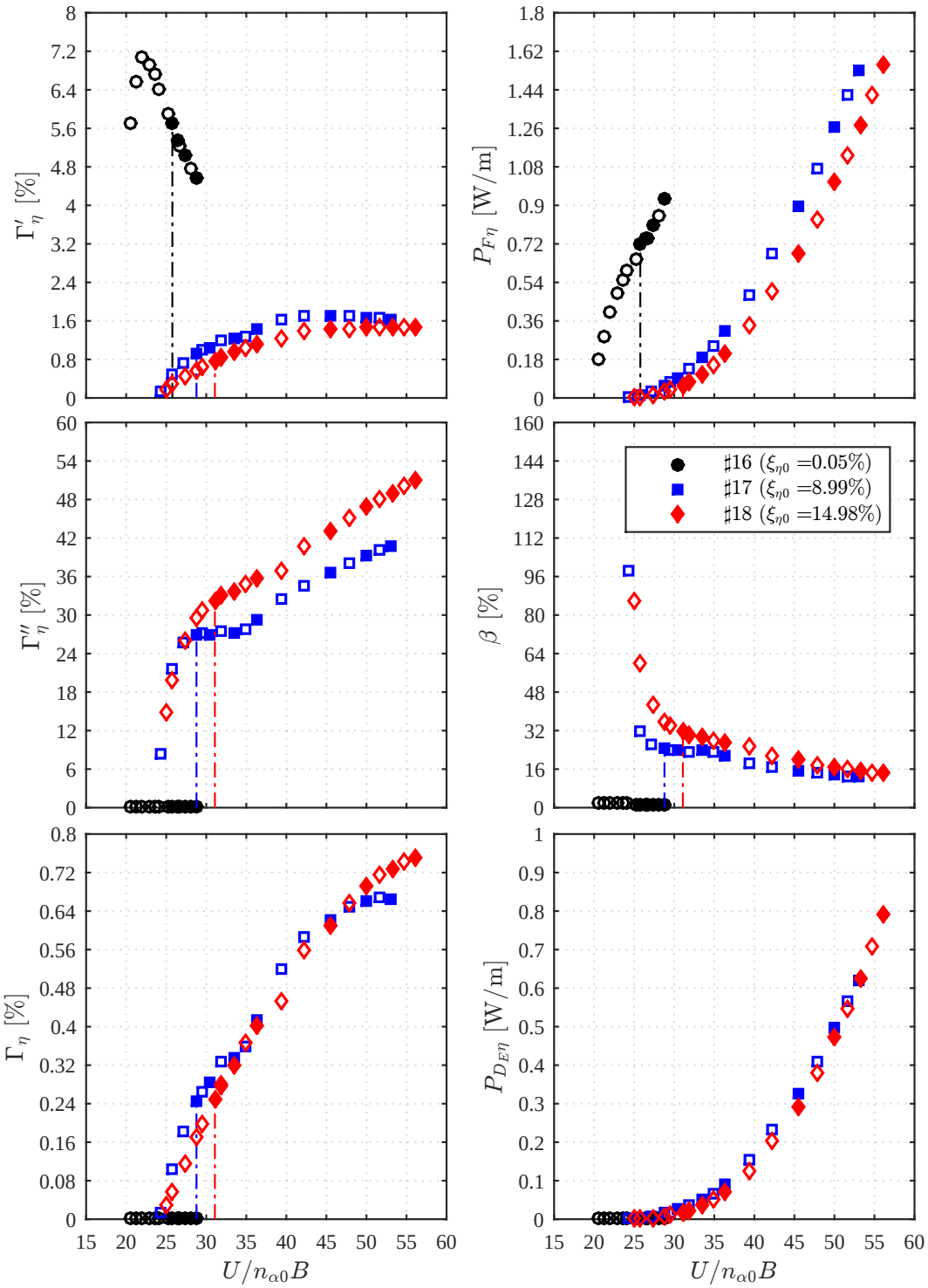

Figure 8.32. Performance evaluation for configurations with still-air frequency ratio γ_n = 1.007 and different heaving-damping levels.

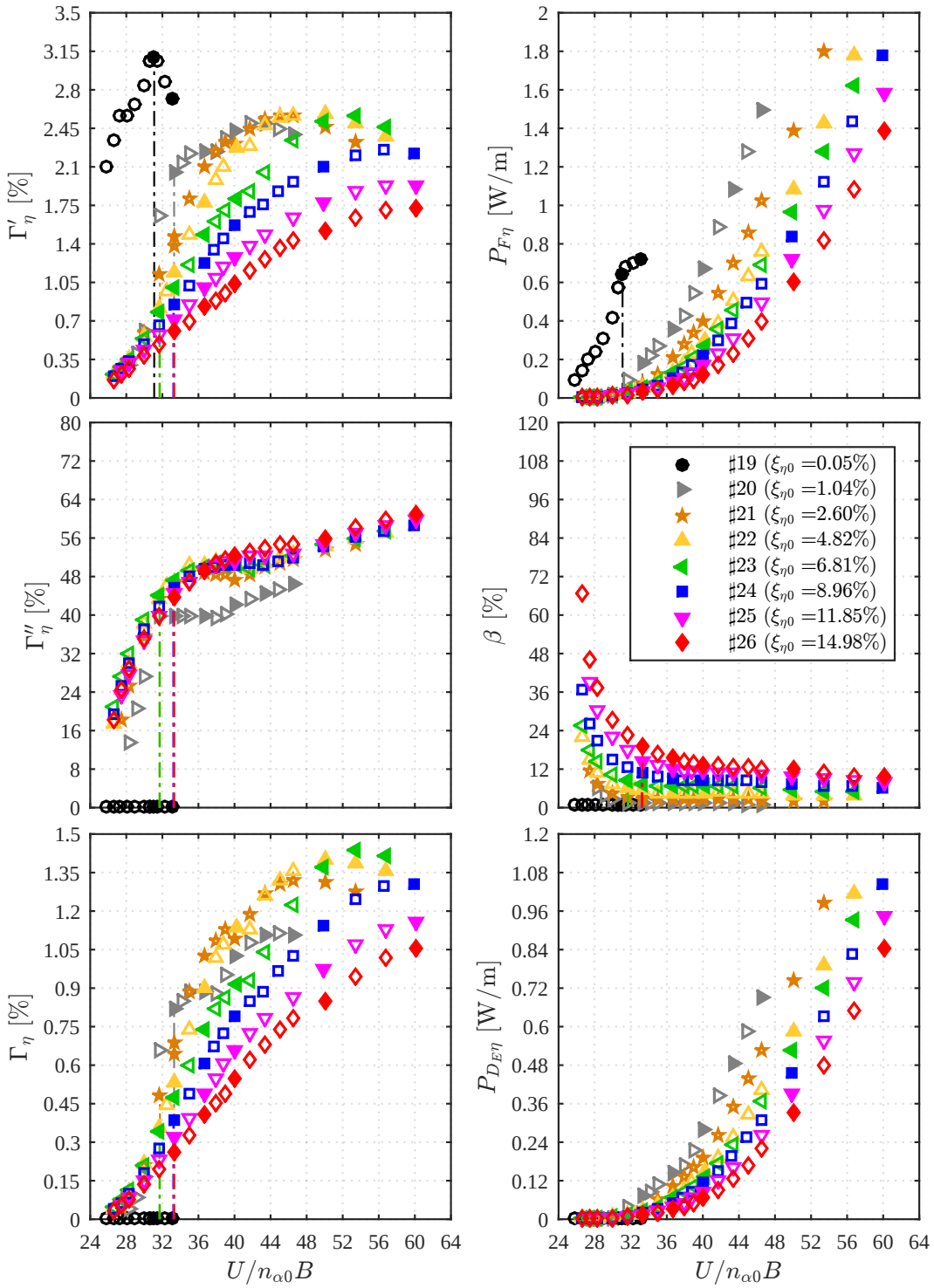

Figure 8.33. Performance evaluation for configurations with still-air frequency ratio γ_n = 0.917 and different heaving-damping levels.

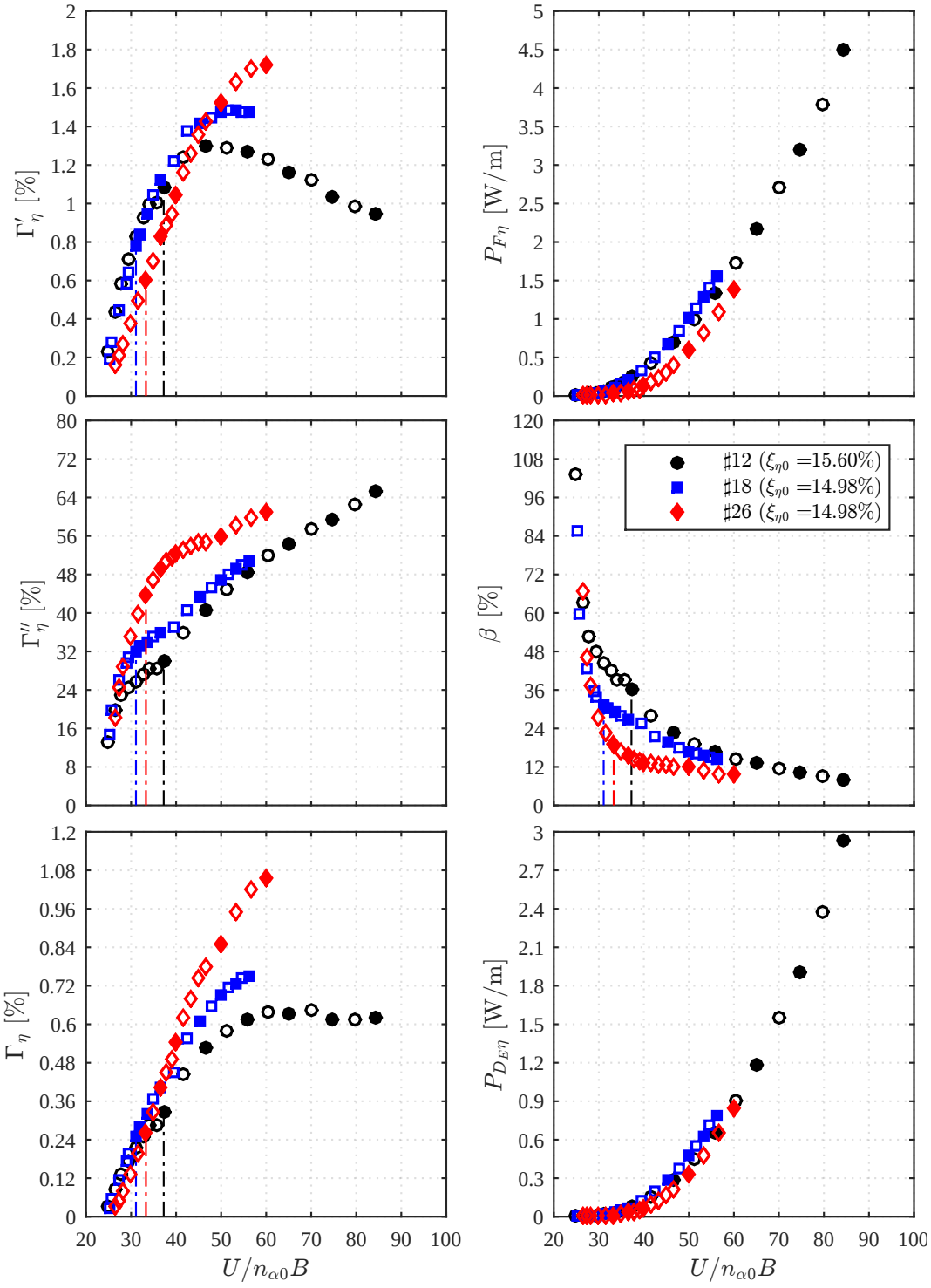

Figure 8.34. Performance comparisons for configurations with different still-air frequency ratio (γ_n = 1.064 for ♯12, γ_n = 1.007 for ♯18, γ_n = 0.917 for ♯26) and maximum heaving-damping level.

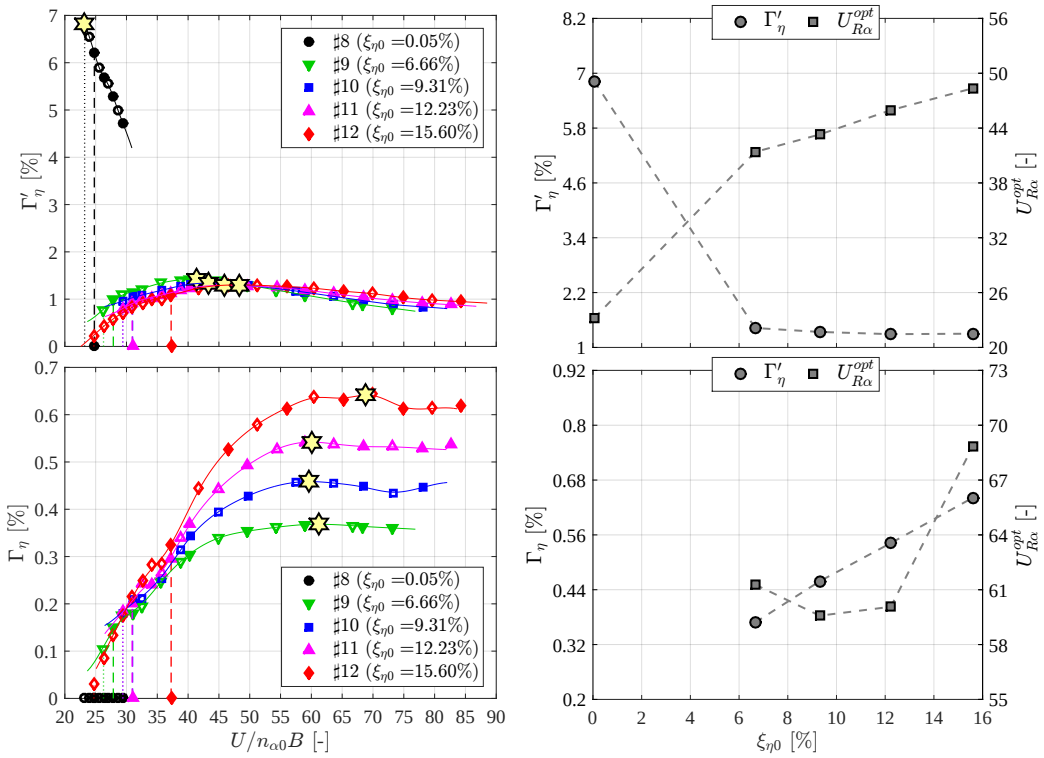

Figure 8.35. Evolution of the maximum performance points for configurations with still-air frequency ratio γ_n = 1.064 and different heaving-damping levels.

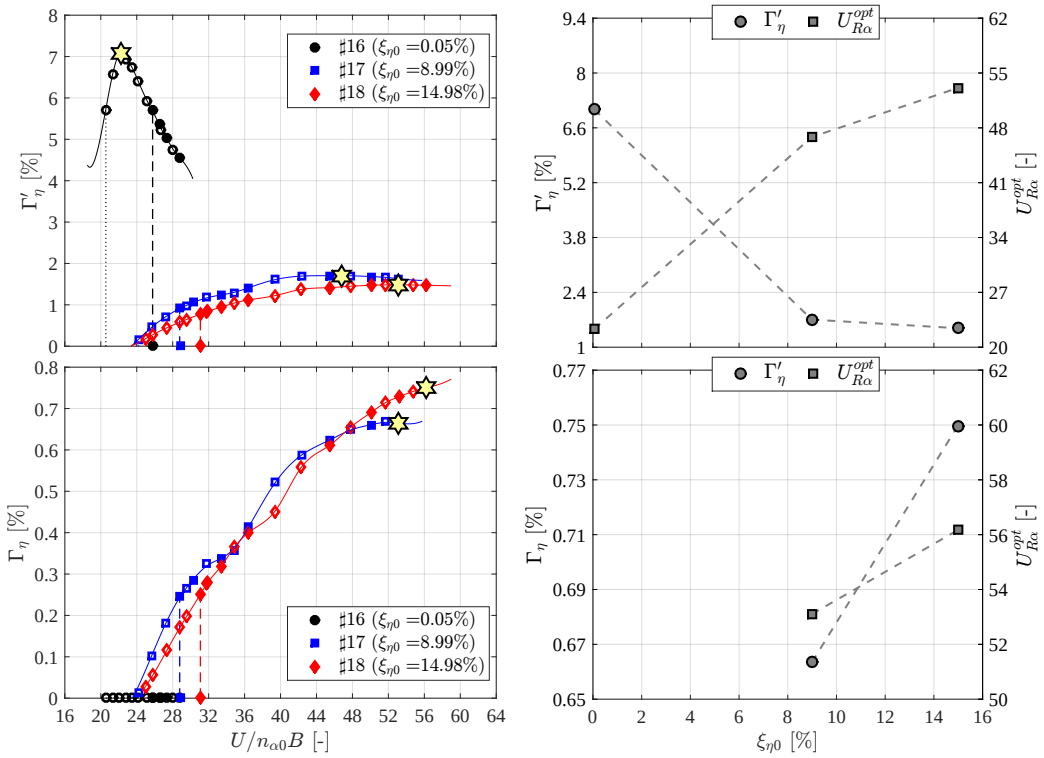

Figure 8.36. Evolution of maximum performance points for configurations with still-air frequency ratio γ_n = 1.007 and different heaving-damping levels.

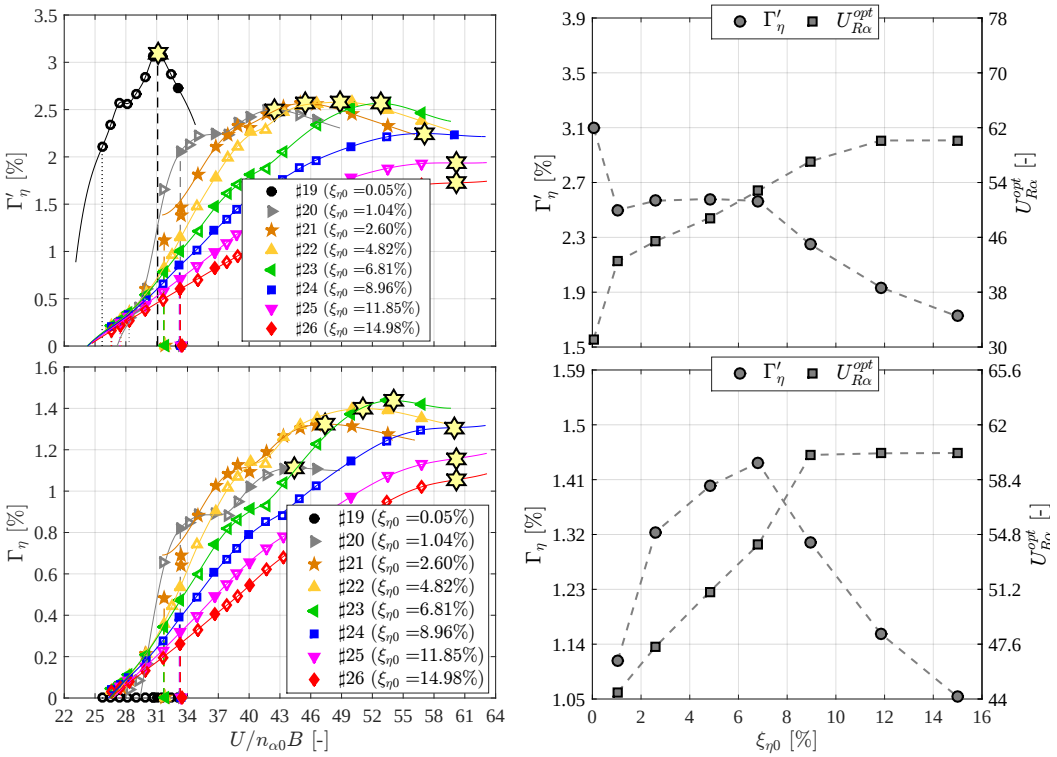

Figure 8.37. Evolution of maximum performance points for configurations with still-air frequency ratio $\gamma_n = 0.917$ and different heaving-damping levels. The points identified for the last two higher levels of $\xi_{\eta 0}$, corresponding to ♯25 and ♯26, have to be carefully considered, since the investigated range of flow speed do not allow the verification of the presence of a maximum in the performance curve.

Chapter 9

Discussions

9.1 Main phenomenological features

9.1.1 Elastic-axis position vs. system inertias

The position of the elastic axis depends on the heaving-damping level (see § 8.1), and the design of flutter-based generators has to take into account this behaviour.

For low-damped systems, the optimal position of the elastic axis is toward the trailing edge when $\gamma_n > 1$, and toward the leading edge when $\gamma_n < 1$. However, this low-damping level does not allow any power generation, and higher damping levels have to be considered to properly simulate a realistically operative power condition. In this case, the linear analysis suggested that the optimal x_e values move toward the upstream quarter-chord with increasing $\xi_{\eta 0}$, requiring also a small positive mass unbalance (see § 8.1).

Fig. 9.1 considers some of the experiments conducted in both Stahlbau Institut and CRIACIV campaigns, and it shows that, for low-damping levels ($\xi_{\eta 0} < 0.1\%$ in the selected configurations), $x_e < 0$ has significant stabilizing effects since γ_n was larger than unity. In fact, comparing configuration #3 ($x_e = 0$, $x_m = 0.034$, $\gamma_n = 1.294$) with #20 ($x_e = -0.10$, $x_m = 0.041$, $\gamma_n = 1.243$) and ♯27 ($x_e = 0$, $x_m = 0.056$, $\gamma_n = 1.254$) with ♯13 ($x_e = -0.25$, $x_m = 0.063$, $\gamma_n = 1.243$), a negative value of the stiffness eccentricity postpones the instability and importantly modifies the motion shape by reducing the pitching amplitudes. Unfortunately, a similar direct comparison, in which only the x_e parameter modifies, is not available among configurations with higher heaving damping, since test cases specific for this aim were not planned due to time limits. Thus, the only information available come from the linear analysis of § 8.1.

It has also to be pointed out a peculiar behaviour experimentally observed in the case of configurations ♯13 and ♯27, both characterised by $\gamma_n \simeq 1.24$. Fig. 9.1 shows the presence of a steady-state regime of oscillation with low amplitude, intermediate between the rest and the large-amplitude stable branch, occurring for a small range of flow velocities immediately after the instability threshold. It recalls a snaking behaviour of the system response [165]. The low-amplitude solutions for the two configurations present similar heaving and pitching amplitudes and phase shift, although the systems are characterised by different positions of the elastic axis. Only few measurements were possible in this short branch, but it is clear that the motion characteristics were markedly different from those of the large-amplitude branch. The LCO in the intermediate branch is characterised by a highly-modulated stationary motion. This behaviour is probably due to the interference of multiple frequency components, as indicated by the presence of higher-order harmonics in the spectra of the motion components (observed in other similar flow-structure-interaction problems, such as in [143], [168] and [130]). However, the low-amplitude response seems to have a different nature compared to the dynamic-stall mechanism, which drives the large-amplitude response branch.

Other key parameters of the flutter problem are the inertial parameters, that is the mass ratio μ and the polar inertia radius r_α, and the linear analyses of § 8.1 showed their significant influence in the critical condition. Thus, it is interesting to observe the effect of combining

positive elastic-axis eccentricity with lower values of the inertial parameters. In particular, lighter systems seem to be more prone to flutter instability, and this could compensate any possible reduction of the amplitudes due to $x_e < 0$, as experimentally observed for low-damped configurations. Indeed, in this case the inertial parameters can help to enhance the motion amplitudes even when $x_e < 0$ is imposed to follow the optimal configuration design. This result is clear when comparing configurations ♯1 ($x_e = 0$, $\mu \simeq 2709$, $\gamma_n = 0.965$) with ♯19 ($x_e = -0.25$, $\mu \simeq 1392$, $\gamma_n = 0.917$) and ♯3 ($x_e = 0$, $\mu \simeq 2605$, $\gamma_n = 1.048$) with ♯8 ($x_e = -0.25$, $\mu \simeq 1378$, $\gamma_n = 1.064$) in Fig. 9.2. The lighter configurations (♯19 and ♯8), although having $x_e = -0.25$, always show lower critical reduced velocities and larger motion amplitudes. This result was obtained by simply halving μ and reducing r_α by 1/3, and it holds also for different values of the still-air frequency ratio γ_n. A direct experimental comparison for higher heaving-damping levels is now available if comparing ♯4 ($x_e = 0$, $\mu \simeq 2605$, $\gamma_n = 1.048$) with ♯9 ($x_e = -0.25$, $\mu \simeq 1378$, $\gamma_n = 1.064$) in Fig. 9.2, which both have $\xi_{\eta 0} \simeq 9.4\%$. In this case, the motion amplitudes of the lighter system are only slightly larger, although the evolutions of the pitching-to-heaving amplitude ratios state that the lighter configuration has a more dominant heaving motion component (positive for energy-harvesting purposes).

It is worth highlighting that the set of planned investigations did not allow a systematic evaluation of μ and r_α influence on the post-critical regime. The values of these parameters strongly depend on the technical features of the aeroelastic setup (in both campaigns), and they cannot be easily modified without altering the boundary conditions. As example, μ is markedly affected by the passive mass of the setup, which is constrained to the setup technology. While adding passive mass is limited by the maximum static displacement allowed with respect the elastic-suspension characteristics and by too large frequency modifications that have to be compensated through heaving/pitching stiffness adjustments. The modification of the model span may be the only effective way (if allowed, as in the case of CRIACIV setup). By contrast, this usually requires a modification of the setup (*e.g.* distance between blade springs) that can affect the comparisons, since the boundary conditions are different. Similar considerations can be made for the polar inertia.

9.1.2 Increasing the heaving damping

9.1.2.1 Destabilizing effect

It is commonly expected that increments of damping lead to system stabilization, postponing the critical condition and reducing the flow-induced effects. This is confirmed by the majority of tested configurations encountered in § 7 and § 8. By contrast, as predicted by the linear theory (see § 8.1), a destabilizing effect of heaving damping can arise for specific sets of the governing parameters.

The effect of damping has extensively been studied in the field of structural dynamics and non-conservative mechanical systems in general (*e.g.* [126, 70, 116, 135] for a review). Dealing with the dynamic behaviour of a 2-DoF segmented column subjected to follower axial forces, Ziegler discovered in 1952 that small damping values can anticipate the buckling instability as compared to the undamped system [224]. Subsequently, several studies focused on the mathematical understanding of this interesting paradox [34, 96, 163, 35, 115], which is characterised by an instability similar to the Hopf bifurcation of Hamiltonian systems [92] and requires a flutter mechanism to occur (in this case interpreted as a general multi-DoF problem with mode-coupling). However, despite the large amount of work done on this topic (see also *e.g.* [89, 174, 120]), the scientific understanding of the originating physical mechanism is still developing [135, 136, 137]. Moreover, very little experimental evidence is available so far [200, 31].

In the context of fluid-structure interaction problems, damping destabilization was observed in the case of a flowing fluid bounded by a flexible surface, and it was explained through the concept of negative energy waves [27]. This was also discussed for energy-harvesting applications of flexible plates in axial flows [155]. To the authors' knowledge, only little research is available on the effect of damping on classical flutter, because of lack of interest for common applications in civil/aeronautical engineering. In particular, Frazer

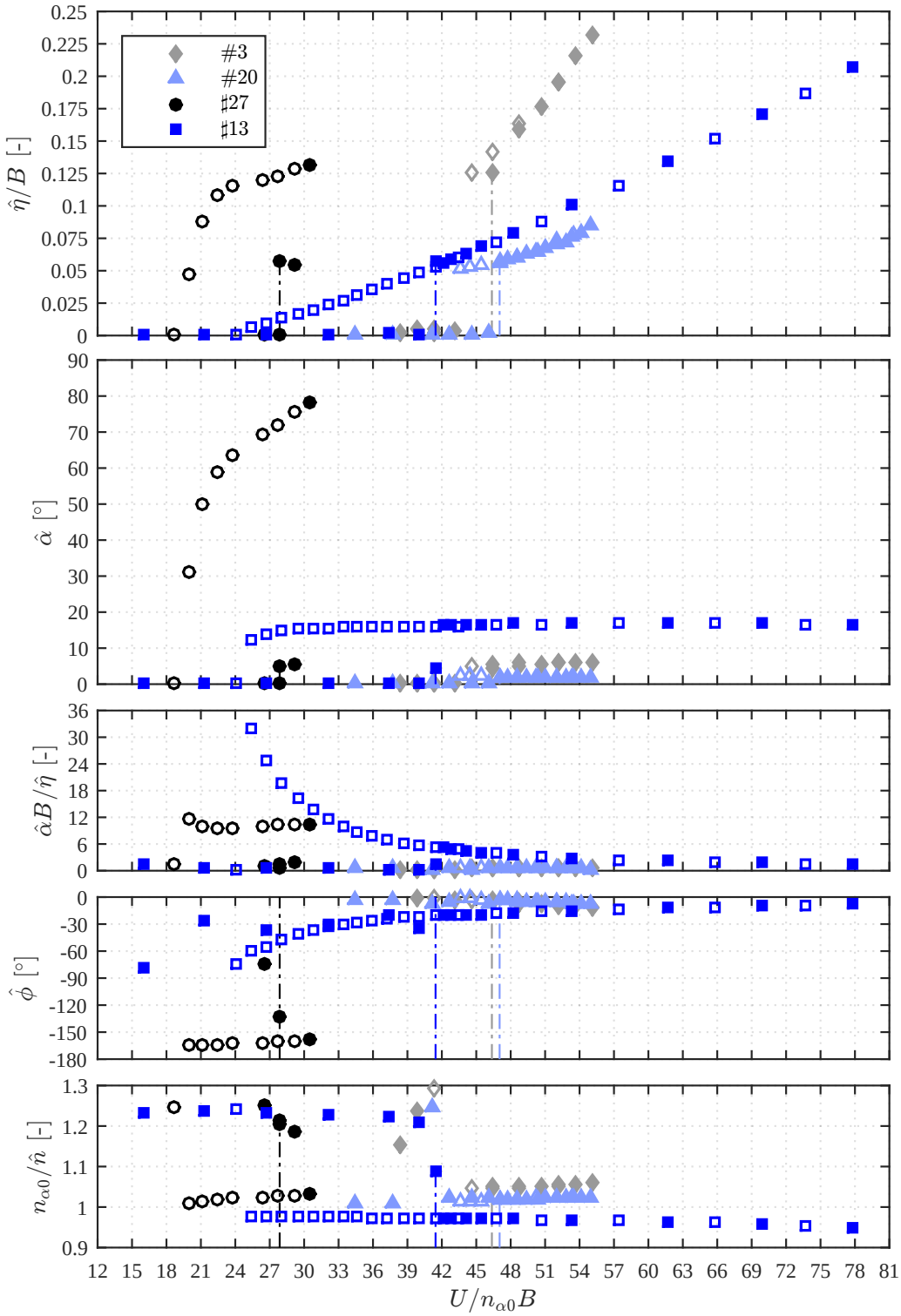

Figure 9.1. Influence of negative elastic-axis positions in the post-critical regime for configurations from both Stahlbau and CRIACIV campaigns, all with low heaving damping ($\xi_{\eta 0} \simeq 0.06\%$). The value of x_e is 0 for #3 and ♯27, -0.1 for #20, -0.25 for ♯13.

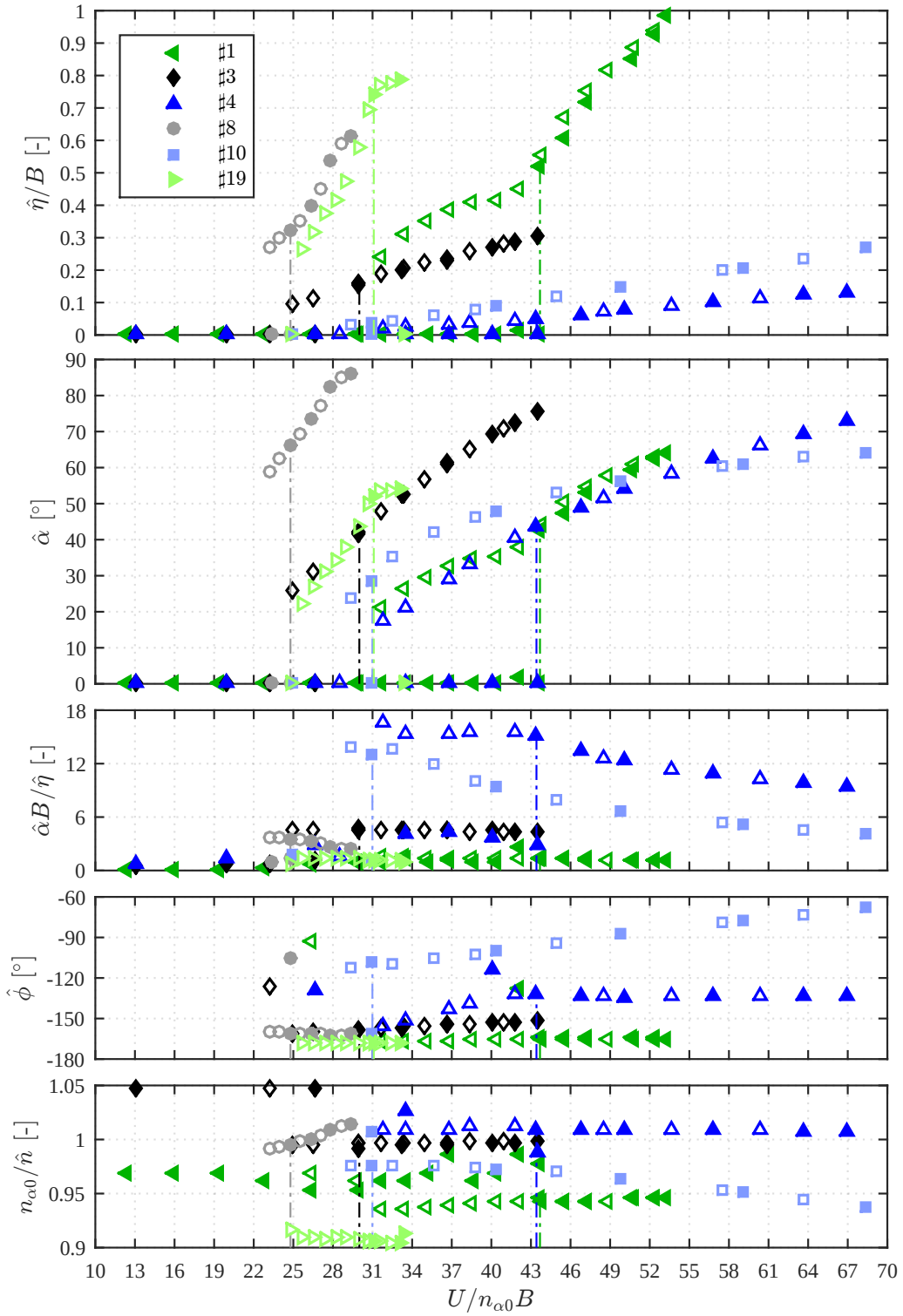

Figure 9.2. Influence in the post-critical regime of negative elastic-axis positions ($x_e = 0$ for ♯1, ♯3 and ♯4, while $x_e = -0.25$ for ♯8, ♯10 and ♯19) when combined with smaller values of the inertial parameters ($\mu \simeq 2650$ and $r_\alpha \simeq 0.62$ for ♯1, ♯3 and ♯4, while $\mu \simeq 1380$ and $r_\alpha \simeq 0.40$ for ♯8, ♯10 and ♯19), for configurations from CRIACIV campaigns. Cases ♯4 and ♯10 have $\xi_{\eta 0} \simeq 9.4\%$, while $\xi_{\eta 0} \simeq 0.05\%$ for the others.

in 1939 [82] (cited in [84]) outlined the possibility to anticipate the instability threshold by means of several types of damping (*e.g.* dry friction, viscous or proportional to the squared amplitude). However, no experimental evidence of damping effects on the post-critical response of 2-DoF aeroelastic systems undergoing classical flutter has been provided yet.

In this thesis work, this behaviour was experimentally observed during the campaign at the Stahlbau Institut for configurations based on #10, as discussed in § 7.1.2. Interestingly, a similar behaviour was also observed during the CRIACIV campaign for configurations based on ♯13, as shown in Fig. 9.3. In this case, a completely different aeroelastic setup was used and also a different sectional model was installed (blade-spring setup with 25:1 plate at CRIACIV, § 5.3.3, while coil-spring setup with 15:1 plate at Stahlbau, § 5.2.3). Moreover, the position of the elastic axis x_e, mass ratio μ and inertial radius r_α were different, while only the mass eccentricity x_m and still-air uncoupled frequency ratio γ_n parameters were maintained as compared to the Stahlbau campaign (compare configurations details in Table 6.3 and Table 6.2).

In both experimental campaigns, the systems became more unstable, anticipating the instability threshold (vertical dashed lines in the figures). Moreover, while the heaving amplitudes of oscillation were practically unaltered, the pitching components were markedly enhanced. The destabilization was also confirmed for larger values of heaving damping, since this time ξ_η was raised up to about 15% during the CRIACIV tests.

The analysis of the linear theory results, combined with the experimental evidence, suggests that non-negligible downstream mass unbalance ($x_m \simeq 0.06$) is required to observe the destabilizing effect of damping. Furthermore, observing the configurations tested in the CRIACIV campaign as compared to the Stahlbau Institute campaign (Fig. 9.4), it is possible to infer that values of the still-air frequency ratio sufficiently larger than unity ($\gamma_n \simeq 1.3$), in addition to small positive mass unbalance, are required for the destabilizing effect of heaving damping to occur. In particular, Fig. 9.5 displays the graphical solution of the complex flutter determinant for two values of the still-air frequency ratio γ_n. For both high values of γ_n (left-hand side of Fig. 9.5) and $\gamma_n \cong 1$ (right-hand side of Fig. 9.5), the increase of $\xi_{\eta 0}$ induces the extension of the real curve and moves down the imaginary curve. Nevertheless, for $\gamma_n = 1.243$ the imaginary curve intersects the real curve in its lower branch for high values of the heaving damping, producing a reduction of U_R^c. Therefore, it is apparent that γ_n plays a key role in the destabilizing effect of damping.

It is worth noting in Fig. 9.4 that, while the amplitude-velocity diagrams of $\hat{\eta}/B$ and $\hat{\alpha}$ of the configurations tested at the Stahlbau Institut and CRIACIV experience similar evolutions, the other motion parameters are markedly different. In particular, the phase $\hat{\phi}$ and motion frequency $\hat{n}$ follows opposite trends with the reduced flow speed, and this may due to the different values of the elastic-axis eccentricity.

Finally, the role of heaving damping on the stability onset characteristics can also depends on other parameters. Considering the governing parameters representing configurations derived from ♯13, Fig. 9.6 explains the sensitivity to variations of μ, r_α and ξ_α. In particular, the destabilizing effect seems to disappear for very-low-inertia systems and for high pitching damping values, as shown in Fig. 9.6.

9.1.2.2 Toward a common configuration

The investigation conducted through the linear analysis (see § 8.1) seemed to indicate that very high heaving-damping levels tend to level out even different configurations, reducing the dependence of the response on the governing parameters. In particular, referring to *e.g.* Fig. 8.26, the mass unbalance and elastic-axis position of optimal configurations converged to $x_m \simeq 0.06$ and $x_e \simeq -0.35$ when the heaving damping was $\xi_{\eta 0} \simeq 25\%$. Moreover, the phase difference tended to $-90°$ and the amplitude ratio to about 8.5, while the motion frequency followed parallel curves with constant slope. Also the optimal critical reduced velocity seemed to follow a convergent path. Hence, a virtual common configuration seems to characterise the response for high values of the heaving damping.

However, it is worth highlighting that the linear theory holds only at the instability threshold (as better explained in § 9.2) and, preliminarily, all these considerations may be

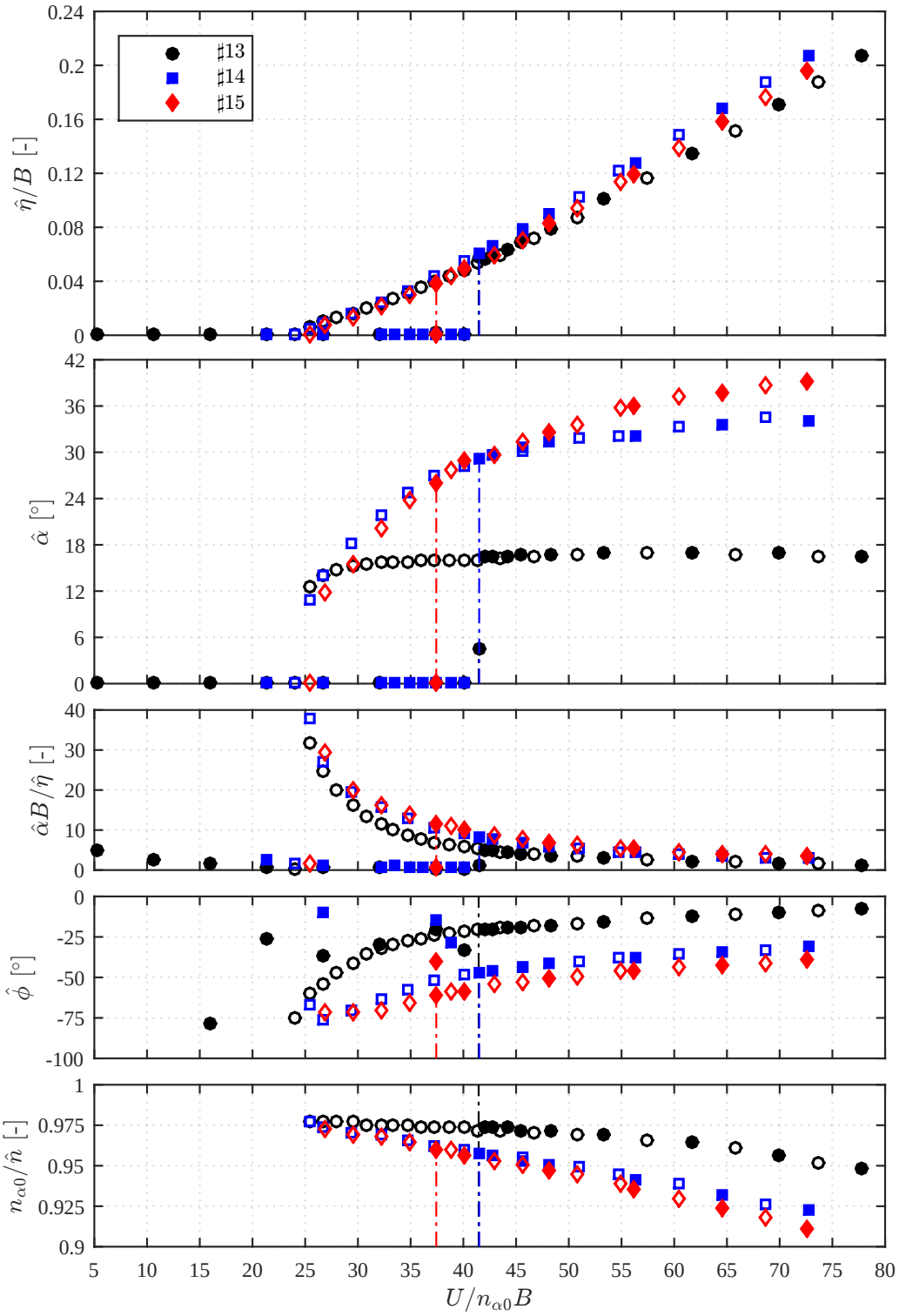

Figure 9.3. Effects of high levels of heaving damping on a configuration with large still-air uncoupled frequency ratio ($\gamma_n = 1.239$) during the CRIACIV campaign. The value of $\xi_{\eta 0}$ is 0.05% for ♯13, 9.38% for ♯14 and 14.57% for ♯15.

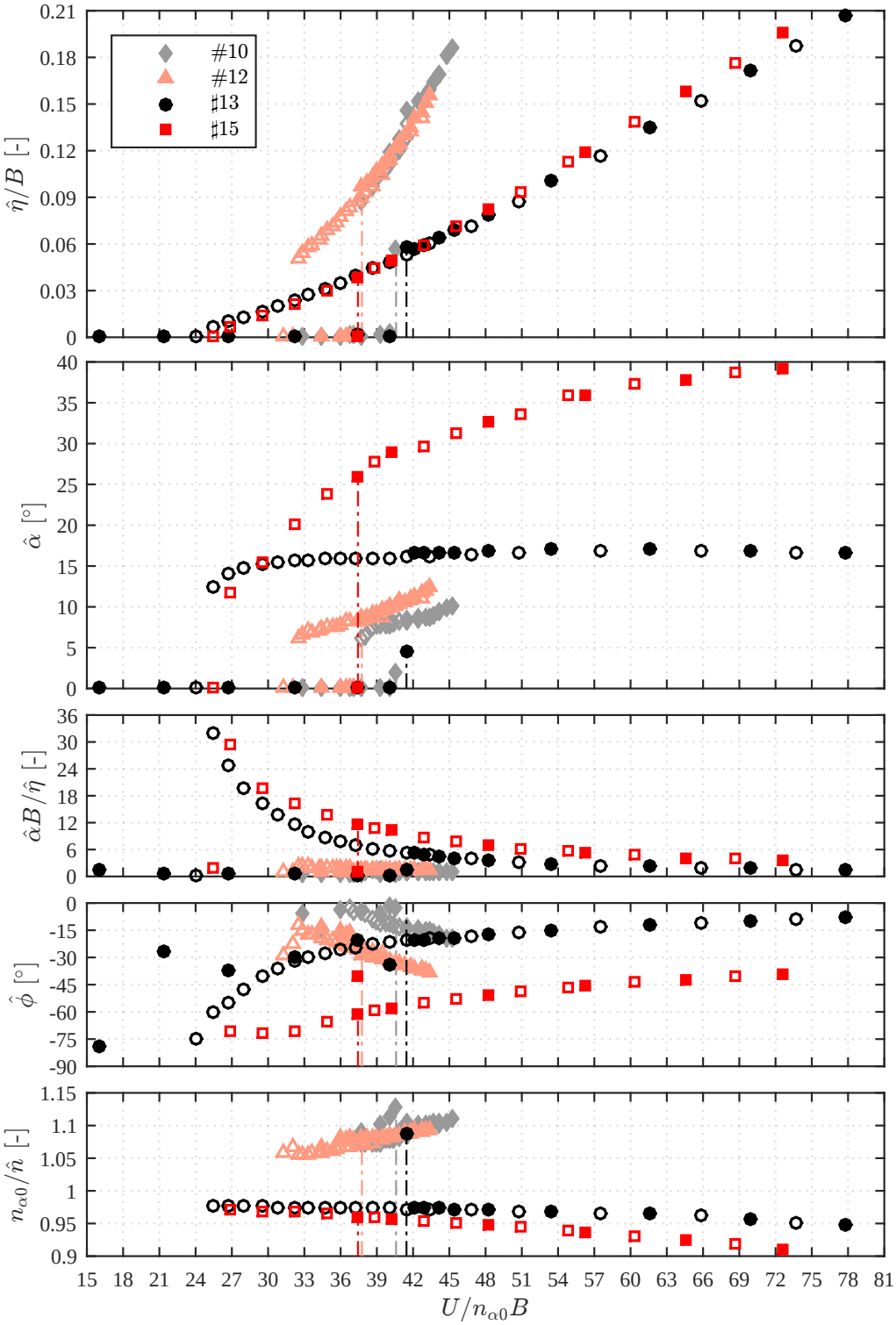

Figure 9.4. Experimental evidence of the destabilizing effect of heaving damping, considering both Stahlbau Institute and CRIACIV results. The value of $\xi_{\eta 0}$ is 0.07% for #10 and 5.67% for #12, while the others parameters are $\xi_{\alpha 0} = 0.17\%$, $x_e = 0$, $\mu \simeq 954$, $x_m = 0.056$, $r_\alpha = 0.84$ and $\gamma_n = 1.316$. The value of $\xi_{\eta 0}$ is 0.05% for ♯13 and 14.57% for ♯15, while the others parameters are $\xi_{\alpha 0} = 1.04\%$, $x_e = -0.25$, $\mu \simeq 1390$, $x_m = 0.053$, $r_\alpha = 0.401$ and $\gamma_n = 1.243$.

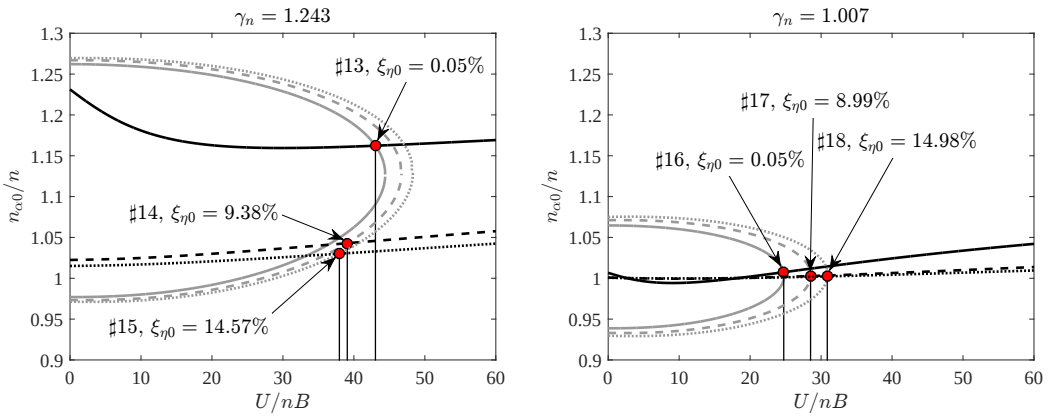

Figure 9.5. Real (black lines) and imaginary (grey lines) solutions of the complex flutter determinant for two still-air frequency ratios. Low (solid lines), medium (dashed lines) and high (dotted lines) damping levels are considered.

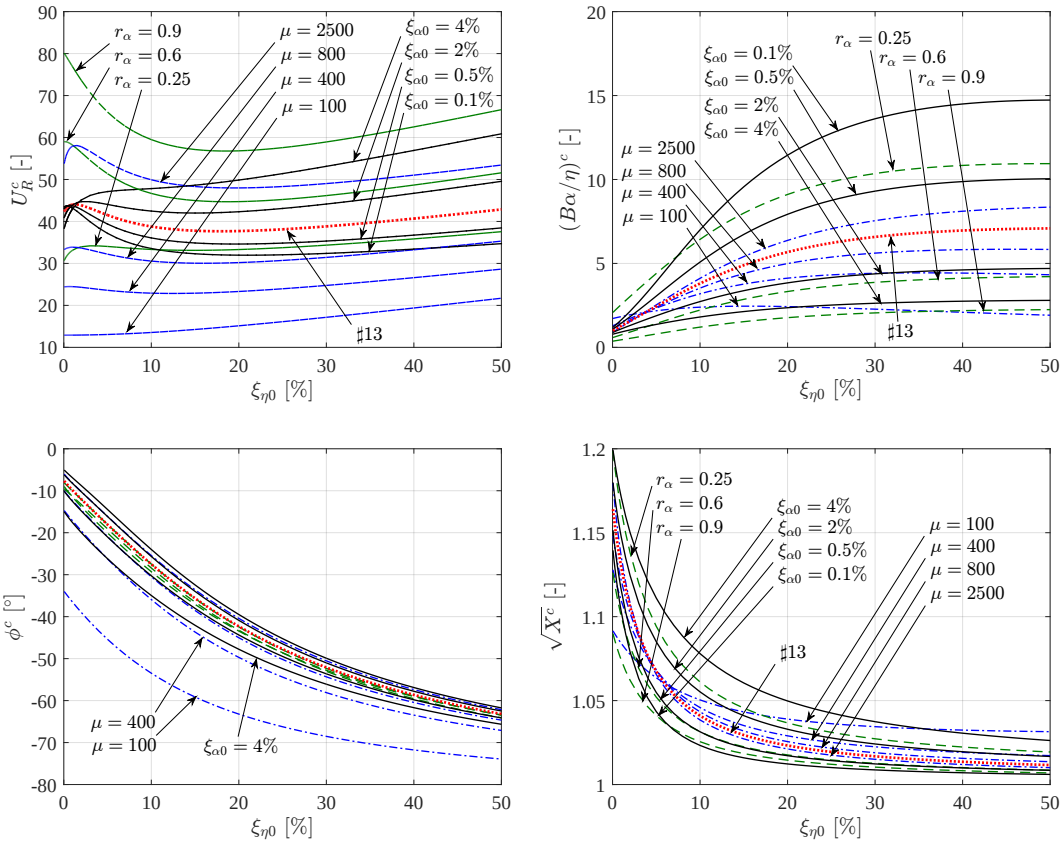

Figure 9.6. Mass ratio (blue-dash-dot lines), polar-inertia radius (green-dash lines) and pitching damping (black-solid lines) influences on the linear predictions of the critical condition, with respect to configuration ♯13 (red-dot lines).

supposed to be valid only for small oscillation amplitudes. Interestingly, Fig. 9.7 seems to experimentally verify the previous result from linear theory, which can be extended also to the post-critical regime. Indeed, the superimposition of configurations based on ♯13, ♯16 and ♯19, which mainly have different values of the still-air uncoupled frequency ratio, shows that the post-critical regime features tend to become more similar with increasing $\xi_{\eta 0}$. The configurations ♯16 and ♯19 manifest a very different motion shape if compared to ♯13, in particular in terms of amplitudes and phase differences. But, when increasing $\xi_{\eta 0}$, configuration ♯13 increases the pitching amplitudes, while both ♯16 and ♯19 decrease the pitching amplitudes. At the same time, the very large heaving amplitudes of ♯16 and ♯19 markedly reduce to be closer to those of ♯13. Moreover, the phase $\hat{\phi}$ gets gradually toward $-90°$ with increasing $\xi_{\eta 0}$.

9.1.2.3 The special case of unity still-air uncoupled frequency ratio

Considering the fixed pair of parameters $x_e = -0.25$ and $x_m = 0.053$, representing configurations derived from ♯13, Fig. 9.8 shows that still-air frequency ratios higher than 1.1 or lower than 0.9 are required to observe the destabilizing effect in a certain range of $\xi_{\eta 0}$. For these configurations, the critical reduced velocity at very low damping levels is always higher than that for higher values of ξ_η and tends to follow a common trend for $\xi_\eta > 40$-50%. Considering also the other curves in Fig. 9.8, it is clear that the configuration with $\gamma_n = 1$ represents a special case. Indeed, it can be considered as a limit configuration corresponding to a lower bound for U_R^c and an upper bound for $(B\alpha/\eta)^c$. Moreover, it represents a divide for the phases and motion frequencies, since configurations with $\gamma_n > 1$ present $\phi^c > -90°$ and $\sqrt{X^c} > 1$, while configurations with $\gamma_n < 1$ are characterised by $\phi^c < -90°$ and $\sqrt{X^c} < 1$. In particular, especially the phase is very sensitive to variations of γ_n when the latter is close to unity. This dependence is more pronounced for low damping values, where any unstable configuration seems to show a phase close to $0°$ and $-180°$, *i.e.* fixed instantaneous center of rotation (downstream the midchord for $\gamma_n < 1$ and upstream for $\gamma_n > 1$).

In general, with increasing the heaving damping all configurations seem to converge to the behaviour of the system with $\gamma_n = 1$, and this further explains the destabilising effect (see § 9.1.2.1). In fact, a reduction of the critical reduced flow speed is observed increasing ξ_η every time U_R^c for low damping values is significantly higher that the corresponding value for $\gamma_n = 1$.

It is worth highlighting that Fig. 9.8 also provides some information supporting the existence of the common configuration for very high $\xi_{\eta 0}$ as depicted in § 9.1.2.2. The classical flutter mechanism needs two DoFs at least to occur, and two modes of oscillation are present slightly before the instability threshold, one having a shape with dominant heaving component and the other with dominant pitching component. However, high values of $\xi_{\eta 0}$ tends to vanish the presence of the heaving component in the motion of the system. In fact, although the heaving is not physically constrained, damping increments reduce the oscillation capability in that DoF. Thus, the mode having a dominant heaving component tends to vanish, forcing the instability to occur through the mode with the dominant pitching component. Therefore, the system would appear as characterised by a single model of oscillation (the one less affected by the heaving damping), and it is less affected by γ_n, explaining the tendency of various configurations to follow the same response of the configuration with $\gamma_n = 1$. Then, the highly damped system adapts to behave according to the configuration that maximises the heaving amplitude, attempting to compensate the influence of high $\xi_{\eta 0}$. This occurs when the pitching-to-heaving phase difference is $-90°$, stating the absence of a fixed instantaneous centre of rotation and producing the maximum heaving amplitude given a fixed pitching amplitude with minimum work of the flow-induced loads. Hence, the heaving amplitude arising in the motion is essentially due to the presence of the mass unbalance, which guarantees a flutter mode with components in both DoFs, preserving the instability to occur.

This instability development reflects also in the post-critical regime, in which the motion tends to manifests through a shape with a dominant pitching component, being not affected by $\xi_{\eta 0}$, and following the evolution of configuration with still-air uncoupled frequency ratio

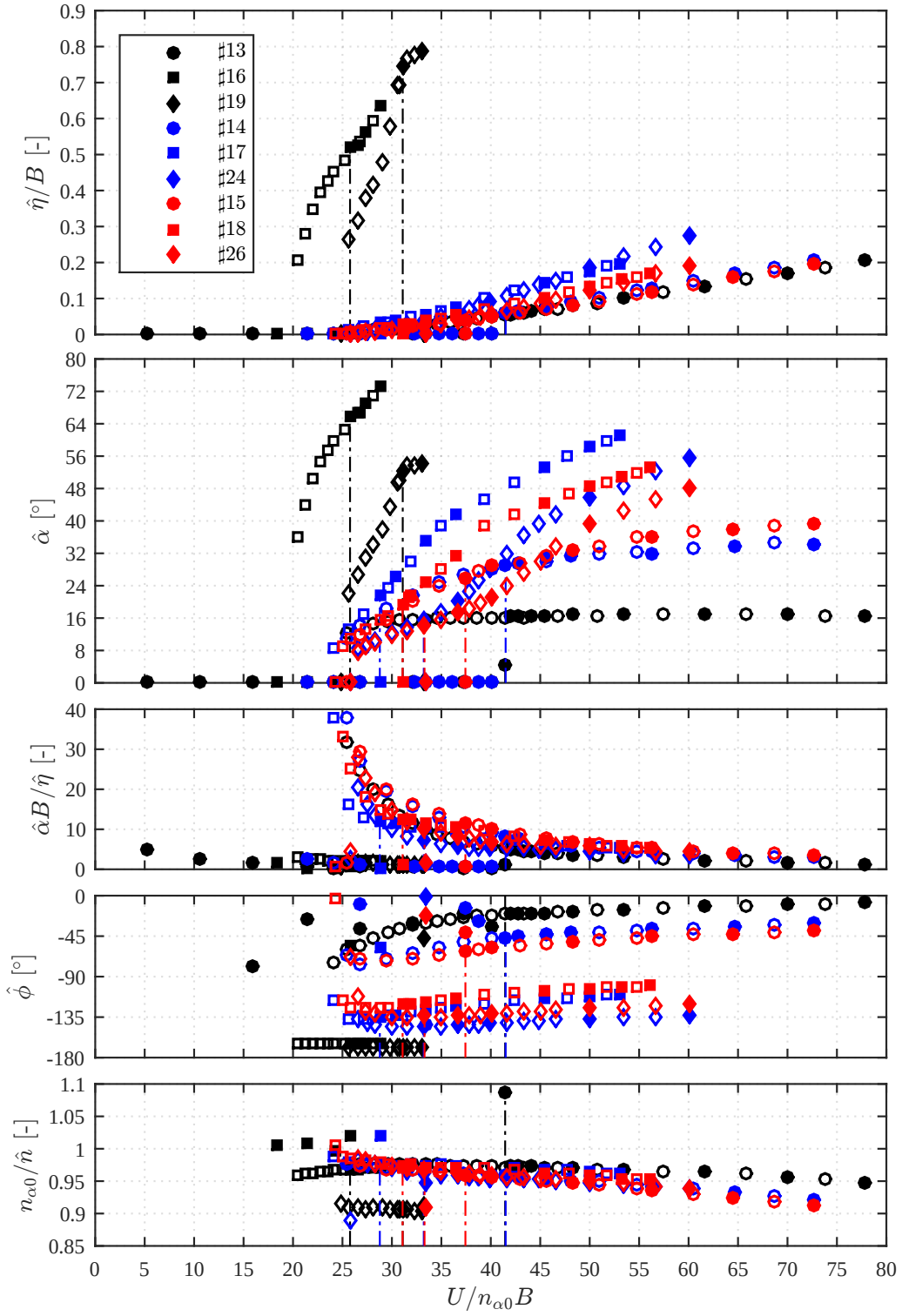

Figure 9.7. Comparison of post-critical paths for configurations with different still-air uncoupled frequency ratio ($\gamma_n = 1.239$ for ♯13-♯16-♯19, $\gamma_n = 1.007$ for ♯14-♯17-♯24, $\gamma_n = 0.917$ for ♯15-♯18-♯26), suggesting a common configuration for high heaving damping ($\xi_{\eta 0} = 0.05\%$ for ♯13-♯16-♯19, $\xi_{\eta 0} \simeq 9\%$ for ♯14-♯17-♯24 and $\xi_{\eta 0} \simeq 15\%$ for ♯15-♯18-♯26).

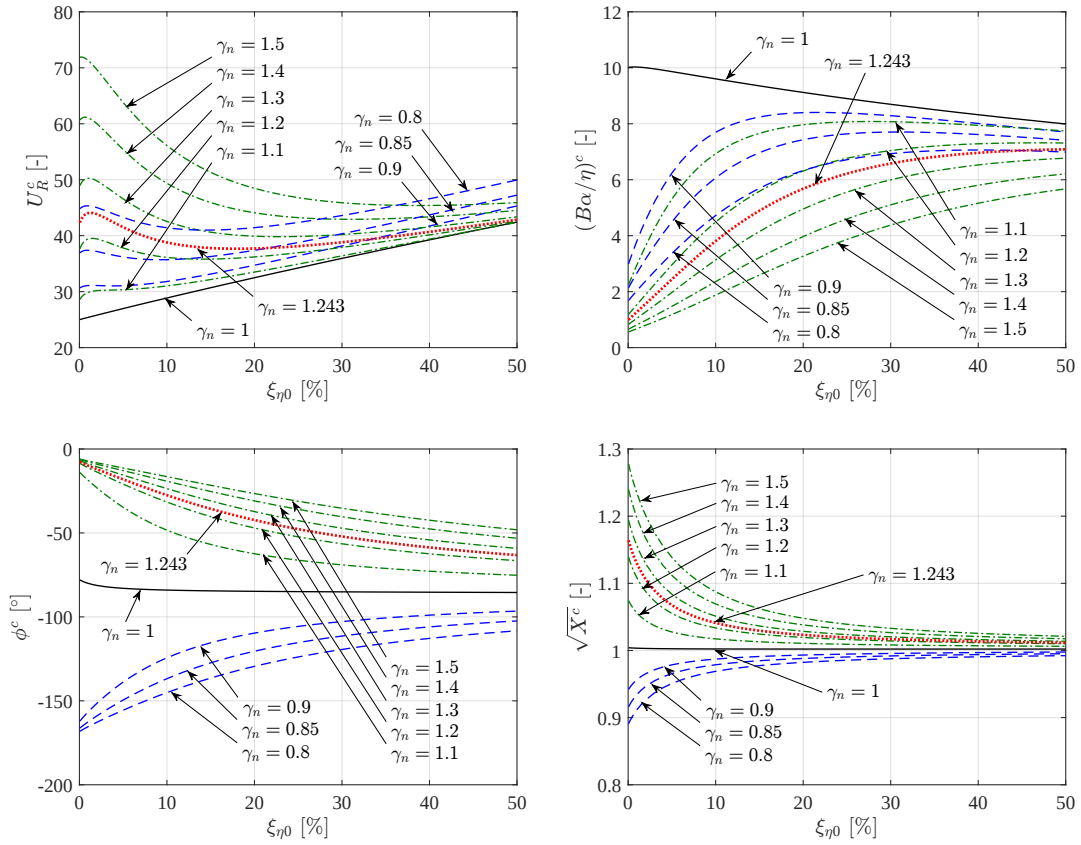

Figure 9.8. Still-air frequency influence, smaller (blue-dash lines) and larger (green-dash-dot lines) than unit (black-solid lines) value, on the linear predictions of the critical condition, with respect to configuration ♯13 (red-dot lines).

closer to unity. Thus, configurations that show large heaving amplitudes for low values of $\xi_{\eta 0}$ (♯16 and ♯19) need to change the motion shape when increasing the heaving damping by significantly reducing the heaving amplitude. By contrast, configurations that low oscillate in heaving for small values of $\xi_{\eta 0}$ (represented by ♯13) are simply fostered to oscillate more in the pitching component, approaching the path of the configuration with γ_n closer to unity (represented by ♯16).

9.1.3 Suitability to harvest energy

9.1.3.1 Performances comparison

The comparisons between different configurations, tested in both Stahlbau Institute and CRIACIV campaigns, but having similar heaving-damping level, are discussed in this section, evaluating their energy-harvesting performances and highlighting the influence of the governing parameters at a given power production level.

Fig. 9.9 compares configurations #12 and #22 (both from the Stahlbau Institute campaign) together with ♯$s4$ and ♯22 (both from CRIACIV campaign), all with $\xi_{\eta 0} \simeq 5\%$. Configurations #12 and ♯$s4$ have no elastic-axis eccentricity, while #22 has $x_e = 0.1$ and ♯22 has $x_e = -0.25$. All configurations have $x_m \simeq 0.05$, while the inertial parameters μ and r_α importantly change between tests at Stahlbau Institut and CRIACIV. The results show that the motion amplitude ratio plays a key role, together with the phase difference. In fact, while configuration ♯$s4$ manifests higher Γ'_η with respect to #12 and #22, these latter have markedly higher conversion factors Γ''_η, and the energy that is flowing in the heaving DoF can be better pumped into the conversion apparatus. Thus, the final performance factors Γ_η of these three configurations are similar. The 15:1 sectional model was characterised by smaller amplitude ratios, and this have beneficial effect on the performance. However, the same figure shows that, after a specific optimization procedure, a more efficient configuration can be designed, that is ♯22, for which the first and last performance factors (Γ'_η and Γ_η) are significantly larger. The presence of the small mass unbalance continues to reduce Γ''_η if compared to the German configurations, but this was necessary to foster the instability and to globally enhance its energy-harvesting suitability.

Fig. 9.10 shows the comparison among some configurations tested during the Italian campaign, which have $\xi_{\eta 0} \simeq 9\%$. Configurations ♯4 and ♯7 have no elastic-axis eccentricity and involve an heavier system ($\mu \simeq 2600$ and $r_\alpha \simeq 0.6$), while the others have $x_e = -0.25$, $\mu \simeq 1400$ and $r_\alpha \in (0.38; 0.5)$. The mass unbalance is always $x_m \simeq 0.06$ and the still-air frequency ratio varies in the range $(0.92; 1.24)$. It is interesting to note that, although the different dynamic parameters, configurations ♯4 and ♯14 markedly differ in terms of Γ'_η and Γ''_η, but follow almost the same Γ_η evolution. Similar considerations can be made for ♯17 and ♯24, and this is again due to differences on the motion shape.

While configuration ♯24 reaches the highest extraction capability, that is Γ'_η, configuration ♯7 produces the highest global performance factor Γ_η. This is caused by the absence of the mass unbalance and null elastic-axis eccentricity, which produced a motion with low amplitude ratios (see Fig. 7.11). For this configuration, there is a perfect conversion of the forcing power to dissipated power, since $\Gamma''_\eta = 1$. Nevertheless, one should consider that configuration ♯7 was not able to start spontaneously the motion in presence of high heaving damping, since it was not prone to flutter instability. Linear theory indicated that small mass unbalance is always required to be prone to spontaneous flutter motion in presence of high $\xi_{\eta 0}$ (see § 8.1). Thus, the high efficiency of this configuration may be misleading, since external triggering is needed to activate its motion.

9.1.3.2 Comments on the swept area

The role of the swept area in the performance estimation is clear from Eqs. (4.8) and (4.18). It is used to define the power of the oncoming flow that interact with the oscillating system through the maximum swept distance in the cross-flow direction. In particular, as explained in [219], the streamlines passing in the maximum swept points can be considered to define

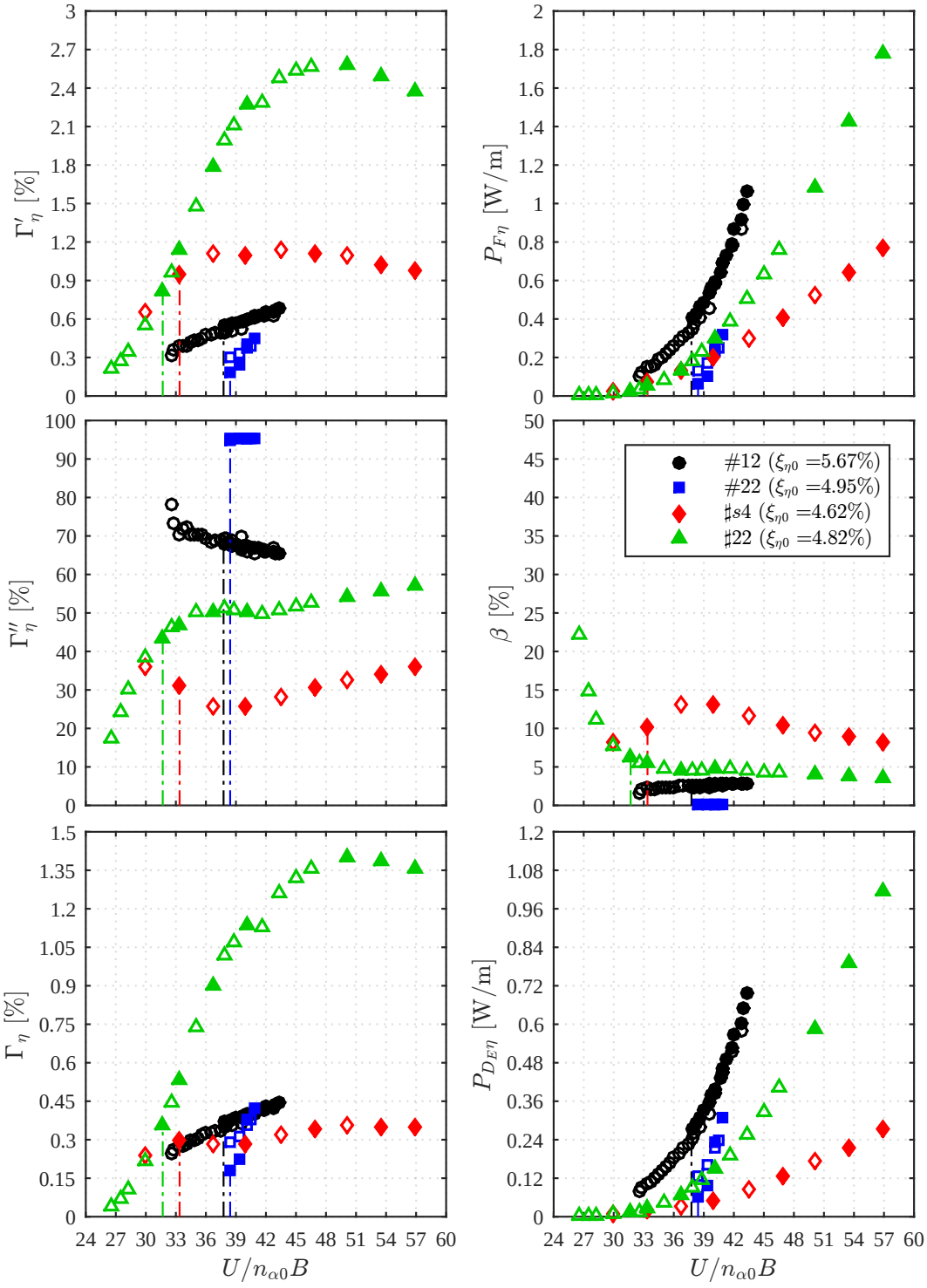

Figure 9.9. Performance comparisons among configurations from the Stahlbau campaign (#12 and 22) and from CRIACIV campaign (♯$s4$ and ♯22), all with a similar heaving-damping level.

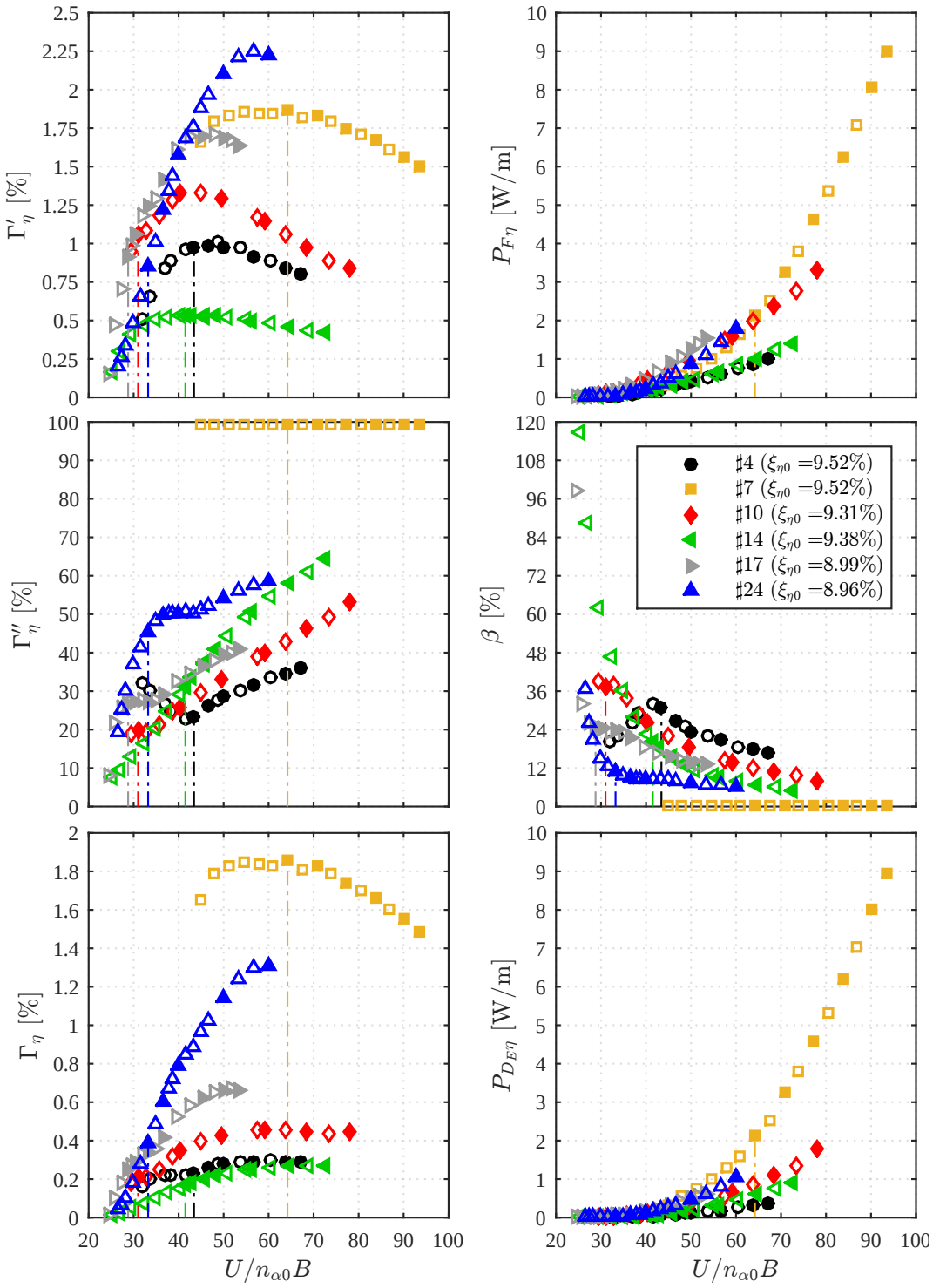

Figure 9.10. Performance comparisons among selected configurations from the CRIACIV campaign, all with a similar heaving-damping level.

the flow-tube boundaries for the Betz analysis. The figures shown from Fig. 9.11 to Fig. 9.13 show the variety of motion shapes that are typically encountered.

Fig. 9.11 shows that, varying only the pitching-to-heaving phase difference while keeping constant the other governing parameters of the motion, $\hat{\phi}$ plays a key role in the evolution of the swept area. In fact, when combined with upstream elastic-axis eccentricity, the in-phase motion gives the largest swept distance, with the instantaneous centre of rotation focused in a small locus region upstream of the midchord. By contrast, it is apparent that the quadrature-phase motion complicates the motion evolution, avoiding a fixed instantaneous centre of rotation.

As shown in Figs. 9.12a and 9.12b, when compared to Fig. 9.11, the elastic-axis eccentricity significantly participates in the motion shape. Thus, the optimal elastic centre position close the upstream quarter-chord, as suggested from the analyses in § 8, can contribute to enlarge the cross-flow swept distance. Thus, although reducing the critical flow speed, the performance factors may experience smaller enhancements due to the larger motion amplitudes.

In Figs. 9.12c, a typical configuration during energy-production conditions, that is with high heaving-damping values, is obtained by reducing down to $0.2B$ the maximum heaving amplitude if compared to those of Fig. 9.11 (the other motion parameters are kept constant). Thus, it is apparent the predominance of the pitching DoF contribution in the definition of the cross-flow swept distance, being the trailing edge to show the largest displacements.

Considering the points of maximum performance Γ_η for selected configurations with $\xi_{\eta 0} \simeq 15\%$ (from **session III**), as depicted in Fig. 9.14, the respective swept areas are evaluated through the parameters of the motion (inferable from Figs. 8.28, 8.29 and 8.30). Thus, Fig. 9.13 shows that these configurations, although having different governing parameters (see Table 6.3), the post-critical regime is characterised by similar motion shapes.

9.2 Relevance of theoretical predictions

The linearised analytical approach was used to predict the instability threshold and to perform systematic parametric analyses looking for optimal configurations (see § 8). Several considerations were based on the evolution of the critical-condition features, in terms of amplitude ratio $(B\alpha/\eta)^c$, phase difference ϕ^c and squared flutter frequency $\sqrt{X^c} = n_{\alpha 0}/n^c$, in addition to the critical reduced velocity $U^c_{R\alpha} = U^c/n_{\alpha 0}B$, with respect to variations of the governing parameters. Thus, it is fundamental to verify the applicability of the linear theory comparing the previously listed output parameters of the critical condition with those experimentally determined about the critical condition. In fact, the parameters describing the critical condition, except for $U^c_{R\alpha}$, are expected to provide only indicative information because they are restricted to the unstable mode appearing during the starting part of the motion build up. Since these may not correspond to the motion characteristics at the limit cycle, the results of the linear analysis should be mainly considered in terms of critical reduced velocity.

This comparison was implemented for some configurations from both Stahlbau and CRIACIV campaigns, and the results are reported from Fig. 9.15 to Fig. 9.20. The figures show the original build-up signals of heaving and pitching DoFs, as resulting from the growing oscillations due to the flutter instability. Then, the first part of the build-up is analysed through the MULS method (see § 5.2.4 or § 5.3.4), which allowed identifying the unstable mode. Suddenly beyond the instability threshold, the system behaves linearly and the exponential growing oscillation is apparent. This identification method is able to supply the estimation of damping, frequency, phase and amplitude parameters, since it performs a complex-eigenvalue-problem identification [24]. The system identification was repeated also in a later part of the build-up signal, where the oscillations were larger but still before the amplitude threshold beyond which aerodynamic nonlinearities start to influence.

Observing Fig. 9.15 and Fig. 9.16, which refer to a configuration tested during the Stahlbau campaign, the linear prediction gives good results in terms of critical reduced velocity and motion frequency, while the phase and amplitude ratio parameters are not

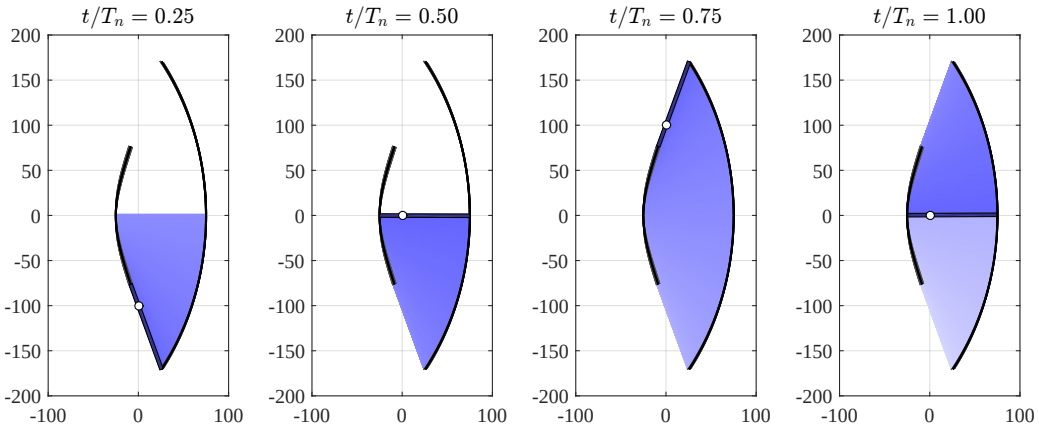

(a) $\hat{\phi} = 0°$.

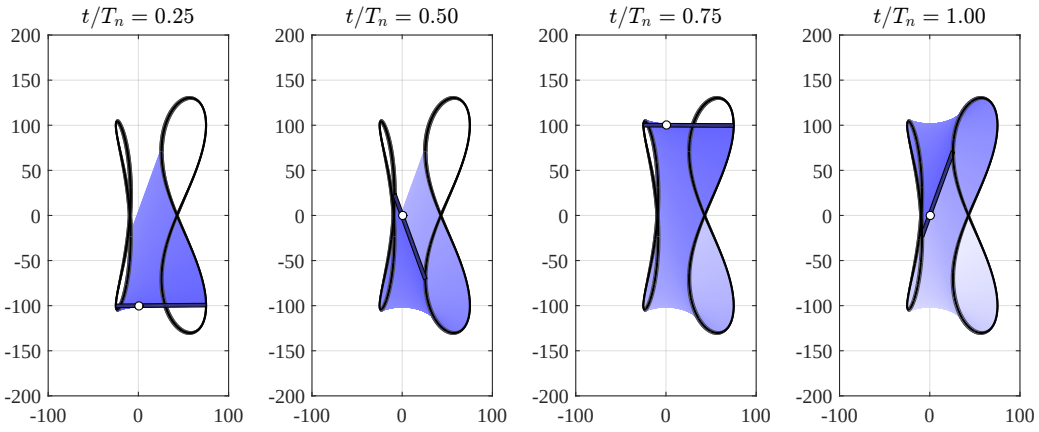

(b) $\hat{\phi} = -90°$.

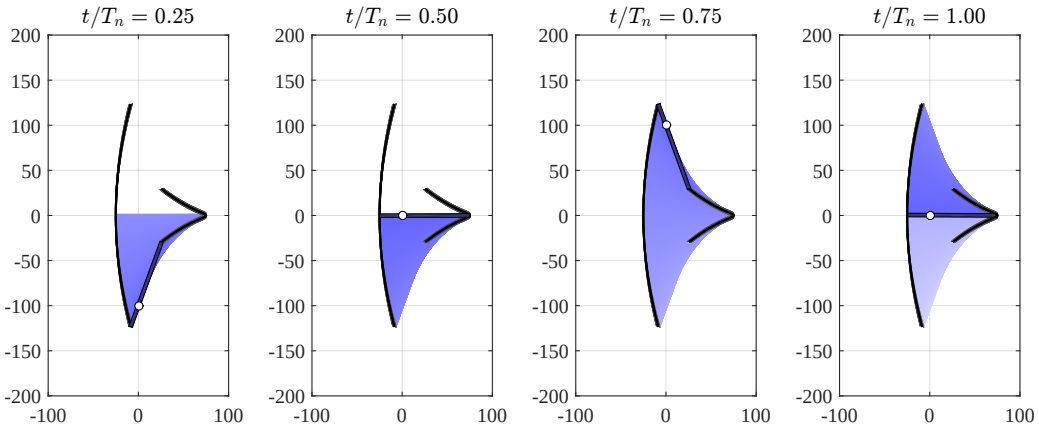

(c) $\hat{\phi} = -180°$.

Figure 9.11. Evaluation of the motion trajectory for configurations with different pitching-to-heaving phase. The other motion parameters are set to $x_e = -0.25$, $\hat{\eta}/B = 1$ and $\hat{\alpha} = 70°$. In the figures the flow comes from left to right and T_n is the oscillation period.

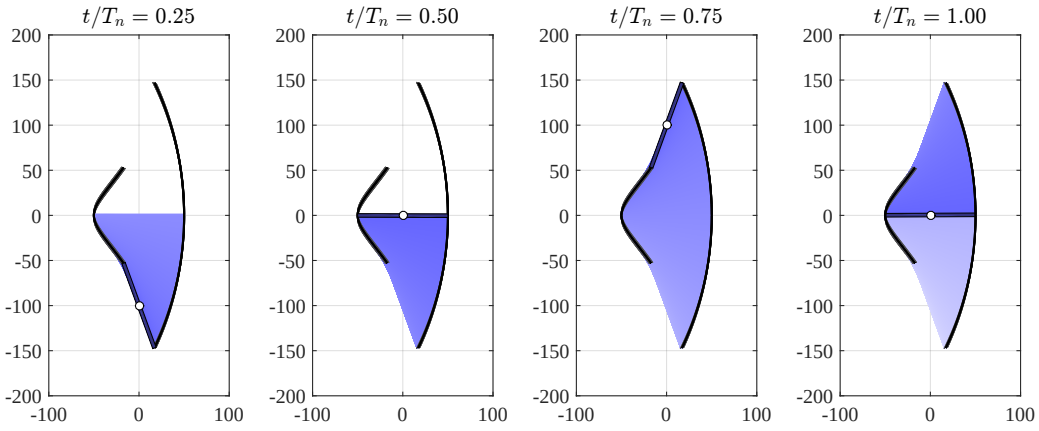

(a) $x_e = 0$, $\hat{\eta}/B = 1$, $\hat{\phi} = 0°$.

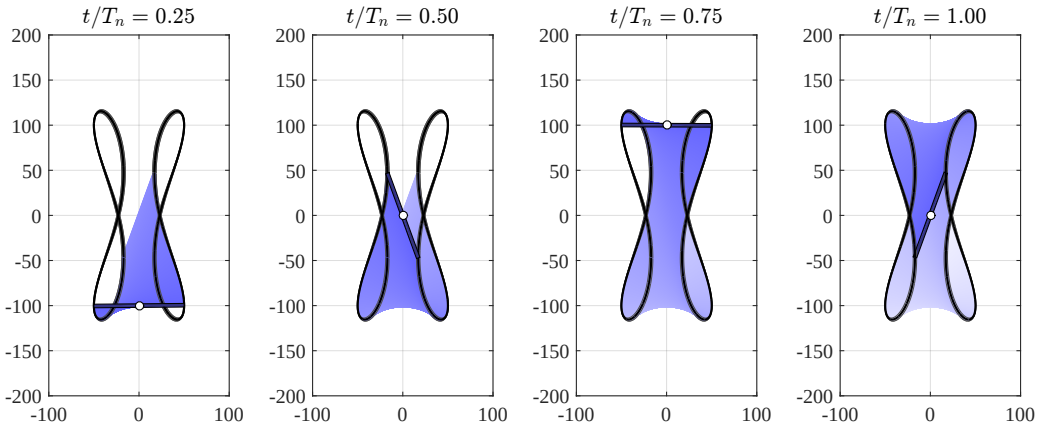

(b) $x_e = 0$, $\hat{\eta}/B = 1$, $\hat{\phi} = -90°$.

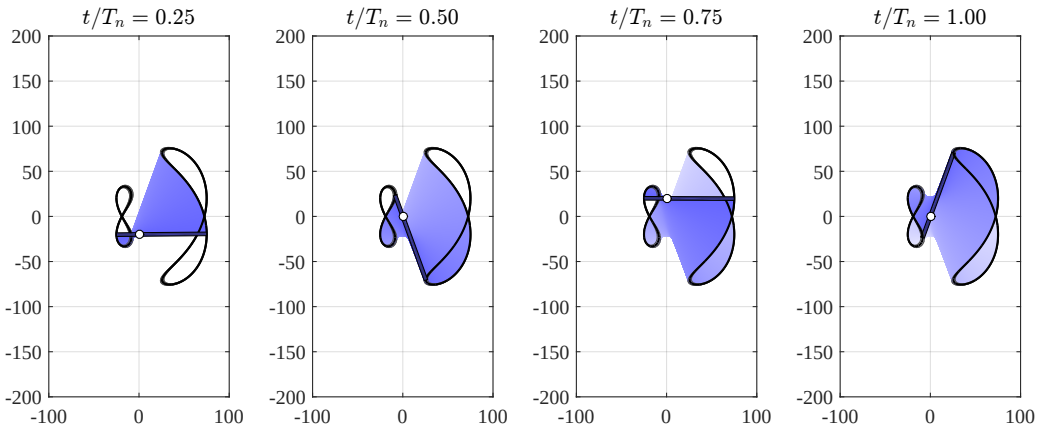

(c) $x_e = -0.25$, $\hat{\eta}/B = 0.2$, $\hat{\phi} = -90°$.

Figure 9.12. Evaluation of the motion trajectory for particular configurations. The other motion parameter is set $\hat{\alpha} = 70°$. In the figures the flow comes from left to right and T_n is the oscillation period.

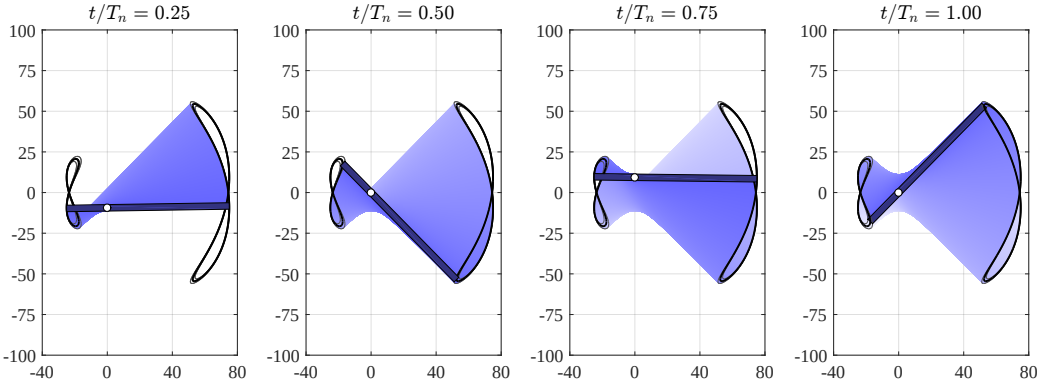

(a) $x_e = -0.25$, $\hat{\eta}/B = 0.094$, $\hat{\alpha} = 45.55°$, $\hat{\phi} = -90.7°$.

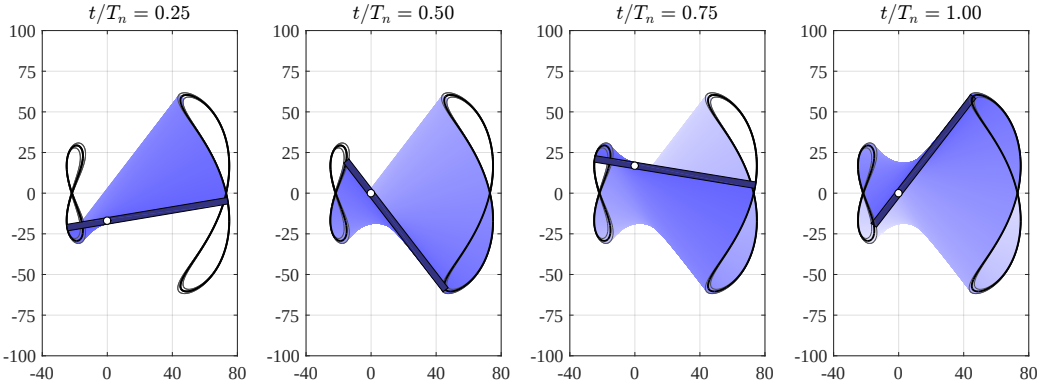

(b) $x_e = -0.25$, $\hat{\eta}/B = 0.170$, $\hat{\alpha} = 53.17°$, $\hat{\phi} = -99.9°$.

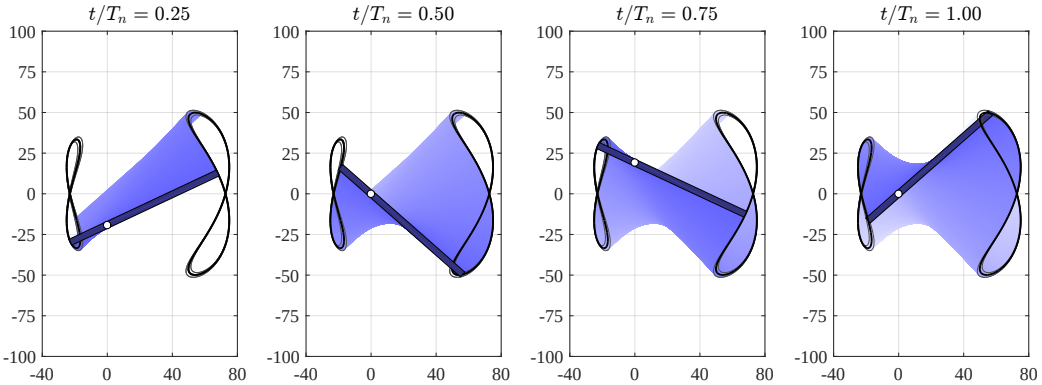

(c) $x_e = -0.25$, $\hat{\eta}/B = 0.191$, $\hat{\alpha} = 48.31°$, $\hat{\phi} = -121.0°$.

Figure 9.13. Evaluation of the motion trajectory for the selected configurations of Fig. 9.14. In the figures the flow comes from left to right and T_n is the oscillation period. (a) Configuration ♯12; (b) configuration ♯18; (c) configuration ♯26;

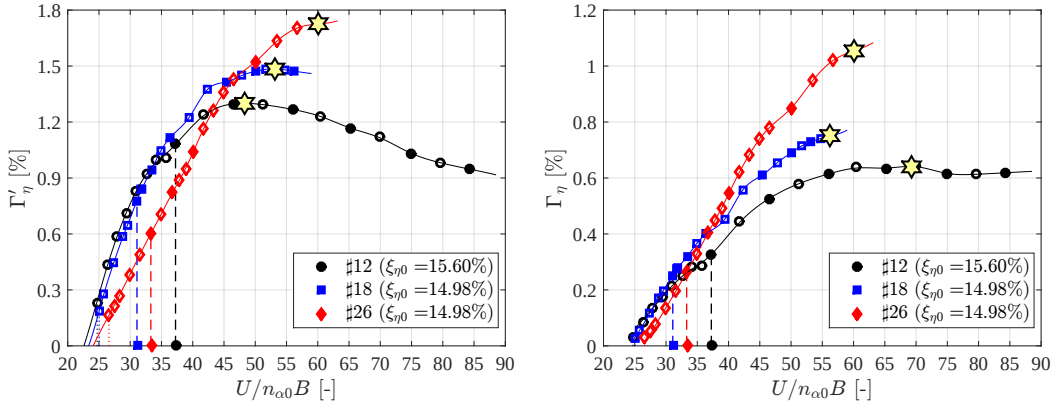

Figure 9.14. Identification and evolution of the maximum performance points for selected configurations of the CRIACIV campaign with similar heaving damping ($\xi_{\eta 0} \simeq 15\%$).

properly obtained. Moreover, the the build-up seems to well follow the exponential growth, then suddenly modifies toward the steady-state LCO amplitude; no marked modulation was detected.

Observing Fig. 9.17 and Fig. 9.18, which refer to a configuration tested during SESSION II at CRAICIV wind tunnel, it is immediately apparent the different behaviour of the system, which produces a marked modulation in the transient regime of the build up. It is worth highlighting that a very small external disturbance in the heaving DoF was introduced to trigger the motion, when the flow speed was close the theoretical critical one. However, focusing on the first part of the build-up signal, the fitting shows very good results. The theoretical predictions of the critical-condition parameters well represent especially the flutter motion shape and phase. Furthermore, also the fitting on the larger amplitudes gives good results, meaning that the system is still oscillating linearly. It may be supposed that the marked modulation arising close to $2800tU/B$ nonlinearly modifies the response and definitely stops the exponential linear growth. This modulation appears when the pitching amplitude gets close to 10°, which may indicate the occurrence of massive flow separation.

Fig. 9.19 and Fig. 9.20 refer to the configuration ♯13, tested during SESSION III in the CRIACIV campaign, for which the destabilizing effect of damping was detected. Firstly, it is interesting to note the evident modulation of the system response. In particular, this motion produces the peculiar stable point in between the rest position and the higher stable branch, as clearly detectable from Fig. 9.3. Observing the results of the system identification, the first part of the build-up signal seems to be better described by the 2$^{\text{nd}}$ mode, although the phase parameter is still quite different from the theoretical one. Nevertheless, the results for larger amplitudes seem to better agree with the 1$^{\text{st}}$ mode. This problem may be linked to the identification procedure that can be complicated by the presence of two modes with close features.

As a general comment, the unstable mode usually is the one showing smaller negative damping, which is highlighted with the symbol '$*$' in the tables of the previously recalled figures.

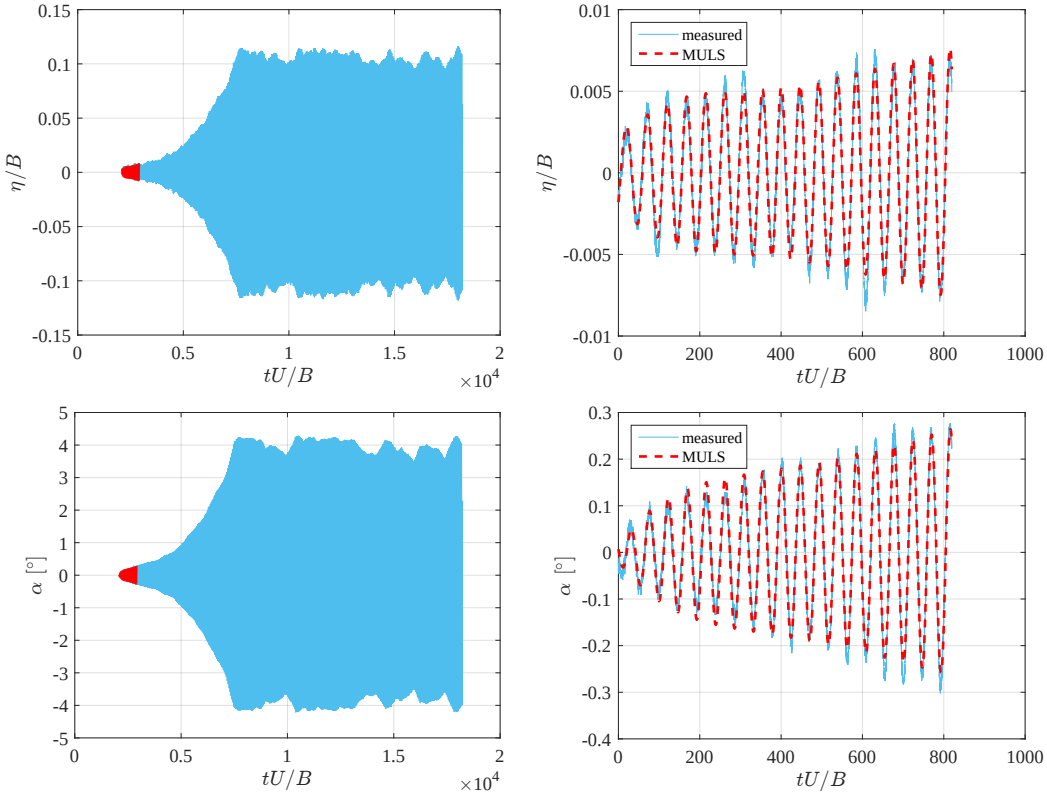

(a) Time histories of the original and elaborated signals.

Mode n.	$\begin{pmatrix} \sigma_\eta \\ \sigma_\alpha \end{pmatrix}$	$B\alpha/\eta$ [–]	ϕ [°]	ξ [%]	$\sqrt{X}$ [–]	$U/n_{\alpha 0}B$ [–]
1*	$\begin{pmatrix} 7-16i \\ -3.2-9.9i \end{pmatrix} \cdot 10^{-4}$	0.60	−7.5	−0.71	1.14	40.6
2	$\begin{pmatrix} -2+27i \\ 3.8+7.7i \end{pmatrix} \cdot 10^{-4}$	0.32	29.7	6.92	1.21	
Linear analysis - Flutter derivatives		1.03	-0.7	0	1.09	39.3
Linear analysis - Theodorsen		0.83	-3.6	0	1.11	46.4

(b) Output parameters from the MULS fitting.

Figure 9.15. Fitting of the incipient flutter motion for configuration #10 ($n_{\alpha 0}$ = 2.244 Hz) - PART I. [Stahlbau Institut campaign]

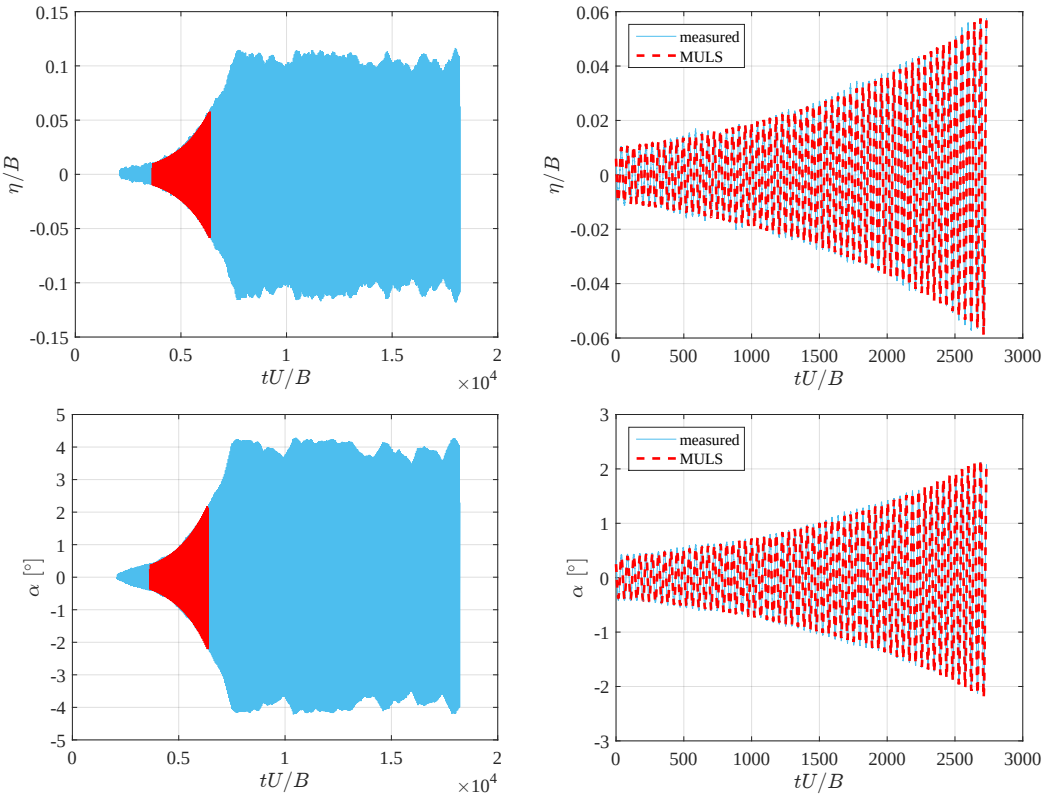

(a) Time histories of the original and elaborated signals.

Mode n.	$\begin{pmatrix} \sigma_\eta \\ \sigma_\alpha \end{pmatrix}$	$B\alpha/\eta$ [–]	ϕ [°]	ξ [%]	$\sqrt{X}$ [–]	$U/n_{\alpha 0}B$ [–]
1*	$\begin{pmatrix} 0.003 - 0.004i \\ 0.0022 - 0.0024i \end{pmatrix}$	0.66	−5.0	−0.48	1.13	40.6
2	$\begin{pmatrix} 9.6 + 7.5i \\ 2.0 - 1.2i \end{pmatrix} \cdot 10^{-6}$	0.13	41.6	−1.21	2.17	
Linear analysis - Flutter derivatives		1.03	-0.7	0	1.09	39.3
Linear analysis - Theodorsen		0.83	-3.6	0	1.11	46.4

(b) Output parameters from the MULS fitting.

Figure 9.16. Fitting of the incipient flutter motion for configuration #10 ($n_{\alpha 0}$ = 2.244 Hz) - PART II. [Stahlbau Institut campaign]

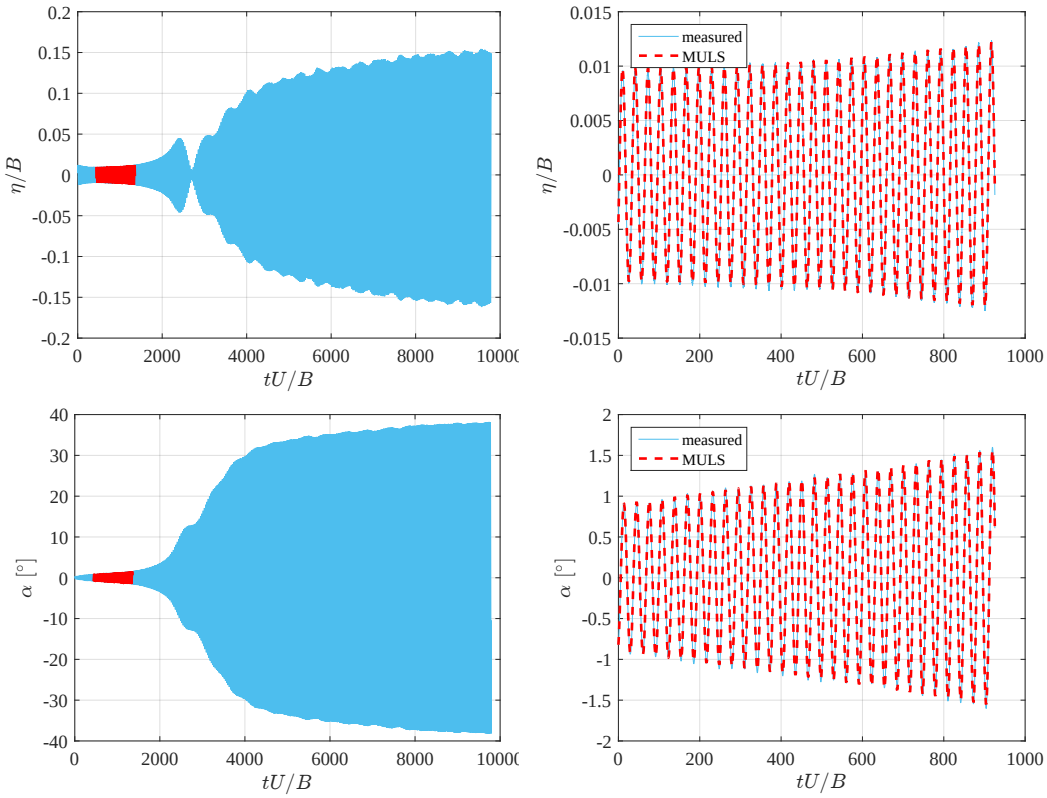

(a) Time histories of the original and elaborated signals.

Mode n.	$\begin{pmatrix}\sigma_\eta\\ \sigma_\alpha\end{pmatrix}$	$B\alpha/\eta$ [–]	ϕ [°]	ξ [%]	$\sqrt{X}$ [–]	$U/n_{\alpha 0}B$ [–]
1*	$\begin{pmatrix}-0.002+0.003i\\ -0.0077+0.0038i\end{pmatrix}$	2.36	−29.7	−0.25	1.04	30.0
2	$\begin{pmatrix}-1+14i\\ 5.7-5.8i\end{pmatrix}\cdot 10^{-4}$	0.59	140.5	0.9	1.04	
Linear analysis - Theodorsen		2.02	-25.4	0	1.05	32.0

(b) Output parameters from the MULS fitting.

Figure 9.17. Fitting of the incipient flutter motion for configuration ♯3 ($n_{\alpha 0}$ = 1.814 Hz) - PART I. [CRIACIV campaign]

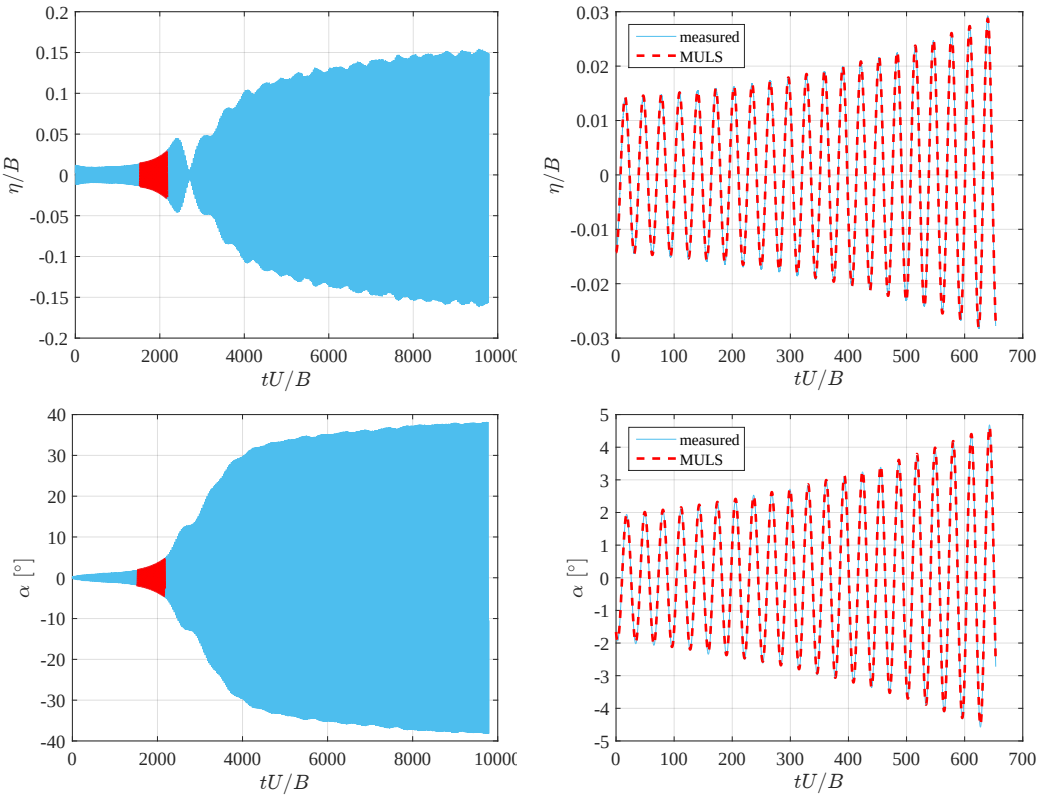

(a) Time histories of the original and elaborated signals.

Mode n.	$\begin{pmatrix}\sigma_\eta\\ \sigma_\alpha\end{pmatrix}$	$B\alpha/\eta$ [–]	ϕ [°]	ξ [%]	$\sqrt{X}$ [–]	$U/n_{\alpha 0}B$ [–]
1*	$\begin{pmatrix}-0.0048+0.0007i\\ -0.0121-0.0062i\end{pmatrix}$	2.79	−35.1	−0.84	1.04	30.0
2	$\begin{pmatrix}-0.0023-0.0006i\\ -0.0024-0.0021i\end{pmatrix}$	1.34	−27.4	0.88	1.05	
Linear analysis - Theodorsen		2.02	-25.4	0	1.05	32.0

(b) Output parameters from the MULS fitting.

Figure 9.18. Fitting of the incipient flutter motion for configuration ♯3 ($n_{\alpha 0}$ = 1.814 Hz) - PART II. [CRIACIV campaign]

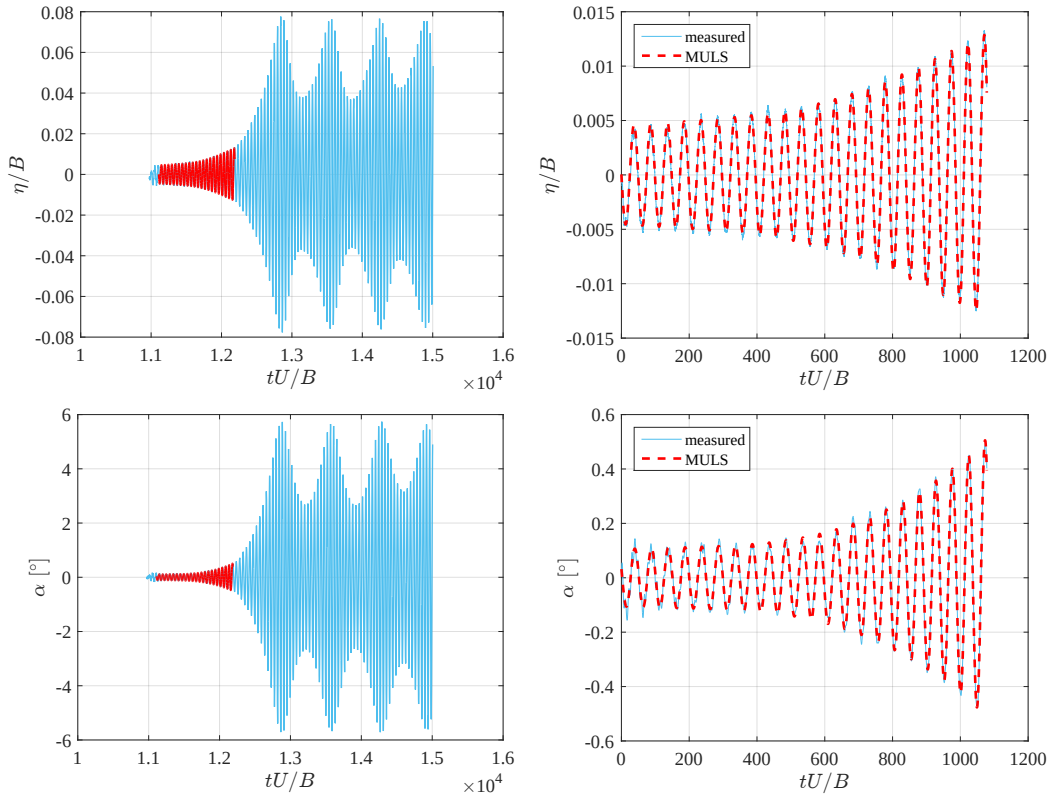

(a) Time histories of the original and elaborated signals.

Mode n.	$\begin{pmatrix}\sigma_\eta \\ \sigma_\alpha\end{pmatrix}$	$B\alpha/\eta$ [–]	ϕ [°]	ξ [%]	$\sqrt{X}$ [–]	$U/n_{\alpha 0}B$ [–]
1*	$\begin{pmatrix}0.3-22i \\ 2.9-8.9i\end{pmatrix}\cdot 10^{-4}$	0.41	−17.6	−0.39	1.19	41.3
2	$\begin{pmatrix}-9.7+2.7i \\ -20+16i\end{pmatrix}\cdot 10^{-6}$	0.91	−31.1	−3.4	1.16	
Linear analysis - Theodorsen		0.94	-7.8	0	1.16	37.1

(b) Output parameters from the MULS fitting.

Figure 9.19. Fitting of the incipient flutter motion for configuration ♯13 ($n_{\alpha 0}$ = 2.273 Hz) - PART I. [CRIACIV campaign]

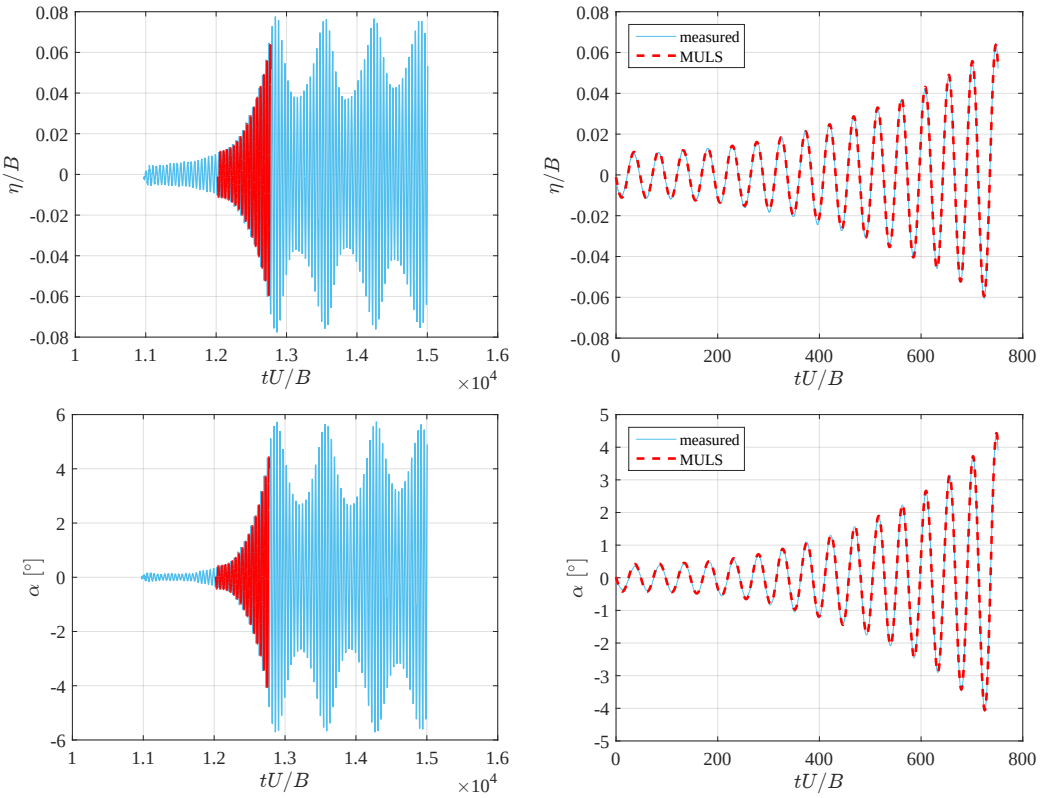

(a) Time histories of the original and elaborated signals.

Mode n.	$\begin{pmatrix}\sigma_\eta\\ \sigma_\alpha\end{pmatrix}$	$B\alpha/\eta$ [–]	ϕ [°]	ξ [%]	$\sqrt{X}$ [–]	$U/n_{\alpha 0}B$ [–]
1*	$\begin{pmatrix}-0.0008-0.006i\\ 0.0002-0.0044i\end{pmatrix}$	0.73	−9.4	−0.46	1.16	41.3
2	$\begin{pmatrix}2.2+5.4i\\ 0.5+7.4i\end{pmatrix}\cdot 10^{-4}$	1.28	−17.6	−3.77	1.11	
Linear analysis - Theodorsen		0.94	-7.8	0	1.16	37.1

(b) Output parameters from the MULS fitting.

Figure 9.20. Fitting of the incipient flutter motion for configuration ♯13 ($n_{\alpha 0}$ = 2.273 Hz) - PART II. [CRIACIV campaign]

Chapter 10

Conclusions

10.1 Summary of thesis outcomes

- *Experimental observation of the phenomenological features of post-critical flutter.*

  The classical-flutter excitation mechanism produces a dynamic instability characterised by a sub-critical bifurcation. The jump at the instability threshold is very pronounced, and the post-critical response evolves almost linearly with the flow speed. Some differences are remarkable for the lighter systems, in which the pitching component seems to follow a quadratic curve with down-side concavity, limiting the pitching amplitude excursions to about 90°. The sub-critical branch usually shows almost constant slope, and it is present for a large range of flow speeds below the critical condition. Moreover, the position of the unstable branch diving the null-amplitude branch and the sub-critical branch depends on the set of dynamic parameters. Small stable branches with intermediate amplitude are encountered immediately beyond the critical flow speed for configurations with still-air frequency ratio larger than unity.

- *Large parametric database of results from linear analyses and wind-tunnel tests.*

  Systematic parametric investigations, both through linear analyses and wind tunnel tests, have been carried out with respect to the space dynamic parameters governing the classical-flutter problem. The linear approach involved Theodorsen's model. The experiments were conducted on two sectional models with 15:1 (width-to-depth ratio) and 25:1 rectangular cross sections. The former model has been tested in the Stahlbau Institute wind tunnel and the latter in the CRIACIV wind tunnel, exploiting respectively coil-spring and blade-spring setups. Thus, the set of investigations supply new information about the large-amplitude, post-critical response of two-degree-of-freedom systems. Given the large attention spent to design as reliable as possible experiments, with particular regards to the aeroelastic-setup features that were identified in detail, the results can be considered reliable and repeatable, being a precious support for the many scholars nowadays dealing with numerical simulation of fluid-structure interaction problems. Moreover, combining critical-condition predictions and experimental results, the governing parameters influence can be cross-validated.

- *Response to high heaving damping and the evidence of damping-induced destabilizing effects.*

  Since the conversion apparatus acts in the heaving motion component, the study of heaving-damping effects on the critical-condition features and on the post-critical response is of crucial importance. Usually, damping increments stabilise the system, postponing the instability threshold and reducing the post-critical motion amplitudes. Nevertheless, the system continues to perform self-sustained motion, even in the presence of very high levels of damping (values of critical damping ratio up to about 18% were achieved). This is a capability typical of two-degree-of-freedom systems, since the presence of one motion component at least that is not disturbed, allows

the system to adapt its response finding a new dynamic equilibrium. Moreover, for configurations with large still-air uncoupled frequency ratio, increments of heaving damping can make the system more prone to flutter instability. This behaviour has been well explained by the linear analysis, which shows the importance of the limit configuration with still-air uncoupled frequency ratio set to unity. As the heaving damping is increased, whatever configuration converges to the behaviour of that special case, as confirmed also by the experimental results in terms of post-critical response.

- *Design guidelines for flutter-based generators.*

  This thesis work is not devoted to develop high-efficiency systems, but mainly to study the phenomenological features of the post-critical response. Nevertheless, it allows explaining that design optimizations can lead to significant improvements of the performance. In particular, it is found that small mass unbalance downstream of the elastic axis is fundamental to allow the flutter instability even in presence of high damping values, anticipating also the instability threshold. Moreover, the optimal position of the elastic axis is expected to depend on the level of heaving damping, moving closer to the upstream quarter-chord when increasing the damping. Then, the still-air uncoupled frequency ratio significantly determines the motion characteristics, in terms of pitching-to-heaving amplitude ratio and phase difference, thus modifying the area swept during the oscillations. Values of the frequency ratio closer to unity can enhance the energy-harvesting performances. Furthermore, designing lighter systems is a very effective way to reduce the critical flow speed and to magnify the post-critical response, thus importantly affecting the performance of the system. Furthermore, the presence of the sub-critical branch wides the operative range of the generator. Toward this purpose, external disturbances introduced by real turbulent flows may be sufficient to trigger the motion.

10.2 Outlooks and future works

- *Investigation of different cross sections.*

  A preliminary study about modifications of the cross-section shapes reported in Appendix D, carried out in the CRIACIV wind tunnel. Installing small screens on the shorter sides of the cross section, so that to obtain H- or U-shape, the aerodynamic properties of the cross section were modified, studying also the influence of different porosity. The wind-tunnel tests showed that the modified cross sections have a wider sub-critical branch, enlarged toward lower flow velocities, and slightly lower instability threshold with respect to the flat plate. The aim should be to understand if modified edges can be used as a solution to widen the range of flow velocities in which flutter oscillations occur, also to anticipate the instability onset and/or to increase the heaving amplitude of oscillation. More unstable configurations lead to larger operative ranges and enhanced potentialities for energy harvesting. Obviously, other typologies of cross section can also be considered, concentrating on the shapes that postpone the flow separation and the vortex shedding, in order to increase the persistence of the lifting load, which is the main responsible of the motion.

- *Turbulent flows effects.*

  Preliminary investigations of the post-critical response in turbulent flows are reported in Appendix E, carried out in the CRIACIV wind tunnel. Two levels of homogeneous turbulence intensity in the along-wind direction were considered (2.45% and 10.68%), showing that the fluttering system still continue to experience very-large motion amplitude even with higher flow turbulence. In the perspective of flutter-based generators installed in real flows, *e.g* urban environments, a detailed study of the turbulence effects should be conducted, in order to understand the capability of extracting energy also in non-optimal flow conditions. However, following these preliminary tests, the classical-flutter mechanism seems to persist even in presence of high-turbulence flows.

- *Analytical modelling of the post-critical response.*

  The parametric investigation of the post-critical flutter response should consider also numerical approaches, since the only experimental approach may be too much time-expensive. However, with exception of computational-fluid-dynamic methods that require high-performance computing, the other numerical methods are still not reliable. Thus, the results of this thesis work can contribute to the development of analytical models for the post-critical regime. For this purposes, static tests to measure the flow-induced loads at different angles of attack and forced-oscillation tests should be implemented in order to improve the quality of the results and to provide complementary information.

- *Improvements of the setup characteristics.*

  Both setups used in this thesis work have positive features and drawbacks, and the development of next technical solutions should mainly improve the linearity of the mechanical features. Focusing on the blade-spring setup at CRIACIV wind tunnel, which was more suitable for large-amplitude oscillation measurements, the ball-bearing system should be improved in order to lower the static friction for very small pitching amplitudes. Since the coil-spring setup of Stahlbau Institute provided better mechanical features for small amplitudes only, a possible alternative is to develop a setup in which, in each side of the model ends, a disc is fixed to model axis, and pairs of parallel coil-springs are connected together through a cable circumscribing the disc. In this way, the distance between the springs is ruled by the disc diameter, and the springs remain in the correct position also during large oscillations, avoiding geometric nonlinearities. Furthermore, a typical problem of post-critical flutter tests is that very large-amplitude motion can be not compatible with the capabilities of the measuring equipment, *e.g.* exceeding the measurement range of the displacement transducers. Thus, a measuring system involving only accelerometers should be considered. Finally, the model should be as rigid as possible to allow reliable large-amplitude measurements, and models made of carbon fiber or consisting of a light-hollow section with a stiff skeleton could be designed.

- *Conversion-apparatus modelling.*

  Within the energy-harvesting context, next studies should address the modelling of the conversion apparatus, studying a complete fluid-solid-electric interaction problem. However, for this aim, experts on electric and mechanical engineering should be involved. Considering the very large motion amplitudes, the simpler conversion method involves linear electromagnetic transducers, *e.g* coaxial solenoids. Nevertheless, with particular regard to the blade-spring setup at CRIACIV wind tunnel, piezoelectric patches could also be installed along the flexible beams of the elastic support to convert heaving-induced bending deformations. The position of the piezo-patches can be optimized to maximise the electromechanical coupling, thus the energy conversion. Morever, following the literature studies (*e.g.* [59]), a global resonance effect between mechanical and electric systems could enhance the system performance. A preliminary modelling of this solution is already taking place.

Bibliography

[1] A. Abdelkefi, M. Ghommem, A. O. Nuhait, and M. R. Hajj, *Nonlinear analysis and enhancement of wing-based piezoaeroelastic energy harvesters*, Journal of Sound and Vibration, 333 (2014), pp. 166–177.

[2] A. Abdelkefi and M. R. Hajj, *Performance enhancement of wing-based piezoaeroelastic energy harvesting through freeplay nonlinearity*, Theoretical and Applied Mechanics Letters, 3 (2013), p. 041001.

[3] A. Abdelkefi, M. R. Hajj, and A. H. Nayfeh, *Phenomena and modeling of piezoelectric energy harvesting from freely oscillating cylinders*, Nonlinear Dynamics, 70 (2012), pp. 1377–1388.

[4] ——, *Piezoelectric energy harvesting from transverse galloping of bluff bodies*, Smart Materials and Structures, 22 (2013), p. 015014.

[5] A. Abdelkefi, F. Najar, A. H. Nayfeh, and S. B. Ayed, *An energy harvester using piezoelectric cantilever beams undergoing coupled bending-torsion vibrations*, Smart Materials and Structures, 20 (2011), p. 115007.

[6] A. Abdelkefi, A. H. Nayfeh, and M. R. Hajj, *Design of piezoaeroelastic energy harvesters*, Nonlinear Dynamics, 68 (2012), pp. 519–530.

[7] ——, *Enhancement of power harvesting from piezoaeroelastic systems*, Nonlinear Dynamics, 68 (2012), pp. 531–541.

[8] A. Abdelkefi, A. H. Nayfeh, and M. R. Hajj, *Modeling and analysis of piezoaeroelastic energy harvesters*, Nonlinear Dynamics, 67 (2012), pp. 925–939.

[9] A. Abdelkefi, R. Vasconcellos, F. Marques, and M. Hajj, *Modeling and identification of freeplay nonlinearity*, Journal of Sound and Vibration, 331 (2012), pp. 1898–1907.

[10] T. Ackermann and L. Söder, *Wind energy technology and current status: a review*, Renewable and sustainable energy reviews, 4 (2000), pp. 315–374.

[11] G. Ahmadi, *Aeroelastic wind energy converter*, Energy Conversion, 18 (1978), pp. 115–120.

[12] G. Ahmadi, *Aeroelastic wind energy converter*, 1979. 20923.

[13] G. Ahmadi, *An oscillatory wind energy convertor*, Wind Engineering, 3 (1979), pp. 207–215.

[14] G. Ahmadi, *Performance of an angular flange aeroelastic wind energy converter*, Journal of Energy, 7 (1983), pp. 285–288.

[15] H. Akaydin, N. Elvin, and Y. Andreopoulos, *Wake of a cylinder: a paradigm for energy harvesting with piezoelectric materials*, Experiments in Fluids, 49 (2010), pp. 291–304.

[16] H. D. Akaydin, N. Elvin, and Y. Andreopoulos, *Energy harvesting from highly unsteady fluid flows using piezoelectric materials*, Journal of Intelligent Material Systems and Structures, 21 (2010), pp. 1263–1278.

[17] D. T. Akcabay and Y. L. Young, *Hydroelastic response and energy harvesting potential of flexible piezoelectric beams in viscous flow*, Physics of Fluids, 24 (2012), p. 054106.

[18] J. J. Allen and A. J. Smits, *Energy harvesting eel*, Journal of Fluids and Structures, 15 (2001), pp. 1–12.

[19] X. Amandolese, X.se, S. Michelin, and M. Choquel, *Low speed flutter and limit cycle oscillations of a two-degree-of-freedom flat plate in a wind tunnel*, Journal of Fluids and Structures, 43 (2013), pp. 244–255.

[20] S. R. Anton and H. A. Sodano, *A review of power harvesting using piezoelectric materials (2003–2006)*, Smart Materials and Structures, 16 (2007), p. R1.

[21] J.-S. Bae and D. J. Inman, *Aeroelastic characteristics of linear and nonlinear piezo-aeroelastic energy harvester*, Journal of Intelligent Material Systems and Structures, (2013), pp. 1–16.

[22] A. Barrero-Gil, G. Alonso, and A. Sanz-Andres, *Energy harvesting from transverse galloping*, Journal of Sound and Vibration, 329 (2010), pp. 2873–2883.

[23] A. Barrero-Gil, S. Pindado, and S. Avila, *Extracting energy from vortex-induced vibrations: a parametric study*, Applied Mathematical Modelling, 36 (2012), pp. 3153–3160.

[24] G. Bartoli, S. Contri, C. Mannini, and M. Righi, *Toward an improvement in the identification of bridge deck flutter derivatives*, Journal of Engineering Mechanics, 135 (2009), pp. 771–785.

[25] G. Bartoli and C. Mannini, *A simplified approach to bridge deck flutter*, Journal of Wind Engineering and Industrial Aerodynamics, 96 (2008), pp. 229–256.

[26] P. W. Bearman, *Vortex shedding from oscillating bluff bodies*, Annual review of fluid mechanics, 16 (1984), pp. 195–222.

[27] T. B. Benjamin, *The threefold classification of unstable disturbances in flexible surfaces bounding inviscid flows*, Journal of Fluid Mechanics, 16 (1963), pp. 436–450.

[28] M. M. Bernitsas, Y. Ben-Simon, K. Raghavan, and E. Garcia, *The VIVACE converter: model tests at high damping and Reynolds number around 10^5*, Journal of Offshore Mechanics and Arctic Engineering, 131 (2009), p. 011102.

[29] M. M. Bernitsas and K. Raghavan, *Fluid motion energy converter*, Feb. 24 2009. US Patent 7,493,759.

[30] M. M. Bernitsas, K. Raghavan, Y. Ben-Simon, and E. Garcia, *VIVACE (Vortex Induced Vibration Aquatic Clean Energy): a new concept in generation of clean and renewable energy from fluid flow*, Journal of Offshore Mechanics and Arctic Engineering, 130 (2008), p. 041101.

[31] D. Bigoni and G. Noselli, *Experimental evidence of flutter and divergence instabilities induced by dry friction*, Journal of the Mechanics and Physics of Solids, 59 (2011), pp. 2208–2226.

[32] R. L. Bisplinghoff and H. Ashley, *Principles of aeroelasticity*, Dover Publications, Inc., New York, 1975.

[33] R. L. Bisplinghoff, H. Ashley, and R. L. Halfman, *Aeroelasticity*, Dover Publications, Inc., New York, 1996.

[34] V. V. Bolotin, *Nonconservative Problems of the Theory of Elastic Stability*, Macmillan, New York, 1963.

[35] V. V. Bolotin and N. I. Zhinzher, *Effects of damping on stability of elastic systems subjected to nonconservative forces*, International Journal of Solids and Structures, 5 (1969), pp. 965–989.

[36] M. Bryant and E. Garcia, *Development of an aeroelastic vibration power harvester*, vol. 7288, 2009, pp. 728812–728812–10.

[37] ——, *Energy harvesting: a key to wireless sensor nodes*, in Proc. SPIE, Second International Conference on Smart Materials and Nanotechnology in Engineering, vol. 7493, 2009, pp. 74931W–74931W–8.

[38] ——, *Modeling and testing of a novel aeroelastic flutter energy harvester*, Journal of Vibration and Acoustics, 133 (2011), p. 011010.

[39] M. Bryant, J. C. Gomez, and E. Garcia, *Reduced-order aerodynamic modeling of flapping wing energy harvesting at low reynolds number*, AIAA Journal, 51 (2013), pp. 2771–2782.

[40] M. Bryant, E. Wolff, and E. Garcia, *Aeroelastic flutter energy harvester design: the sensitivity of the driving instability to system parameters*, Smart Materials and Structures, 20 (2011), p. 125017.

[41] T. Burton, D. Sharpe, N. Jenkins, and E. Bossanyi, *Wind energy handbook*, John Wiley & Sons, 2001.

[42] L. Caracoglia, *Feasibility assessment of a leading-edge-flutter wind power generator*, Journal of Wind Engineering and Industrial Aerodynamics, 98 (2010), pp. 679–686.

[43] C. B. Carroll, *Energy harvesting eel*, July 23 2002. US Patent 6,424,079.

[44] L. Chen, F. L. Ponta, and L. I. Lago, *Perspectives on innovative concepts in wind-power generation*, Energy for Sustainable Development, 15 (2011), pp. 398–410.

[45] W. C. Chen and J. Dugundji, *A formulation of nonlinear limit cycle oscillation problems in aircraft flutter.*, tech. report, DTIC Document, 1993.

[46] A. K. Chopra, *Dynamics of structures: theory and applications to earthquake engineering*, Pearson Education, Inc., New York (US), 4th ed., 2012.

[47] K. A. Cook-Chennault, N. Thambi, and A. M. Sastry, *Powering mems portable devices: a review of non-regenerative and regenerative power supply systems with special emphasis on piezoelectric energy harvesting systems*, Smart Materials and Structures, 17 (2008), p. 043001.

[48] A. Cunningham Jr, *A generic nonlinear aeroelastic method with semi-empirical nonlinear unsteady aerodynamics, vol 1 and 2*, tech. report, AFRL-VA-WP, 1999.

[49] H. Dai, A. Abdelkefi, U. Javed, and L. Wang, *Modeling and performance of electromagnetic energy harvesting from galloping oscillations*, Smart Materials and Structures, 24 (2015), p. 045012.

[50] M. J. de C. Henshaw, K. J. Badcock, G. A. Vio, C. B. Allen, J. Chamberlain, I. Kaynes, G. Dimitriadis, J. E. Cooper, M. A. Woodgate, A. M. Rampurawala, D. Jones, C. Fenwick, A. L. Gaitonde, N. V. Taylor, D. S. Amor, T. A. Eccles, and C. J. Denley, *Non-linear aeroelastic prediction for aircraft applications*, Progress in Aerospace Sciences, 43 (2007), pp. 65–137.

[51] C. De Marqui and A. Erturk, *Electroaeroelastic analysis of airfoilbased wind energy harvesting using piezoelectric transduction and electromagnetic induction*, Journal of Intelligent Material Systems and Structures, 24 (2012), pp. 846–854.

[52] C. De Marqui, A. Erturk, and D. J. Inman, *Piezoaeroelastic modeling and analysis of a generator wing with continuous and segmented electrodes*, Journal of Intelligent Material Systems and Structures, 21 (2010), pp. 983–993.

[53] C. De Marqui, W. G. Vieira, A. Erturk, and D. J. Inman, *Modeling and analysis of piezoelectric energy harvesting from aeroelastic vibrations using the doublet-lattice method*, Journal of Vibration and Acoustics, 133 (2011), p. 011003.

[54] R. Decher, *Direct Energy Conversion: fundamentals of electric power production*, Oxford University Press, 1997.

[55] J. Derakhshandeh, M. Arjomandi, B. Cazzolato, and B. Dally, *Harnessing hydro-kinetic energy from wake-induced vibration using virtual mass spring damper system*, Ocean Engineering, 108 (2015), pp. 115–128.

[56] J. F. Derakhshandeh, M. Arjomandi, B. Dally, and B. Cazzolato, *The effect of arrangement of two circular cylinders on the maximum efficiency of vortex-induced vibration power using a scale-adaptive simulation model*, Journal of Fluids and Structures, 49 (2014), pp. 654–666.

[57] J. Dias, C. De Marqui Jr, and A. Erturk, *Hybrid piezoelectric-inductive flow energy harvesting and dimensionless electroaeroelastic analysis for scaling*, Applied Physics Letters, 102 (2013), p. 044101.

[58] ——, *Three-degree-of-freedom hybrid piezoelectric-inductive aeroelastic energy harvester exploiting a control surface*, AIAA Journal, 53 (2014), pp. 394–404.

[59] O. Doaré and S. Michelin, *Piezoelectric coupling in energy-harvesting fluttering flexible plates: linear stability analysis and conversion efficiency*, Journal of Fluids and Structures, 27 (2011), pp. 1357–1375.

[60] E. H. Dowell, *A Modern Course in Aeroelasticity*, vol. 217, Springer, 2014.

[61] E. H. Dowell, J. Edwards, and T. Strganac, *Nonlinear aeroelasticity*, Journal of Aircraft, 40 (2003).

[62] E. H. Dowell and K. C. Hall, *Modeling of fluid-structure interaction*, Annual Review of Fluid Mechanics, 33 (2001), pp. 445–490.

[63] E. H. Dowell, K. C. Hall, R. Kielb, D. Tang, and J. Thomas, *Nonlinear aeroelasticity of current and future aerospace vehicles*, Tech. Report September, 2008.

[64] E. H. Dowell and D. Tang, *Nonlinear aeroelasticity and unsteady aerodynamics*, AIAA Journal, 40 (2002), pp. 1697–1707.

[65] W. Duncan, *The fundamentals of flutter*, Aircraft Engineering and Aerospace Technology, 17 (1945), pp. 32–38.

[66] W. Duncan and A. Collar, *Xv. matrices applied to the motions of damped systems*, The London, Edinburgh, and Dublin Philosophical Magazine and Journal of Science, 19 (1935), pp. 197–219.

[67] P. Dunn and J. Dugundji, *Nonlinear stall flutter and divergence analysis of cantilevered graphite/epoxy wings*, AIAA Journal, 30 (1992), pp. 153–162.

[68] J. A. Dunnmon, S. C. Stanton, B. P. Mann, and E. H. Dowell, *Power extraction from aeroelastic limit cycle oscillations*, Journal of Fluids and Structures, 27 (2011), pp. 1182–1198.

[69] J. W. Edwards, *Unsteady aerodynamic modeling for arbitrary motions*, AIAA Journal, 17 (1979), pp. 365–374.

[70] I. Elishakoff, *Controversy associated with the so-called "follower forces": critical overview*, Applied Mechanics Reviews, 58 (2005), pp. 117–142.

[71] N. Elvin and A. Erturk, *Advances in energy harvesting methods*, Springer Science & Business Media, 2013.

[72] N. G. Elvin and A. A. Elvin, *An experimentally validated electromagnetic energy harvester*, Journal of Sound and Vibration, 330 (2011), pp. 2314–2324.

[73] C. W. Emory, *Prediction of limit cycle oscillation in an aeroelastic system using nonlinear normal modes*, PhD thesis, Aerospace and Ocean Engineering, Virginia Polytechnic Institute and State University, Blacksburg, Virginia, 2010.

[74] H. Erich and H. Renouard, *Wind turbines fundamentals, technologies, application*, Economics, 2 (2005).

[75] A. Erturk, W. G. R. Vieira, C. De Marqui, and D. J. Inman, *On the energy harvesting potential of piezoaeroelastic systems*, Applied Physics Letters, 96 (2010), p. 184103.

[76] M. L. Facchinetti, E. De Langre, and F. Biolley, *Coupling of structure and wake oscillators in vortex-induced vibrations*, Journal of Fluids and structures, 19 (2004), pp. 123–140.

[77] F. Fei and W. J. Li, *A fluttering-to-electrical energy transduction system for consumer electronics applications*, 2009 IEEE International Conference on Robotics and Biomimetics (ROBIO), (2009), pp. 580–585.

[78] F. Fei, J. D. Mai, and W. J. Li, *A wind-flutter energy converter for powering wireless sensors*, Sensors and Actuators A, 173 (2012), pp. 163–171.

[79] I. Fenercioglu, B. Zaloglu, J. Young, M. Ashraf, J. C. S. Lai, and M. F. Platzer, *Flow structures around an oscillating-wing power generator*, AIAA Journal, 53 (2015), pp. 3316–3326.

[80] G. Fragiskatos, *Non-linear response and instabilities of a two-degree-of-freedom airfoil oscillating in dynamic stall*, master's thesis, Dept. of Mechanical Engineering, McGill University, Montreal, Canada, 1999.

[81] S. M. Frayne, *Generator utilizing fluid-induced oscillations*, June 05 2008. US Patent 2,008,129,254.

[82] R. A. Frazer, *On the power input required to maintain forced oscillations of an aeroplane wing in flight*, Tech. Report 1872, Aeronaut. Research Com., R. & M., 1939.

[83] P. P. Friedmann, *Renaissance of aeroelasticity and its future*, Journal of Aircraft, 36 (1999), pp. 105–121.

[84] Y.-C. Fung, *An introduction to the theory of aeroelasticity*, Dover Publications, Inc., New York (US), 2008.

[85] B. Gjerek, R. Drazumeric, and F. Kosel, *A novel experimental setup for multiparameter aeroelastic wind tunnel tests*, Experimental Techniques, 38 (2014), pp. 30–43.

[86] H. Goldstein, *Classical Mechanics*, Addison-Wesley series in physics, Addison-Wesley Publishing Company, 1980.

[87] C. Grouthier, S. Michelin, R. Bourguet, Y. Modarres-Sadeghi, and E. de Langre, *Energy harvesting using vortex-induced vibrations of tensioned cables*, Journal of Fluids and Structures, 49 (2014), pp. 247–440.

[88] M. Gu, R. Zhang, and H. Xiang, *Identification of flutter derivatives of bridge decks*, Journal of Wind Engineering and Industrial Aerodynamics, 84 (2000), pp. 151–162.

[89] P. Hagedorn, *On the destabilizing effect of non-linear damping in non-conservative systems with follower forces*, International Journal of Non-Linear Mechanics, 5 (1970), pp. 341–358.

[90] A. Harb, *Energy harvesting: State-of-the-art*, Renewable Energy, 36 (2011), pp. 2641–2654.

[91] R. L. Harne, *Theoretical investigations of energy harvesting efficiency from structural vibrations using piezoelectric and electromagnetic oscillators*, Journal of the Acoustical Society of America, 132 (2012), pp. 162–172.

[92] B. D. Hassard, N. D. Kazarinoff, and Y.-H. Wan, *Theory and applications of Hopf bifurcation*, vol. 41, Cambridge University Press Archive, 1981.

[93] E. Hau, *Wind turbines-fundamentals, technologies, application, economics.*, IEEE Electrical Insulation Magazine, 19 (2003), p. 48.

[94] X.-F. He and J. Gao, *Wind energy harvesting based on flow-induced-vibration and impact*, Microelectronic Engineering, 111 (2013), pp. 82–86.

[95] P. Hémon, X. Amandolese, and T. Andrianne, *Galloping oscillations of prisms and energy harvesting wind tunnel*, in Proceedings of First International Symposium on Flutter and its Applications, May 15-17, Tokyo, Japan, 2016.

[96] G. Herrmann and C. Jong, *On the destabilizing effect of damping in nonconservative elastic systems*, Journal of Applied Mechanics, 32 (1965), pp. 592–597.

[97] J. D. Hobeck and D. J. Inman, *Artificial piezoelectric grass for energy harvesting from turbulence-induced vibration*, Smart Materials and Structures, 21 (2012), p. 105024.

[98] C. M. Hoke, J. Young, and J. C. S. Lai, *Effects of time-varying camber deformation on flapping foil propulsion and power extraction*, Journal of Fluids and Structures, 56 (2015), pp. 152–176.

[99] F. S. Hover, Ø. Haugsdal, and M. S. Triantafyllou, *Effect of angle of attack profiles in flapping foil propulsion*, Journal of Fluids and Structures, 19 (2004), pp. 37–47.

[100] G. Huxham, S. Cochard, and J. Patterson, *Experimental parametric investigation of an oscillating hydrofoil tidal stream energy converter*, in Proceedings of 18th Australasian Fluid Mechanics Conference AFMC, 2012.

[101] K. Isogai and H. Abiru, *Study of multi-wing configurations of elastically supported flapping wing power generator*, Japan Society of Aeronautical Space Science, 55 (2012), pp. 133–142.

[102] K. Isogai, M. Yamasaki, M. Matsubara, and T. Asaoka, *Design study of elastically supported flapping wing power generator*, in International Forum on Aeroelasticity and Structural Dynamics, Amsterdam, 2003.

[103] K. D. Jones, S. Davids, and M. F. Platzer, *Oscillating-wing power generation*, in Proceedings of the 3rd ASME/JSME Joint Fluids Engineering Conference, San Francisco, California, USA, 1999, pp. 1–6.

[104] K. D. Jones, K. Lindsey, and M. F. Platzer, *An investigation of the fluid-structure interaction in an oscillating-wing micro-hydropower generator*, in WIT Transactions on The Built Environment, vol. 71, 2003, ch. Fluid Structure Interaction II, pp. 73–82.

[105] K. D. Jones and M. F. Platzer, *Numerical computation of flapping-wing propulsion and power extraction*, in AIAA 35th Aerospace Sciences Meeting & Exhibit, Reno, NV, 1997, pp. 1–16.

[106] H.-J. Jung and S.-W. Lee, *The experimental validation of a new energy harvesting system based on the wake galloping phenomenon*, Smart Materials and Structures, 20 (2011), p. 055022.

[107] H.-J. Jung, S.-W. Lee, and D. D. Jang, *Feasibility study on a new energy harvesting electromagnetic device using aerodynamic instability*, EEE Transactions on Maqnetics, 45 (2009), pp. 4376–4379.

[108] M. A. Karami and D. J. Inman, *Equivalent damping and frequency change for linear and nonlinear hybrid vibrational energy harvesting systems*, Journal of Sound and Vibration, 330 (2011), pp. 5583–5597.

[109] T. M. Kier, *Comparison of unsteady aerodynamic modelling methodologies with respect to flight loads analysis*, AIAA Paper, 6027 (2005), p. 2005.

[110] T. Kinsey and G. Dumas, *Parametric study of an oscillating airfoil in a power-extraction regime*, AIAA Journal, 46 (2008), pp. 1318–1330.

[111] ——, *Testing and analysis of an oscillating hydrofoils turbine concept*, in ASME 2010 3rd Joint US-European Fluids Engineering Summer Meeting collocated with 8th International Conference on Nanochannels, Microchannels, and Minichannels, American Society of Mechanical Engineers, 2010, pp. 9–22.

[112] ——, *Optimal tandem configuration for oscillating-foils hydrokinetic turbine*, Journal of Fluids Engineering, 134 (2012), p. 031103.

[113] ——, *Three-Dimensional Effects on an Oscillating-Foil Hydrokinetic Turbine*, Journal of Fluids Engineering, 134 (2012), p. 071105.

[114] T. Kinsey, G. Dumas, G. Lalande, J. Ruel, A. Mehut, P. Viarouge, J. Lemay, and Y. Jean, *Prototype testing of a hydrokinetic turbine based on oscillating hydrofoils*, Renewable Energy, 36 (2011), pp. 1710–1718.

[115] O. N. Kirillov, *A theory of the destabilization paradox in non-conservative systems*, Acta Mechanica, 174 (2005), pp. 145–166.

[116] O. N. Kirillov and F. Verhulst, *Paradoxes of dissipation-induced destabilization or who opened Whitney's umbrella?*, ZAMM-Journal of Applied Mathematics and Mechanics/Zeitschrift für Angewandte Mathematik und Mechanik, 90 (2010), pp. 462–488.

[117] J. Ko, A. Kurdila, and T. Strganac, *Nonlinear control theory for a class of structural nonlinearities in a prototypical wing section*, in Proc. of the 35th AIAA Aerospace Scinece Meeting and Exhibit, AIAA paper 97, vol. 580, 1997.

[118] J. Ko, A. J. Kurdila, and T. W. Strganac, *Nonlinear control of a prototypical wing section with torsional nonlinearity*, Journal of Guidance, Control, and Dynamics, 20 (1997), pp. 1181–1189.

[119] J. Ko, T. W. Strganac, and A. J. Kurdila, *Stability and control of a structurally nonlinear aeroelastic system*, Journal of Guidance, Control, and Dynamics, 21 (1998), pp. 718–725.

[120] A. N. Kounadis, *On the paradox of the destabilizing effect of damping in non-conservative systems*, International Journal of Non-Linear Mechanics, 27 (1992), pp. 597–609.

[121] R. Král, S. Pospíšil, and J. Náprstek, *Experimental set-up for advanced aeroelastic tests on sectional models*, Experimental Techniques, (2013).

[122] ——, *Wind tunnel experiments on unstable self-excited vibration of sectional girders*, Journal of Fluids and Structures, 44 (2014), pp. 235–250.

[123] H. G. Kussner, *Zusammenfassender bericht uber den instationaren auftrieb von flugeln*, Luftfahrtforschung, 13 (1936), pp. 410–424.

[124] S.-D. Kwon, *A t-shaped piezoelectric cantilever for fluid energy harvesting*, Applied Physics Letters, 97 (2010), p. 164102.

[125] C. K. Kwuimy, G. Litak, M. Borowiec, and C. Nataraj, *Performance of a piezoelectric energy harvester driven by air flow*, Applied Physics Letters, 100 (2012), p. 024103.

[126] M. A. Langthjem and Y. Sugiyama, *Dynamic stability of columns subjected to follower loads: a survey*, Journal of Sound and Vibration, 238 (2000), pp. 809–851.

[127] J. W. Larsen, S. R. Nielsen, and S. Krenk, *Dynamic stall model for wind turbine airfoils*, Journal of Fluids and Structures, 23 (2007), pp. 959–982.

[128] B. Lee, S. Price, and Y. Wong, *Nonlinear aeroelastic analysis of airfoils: bifurcation and chaos*, Progress in Aerospace Sciences, 35 (1999), pp. 205–334.

[129] J. Lee and M. Bernitsas, *High-damping, high-reynolds viv tests for energy harnessing using the vivace converter*, Ocean Engineering, 38 (2011), pp. 1697–1712.

[130] Y. S. Lee, A. F. Vakakis, L. A. Bergman, D. M. McFarland, and G. Kerschen, *Triggering mechanisms of limit cycle oscillations in a two degree-of-freedom wing flutter model*, in ASME. International Design Engineering Technical Conferences and Computers and Information in Engineering Conference. Volume 1: 20th Biennial Conference on Mechanical Vibration and Noise, Parts A, B, and C, September 24-28, Long Beach, California, USA, 2005, pp. 1863–1872.

[131] J. Leishman and T. Beddoes, *A semi-empirical model for dynamic stall*, Journal of the American Helicopter society, 34 (1989), pp. 3–17.

[132] G. A. Lesieutre, G. K. Ottman, and H. F. Hofmann, *Damping as a result of piezoelectric energy harvesting*, Journal of Sound and Vibration, 269 (2004), pp. 991–1001.

[133] S. Li, J. Yuan, and H. Lipson, *Ambient wind energy harvesting using cross-flow fluttering*, Journal of Applied Physics, 109 (2011), p. 026104.

[134] M. Lighthill, *Large-amplitude elongated-body theory of fish locomotion*, Proceedings of the Royal Society of London B: Biological Sciences, 179 (1971), pp. 125–138.

[135] A. Luongo and F. D'Annibale, *On the destabilizing effect of damping on discrete and continuous circulatory systems*, Journal of Sound and Vibration, 333 (2014), pp. 6723–6741.

[136] ——, *A paradigmatic minimal system to explain the Ziegler paradox*, Continuum Mechanics and Thermodynamics, 27 (2015), pp. 211–222.

[137] A. Luongo, M. Ferretti, and F. D'Annibale, *Paradoxes in dynamic stability of mechanical systems: investigating the causes and detecting the nonlinear behaviors*, SpringerPlus, 5 (2016), p. 1.

[138] K. H. Ly and V. A. L. Chasteaut, *Experiments on an oscillating aerofoil and applications to wind-energy converters*, AIAA Journal, 5 (1981), pp. 116–121.

[139] C. Mannini, *Flutter vulnerability assessment of flexible bridges*, PhD thesis, 2006.

[140] C. Mannini, A. M. Marra, and G. Bartoli, *VIV-galloping instability of rectangular cylinders: review and new experiments*, Journal of Wind Engineering and Industrial Aerodynamics, 132 (2014), pp. 109–124.

[141] C. Mannini, A. M. Marra, and G. Bartoli, *Experimental investigation on VIV-galloping interaction of a rectangular 3:2 cylinder*, Meccanica, 50 (2015), pp. 841–853.

[142] C. Mannini, A. M. Marra, T. Massai, and G. Bartoli, *Interference of vortex-induced vibration and transverse galloping for a rectangular cylinder*, Journal of Fluids and Structures. (submitted).

[143] C. Mannini, G. Sbragi, and G. Schewe, *Analysis of self-excited forces for a box-girder bridge deck through unsteady RANS simulations*, Journal of Fluids and Structures, 63 (2016), pp. 57–76.

[144] L. Mateu and F. Moll, *Review of energy harvesting techniques and applications for microelectronics (keynote address)*, in Microtechnologies for the New Millennium 2005, International Society for Optics and Photonics, 2005, pp. 359–373.

[145] M. Matsumoto, *Aerodynamic damping of prisms*, Journal of Wind Engineering and Industrial Aerodynamics, 59 (1996), pp. 159–175.

[146] M. Matsumoto, *Flutter and its applications - flutter mode and ship navigation*, Journal of Wind Engineering and Industrial Aerodynamics, 122 (2013), pp. 10–20.

[147] M. Matsumoto, K. Mizuno, K. Okubo, and Y. Ito, *Fundamental study on the efficiency of power generation system by use of the flutter instability*, in ASME. Proceedings of Pressure Vessels and Piping Division Conference, Volume 9: 6th FSI, AE and FIV and N Symposium, July 23-27, Vancouver, BC, Canada, 2006, pp. 277–287.

[148] M. Matsumoto, K. Okubo, Y. Ito, H. Matsumiya, and G. Kim, *The complex branch characteristics of coupled flutter*, Journal of Wind, 96 (2008), pp. 1843–1855.

[149] M. Matsumoto, H. Shirato, K. Mizuno, R. Shijo, and T. Hikida, *Flutter characteristics of h-shaped cylinders with various side-ratios and comparisons with characteristics of rectangular cylinders*, Journal of Wind Engineering and Industrial Aerodynamics, 96 (2008), pp. 963–970.

[150] M. Matsumoto, T. Yagi, H. Tamaki, and T. Tsubota, *Vortex-induced vibration and its effect on torsional flutter instability in the case of b/d= 4 rectangular cylinder*, Journal of Wind Engineering and Industrial Aerodynamics, 96 (2008), pp. 971–983.

[151] W. McKinney and J. DeLaurier, *Wingmill: an oscillating-wing windmill*, Journal of Energy, 5 (1981), pp. 109–115.

[152] A. Mehmood, A. Abdelkefi, M. R. Hajj, A. H. Nayfeh, I. Akhtar, and A. O. Nuhait, *Piezoelectric energy harvesting from vortex-induced vibrations of circular cylinder*, Journal of Sound and Vibration, 332 (2013), pp. 4656–4667.

[153] L. Meirovitch, *Fundamentals of Vibrations*, McGraw-Hill higher education, McGraw-Hill, 2001.

[154] S. Meninger, J. O. Mur-Miranda, R. Amirtharajah, A. P. Chandrakasan, and J. H. Lang, *Vibration-to-electric energy conversion*, IEEE Transactions on Very Large Scale Integration (VLSI) Systems, 9 (2001), pp. 64–76.

[155] S. Michelin and O. Doaré, *Energy harvesting efficiency of piezoelectric flags in axial flows*, Journal of Fluid Mechanics, 714 (2013), pp. 489–504.

[156] P. D. Mitcheson, T. C. Green, E. M. Yeatman, and A. S. Holmes, *Architectures for vibration-driven micropower generators*, Journal of Microelectromechanical Systems, 13 (2004), pp. 429–440.

[157] J. Náprstek, *Bifurcation and post-critical flutter-type random vibrations of slender structures*, in Proc. 8th ASCE Joint Spec. Conf. Probabilistic Mechanics and structural reliability. University of Notre Dame, paper PMC2000-006, 2000.

[158] ——, *Stability domains of wind-excited random nonlinear systems through Lyapunov function*, Journal of Wind Engineering and Industrial Aerodynamics, 89 (2001), pp. 1499–1512.

[159] J. Náprstek, C. Fischer, and S. Pospíšil, *Some properties of limit cycles of multi-degree of freedom non-linear systems*, in Proc. 10th Int. Conf. on Recent Advances in Structural Dynamics, M. Brennan edt., Univ. Southampton, Inst. Sound Vibr. Res., Southampton, 2010, pp. 1–16.

[160] J. Náprstek and S. Pospíšil, *Post-critical behavior of a simple non-linear system in a cross-wind*, Engineering Mechanics, 18 (2011), pp. 193–201.

[161] ——, *Response types and general stability conditions of linear aero-elastic system with two degrees-of-freedom*, Journal of Wind Engineering and Industrial Aerodynamics, 111 (2012), pp. 1–13.

[162] E. Naudascher and D. Rockwell, *Flow-induced vibrations: an engineering guide*, Courier Corporation, 2012.

[163] S. Nemat-Nasser and G. Herrmann, *On the stability of equilibrium of continuous systems*, Ingenieur-Archiv, 35 (1966), pp. 17–24.

[164] K. S. O'donnell, P. Marzocca, A. Milanese, C. McNall, R. Jha, and E. M. Bollt, *Design of a wind tunnel apparatus to assist flow and aeroelastic control via zero net mass flow actuators*, methods, 5 (2007), p. 7.

[165] A. Papangelo, A. Grolet, L. Salles, N. Hoffmann, and M. Ciavarella, *Snaking bifurcations in a self-excited oscillator chain with cyclic symmetry*, Communications in Nonlinear Science and Numerical Simulation, 44 (2017), pp. 108–119.

[166] G. Parkinson and J. Smith, *The square prism as an aeroelastic non-linear oscillator*, The Quarterly Journal of Mechanics ..., XV (1964).

[167] Z. Peng and Q. Zhu, *Energy harvesting through flow-induced oscillations of a foil*, Physics of Fluids, 21 (2009), p. 123602.

[168] D. Pereira, R. Vasconcellos, M. Hajj, and F. Marques, *Insights on aeroelastic bifurcation phenomena in airfoils with structural nonlinearities*, Journal | MESA, 6 (2015), pp. 399–424.

[169] D. A. Peters, *Two-dimensional incompressible unsteady airfoil theory—an overview*, Journal of Fluids and Structures, 24 (2008), pp. 295–312.

[170] D. A. Peters, S. Karunamoorthy, and W.-M. Cao, *Finite state induced flow models. i-two-dimensional thin airfoil*, Journal of Aircraft, 32 (1995), pp. 313–322.

[171] D. Petot, *Differential equation modeling of dynamic stall*, La Recherche Aérospatiale, 5 (1989), pp. 59–72.

[172] L. Pigolotti, C. Mannini, G. Bartoli, and K. Thiele, *Wind tunnel tests on elongated rectangular plates under flutter motion: limit-cycle oscillations and preliminary energy harvesting considerations*, in 14th International Conference on Wind Engineering, June 21-26, Porto Alegre, Brazil, 2015.

[173] M. F. Platzer and R. A. Bradley, *Oscillating-wing power generator with flow-induced pitch-plunge phasing*, Nov. 7 2008. US Patent App. 12/266,553.

[174] R. H. Plaut and E. F. Infante, *The effect of external damping on the stability of Beck's column*, International Journal of Solids and Structures, 6 (1970), pp. 491–496.

[175] S. Pobering, S. Ebermeyer, and N. Schwesinger, *Generation of electrical energy using short piezoelectric cantilevers in flowing media*, in Proceedings of SPIE 7288, Active and Passive Smart Structures and Integrated Systems, vol. 7288, International Society for Optics and Photonics, 2009.

[176] S. Pobering, M. Menacher, S. Ebermaier, N. Schwesinger, and T. U. Muenchen, *Piezoelectric power conversion with self-induced oscillation*, Power MEMS, (2009), pp. 384–387.

[177] S. Pobering and N. Schwesinger, *A novel hydropower harvesting device*, Proceedings of the International Conference on MEMS, NANO and Smart Systems, ICMENS, (2004), pp. 431–436.

[178] J. Pons, *Entwicklung und auslegung eines wirbelstromdämpfersystems zur schwingungsdämfung von windkanalmodellen*, master's thesis, Institut für Stahlbau TU Braunschweig, 2014.

[179] S. Priya and D. Inman, *Energy harvesting technologies*, 2008.

[180] M. Ragheb and A. M. Ragheb, *Wind turbines theory-the betz equation and optimal rotor tip speed ratio*, INTECH Open Access Publisher, 2011.

[181] M. Righi, *Aeroelastic stability of long span suspended bridges: flutter mechanism on rectangular cylinders in smooth and turbulent flow*, PhD thesis, University of Florence, 2003.

[182] S. Roundy, *On the effectiveness of vibration-based energy harvesting*, Journal of Intelligent Material Systems and Structures, 16 (2005), pp. 809–823.

[183] S. Roundy and P. K. Wright, *A piezoelectric vibration based generator for wireless electronics*, Smart Materials and Structures, 13 (2004), p. 1131.

[184] S. Roundy, P. K. Wright, and K. S. Pister, *Micro-electrostatic vibration-to-electricity converters*, in ASME 2002 International Mechanical Engineering Congress and Exposition, American Society of Mechanical Engineers, 2002, pp. 487–496.

[185] S. Roundy, P. K. Wright, and J. Rabaey, *A study of low level vibrations as a power source for wireless sensor nodes*, Computer Communications, 26 (2003), pp. 1131–1144.

[186] P. P. Sarkar, N. P. Jones, and R. H. Scanlan, *Identification of aeroelastic parameters of flexible bridges*, Journal of Engineering Mechanics, 120 (1994), pp. 1718–1742.

[187] R. H. Scanlan and J. J. Tomko, *Airfoil and bridge deck flutter derivatives*, Journal of the Engineering Mechanics Division, 97 (1971), pp. 1717–1737.

[188] G. Schewe, H. Mai, and G. Dietz, *Nonlinear effects in transonic flutter with emphasis on manifestations of limit cycle oscillations*, Journal of Fluids and Structures, 18 (2003), pp. 3–22.

[189] W. R. Sears, *Operational methods in the theory of airfoils in non-uniform motion*, Journal of the Franklin Institute, 230 (1940), pp. 95–111.

[190] ——, *Some aspects of non-stationary airfoil theory and its practical application*, Journal of the Aeronautical Sciences (Institute of the Aeronautical Sciences), 3 (1941).

[191] E. Shimizu, *Multi-objective design study of a flapping wing generator*, in The 24th International Congress of the Aeronautical Sciences, 2004, pp. 1–8.

[192] E. Simiu and R. H. Scanlan, *Wind Effects on Structures: Fundamentals and Application to Design*, New York: John Wiley & Sons, 1996.

[193] B. Simpson, F. Hover, and M. Triantafyllou, *Experiments in direct energy extraction through flapping foils*, in Proceeding of the 18th International Offshore and Polar Engineering Conference, Vancouver, BC, Canada, 2008, pp. 370–376.

[194] K. Singh, S. Michelin, and E. De Langre, *The effect of non-uniform damping on flutter in axial flow and energy-harvesting strategies*, Proceedings of the Royal Society A: Mathematical, Physical and Engineering Sciences, 468 (2012), pp. 3620–3635.

[195] K. Singh, S. Michelin, and E. de Langre, *Energy harvesting from axial fluid-elastic instabilities of a cylinder*, Journal of Fluids and Structures, 30 (2012), pp. 159–172.

[196] V. C. Sousa, M. de M. Anicézio, C. De Marqui Jr, and A. Erturk, *Enhanced aeroelastic energy harvesting by exploiting combined nonlinearities: theory and experiment*, Smart Materials and Structures, 20 (2011), p. 094007.

[197] D. St. Clair, a. Bibo, V. R. Sennakesavababu, M. F. Daqaq, and G. Li, *A scalable concept for micropower generation using flow-induced self-excited oscillations*, Applied Physics Letters, 96 (2010), p. 144103.

[198] T. Sterken, K. Baert, C. Van Hoof, R. Puers, G. Borghs, and P. Fiorini, *Comparative modelling for vibration scavengers [mems energy scavengers]*, in Proceedings of IEEE Sensors, 2004, pp. 1249–1252.

[199] T. W. Strganac, J. Ko, and D. E. Thompson, *Identification and control of limit cycle oscillations in aeroelastic systems*, Journal of Guidance, Control, and Dynamics, 23 (2000), pp. 1127–1133.

[200] Y. Sugiyama and M. A. Langthjem, *Physical mechanism of the destabilizing effect of damping in continuous non-conservative dissipative systems*, International Journal of Non-Linear Mechanics, 42 (2007), pp. 132–145.

[201] L. Tang, *The Dynamics of Two-Dimensional Cantilevered Flexible Plates in Axial Flow and a New Energy-Harvesting Concept*, PhD thesis, McGill University of Montréal, 2007.

[202] L. Tang and M. P. Païdoussis, *On the instability and the post-critical behaviour of two-dimensional cantilevered flexible plates in axial flow*, Journal of Sound and Vibration, 305 (2007), pp. 97–115.

[203] L. Tang, M. P. Païdoussis, and J. Jiang, *Cantilevered flexible plates in axial flow: energy transfer and the concept of flutter-mill*, Journal of Sound and Vibration, 326 (2009), pp. 263–276.

[204] G. W. Taylor, J. R. Burns, S. A. Kammann, W. B. Powers, and T. R. Welsh, *The energy harvesting eel: a small subsurface ocean/river power generator*, IEEE Journal of Oceanic Engineering, 26 (2001), pp. 539–547.

[205] T. Theodorsen, *General theory of aerodynamic instability and the mechanism of flutter - Report No. 496*, tech. report, 1935.

[206] T. Theodorsen and I. E. Garrick, *General potential theory of arbitrary wing sections - Report No. 452*, tech. report, 1934.

[207] F.-B. Tian, J. Young, and J. C. S. Lai, *Improving power-extraction efficiency of a flapping plate: From passive deformation to active control*, Journal of Fluids and Structures, 51 (2014), pp. 384–392.

[208] C. Tran and D. Petot, *Semi-empirical model for the dynamic stall of airfoils in view of the application to the calculation of responses of a helicopter blade in forward flight*, Vertica, 5 (1981), pp. 35–53.

[209] G. A. Van Kuik, *The lanchester–betz–joukowsky limit*, Wind Energy, 10 (2007), pp. 289–291.

[210] T. Von Karman, *Airfoil theory for non-uniform motion*, Journal of the Aeronautical Sciences (Institute of the Aeronautical Sciences), 5 (1938).

[211] H. Wagner, *Über die entstehung des dynamischen auftriebes von tragflügeln*, ZAMM-Journal of Applied Mathematics and Mechanics/Zeitschrift für Angewandte Mathematik und Mechanik, 5 (1925), pp. 17–35.

[212] D.-A. Wang, C.-Y. Chiu, and H.-T. Pham, *Electromagnetic energy harvesting from vibrations induced by kármán vortex street*, Mechatronics, 22 (2012), pp. 746–756.

[213] J. Wu, J. Wu, F.-B. Tian, N. Zhao, and Y.-D. Li, *How a flexible tail improves the power extraction efficiency of a semi-activated flapping foil system: A numerical study*, Journal of Fluids and Structures, 54 (2015), pp. 886–899.

[214] J. Xiang, Y. Wu, and D. Li, *Energy harvesting from the discrete gust response of a piezoaeroelastic wing: Modeling and performance evaluation*, Journal of Sound and Vibration, 343 (2015), pp. 176–193.

[215] Q. Xiao and Q. Zhu, *A review on flow energy harvesters based on flapping foils*, Journal of Fluids and Structures, 46 (2014), pp. 174–191.

[216] J. Young, M. A. Ashraf, J. C. S. Lai, and M. F. Platzer, *Numerical simulation of fully passive flapping foil power generation*, AIAA Journal, 51 (2013), pp. 2727–2739.

[217] J. Young, J. C. Lai, and M. F. Platzer, *A review of progress and challenges in flapping foil power generation*, Progress in Aerospace Sciences, 67 (2014), pp. 2–28.

[218] J. Young, S. Lai, and C. Joseph, *Mechanisms influencing the efficiency of oscillating airfoil propulsion*, AIAA Journal, 45 (2007), pp. 1695–1702.

[219] J. Young, F.-B. Tian, and J. C. Lai, *Betz analysis of a single flapping foil power generator*, in Proceedings of First International Symposium on Flutter and its Applications, May 15-17, Tokyo, Japan, 2016.

[220] Q. Zhu, *Optimal frequency for flow energy harvesting of a flapping foil*, Journal of Fluid Mechanics, 675 (2011), pp. 495–517.

[221] ——, *Energy harvesting by a purely passive flapping foil from shear flows*, Journal of Fluids and Structures, 34 (2012), pp. 157–169.

[222] Q. Zhu, M. Haase, and C. H. Wu, *Modeling the capacity of a novel flow-energy harvester*, Applied Mathematical Modelling, 33 (2009), pp. 2207–2217.

[223] Q. Zhu and Z. Peng, *Mode coupling and flow energy harvesting by a flapping foil*, Physics of Fluids, 21 (2009), p. 033601.

[224] H. Ziegler, *Die Stabilitätskriterien der Elastomechanik*, Archive of Applied Mechanics, 20 (1952), pp. 49–56.

Appendix A

Flow measurement, Stahlbau wind tunnel

Example of low-pass filtering

Time histories

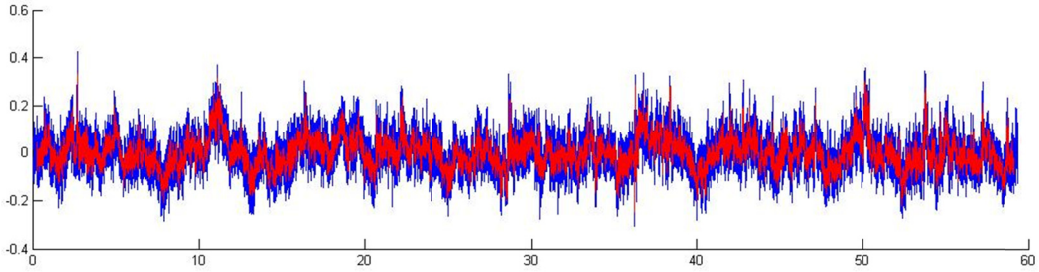

Auto-spectra

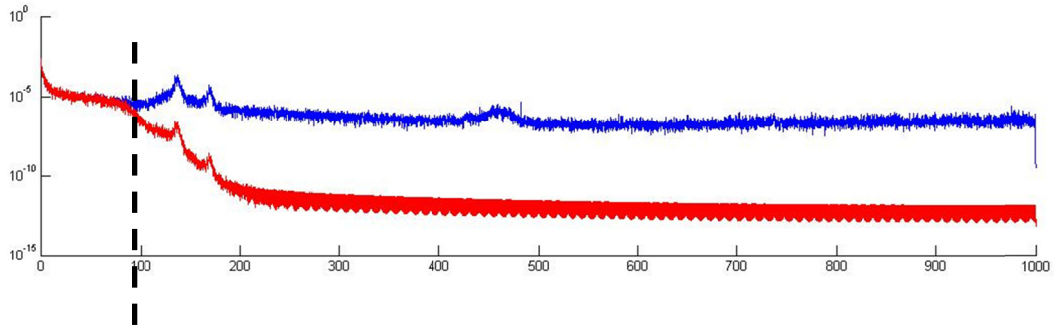

90 *Hz*

Filtering procedure of the real data, which applies a low-pass filter with cut-off frequency of 90 Hz. What happens above 100 Hz is considered to not be of physical interest for the next aeroelastic tests and just noise.

The filter is constructed using the MatLab's routine `[b,a] = butter(n,Wn)`, which designs an order `n` low-pass digital Butterworth filter with normalized cutoff frequency `Wn`. It returns the filter coefficients in length `n+1` row vectors `b` and `a`, with coefficients in descending powers of z:

$$H(z) = \\ = \frac{b(1) + b(2)z^{-1} + \cdots + b(n+1)z^{-n}}{1 + a(2)z^{-1} + \cdots + a(n+1)z^{-n}} \quad . \tag{2-1}$$

The chosen order of the filter is 6.

Maps of flow data, without filtering

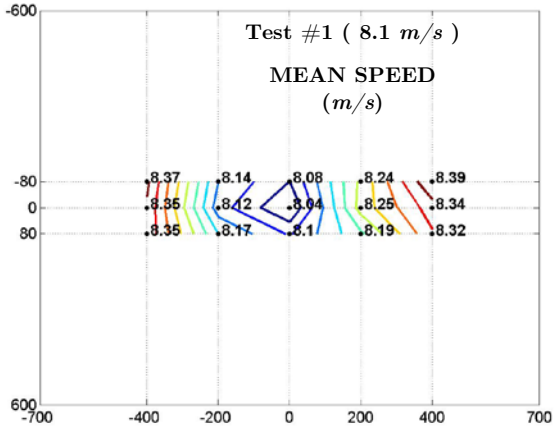

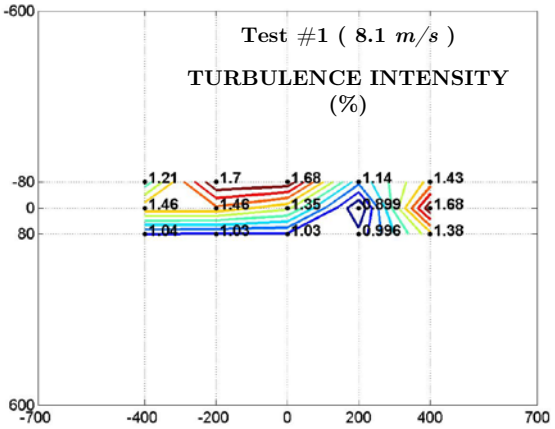

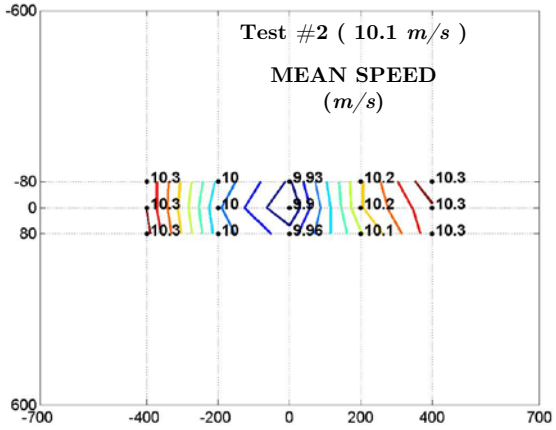

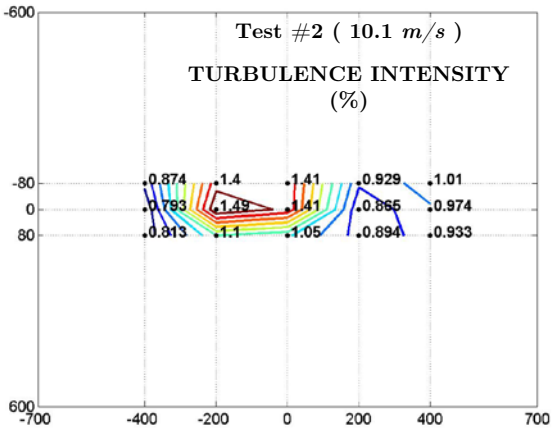

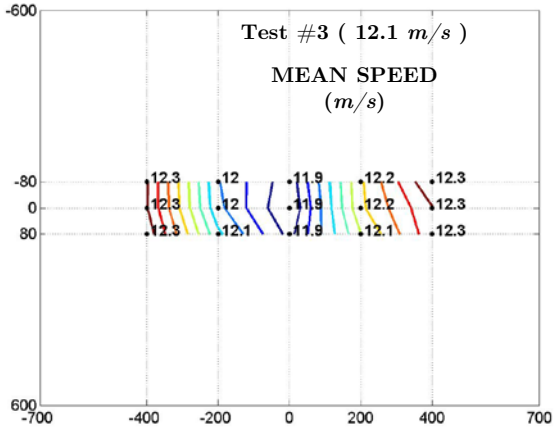

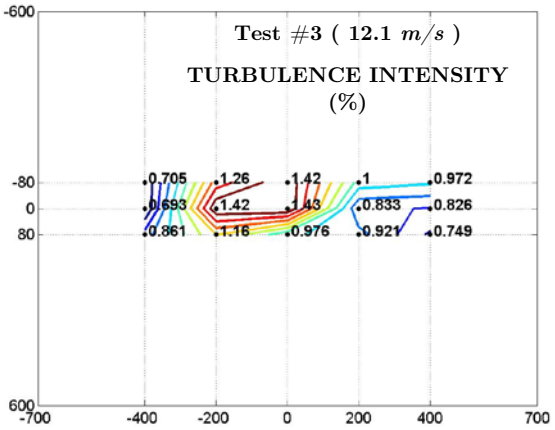

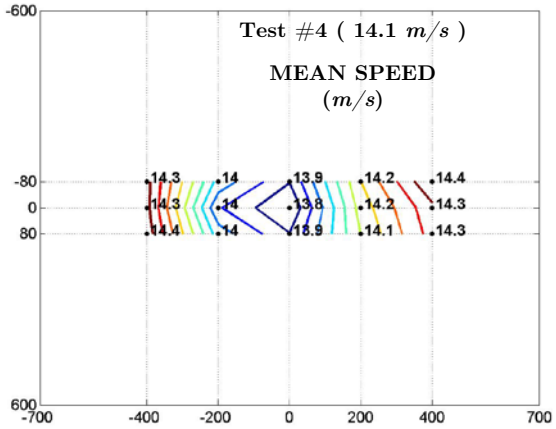

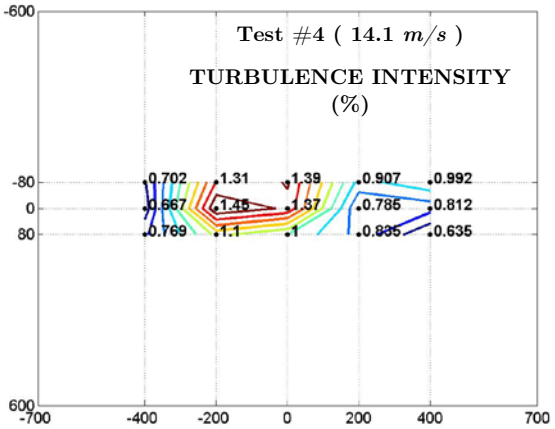

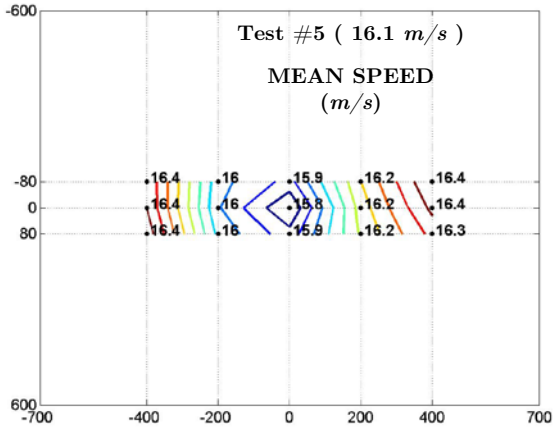
Test #5 (16.1 m/s)
MEAN SPEED
(m/s)
16.4
16
15.9
16.2
16.4
16.4
16
15.8
16.2
16.4
16.4
16
15.9
16.2
16.3
-600
-80
0
80
600
-700
-400
-200
0
200
400
700

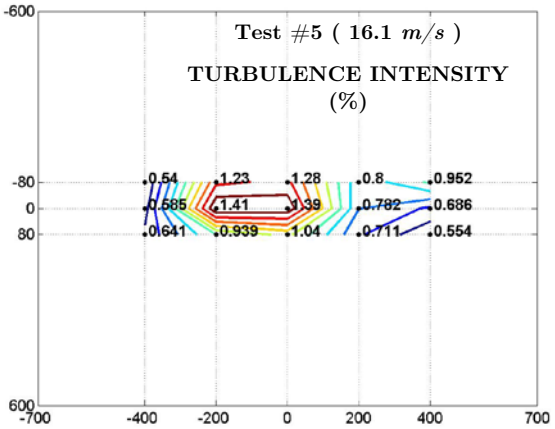
Test #5 (16.1 m/s)
TURBULENCE INTENSITY
(%)
0.54
1.23
1.28
0.8
0.952
0.585
1.41
1.39
0.782
0.686
0.641
0.939
1.04
0.711
0.554
-600
-80
0
80
600
-700
-400
-200
0
200
400
700

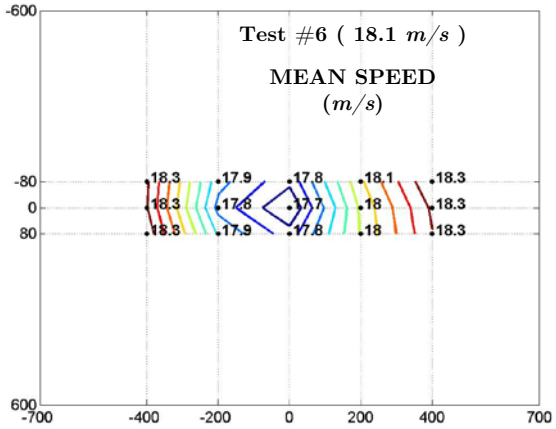
Test #6 (18.1 m/s)
MEAN SPEED
(m/s)
18.3
17.9
17.8
18.1
18.3
18.3
17.8
17.7
18
18.3
18.3
17.9
17.8
18
18.3
-600
-80
0
80
600
-700
-400
-200
0
200
400
700

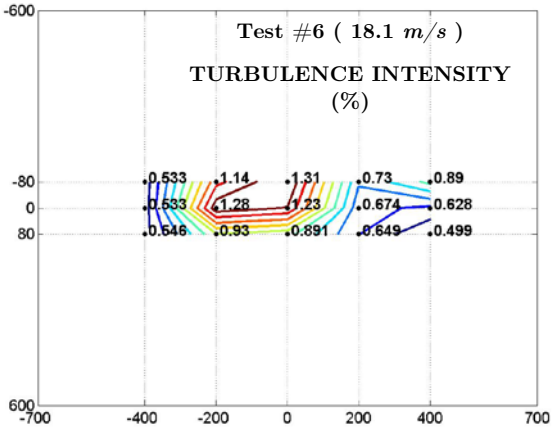
Test #6 (18.1 m/s)
TURBULENCE INTENSITY
(%)
0.533
1.14
1.31
0.73
0.89
0.533
1.28
1.23
0.674
0.628
0.546
0.93
0.891
0.649
0.499
-600
-80
0
80
600
-700
-400
-200
0
200
400
700

Maps of flow data, filtered with a low-pass filter at 90 *Hz*

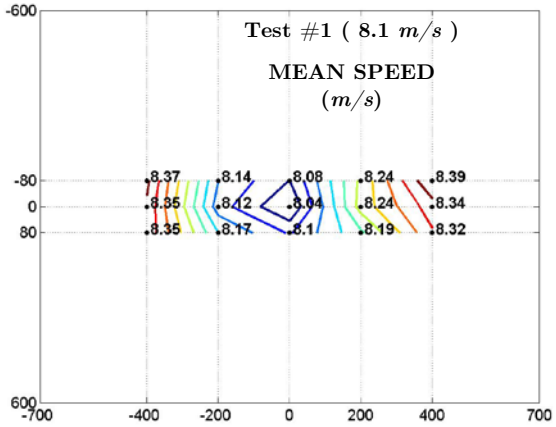

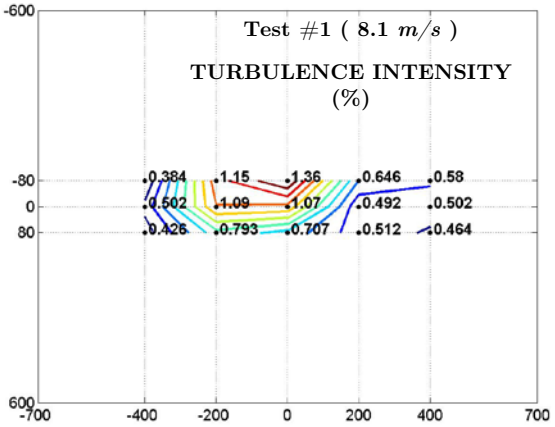

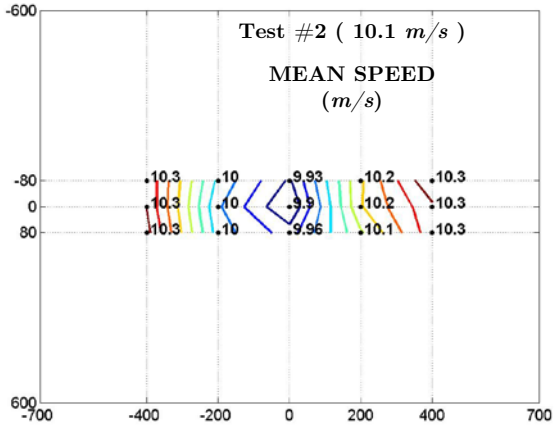

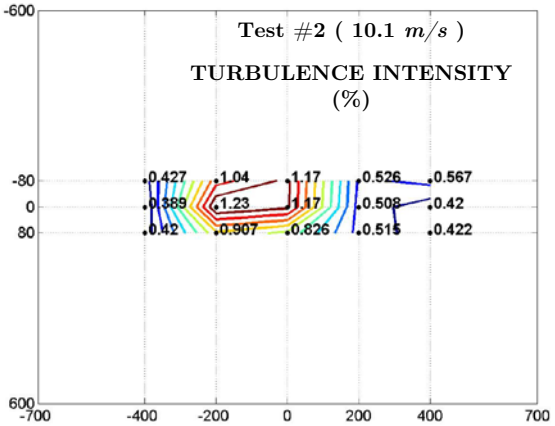

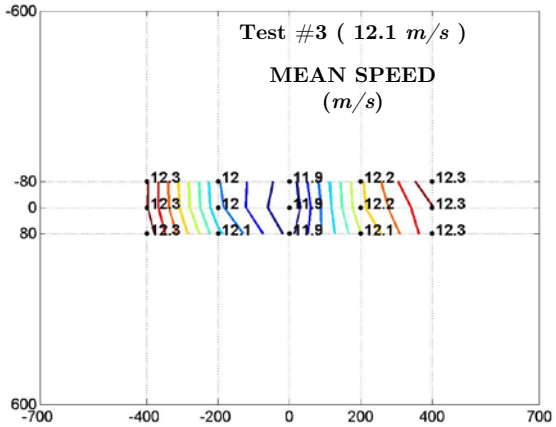

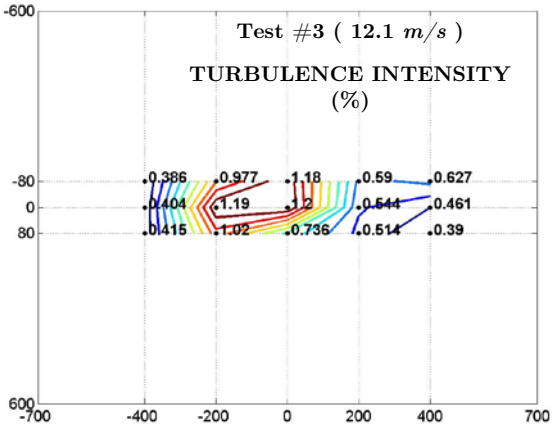

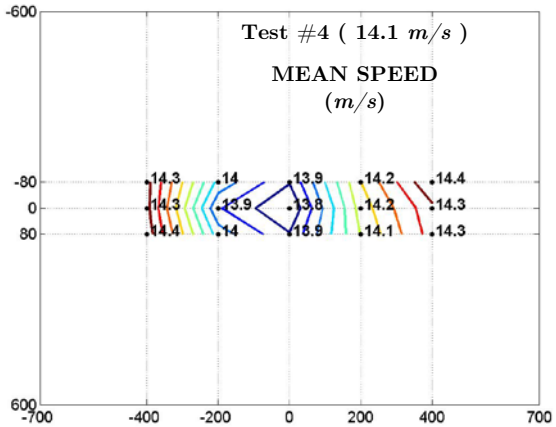

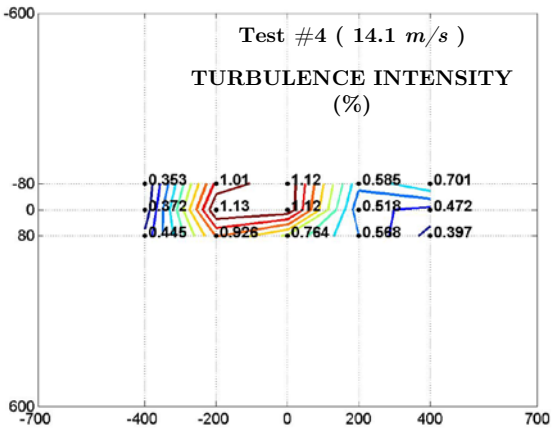

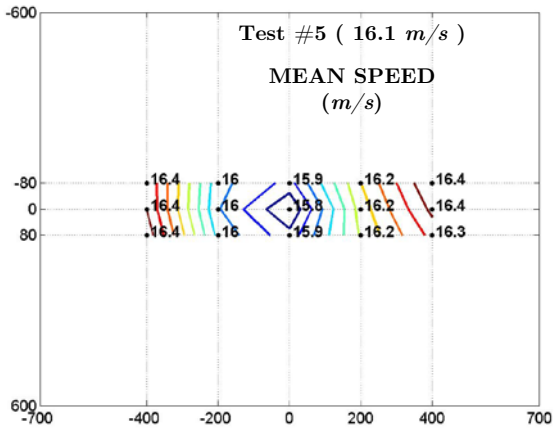
Test #5 (16.1 m/s)
MEAN SPEED
(m/s)
16.4
16
15.9
16.2
16.4
16.4
16
15.8
16.2
16.4
16.4
16
15.9
16.2
16.3
-600
-80
0
80
600
-700
-400
-200
0
200
400
700

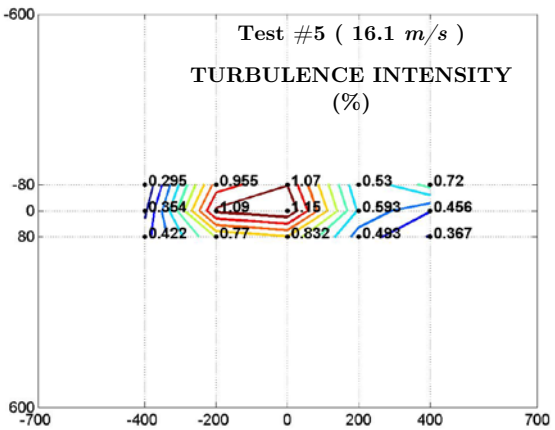
Test #5 (16.1 m/s)
TURBULENCE INTENSITY
(%)
0.295
0.955
1.07
0.53
0.72
0.354
1.09
1.15
0.593
0.456
0.422
0.77
0.832
0.493
0.367
-600
-80
0
80
600
-700
-400
-200
0
200
400
700

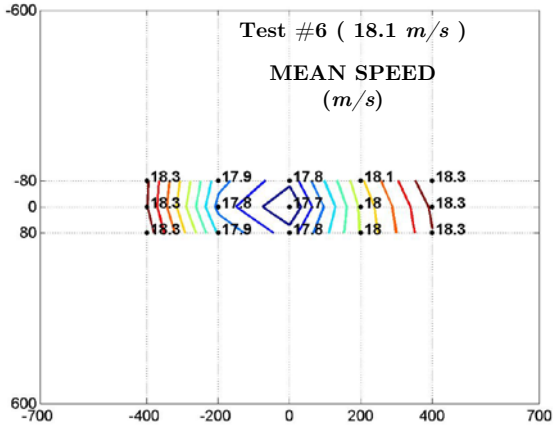
Test #6 (18.1 m/s)
MEAN SPEED
(m/s)
18.3
17.9
17.8
18.1
18.3
18.3
17.8
17.7
18
18.3
18.3
17.9
17.8
18
18.3
-600
-80
0
80
600
-700
-400
-200
0
200
400
700

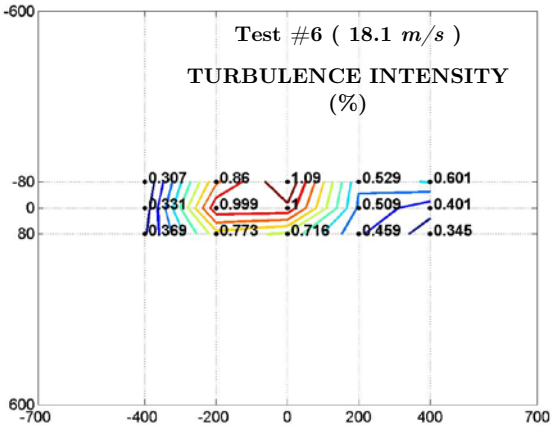
Test #6 (18.1 m/s)
TURBULENCE INTENSITY
(%)
0.307
0.86
1.09
0.529
0.601
0.331
0.999
1
0.509
0.401
0.369
0.773
0.716
0.459
0.345
-600
-80
0
80
600
-700
-400
-200
0
200
400
700

Appendix B

Flow measurement, CRIACIV wind tunnel

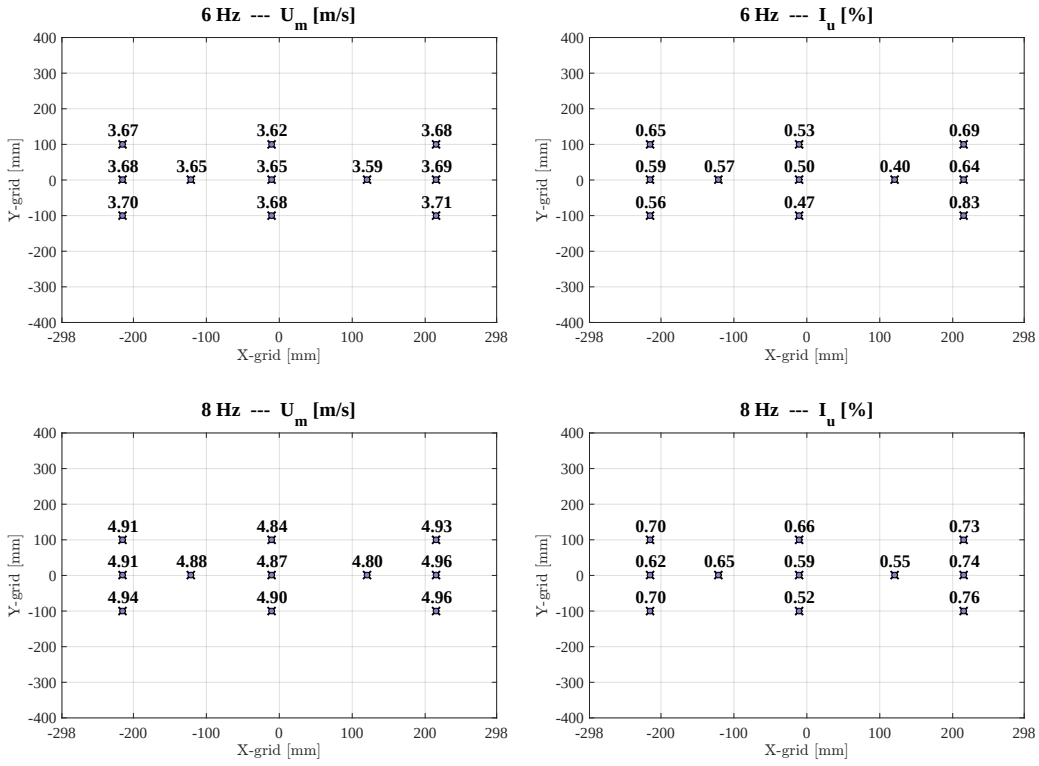

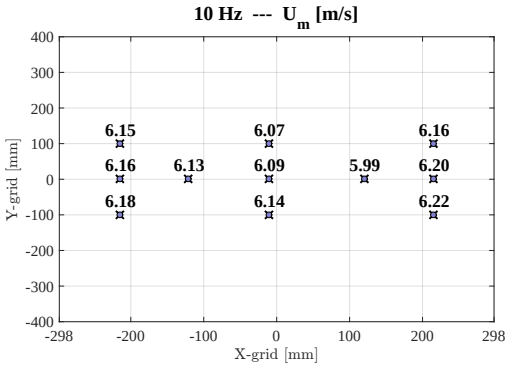
10 Hz --- U_m [m/s]
6.15 6.07 6.16
6.16 6.13 6.09 5.99 6.20
6.18 6.14 6.22
Y-grid [mm]
X-grid [mm]

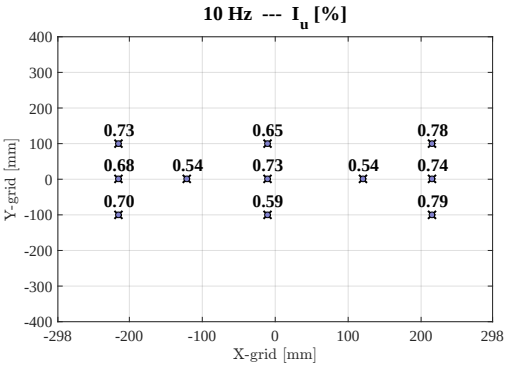
10 Hz --- I_u [%]
0.73 0.65 0.78
0.68 0.54 0.73 0.54 0.74
0.70 0.59 0.79
Y-grid [mm]
X-grid [mm]

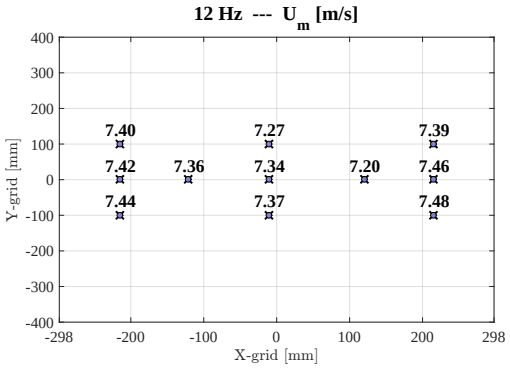
12 Hz --- U_m [m/s]
7.40 7.27 7.39
7.42 7.36 7.34 7.20 7.46
7.44 7.37 7.48
Y-grid [mm]
X-grid [mm]

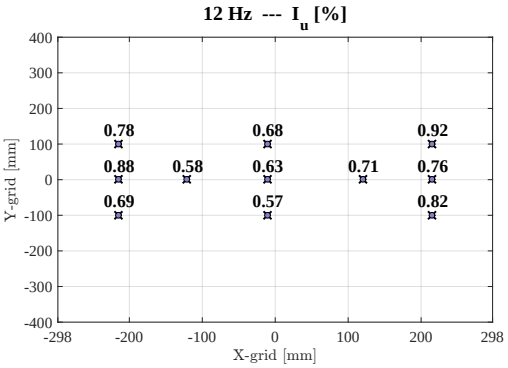
12 Hz --- I_u [%]
0.78 0.68 0.92
0.88 0.58 0.63 0.71 0.76
0.69 0.57 0.82
Y-grid [mm]
X-grid [mm]

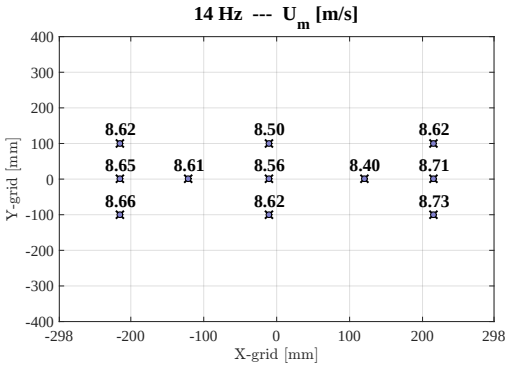
14 Hz --- U_m [m/s]
8.62 8.50 8.62
8.65 8.61 8.56 8.40 8.71
8.66 8.62 8.73
Y-grid [mm]
X-grid [mm]

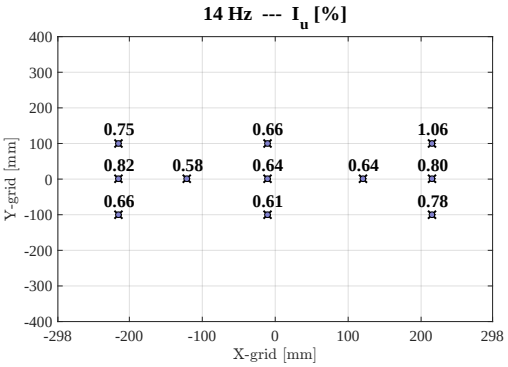
14 Hz --- I_u [%]
0.75 0.66 1.06
0.82 0.58 0.64 0.64 0.80
0.66 0.61 0.78
Y-grid [mm]
X-grid [mm]

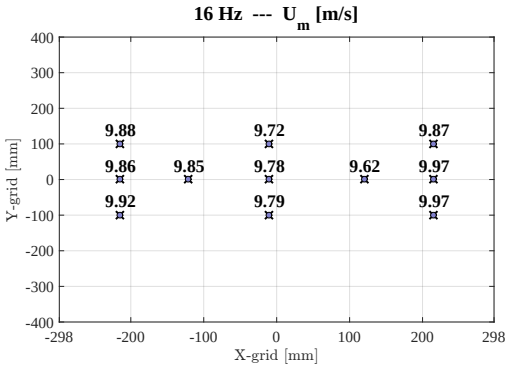
16 Hz --- U_m [m/s]
9.88 9.72 9.87
9.86 9.85 9.78 9.62 9.97
9.92 9.79 9.97
Y-grid [mm]
X-grid [mm]

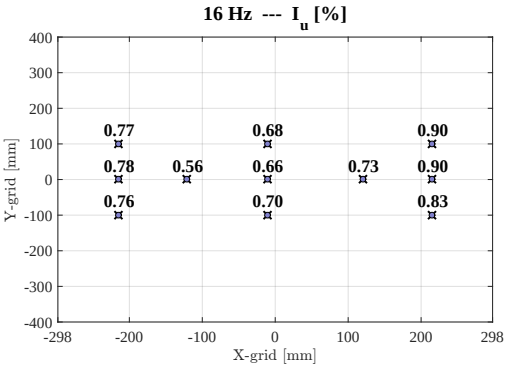
16 Hz --- I_u [%]
0.77 0.68 0.90
0.78 0.56 0.66 0.73 0.90
0.76 0.70 0.83
Y-grid [mm]
X-grid [mm]

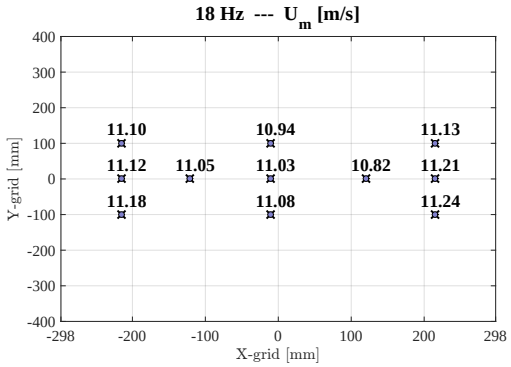
18 Hz --- U_m [m/s]
11.10
10.94
11.13
11.12
11.05
11.03
10.82
11.21
11.18
11.08
11.24
Y-grid [mm]
X-grid [mm]

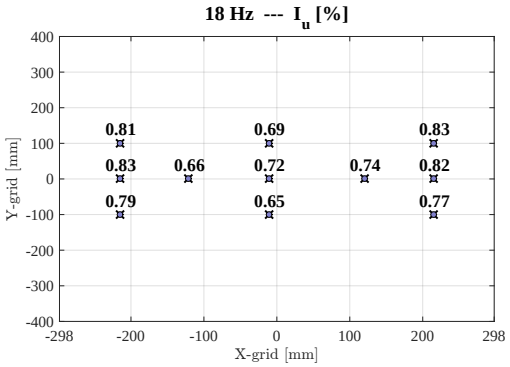
18 Hz --- I_u [%]
0.81
0.69
0.83
0.83
0.66
0.72
0.74
0.82
0.79
0.65
0.77
Y-grid [mm]
X-grid [mm]

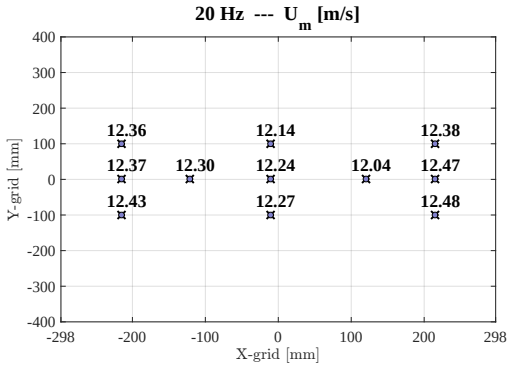
20 Hz --- U_m [m/s]
12.36
12.14
12.38
12.37
12.30
12.24
12.04
12.47
12.43
12.27
12.48
Y-grid [mm]
X-grid [mm]

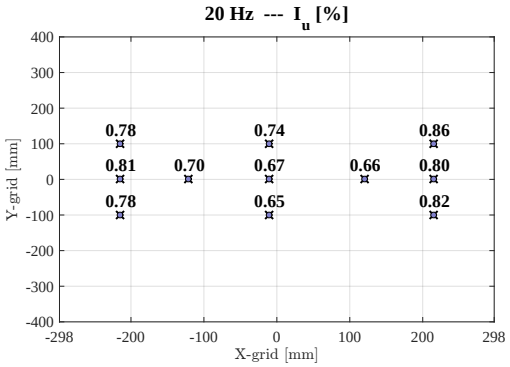
20 Hz --- I_u [%]
0.78
0.74
0.86
0.81
0.70
0.67
0.66
0.80
0.78
0.65
0.82
Y-grid [mm]
X-grid [mm]

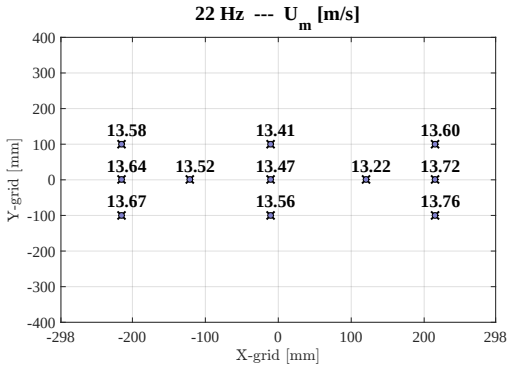
22 Hz --- U_m [m/s]
13.58
13.41
13.60
13.64
13.52
13.47
13.22
13.72
13.67
13.56
13.76
Y-grid [mm]
X-grid [mm]

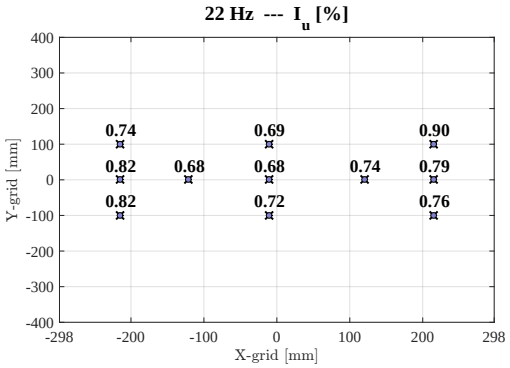
22 Hz --- I_u [%]
0.74
0.69
0.90
0.82
0.68
0.68
0.74
0.79
0.82
0.72
0.76
Y-grid [mm]
X-grid [mm]

Appendix C

Influence of ball-bearings and carters

With respect to Table 6.4 in § 6.3.2, the tested configurations reported in Figs. C.1 are:

- $\sharp\, p2$, small ball-bearing system (identified as BS1 in § 5.3.3, see also Figs. 5.34d and 5.34c), without carters (see Fig. 5.37 in § 5.3.3);
- $\sharp\, g2$, large ball-bearing system (identified as BL in § 5.3.3, see also Fig. 5.34c and 5.43), without carters (see Fig. 5.37 in § 5.3.3);
- $\sharp\, 10$, large ball-bearing system, with carters (see Fig. 5.38 in § 5.3.3).

It is worth highlighting that all configurations have critical heaving-damping ratio of $\xi_{\eta 0} = 9.4\%$. Moreover, during the measurements with decreasing flow speeds in the post-critical response of configuration $\sharp\, p2$, the ball-bearing system BS1 brake gradually, increasing the pitching damping $\xi_{\alpha 0}$. As clear from Fig. C.1, the increments of $\xi_{\alpha 0}$ reduce the pitching amplitude and slightly increase the heaving amplitude. Thus, a system with higher values of $\xi_{\alpha 0}$ is expected to perform smaller post-critical pitching-to-heaving amplitude ratios.

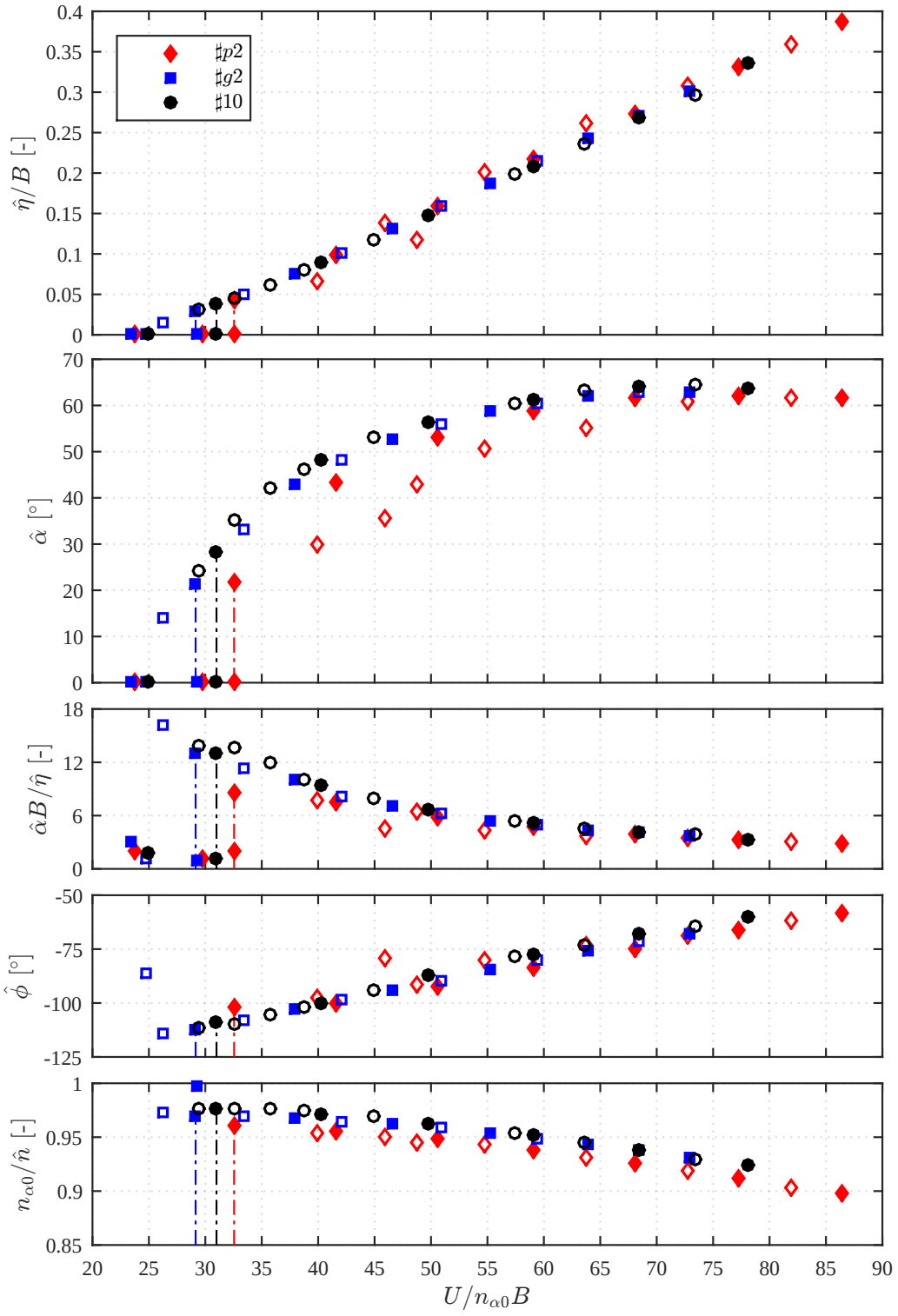

Figure C.1. Influence of ball-bearings and carters in the post-critical response of configurations with $\xi_{\eta 0} \approx 9.4\%$.

Appendix D

Cross section with porous screens

The results presented in this section come from a specific experimental campaign conducted in collaboration with Dr. Mikel Ogueta Gutiérrez, from Polytechnic University of Madrid, who I wish to thank.

With respect to Table 6.4 in § 6.3.2, the tested configurations reported in Figs. D.3 and D.4 are:

- $\sharp 2$, reference case without screens (see also Fig. D.1);
- $\sharp b1$, symmetric screens with 0% porosity (see also Fig. D.2a);
- $\sharp b2$, symmetric screens with 25% porosity (see also Fig. D.2b);
- $\sharp b3$, symmetric screens with 50% porosity (see also Fig. D.2c);
- $\sharp b4$, asymmetric screens with 0% porosity (see also Fig. D.2d);
- $\sharp b5$, asymmetric screens with 50% porosity (see also Fig. D.2e).

Figs. D.3 and D.4 show the evolution of the amplitudes of the limit-cycle oscillations with respect the flow speed. As a general remark, a sub-critical bifurcation with a long stable branch below the critical threshold characterises the system response also the cases of screens installed. The installation of the screens widened the sub-critical branch toward lower flow velocities, and slightly anticipated the instability threshold. These effects are magnified for configurations with the solid screens. Moreover, the heaving amplitudes seemed to not be affected by the presence of the screens, while the pitching amplitudes were reduced. Additional tests were conducted to observe the build up after the release of different initial conditions in both degrees of freedom. A very small initial condition of pitching was usually sufficient to trigger the instability. By contrast, weaker sensitivity to heaving disturbances was observed for the porous screens, and this behaviour magnified in the case of solid screens.

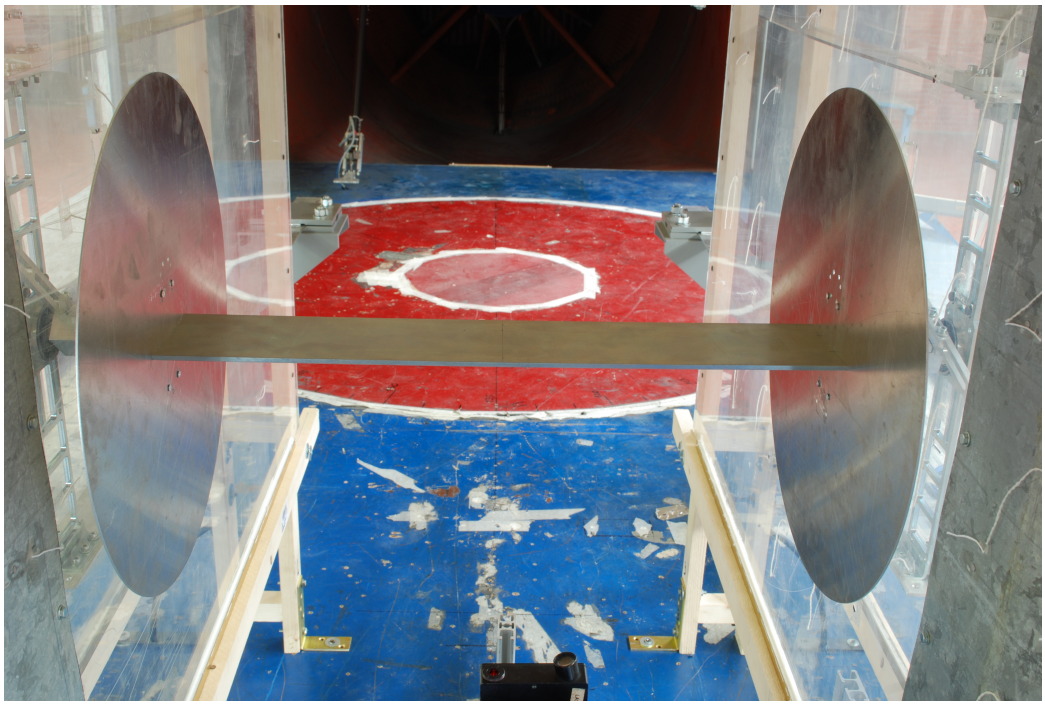

Figure D.1. View of the reference configuration of the model without screens (♯2).

(a) Symmetric screens with 0% porosity.

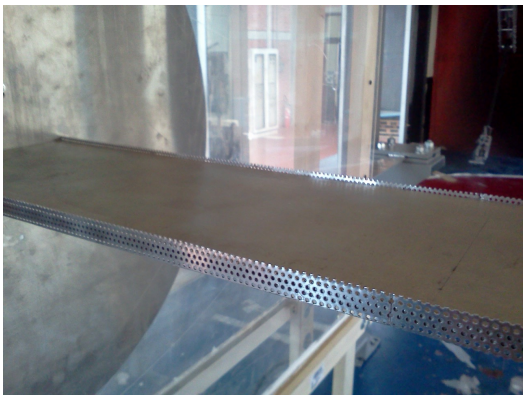

(b) Symmetric screens with 25% porosity.

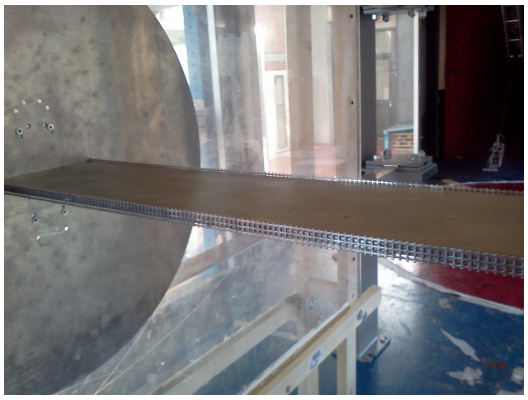

(c) Symmetric screens with 50% porosity.

(d) Asymmetric screens with 0% porosity.

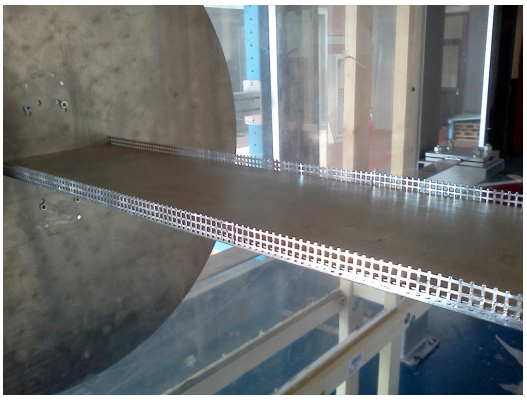

(e) Asymmetric screens with 50% porosity.

Figure D.2. Details of the configurations with symmetric screens (H-shaped arrangement) and with asymmetric screens (U-shaped arrangement).

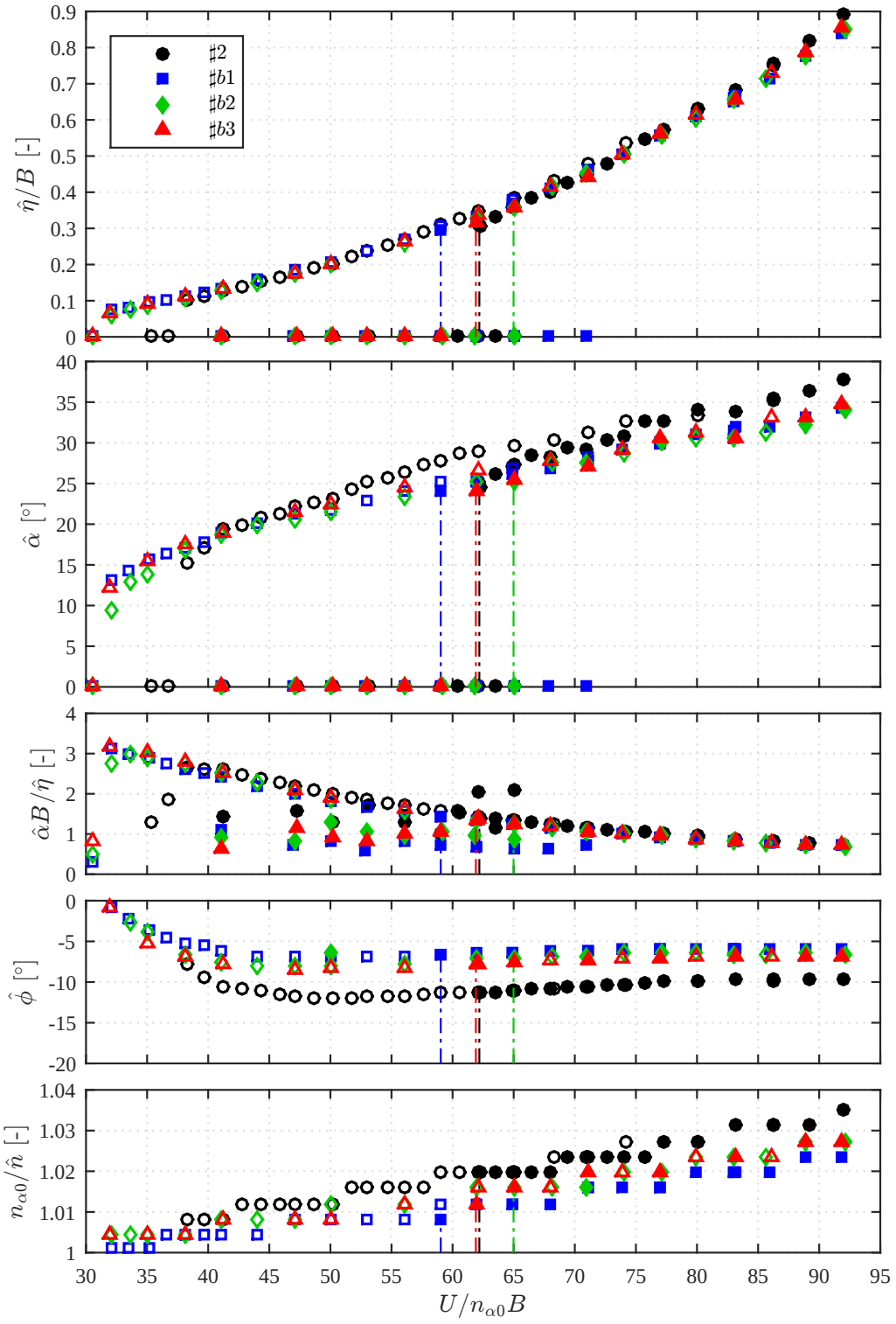

Figure D.3. Effect of symmetric screens with different porosity (0% for ♯b1, 25% for ♯b2, 50% for ♯b3) on the post-critical response with respect to the reference configuration (♯2).

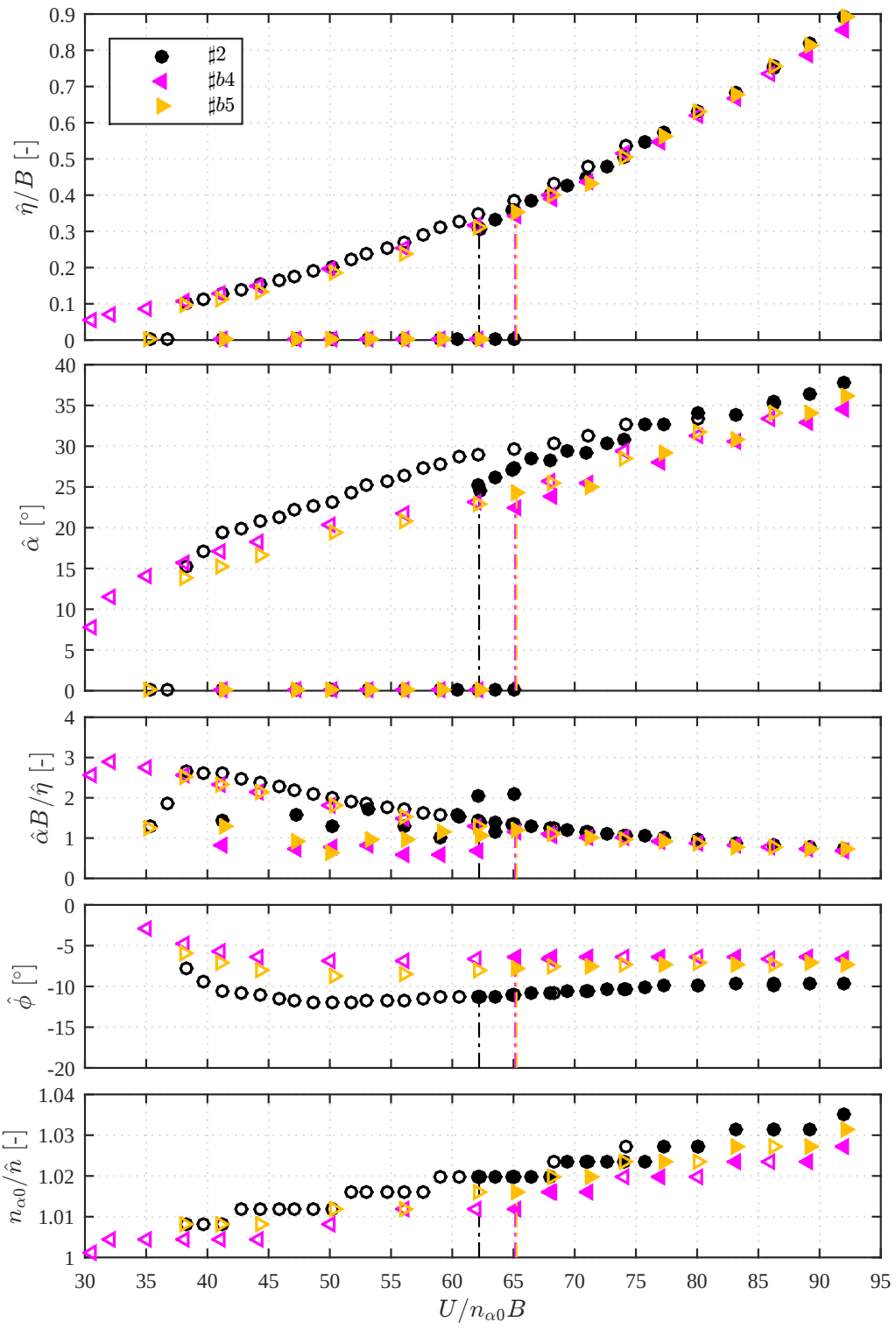

Figure D.4. Effect of asymmetric screens with different porosity (0% for ♯b4, 50% for ♯b5) on the post-critical response with respect to the reference configuration (♯2).

Appendix E

Homogenous-turbulence effects

The preliminary results about the post-critical regime of flutter in turbulent flow are discussed in the following.

With respect to Table 6.4 in § 6.3.2, the tested configurations reported in Figs. E.4 are:

- ♯ $s4$, reference case in smooth flow, $I_u = 0.7\%$;
- ♯ $s4T1$, small grid (see Fig. E.1a) placed at about 4.48 m upstream the model position, $I_u = 2.45\%$ and $L_u x/B = 0.8$ (see Fig. E.2a);
- ♯ $s4T2$, large grid (see Fig. E.1b) placed at about 4.48 m upstream the model position, $I_u = 10.68\%$ and $L_u x/B = 2.3$ (see Fig. E.2b);

It is worth highlighting that all configurations have an heaving damping ratio of $\xi_{\eta 0} = 4.62\%$. Moreover, the mean flow velocity conversion from the upstream Prandtl tube to the model position are reported in Figs. E.3a and E.3b.

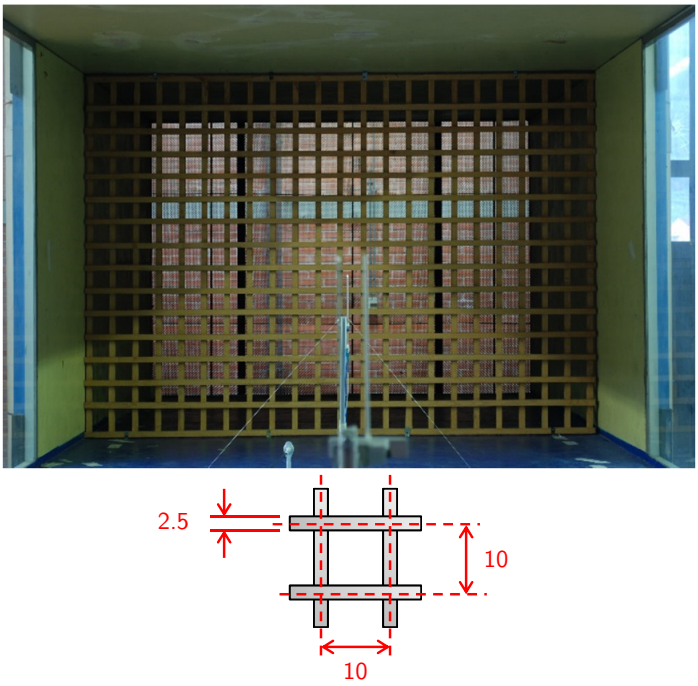

(a) Small grid.

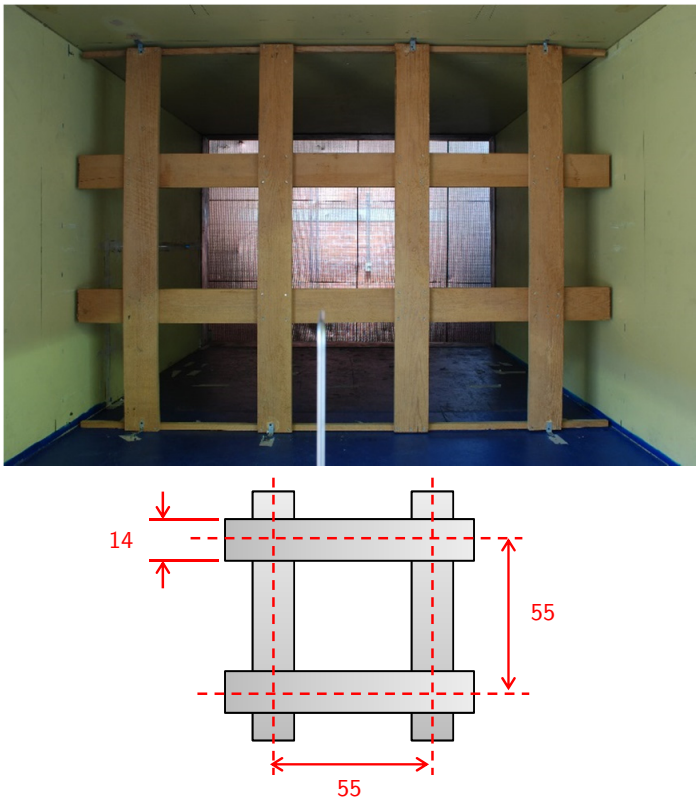

(b) Large grid.

Figure E.1. Geometry of the turbulence grids. Dimensions are in centimetres.

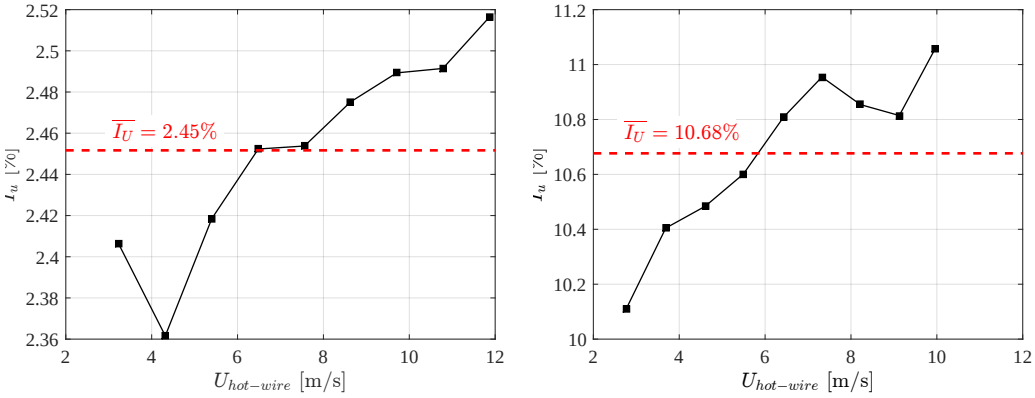

(a) Small grid. **(b)** Large grid.

Figure E.2. Mean turbulence intensity for small and large grids.

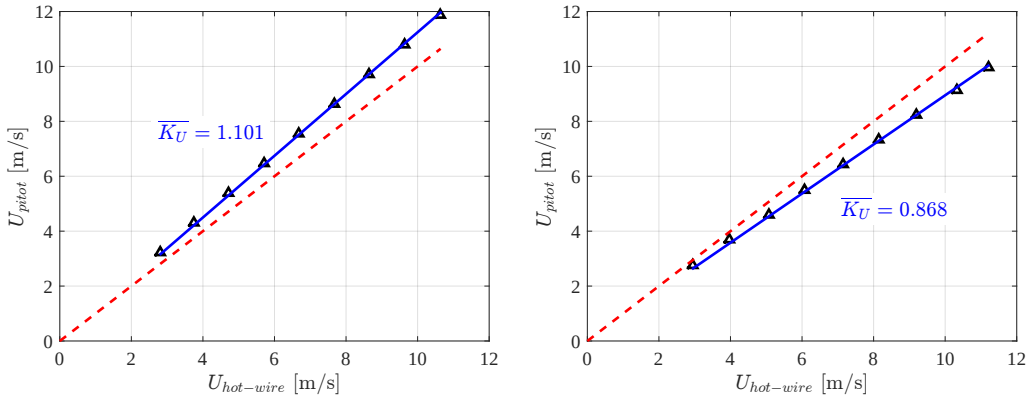

(a) Small grid (I_u = 2.45%). **(b)** Large grid (I_u = 10.68%).

Figure E.3. Mean flow velocity conversions for high turbulence. In the ordinates, U_{pitot} refers to the flow speed measured by the upstream Prandt tube.

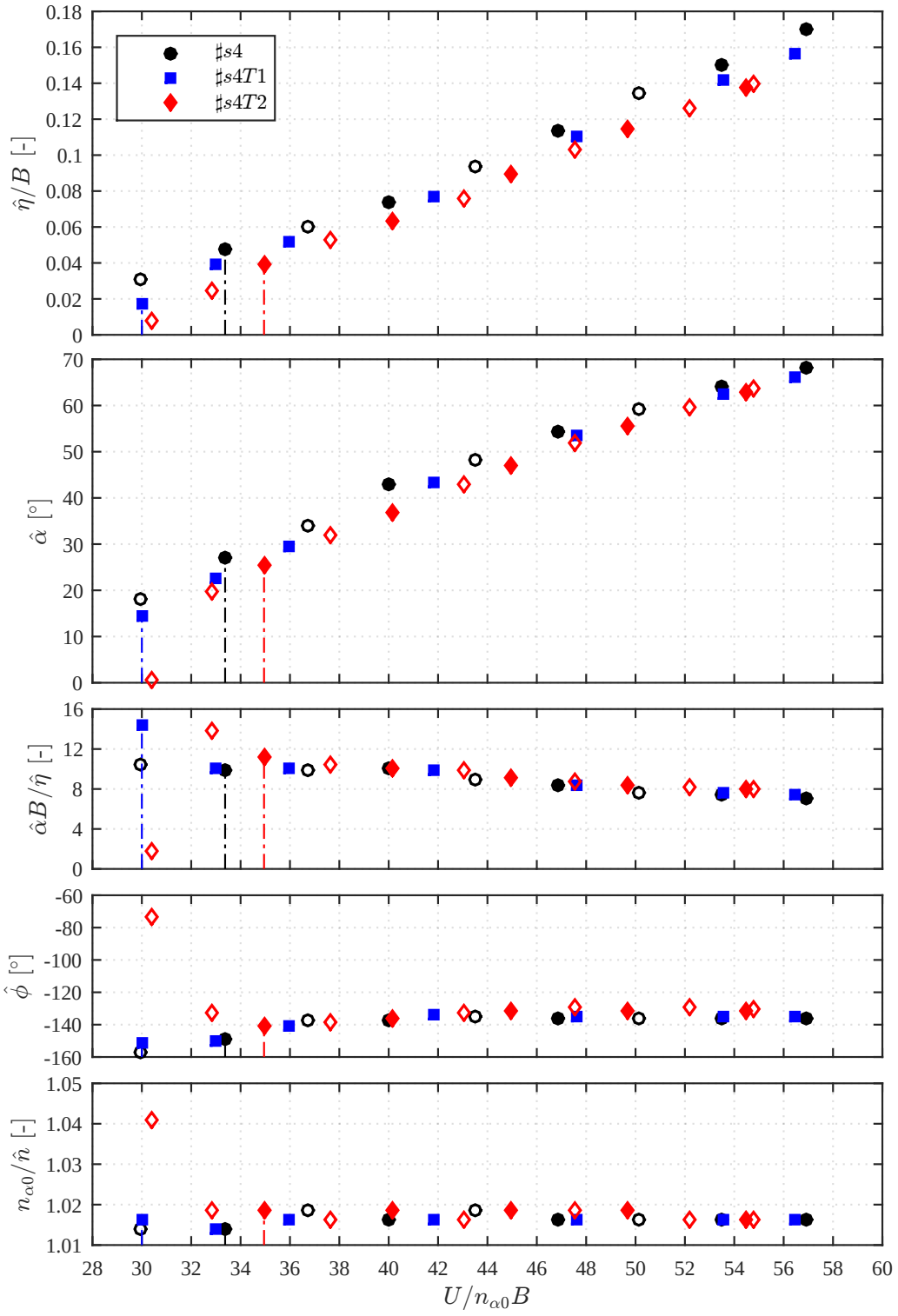

Figure E.4. Effect of different levels of homogeneous alongwind turbulence (I_u = 0.7% for ♯ $s4$, I_u = 2.45% for ♯ $s4T1$, I_u = 10.68% for ♯ $s4T2$) on the post-critical response of configurations with $\xi_{\eta 0}$ = 4.62%.